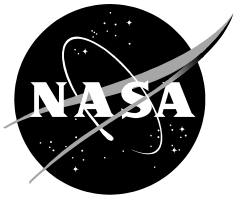
NASA/TM–20210020973



NASA Ground-Based Layered Pressure Vessels Nondestructive Evaluation Report

Owen R. Greulich
Jacobs Space Exploration Group, Huntsville, Alabama
NASA Headquarters, Washington, DC

Brian C. Stoltz
Jacobs Space Exploration Group, Huntsville, Alabama

Clifton T. Arnold, Jr.
National Aeronautics and Space Administration, Office of Safety and Mission Assurance, Washington, DC

January 2024

NASA STI Program Report Series

The NASA STI Program collects, organizes, provides for archiving, and disseminates NASA's STI. The NASA STI program provides access to the NTRS Registered and its public interface, the NASA Technical Reports Server, thus providing one of the largest collections of aeronautical and space science STI in the world. Results are published in both non-NASA channels and by NASA in the NASA STI Report Series, which includes the following report types:

- TECHNICAL PUBLICATION. Reports of completed research or a major significant phase of research that present the results of NASA Programs and include extensive data or theoretical analysis. Includes compilations of significant scientific and technical data and information deemed to be of continuing reference value. NASA counterpart of peer-reviewed formal professional papers but has less stringent limitations on manuscript length and extent of graphic presentations.

- TECHNICAL MEMORANDUM. Scientific and technical findings that are preliminary or of specialized interest, e.g., quick release reports, working papers, and bibliographies that contain minimal annotation. Does not contain extensive analysis.

- CONTRACTOR REPORT. Scientific and technical findings by NASA-sponsored contractors and grantees.

- CONFERENCE PUBLICATION. Collected papers from scientific and technical conferences, symposia, seminars, or other meetings sponsored or co-sponsored by NASA.

- SPECIAL PUBLICATION. Scientific, technical, or historical information from NASA programs, projects, and missions, often concerned with subjects having substantial public interest.

- TECHNICAL TRANSLATION. English-language translations of foreign scientific and technical material pertinent to NASA's mission.

Specialized services also include organizing and publishing research results, distributing specialized research announcements and feeds, providing information desk and personal search support, and enabling data exchange services.

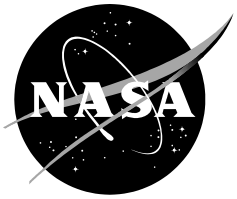
For more information about the NASA STI program, see the following:

- Access the NASA STI program home page at http://www.sti.nasa.gov

- Help desk contact information:

https://www.sti.nasa.gov/sti-contact-form/ and select the "General" help request type.

NASA/TM–20210020973



NASA Ground-Based Layered Pressure Vessels Nondestructive Evaluation Report

Owen R. Greulich
Jacobs Space Exploration Group, Huntsville, Alabama
Marshall Space Flight Center, Huntsville, Alabama

Brian C. Stoltz
Jacobs Space Exploration Group, Huntsville, Alabama

Clifton T. Arnold, Jr.
National Aeronautics and Space Administration, Office of Safety and Mission Assurance, Washington, DC

National Aeronautics and
Space Administration

Marshall Space Flight Center
Huntsville, AL 35805

January 2024

Contents

1. Notification and Authorization 7
2. Disclosure Page 8
3. Team List 9
4. Executive Summary 11
5. Introduction, Objective 13
6. Past Work, Concerns 13
   6.1 1975 LaRC Investigation 14
   6.2 Leaking Helium Vessel at KSC 15
   6.3 Early OSMA Efforts 15
   6.4 NESC Study 15
7. Historically Found Flaws, Failures, and Techniques 16
   7.1 Industry 16
   7.2 NASA Center LPV Failure History 16
      7.2.1 KSC Helium Vessel 17
      7.2.2 MSFC Vessel V0256 17
      7.2.3 MSFC Vessel V0111 18
      7.2.4 MSFC Vessel V0012 18
      7.2.5 MSFC Vessel V0023 21
      7.2.6 Other MSFC Vessels 22
      7.2.7 LaRC HTT Support Vessels 22
      7.2.8 LaRC Methane Vessels 22
      7.2.9 ARC High Pressure Air Storage Field 22
      7.2.10 ARC High Pressure Air Storage 23
      7.2.11 GRC Vessels 24
      7.2.12 KSC Vessels with Outer Shell Cracks 24
      7.2.13 Other KSC LPVs 25
      7.2.14 SSC Vessels 25
      7.2.15 WFF Vessels 25
   7.3 Historical/Legacy Inspections 26
      7.3.1 Surface Inspections 26
      7.3.2 Weld Volume Inspections 26

7.3.3 Leak Detection 26
7.3.4 AE Inspections 27
7.4 Contemporary Dissection 27
8. Flaws/Regions of Interest 27
8.1 Flaw Map Diagrams 27
8.2 Flaw Mitigation Matrix 33
9. Demonstration Block Construction 35
9.1 Head-to-Shell 36
9.2 Shell-to-Shell blocks 38
9.2.1 Shell-to-Shell Demonstration Ring 38
9.2.2 Vendor Radiography (Post Flaw) 40
10. Industry Polling, RFI 40
10.1 RFI Responses 40
10.1.1 PAUT 40
10.1.2 Health Monitoring Systems 41
10.1.3 Eddy Current Arrays 41
10.1.4 Miscellaneous Proposals 42
10.2 RFI Down Select Process 42
10.3 Rating Criteria 42
10.3.1 Prognosis 42
10.3.2 Overall Benefit/Value 42
10.3.3 LPV Inventory Applicability/Constraints 42
10.3.4 Agency Cost 43
10.3.5 Practicality of Use at Centers 43
10.4 NASA Response 43
10.5 RFI Outcome Summary 43
10.5.1 PAUT 43
10.5.2 Health Monitoring Systems 44
10.5.3 Defect Screening Technologies 44
10.5.4 Tangential Eddy Current Array 45
11. Analytical Modeling 46
11.1 AE 46

11.2 Guided Wave 47
11.3 PAUT 47
12. NDE Lab Scale Demonstration 47
12.1 Head-to-Shell Demo Block Inspections 48
12.1.1 In-House Head-to-Shell Demo Block Inspections 48
12.1.2 Vendor In-House Head-to-Shell Demo Block Demonstrations 49
12.1.3 PAUT Two-Dimensional Matrix Arrays on Head-to-Shell Demo Block 49
12.1.4 PAUT Full Matrix Capture Methods (FMC) 50
12.2 Shell-to-Shell Demonstration Block Inspections 50
12.3 AE Lab Scale 50
12.4 Shell-to-Shell Demonstration Ring Inspections 52
12.4.1 Guided Wave on Shell-to-Shell Weld on Vessel Section 52
12.4.2 In-House Conventional PAUT 53
12.4.3 In-House 2D Array PAUT 53
12.4.4 Vendor 2D PAUT 54
13. NDE Field Trials 54
13.1 Head-to-Shell Weld Inspections 54
13.1.1 In-House PAUT 54
13.1.2 Past Inspections at MSFC 56
13.2 Shell-to-Shell Weld Inspections 56
13.3 Surface, Outer (TECA, MT) Inspections 57
13.4 Surface, Inner Inspections 57
13.5 Nozzle Inspections 57
13.5.1 Nozzles (Including Manways) in Heads 57
13.5.2 Nozzles in Shells 58
13.5.3 GRC Nozzle Inspection, Ultrasonic 58
13.5.4 In-House PAUT 59
13.6 Radiography 59
13.6.1 V0023 Pre-Dissection 59
13.6.2 Field Radiography 62
13.6.3 Cautions Regarding Use of Radiographic Testing 65
13.7 Layer Efficiency 66

13.7.1 ARC 16-Bank and MSFC 19-Bank Circumferential Growth Measurements 69
13.8 Pi-Tape Process Interpretation of Variables 79
13.8.1 Measurement Irregularities Showing Efficiency < 50% - Causes 83
13.8.2 Causes of Measurement Irregularities Showing Efficiency > 100% 84
13.8.3 Physical Causes for Accurate Measurements with Anomalous Results 84
13.8.4 Physical Causes for Accurate Measurement Showing Efficiency < 50% 85
13.8.5 Physical Causes for Accurate Measurement Showing Efficiency > 100% 85
13.8.6 Conclusions 86
13.8.7 V0023 Circumferential Growth Measurements 86
13.8.8 MSFC West Test Area Hydrogen Bank Circumferential Growth Measurements .. 87
13.8.9 V0023 Layer Sliding During AE Testing 87
13.9 AE Testing 89
13.9.1 MV50466-8 DW Test (High Level Summary, NESC Report) 90
13.9.2 V0023 AE Test 95
13.9.3 Limitations for Vintage LPV Structures 97
13.10 Vent Hole Leakage 98
13.10.1 Vessels Containing Gas 99
13.10.2 Vessels Containing Liquid: 101
13.11 Inspection of Plate Acreage 102
13.12 Detecting Loss of Layer 102
13.12.1 Self-Rescue Capacity 102
13.12.2 Inspection Feasibility 103
13.13 Visual Inspections 104
14. Recommendations 105
14.1 General 105
14.2 Head-to-Shell Welds 105
14.3 Shell-to-Shell Welds 106
14.4 Nozzles in Heads 106
14.5 Nozzles in Shells 107
14.6 Longitudinal Welds 107
14.6.1 Outer Layer Welds 108
14.6.2 Inner Layer (Liner) Welds 108

14.6.3 Intermediate Layer Welds 108
14.7 Vent Hole Inspection 108
14.8 Leakage Through Vent Holes 108
14.8.1 Gas Containing Vessels 109
14.8.2 Liquid Containing Vessels 110
14.8.3 Vessels Containing Lethal Fluids 110
14.9 Efficiency 110
14.9.1 Circumferential growth measurement 111
14.9.2 Efficiency Calculation 111
14.10 Acreage 112
14.11 Inspection for Loss of Layer 112
14.12 Visual on OD 112
15. Lessons Learned 113
16. Conclusion 114
17. Acronym list 114
18. References 117
19. Appendices 119
A. A Synopsis of Known Catastrophic Failures of Layered Vessels 120
B. PVS-15-012 V0111 Inspection and Excavation 136
C. Demo Block and Ring Configurations 210726 143
D. PVS 16-004, MSFC Phased Array Ultrasonic Test (PAUT) for Layered Pressure Vesselsé .153
E. Request for Information (RFI) NNM17ZQD001L entitled ñFeasible Technologies for Non-Destructive Evaluation (NDE) of Layered Pressure Vesselsò 162
F. Simulation Work for Layered Pressure Vessels 168
G. Ultrasonic Testing Simulation Documentation 177
H. Detection of Transverse Flaw in a Root of Multi-Layered Vessel 196
I. Examination/Analysis of Acoustic Emission Waveform Data from Tensile Testing of Notched Curved Sample of LPV Steel 211
J. Tensile Testing of LPV Material at NIST Boulder 227
K. Far-Field Wave Propagation Signals from Pencil Lead Breaks on the Open End of a Thick-Walled Layered Cylinder, Part 1: Amplitudes and Frequency Content 304
L. Far-Field Wave Propagation Signals from Pencil Lead Breaks on the Open End of a Thick-Walled Layered Cylinder, Part 2: Modes of Wave Propagation 326
M. Summary of Zetec Dynaray System Demonstration, Document Number PVS-20-008é .é 347
N. GRC UT Bore Probes, Dirienzo and Samuele 352

O. GRC Radiographic Specification for A.O. Smith PV 360
P. Circumferential Growth Measurement of Layered Pressure Vessels 365
Q. MPFR-16-016 Pi Tape Measurements of V0023 369
R. Efficiency Tables 20210325 379
S. PVS-19-011, Pi Tape Measurements of West Test Area (WTA) Hydrogen Bottles 388
T. Test on Vessel V0023 MISTRAS Group AE Measurements & Analysis, 09/13/16 394
U. Acoustic Emission Test Report for Vessel V0023, Report No. AE-V0023-2016 417
V. V0023 Vertical Multilayered Vessel Acoustic Emission Sensor Layout 452
W. Report on the Modal Acoustic Emission Testing of A.O. Smith Pressure Vessel V0023 454

1. Notification and Authorization

On January 23, 2014, the NASA Office of Safety and Mission Assurance (OSMA) chartered an agency-wide team to perform the following work:

Implement the following recommendations contained within the *NESC Report NESC-RP-13-00852, Evaluation of Agency Non-Code (ASME) Layered Pressure Vessels (LPVs)*:

- R-5. Agency develop and implement a consistent program of minimum maintenance and vessel inspection requirements.
- R-7. Agency formulate and support an Agency-wide team to continue efforts to assess and reduce risks associated with LPVs with the goal of developing a standard Agency process for their continued usage.
- R-8. Agency develop a centralized database that documents, to the extent practical, LPV design, fabrication, materials, operation, inspection, maintenance, and repair data.
- R-9. Agency expand efforts to gather LPV weld and parent materials property data.
- R-10. Agency expand efforts to develop and validate analysis methods to address identified highest risk conditions and regions of LPVs.
- R-11 Agency develop and validate Nondestructive Evaluation (NDE) techniques to address the highest risk conditions and regions of LPVs.

In addition:

- Develop draft procedures for incorporation into an Occupational Safety and Health Administration (OSHA) Alternate Standard for Non-Code LPVs.

Funding was provided by OSMA and team members were identified, with the lead at Marshall Space Flight Center (MSFC).

The primary stakeholders for this assessment were OSMA, as represented by Clifton Arnold and his predecessor Owen Greulich, Technical Discipline Manager for Pressure Systems, and the Centers responsible for the safe operation of these LPVs as represented by their respective Pressure Systems Managers (PSMs).

2. Disclosure Page

Findings, observations, and recommendations compiled in this report are factually based on data extracted from program/project documents, contractor reports, and open literature, and/or generated from independently conducted tests, analyses, and inspections.

3. Team List

Core Team		
Name	**Discipline**	**Organization**
Clifton T. Arnold, Jr.	Program Executive for Pressure Systems, Lifting Devices, and Propellants and Pressurants	OSMA/HQ
Benjamin D. Barrentine	NDE Specialist	NASA/MSFC
Calogero Dirienzo	Pressure Systems Manager	NASA/GRC
Douglas R Fraser	Pressure Systems Manager	NASA/ARC
Elizabeth D. Gregory	Research Engineer	NASA/LaRC
Owen R. Greulich	Pressure Systems Subject Matter Expert	Jacobs Space Exploration Group
Joel R. Hobbs	Damage Tolerance Engineer	NASA/MSFC
Maan H. Jawad	ASME Code and LPV Subject Matter Expert	Global Engineering & Technology
Edward F. Johnson	Pressure Systems Manager	NASA/MSFC
Peter D. Juarez	Mechanical and Electronics Engineer	NASA/LaRC
Matt Kirby	Senior Research Engineer	Southwest Research Institute
Son Le	Pressure Systems Manager	NASA/SSC
Matthew Leith	NDE Specialist	Bastion Technologies Inc. /MSFC
Benjamin Melia	Damage Tolerance	NASA/MSFC
Frank Monroe	Pressure System Certification Engineer	Bastion Technologies Inc./MSFC
William Prosser	NDE	NASA Engineering & Safety Center
Ronald L. Shelton	Damage Tolerance	NASA/MSFC
Brian C. Stoltz	Damage Tolerance	Jacobs Space Exploration Group

William Vesely (Retired)	Risk Management	NASA/HQ
Douglas N. Wells	Damage Tolerance	NASA/MSFC
William P. Winfree	NDE	AMA/LaRC

Consultants		
Name	**Discipline**	**Organization**
Marv Hamstad	Mechanical and Materials Engineering	National Institute of Standards and Technology
Adrian Pollock	Acoustic Emissions	MISTRAS Group
Steve Ziola	Modal Acoustic Emissions	Digital Wave Corporation

4. Executive Summary

This NASA Technical Memorandum documents the results of a study undertaken to identify effective means of inspecting Layered Pressure Vessels (LPV) as part of a larger Risk Mitigation Project (RMP) to ensure their integrity, fitness for service, and remaining safe life, including both structural and materials aspects.

This effort reviewed and documents past work in the field, and past flaws and failures. It includes a review of past NDE work performed at various NASA Centers as well as summary results of a poll of industry using a Request for Information (RFI) sent out by Marshall Space Flight Center.

The RMP team considered Acoustic Emissions (AE, or MAE for modal AE), circumferential growth measurements, guided wave, inspection of vent holes for leakage, magnetic particle, Phased Array Ultrasonic Testing (PAUT) (including with full matrix capture and use of two dimensional (2D) arrays), radiography, Tangential Eddy Current Array (TECA), and ultrasonic and visual inspection techniques. In conjunction with the assessment of these technologies, the team assessed anticipated defects, their likelihood of occurrence, and the likelihood of their propagation to ultimate catastrophic failure through materials studies, structural and fracture mechanics analyses, and probabilistic studies. These other studies are documented in *NASA Ground-Based Layered Pressure Vessels Fitness for Service Handbook NASA/TM-20210020974* [1], *NASA Ground-Based Layered Pressure Vessels Materials Report NASA/TM-20210019043* [2], and *NASA Ground-Based Layered Pressure Vessels Structural Analysis Report NASA/TM-20210020972* [3]. Assessments included evaluations based on prior knowledge of involved personnel, literature reviews, hardware demonstrations on actual LPV's and test blocks, and simulations.

Team members identified PAUT as one of the most promising inspection technologies, although the technology needs additional development so that researchers can use it to identify all defects consistently. For several years, the Marshall Space Flight Center (MSFC) Team has achieved good results using the technology to inspect LPV head-to-shell welds. PAUT use on shell-to-shell welds is not fully developed, but one vendor demonstrating the use of 2D phased array probes successfully identified all defects in a circumferential weld that had been machined to present a flat surface for coupling the transducer. NASA followed up on the success of that demonstration with the purchase of 2D phased array probes and began in-house testing. This testing resulted in a high level of confidence that PAUT technology can be adapted to inspect both shell-to-shell and head-to-shell circumferential welds and some nozzle welds.

Assessment of Acoustic Emissions (AE) technology included analytical modeling, lab tests, and actual field testing. AE demonstrated the capability of recognizing the difference between crack growth and other sounds in LPV and was able to detect ductile tearing. It was not pursued further because of its development level, resource availability, and the greater immediate promise currently shown by PAUT. AE showed potential as an alternate strategy to measurement of circumferential growth as a means of assessing load sharing among layers and for leak detection,

however these potential applications were never specifically studied as part of the overall LPV effort.

Another phase of work included studies of the ability of circumferential growth measurements to provide information regarding efficiency of load sharing among layers and the possibility of a failed intermediate layer.

Based on the work described above, this document concludes with a number of recommendations for ensuring the integrity of LPVs.

Recommendations applicable to LPVs generally include those related to development and implementation of inspection plans, determination of critical initial flaw size (CIFS), development of calibration standards and demonstration rings, and use of ray tracing software to assist in developing scan plans and designing calibration standards.

The report also provides a number of recommendations applicable to the use of specific technologies or processes to particular portions of the vessels or to vessels operating in particular media.

This report recommends the use of PAUT for examination of head-to-shell welds, shell-to-shell welds, and some nozzle-to-head welds, along with Magnetic Particle Testing (MT), Penetrant Testing (PT), or Tangential Eddy Current Array (TECA) for surface examination in certain cases. For nozzles located in shells, it generally recommends use of eddy current bolt hole probes or bobbin-type probes, in conjunction with MT, PT, Eddy Current Testing (ET), or TECA for exterior attachment welds.

For outer layer welds, a fracture mechanics analysis may, in some cases, obviate the need for inspection. If it does not, then the report recommends Visual Testing (VT) followed by TECA, MT, or PT, with PAUT for subsurface flaws if needed (e.g., in thick layers such as on autofrettage vessels).

Inner layer (liner) welds do not require direct inspection because inspection of vent holes allows recognition of a leaking liner, while materials studies and structural analysis have determined that a catastrophic failure due to an inner shell flaw is highly unlikely prior to leakage. A number of recommendations in this report relate to the inspection of vent holes, both for functionality and for leakage.

Except for a very small portion of the weld adjacent to circumferential welds, intermediate layer welds are extremely difficult to inspect, but structural analysis demonstrates that they are not critical to LPV integrity.

The report provides recommendations specific to LPVs containing gas, liquid and lethal fluids.

Finally, the report recommends that each LPV shell course be subjected once to a circumferential growth measurement to assess load sharing if recorded results that such a test has been previously performed are not available.

A number of references and appendices include further details that either explain, provide background for, or amplify the information provided in this report. If the recommendations included in this report are followed for each LPV, then the Team believes that a catastrophic failure is highly unlikely.

Note: This report mentions various products and vendor names. This reflects the fact that research and testing are performed by personnel who use equipment, and that at times mentioning a particular product or company is the most efficient way of making clear what work was done and how it was accomplished. It is neither an endorsement nor a commentary on such products or organizations.

5. Introduction, Objective

NASA had approximately 300 LPVs in service in 2015. Most of these vessels were acquired between 1960 and the mid-1970s, and were not constructed in accordance with the American Society of Mechanical Engineers (ASME) Boiler and Pressure Vessel Code (BPVC), Section VIII Rules for Construction of Pressure Vessels [4]. In the past, NASA addressed the challenges associated with certifying the LPVs' safety and integrity for operation only in a fragmentary fashion. In 2014, the NASA Office of Safety and Mission Assurance (OSMA) began a significant effort to address these vessels in a comprehensive manner, including structural and material evaluations and NDEs. This NASA Technical Memorandum (TM) is a product of that effort.

Assessing the risk associated with Agency LPVs presented a particular challenge because of the difficulty in inspecting intermediate layers; the analytical complexities of layer, weld, and defect interactions; and the lack of documented material fracture properties for most of the vessels at NASA. This TM documents the research and development effort to find means and methods for identifying defects relevant to fitness for service and remaining life in LPVs. Other reports referred to in Section 4 document the efforts associated with analytical work and material properties.

The results of the materials studies and the analytical work performed in this effort demonstrate that some defects in locations and orientations that would be critical in other types of pressure vessels do not have a credible risk of leading to LPV failure. Thus, these particular defects, identified in Section 8, do not need to be detected. Section 8 also identifies defects that could potentially lead to vessel failure and which therefore require detection.

This report documents the work performed to identify or develop means of detecting, locating, and characterizing potentially critical pressure vessel defects in LPVs and, in particular, defects associated with welds.

6. Past Work, Concerns

NASA safety and engineering personnel have been concerned about LPVs for a number of years. The Agency first began acquiring and putting LPVs into service at NASA in the late 1950s,

adding many more during the 1960s, and a few during the 1970s. Most were acquired before inclusion of LPVs in the ASME BPVC.

NASA has never had a catastrophic failure of an LPV. However, NASA has removed many vessels from service due to cracks, industry has suffered a number of catastrophic failures, and multiple aspects of these vessels cause concern.

Most NASA LPVs include non-code materials, and examinations specified on LPV construction drawings rarely met all the requirements of either the current version of the *ASME BPVC* [4] or the earlier versions of that standard that first addressed LPV. Lack of full understanding of material properties and shell layer interactions had reduced confidence in the effectiveness of structural analysis. The lack of a credible means of inspecting the LPV's has prevented understanding of what defects may be contained in the vessels. And, finally, the lack of ASME BPVC stamping means that, in many cases, LPV are not in compliance with OSHA regulations.

The following provides a history of NASA investigations of LPV:

6.1 1975 LaRC Investigation

Dr. C. Michael Hudson at Langley Research Center (LaRC) led the earliest NASA investigation unearthed by the RMP regarding LPV, formally reporting out in December, 1975, though approximately a year prior much of the work had already been reported and was being used in making decisions. Hudson's study, titled "An Investigation of Fracture Toughness, Fatigue-Crack Growth, Sustained-Load Flaw Growth, And Impact Properties of Three Pressure Vessel Steels" [5], did not address NDE of LPV.

The report does not describe a specific initiating event that led to Hudson's investigation, but the report summary stated its purpose was to "relieve the general paucity of such data for these [*layered*] pressure vessel steels", which were in service at LaRC. At that time, LaRC operated a number of LPVs, including 12 vertical vessels enclosed in a large building. Records indicate that growing cracks had been identified, monitored, and stop-drilled in these vessels over a number of years. Also, a prior LaRC internal memorandum stated, "In order to preclude a catastrophic fatigue failure of these vessels, it was decided to analyze, inspect, and test these vessels to ensure their continued safe operation." [Hudson Memo (1975) [6]. The investigators procured VMS 5002, VMS 1146A, and A-225 Grade B steels to provide material for testing.

The minutes of meetings of the LaRC Pressure Systems Committee for November 19, 1974 [7] and December 12, 1974 [8] indicate that the building constructed around the 12 LPVs in the 8-Foot High Temperature Structures Tunnel Air Storage System was referred to as a Thermal Enclosure. Factors other than temperature were also considered in the decision to construct it. These included a reduced chance of wind induced vibration, access for maintenance and inspection, and protection for acoustic emission equipment. According to the meeting minutes, however, "Lastly and probably the most important consideration is the additional confidence in the integrity of the entire system by operation well above the material's nil-ductility temperature (NDT)."

The twelve LPV were constructed by A.O. Smith in accordance with drawings MV 50562, MV 50562A, and MV 50562B (four each).

Section 7.2.7 also briefly discusses these 12 vessels.

6.2 Leaking Helium Vessel at KSC

In 1980, Kennedy Space Center (KSC) performed a study regarding the failure of a 6000 psig gaseous helium vessel at KSC after it developed an audible blowing leak from one of its vent holes. The study described the results of radiographic inspection (RT) after identification of the leak as "with little detail shown." There was apparently no indication of the crack on the radiographs. (See cautions in Section 13.6.3 regarding use of radiography.) NASA contracted with Dunegan Endevco Field Testing Service to instrument the vessel with AE equipment. Acoustic indications and pressure measurements both detected leakage during pressurization to 2100 psi with Gaseous Nitrogen (GN2). During pressurization with water at up to 10,000 psi, the acoustic emissions were inconsistent. One head was cut off and the vent holes were pressurized, with water seepage revealing a crack that appeared 4.5 inches long in a photo. Dye penetrant inspection revealed a crack described as "four times longer than was indicated during the visual inspection." *MMA-1884-80 Discussion of Gaseous Helium LPV That Developed a Blowing Leak During Operation* [9] and *Malfunction Investigation of A 6000 Psig Laminated Pressure Vessel* [10] describe the study performed.

6.3 Early OSMA Efforts

OSMA promulgated efforts beginning in fiscal year 2011 involving a layered AO Smith pressure vessel (MV-50466-8) cycled by Digital Wave Corporation (DWC) and monitored using MAE technology. *NASA-CR-2014-218156 – Cyclic Crack Growth Testing of an A. O. Smith Multilayer Pressure Vessel with Modal Acoustic Emission Monitoring and Data Assessment* [11] describes this effort. Using a video microscope, the study identified fatigue crack growth and later review of MAE results identified corresponding signals. After completion of cycling, Southwest Research Institute (SwRI) dissected the vessel and obtained material properties for major components. *NASA-CR-2014-218157 Multilayer Pressure Vessel Materials Testing and Analysis, Phase 1* [12], and *NASA-CR-2014-218158 Multilayer Pressure Vessel Materials Testing and Analysis, Phase 2* [13] provide results of these investigations, with final reporting completed in 2013. MSFC later used portions of this vessel to produce shell-to-shell demonstration rings, seeding them with known defects to allow demonstration of NDE technologies (Section 9.2).

6.4 NESC Study

The NASA Engineering Safety Center (NESC) began a study in 2013 which reported out in 2014, *NASA-TM-2014-218505 Evaluation of Agency Non-Code LPVs Volume I* (corrected copy) and *Volume II* [14], containing recommendations that resulted in interim work by OSMA in 2015 followed by the current effort.

7. Historically Found Flaws, Failures, and Techniques

Estimates of the total number of LPVs constructed worldwide range between 15,000 and 23,000. Of these vessels, about 10 are known to have failed catastrophically, while a number of others have failed in a more benign fashion. NASA and other organizations have removed LPVs from service because of identified defects or potential problems. This section discusses significant known failures and some of the less significant ones.

7.1 Industry

Appendix A: A Synopsis of Known Catastrophic Failures of Layered Vessels provides a list of documented catastrophic LPV failures. Some cases involved vessels left in service in spite of obvious leaks from the vent holes. Anecdotal reports describe several additional such failures, but no documentation for them has been found. All of the catastrophic failures identified involved more aggressive internal environments than those found in NASA operations, though NASA has used, and continues to use some LPV's in hydrogen service.

In addition to the catastrophic failures described in *Appendix A*, reports describe a number of non-catastrophic failures and provide documentation of some of them. This report uses the term "non-catastrophic failure" broadly, including any failure not involving a vessel splitting open or fragmenting. Thus, it includes not only leakage, but also cracking or other significant service-related defects identified prior to catastrophic failure, resulting in removal from service or repair of the LPV. (The failure discussed in Section 6.2 and Section 7.2.1 is an example of a vessel falling into the category of non-catastrophic failure.)

Centers repaired some vessels with defects and returned them to service. In other cases, vessels were scrapped or used for research into LPV material properties, failure mechanisms, or inspection techniques. Repairs most commonly involved grinding out surface defects. Sometimes stop-drilling and/or welding was performed. The conflict between heat treatment requirements and the negative effect of heat treatment on layer tightness typically prevents welding on heads near the head-to-shell weld.

NASA CR-1305, Hydrogen Gas Pressure Vessel Problems in the M-1 Facilities [15], describes cracking problems that occurred in 1963-1965 in nozzles and longitudinal welds of seven multi-layer vessels constructed by AO Smith and Struthers-Wells and operated at 5000 psi at the Aerojet General facility in Sacramento, California. Four of the vessels were in hydrogen service and three in nitrogen service. All seven vessels failed by cracking, but defects were identified in time to prevent catastrophic failure. The cracks were identified after low numbers of cycles and nine months or less of service, with most cycling less than the full pressure range. (A NASA Contractor Report documents these problems, but Aerojet General apparently owned and operated the vessels, so this report is included with industry failures rather than in Section 7.2.)

7.2 NASA Center LPV Failure History

Specific defects, or suspicion of defects, resulted in removal from service or repairs of a number of NASA LPVs as a result of findings during testing/inspection using acoustic emissions or other

inspection technologies. This section provides a brief description of some of these cases. Note also that a far greater number of vessels remain in service with no problems.

7.2.1 KSC Helium Vessel

In 1980, KSC personnel identified a leak in an LPV containing helium at ambient temperature. A.O. Smith Corporation had constructed this vessel in 1958 and rated it for a working pressure of 6600 psi at a temperature of -20°F to 150°F. This was a relatively small vessel with a water volume capacity of 78.5 cubic feet. Section 6.2 of this report provides further discussion regarding this vessel and References [9] and [10] provide further details.

7.2.2 MSFC Vessel V0256

In 2013, inspections identified a 2.25-inch-long longitudinal crack in the outer layer adjacent to the head-to-shell weld of a large LPV built by Chicago Bridge and Iron Company (CB&I) and used in air service. Subsequent examination determined that this was an original construction defect with no indication of service-induced crack growth. The vessel was repaired and returned to service.

Table 7.2.2.1: V0256 Design Information

General Information	
Manufacturer	CB&I
Manufacturer's Number	M-108
Manufacturer's Drawing Number	8-8456
Year Built	1963
MAWP	5000 psi
Manufacturer Hydrotest Pressure	7500 psi
Volume	1250 cu ft
Materials	
Head	A225 Gr B FBX
Inner Layer	MLP 1143 mod
Wrapper Layers	MLP 1146
Geometry (Nominal)	
Shell Inner Diameter	60.25 in
Head Inner Diameter	60 in
Head Thickness	3.699 in
Total Shell Thickness	4.125 in
Inner Layer Thickness	15/32 in
Wrapper Layer Thickness	9/32 in
Number of Wrapper Layers	13

7.2.3 MSFC Vessel V0111

Inspection of this vessel during the summer of 2015 using PAUT identified a rejectable indication within the head-to-shell weld. MSFC removed the vessel from service for weld defect excavation and examination and eventually scrapped it. *Appendix B, PVS-15-012 V0111 Inspection and Excavation* provides the report documenting the inspection, weld excavation, and defect characterization.

Table 7.2.3.1: V0111 Design Information

General Information	
Manufacturer	A.O. Smith
Manufacturer's Number	MV50223-6
Manufacturer's Drawing Number	MV50223
Year Built	1958
MAWP	3500 psi
Manufacturer Hydrotest Pressure	5250 psi
Volume	120 cu ft
Materials	
Head	AOS 1148b
Inner Layer	AOS 1148b
Wrapper Layers	AOS 1148b
Geometry (Nominal)	
Shell Inner Diameter	33 in
Head Inner Diameter	33 in
Head Thickness	1.19 in
Total Shell Thickness	2.188 in
Inner Layer Thickness	0.50 in
Wrapper Layer Thickness	0.25 in
Number of Wrapper Layers	7

7.2.4 MSFC Vessel V0012

Identification of outside surface-connected cracks in a longitudinal outer layer weld heat affected zone (HAZ) of MSFC Vessel V0012 resulted in its temporary removal from service. Extensive analysis indicated that the vessel could be returned to service at a pressure not to exceed 3275 psig and a temperature not less than 0°F, with annual monitoring for crack growth. The findings and limits on future service are further described in the balance of this section.

Table 7.2.4.1: V0112 Design Information

General Information	
Manufacturer	A.O. Smith

Manufacturer's Number	MV50565-18
Manufacturer's Drawing Number	MV50565
Year Built	1960
MAWP	4400 psi
Manufacturer Hydrotest Pressure	7475 psi
Volume	618 cu ft
Materials	
Head	A225 Gr B FBX
Inner Layer	AOS 1146a
Wrapper Layers	AOS 1146a
Geometry (Nominal)	
Shell Inner Diameter	58 in
Head Inner Diameter	58 in
Head Thickness	3.0 in
Total Shell Thickness	3.3 in
Inner Layer Thickness	0.47 in
Wrapper Layer Thickness	0.28 in
Number of Wrapper Layers	10

Pressure vessel inspections at MSFC in late 2018 identified the presence of cracks in the outer layer of Vessel V0012 (Figure 7.2.4.1). V0012 is a 625 cubic foot vessel originally designed for 4,400 psig and was in 3,275 psig high purity air service at time of the inspection. The vessel and its 18 sister vessels, which are all connected via common piping manifold, had previously operated in high pressure hydrogen service and MSFC planned to return them to hydrogen service in 2020. Vessel V0012 is a sister vessel of V0023, which also had defects identified, and which is addressed separately in Section 7.2.5. This bank of vessels originally had 20 vessels, including Vessels V0012 and V0023.

Magnetic particle inspection identified two surface-connected cracks adjacent to the outer layer longitudinal weld on the lower shell course at the approximate location shown Figure 7.2.4.1. The cracks run parallel to the longitudinal weld with one crack measured to be approximately ½ inch long and the other approximately 1-inch long (Figure 7.2.4.2).



Figure 7.2.4.1: Vessel V0012 defective welds. The arrow identifies the area where MT inspection revealed two cracks adjacent to the longitudinal weld seam.

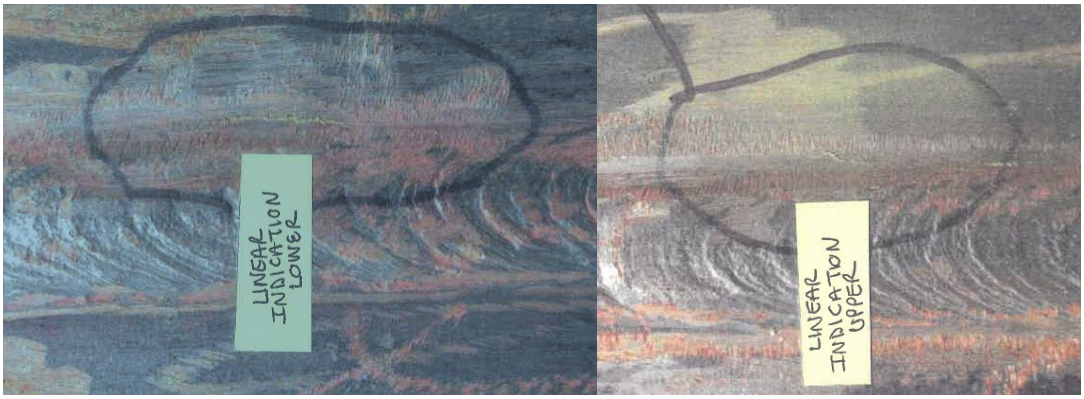


Figure 7.2.4.2: Cracks adjacent to longitudinal weld on Vessel V0012.

The MSFC Materials and Processes Laboratory (EM) performed damage tolerance analysis for vessel V0012 and concluded that the vessel could remain in service at 3,275 psig and a minimum operating temperature of 0°F provided the cracks were monitored annually for growth. Analysis has demonstrated that the remaining safe life based on current operations is greater than or equal to two years. Vessel V0012 was returned to hydrogen service in 2020 at 3,100 psig and with annual monitoring of the cracks for growth. Any growth detected will require additional damage tolerance analysis to ensure the vessel remains fit-for-service, with the inspection intervals adjusted accordingly.

7.2.5 MSFC Vessel V0023

MSFC removed Vessel V0023 from service in 1983 due to an AE emission which, according to anecdotal information, was characterized at that time as being a classic crack signature. The AE data indicated that the defect was buried within the layers of the vessel. At that time the vessel was removed from service and no further efforts were to made to locate or more fully characterize the defect. In 2016, the LPV Program performed AE testing on this vessel, followed by radiography, dissection, and a fracture mechanics evaluation. Investigations determined that the defect was a crack that, while "noisy," had been present since original manufacture due to weld technique, and that it was not a growing service-related crack. The Team used sections of this vessel for a study of sound propagation through the layers and to create rings that were welded together to produce demonstration rings with embedded defects that were then cut into blocks for shipment to vendors for demonstration and assessment of the capabilities of various NDE techniques (see Section 9.2).

Table 7.2.5.1: V0023 Design Information

General Information	
Manufacturer	A.O. Smith
Manufacturer's Number	MV50565-4
Manufacturer's Drawing Number	MV50565
Year Built	1960
MAWP	4400 psi
Manufacturer Hydrotest Pressure	7475 psi
Volume	623 cu ft
Materials	
Head	A225 Gr B FBX
Inner Layer	AOS 1146a
Wrapper Layers	AOS 1146a
Geometry (nominal)	
Shell Inner Diameter	58 in
Head Inner Diameter	58 in
Head Thickness	3.0 in
Total Shell Thickness	3.3 in
Inner Layer Thickness	0.47 in
Wrapper Layer Thickness	0.28 in
Number of Wrapper Layers	10

7.2.6 Other MSFC Vessels

MSFC also made a number of LPV nozzle and head-to-shell weld repairs in the 1980s and 1990s after detection of manufacturing flaws including porosity, inclusions, and lack of fusion. During that period, they employed conventional ultrasonic techniques. Although the ultrasonic techniques could not provide full examination of the vessel welds, these examinations were considered best effort and acceptable for the time. MSFC eventually returned all of the repaired LPVs to service. These LPVs continued in service for decades without any known failures or leakage problems.

7.2.7 LaRC HTT Support Vessels

LaRC used 12 vertically oriented A.O. Smith LPVs in a blowdown application. In time, one or more of these vessels developed cracks in the outer layer and in internal components. Studies attributed the internal cracking to a combination of thermal cycling due to adiabatic cooling and acoustic shocking from their blowdown service. The Center removed these vessels from service and scrapped them in the early 1990s.

7.2.8 LaRC Methane Vessels

LaRC removed two A.O. Smith LPVs from service in 2015 due to cracking in welds. In one case, the crack extended from the head-to-shell weld into the head material.

7.2.9 ARC High Pressure Air Storage Field

Ames Research Center (ARC) placed 16 large A.O. Smith LPVs obtained from the Nevada test site at Jackass Flats into compressed air service in 1987. The vessels had been in methane service at the test site. Prior to placing the vessels in service, ARC stripped the vessels of paint entirely and recoated them, inside and out. They removed the support rings and treated local corrosion beneath. Internal welds were MT inspected (these LPVs all have 16 inch diameter access ports in one head). Prior to installation, RT was performed on 3 of the 10 circumferential welds on each vessel, and an external surface examination was performed on all of them as part of the installation project. The inspections identified many volumetric defects and surface cracks. The contractor installing the vessels repaired the surface cracks and some, but not all, of the volumetric defects. During or after the hydrotest, the water was chemically treated to develop a conversion coating on the inside of the vessels. This protected the vessel interior from further rust or corrosion, but had the collateral effect of making MT no longer a viable inspection technique for the interior.

Table 7.2.9.1: ARC Storage Field Vessel Design Information

General Information	
Manufacturer	A.O. Smith
Manufacturer's Number	MV50527
Manufacturer's Drawing Number	MV50527
Year Built	1960
MAWP	3500 psi
Manufacturer Hydrotest Pressure	5250 psi
Volume	1773 cu ft
Materials	
Head	A225 Gr B
Inner Layer	AOS 1146a
Wrapper Layers	AOS 1146a
Geometry (Nominal)	
Shell Inner Diameter	60 in
Head Inner Diameter	60 in
Head Thickness	2.5 in
Total Shell Thickness	2.93 in
Inner Layer Thickness	0.5 in
Wrapper Layer Thickness	0.27 in
Number of Wrapper Layers	8

7.2.10 ARC High Pressure Air Storage

ARC used a large LPV, constructed by CB&I, in air service for a number of years in the 1970s through the 1990s. An internal inspection performed in the 1986 identified a significant zone of weld porosity in a head-to-shell weld. CB&I was retained to remove the defects and to perform a repair of the weld. NASA re-hydrotested the vessel at 4950 psi based on a 3300 psi relief valve setting and returned it to service at 3000 psi operating pressure in air service for a number of years. It was removed from service in about 1999 because it was no longer needed.

Table 7.2.10.1: ARC High Pressure Air Storage Vessel Design Information

General Information	
Manufacturer	CB&I
ARC Drawing Number	A8---6630-V1
Manufacturer's Drawing Number	M282
Year Built	1967
MAWP	3000 psi

Manufacturer Hydrotest Pressure	4500 psi
Volume	2615 cu ft
Materials	
Head	A225 Gr B
Inner Layer	CBI 1143
Wrapper Layers	CBI 1146
Nozzle	A350-LF3
Geometry (Nominal)	
Shell Inner Diameter	86 in
Head Inner Diameter	86.38 in
Head Thickness	3.52 in (measured 3.538 in)
Total Shell Thickness	5.40 in
Inner Layer Thickness	0.63 in
Wrapper Layer Thickness	0.28 in
Number of Wrapper Layers	17
Number of Shell Courses	6
Tangent-to-Tangent Length	720 in

7.2.11 GRC Vessels

Glenn Research Center (GRC) has rejected a total of 51 LPVs due to unacceptable defects. The defects included linear indications in or associated with longitudinal or circumferential welds as well as lack of fusion in nozzle welds. Some LPV rejections involved defects in both locations.

The 51 rejected LPVs included 25 with rejectable linear indications in or associated with longitudinal or circumferential welds. Four of the 25 had exterior linear indications found using MT that were ground out and the vessels returned to service. Sixteen were repaired by welding and returned to service. Five were removed from service because of such defects.

Conventional Ultrasonic Testing (UT) inspection resulted in rejection of 60 nozzles among the 51 LPVs because of lack of fusion. Thirty-three of the nozzles were repaired and returned to service, 19 were analyzed per API 579 and returned to service, and 8 were removed from service for other reasons.

GRC operated two LPVs with linear indications for a number of years and monitored the flaws using radiography since the time the flaws were discovered in 1994 and 1995. They removed one of the LPVs from service after 16 years of operation and repaired the other after 11 years of service.

7.2.12 KSC Vessels with Outer Shell Cracks

KSC identified cracks in the outer shell plates, away from the welds, of two A.O. Smith LPVs (Drawing MV-50226) located at Cape Canaveral (Figure 7.2.12.1). The vessels had previously

been removed from service due to lack of need and have since been removed from inventory. Specific study of these cracks was not performed, but it appeared that they may have occurred at locations where lugs had previously been removed.



Figure 7.2.12.1: General and detail views, shell plate crack.

7.2.13 Other KSC LPVs

While the specific details, reasons, and any corresponding test results appear to be lost to history, Owen Greulich observed a number of LPVs at KSC with samples removed from the outer layer, indicating possible concerns and a need to investigate material properties and/or defects.

Two sources [Douglas Fraser and Raymond Norman] verbally reported that two KSC LPVs were removed from service due to results of AE examination, but no reports or other documentation have been found.

A long-term agreement between KSC and SpaceX in 2014 included the loan of two small LPVs for use at Launch Complex 40. A mishap on the pad reportedly destroyed these vessels in 2016.

7.2.14 SSC Vessels

Stennis Space Center (SSC) removed several vessels from service for various reasons, including identified defects.

7.2.15 WFF Vessels

In approximately 2012, Wallops Flight Facility (WFF) entered into a long-term agreement to loan the Virginia Commercial Space Flight Authority (VCSFA), a political subdivision of the Commonwealth of Virginia, 12 “conventional” non-code LPVs and 5 autofrettage vessels. The VCSFA operates these vessels in support of activities of the Mid-Atlantic Regional Spaceport (MARS) at Launch Pad 0-A.

Thus, these vessels, operated by a non-NASA entity through a loan agreement between WFF and the Commonwealth of Virginia, are subject to the Virginia Occupational Safety and Health Program rather than federal OSHA. Contractual requirements may address certification and recertification of these vessels and their return to NASA at the end of the loan agreement in the same condition in which they were received. The WFF Pressure Vessels and Systems (PVS) certification/recertification program does not cover these vessels and the current NASA RMP for non-code LPVs excludes them.

The LPVs in question include: 5 Taylor Forge vessels, 3 per manufacturer's drawing 13676 and 2 per manufacturer's drawing 11648, and 12 A.O. Smith vessels: numbered 50457-1, -2, and -5; 50465-1, -2, and -5; and 50457A-10, -11, and -15; and 50464-1, -2, and -5.

7.3 Historical/Legacy Inspections

Prior to the initiation of the RMP, risk management efforts for LPVs were fragmented across the Agency. Each Center developed and implemented its own plans. Centers communicated to some extent, and general knowledge of NDE techniques resulted in some commonality, but, generally, individual Centers did not effectively share techniques and lessons learned. Sections 7.3.1 through 7.3.4 describe some of the inspection methods used prior to the completion of this effort:

7.3.1 Surface Inspections

Centers commonly used MT and PT, techniques long recognized as effective in identifying relevant surface defects, particularly for vessel exterior welds. Both of these techniques generally required removal of paint or other coatings, though one or more Centers developed and qualified MT procedures for use through a certain amount of paint. Heavy weld contours sometimes hampered the effectiveness of these techniques.

7.3.2 Weld Volume Inspections

Inspection of weld volumes was typically accomplished using RT. RT is well-recognized for its ability to identify volumetric defects, but recognized weaknesses include: inability to identify laminations and closed cracks (particularly those perpendicular or nearly perpendicular to the direction of the radiation), potential masking by layer wash of defects in circumferential welds, the need to wrap nearly the entire vessel in film if longitudinal welds are to be inspected, and the inability to identify small defects in layer longitudinal welds because of the overall shell wall thickness.

7.3.3 Leak Detection

Centers have generally practiced inspection of vent (weep) holes, though not always on well-defined intervals. NASA identified only a single LPV with an actual leak (see Section 6.2). That vessel was removed from service.

7.3.4 AE Inspections

NASA has used AE technology for evaluation of LPVs since the 1980s. Initial efforts used the MONPAC technology, whereas later work used a modal approach. AE has the advantage of potentially assessing the whole vessel at once. Disadvantages are the difficulty in discerning significant emissions from other noise coming from these inherently noisy vessels. Not only is this a general problem, but even with a quiet vessel, the determination of which crack growth is important is hard. MSFC removed a vessel from service in 1983 (Section 7.2.5) because of indications deemed critical at the time, and in 2016 it was determined that there were no growing cracks in that vessel.

7.4 Contemporary Dissection

The LPV Team studied a number of vessels and various defects therein. Defects included a number of longitudinal weld defects, some head-to-shell weld defects, and cracks near welds and in the HAZ. Defects were typically excavated and fractography performed. Some vessels were later repaired and returned to service, while other vessels were removed from service and were in some cases scrapped. The materials report [2] provides details of this work. This work included vessels V0023, V0348, and V0256 at MSFC, vessel MV50466-8 from KSC, and others.

8. Flaws/Regions of Interest

Sections 8.1 and 8.2 provide information regarding flaw locations, risk, and mitigation techniques. Section 8.1 provides a graphical explanation, while Section 8.2 provides the information in a table format. Flaw criticality information in these sections is based on work documented in reference[2].

8.1 Flaw Map Diagrams

Table 8.1.1, which follows, provides a naming convention which is then used in Figure 8.1.1-Figure 8.1.5 to show flaw criticality, inspection methods, and the ability to identify each flaw reliably. These charts identify the credible defect locations and orientations. Two charts are provided for each view: The first identifies the primary inspection method for each defect, while the second provides an assessment of risk associated with the defect. The associated risk is identified as red for critical and not easily found, orange for not easily found but of limited consequence, and green for easily found using existing or known methods.

Table 8.1.1: Flaw Naming Convention (see Figure 8.1.1)

Region:
NH = Nozzle to Head
NS = Nozzle to Shell
HS = Head to Shell
SS = Shell to Shell
HM = Head to Manway
LW = Longitudinal Weld
NP = Nozzle Parent
HP = Head Parent
WP = Wrapper Parent
IP = Inner Parent

Orientation (opening stress):
H = Hoop
A = Axial
M = Meridional (Spherical)
C = Circumferential(Spherical)

Flaw Type:
T = Through
Si = Surface, inner surface
So = Surface, outer surface
C = Corner
E = Embedded

Flaw Location:
H = HAZ
W = Weld
F = Fusion Line
P = Parent
A = All/Any

Flaw Size (in):
D = 1 x a Depth
L = 1 x c Length

Naming Convention:
Region-Orientation-Type-Location-D-L

Examples:
SS-A-Si-F-1-2 = Shell to shell weld, axially opened, semi-elliptical inner surface, located in fusion line, 1” deep by 4” total surface length

NS-H-C-P-0.5-1 = Nozzle, hoop oriented, corner crack, located in parent material, 0.5” depth 1” surface length

WP-H-S-H-0.25-2 = wrapper parent, hoop oriented, surface crack, located in HAZ, 0.25” in depth with 4” total length. Since this is wrapper parent it must be in the LW backer layer.

Figure 8.1.1 shows the potential flaw location referred to in the flaw naming convention. Additional information about the flaw is provided by the Orientation, Flaw Type, and Flaw Location descriptors in Table 8.1.1.

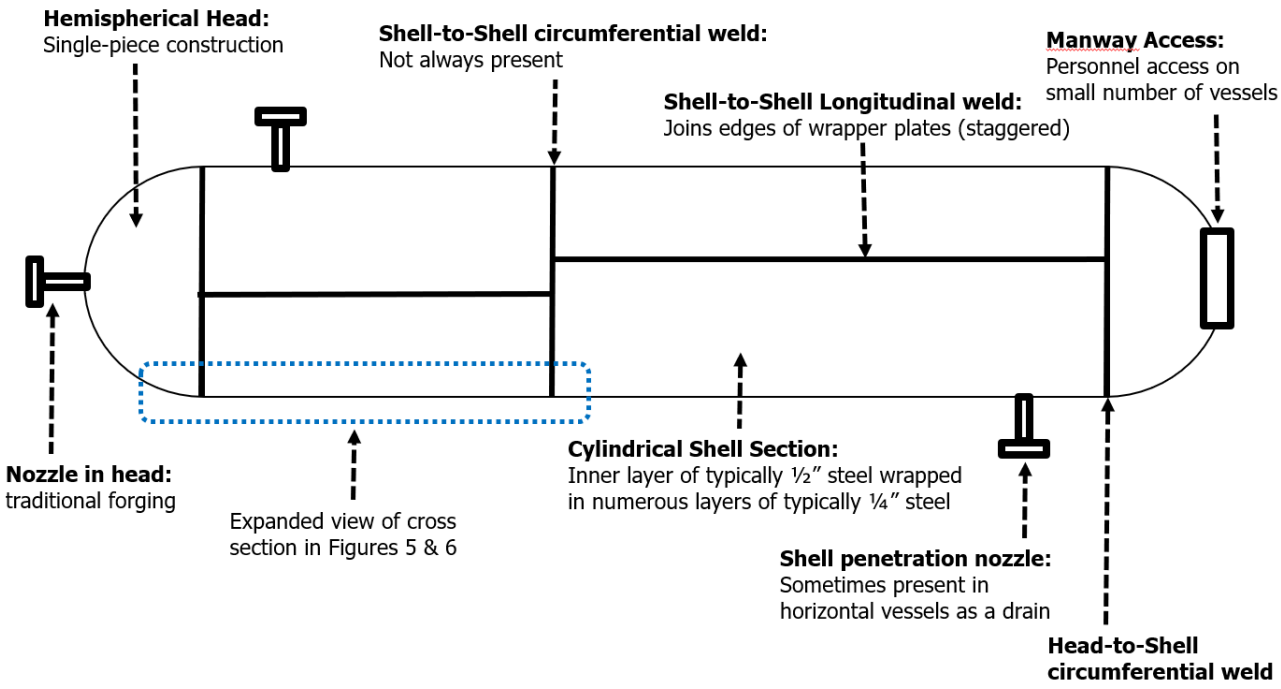


Figure 8.1.1: General View: postulated, and known flaw locations for an LPV. (Figure 8.1.2-Figure 8.1.5 provide section details.)

Figure 8.1.2 ties circumferentially-oriented flaws in the head, shell, and associated welds to their designations using the naming convention, and, in addition, indicates inspection methods and the ease with which a particular defect is found.

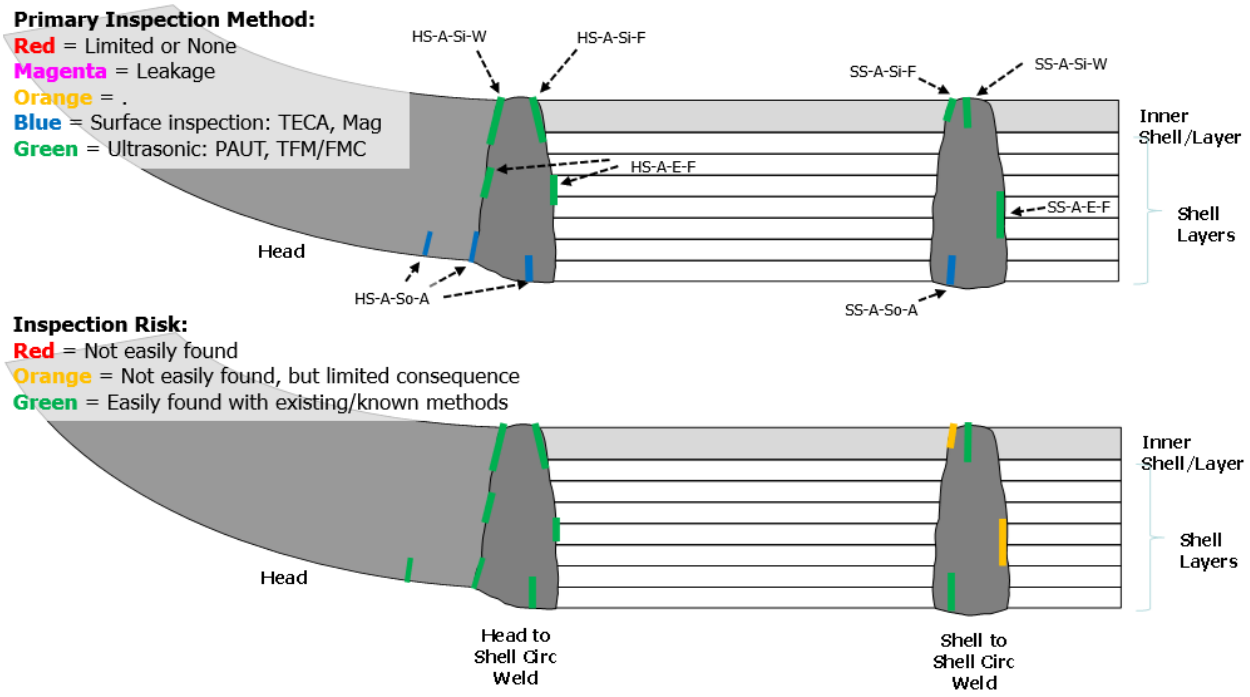


Figure 8.1.2: Circumferentially-oriented shell, head, and weld flaws – inspection methods and inspection risk.

Figure 8.1.3 performs the same functions as Figure 8.1.2, but for longitudinally-oriented flaws.

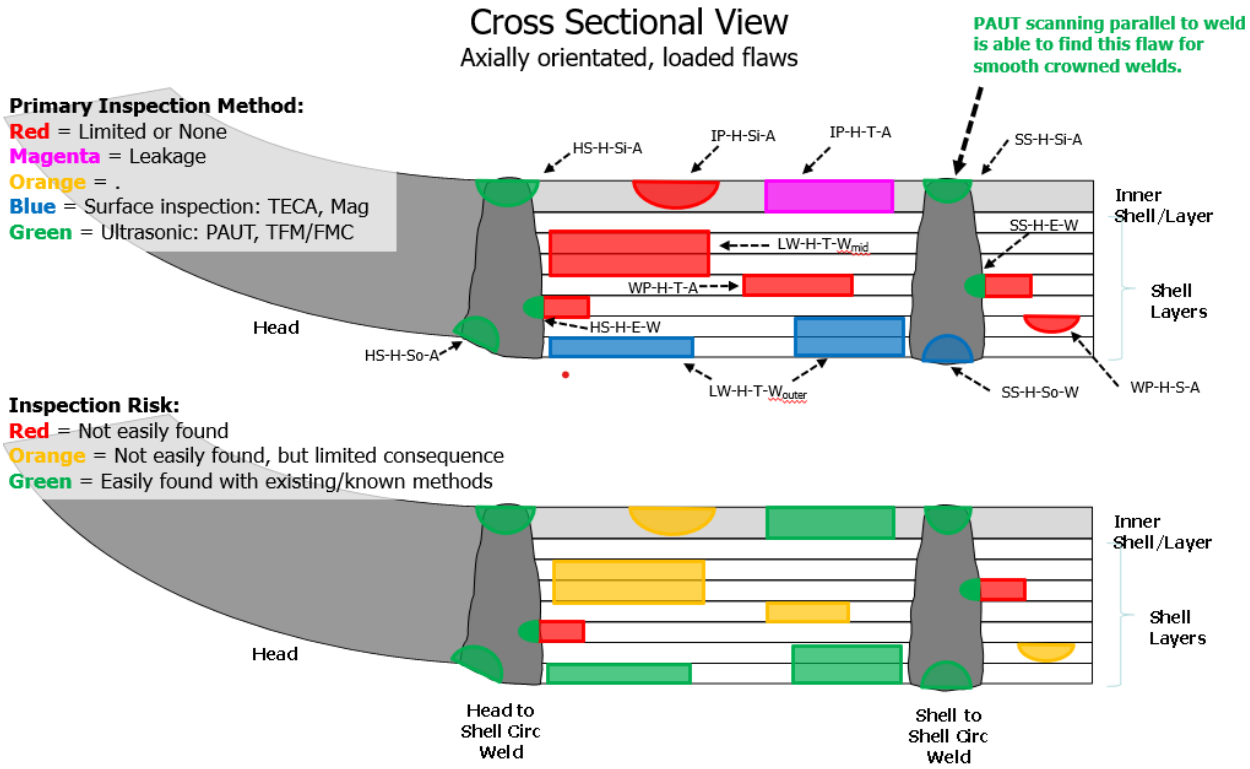


Figure 8.1.3: Axially oriented shell, head, and weld flaws – inspection methods and inspection risk.

Figure 8.1.4 and Figure 8.1.5 provide the same information as Figure 8.1.2 and Figure 8.1.3 for a nozzle penetration in a layered shell section and one in a monolithic head, respectively.

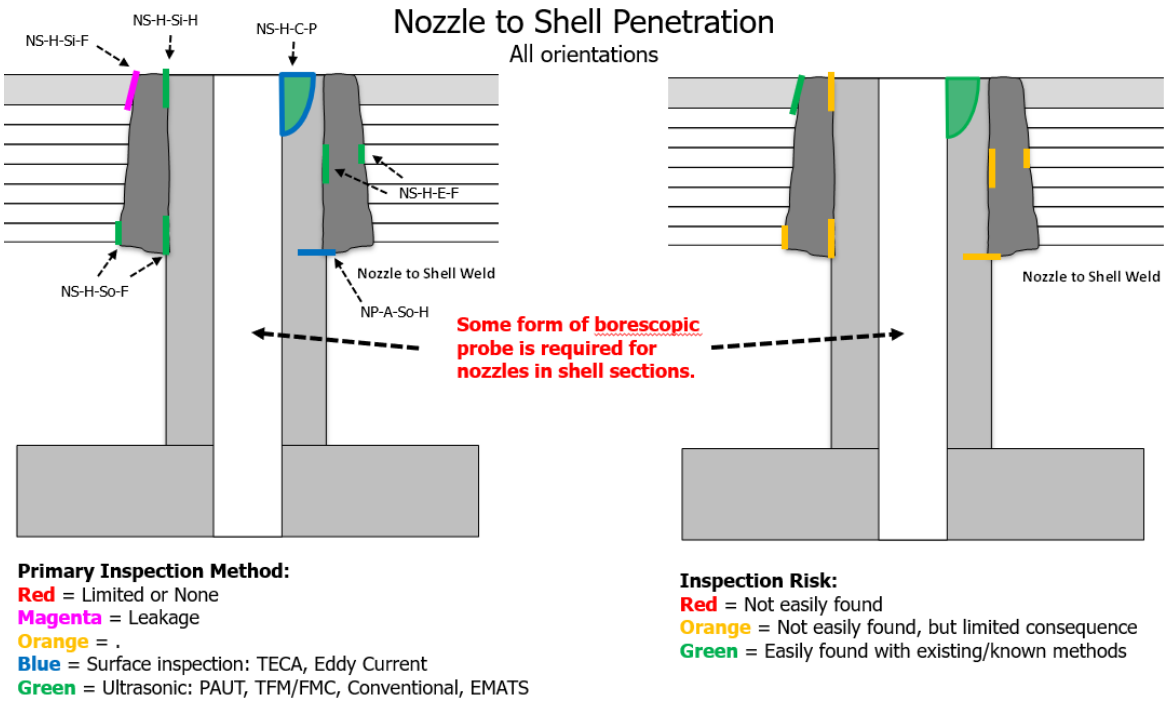


Figure 8.1.4: Nozzle-to-Shell Penetration.

Inspection methods and inspection risk for all orientations. Figure 8.1.4 provides the same information as Figure 8.1.2 and Figure 8.1.3, but for a nozzle penetration in a layered shell section.

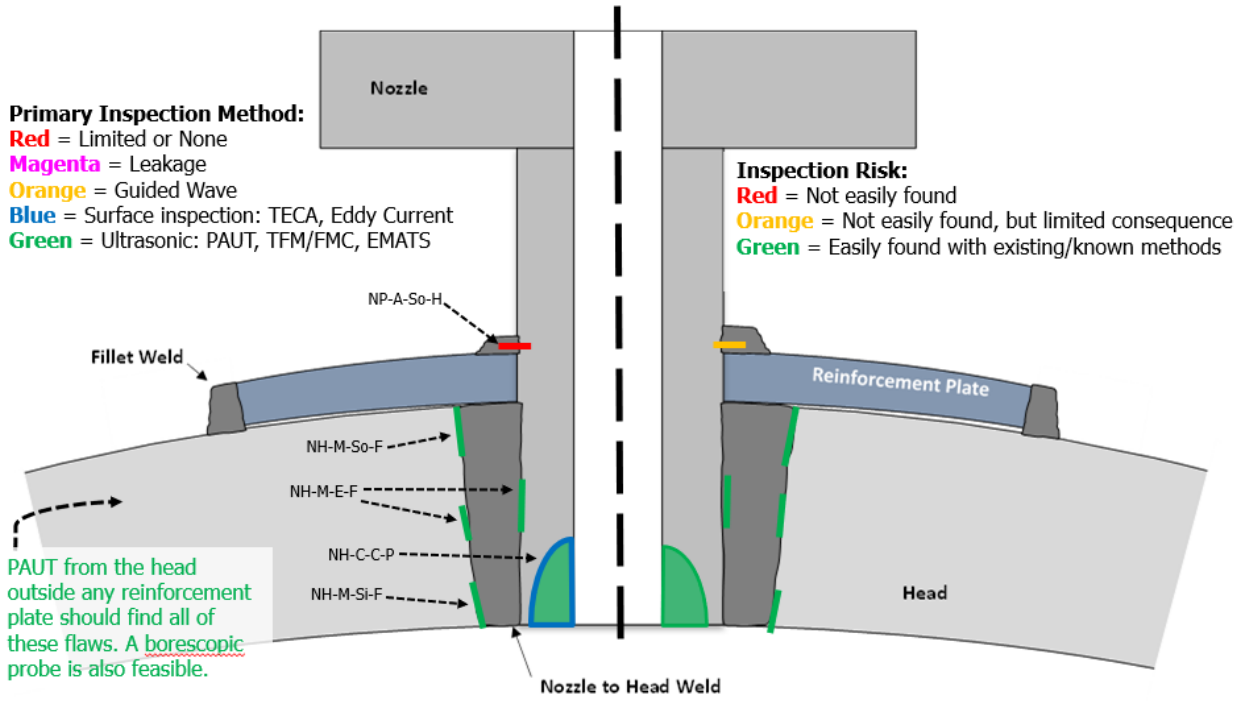


Figure 8.1.5: Nozzle-to-head penetration.

Inspection methods and inspection risk for all orientations. Figure 8.1.5 provides the same information as Figure 8.1.2 and Figure 8.1.3, but for a nozzle penetration in a monolithic head.

8.2 Flaw Mitigation Matrix

The matrix shown in Table 8.2.2 summarizes information regarding the various flaws anticipated in an LPV. The naming convention is the same as that provided in Section 8.1.

Flaws are identified based on region of the vessel, orientation, flaw type, and location. That is followed by an assessment of risk, then mitigation methods, identified as primary (P), secondary (S), tertiary (T), or not applicable (N/A).

The Risk Percentage is a qualitative assessment derived from the values of severity, probability of occurrence, likelihood of detection values (the prior three columns in Table 8.2.2). These three numbers are relative values estimated based on engineering judgment, considering the structural analysis [2], historical records, and flaws identified during this project either through inspection or vessel dissection, whether a particular flaw provides access to the full thickness, and the expected detection capability. For shell-to-shell weld inspection using 2D PAUT, detection capability is that anticipated based on past vendor demonstrations and initial in-house experimentation, though not yet fully verified under this project. A number of recommendations in Section 14 relate to qualification of PAUT procedures for shell-to-shell welds prior to proceeding.

Name				Risk Cube Classification: 1 (good) — 5 (bad)				Mitigation Method(s): Primary (P), Secondary (S), Tertiary (T), Non-Applicable (N/A)											
Region	Orientation	Flaw Type	Location	Severity	Probability	Detection	Risk % S^2*P*D .	PAUT	TFM/FMC	EMATS	TECA	EC	RT	Mag	AE	Leak	GW	Analyt.	Hydro Proof
HS	A	So	A	5	3	2	24.0	P	S	N/A	P	N/A	T	T	N/A	N/A	N/A		
SS	H	E	W	5	2	2	16.0	P	S	N/A	N/A	N/A	T	N/A	N/A	N/A	T		
HS	H	E	W	5	2	2	16.0	P	S	N/A	N/A	N/A	T	N/A	N/A	N/A	T		
SS	H	Si	A	5	1	3	12.0	P	P	N/A	N/A	N/A	S	N/A	N/A	S	T	S	
SS	A	So	A	5	3	1	12.0	S	S	N/A	P	N/A	T	S	N/A	N/A	N/A		
HS	A	Si	F	3	4	2	11.5	P	S	N/A	N/A	N/A	T	N/A	N/A	P	N/A		
NS	H	C	P	4	2	2	10.2	T	T	S	S	P	N/A	N/A	N/A	S	N/A		
HS	H	So	A	4	2	2	10.2	S	S	N/A	P	N/A	T	S	N/A	N/A	T		
HS	H	Si	A	4	2	2	10.2	P	S	N/A	N/A	N/A	T	N/A	N/A	T	T		
WP	H	T	A	2	3	5	9.6	N/A	N/A	N/A	N/A	N/A	S	N/A	T*	N/A	N/A	P	
NS	H	Si	H	3	2	3	8.6	P	P	P	N/A	N/A	N/A	N/A	N/A	N/A	N/A		
HS	A	Si	W	5	2	1	8.0	P	S	N/A	N/A	N/A	T	N/A	N/A	N/A	N/A		
IP	H	T	A	3	2	2	5.8	N/A	N/A	N/A	N/A	N/A	T	N/A	N/A	P	N/A	P	P
NH	M	Si	F	2	4	2	5.1	P	P	S	N/A	N/A	N/A	N/A	N/A	N/A	N/A		
SS	H	So	W	4	1	2	5.1	S	S	N/A	P	N/A	T	S	N/A	N/A	T		
NH	C	C	P	4	2	1	5.1	P	S	T	T	S	N/A	N/A	N/A	N/A	T		
LW[1]	H	T	W	1	5	5	4.0	N/A	N/A	N/A	N/A	N/A	S	N/A	T*	N/A	N/A	P	
SS	A	E	F	1	5	5	4.0	S	P	N/A	N/A	N/A	T	N/A	N/A	N/A	N/A	P	
WP	H	S	A	1	5	5	4.0	N/A	N/A	N/A	N/A	N/A	S	N/A	T*	N/A	N/A	P	
NH	M	So	F	2	3	2	3.8	P	P	S	N/A	N/A	N/A	N/A	N/A	N/A	N/A		
NS	H	So	F	2	2	3	3.8	P	P	N/A	S	N/A	N/A	T	N/A	N/A	N/A		
SS	A	Si	F	2	3	2	3.8	S	S	N/A	N/A	N/A	N/A	N/A	N/A	P	N/A		
NP	A	So	H	1	4	5	3.2	P	P	N/A	N/A	N/A	N/A	T	N/A	N/A	N/A		
NS	H	E	F	1	5	4	3.2	P	P	S	N/A	N/A	N/A	N/A	N/A	N/A	N/A		
HS	A	E	F	1	5	2	1.6	P	S	N/A	N/A	N/A	T	N/A	N/A	N/A	N/A		
NH	M	E	F	1	5	2	1.6	P	P	S	N/A	N/A	N/A	N/A	N/A	N/A	N/A		
IP	H	Si	A	1	2	5	1.6	N/A	N/A	N/A	N/A	N/A	T	N/A	N/A	N/A	N/A	P	
NS	H	Si	F	1	4	2	1.3	P	P	S	N/A	N/A	N/A	N/A	N/A	P	N/A		
LW[2]	H	T	W	1	5	1	0.8	S	N/A	N/A	P[2]	N/A	S	S[2]	N/A	N/A	N/A		

[1]	Intermediate layers only; severity depends on layer count
[2]	Outer layer only
Gen	Table is general guide. Re-evaluate depending on specific flaw, vessel, loading, geometry, etc.

Table 8.2.1: Risk Classification and Mitigation Summary

Abbreviations used in Table 8.2.1 are repeated in Table 8.2.2 for easy reference.

Table 8.2.2: Abbreviations from Table 8.2.1

Region: NH = Nozzle-to-Head NS = Nozzle-to-Shell HS = Head-to-Shell SS = Shell-to-Shell HM = Mead-to-Manway LW = Longitudinal Weld NP = Nozzle Parent HP = Head Parent WP = Wrapper Parent IP = Inner Parent	**Orientation (Opening Stress):** H = Hoop A = Axial M = Meridional (Spherical) C = Circumferential (Spherical)		**Flaw Location:** H = HAZ W = Weld F = Fusion Line P = Parent A = All/Any
	Flaw Type: T = Through Si = Surface, Inner So = Surface, Outer C = Corner E = Embedded		**Flaw Size (inches):** D = 1 x a Depth L = 1 x c Length
Naming Convention: Region-Orientation-Type-Location-D-L			

9. Demonstration Block Construction

Validation of test and inspection procedures requires an inspection of a representative sample of the product to be inspected, with representative defects. In addition to the parent material, LPVs have multiple welds that need inspection including: head-to-shell welds, shell-to-shell welds, nozzle-to-head and nozzle-to-shell welds, and shell section-to-shell section longitudinal welds. The overall complexity of the NDE effort led to use of an incremental approach so that each vessel weld location could be separately evaluated.

In 2014, MSFC contracted for the construction of an NDE demonstration block intended to represent an LPV head-to-shell weld with various embedded defects. Later efforts involved shell-to-shell configurations using sections produced from an actual LPV. Modeling did not

encompass every configuration and defect, but representative samples intended to encompass the range of defects and the most difficult to inspect configurations were produced.

Appendix C provides details of demonstration block and ring configurations.

9.1 Head-to-Shell

Section 2.2 of *Appendix D, PVS-16-004, MSFC Phased Array Ultrasonic Test (PAUT) for Layered Pressure Vessels* describes the construction of the first demonstration block produced for this effort. This block was fabricated using a section of 3-inch plate butt welded to one layer of ½ inch plate and 10 layers of ¼ inch plate. Researchers placed a total of 26 flaws (manufactured planar discontinuities) of different sizes, locations (depth in weld and distance from centerline, or in the parent material), and orientations in the block. After initial fabrication, one end of the demonstration block was cut off to reveal three of the embedded flaws, allowing verification of the accuracy with which the flaws were "installed" into the block.

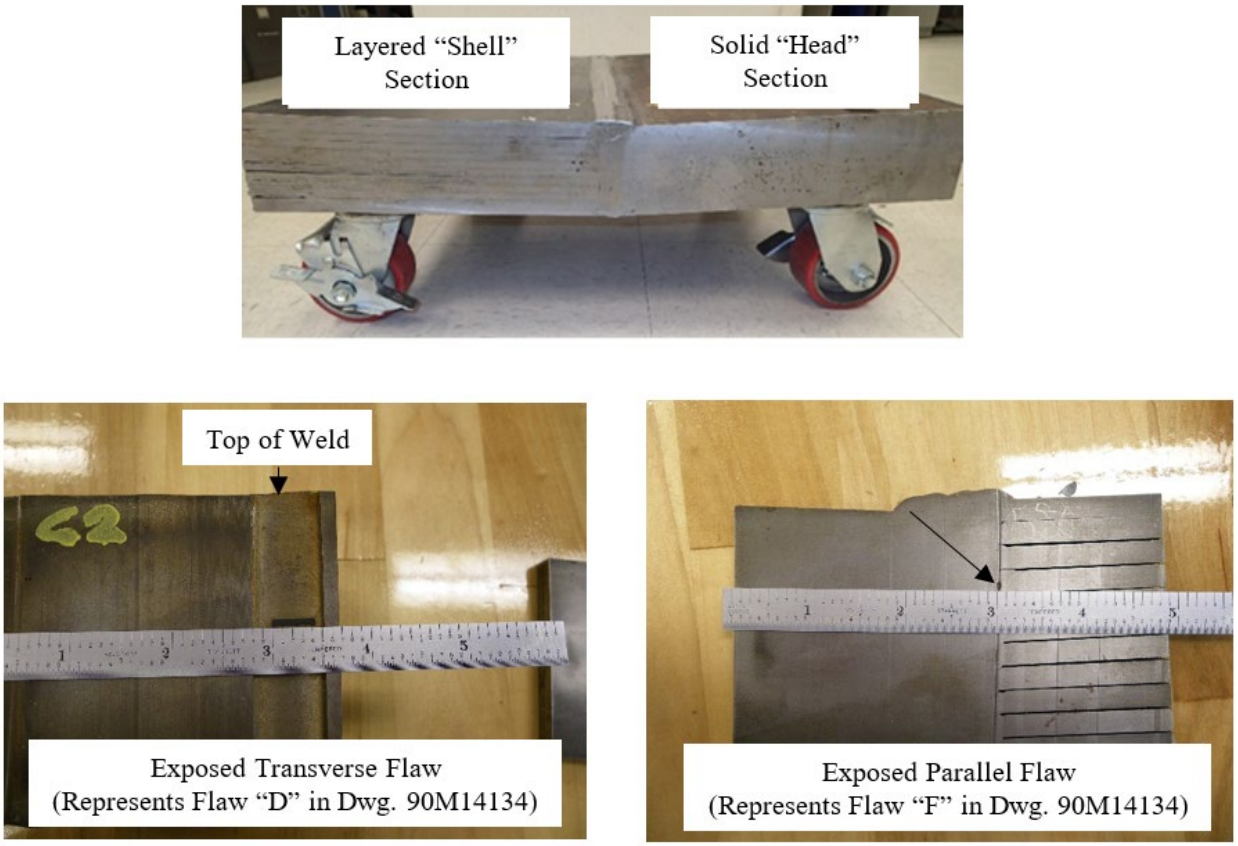


Figure 9.1.1: Shell-to-shell demonstration block

Shell-to-shell demonstration block verification included location, size, and orientation of several flaws compared with the demonstration block fabrication drawing. It was not possible to expose and verify all defect types and orientations, but verified defects showed good correlation with intended size, location, and orientation.

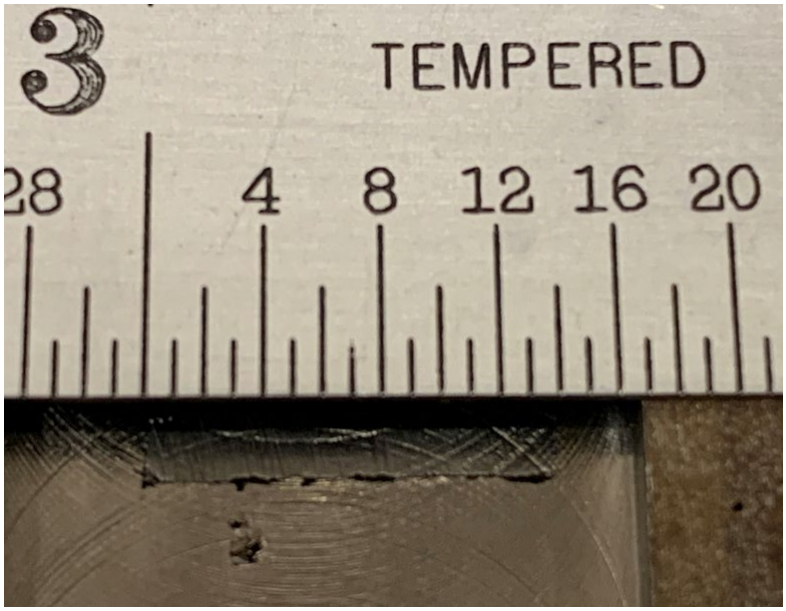


Figure 9.1.2: Detail of section of subsurface defect exposed for verification

Figure 9.1.2 shows a detail of a transverse, subsurface flaw. The figure, looking in the direction of welding, clearly shows an inclusion of a precisely defined rectangular cross-section, measuring (with an engineer's scale) slightly more than 1/16 inch by slightly less than 7/16 inch. This compares well with the targeted size of 0.090 inch by 0.450 inch (the desired 0.040 inch in the depth direction is not shown).

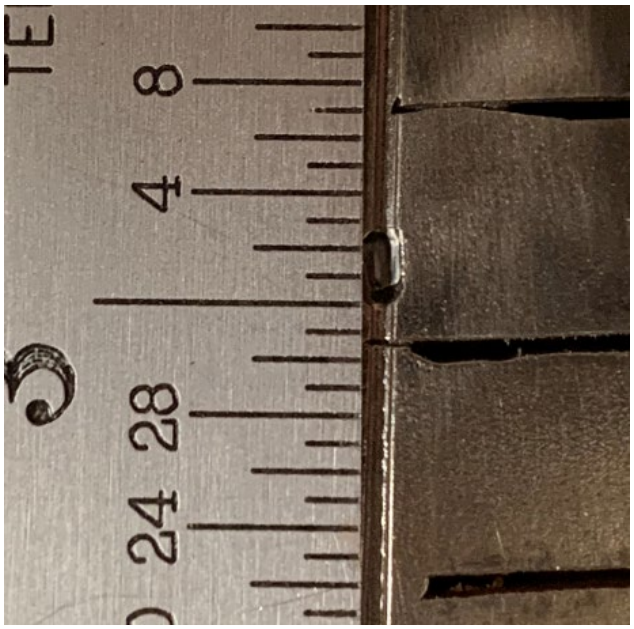


Figure 9.1.3: Detail of subsurface simulated lack of sidewall penetration at the layered side of the weld

Figure 9.1.3, again looking in the direction of welding, shows another subsurface flaw. This time the flaw is oriented in the direction of welding, simulating lack of sidewall penetration to the layered side. As viewed, the end of the defect measures approximately 1/32 inches wide by 5/64 inches vertically (length not shown). The targeted surface flaw was 0.075 inch depth by 0.040 inch width by 0.375 inch length. To the accuracy of the measuring tool, 5/64 inches or (0.078 inch) matches the desired depth, and the 1/32 inches (0.031 inches) approximates the intended 0.040 width. The length is not shown.

9.2 Shell-to-Shell blocks

No flat shell-to-shell demonstration blocks were produced or examined. Instead, the RMP fabricated radiused shell-to-shell demonstration blocks by inserting known defects into an original shell-to-shell weld in a ring section cut from vessel V0023 and cutting it into pieces. The pieces were sent to vendors to provide a means of demonstrating inspection capability. Section 9.2.1 describes production of these blocks.

9.2.1 Shell-to-Shell Demonstration Ring

The RMP produced a demonstration ring including two circumferential welds using sections of a scrap vessel (MV50466-8) as part of the effort to fully investigate the capability of the guided wave ultrasonic examination, PAUT using both linear and 2D ultrasonic arrays, and tangential eddy current arrays. One circumferential weld was left in the as-welded condition, while the other was “flat topped” (machined to provide a smooth surface for coupling of UT transducers) (See Figure 9.2.1.1).

Three rings were cut from the scrap vessel and weld preparations were machined. An outside contractor submerged arc welded the rings back together. The contractor performed welding in accordance with *ASME Section IX Welding, Brazing, and Fusing Qualifications* [16] requirements, and consistent with *ASME Section VIII* [4]. As is usual and code compliant for LPV, no post-weld heat treatment was performed. These ring coupons were subsequently sent to Flawspec Manufacturing, Inc. to have actual crack-like indications implanted within the weld volume. RMP personnel selected this company due to their ability to handle the large coupon size, their welding capabilities, and their ability to produce actual crack-like indications rather than simple EDM notches or other simulated defects. Seven flaws each were inserted into Weld A and Weld B. Because the flaws in the two welds were identical in size, but had different locations, they provided two individual tests (*Appendix C*). These flaws were indicative of transverse weld cracks, longitudinal weld cracks, ID/OD weld cracks, lack of fusion in the weld volume, and cracks emanating from the air gap between layers.

Because of the difficulty in coupling the UT probe to an as-welded surface, the weld in one of the rings was machined flat ("flat-topped"). Techniques that permit inspection through an as-welded surface are desirable, but the current technologies require a smoother surface. Sections 11.3 and 12.1.2 discuss the difficulty of performing inspections through an as-welded surface.

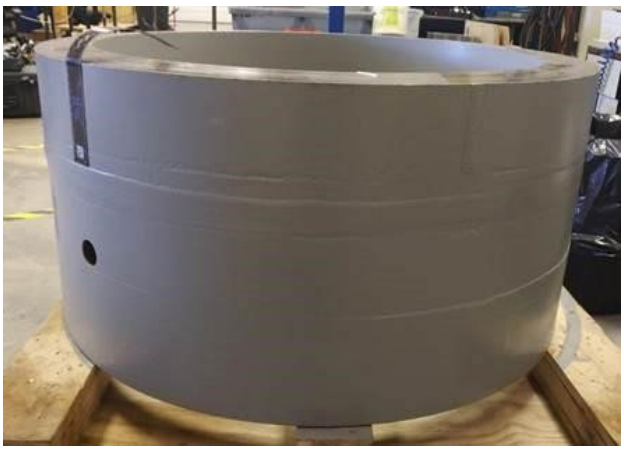


Figure 9.2.1.1: Layered demonstration ring (pre-flawed)

MSFC personnel performed radiography on this assembly after the welding process to ensure integrity of the weld zone and the absence of extraneous flaws. The source was a 450kV Varian accelerator, operating at 420kV. Radiography was performed in accordance with *ASME BPVC Section V* [17], using the single wall/single view technique. This examination revealed isolated areas of slag, isolated minor lack of fusion, and layer wash at the weld/base metal fusion face (Figure 12.3.1). (No radiograph is presented here because of the difficulty of reproducing them well.) NDE personnel evaluated these indications in accordance with *ASME BPVC Section VIII* [4], *Division 1* acceptance criteria. The lack of fusion was found to be rejectable by code, but was deemed to be useful for the purpose of evaluating inspection techniques. The *ASME BPVC Section VIII*, *Division 1* defines layer wash as "the indications resulting from slight weld penetration at the layer interfaces" and does not consider it to be a detrimental defect. Insertion

of the manufactured defects was carefully planned and monitored so as to not encroach on existing unplanned flaws from the welding process.

Note that while radiography is an NDE technique that was used on the demonstration block and rings, it was used to verify quality of the products radiographed, not to assess capability of the technique.

9.2.2 Vendor Radiography (Post Flaw)

Radiography of the coupon post flaw insertion was performed utilizing a Cobalt 60 source to verify existence, location and placement orientation of intended defects, and to confirm lack of extraneous defects from the insertion process. The single wall/single view technique was employed. This examination revealed the inserted flaws, roughly determined their dimensions (to the extent that that could be determined by radiography), and identified very minimal extraneous defects. This test also verified that no two flaws existed in the same location along the two welds. Reviewers found the flaw quality after insertion as evaluated by radiography to be high, with multiple faceted areas on crack-like indications. Lack of fusion indications were smooth faced and of lengths that were acceptable per the flaw size requested. The purpose of RT performed in-house and by vendors was to assess the quality of the product, not the capability of the RT process.

10. Industry Polling, RFI

In September 2017, the Government released an RFI *NNM17ZQD001L* entitled “Feasible Technologies for Non-Destructive Evaluation (NDE) of Layered Pressure Vessels” to solicit potential sources for technologies to be used explicitly for examination of LPV welds. The language of the RFI was very clear; the government was not committing to procure any NDE equipment or services nor was the government required to respond to any of the companies providing RFI submittals (hereinafter referred to as respondents). The RFI was only intended to survey the market for information which might have technical merit for examination of LPVs.

10.1 RFI Responses

Eleven companies responded to the RFI, providing 14 separate proposals. The 11 responding organizations represented a combination of NDE equipment vendors, research and development organizations, NDE service providers, and engineering solution providers. They included some of the leading NDE companies in the US and Canada. The 14 proposals in response to the RFI can be generally summarized as follows:

10.1.1 PAUT

The majority of the proposals recommended various forms of PAUT as the primary weld volume examination method with various options and features including water-filled flexible wedges, weld surface mapping software, and 2D probes.

Vendors used different approaches to analyze the data. One of the major differences was the analysis software used to interpret the results of an inspection. For example, one of the suppliers demonstrated software with algorithms that were able to filter out indications from known geometric features.

There were, however other significant differences.

The full matrix capture (FMC) approach sequentially uses each individual transducer element in an array to produce a signal while all others receive. This is a much more data and analysis intensive approach, and while it may ultimately produce better results, the differences observed (primarily on-screen data presentation) during the demonstration were not sufficient to justify the added cost. The Team did not observe that using this technique provided a significantly greater ability to identify or characterize defects than with conventional PAUT. However, they did observe that the FMC system had, compared to normal PAUT, reduced inspection speed and increased data file size. Also, it has the same need for coupling between the transducer and the workpiece being inspected as does conventional PAUT.

The use of 2D transducer arrays showed a potential for improved defect detection. These allow greater flexibility in steering the sound into the required regions of a part, and the ability to program the direction of the sound increases the probability of sound hitting a defect from the direction that would result in the greatest specular reflection. This technique was able to detect a defect that had not been identified by any of the other inspections. This approach is expected to be especially valuable for inspection of shell-to-shell welds, in which inspection must take place from the top of the weld. It is, however, expected to require “flat-topping” of the welds.

Resource and time limitations made it impossible to fully verify the capabilities of the PAUT using 2D arrays prior to publication of this document, but initial successes provide confidence that this technique will be successful in identifying required defects in the shell-to-shell circumferential welds.

10.1.2 Health Monitoring Systems

Two submittals proposed health monitoring systems (HMS) for early warning of incipient vessel structural failure. One submittal proposed the use of a vibratory/acoustic technique to monitor change in the vessel structure from a pre-established baseline. The Team did not pursue this proposal because the only baseline that could be established is the current state of the LPV, but that is what requires evaluation. Other submittals proposed continuous monitoring of the vessel vent holes for leakage which would indicate the inner vessel layer has been compromised. Industry already recognizes the validity of this technique, though it is rarely used because of cost and various associated technical challenges.

10.1.3 Eddy Current Arrays

Several submittals proposed Eddy Current Array (ECA) technology, including Tangential Eddy Current Array (TECA), for detection of weld surface/near-surface defects. Some proposals paired ECA with PAUT to cover both weld surface and weld volume examinations.

The TECA technology uses multiple coils oriented in different directions so as to permit detection of flaws both transverse to and parallel with the direction of travel. This is an enhancement of conventional eddy current technology that increases efficiency of scans, but is not new technology that requires validation from first principles. Also, because it is a technology that needs a surface-connected defect in order to be effective, TECA inspections of an LPV are essentially the same as those of a monolithic vessel, so no additional efforts were needed to justify use of the technology on NASA LPVs

10.1.4 Miscellaneous Proposals

The remaining proposals focused on LPV defect screening technologies including MAE, ultrasonic guided wave, digital image correlation, ultrasonic spectroscopy and magnetic flux leakage techniques.

10.2 RFI Down Select Process

Representatives of the affected NASA Centers and NASA Headquarters participated in the down select process for NDE proposals.

10.3 Rating Criteria

The evaluation team rated each proposal on the following criteria: prognosis, overall benefit/value, LPV inventory applicability/constraints, agency cost (initial cost to develop or validate prior to deployment), and practicality of use at Centers (logistical considerations). Sections 10.3.1-10.3.5 explain the 5 criteria used to evaluate the proposals.

10.3.1 Prognosis

Prognosis was the likelihood that using the proposed technology would ultimately succeed in accomplishing the objective as proposed by the vendor.

10.3.2 Overall Benefit/Value

The overall benefit/value was an evaluation of how valuable the technology would be if successful as proposed. This included consideration of such things as how much of the vessel (or vessel welds) would be covered by the technology, the types of defects that the technology would identify, and whether the technique would allow flaw characterization or whether follow-up inspection using another technology would be required.

10.3.3 LPV Inventory Applicability/Constraints

LPV inventory applicability/constraints represents a measure of the portion of the agency fleet that could be evaluated using the vendor’s technology. This metric includes, for example, whether a technology was so non-portable and high cost that it could be implemented only at one Center, or whether it might only be applied effectively to horizontal vessels with large amounts of space around them.

10.3.4 Agency Cost

Agency cost was calculated as the initial cost for further developing or validating the technology prior to deployment on NASA LPVs.

10.3.5 Practicality of Use at Centers

The Team defined practicality of use at Centers by looking at logistical considerations, initial investment, and recurring costs. The team evaluated items such as vessel access, vessel availability, process disruption, vessel contamination/recleaning, etc. Initial investment was the estimated cost to implement the examination or monitoring technique, including equipment procurement, hiring additional personnel, funding contractor services, procuring calibration standards, and possibility of sharing costs or resources with other NASA Centers. Recurring costs were those associated with the technique on an ongoing basis, including additional labor resources, equipment calibration, vessel re-examination, and equipment maintenance/upkeep. In addition, some proposals appeared to require a contract structure that would have been very limiting for the Government and would have resulted in higher recurring costs. The team therefore scored these lower.

10.4 NASA Response

In March 2018, after initial review of the RFI responses, NASA invited many of the respondents with promising technology submittals to present their proposals via teleconference to the NASA LPV Working Group. The discussions focused primarily on specific applicability of the proposed technologies for LPV construction, the technology maturity level of the methods proposed, and the overall scope and costs of any efforts required to validate technologies deemed to have merit.

10.5 RFI Outcome Summary

10.5.1 PAUT

A number of respondents proposed the use of PAUT, a technology that was already being investigated by NASA, but the Team did not identify any respondents who had undertaken any specific development or validation initiatives to understand capabilities and limitations of PAUT for examination of LPV welds. Further discussion with a number of the respondents revealed that their primary interest was in performing PAUT research and development efforts for LPV applications. These efforts would have been redundant with ongoing efforts by the NASA LPV Working Group. NASA had been researching the use of PAUT for LPV examination since 2014 and had already made substantial investments in PAUT equipment and technique validation efforts as described in Section 12.3. Although most of the PAUT proposals resulted in little new information, one proposal involving use of 2D arrays was of interest. While the initial proposal and results were not sufficient to result in any immediate change of course on the part of NASA, NASA encouraged the company to develop the technology and to advise NASA when certain progress had been made. Approximately two years later, the company was able to demonstrate

the ability to identify and characterize defects in shell-to-shell welds. As a result, NASA has begun pursuing this technology.

10.5.2 Health Monitoring Systems

The two continuous HMS which were proposed, one involving vibro-acoustic technology, and the other regarding vent hole monitoring, were not deemed practical to pursue.

The Team considered use of the specific vibratory/acoustic technology to monitor the LPVs impractical and very costly due to the requirement to establish a known structural baseline for each individual vessel and then to install and maintain the instrumentation and data acquisition system for such a large number of vessels, many of which are located in remote areas without immediate access to electrical power. The vibratory/acoustic system would also require an initial, and possibly protracted, validation effort to demonstrate that the system could indeed detect growing flaws in large, heavy wall vessels in advance of catastrophic failure.

The separate HMS proposal to continuously monitor vent holes for leakage was also considered impractical for NASA. NASA had already taken steps to check LPV vent holes for leakage and considers a periodic leak check sufficient rather than attempting to "continuously" monitor so many vent holes across such a large fleet of vessels. The vent hole monitoring system would require initial installation and continued maintenance of instrumentation on large numbers of vessels, each with multiple vent hole locations. As in the case of vibratory/acoustic HMS, the system would require providing electrical power to vessels at remote locations, thereby causing NASA to accrue additional costs.

Lastly, both health monitoring systems proposed would require the use of other NDE technologies to investigate suspect areas of the vessel identified by the HMS and to characterize any flaws present. Section 14.7 addresses inspection of vent holes themselves, while Section 14.8 discusses identification of leakage through them.

10.5.3 Defect Screening Technologies

The LPV defect screening technology proposals included some technologies that NASA was currently investigating and some that NASA had never considered. To some extent, NASA had already investigated the use of AE and digital image correlation (discussed further in Section 11.1 and the *NESC Report* [14], respectively). The RFI proposals for digital image correlation did not provide any additional insight into that technology, while the proposal for MAE using multiple phased array sensors did indicate that significant improvements in sensitivity and defect location were achievable, potentially overcoming the primary difficulty encountered during the cyclic testing project (active ductile crack emissions on the threshold of detectability) as is discussed later in Section 13.9.1.

MAE using phased array sensors was successfully applied by the contractor on the V0023 AE test (also described in Section 13.9.2.3). Following this, several LPV team members visited the home facility of the submitter to assess the maturity level of the phased array MAE approach in detail. The detection capabilities of this technology were, however, somewhat redundant with

those of PAUT without providing the flaw characterization capabilities of the flaws that PAUT could detect (e.g., welds in solid sections). In addition, the flaws that could be detected by Phased Array MAE that were not accessible to PAUT (e.g., in longitudinal layer welds) were determined through structural analysis not to be critical to vessel safety. Ultimately the LPV Team decided that further work in AE and MAE would not be pursued by the LPV Project due to the rapidly increasing confidence in PAUT.

Ultrasonic guided wave and magnetic flux leakage were technologies which NASA had not previously considered for LPV examination or defect screening. NASA provided low level funding to one RFI respondent for a demonstration of ultrasonic guided wave technology as this was considered a novel approach which might have technical merit (and was considered in some respects similar to PAUT technology) (See Section 11.2). The magnetic flux leakage proposal, although interesting technology, was considered low maturity level for heavy wall LPV applications. NASA considered pursuit of this technology another potentially costly and protracted effort which, in the end, may not have application for heavy wall layered construction and would still require supplemental NDE techniques to characterize suspected flaws.

10.5.4 Tangential Eddy Current Array

NASA had already been evaluating Tangential Eddy Current Array (TECA) systems (beginning in 2015) for weld surface examination prior to the release of the RFI. The TECA technology had matured significantly in recent years and NASA subsequently procured a TECA system which is further described in Section 13.3 of this report.

This technology uses an array of eddy current coils arranged to enable detection of both longitudinal and transverse surface-connected indications in a single pass. In addition to that capability, attractive characteristics of TECA include the manufacturer's published capability of detecting and sizing surface-connected defects of 0.08 inches (2 mm) minimum length and 0.02 inches (0.5 mm) depth, and compensation for "lift-off" caused by tightly adhered, non-conductive, non-peeling, and non-flaking surface coatings of up to 0.12 inch (3 mm). (Lift-off refers to the pronounced signal change that occurs with a very small change in coil-to-part distance.) [20]

TECA holds the promise of improved detection capability over MT and PT inspections, including the ability to determine the depth of indications. Eliminating the need to remove surface coatings will, in some cases, result in cost savings, although for those welds requiring flat topping, whether for TECA or for PAUT, this issue is moot.

NASA produced a painted carbon steel coupon with 0.375 inch long with 0.040 inch deep square bottom EDM notches for demonstration purposes. In addition to the paint, the area containing the defects was covered with nonconductive cloth duct tape, adding thickness and obscuring visual evidence of the surface defects.

Initial evaluations of the technology in 2015 were promising, but the technology, especially the software, was still evolving and maturing. It reliably detected defects, but its locating capability was insufficient. This deficiency was discussed with the vendor at the time, and the vendor

agreed to work to refine the software to improve the capability. In 2018, following responses to the RFI discussed in Section 10, NASA requested another demonstration of the technology. During this second review, TECA accurately detected, located, and sized all surface-breaking defects in the OD of the 24 inch LPV head-to-shell demonstration block.

11. Analytical Modeling

Experimental approaches are widely utilized for the development of inspection techniques, but as the complexity of the geometry increases, both fabricating realistic test articles and developing techniques become more difficult. Computational NDE simulations can assist in the development of new inspection methodologies or optimization of existing NDE techniques for these configurations by providing an improved understanding of the interaction of instrumentation with the item to be inspected.

NDE simulations use physics-based models of the interaction of the measurement system with the object to be inspected. Accurate prediction of the acquired signals requires accurate inputs for many parameters. These include such items as the exact geometry of the object, a map of pertinent material properties, and the details of the operating characteristics of the measurement system. It is unlikely that all of the information required for a precise prediction of the system response is available when performing simulations. However, simulations have provided important insights into the capabilities of an inspection, assisted in the interpretation of inspection results, and predicted trends in inspection results as changes occur in important characteristics such as flaw size and location.

The two primary sets of NDE simulations performed for this effort were PAUT of the circumferential weld of an LPV and the propagation of AE generated by the growth of a crack in an LPV. Both are cases where it is difficult to obtain significant measurement data due to the fabrication cost of test articles (vessel test coupons). The whole system (sensor excitation, couplant, test article, and receiver response) was modeled for the PAUT inspection. Using these simulations, it was possible to explore the sensitivity of the inspection to small changes in test article (and therefore, vessel) geometry or flaw characteristics.

For AE, simulations to determine the amplitude of the generated acoustic wave were not possible with the limited knowledge available on the crack growth mechanisms in these materials. Rather, the simulations focused on how generated waves would propagate from inner layers to the outer layer in the presence of limited contact points between plates and how the frequency content changes as the acoustic wave propagates. An independent experimental effort was performed to measure the amplitude of these waves (Appendices I, J).

11.1 AE

AE technology has been applied to LPVs for some time. The technology has detected signals associated with cracks and other flaws, but questions have remained regarding the true capability of the technology to detect all significant defects in LPVs. In addition to a concern regarding effective identification of growing cracks in time to avert a failure, the extent to which signals in inner layers will find their way to surface-mounted sensors is a concern. In an effort to better

understand the capabilities of this technology, an analytical study was performed using the in-house elastodynamic finite integration technique (EFIT) code. The study modeled signal transmission between layers for 25%, 50%, 75%, and 100% contact. For the dipole signal modeled, the conclusion was that, even with variable contact, the wave is observable on both inner and outer surfaces. This was consistent with documented results of testing at ARC and DWC (*Cyclic Crack Growth Testing of an A. O. Smith Multilayer Pressure Vessel with Modal Acoustic Emission Monitoring and Data Assessment*, NASA-CR-2014-218156, https://archive.org/details/NASA_NTRS_Archive_20140008836) [11]. Further details regarding this analysis are found in *Appendix F*, *Simulation Work for Layered Pressure Vessels.*

11.2 Guided Wave

No documented use of guided wave technology applied to LPV was found, but researchers speculated that the technology might provide another means of gathering information in otherwise hard to inspect areas. While some discussion focused on sending sound into the layers from the head, this analytical work studied the injection of sound from the outside surface of a vessel circumferential weld, looking for a crack on the inside surface. The study concluded that cracks in the direction of the wave were nearly impossible to detect, and that the ability to transmit the required ultrasound through layers was limited. Further discussion of this analysis is also found in Section 12.4.1 and in *Appendix F Simulation Work for Layered Pressure Vessels*.

11.3 PAUT

MSFC has used PAUT to inspect LPVs since 2015. The technology has successfully identified a number of defects in LPV head-to-shell welds. While defects were found to correlate with PAUT indications, a better understanding of capabilities was desired. NDE simulation software was used to simulate inspections of head-to-shell and shell-to-shell welds, each with a circumferential and an axially-oriented crack. Modeling was thorough, including simulation of weld anisotropy, and actual defects in the demonstration block were modeled. The model also accounted for weld surface roughness. For an axial crack, a difference in signal response of 8.9 decibel (dB) was observed between a smooth finish and a 250 μm finish, but when actual weld contour was modeled there was little difference in response level, though a higher presence of artifacts. Identifying defects by the loss of signal caused by a vertical discontinuity was modeled. The simulation showed limited promise of finding vertical discontinuities using this potential inspection technique. Details of this study are provided in *Appendix G*, *Ultrasonic Testing Simulation Documentation.*

12. NDE Lab Scale Demonstration

This Section addresses several lab-scale evaluations that were used to measure the feasibility and proficiency of various NDE methods. These evaluations were performed on samples that were manufactured from LPV remnants or from plates and that included induced flaws of various types and dimensions. Flaws of particular interest in the weld zone were simulated using EDM notches and other techniques (See Section 9.2). The samples varied in thicknesses and dimensions proportionate with the method, technique, and flaws to be identified. Samples

included pre-cracked individual plates, a fabricated flat section simulating a head-to-shell joint, portions of an actual vessel that had been cut into rings and circumferentially welded back together, and vessel remnants with EDM flaws.

12.1 Head-to-Shell Demo Block Inspections

The first of the lab scale evaluations performed was on a head-to-shell weld joint sample. This demonstration intended to replicate the inspection of a head-to-shell weld joint in an LPV using the performance demonstration (PD) block described in Section 9.1. The sizes of the flaws implanted in the PD block were the largest non-rejectable flaws determined from *ASME VIII-2* [4], *Table 7.10* based on an assumed aspect ratio of 0.2. Successful detection and characterization of these "acceptable" flaws would serve as validation that larger, rejectable flaws would be detected. The successful detection and sizing of an ID, OD, and one volumetric flaw in this block would provide qualification of the PAUT procedure, equipment, and operator in accordance with the *ASME BPVC*, *Section V* [17], *Article 4*, *Mandatory Appendix IX*.

PAUT offered the best chance of detecting these defects, largely due to the multiple angles in the sector scan, which increased the probability of specular reflection of sound. Throughout the qualification, PAUT excelled in the detection and sizing of circumferentially-oriented defects in head-to-shell welds. Defects in both the near and far fusion zones were detectable at multiple depths and simulated ID and OD cracking were easily detected, in addition to indications further back in the layers beyond the fusion zone. The performance of the system, sensitivity, and scanning and sizing techniques used in the qualification were deemed satisfactory based on the flaw data obtained; and the procedure was considered qualified for the detection of circumferentially-oriented defects. Transverse defects still pose a challenge for the technique at this time, and will require further development due to the incident angle limitations associated with having to introduce sounds waves from directly above the weld.

12.1.1 In-House Head-to-Shell Demo Block Inspections

While initial in-house PAUT inspections did not result in defect identification with full confidence, practice on the flat head-to-shell demo block refined the ability to identify defects accurately and consistently. An inspector experienced in the technique on a layered fabrication was able to identify defects and determine their orientation and size. While a formal report was not produced to document this effort, refinement of the technique was continued until acceptable flaw characterization was achieved repeatably. Further documentation was not pursued because of the development of additional demonstration blocks representing the shell-to-shell joints and more sophisticated inspections that followed.

Complete examination of LPV welds requires inspection of both the volume and the surface of the weld. Past inspections have used various methods, primarily MT and PT, to detect surface-breaking flaws in LPVs. While effective, both of these methods have proven to be relatively time-consuming and costly. In addition, PT always requires an unpainted surface, and while MT has been qualified on certain painted surfaces in the past, best results are obtained if the paint is removed. Both paint removal and repainting added to the cost of the inspection, and coordination

of paint removal with the inspection often further delayed the process and the availability of results. These problems gave urgency to the need to find another surface inspection technique.

In 2018, MSFC purchased a TECA system (*ASME Section V*, *Article 8*, *Mandatory Appendix X* [17]). This system has been used to evaluate surface-breaking defects in a demonstration block and in rings with artificial and realistic flaws. Due to favorable laboratory results during the demonstration of the equipment on the 24 inch LPV head-to-shell block, MSFC field-deployed the TECA system in 2019, where it was initially used for surface examination of LPV longitudinal welds. Since TECA is a surface technique, it is not affected by the vessel layers. As a result, testing on the demo ring was not required. The technique was tested on both as-welded and "flat-topped" welds on shell-to-shell blocks, and was found to work best on "flat-topped" welds.

12.1.2 Vendor In-House Head-to-Shell Demo Block Demonstrations

In an effort to continue refining the inspection process, NASA allowed multiple vendors to demonstrate their capabilities on the same head-to-shell demonstration block that was used to qualify the NASA PAUT procedure. These demonstrations were performed "blind." The vendors were only supplied with the weld joint geometry for scan plan development. The various demonstrations yielded mixed results. However, these vendor demonstrations further validated the use of ultrasonic methods as the most promising technique for LPVs. A common point of failure proved to be coupling any type of probe to the weld surface in the "as-welded" condition. This led to investigating the removal of the weld cap reinforcement which would leave a smooth flat surface and improving probe coupling capability. The sections below provide some information regarding specific findings, but a detailed accounting of inspection successes and failures is not provided in this section because this work was largely confined to determining which technique to pursue, rather than investigating actual capabilities of the techniques.

12.1.3 PAUT Two-Dimensional Matrix Arrays on Head-to-Shell Demo Block

NASA began investigation of 2D array PAUT technologies in an effort to identify defects in shell-to-shell welds. Use of this approach on the head-to-shell demonstration block showed that the technology is also effective for head-to-shell welds. While traditional PAUT had been effective for inspection of these welds, inspecting them using 2D arrays allows the same technology to be used for both head-to-shell and shell-to-shell welds, reducing equipment set up time.

Two-dimensional transducer arrays offer more flexibility in beam steering and provide a possible method for the detection of transverse defects in head-to-shell welds. The technique offers the capability of the traditional sector scan, but allows it to be directed into the volume of the weld and also electronically skewed electronically a predetermined amount on either side of the center of the probe. It is expected that this technique will allow detection of transverse (perpendicular to the weld direction) defects, but that it will require further development for the detection of circumferentially-oriented defects.

12.1.4 PAUT Full Matrix Capture Methods (FMC)

Another NDE technology that was considered during the LPV inspection evaluations was Full Matrix Capture. FMC is a method of collecting phased array data that doesn't require prior knowledge of the piece that is being inspected. Code requirements are found in *ASME V*, *Article 4*, *Mandatory Appendix XI* [17].

FMC uses a phased array ultrasonic probe. Each element in the array is sequentially used as a transmitter while all the other elements act as receivers. Thus, this method captures and stores every possible transmit-receive combination. After capturing the data matrix, post-processing algorithms enable computational focusing of the ultrasonic beam to different locations within the inspection volume. For conventional PAUT, the beam is electronically focused and cannot be refocused after the data has been acquired. Discussions with NDE vendors about the capabilities of this emerging technology and an equipment demonstration at MSFC did not reveal any current significant strengths or benefits of using this method over PAUT for LPV weld examination, especially since FMC is more expensive and takes additional time to perform. As FMC technology continues to evolve, this method may prove to be worthy of reconsideration for LPV weld examination, although substantial equipment investment would be required.

12.2 Shell-to-Shell Demonstration Block Inspections

Initially construction of a flat shell-to-shell demonstration block was planned, but it was never constructed. Instead, a shell-to-shell ring with two welds was produced using shell rings cut from remnants of the vessel cycled at DWC (MV50466-8), and vessel shell-to-shell weld sections from Vessel V0023 were excised and cut into blocks after completion of the AE test of that vessel in 2016, then seeded with flaws. Inspections of the demonstration rings are detailed in Section 12.4.

12.3 AE Lab Scale

AE is a well-accepted technique for detection of acoustically active defects in monolithic pressure vessels. It is a unique inspection technique in that the ultrasonic waves under study are created within the material itself by the pressure loading, rather than using an external source to propagate energy to a crack and having that energy propagate back to a sensor. For pressure vessel AE inspection, the intent is to take the vessel to a high enough pressure to result in crack growth during the single application of pressure. In theory, the crack growth generates an acoustic wave that can be detected, recognized, and located from a location remote to the crack. Methods of AE pressure vessel inspection are documented in *ASME V Article 11* [17], *ASME Section X*, *Appendix 8*, *Article 8-600* [18], and the *National Board Inspection Code NB-23*, *Part 2*, *Supplement 10* [19].

Two important aspects of AE inspections are: only acoustically active defects have a potential of being detected, and testing requires pressurizing the vessel past its maximum normal operating pressure.

One unavoidable fact is that there is often much non-relevant noise detected during an AE test, and distinguishing noise from flaw growth is essential to a meaningful test.

To better understand the potential and limitations of the AE technique for NASA LPVs, laboratory measurements were also performed at the National Institute of Standards and Technology (NIST) in Boulder, CO. These measurements focused on the number of events, amplitude, and frequency content of AE signals in coupon specimens under uniaxial tensile loading conditions. Digital Image Correlation (DIC) techniques were used to observe the strain field in crack tip regions. Measurements were performed on pre-notched samples of both shell material and weld material provided by MSFC. Additionally, measurements were performed with multiple resonant and broadband transducers from the major vendors to compare their relative performance for NASA needs. These measurements indicated that while a significant number of AE signals were generated during actual crack extension, signal amplitudes were relatively small, and the principal investigator expressed some concern about their detectability in field conditions. This work is reported in *Appendix I*, *Examination/Analysis of Acoustic Emission Waveform Data from Tensile Testing of Notched Curved Sample of LPV Steel*. Prior to this effort, a study was performed regarding means of minimizing grip noise. *Appendix J*, *Tensile Testing of LPV Material at NIST Boulder* provides study details.

To determine whether AE signals manually generated in the interior layers would be detectable at the outer surface where sensors were attached, a final set of tests was performed on a section of one shell course of V0023 that had been cut from the LPV after completion of AE testing. Since this vessel section was both unpressurized and open-ended (see Figure 12.3.1), its value as an analog to fully pressurized service conditions where shell contact forces are much greater was limited. Rather, it represented a lower bound of the effect of shell tightness on the ability of AE to propagate through shell layers.

To simulate AE events, pencil lead breaks in accordance with ASTM E-1419 (an industry-accepted method for simulating AE events as adopted by *ASME V Article 29* [17]) were initiated at the exposed end of the shell layers. Four different pairs of sensors were placed opposite each other on the inner and outer surfaces of the vessel 66 inches from the exposed ends of the layers to represent typical sensor spacing during a customer field test. The test demonstrated that the AE signal was detectable on the outer surface (where sensors are placed in pressurized vessels) when the source was on the inner-most layer, which is the worst-case location for emission detection. Wave propagation through multiple layers significantly attenuated the amplitude of the acoustic signals, but they were recorded by each of the vendor's sensors nonetheless. Also, the higher frequencies of the signal were more attenuated than the lower frequencies. *Appendix K, Far-Field Wave Propagation Signals from Pencil Lead Breaks on the Open End of a Thick-Walled Layered Cylinder, Part 1: Amplitudes and Frequency Content* and *Appendix L, Far-Field Wave Propagation Signals from Pencil Lead Breaks on the Open End of a Thick-Walled Layered Cylinder, Part 2: Modes of Wave Propagation* document this work.

Since these tests were performed on an unpressurized open-ended shell, layer-to-layer contact was much less than would occur in a fully pressurized LPV, so these results confirmed previous

work performed at Ames Research Center (ARC) demonstrating that sensor placement on the outer shell layer of the LPV was acceptable. In addition, an analytical study addressed elsewhere in this document (Section 11.1, and *Appendix F*) concluded that with variable contact at a small scale, as is likely for a pressurized LPV, the signal is observable on both the inside and outside surfaces.



Figure 12.3.1: A section of V0023 used to determine whether AE signals generated in the interior layers would be detectable at the outer surface.

12.4 Shell-to-Shell Demonstration Ring Inspections

Two shell-to-shell demonstration rings (Figure 9.2.1.1) were produced using shell sections cut from MV50466-8 (the "Digital Wave Vessel" dissected at SwRI). Defects were implanted in the welds of these rings, which were provided (blind) to various vendors to permit experimenting with and demonstrating their techniques.

12.4.1 Guided Wave on Shell-to-Shell Weld on Vessel Section

One vendor evaluated the guided wave method on one of the demonstration rings manufactured from remnants of Vessel MV50466-8 (the vessel cycled at DWC to study AE capabilities) and shown in Figure 9.2.1.1 using magnetostrictive transducers (MST) placed on top of (outside), next to, and on the inside surface of circumferential shell-to-shell welds on the vessel. It was believed that the MST might be excited at a frequency that would produce a guided ultrasonic wave that would travel most of the way, if not all the way, around the circumference of a vessel and that

the received response would have indications of the implanted flaws along the path. This method had proved useful in inspection of single layer underground pipelines (in accordance with requirements found in *ASME V* [17], *Article 19*) and typical solid walled pressure vessels. In those applications, the ultrasound had been directed in the longitudinal direction in the pipe or vessel.

Considerable time and effort were expended attempting to demonstrate this capability with minimal success. The method detected transverse flaws with the MST on top of the weld, but the method could not reliably detect circumferentially-oriented flaws from this position. A second probe placement beside the weld in the area of the HAZ was tried in an effort to detect circumferential defects, but was also unsuccessful. It is believed that this was due to the layered shell sections directly adjacent to the weld impeding the transfer of sound into the weld zone. After evaluation, researchers deduced that for this method to beneficial, the weld cap would have to be removed to allow coupling of the magnetostrictive transducer, just as if PAUT were used Given the weld cap preparation requirements and the limited detection of defects in the remnant, the guided wave method failed to provide an advantage over PAUT in the evaluation of shell-to-shell welds. *Appendix H, Detection of Transverse Flaw in a Root of Multi-Layered Vessel* provides details of this evaluation.

12.4.2 In-House Conventional PAUT

MSFC investigated the possibility of "flat-topping" the shell-to-shell welds of LPVs to facilitate coupling when performing UT inspections. This was done on one of the welds in the ring described in Section 12.4. In-house tests were performed, demonstrating that transverse indications (perpendicular to the weld direction) can be detected, located, and sized reliably using this method on smooth-topped welds, but circumferentially-oriented defects (parallel to the weld direction) still pose a challenge for detection. It is believed that this is because the major dimension of the circumferentially-oriented defects lies parallel to the sound waves produced by the search unit.

Section 12.4.3 provides further information regarding the capabilities of PAUT using a 2D array.

12.4.3 In-House 2D Array PAUT

A vendor demonstration (*Appendix M, Summary of Zetec Inc. Dynaray System Demonstration, Document Number PVS-20-008*) showed that the addition of 2D array techniques would assist in detecting, sizing, and accurately locating flaws that are oriented in directions that are not easily detected using a traditional approach (both axial and circumferential flaws). Section 12.4.4 describes results of this effort. MSFC has purchased a 2D transducer array to permit in-house experimentation with this approach. Equipment purchased for this effort includes a custom made 252 element matrix array probe fitted with an angled wedge capable of producing shear waves in steel at angles between 35 and 70 degrees and a separate wedge that can be used with the same transducer to produce angled longitudinal waves in the part under inspection. A separate 63 element matrix array probe and angled wedge with a much smaller footprint was also purchased for the purpose of locating and characterizing near surface defects on the outside diameter of the

weld. These transducers are driven using a Zetec Dynaray 256/256 instrument and the Zetec Ultravision software for data acquisition and analysis.

12.4.4 Vendor 2D PAUT

During the demonstration of 2D array technology on the layered demonstration ring, Zetec was able to show the technique to be effective for the detection and sizing of axial and circumferentially-oriented defects in “flat-topped” shell-to-shell welds. The results of that inspection are detailed in the *Appendix M, Summary of Zetec Inc. Dynaray System Demonstration, Document Number PVS-20-008*.

13. NDE Field Trials

In the effort to surmount the challenges of LPV inspections, many techniques have been evaluated with varying degrees of success. Equipment to perform the techniques with the highest level of promise has been acquired and employed for further field evaluation and implementation. Confidence in examination integrity depends on demonstrating the capability to locate, identify, and characterize any defects equal in size to the CIFS or larger. For PAUT, for example, this is accomplished by using scan plans designed to detect discontinuities in all orientations, specifying the surfaces from which inspections are to be performed, the ultrasonic beam paths, the scan paths, and the scanning index. The effectiveness of the scan plans is demonstrated on calibration blocks or rings with defects representative of the CIFS that must be found in any particular location and orientation. Efficient development of scan plans is facilitated by the use of ray tracing software that simulates the paths of the ultrasonic waves for defined material configurations. This approach uses software to optimize techniques and to assess prototype calibration block configurations without actually constructing them, reducing the likelihood that multiple actual prototype calibration blocks will need to be produced and tested in the process of producing the final calibration block.

The following sections provide brief discussions of the use of the examination techniques studied and some of the ASME code requirements for their validation.

13.1 Head-to-Shell Weld Inspections

Inspection techniques for LPV head-to-shell welds have evolved from conventional ultrasonic techniques to PAUT. Current PAUT techniques using a one dimensional array appear to be effective for the inspection of head-to-shell welds when working from the vessel head, but implementation may involve use of a 2D array to eliminate equipment changes from the configuration used for the shell-to-shell welds, which are better inspected with the latter technique.

13.1.1 In-House PAUT

MSFC began evaluating the possibility of using PAUT to evaluate LPV welds in late 2012. At that time, only one manufacturer capable of providing a solution beneficial to the effort was identified. MSFC procured this system after thorough evaluation and began to adapt the

equipment, scan plans, and scanning techniques to target the unique inspection requirements of LPVs. The system showed a distinct increase in the probability of detection and defect interpretation/characterization over more conventional ultrasonic methods due to the additional scan views (B, S, and C scan views) afforded to the operator during data review for head-to-shell welds.

The additional information obtained from the PAUT array data has proven to be invaluable in the detection and characterization of defects when compared to conventional ultrasonic techniques. These inspections are performed using traditional phased array ultrasonic equipment that is commercially available off the shelf and is manipulated by a robotic crawler with magnetic wheels. The crawler allows for improved data acquisition and reliability, as well as complete distance encoding along the scan. While greatly facilitating inspections, the crawler may sometimes cause damage to vessel coatings, requiring follow-up paint touch-up to avoid corrosion.

The RMP team qualified a PAUT inspection procedure for thicknesses up to 3 inches in accordance with the *ASME Boiler and Pressure Vessel Code Section V* [17] – *Article 4; Mandatory Appendix IX*. Although this qualification is considered to have a low level of rigor, it appears to be adequate for the inspections of head-to-shell and nozzle welds located in solid heads. This method has repeatedly demonstrated the capability to fully characterize ID and volumetric defects much smaller than the sizes calculated to be the CIF in both locations. The process will also sometimes identify OD-connected flaws, but, unless a procedure has been optimized for this purpose, it will not do so reliably. For OD flaws, surface techniques such as MT, PT, and TECA are more reliable and efficient. Surface flaws contained in the inspection procedure demonstration block are on the order of 0.055 inches shorter in height, but 0.115 inches longer in total length than the CIF size based on analysis. The defect in the block with the shorter height dimension (0.075 inches high x 0.375 inches long) is, in fact, harder to detect and size than what might typically be expected for the CIF size in a circumferential weld. Actual CIF must be the calculated CIF for a surface defect in the circumferential weld in question for the specific vessel and geographical location (and corresponding temperature range) under examination (see *Structural Report* [2] for more details). The accurate detection, characterization, and sizing of the smaller flaws would well qualify the inspection system for larger size defects. The calculated CIF for an embedded flaw would be significantly larger than the size for a surface flaw under the same stress state since the stress intensity factor is higher for the surface flaw.

Performance of the inspection system implies that these defects would also be detected easily.

Since qualification of the PAUT procedure noted above, head-to-shell welds and nozzle welds in solid heads have been inspected in 173 LPVs at MSFC. Many manufacturing defects in the weld volume have been detected and sized. The defects discovered to date have been consistent with expectations for the welding processes used during fabrication, including slag, porosity, undercut (root and cap), lack of fusion, lack of penetration, and an isolated event of verified cracking inside the weld volume emanating from the root area in MSFC Vessel V0111. This particular

head-to-shell crack was excavated to further validate the characterization of defects using PAUT (see *Appendix B*).

All defects found during these inspections were evaluated using fracture mechanics sizing and evaluation criteria found in *ASME BPVC Section VIII* [4], *Division 2*, *Table 7.10* for the corresponding solid wall material thickness. Inspection reports documented any indications that were accepted by this evaluation for future comparison to identify growth, if any. Indications that exceeded this evaluation criteria were rejected, and further evaluation using *API 579 Fitness for Servic*e [21] was performed. Depending on the results of these evaluations, the vessel was removed from service, the defect was repaired, or the vessel was allowed to remain in service with shortened defect monitoring intervals. Any defect growth detected during subsequent inspections would result in reevaluation of vessel fitness for service.

Further research and development may lead to use of nonstandard angles of introduction and reflection of sound, hitting circumferentially-oriented defects from a different direction, thereby causing specular reflection of the sound and resulting in a higher probability of detection. Two-dimensional probes and supporting software have been acquired in hopes that they will allow detection of circumferentially-oriented defects in shell-to-shell welds, and will likely also be used for head to shell welds.

13.1.2 Past Inspections at MSFC

Past inspections at MSFC have included the PAUT inspection of the head-to-shell welds on the entire fleet of 173 LPVs, not all of which are currently in service. During these inspections, suspect areas were identified and evaluated according to flaw acceptance criteria provided in the *ASME BPVC VIII* [4]*, Division 2, Table 7.10*. Indications exceeding the acceptable criterion listed were sized using the ultrasonic data, documented, and evaluated using *API 579 Fitness for Service* [21] calculations. In the instance of Vessel V0111 at MSFC, PAUT provided identification and sizing of the defect, which was then rejected and excavated to validate system capability. After excavation, physical measurement demonstrated that the height of the actual flaw was, in fact, measured accurately within the resolution capabilities of the ultrasonic inspection system.

13.2 Shell-to-Shell Weld Inspections

Surface inspection of shell-to-shell welds on LPVs can be conducted using the same techniques as are used on monolithic vessels. Efforts regarding surface inspections of these welds have therefore focused on techniques that can improve the efficiency of these inspections, either through automation, more efficient processes, or elimination of steps.

Effective inspections of the full volume of shell-to-shell welds on LPVs have heretofore not been possible, so efforts have been directed towards developing techniques that make inspections for critical defects throughout the weld either possible or unnecessary.

13.3 Surface, Outer (TECA, MT) Inspections

After favorable laboratory results during the demonstration of the equipment on the 24 inch LPV head-to-shell block, MSFC field deployed the TECA system in 2019, initially using it for surface examination of LPV longitudinal welds. Surface indications (cracks of approximately 1 inch in length) in the HAZ of longitudinal LPV welds have been detected and sized using the TECA system, and verified on the surface using MT and below the surface using UT.

In field deployment, the deepest defect indication that the system has found is 0.037 inches by 1.075 inches long. Field depth sizing accuracy has been found by comparison to PAUT results to be ± 10-20%, and length accuracy ±0.080 inches. Experiments have been run with some success on "flat-topped" circumferential welds. Two scans have been required to cover the full width of welds plus the HAZ. Mounting the system to the same robotic crawler used for PAUT inspections was originally anticipated, allowing simultaneous surface and volumetric inspections. This has not been possible because of conflicting mounting needs of the two systems.

Experiments have been run with some success on "flat-topped" circumferential welds.

The capabilities of MT for surface inspections of ferromagnetic materials are well known and documented, so no field trials were needed or performed.

13.4 Surface, Inner Inspections

Leak testing and inspection for leaks in the inner shell liner are standard techniques for LPV and no NDE field trials were performed regarding finding leaks.

13.5 Nozzle Inspections

13.5.1 Nozzles (Including Manways) in Heads

For inspection purposes, manways present the same issues and concerns as nozzles, so the term "nozzles" used in this section is understood to apply to manways as well. The inspection of nozzles located in the head sections of the pressure vessels was typically performed using conventional ultrasonic techniques until the application of PAUT. By passing sound through the weld and nozzle shell volumes, weld defects and inclusions and nozzle defects with their major dimension lying perpendicular, or mostly perpendicular, to the sound beams can be reliably detected. As was the case for the head-to-shell welds, the additional views (sectoral S-scan view) constructed from the raw "A" scan data have proved invaluable in evaluating indications in nozzle attachment welds. Use of these views permits assessment of the inside wall of the nozzle. With careful planning of the scan using the actual measured dimensions of the weld cap, and bevel angles shown on manufacturing drawings, the location of most defects can be accurately determined. Not all nozzle defects can be detected at this time, but volumetric flaws can be detected and sized successfully using traditional PAUT techniques.

Based on vendor demonstrations described in Section 12.4.2 of this document, inspection personnel expect that the addition of 2D array techniques will improve both characterization of the flaws described above, and detection, sizing, and locating of flaws oriented in directions that

have heretofore been difficult to identify. A system to test this capability has been procured and testing is in process, but results were not available in time for inclusion in this TM.

A particular flaw of interest is a flaw that originates at the inner diameter of the nozzle wall and extends around the corner toward the root of the nozzle attachment weld. Traditional eddy current using a bolt hole type probe, or angled surface probe will be the method of choice for this inspection. A host of industries has successfully used traditional eddy current for many years to detect this type of flaw.

13.5.2 Nozzles in Shells

Nozzles installed in the layered shell sections of LPVs pose a particular challenge. While fracture mechanics investigations have identified defects on nozzle interiors as among the most critical, most NDE techniques are not successful in identifying and characterizing them when working through a layered shell. Ultrasonic techniques have proved ineffective in the examination of these nozzles due to the inability to pass sound through the layer stack. Radiography cannot be used effectively due to challenges relating to film placement, source alignment, long exposure times, and high contrast due to thickness differences.

To detect these flaws, traditional eddy current testing with conventional long handle bobbin coils or specially made bolt hole type probes is recommended. These methods have been used successfully in the aviation and power generation industries, as well as within NASA for various applications. The bolt hole type probe has a distinct advantage over conventional bobbin coils due to speed of inspection and internal encoding that can more accurately pinpoint the zone containing any defects found. Although the eddy current techniques mentioned require the vessel to be taken offline and the nozzles opened, it is believed that this is the only method currently available that can detect these defects reliably.

13.5.3 GRC Nozzle Inspection, Ultrasonic

Beginning in the 1980s, NASA Glenn Research Center (GRC) developed UT bore probes to perform examinations of PV nozzle full penetration welds from the inside diameter (ID) of the nozzle. These probes were used for a number of years and successfully identified a number of defects within nozzles and nozzle welds. However, because of the inherent limitations of the technique and the technical advantages of eddy current and TECA inspections, the bore probe and calibration standard advancement work has been suspended. In addition, while the calibration blocks used for the bore probes were constructed in accordance with ASME Code criteria, recent discussions have called into question the degree to which the included flaws are representative of actual flaws of concern. Use of this technology is being phased out in light of the demonstrated capabilities of other technologies, but *Appendix N* provides information regarding the probes, their use, and their calibration.

13.5.4 In-House PAUT

It is not possible to perform UT of the shell nozzles from the shell exterior because of the layers, and, because the nozzles themselves are typically fairly short, working from the nozzle itself is difficult. Thus, PAUT of shell nozzles is not anticipated and no significant work was done in this area. While UT from the interior might be used, no work was done in this area as this is a standard inspection technique and because the use of couplants inside the vessel is undesirable.

13.6 Radiography

Radiography has been performed on the demonstration blocks as well as on various LPV, including Vessel V0023. The technique is popular because it is relatively easy to perform, and because it provides a visible and permanent record of features and defects that have been identified, available for later examination by others. (Historically such a record was not available with UT, but now common PAUT systems automatically record all data and produce a permanent electronic record.)

Regions of vessel V0023 indicated by AE as having high activity were radiographed following completion of the AE testing. RT is not always successful in detecting cracks and is dependent on the extent of crack opening and orientation relative to the x-ray beam (source orientation), but, in this case, RT films clearly showed longitudinal weld cracks. Upon dissection of the LPV, it was learned that the cracks were original welding defects, had not been growing, and were clearly open, allowing easy passage of radiation. Hence, the cracks in question were clearly visible using RT.

This study of NDE capabilities used film radiography a number of times. Radiography was used largely as a tool to determine existence and location of specific postulated flaws, and was not a subject of evaluation during the study. In some cases, an LPV weld was radiographed and the results compared to the PAUT inspection data. RT and PAUT findings were compared to look for correlations with the knowledge that the two methods typically complement each other in detection of certain flaws. This complementary behavior held true for weld defects. PAUT excelled at the detecting cracks and planar defects, and RT effectively detected rounded or other volumetric defects where traditional introduction of a sound beam would not produce enough reflection for effective detection. RT also detected open cracks in the vessel layer weld regions after AE testing had identified a suspect area.

13.6.1 V0023 Pre-Dissection

During evaluation of the AE testing method, MSFC made available an LPV (Vessel V0023, previously described in Section 7.2.5 and in the AE testing procedures in Section 12.3). This vessel had been identified during the 1980s as having an AE “crack-like signature” and MSFC removed the vessel from service at that time. Locations with anomalously high sound sources were identified by MSFC AE testing personnel during recent testing (2016) and flagged for further evaluation to better understand the source of the AE signals. These areas were located in the shell acreage away from a shell-to-shell weld zone. Due to their location and the pressure

vessel wall thickness, film radiography using the Cobalt 60 isotope was determined to be the best NDE method for the potential evaluation of these indications.

The panoramic RT technique (Figure 13.6.1.1) was chosen for efficient exposure. A 3/16 inch aircraft cable with 2 inch sections of 3/8 inch stainless tubing threaded onto it was introduced into the vessel ID through the nozzle at each end of the vessel, one end of the cable affixed to a bar across the flange and a chain come-along (ratcheting tensioner) used to pull tension from the opposite end. The 2-inch sections of tubing provided a movable point to which the guide tube for the exposure device could be attached and moved to the correct position for exposure inside the vessel. The outside of the suspect area was wrapped with film and the exposure recorded. After development and film review, several areas of layer cracking were noted in the weld and heat affected zone of intermediate layer longitudinal welds. These areas were flagged for further dissection and evaluation by destructive testing. After dissection, it was obvious that the cracks identified with RT were open and radially-oriented, and also that they were original weld defects that had not grown during the life of the LPV (Figure 13.6.1.2 through Figure 13.6.1.4).

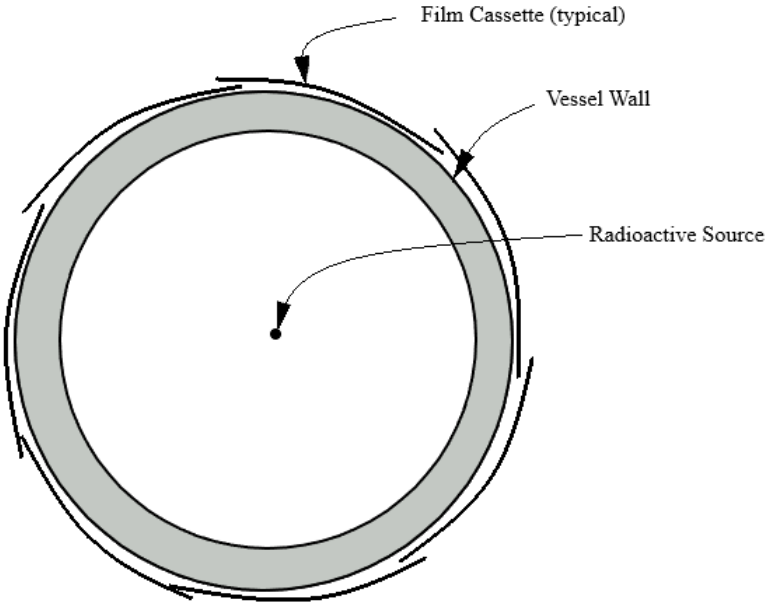


Figure 13.6.1.1: Panoramic radiographic exposure.

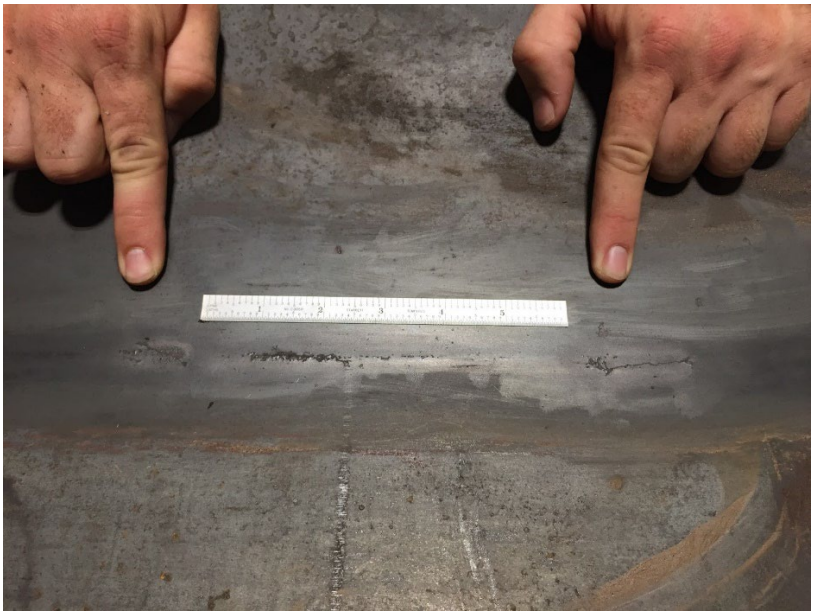


Figure 13.6.1.2: Surface connected crack associated with a longitudinal weld.



Figure 13.6.1.3: Detail view of surface connected crack associated with longitudinal weld.

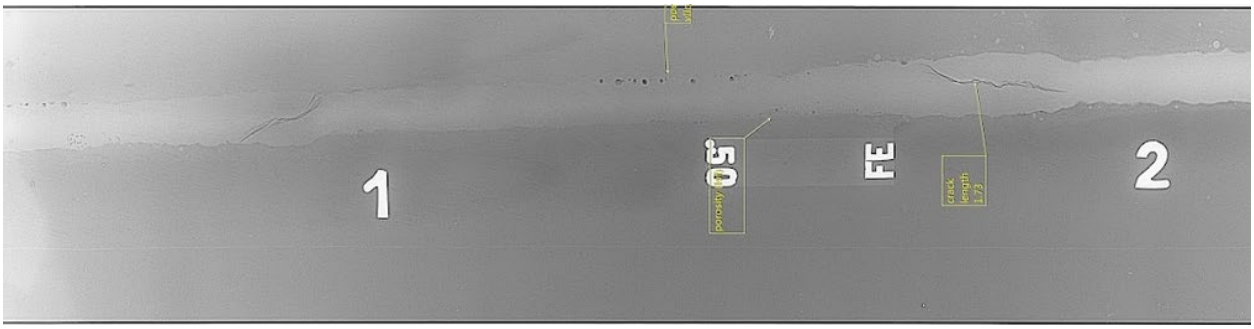


Figure 13.6.1.4: Radiograph of longitudinal weld with cracks and porosity.

13.6.2 Field Radiography

This Section describes the radiographic examination techniques and interpretations that have been historically utilized by NASA GRC for LPVs. It also describes the procedures developed to utilize radiography to examine LPV full penetration welds as required by the current *ASME B&PV Code* [4]. Interpretation of LPV weld radiography can be difficult unless there is a clear understanding of the joint design, discontinuities, welding, examination procedures, and code acceptance criteria. Although LPV manufactures' designs vary and the radiography techniques described within this Section focus on typical GRC A.O. Smith circumferential head-to-shell and shell-to-shell weld designs, the basic techniques are valid for similar vessels produced by other manufacturers as well. The head-to-shell weld design examined is limited to a monolithic head welded to a shell consisting of multiple concentric wraps (see Figure 13.6.2.1). The shell-to-shell weld design examined consists of a full penetration circumferential weld of layered shell course to layered shell course (see Figure 13.6.2.2).

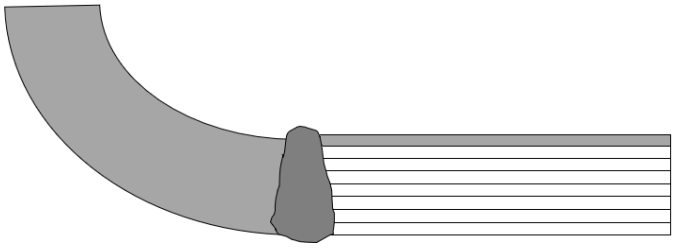


Figure 13.6.2.1: Monolithic head-to-layered shell weld

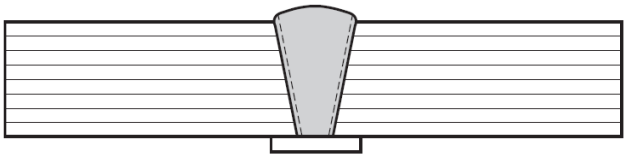


Figure 13.6.2.2: Layered-to-layered shell weld

13.6.2.1 Radiography Techniques

The panoramic exposure is created when the radiographer places the source of radiation at the center of a pressure vessel (Figure 13.6.1.1). The film cassettes are placed on the outside of the surface to be examined. This exposure arrangement is preferred for its efficiency. When properly arranged and exposed, all portions of all exposed film will be of approximately the same density. In panoramic exposures, the radiation only penetrates the wall being viewed, as opposed to both walls in the case of a double wall shot, in which the source is on the opposite side and outside of the vessel. A panoramic exposure typically examines a full circumferential weld in a single shot, while double wall exposures typically require at least three shots to show the full circumference of a vessel. Penetrating only a single wall reduces the exposure time significantly (as an estimate, for a 1 inch iron wall thickness, the ratio is about 5 and for a 2 inch iron wall thickness, the ratio is about 23.). Finally, because the source-to-film distance is reduced by a factor of two, exposure time is reduced by an additional factor of about four. The use of panoramic exposures is a well-accepted technique which is regularly employed for inspection of pressure vessels, whether monolithic or layered.

13.6.2.2 Image Quality Indicator and Quality Level

The purpose of an Image Quality Indicator (IQI) is to indicate the overall sensitivity of a technique, providing a measure of how well the radiograph reveals discontinuities. An IQI is a device made from the same material as the test specimen. It is placed on the test specimen in the general area of investigation in a position where its image will be recorded on the radiograph without obscuring the area of interest.

The quality of a radiographic image can be assessed in terms of three factors:

1. Image Sharpness. Usually in radiography, the inverse of sharpness – unsharpness or blurring – is used.
2. Image Contrast. Image contrast is the density change on a film for a given thickness change in the specimen. If a small image detail shows only faintly, this is a low contrast image. If the image detail is easily seen, this is a higher contrast image.
3. Image Noise. For film radiography, image noise is effectively graininess. In radioscopy, other factors affect image noise.

A good IQI design shows changes that occur in any of these three factors. The applicable standard for hole-type IQIs is *ASTM E1025-18 Standard Practice for Design, Manufacture, and Material Grouping Classification of Hole-Type Image Quality Indicators (IQI) Used for Radiography* [22].

The quality level usually required for radiography is 2% (2-2T when using hole type IQI), unless a higher or lower quality is agreed upon between the purchaser and the supplier. At the 2% subject contrast level, three quality levels of inspection (2-1T, 2-2T, and 2-4T) are available through the IQI design and application (*Practice E1025* [22]*, Table 1*). The quality level designation's first number refers to IQI thickness expressed as a percentage of specimen thickness. The second number refers to the diameter of the IQI hole that must be visible on the radiograph expressed as a multiple of penetrometer thickness (T).

Other levels of inspection are available in *Practice E1025, Table 1*. The specified inspection level should be based on the service requirements of the product. Great care should be taken in specifying quality levels 2-1T, 1-1T, and 1-2T by first determining that these quality levels can be maintained in production radiography. Since this application of radiography is to non-code pressure vessels, the flaw sizes determined to be acceptable by the ASME BPVC may not apply. Thus, while use of an IQI ensures a certain quality level for the radiograph, assessment must also be performed of the capability of the technique to identify the critical initial flaw, as well as to determine the appropriate IQI to ensure its detection.

It should be noted that even if 2-2T sensitivity is indicated on a radiograph, a defect of the same diameter and material loss may not be visible. The holes in the IQI represent sharp boundaries and a small thickness change. Discontinuities within the part may contain gradual changes and are often less visible. The IQI is used to indicate the quality of the radiographic technique and is not intended to be used as a measure of the size of a cavity that can be located on the radiograph.

13.6.2.3 Joint Layout and Interpretation

Film interpretation of layered-to-layered and layered-to-solid welded joints (Figure 13.6.2.3.1) is critical to the acceptance of the weld joint and can be difficult due to layer wash. *ASME BPVC, Section VIII, Division 1* [4] *Part ULW Requirements for Pressure Vessels Fabricated by Layered Construction* states that layer wash indications result from slight weld penetration at the layer interfaces. Layer wash can be difficult to distinguish from slag on the radiographic film, therefore experience in the interpretation of LPV weld radiography is critical.

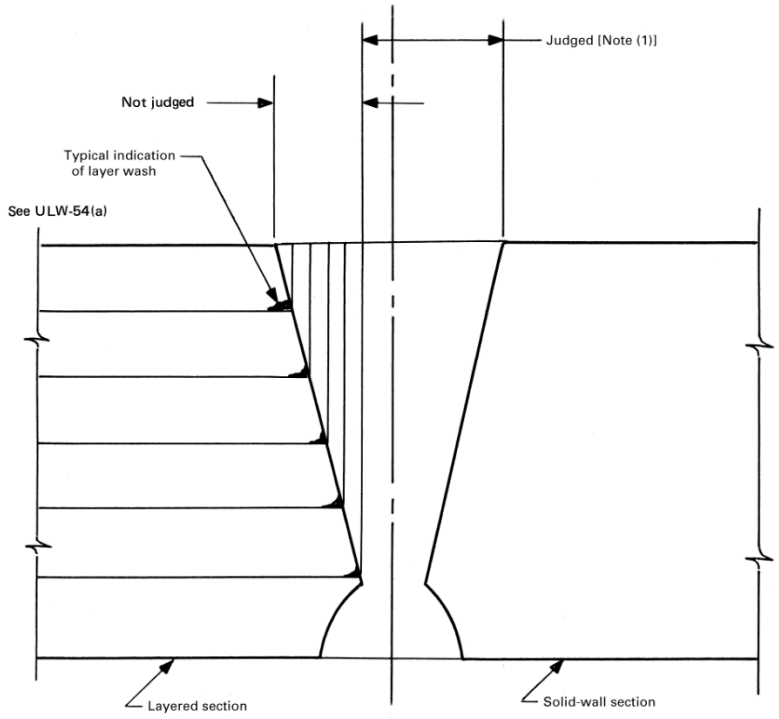


Figure 13.6.2.3.1: Weld between a layered and a solid-wall section.

The actual RT procedure used by NASA GRC to perform radiography for multilayer weld flaw detection is provided in *Appendix O, GRC Radiographic Specification for A.O. Smith PV.*

13.6.3 Cautions Regarding Use of Radiographic Testing

The ASME BPVC has included RT at least since the 1940s. It specifies the use of RT for the inspection of certain original construction configurations as a means of detecting slag, porosity, cracks, and other volumetric welding defects. The film is exposed by radiation passing through the component. Thicker areas of the part will stop more radiation resulting in light areas on the film relative to thinner areas. Thus, areas of reduced total material thickness, such as zones of porosity, will show dark on the film. Areas of greater thickness, such as zones of excessive welding reinforcement, will result in lighter areas on the film (as will tungsten inclusions resulting from improper technique when using gas tungsten arc welding).

Vessel V0023 at MSFC has been extensively examined using a number of techniques. RT identified a number of cracks in this vessel. When the vessel was dissected, it was determined that the RT had been very effective at identifying both the location and extent of all of these defects. The cracks in question were original welding defects which were perpendicular to the plate surface (aligned with the direction of the radiation) and were open. Thus, they provided a clear path of reduced thickness for the radiation to pass through on its way to the film.

Identification of such defects using RT has, at times, led to the assumption that cracks are generally observable on radiographs and that the crack growth can be monitored using RT. Because growing cracks often have very small crack openings, and because they are not always in the direction of the radiation, the ability to detect them using RT is inconsistent. Inspectors are aware that cracks detected using RT are often found to be of greater extent when follow-up PT or MT is performed. In such cases, the RT has failed to characterize accurately the extent of the cracks, making it generally undependable as a crack growth monitoring technique. This can occur either because a crack is closed at the ends or, in some cases, when the crack twists and no longer causes a significant reduction in the thickness of material through which the radiation must pass.

Explanations of the difficulty of locating the ends of a crack using RT include the following:

(1) If the crack follows the grain boundaries, which might be described as interlocking, and if it is not open, then there is no direct path for the radiation to follow from the source to the film and no zone of significantly reduced thickness through which the radiation can pass. RT will then see the crack area as no different from the surrounding metal.
(2) It is common for a surface or embedded crack to have greater depth in the middle, tapering to near nothing at the ends. In this case, even an open crack may not be deep enough at the ends to result in an indication on the film.
(3) Not all cracks will be oriented in the direction of the radiation. For monitoring purposes, this may present a particular challenge, since a small change in the location of the radiation source can result in a sufficient change in angle, such that the crack and the direction of the radiation are no longer aligned. Non-aligned cracks may show on a radiograph if they are sufficiently open. The required degree of alignment of the crack and radiation beam for a given crack opening for reliable RT detection may be calculated approximately using the thickness of the penetrameter used to verify the quality of the inspection.

Thus, while RT is a useful tool for identifying welding defects and will successfully identify some cracks, it should not be used as the sole means of inspecting for them. It is more valuable for finding other welding defects that might cause cracking, following which such techniques as PAUT may be more applicable. RT may also be more effective if multiple radiographs are produced, varying the angles of the shots, but this is generally impractical.

13.7 Layer Efficiency

The construction of a monolithic pressure vessel results inherently in a sharing of the pressure load across the vessel wall. While the actual stress at any point in the wall is affected by other factors such as residual stresses and local material properties, the possibility of shall layers being individually loaded or unloaded does not exist as it does in an LPV.

Layered construction offers the possibility of layer gaps and of bridging at longitudinal welds, both undesirable features that can result in an unequal loading distribution among the layers with the potential for overstress. It is not possible to ensure completely against unequal loading of

shell layers, but it must be controlled. NASA has evaluated these effects extensively in this Program, and the structural report Reference [3] provides more information in this area.

The *ASME BPVC VIII-1* [4] and *VIII-2* [4] first included LPVs in 1977. Both the 1977 ASME Code and the current ASME Code offer two ways of addressing the problem of layer gaps for code LPV's. *ASME BPVC VIII-1* [4], paragraph *ULW-77* requires measurement of gaps at the ends of shell courses prior to vessel assembly, and *ULW-78* provides an alternative to this, allowing measurement of circumferential growth under pressure instead, performed at the time of the vessel hydrotest.

Since most NASA LPV's were constructed prior to 1977 (thus, not in accordance with the applicable codes) and detailed documentation is typically lacking, it is not known whether such measurements to determine the extent to which the pressure load is effectively shared among layers were performed by the original manufacturers.

Because the LPVs in the NASA fleet are already fabricated and have no record of layer gap measurements and there is no possibility of measuring layer gaps directly, NASA has often used the *ASME VIII-1* [4]*, ULW-78* circumferential growth measurement as a means of assessing the effectiveness of load distribution among layers, albeit only up to maximum normal operating pressure.

Since most NASA LPVs are non-code pressure vessels, this information on code requirements is provided as background regarding what has been found acceptable in practice in code construction of LPVs, but may not entirely apply.

The ASME Code requires that when the circumferential expansion of the shell courses is used as a measure of load-sharing effectiveness, the expansion must be measured midway between adjacent circumferential joints or between circumferential joints and any nozzles in a shell course. The average expansion for any shell course must not be less than 0.5 times the theoretical value using the equation shown in *ASME VIII-1, ULW-78(b).* (This value was not arrived at by analysis, but rather was agreed on by manufacturers as a value that they were generally confident of meeting.) While not ensuring uniform loading, it ensures, at least to some extent, that the pressure loading is distributed throughout the layers. This report uses the term “efficiency” as a brief way of referring to LPV expansion ratios during pressurization.

The usual way of measuring vessel circumferential expansion is through the use of a Pi Tape. A Pi Tape is a precision measuring tape, graduated in increments of pi inches and with a vernier scale to permit reading measurements with a precision of 0.001 inches of diameter. Such tapes are commonly used in machine shops for accurately measuring machined cylinders too large to be measured easily with micrometers or calipers. Although they are graduated in units of pi inches and thereby read in inches of diameter, it should be noted that these tapes actually measure circumference. Thus Pi Tape measurement meets the requirement of ULW-78 that the increase in circumference in going from zero pressure to design pressure be measured, and the vernier scale or digital readout that is available ensures that it can be read accurately.

Observations regarding use of circumferential growth measurements for pressure vessels:

(1) A rolled and welded shell may be expected to vary slightly in dimension over its length. Therefore, for repeatability and for comparison of measurements, the measurement must be taken at the same location each time.
(2) The longitudinal weld(s) of a shell course are typically not ground-flush and often have a varying contour. Special care is thus needed to ensure that the tape crosses each longitudinal weld at the same place each time the shell course is measured. The place at which the tape is actually read should not be over a weld or other discontinuity on the shell surface, and the shell zone in which measurement is taken should be reasonably clean so that dirt or debris under the tape does not result in an apparent increase in diameter.
(3) Accurate measurement requires that the tape measures a circle, not an ellipse which would have a larger circumference. If care is not taken to ensure that the tape lies in a plane perpendicular to the axis of the vessel, either an ellipse or an undulating curve will be measured. If this occurs, then, while placing the tape in the same location for two measurements would result in dimensions that could be compared to each other, this would result in a measurement greater than the actual circumference/diameter of the vessel.
(4) The Pi Tape measures circumference divided by pi, not true diameter, since a vessel is rarely truly round.
(5) It is possible to misread the Pi Tape in several ways, resulting in an incorrect measurement.

The effects of observations (1)-(3) are mitigated if measures are taken to ensure that the tape follows the same path around the LPV for all measurements, that it is pulled taut, and that it is jiggled back and forth to ensure that the minimum dimension is measured. Observation (4) need not be a concern, but personnel using the information should be aware that out-of-roundness can be a separate issue. Observation (5) is a significant concern, but can be mitigated by taking extreme care in reading the measurement, having two people read the measurement separately, and by photographing the tape for each measurement, so that measured values can be verified later, and errors rectified if needed.

Appendix P, Circumferential Growth Measurement of Layered Pressure Vessels, provides a recommended procedure for this measurement on legacy vessels.

Unusual layer gap and load distribution could result in meeting the 0.5 requirement while significantly overloading one or more layers, but devising a realistic configuration in which this would be the case is difficult. Thus, to some degree, the expansion ratio can be considered to provide an assessment of the loading efficiency of the system.

During the pressurization of Vessel V0023 for AE testing, it was observed that the expansion of the outer layer lagged the theoretical values during the early part of pressurization, but that later in the process expansion continued more or less as expected. Similarly, during the early part of the pressurization cycle, non-relevant AEs (e.g., noise due to friction, rubbing, etc.) were at a relatively high level, then dropped to a lower, more expected value. Both phenomena, which

essentially coincided, could be explained by the existence of layer gaps that gradually closed under pressurization, resulting finally in a condition under which all layers were sharing additional pressure loads as they were applied. Until the layers achieved essentially 100% contact, motion and rubbing between layers could be expected, producing the observed AE. At the same time, the outer layer would not be fully engaged in carrying the pressure load until the gaps had closed.

It is further noted that the probability of AE testing detecting relevant emissions from inner layers improves as pressure rises in a vessel and contact between the layers becomes more uniform. *Appendix F: Simulation Work for Layered Pressure Vessels,* documents theoretical work in this area and provides a discussion of the extent to which sound may be transmitted between layers in the absence of complete contact.

13.7.1 ARC 16-Bank and MSFC 19-Bank Circumferential Growth Measurements

13.7.1.1 Layer Effectiveness Ratio

Pi Tape measurements provide an assessment of the degree to which the outer layers of an LPV share the pressure loading in the vessel. Comparison of the actual expansion of the outer layer of each shell course of an LPV to the theoretical expansion obtained from the equation in *Section ULW-78 of ASME BPVC Section VIII, Division 1* [4] is used for this assessment. The layer effectiveness ratio obtained in this way doesn't provide definitive information as to stress values in individual inner layers. If the value is sufficiently high, however, it provides a reasonable level of confidence that inner layer stress is not excessive. Also, with carefully developed assumptions, it can be used to calculate probable bounding values for stresses in the shell liner and inner layers.

In this study, vessel efficiency (η) was quantified using circumferential growth measurements for 16 LPVs at ARC and 19 LPVs at MSFC, all fabricated by A.O. Smith. The ARC LPVs have 9 shell courses each, resulting in a total of 144 measurements, while the MSFC vessels have 2 courses each, for a total of 38 measurements. The ARC vessels are mounted horizontally and the MSFC vessels are mounted vertically. Vessel orientation is not anticipated to affect efficiency in any way, but measurements are considerably easier to perform on horizontal vessels than on vertical vessels because the Pi Tape has less tendency to slide out of alignment. In addition, to ensure measurement accuracy, the diametric expansion of the MSFC vessels was measured twice at each location on the vessels and photos were taken of the Pi Tape measurements for later verification.

To calculate the diametric expansion (δ_{OD}), Pi Tape measurements of the diameter were recorded for both an unpressurized (or nearly unpressurized, ≤ 50 psi) and a pressurized state. Because the manufacturer's nameplate maximum allowable working pressures (MAWP) (3500 psi for ARC, 4400 psi for MSFC) exceed those allowed by the ASME BPVC, pressures have been downrated, with new MAWP and operating pressures established.

provides information regarding operating and testing parameters (pressures in psi). Both sets of vessels have considerable risk mitigations. The ARC vessels are enclosed within a significant berm designed to contain a vessel half in the event of a failed circumferential weld mid-vessel, while the MSFC vessels are located in a relatively isolated area of the Center, to which access is limited.

Table 13.7.1.1.1: Vessel Rating and Growth Measurement Parameters (Pressures in psi)

	ARC	**MSFC**
Mfr. Nameplate Rating	3500	4400
MAWP (Factor of Safety of 3)	2946	3874
Current Relief Valve Setting	3150	3100
Current Operating Pressure	3000	2950-2975
Growth Measurement Upper Pressure	2950-3000	2780-2950

13.7.1.2 Efficiency Calculation and Extrapolation

The efficiency at the down-rated pressure of each shell course was calculated according to Equation (1), in which $\delta_{OD,actual}$ is the Pi Tape measured diametric expansion and $\delta_{OD,theoretical}$ is the calculated diametric expansion for a monolithic vessel of equivalent geometry based on *ASME VIII* [4] *Division 1 or 2* (both standards use the same formula).

$$\eta = \frac{\delta_{OD,actual}}{\delta_{OD,theoretical}} \quad (1)$$

Note that the measured efficiency is a function of the internal pressure, but once the efficiency is known for one internal pressure, the efficiency at another pressure can easily be approximated using Equation (2).

Equation (2) provides a simplified expression for calculating the vessel efficiency at additional internal pressures based on the relationship between the theoretical closure pressure ($P_{closure}$) and the applied internal pressure ($P_{applied}$). This formulation assumes that the outer shell layer does not begin to expand until the internal pressure reaches $P_{closure}$. It also assumes that the outer shell layer is carrying its full share of the additional load once $P_{closure}$ is reached. The outer layer only takes its share of the additional loading and never takes over loading that occurred in closing gaps between layers at pressures below $P_{closure}$. These assumptions ignore the reality (1) that some expansion does takes place prior to $P_{closure}$ and (2) that the outer shell layer does not take its full share of the additional load until some higher pressure, denoted as

P_{solid}. Figure 13.7.1.2.1 illustrates the difference between the actual expansion of the outer layer and the assumed expansion inherent in the formulation of Equation (2).

$$\eta = 1 - \frac{P_{closure}}{P_{applied}} \tag{2}$$

Notice that when $P_{applied}$ is in the vicinity of $P_{closure}$, the assumed expansion of the outer layer deviates significantly from the actual expansion and, by extension, Equation (2) breaks down. However, if $P_{applied}$ is significantly greater than $P_{closure}$ (at least 50 percent greater than $P_{closure}$, meaning that $P_{applied}$ is likely greater than P_{solid} as well) , the assumed expansion provides a sufficient estimate of the true expansion. Adding a correction term to Equation (2), such as $\frac{\delta_{OD,closure}}{\delta_{OD,theoretical}}$, where $\delta_{OD,closure}$ is the diametric expansion at $P_{closure}$, may provide a better estimate of the efficiency throughout pressurization of the vessel, but obtaining an accurate measure of $\delta_{OD,closure}$ proves to be difficult and would limit the ease of use and practicality of the current formulation. It should further be noted that the inaccuracy of Equation (2) in the vicinity of $P_{closure}$ and the difficulty of accurately determining $P_{closure}$ limit the value of this modeling at relatively low pressures. However, at such pressures, stresses are relatively low, so the need for such modeling is greatly reduced and the value of taking measurements of circumferential growth is likewise limited.

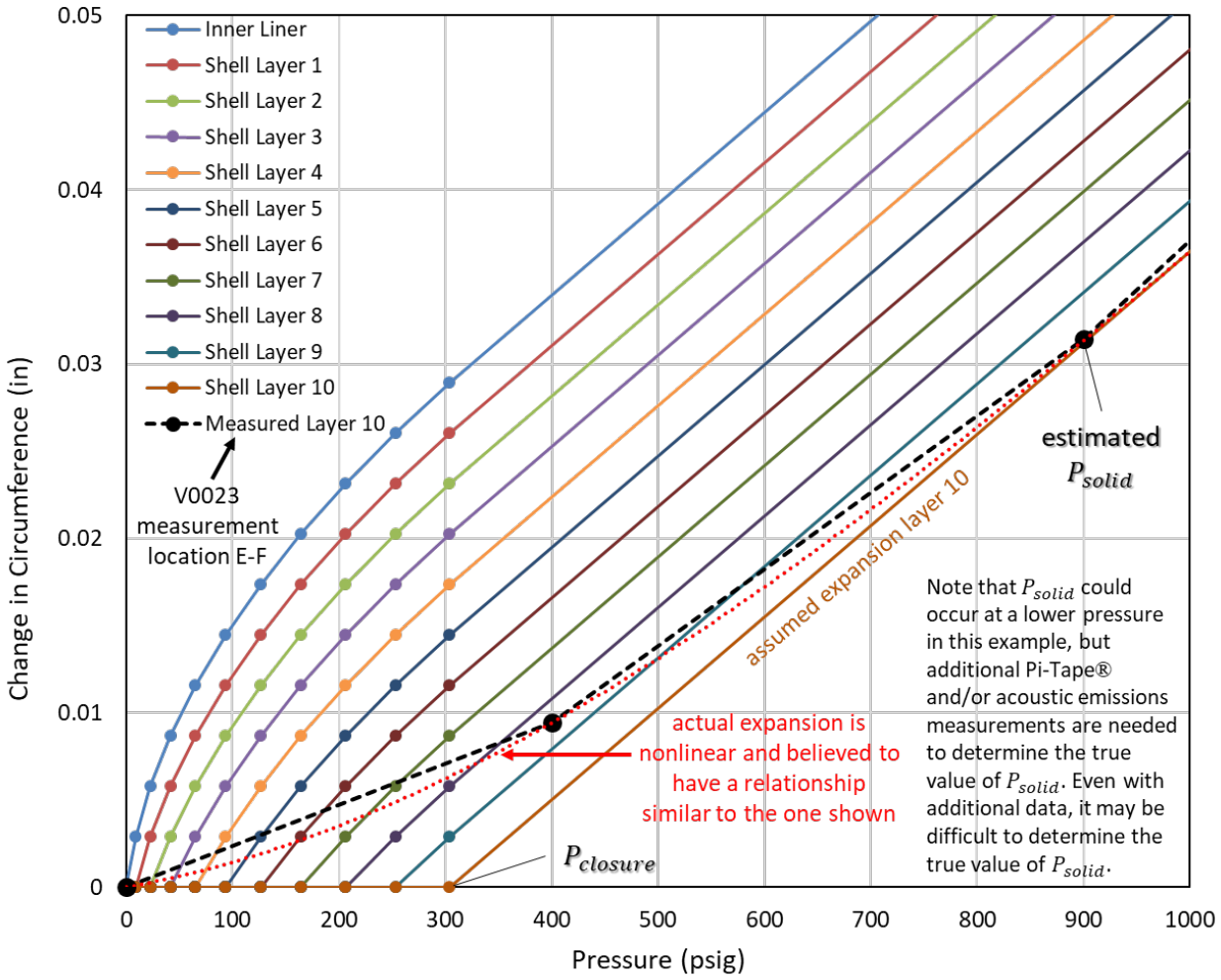


Figure 13.7.1.2.1: Conceptual illustration of the difference between the actual and assumed expansion of the outer shell layers in an example 11-layer LPV based on V0023 measurement location E-F, which had a measured efficiency of 90.2 percent at 3100 psi (see *Appendix Q*). The actual expansion is nonlinear and begins prior to $\boldsymbol{P_{closure}}$.

In order to estimate the efficiency at a new pressure after using Equation (1) to determine the efficiency at the test pressure, first, $P_{closure}$ is calculated by rearranging Equation (2), for which $P_{applied}$ is the internal pressure at the time of the measurement of circumference. Then, the efficiency at the new pressure can be calculated via Equation (2) again, using the previously determined $P_{closure}$ and setting $P_{applied}$ equal to the new pressure. Equation (2) provides a sufficiently accurate representation of efficiency if $P_{applied}$ is significantly greater (at least 50 percent greater) than $P_{closure}$. If $P_{applied}$ is not significantly greater than $P_{closure}$, then the efficiency estimate using Equation (2) may be non-conservative. Using V0023 measurement location E-F as an example (see *Appendix Q*), the vessel efficiency can be determined from the Pi Tape measurements at 3100 psi according to Equation (1) and $P_{closure}$ can be calculated by rearranging Equation (2):

$$\eta = \frac{\delta_{OD,actual}(3100\text{ psi})}{\delta_{OD,theoretical}(3100\text{ psi})} = \frac{0.046\text{ in}}{0.051\text{ in}} = 0.902$$

$$P_{closure} = -(\eta - 1) \cdot P_{applied} = -(0.902 - 1) \cdot 3100\text{ psi} = 303.8\text{ psi}$$

Now consider what would happen if a circumferential measurement was unknowingly taken at $P_{closure}$. Assume that neither vessel efficiency nor $P_{closure}$ are known and a Pi Tape measurement was taken at 303.8 psi. Equation (2) makes the simplifying assumption that Layer 10 does not expand prior to $P_{closure}$, however Figure 13.7.1.2.1 shows that expansion of the outer layer does occur prior to $P_{closure}$. Since there is not a Pi Tape measurement at $P_{closure}$, it is unclear exactly how much outer layer expansion has occurred once the internal pressure equals $P_{closure}$. Based on the depiction of the "actual expansion" shown in Figure 13.7.1.2.1 as the red dotted line, the circumferential change of the outer layer at 303.8 psi is roughly 0.0057 inches, which equates to approximately 0.0018 inches of diametric expansion. Thus, assume a Pi Tape measurement is taken at 303.8 psi and the measured diametric expansion is 0.0018 inches, then, according to Equation (1), the measured efficiency would be:

$$\eta = \frac{\delta_{OD,actual}(303.8\text{ psi})}{\delta_{OD,theoretical}(303.8\text{ psi})} = \frac{0.0018\text{ in}}{0.0051\text{ in}} = 0.353$$

Again, assuming that vessel efficiency and $P_{closure}$ are not known, the next step is to calculate $P_{closure}$ using Equation (2) based on a measured efficiency of 35.3 percent at 303.8 psi, as shown:

$$P_{closure} = -(\eta - 1) \cdot P_{applied} = -(0.353 - 1) \cdot 303.8\text{ psi} = 196.6\text{ psi}$$

This estimated $P_{closure}$ is inaccurate, but there is no indication of the inaccuracy unless the true $P_{closure}$ or vessel efficiency at (or near) MAWP or the relief valve setting is known beforehand. Then, in order to estimate the efficiency at MAWP or the relief valve setting, Equation (2) would again be employed and would yield a non-conservative estimate for efficiency:

$$\eta = 1 - \frac{P_{closure}}{P_{applied}} = 1 - \frac{196.6\text{ psi}}{3100\text{ psi}} = 0.937$$

Therefore, this example highlights the importance of taking the pressurized circumferential growth measurements at an internal pressure ($P_{applied}$) that is significantly greater (at least 50 percent greater) than $P_{closure}$. If these measurements are taken too close to $P_{closure}$ and Equation

(2)is used to estimate the efficiency at a higher internal pressure, then the estimated efficiency at the higher pressure may be non-conservative.

To mitigate the possibility of inaccuracies and non-conservative results, circumferential growth measurements should be taken in accordance with Section 14.9.1, which requires that the pressurized measurement be taken at a pressure above the closure pressure for an assumed 40 percent efficient vessel. If the measured efficiency is greater than or equal to 50%, the other prescribed inspections and assessments of the vessel must still occur, but no further efficiency evaluation is required. However, if the measured efficiency is less than 50%, then further investigation is necessary. The pressure used in the pressurized Pi Tape measurement along with the measured efficiency dictate the options for further investigation. If the pressurized Pi Tape measurement was taken at a pressure less than MAWP and the measured efficiency is greater than or equal 40%, then Equation (2) can be used to estimate the efficiency at MAWP. If the pressurized Pi Tape measurement was taken at a pressure less than MAWP and the measured efficiency is less than 40%, then Equation (2) cannot be used to estimate efficiency at a higher internal pressure because it may give nonconservative estimates. Instead of using Equation 2, the efficiency must be re-measured at a higher internal pressure to ensure accurate results if the measured efficiency is less than 40 percent. Ultimately, if the efficiency at MAWP is greater than or equal to 50%, then no additional efficiency investigation is necessary, but if the efficiency at MAWP (or as close as possible to MAWP, for cases in which it is not possible to re-take the pressurized measurement at a higher pressure and Equation (2) cannot be used to calculate the efficiency at a higher pressure) is less than 50% the vessel must be removed from service or further investigation performed. Vessels with an efficiency of less than 50% at MAWP are out-of-family compared to nearly all of the data collected in this study, and such a low efficiency indicates inadequate sharing of the load among layers. A helpful decision tree that summarizes this information and can be used to determine whether additional investigation is necessary is provided in Recommendation Section 14.9.2 on Efficiency Calculation (see Figure 14.9.2.1).

Another important consideration when taking circumferential growth measurements is the vessel temperature at which the pressurized and unpressurized measurement are taken. If there is a difference between the vessel temperature at the time of the pressurized and unpressurized measurements, then thermal expansion/contraction of the vessel must be accounted for in the calculation of the diametric expansion, $\delta_{OD,actual}$, as shown in Equation (3).

$$\delta_{OD,actual} = \left(OD_{press} - OD_{unpress}\right) + OD_{unpress} \cdot \alpha \cdot (T_{press} - T_{unpress}) \qquad (3)$$

Where OD_{press} is the measured outer diameter of the pressurized LPV, $OD_{unpress}$ is the measured outer diameter of the unpressurized LPV, α is the coefficient of thermal expansion for the vessel material (6.5×10^{-6} F^{-1} for steel in this program), T_{press} is the vessel temperature at the time of the pressurized diameter measurement, and $T_{unpress}$ is the vessel temperature at the time of the unpressurized diameter measurement. A measurement temperature difference may

result in as much as roughly a 1% efficiency change per degree of temperature change. Note that T_{press} and $T_{unpress}$ should reflect the bulk metal temperature and individuals taking the temperature readings should be careful to avoid locations of the vessel at which the surface temperature is not representative of the bulk metal (e.g. localized sun-lit regions on the vessel).

13.7.1.3 ARC 16-Bank Circumferential Growth Measurements

Each shell course efficiency measurement was treated as an independent sample because shell courses were fabricated independently prior to being joined together by circumferential welds. Of the 288 shell course measurements taken at ARC, 3 were identified as erroneous due to either a misread or transcription error, resulting in calculated efficiencies at 2946 psi internal pressure of -99 percent, -13 percent, and 245 percent (see *Appendix R*). Figure 13.7.1.3.1 shows a histogram of the vessel efficiency at 2946 psi (the MAWP for a factor of safety of 3) based on the circumferential growth measurements after the removal of the three erroneous data points (but including the two anomalous but credible measurements discussed later in this section).

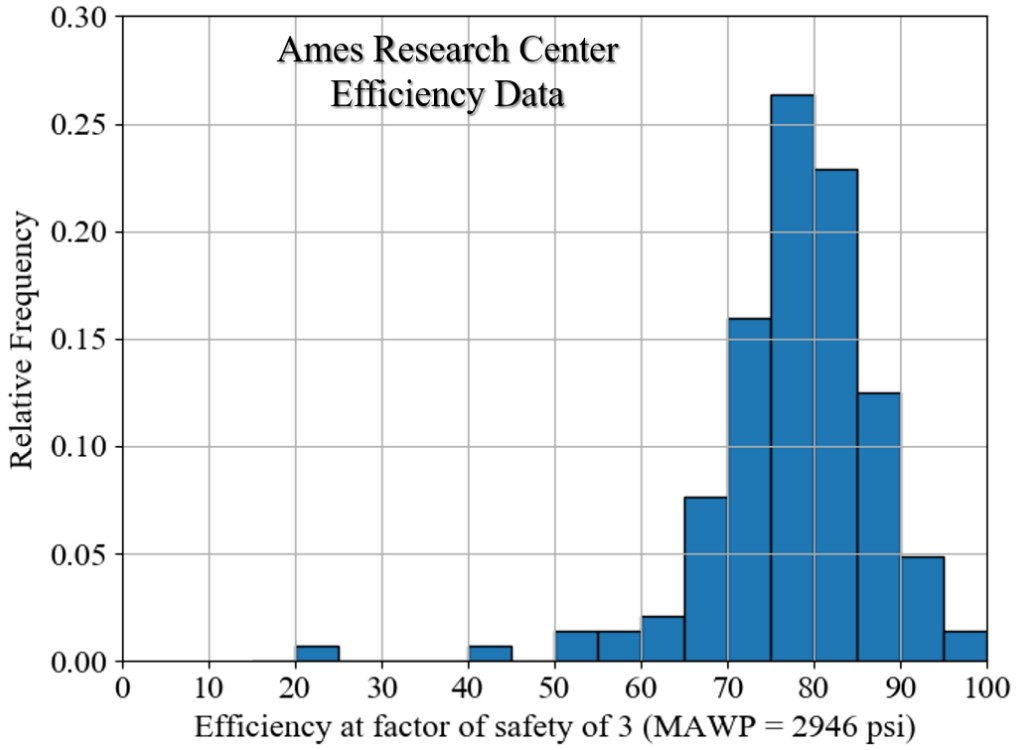


Figure 13.7.1.3.1: Histogram of vessel efficiency measurements of 141 shell courses from 16 LPVs at ARC at N250A.

The *ASME BPVC Sec VIII* [4] requires either measurement of layer gaps prior to placement of circumferential welds during fabrication, with specific limits on gap size and area, or measurement of circumferential growth at design pressure following the hydrotest. If the circumferential growth measurement is used, the *ASME BPVC* [4] requires that new LPVs have an efficiency greater than 50% at design pressure. None of the vessels involved in this

circumferential growth testing was fabricated in accordance with the *ASME BPVC*, since the Code at the time did not cover LPVs. No information is available as to whether any growth measurements were made during fabrication of these LPVs. The same holds true for the majority of the NASA fleet of LPVs, with only three LPVs being ASME Code stamped. Thus, the assumption that the original efficiency of each shell section exceeded 50% based on original measurements is not possible.

Two shell course measurements are well below 50%, one having a measured efficiency of 21.5% and the other having a measured efficiency of 42.9%. It is possible (even probable, since AE testing did not indicate any abnormalities in this vessel) that these are also measurement errors given the consistency of the other 139 shell courses measured, but these are not unrealistic values and, if correct, indicate that the outer layer of the shell course is not sharing the load properly. Note that failure of the outer layer to accept its share of the load is not always indicative of a significant increase in stress, as the stress state is also dependent on how well the load is shared among the other layers. Therefore, these data points were not removed from the vessel efficiency dataset. While neither Figure 13.7.1.3.1 nor the ASME Code limit of 50% can be used to determine the efficiency of any particular vessel, Figure 13.7.1.3.1 provides a reasonable level of confidence as to limiting values that can be expected.

> *Note: The ARC data was obtained by operations mechanics on a single pass long before any of the theoretical bases were developed by the LPV team and without benefit of lessons learned from later studies. It is notable that only 3 of the 144 measurements were shown later to be erroneous and in need of rework, and that only two measurements indicated a possible vessel problem.*

13.7.1.4 MSFC 19-Bank Circumferential Growth Measurements

Of the 38 Pi Tape comparisons performed at MSFC, only one was identified by the measurement team to be a misread error (see Appendix *S*). The diameter of the lower shell course of V0019 at a pressure of 2950 psi was recorded as 64.716 inches for the first Pi Tape reading and 64.715 inches for the second Pi Tape reading. However, the measurement team identified these values as errors after reviewing photos of the Pi Tape. The values should be 64.726 inches and 64.725 inches respectively. Therefore, these values were changed in the dataset and yielded an efficiency of 71.0% at a pressure of 3874 psi. Note that if left unchanged, these values would yield an efficiency of 55.6% at 3874 psi.

In general, the practice of taking two Pi Tape measurements in both the unpressurized and pressurized states at the same location, as was done on the MSFC LPVs, should help catch errors. If the measurements are compared in the field, Pi Tape alignment issues may be identified as well. The practice of photographing the measurements, also done on the MSFC LPVs, allows after-the-fact correction of Pi Tape reading errors, without the need to go into the field to take new measurements. These repeat Pi Tape measurements of the vessel diameter were very consistent – on average the repeat measurements had only a 0.001-inch difference and the maximum difference was 0.007 inches.

During the initial MSFC measurements, the vessel temperature was thought to have a minimal impact, if any, and the readings were collected only for incidental data purposes. The Pi Tape measurements were made over multiple days and the vessel temperature measurements varied depending on the specific day and time of day when the Pi Tape measurements were taken. After further development of the efficiency calculations, it was obvious that the vessel temperature had more of an impact than originally thought. Since some of the vessel temperature measurements were taken in direct sunlight while others were taken on the shaded side of others vessels, the surface temperature measurements varied much as 25°F in readings during the same collection period. This significant difference in surface temperature measurements required a different approach for use in the efficiency calculations. After some discussion, the average surface temperature for the collection period was chosen as the best representation of the vessel temperature measurement. There were four different collections periods: 2950 psi High Pressure, 2780 psi High Pressure, 50 psi Low Pressure, and 0 psi Low Pressure. The vessel temperature measurements of each vessel were averaged for each collection period and used to calculate the temperature-corrected diametric expansion of the vessel Equation (3) . The 2950 psi High Pressure collection group had an average temperature of 45.2°F, the 2780 psi High Pressure collection group had an average temperature of 76.9°F, the 50 psi Low Pressure collection group had an average temperature of 70.3°F, and the 0 psi Low Pressure collection group had an average temperature of 44.8°F.

In each case, the lesser of both the pressurized and unpressurized Pi Tape measurements was used to calculate the temperature-corrected diametric expansion according to Equation (3).The lowest measurement was used in each case because, when using a Pi Tape to measure the outside of a cylinder, misalignment of the tape can result in a measurement that is larger than the true value, but with the exception of simply misreading the Vernier scale, it is not possible to obtain a value that is too low. Then, a representative efficiency was computed for each shell course based on the temperature-corrected diametric expansion according to Equation (1), and the efficiency at MAWP was calculated according to Equation (2). Figure 13.7.1.4.1 shows a histogram of the vessel efficiency at the MAWP of 3874 psi based on the Pi Tape measurements.

Similar to Figure 13.7.1.3.1, Figure 13.7.1.4.1 provides confidence as to the limiting efficiency values that can be expected in the shell courses of NASA’s LPV fleet. A discussion of the similarities and differences between the ARC and MSFC calculated efficiency distributions at a factor of safety of 3 and recommendations for using this data in structural analyses are provided in the *Structures Technical Memorandum* [3] (Section 9.2.1).

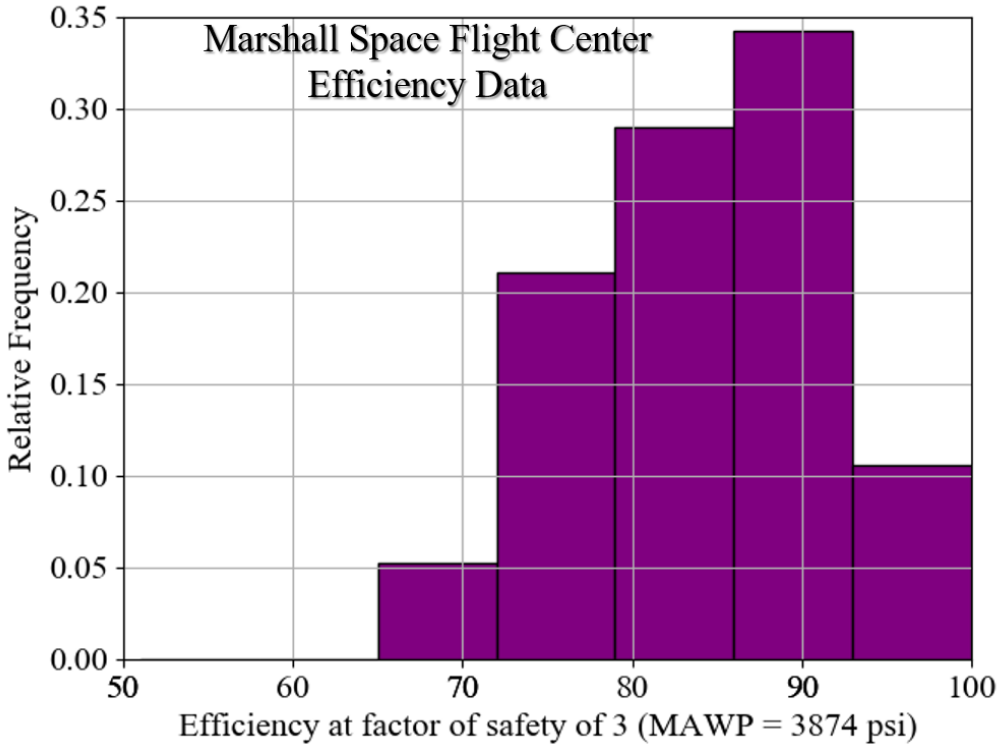


Figure 13.7.1.4.1: Histogram of vessel efficiency measurements of 38 shell courses from 19 hydrogen LPVs at MSFC.

13.7.1.5 Combined ARC and MSFC Efficiency Data

A review of the ARC and MSFC vessel efficiency measurements shows that they represent two distinct populations, so combining them is not appropriate. Figure 13.7.1.5.1 shows that while the curves of the cumulative distribution functions are similar, the MSFC data shows generally higher efficiencies. For example, approximately 73% (1.0 – 0.27) of the MSFC vessels had efficiencies exceeding 80%, while only about 40% (1.0 – 0.6) of the ARC vessels did.

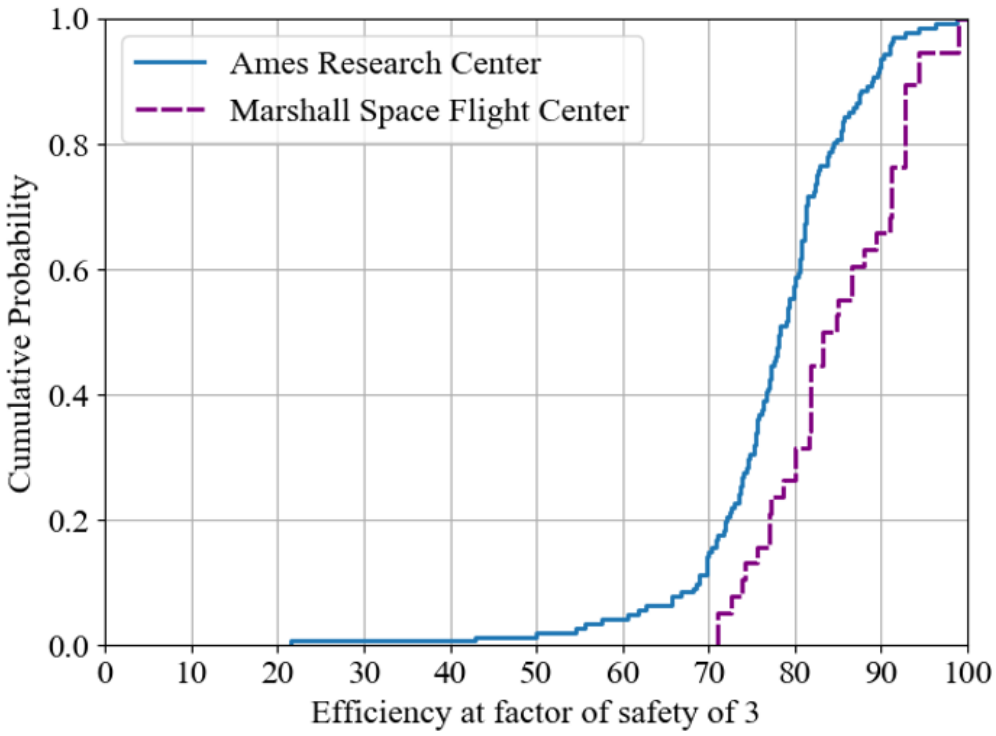


Figure 13.7.1.5.1: Comparison of the empirical cumulative distribution function of the ARC efficiency data and the MSFC efficiency data.

13.8 Pi-Tape Process Interpretation of Variables

Of the 235 active vessels in the LPV fleet, 16 of ARC's LPVs were measured over multiple shell courses. This data provides a basis for the expected range of efficiency values as seen in Figure 13.7.1.5.1. Most shell courses measured fall within a range of 75%-95%.

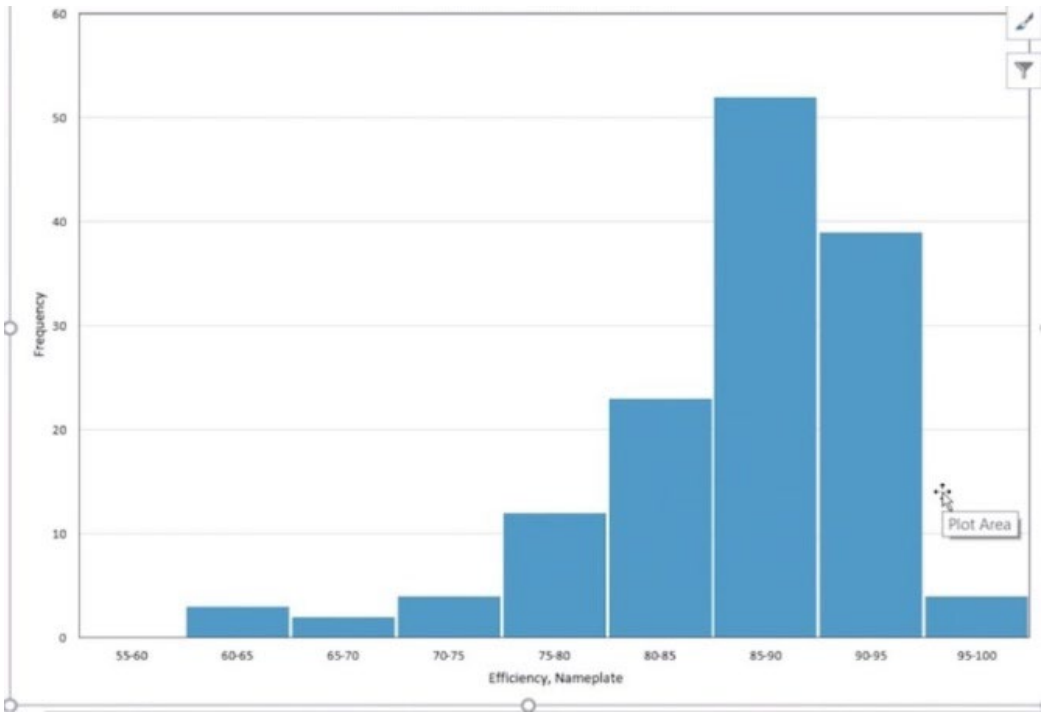


Figure 13.7.1.5.1: Efficiency at nameplate pressure.

Therefore, if a value below 50% or above 100% is recorded, the measurement should be validated using the logic as outlined in Figure 13.7.1.5.2 and Figure 13.7.1.5.3. The basis for these figures is discussed in Sections 13.8.1 through 13.8.6.

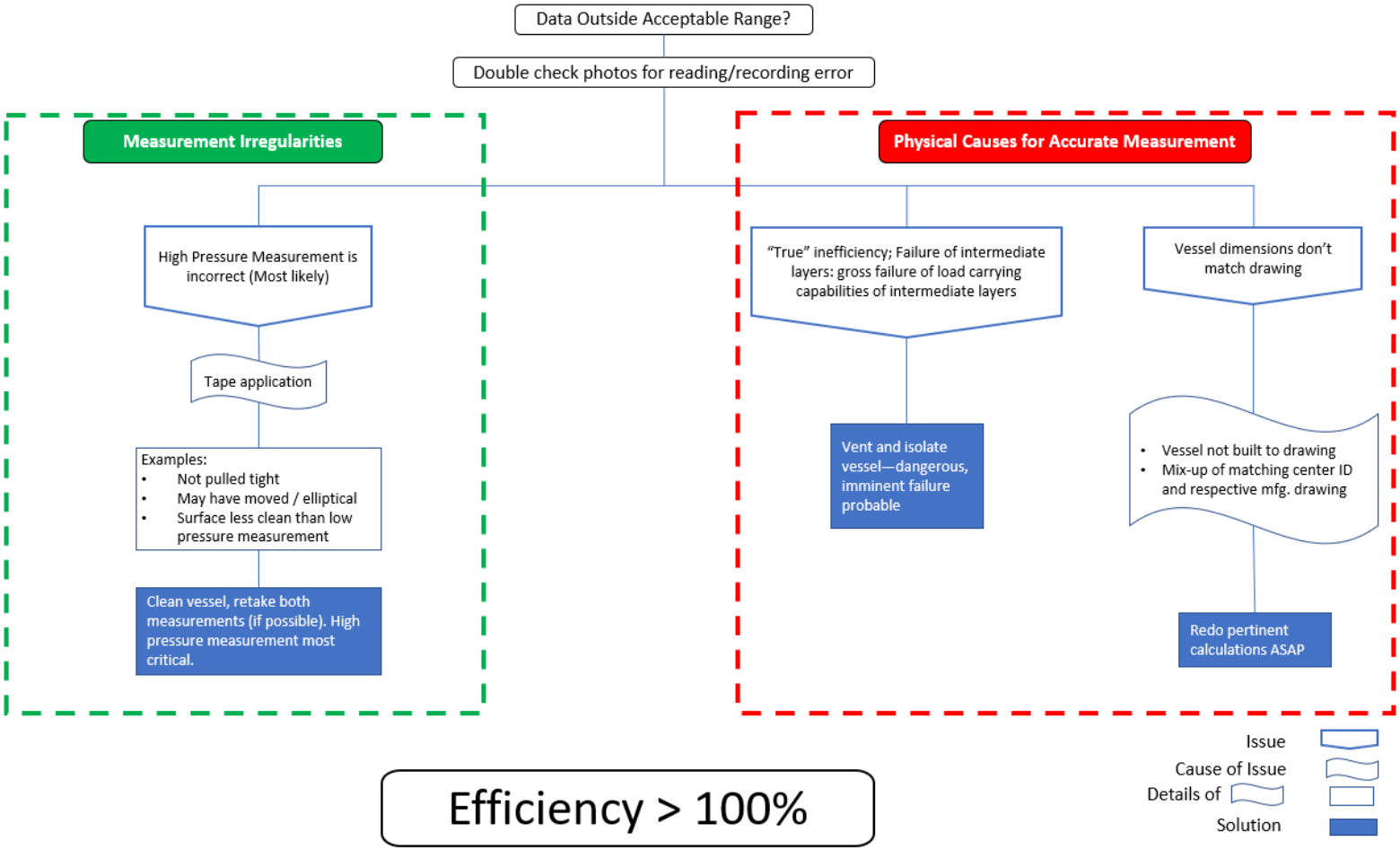


Figure 13.7.1.5.2: Data interpretation > 100%.

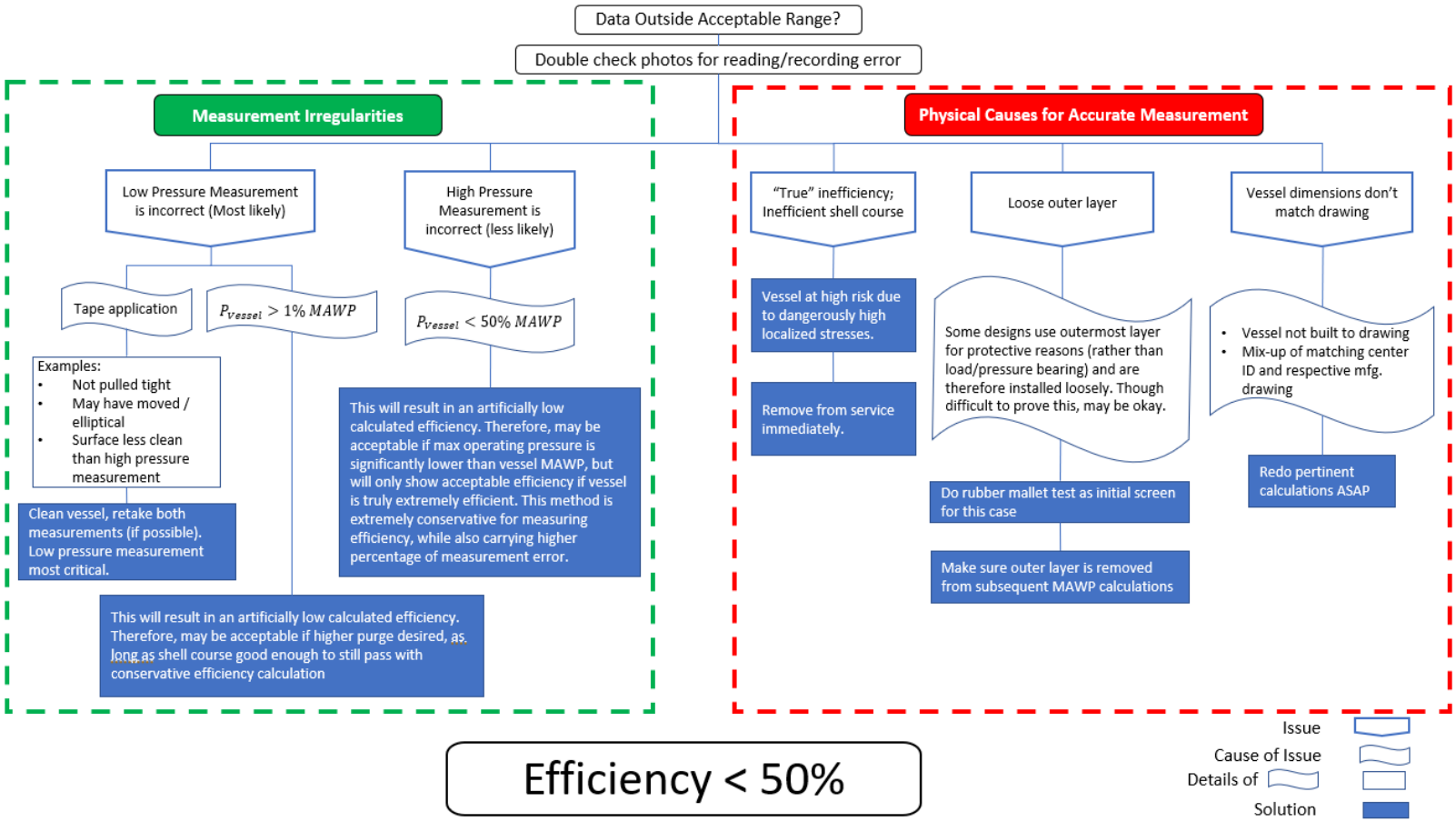


Figure 13.7.1.5.3: Data interpretation < 50%.

Any recorded measurements outside of the expected/acceptable range can be split into two primary categories: measurements based on true physical causes and those based on measurement errors. Physical causes of measurements that lie outside of the acceptable bounds set by the standard should be treated with extreme caution as they may represent a dangerous vessel that is likely to fail unexpectedly. However, measurement irregularities can be resolved in the field with minimal time and effort if identified.

13.8.1 Measurement Irregularities Showing Efficiency < 50% - Causes

An underestimate of the true efficiency of the vessel has two likely causes: incorrect tape application or an unusual P_{Vessel}. If P_{Vessel} > 1% MAWP, an artificially low efficiency will be calculated. Using a low pressure >1% MAWP may be acceptable for higher pressure purges, so long as the shell course can still satisfy the efficiency 50% requirement despite the conservatism.

Incorrect tape application should be checked next because it can readily be corrected. Examples of common tape application errors include the user not pulling the tape tight or with the same resistance between measurements, lateral/angular movement causing a loss in coaxiality with the vessel (Figure 13.8.1.1, or the surface of the low-pressure measurement suffering from a buildup of superficial debris (especially when compared to the high-pressure measurement (Figure 13.8.1.2)).

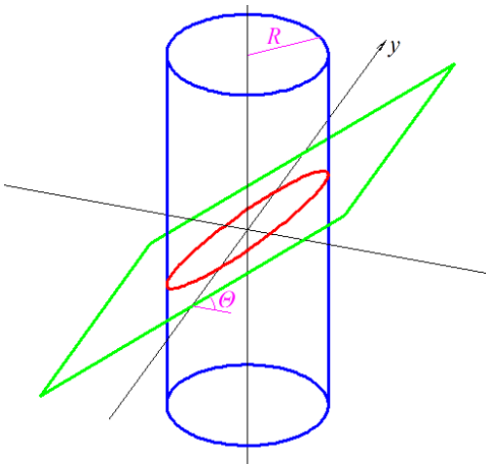


Figure 13.8.1.1: Ellipse from loss of coaxiality (exaggerated).

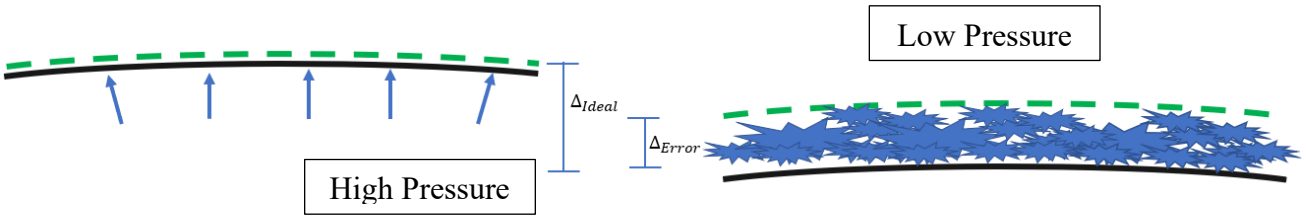


Figure 13.8.1.2: Surface debris for < 50 %.

If incorrect tape application is suspected, cleaning the vessel and retaking both measurements are recommended, with the low-pressure measurement being the most critical.

An error in the high pressure reading for efficiencies calculated < 50% is highly unlikely, but could be caused by the high-pressure reading being taken with the vessel below 50% of MAWP. The resulting delta would produce an artificially low calculated efficiency but might be acceptable provided the maximum operating pressure is significantly lower than the vessel MAWP. However, this solution should only be utilized as a last resort as it carries significant measurement uncertainty and conservatism.

13.8.2 Causes of Measurement Irregularities Showing Efficiency > 100%

Incorrect tape application is the only measurement error that can cause a false efficiency measurement above 100%. As with the <50% irregularities, examples of common tape application errors include the user not pulling the tape tight (or with the same resistance between measurements), lateral/angular movement causing a loss in coaxiality with the vessel (Figure 13.8.1.1), or the surface of the high-pressure measurement suffering from a buildup of superficial debris (especially when compared to the low-pressure measurement Figure 13.8.2.1). If incorrect tape application is suspected, it is recommended to clean the vessel and retake the measurements, with the high-pressure measurement being the most critical.

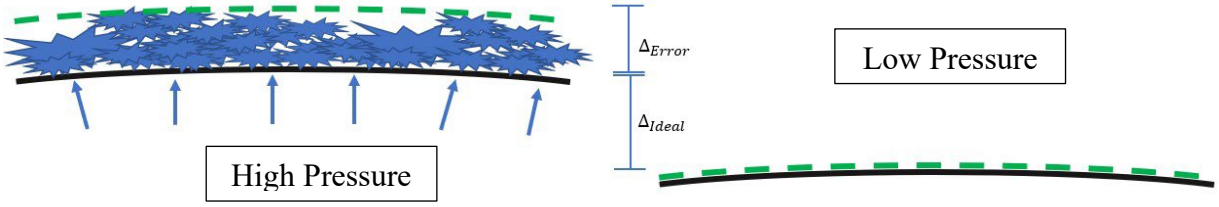


Figure 13.8.2.1: Surface debris for >100%.

13.8.3 Physical Causes for Accurate Measurements with Anomalous Results

Inaccurate drawings/calculations: When the actual vessel total wall thickness doesn't match the value specified on the drawing, the analysis will provide incorrect expected expansion values. With the vessels being built so long ago and sometimes being built at breakneck speeds, documentation and change records have often been lost. Additionally, many vessels in the fleet have moved between Centers or agencies one or more times and some may have suffered mix-ups of their center IDs with their corresponding manufacturer drawings. However, the pertinent

calculations can be re-run to accurately assess the risk if the correct drawings are provided or generated. This effect can result in measured efficiencies of either < 50% or > 100%.

13.8.4 Physical Causes for Accurate Measurement Showing Efficiency < 50%

There are 3 primary causes for accurate efficiency measurements that are below 50%: inefficient shell course, loose outer layers, and the vessel total wall thickness doesn't match the drawing. A truly inefficient shell course (Figure 13.8.4.1) can result in dangerously high localized stresses, and therefore necessitates emergency removal from service.



Figure 13.8.4.1: Inefficient shell course.

Some vessel designs utilized the outermost layer as an environmental protective barrier only, lacking the load-bearing functionality of the other layers. Alternatively, sometimes the nature of construction led to the outermost layer not being wrapped as tightly. This condition can be verified by the rubber mallet test as an initial screen. If a vessel is proven to have a loose outer layer, the outer layer must be omitted from all MAWP calculations.

13.8.5 Physical Causes for Accurate Measurement Showing Efficiency > 100%

There are 2 primary causes for accurate efficiency measurements greater than 100%: failure of intermediate layers and failure of the total wall thickness to match the drawing. Failure of intermediate layers (Figure 13.8.5.1) indicates a gross failure of load carrying capabilities within the layers of the vessel and, therefore, necessitates emergency removal from service.

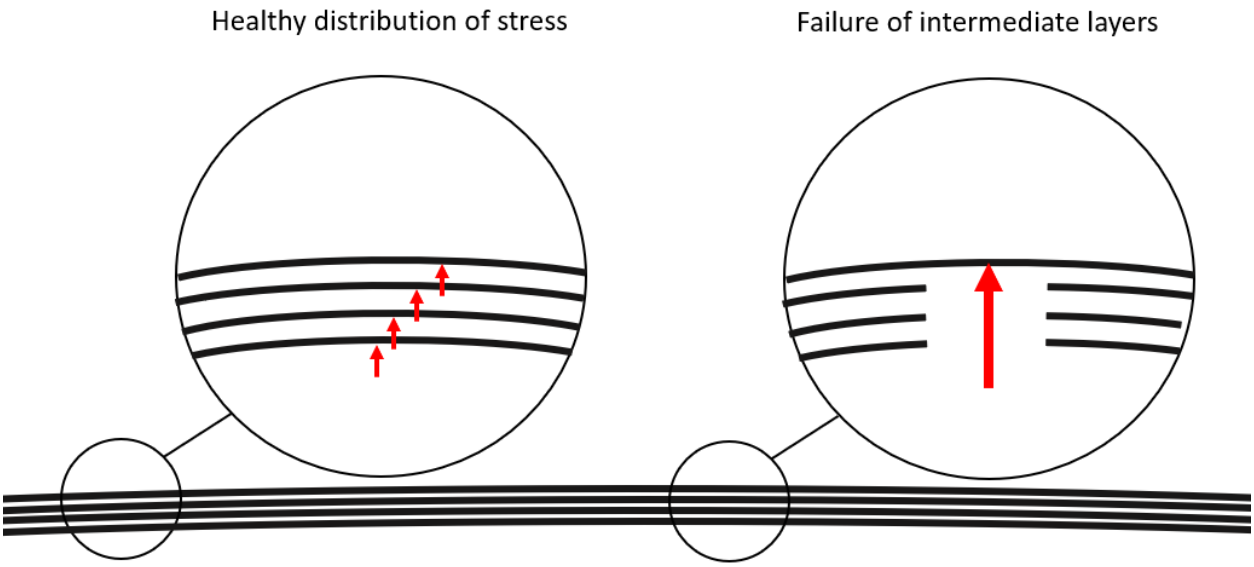


Figure 13.8.5.1: Failure of intermediate layers.

13.8.6 Conclusions

The consistency of the measurements throughout implies both the ability to take repeated and accurate measurements and an extraordinary consistency in fabrication of these vessels. The uniformity in the difference between two measurements at different pressures on each shell course reinforces confidence that Pi Tape measurements performed in accordance with a well thought-out and repeatable procedure can be performed accurately. Thus, the use of Pi Tape measurements as a basis for helping to understand stresses in inner layers of an LPV is highly reasonable.

13.8.7 V0023 Circumferential Growth Measurements

During depressurization of V0023 following its AE test on September 14, 2016, the vessel diameter was periodically monitored using a Pi Tape at the same time that AE monitoring continued. As the pressure was reduced, the reduction in diameter slowed slightly after about 400 psi. At the same time and pressure, a significant increase in acoustic emissions was observed, explained by an increase in sliding between layers as they became less tight.

Thus, while Pi Tape measurements provide an effective means of determining LPV efficiency, it appears that some quantification of LPV efficiency might also be obtained through use of AE. This possibility warrants further investigation, as the AE approach might be more easily accommodated by test schedules, etc.

Documentation of Pi Tape measurements on V0023 and the correlation with AE is found in *Appendix Q, MPFR-16-016 Pi Tape Measurements of V0023*.

13.8.8 MSFC West Test Area Hydrogen Bank Circumferential Growth Measurements

Appendix S, PVS-19-011, Pi Tape Measurements of West Test Area (WTA) Hydrogen Bottles, provides the report on the actual Pi Tape measurements of these vessels.

13.8.9 V0023 Layer Sliding During AE Testing

During the AE test of vessel V0023, the onset of significant layer sliding could be clearly discerned in the AE signals. Highlighted below in Figure 13.8.9.1 is the transition point at which the vessel is "solid", the pressure at which this occurs is "$P_{Closure}$" in the LPV Gap Closure Tool (LPVGCT).

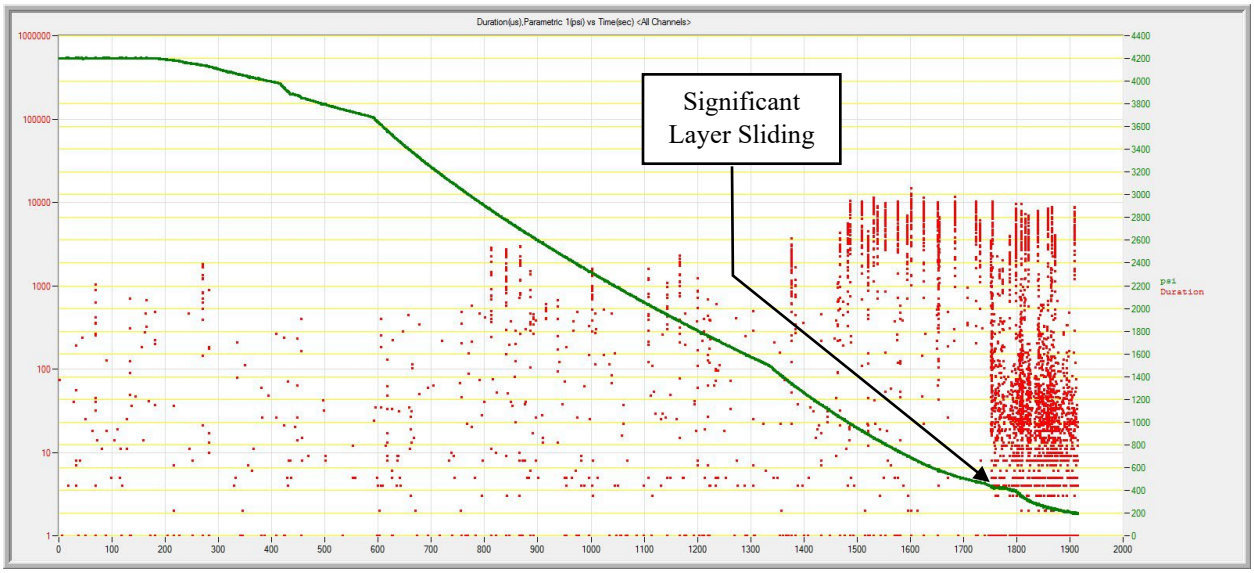


Figure 13.8.9.1: Pressure and AE signals during depressurization test

This method of measuring efficiency by directly detecting P closure may be especially helpful in instances in which the vessel is operating well below MAWP, and diametral expansion measurements have greatly reduced efficacy because the range of expected measurement is of similar magnitude to the typical range in measurement precision. Since measurement precision is a fixed range and not a function of pressure, separating the high and zero pressure measurements as much as possible helps lessen their effect over a larger range. However, system configurations often make a high pressure reading impractical. See Figure 13.8.9.2 and Figure 13.8.9.3.

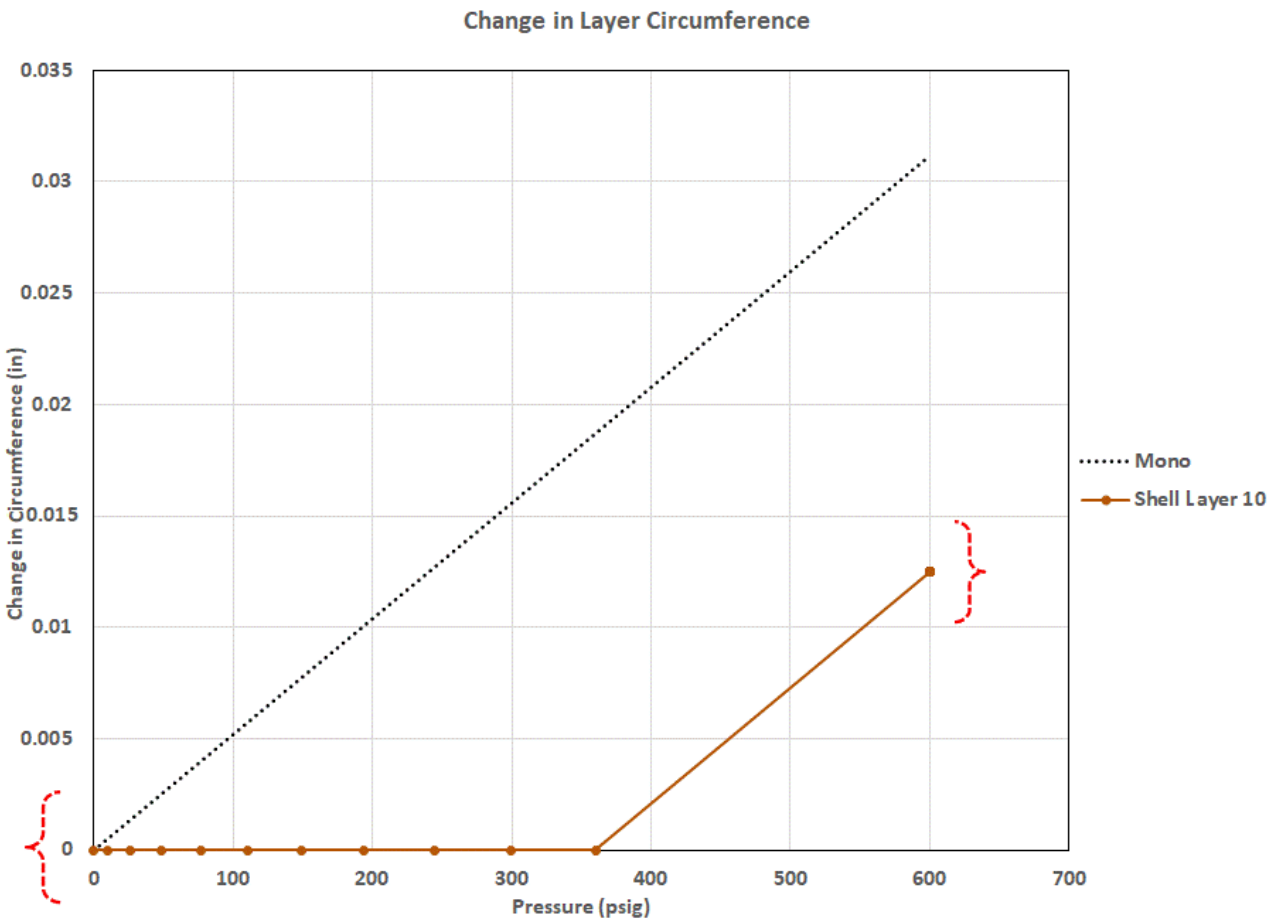


Figure 13.8.9.2: Diametral expansion at low pressure range.

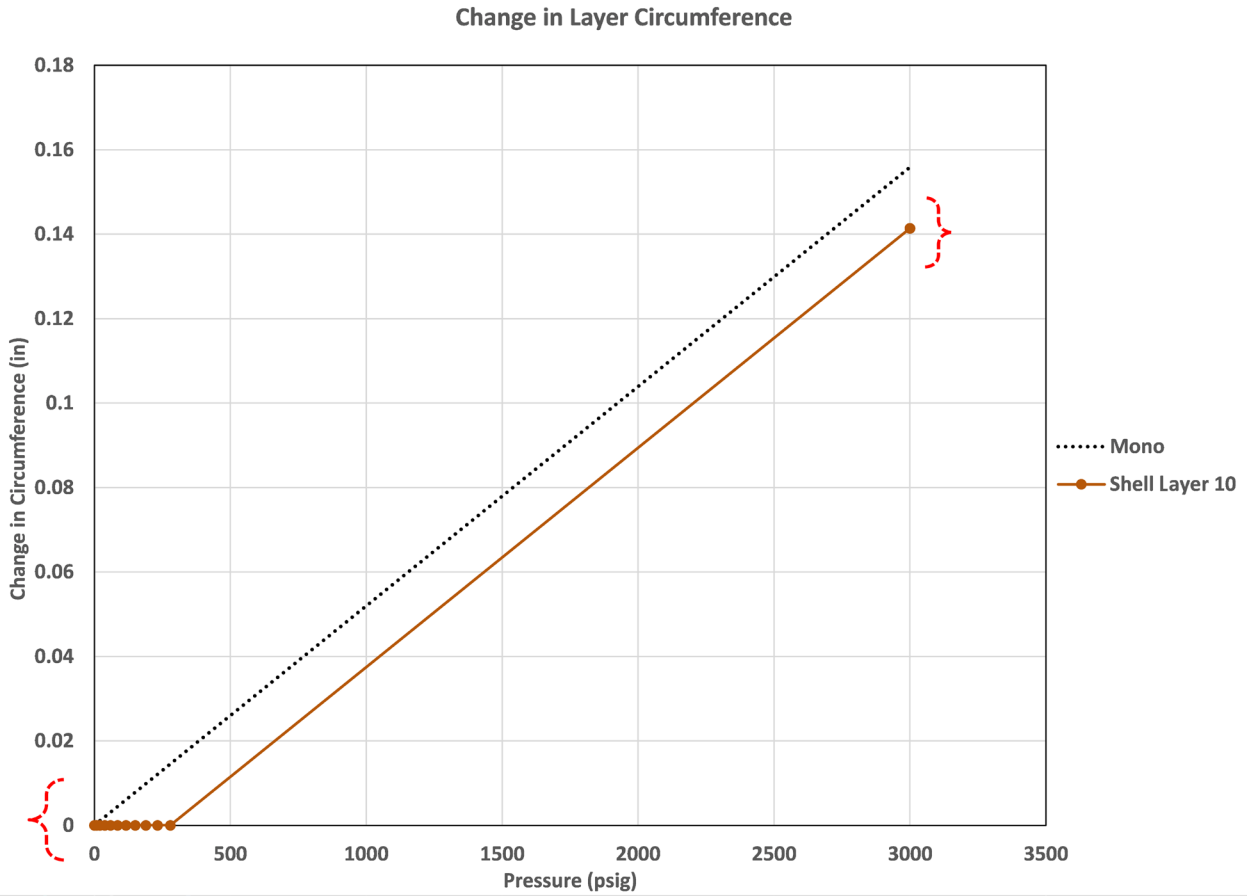


Figure 13.8.9.3: Diametral expansion at high pressure range.

Experimentation regarding this approach to determining vessel efficiency by directly measuring the $P_{closure}$ is limited and requires further validation if is to be pursued. This approach may also be applicable for detecting large intermediate layer failures which result in significant layer sliding, but that would be otherwise undetectable.

13.9 AE Testing

For LPVs, AE offered the potential for practically inspecting the large regions of the vessels that are inaccessible to conventional surface and volumetric NDE techniques. ARC and others have used AE on LPVs since the 1980s, and while many aspects of AE application for use on LPVs were validated, there was no known correlation to an actual growing crack signal. Therefore, ARC contracted and managed an OSMA funded effort with Digital Wave Corporation (DWC) in 2011 using their broadband MAE method to monitor an LPV while pressure cycling it 4,688 times at or above its nameplate rating to induce crack extension at a milled sharp notch defect (see Section 13.9.1). They concluded that it was marginally possible to identify this ductile crack growth through analysis of the frequency content of the received signals, separating the relevant signals using sensors and filters available at that time from other non-relevant signals in these

very noisy (due to layer rubbing, slag crushing at welds, etc.) pressure vessels. However, additional testing, higher sensitivity sensors, and improved analysis techniques (e.g., wavelet transformations) were required to further validate this one test to establish a reasonable confidence level in the results. The results of the testing and analysis are reported in *Cyclic Crack Growth Testing of an A. O. Smith Multilayer Pressure Vessel with Modal Acoustic Emission Monitoring and Data Assessment* [11].

More recent efforts have also been performed to determine whether AE would meet NASA's needs as an inspection technique for LPVs. One of the most significant efforts was a full-scale test at MSFC on Vessel V0023, a vessel that had been out of service since 1983 after parametric (MONPAC) AE testing revealed extensive unacceptable signal levels when the LPV was pressurized to 2750 psig. At the time, these signals were considered as possible indications of incipient failure of the vessel. In 2016, after instrumentation of the vessel with DWC, MISTRAS Group, and NASA-owned systems using both parametric and broadband/modal AE methods, the vessel was pressurized in steps to 4317 psig. While significant high amplitude AE event clusters were recorded during the pressurization and holds, none were assessed to be due to ductile or brittle crack growth. One vendor (DWC) called the events "cold-cracking" of existing defects (i.e., corroded metal faces pulling apart at pre-existing locations). Subsequent radiographs, dissection of the vessel, and examination of cracks showed extensive original manufacturing defects such as cracks and burn-through at welds, but did not yield any evidence of crack growth during the test or crack extension under operational loads (see Figure 13.9.1).

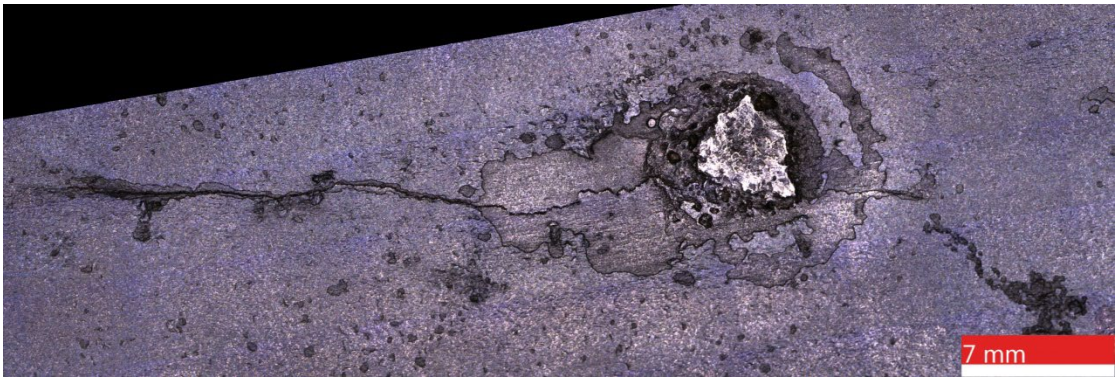


Figure 13.9.1: Optical image of the crack and weld defect of sample 10AC along the surface of the inner-most plate of the pressure vessel V0023

.

13.9.1 MV50466-8 DW Test (High Level Summary, NESC Report)

ARC contracted with DWC and SwRI in 2011 to perform cyclic-pressure crack-growth AE and material fracture toughness testing on a full size LPV with 11 layers obtained as surplus from KSC (A.O. Smith serial number MV50466-8). The vessel's nameplate rating was 6,600 psig, which was based on 1/2 of the yield strength of the shell material used in construction. The original hydrotest pressure was 9,900 psig. This vessel was instrumented with DWC's broadband waveform capture and analysis MAE system, strain gauges, and a magnifying video camera and

waveform analysis was performed using DWCs WaveExplorer™ software. This method had been used at NASA ARC since 2001 on its A.O. Smith layered vessels and other single layer vessels. The vessel is shown in Figure 13.9.1.1 after being prepared by DWC for radiographic examination of the welds.



Figure 13.9.1.1: Vessel after preparation for radiographic examination of welds.

Specific test objectives were to:

1) Document the ability to detect modal AE events from fatigue crack growth under realistic field-testing condition.
2) Monitor strain readings during the cyclic testing to ensure that the vessel was not plastically deforming.
3) Perform fractographic analysis of the crack growth and obtain ASTM tensile, fracture toughness, stress intensity, and fatigue crack growth (da/dn) material properties of the vessel.
4) Correlate actual measured incremental crack growth with MAE signals to establish energy release sensitivity and nonrelevant noise discrimination capability in order to improve LPV structural integrity assessments using the MAE waveform assessment methodology.

While not an explicit objective of this test, the long-range objective was to be able to establish a relationship between detected crack acoustic emission characteristics (e.g., intensity, frequency,

amplitude, etc.) and crack size as a percentage of CCS in order to estimate or screen for remaining safe life before brittle fracture.

Broadband waveform analysis using DWC's MAE methodology was selected as the most likely to succeed based on previous comparative testing at ARC versus the resonant sensor, parameter-based methodology that is also commonly used in the AE inspection industry. Although the wave propagation theory and acoustic science behind MAE is well established, no prior crack-correlation validation testing of this nature had been attempted on multilayer vessels, which exhibit significant non-relevant (i.e., not related to crack growth) noise emissions under loading and which are thicker-walled with tougher material than the vessels on which the method was originally validated.

From DWC's prior work and that of others, it was known that stable crack growth in ductile material does not emit strong AE signals, and such cracks likely would not become detectable until the crack was a significant percentage of critical size. Therefore, a large starter defect, approximately 2 inches long with a center depth of 0.175 inches (in a layer thickness of 0.265 inches), was milled into the outer layer of the vessel to accelerate the crack initiation process. Using toughness properties from work performed in 1975 by LaRC, this milled defect was believed to be closer to critical size than it was later determined to be based on post-test fracture toughness material testing. That is, the shell material was tougher than originally believed. Thus, while the intent had been to initiate crack growth at about 50% of critical size, it was later determined that the milled defect was only on the order of 10% of critical size.

With the milled defect in place, the vessel was placed in an underground bunker for safety and was pressure-cycled using high-pressure Haskel and Sprague hydraulic pumps a total of 4,688 times, mostly between a low of about 1000 psig (less than 10% nominal yield stress) and a high of 50% of yield (that is, to the nameplate pressure of 6,600 psig), with a number of cycles toward the end to over 100% nominal yield stress of the shell material (14,000 psig maximum). These were significantly higher stress cycle ranges than typically imposed during AE testing, which traditionally uses 10% over maximum operating pressure as standard procedure, as specified in *ASTM E-1419, Examination of Seamless, Gas-Filled, Pressure Vessels Using Acoustic Emission* [24]. This was done in order to accelerate crack growth since equipment and funding constraints limited the amount of time available to conduct the test. The test configuration in the bunker and instrument display as provided by DWC are shown in Figure 13.9.1.2 and Figure 13.9.1.3.



Figure 13.9.1.2: Test configuration.



Figure 13.9.1.3: Instrument display.

A visible crack indication was seen in the center-shell crack under a video magnifier after about 2,000 cycles, but its depth could not be determined during testing. Figure 13.9.1.4 and Figure 13.9.1.5 show the milled starter notch and micro video display during testing.



Figure 13.9.1.4: Starter notch.

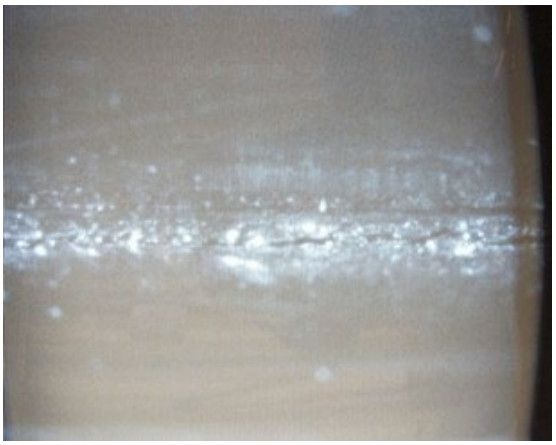


Figure 13.9.1.5: Micro video display.

No MAE signals indicating crack growth were recognized real-time during this phase of testing, but some were revealed in later examination after filtering. Figure 13.9.1.6 shows an example MAE crack growth indication from Cycle 2462 as displayed by DWC's WaveExplorer software.

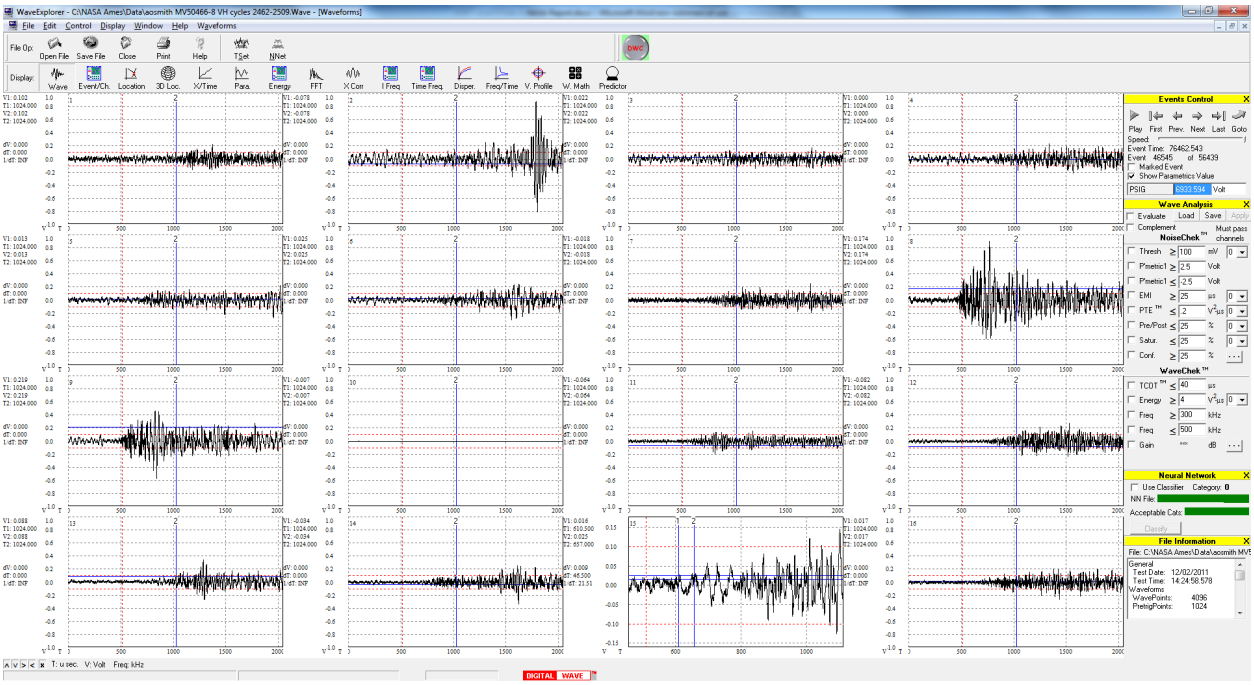


Figure 13.9.1.6: Example MAE crack growth indication.

Due to funding limitations and the wearing out of the last available hydraulic pump, researchers ultimately terminated the test with the application of several cycles of yield-level stress to force crack extension. MAE crack signals were also captured during these final cycles. In general, the MAE response was less than anticipated, and it is likely that this crack, if hidden, would not have been identified with the normal test level of effort available up to that time. Refinements in filtering made possible by this test would improve future field assessments, although the sensitivity and crack size correlation to signal strength were not clearly established because the crack was at the threshold of detectability for this tough material. Future cyclic testing was recommended to focus on welds and weld HAZ which are more likely to crack in service and are also more likely to emit stronger AE signals, assuming they are lower toughness material.

Reference [11] provides the complete report for this work.

The vessel was subsequently sent to SwRI for fractographic analysis of the center crack and for testing of strength, fracture toughness, and fatigue crack growth properties of shell, head, and weld material to facilitate correlation of the actual crack with fracture mechanics calculations. References [12] and [13] report on these efforts. This material testing work provided extensive fracture toughness data and demonstrated that the crack grew 0.064 inches before the final, rapid through-wall extension under yield level stress. The photomicrographs also showed that the crack growth was not uniform across the crack front and was highly plastic, which also had an unanticipated negative effect on the ability to identify the crack using MAE because of the more diffuse plastic energy release mechanism. A micrograph of the cracked section provided by SwRI is shown in Figure 13.9.1.7.

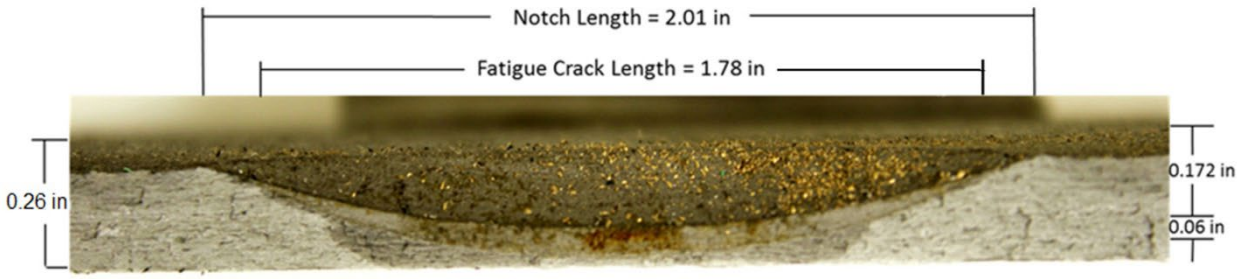


Figure 13.9.1.7: Micrograph of cracked section.

In retrospect, a smaller, elastic-mode crack extension may have been easier to detect but would have required much more pressure-cycling at lower stress levels, substantially lengthening the time and increasing testing cost, which was not feasible. Nonetheless, the filtering developed to evaluate these results was thought at the time to significantly improve the accuracy of data assessments for future testing, although subsequent developments in methodology including incorporation of emission wavelet transforms and image analysis have likely outpaced these conclusions and would reportedly yield orders of magnitude improvements in detectability.

13.9.2 V0023 AE Test

Vessel V0023 was an LPV removed from service at MSFC in 1983 based on the results of a MONPAC AE test performed at that time. The test showed a high level of activity with signals described as having “classic crack-like characteristics”. Because this vessel was known to have an active noise source, it was pressurized on September 13, 2016, to permit the application and assessment of more advanced AE technology.

Jacobs Engineering (MSFC onsite personnel), DWC, and MISTRAS all performed AE monitoring of Vessel V0023 concurrently during that pressurization.

All of the organizations participating in this AE test also participated to some extent in the test planning and, during the test, all identified areas of significant activity. After completion of the test, the vessel was inspected using RT, then subjected to destructive examination for detailed inspection, testing, and analysis of vessel features. Equipment and techniques varied among the testing organizations. All the organizations participating in the test located noise sources in the expected area, however only DWC was successful in locating the sources as well as clearly and accurately characterizing them as not involving actual crack growth.

The vessel was pressurized to 1000 psig twice on the day before the actual test to determine the level of background noise that could be expected. The level of background noise was significantly lower during the second loading sequence, and only flow noise was detected.

Sections 13.9.2.1, 13.9.2.2, and 13.9.2.3 provide brief descriptions of that work, while more detail is provided in appendices as referenced below.

13.9.2.1 MISTRAS (contractor report)

MISTRAS used an 8-channel system to monitor a section of the vessel centered on the reported location of the 1983 AE source. This focus on the location of prior activity meant that MISTRAS efforts had less ability to examine other areas of the vessel, were any significant activity to be noted elsewhere.

The MISTRAS data analysis reported identification of sliding events as well as activity related to what was later determined, by RT and destructive examination, to be a crack. A discussion of MAE techniques is provided, along with some assessment of the significance of the findings. With knowledge of RT results showing a crack in the expected area, the MISTRAS report discusses possible interpretations of the data and provides possible explanations for the observed test results, including breaking of oxide layers and rubbing between layers.

Appendix T, Test on Vessel V0023 MISTRAS Group AE Measurements and Analysis, September 13, 2016, September 13, 2016 provides the full MISTRAS report.

13.9.2.2 MSFC (In-House)

Jacobs Engineering applied a total of 43 sensors to Vessel V0023, including 36 R15I resonant sensors and 7 broadband sensors, connected to a Physical Acoustics Corporation (PAC) DisP System. The broadband sensors were located around the approximate area in which activity had occurred during the 1983 AE test. Jacobs reported that relevant crack-like signals were identified during the test and verified during post-test data analysis. During the first pressurization to 1000 psig on the day prior to the actual test, it was noted that there was a high level of background noise below 1000 psig, something that did not occur during the second pressurization.

Jacobs reported clusters of sound emanating from the area of the supposed defect, including 30 hits described as “relevant crack-like signals.” They recommended follow-up radiography. They also stated that they suspected that the source would be found to be shallow (closer to the outside surface than the inside surface) because of the lack of signal distortion, and they reported a number of non-significant hits from various locations across the vessel.

Appendix U, Acoustic Emission Test Report for Vessel V0023, Report No. AE-V0023-2016 provides the full report by Jacobs Engineering.

13.9.2.3 Digital Wave Corporation

DWC placed 28 broadband sensors on Vessel V0023, covering the full area of the vessel. They reported that two locations had groups of events and stated unequivocally that neither location showed active crack growth indications, an assertion later shown to be accurate by post-test dissection and fractography (Section 13.9.2.4). DWC further noted that the waveforms from these locations occurred at pressures well below the prior maximum pressurization, indicating that the emissions were not from active crack growth, and confirmed this assessment with their analysis and evaluation of the waveforms. The indications at one of the locations were described

as consistent with cold-weld cracking of crack faces (that is, separation of already cracked faces that had cold-welded together when the LPV was depressurized). This statement also appeared consistent with the fractography.

The full DWC report is provided in *Appendix V, V0023 Vertical Multilayered Vessel Acoustic Emission Sensor Layout.*

13.9.2.4 Post-Test Destructive Evaluation

Following the AE testing of Vessel 23, MSFC personnel performed destructive evaluation of the cracks identified both by AE and by radiographic examination. Scanning electron microscope (SEM) examination determined that the cracks were original manufacturing defects and that there had been no crack growth during the life of the vessel. Details of the examination and evaluation are found in *2017-0376 Pressure Vessel V0023 Fractography and Metallography of Weld*, which is included as part of the Structures Report [3].

13.9.3 Limitations for Vintage LPV Structures

AE technology has been used for a number of decades to detect leaks in pressure vessels. Companies began to develop the technology in the 1970s in an attempt to detect AE that represented precursors to vessel failures. The idea of listening for such precursor events is attractive in that this approach to inspection can, at least in principle, reduce process disruptions, downtime, and the cost of vessel inspection. Analysis of when an emission is received by various sensors permits location of the sound source.

Because the layered structure of LPV results in potential for layer rubbing, cracking of slag or oxidation, and other acoustic events, these vessels have always presented a challenge to effective use of AE testing.

Beginning in the 1980s, several NASA Centers began using AE to evaluate pressure vessels. MSFC began using the MONPAC technology on a regular basis, including for assessment of LPV. Beginning in 2001, ARC used modal AE for evaluation of 16 large LPVs, and some other Centers followed suit.

The MONPAC technique uses zone intensity classifications of A through E, with E the most severe. When used on LPVs, it has often resulted in zone intensity classification of C, D, or E, with recommendations varying from a relatively mild "Immediate follow-up inspection and evaluation required" to a dire "Major defect requiring immediate shutdown and follow-up nondestructive examination." However, only a single LPV has ever been permanently removed from service as a result of AE inspection (MSFC Vessel V0023 in 1983). Dissection and fractography of this vessel after additional AE testing in 2016 showed clearly that original welding defects and weld cracks existed in the vessel, but that all had been in place since construction of the vessel and none of the cracks or other defects had grown in the interim.

The more advanced techniques and analytical capabilities of modal/broadband AE provide for characterization of signals based on their waveforms. This allows many signals that might in the

past have been considered relevant to be discounted as insignificant. However, the problem remains that very small amounts of ductile crack growth result in very small signals. The use of phased array modal AE and more recent developments in application of wavelet transform and image analysis show promise of detecting and characterizing very low energy signals. Rejection criteria for such low energy indications has not been determined. If the location of the indication is such that it can be inspected by other means, following the AE testing such inspection will normally be performed. If the presence of a defect cannot be dealt with analytically in otherwise un-inspectable locations, the LPV may need to be removed from service.

13.10 Vent Hole Leakage

Vent holes in LPVs serve two purposes. First, they prevent pressure build up between shell layers in the event of a liner leak, preventing over-pressurization and catastrophic failure of the layers. Second, they provide a means of monitoring for leakage through the inner layer (liner).

The *ASME BPVC* permits a shell course or head segment layer to be made up of one or more plates. To ensure that a leak in the vessel liner will vent to atmosphere, avoiding the possibility of layers failing to share the pressure load properly, the Code requires that each layer plate has at least 2 vent holes, each at least ¼ inch diameter. If layer plates don't all cover equal portions of the circumference (whole cylinders, halves, thirds, etc.), more holes may be needed to ensure that all inner volumes are adequately vented [4].

The Code permits the holes to be drilled radially through multiple layers, to be staggered in individual layer plates, or a combination of these two approaches. Providing holes in individual plates before they are assembled may result in greater resistance to the outward flow of air from a liner leak since holes in successive layers will not line up, but with the pressures involved in operating a typical LPV, this lack of alignment is not likely to be a concern if monitoring is performed on a regular basis. Drilling the plates before assembly also ensures that, even if layer segments do not cover equal portions of the circumference of the LPV, inner shell leakage will make its way through to the outside.

Radial holes drilled through multiple or all layers at one time after assembly probably dissipate pressure more readily and may thereby make leakage more obvious. This is the approach most commonly used on A.O. Smith vessels.

Holes drilled after assembly have the added advantage that they can be checked easily for functionality by running a wire into the holes, followed by use of a flat-bottomed drill if needed to remove corrosion, potential product buildup from a leak, or mud dauber nests, ensuring effectiveness of the vents. Both the wire and the drill should be marked to ensure that the hole is functional to its full depth, but that the drill bit doesn't damage the inner liner. Also, if a drill bit is used to clear the holes, it should have a flat bottom to ensure that it does not damage the inner liner.

If holes are drilled after assembly of a shell course, they must not pass through longitudinal welds or they may to fail to vent effectively.

A through-wall defect in the liner of an LPV will normally manifest itself in leakage through two or more vent holes in the outer shell layer, provided neither vent hole in that plate is blocked. If periodic maintenance is performed to clean exposed vent holes, or if other means are used to ensure their functionality, and care is taken to monitor them, leakage will indicate when such a defect exists. The second hole in each layer plate provides redundancy. Multiple approaches are available for detecting leakage through vent holes, as follows:

In the past, vent holes have been protected from extraneous materials and rain by placement of unthreaded plastic plugs, a dab of grease, or by other means. Some vessels have thin covers welded over the vent holes. These covers are intended to protect the vent holes and to fail at low pressure should a liner leak occur. This precludes inspection, but presumably also prevents rust, corrosion, and accumulation of debris within the hole. While vent hole protection is important, it is also important that the means of protection be verified not to impair vent hole functionality.

Welded covers over vent holes should not be added to vessels that do not already have them, and it is essential that existing covers be designed to fail before the outer shell does. Use of such covers has been a violation of the *ASME BPVC Section VIII-1* and *-2* [4] since LPV were first included in the 1977 Addenda to the code. (“Vent holes shall not be obstructed. If a monitoring system is used, it shall be designed to prevent buildup of pressure within the layers.”)

Although 1/4 inch diameter vent holes still comply with ASME code requirements, the industry standard practice has since moved to a 3/8 inch diameter hole, helping to reduce the risk of clogging due to corrosion products, however, existing 1/4 inch holes need not be drilled out to 3/8 inch.

Only one LPV is known to have been removed from service at NASA due to leakage. This vessel is discussed in Section 6.2 and References [9] and [10] .

13.10.1Vessels Containing Gas

For vessels containing gas, various monitoring alternatives are available, sometimes requiring PPE or precautionary measures such as the use of monitoring equipment in the case of vessels containing flammables, toxics, or asphyxiants:

13.10.1.1 Listening to Detect Leaks.

Listening for the sound of escaping gases while passing near all portions of the vessel is inexpensive. While not tested as a part of this effort, gas leaks are easily heard at leaking components and fittings, and auditory monitoring is generally considered effective in relatively quiet environments. Limitations include the hearing ability of the listener and high ambient noise levels in industrial areas. This should not be the sole technique used in areas of high noise. If access is a problem, such as in the case of vertical vessels, this technique can be aided with a parabolic microphone for inspection of targeted areas from a distance. Each vent hole should then be targeted with the microphone to ensure full coverage. Marking of vent holes will facilitate their identification from a distance.

13.10.1.2 Ultrasonic or AE Monitoring.

Ultrasonic or acoustic emission monitoring equipment can be used for either continuous or intermittent monitoring for high frequency sound emitted by leaks and can be used for location determination if multiple sensors are used. Ultrasonic leak detection devices are readily available at industrial supply houses. The supplemental requirements provided in *ASME BPVC, Section V* [17]*, Mandatory Appendix VI Leak Detection Applications* may be used as guidance for those cases requiring continuous AE monitoring for leaks from the pressure boundary, though because of their service, continuous monitoring is not normally a requirement for NASA LPVs.

13.10.1.3 Bubble Leak Tests.

A bubble leak test of the vent holes provides an alternative to the audible test, eliminating dependency on auditory perception of individual personnel and providing a more effective test in areas of high background noise. However, a bubble leak test is more labor intensive because test personnel must access each vessel vent hole. Direct access to the vent holes is typically more difficult for vertical vessels or vessels with other direct access limitations (e.g., close proximity to support structures or tight spacing between vessels). Each vent hole must be bubble leak tested individually since, depending on location, an inner liner leak can manifest itself in different vent holes in the outer layer. It should also be noted that changes in temperature and atmospheric pressure may cause a small amount of "breathing" (i.e., aspiration). Further investigation of any vent holes found to have very small bubbles may be considered to rule out aspiration as a potential cause.

13.10.1.4 Pressure Monitoring.

Pressure monitoring may be used, connecting pressure gauges or other pressure activated indicators to each vent hole on a vessel. This technique can be expensive, depending on the number of vent holes that require monitoring and the need to periodically calibrate or functionally verify operation of the monitoring devices.

13.10.1.5 Sniffers.

For gasses such as methane, which are easily detectable in air, sniffers may be used. These instruments will also require calibration and verification of functionality on a periodic basis.

13.10.1.6 Using Vent Hole Covers.

Some NASA LPVs have vent hole covers welded over the vent holes. Such covers are shown on some AO Smith drawings and are currently in service at GRC, MAF, and possibly other Centers. The method has the advantage of keeping rust and contamination from the vent holes. It requires monitoring, however, to identify any covers that have been compromised because a cover with a cracked weld that leaks gas may not be visually obvious without careful screening. *The ASME BPVC* does not permit this method of protection and failed vent hole covers should not be replaced.

13.10.1.7 Frost Checks.

A significant leak will likely result in frost due to adiabatic cooling on the exterior of the vessel in the vicinity of the vent hole that is expelling gas. If such frost is visible, it should never be ignored, even in the absence of audible indications, but such an indication should not be used as a sole means of monitoring vent holes.

13.10.2Vessels Containing Liquid:

NASA does not currently have any LPVs in liquid service. If any LPV is placed in such service, the following methods may be used to check for liner leaks.

13.10.2.1 Physical Monitoring.

Physical monitoring can be effective, using connected pressure gauges or other indicators to each vent hole on a vessel. It may also be possible to devise other indicators that provide an obvious visual indication of leakage.

13.10.2.2 Observation of Leakage.

It is likely that liquid leaking from an LPV will be obvious from evidence on the outside surface of the vessel in the vicinity of one or more vent holes. Inspection for drips, rust, or product buildup should be effective. It is important to note, however, that certain leaking fluids may gradually clog the flow path, preventing further evidence of the failure from accumulating and resulting in pressure buildup between layers. Prior to one or more catastrophic, industrial LPV failures, indications such as these were present for many months, and ignored, possibly in part because they stopped accumulating further evidence of the leakage [25] .

Cautionary Notes:

(1) Threaded vent hole plugs are not safe because they can retain a high pressure, putting the outer shell at risk. If a vessel is found to have vent holes with threaded plugs, the plugs should be removed, as they would defeat the intent of the vent hole in its dual role of providing an early warning of inner liner leakage and ensuring venting of pressure in the event of a liner leak. Prior to implementation, users should verify that any means of protecting vent does not impair their functionality.

(2) If pressure monitoring is used, because of potential aspiration an important consideration is the alarm pressure. Also, provisions to avoid building up excessive pressure within shell layers will be needed.

(3) Welded vent hole covers were installed by the manufacturer on some vessels. These have the advantage of protecting the vent holes from contamination, rust, etc., but present some risk that they will not blow off at a pressure low enough to fully protect the vessel and need to be analyzed to ascertain that they cannot permit pressure buildup sufficient to endanger the outer layer. Such covers are not permitted by the current ASME BPVC, and should not be installed on any LPV.

(4) Inspection of vessels with vent hole covers should be thorough, recognizing the possibility that a vent hole cover may initially appear to be intact, but actually be compromised and leaking.
(5) LPVs that contain lethal fluids will likely require a manifolded fluid collection system to continuously monitor leakage for all vent holes. Industry literature has reported on such systems, but NASA does not currently have any LPVs in lethal fluid service.
(6) NASA currently requires that all vent holes in non-code metallic LPVs be monitored on an annual basis or more frequently (NASA-STD-8719.26 [26]*).*

13.11 Inspection of Plate Acreage

While weld metal is often alloyed to yield slightly higher properties than parent material, ensuring that the weld is not weaker than associated plates or other components, the process of weld deposition is more variable and subject to production of defects than plate-rolling. While defects in plate material are not unheard of, they are unusual and most often relate to such features as laminar inclusions, cold laps, or prior welds. Plate cracking away from longitudinal or circumferential vessel welds has been identified in only two vessels, and these cracks appear to have been associated with local welding for lug installation, with lugs later removed (Figure 7.2.12.1).

Other defects in plate material have all occurred in the vicinity of welds, typically within, or running from the HAZ.

Therefore, inspection and analysis both focus on LPV welds and the immediate surrounding area, but a visual inspection of an LPV should include all areas, and cracks or other significant defects must be addressed.

13.12 Detecting Loss of Layer

Identification of a compromised intermediate layer of an LPV is challenging. However, the likelihood of such a failure occurring appears to be small, and the consequences may not be large.

13.12.1 Self-Rescue Capacity

If a crack were to propagate the full length of a longitudinal shell layer weld, there would be a local reduction in load carrying capacity proportional to the percentage of the total thickness of shell that is lost. Thus, the reduction in carrying capacity is more significant in an LPV with few layers than in one with many. However, due to friction between layers, except for the outer layer (where the failure would be obvious), the effect is localized and does not produce a situation comparable to the whole layer being absent. Because this is the case, missing or ineffective welds that are distant from each other in the circumferential direction affect vessel integrity less than would otherwise be expected.

The effectiveness of such a vessel was dealt with in a physical test of a five layer LPV by Krupp Company, reported in a paper by Y. Wang, A.I. Soler, and G.L. Chen, The *"Self-Rescue"*

Capacity of Wrapped Vessels – A Theoretical and Experimental Analysis [23]. The report also contains an analytical assessment of a generalized vessel consisting of *n* layers. The five layer vessel tested by Krupp had three internal layers purposely not welded. Only the inner and the outer shell layers were intact, yet the vessel burst at about 75% of the predicted bursting pressure for a normal wall vessel. The vessel design that was tested incorporated a single shell course, had a length about twice its diameter, and was assembled from machined cylinders that were heat-shrunk together. While informative, this test series may not accurately represent the typical LPV in the NASA fleet. The low aspect ratio of this vessel may have resulted in excessive support from the welds to the end plates, and heat-shrunk machined cylinders probably had better contact between layers than a typical rolled and welded vessel.

Analysis demonstrates that, in the case of good contact between layers, the absence of a weld affects only a small sector in the neighborhood of the missing weld before friction effectively transfers hoop stress loads back into the layer with the missing weld. Therefore, if missing welds are circumferentially distant from each other, they are unlikely to have a significant effect on each other. Further details are provided in the *NASA Ground-Based Layered Pressure Vessels Structures Report* [3], Sections 6.2.5 and 8.3.1.

13.12.2 Inspection Feasibility

The practice of Pi Taping is sometimes cited as a means of ensuring that a weld has not been "lost" due to cracking. The effectiveness of this technique for this purpose is questionable.

If gaps between layers were not measured during the fabrication process, then the *ASME BPVC, Section VIII* [4]*, Divisions 1* and *2* require measurement of circumferential growth of the LPV during hydrotest to ensure that pressure loading is adequately shared among the layers (i.e., gaps between layers are small). The analysis by Wang [23] refers to an angle 2α of about π radians, or approximately 180 degrees, before the layer is again effective due to load sharing through friction between layers. The analysis in [3], Section 6.2.5, indicates a significantly smaller angle is needed for load sharing.

A simplified example will allow assessment of the effectiveness of an expansion measurement to determine whether or not a shell layer weld has failed:

Take as an example an LPV with a shell consisting of 8 layers of ¼ inch plate and an internal liner of ½ inch plate, for a total shell thickness of 2.5 inches, with a diameter D. During normal pressurization from 0 psig to MAWP, assuming that all layers are tight and share the load with the same hoop stress, the shell increases in diameter ΔD. If a shell layer were removed entirely, then the stress would rise to approximately 10/9 of its previous value, with expansion increasing proportionally, or ΔD^* equals approximately $1.11\Delta D$.

If we assume that the layer remains in place, and if the Wang assumption of $2\alpha = \pi$ radians (180 degrees), is accepted, and if within that angle the shell is considered to be entirely ineffective, then 1/2 of the shell would be assumed ineffective, and 1/2 would be assumed to function normally. Then the shell expansion ΔD^* for a layer with a missing weld would be expected to be

an increase over the intact ΔD one-half of the increase for a missing layer. Thus, the expansion would be (1+0.11*(1/2))ΔD, or about 1.055*ΔD.

Since the Code permits an expansion equal to 50% of the expected expansion (0.5*ΔD), and typical values are in the range of 80% of the expected expansion, it is clear that the difference in measured expansion of a vessel would most likely not result in detection of the failure of a single weld in a shell layer and that even multiple failed welds could be missed using this test. The manufacturing process, including running the shell courses on rollers during welding of circumferential welds, can result in expansion of the outer layer, also resulting in relatively low expansion results for the outer layer while inner layers remain tight.

Further information regarding stresses, layer interactions, etc., is available in Reference [3].

13.13 Visual Inspections

All NASA LPV's have all been in service for many years, so the inspection performed is an in-service inspection, not an inspection as for a new vessel. Some assessments such as the fit-up inspection would normally not be needed at this stage. However, the vessels are essentially all non-code, so there is not complete confidence that appropriate fit-up inspections were adequately performed when the vessels were in process. For those vessels that have not undergone a complete inspection, such should be performed.

Visual inspection of accessible surfaces, whether outside or inside, is essentially the same as for monolithic pressure vessels, with the exception of the addition of vent hole inspections, discussed in Section 14.7. Inspections should cover: weld contour and fill, head to shell thickness transitions, quality of alignment and fit-up, surface and coating condition, external corrosion, and a careful examination for any cracking that may have occurred.

Many LPV welds were produced using processes and techniques that provided smooth contours, and some LPV's had their welds ground flush. In some cases, however, the weld contours are fairly sharp or rough, and sometimes there is undercut. Defects in weld contour must be assessed to determine whether repair is required, involving welding or grinding, or both.

Some LPV have head-to-shell transition welds steeper than the 3:1 taper permitted by the *ASME BPVC, Section VII*I [4], Div*isions 1* and *2*. Such conditions should be documented and may require additional evaluation including structural analysis.

Alignment and fit-up are typically good on these vessels, but defects should be noted and assessed.

Surface coating protects from atmospheric corrosion. While the thick walls associated with most LPV's alleviate some concerns in this regard, a coating defect that is allowed to persist can result in corrosion that could mask underlying defects and needs to be addressed.

Shell cracking is often not visually obvious, but it is sometimes revealed by rust that forms because of the break in coating that may occur at a crack (Figure 7.2.12.1). Also, as seen at the

right in Figure 7.2.12.1, existing cracks may have been painted over, yet can sometimes be observed visually.

14. Recommendations

The recommendations that follow are based on the best knowledge when this Technical Memorandum was written. They apply to the "traditional" LPV constructed with an inner layer of approximately ½ inch and multiple layers of approximately ¼ inch, and other similar vessels. Special cases with unique construction elements will require more evaluation. More capable inspection technologies, or more efficient technologies of the same capability, may and should be adopted as they become available.

14.1 General

The following recommendations apply to all later portions of Section 14.1 (numbers at the end of recommendations indicate the source of the recommendation):

(1) Develop and implement an inspection plan consistent with the requirements of [1].

(2) Determine either a CIFS or a conservative value to be substituted for it for each condition, location, and orientation to be inspected consistent with [3].

(3) Determine appropriate calibration standards applicable to the CIFS that need to be found and the vessel locations and configurations of concern. Section 9, Section 10.3.5, Section 13)

(4) Develop and produce updated demonstration rings, blocks, or calibration standards to reflect new CIFS information if the current rings are determined not to be adequate to demonstrate the required inspection capabilities. Section 9, Section 13)

(5) Perform all surface and volumetric inspections and other assessments as indicated in Sections 14.2 through 14.12 in accordance with formal procedures and scan plans developed and qualified in accordance with applicable standards such as *ASME V* [17] to detect flaws equal to and greater than the CIFS. (Section 13.1.1)

(6) Create scan plans using ray tracing software to provide confidence in the selection of beam direction and behavior for each specific weld configuration and expected flaw location, configuration, and orientation. (Section 13.1.1)

(7) After completion of inspections, touch up paint where required due to weld "flat-topping," paint removal to facilitate inspections, abrasion by robotic crawler during inspections, etc., to prevent corrosion of exposed metal surfaces. (Section 13.1.1)

14.2 Head-to-Shell Welds

Head-to-shell welds are best inspected using PAUT.

(1) Use PAUT with the transducer running on the LPV head, mounted on a crawler running on the LPV shell to identify surface, and, if the technique is qualified for them, subsurface defects based on the CIFS for the weld material and loading in question. This may be done using either conventional PAUT or PAUT using a 2D array, if qualified in accordance with Section 14.1(5). Multiple transducers or multiple passes may be needed to cover the full weld volume and the surface. (13.1.1)

(2) If PAUT is not optimized to ensure detection of surface flaws, inspect for flaws connected to accessible surfaces using MT (ferromagnetic metals), PT (any metal) with paint removed, or TECA with or without paint removal. (13.1.1**,** 13.3)
Note: It is possible that lead paint can interfere with effective use of TECA, so the qualification standard used to develop the inspection qualification should include paint similar to that on the vessels to be inspected; otherwise, paint should be removed.

14.3 Shell-to-Shell Welds

(1) Ensure that the weld surface is sufficiently flat and smooth to permit effective coupling of ultrasonic transducers and to ensure the transducer is stable on the weld surface (i.e., no rocking or tilting). (9.2**.,** 10.1.1, 11.3)

(2) Perform inspections to detect both circumferential and axial subsurface flaws using a 2D PAUT array. (10.1.1)

(3) If PAUT is not optimized to ensure detection of surface flaws, inspect for flaws connected to an accessible surface using MT (ferromagnetic metals), PT (any metal) with paint removed, or TECA with or without paint removal. (See note in 14.2(2).) (10.5.4**,** 12.1.1)

14.4 Nozzles in Heads

Nozzle size and accessibility create challenges to effective inspection.

(1) Develop and follow an inspection regime capable of identifying defects in the surface of the nozzle (especially nozzle corner cracks) and the material volume, including parent and weld metal. (8.1)

(2) Inspect for defects in the nozzle weld and parent metal volumes using conventional UT, PAUT, or ET, working from the head, the nozzle extension, or the nozzle interior as needed. (13.5.1)

(3) Create scan plans using ray tracing software to provide confidence in the selection of beam direction and behavior with specific nozzle configurations. (13)

(4) Inspect for flaws connected to accessible surfaces using MT (for ferromagnetic metals), PT (for any metal) with paint removed, or ET or TECA with or without paint removal, and using a bolt-hole ET probe or standard bobbin coil for inner surfaces. (See note in Section 14.2.(2).) (13.5.1)

14.5 Nozzles in Shells

(1) Develop and follow an inspection regime capable of identifying defects in the surface of the nozzle (especially nozzle corner cracks) and the material volume, including parent and weld metal. (13.5.2)

(2) Use standard industry eddy current bolt-hole or standard bobbin type probes to inspect from the nozzle interior. UT probes may also be used but present the disadvantage of potential vessel contamination and require cleanup of couplant following inspection. (13.5.2)

(3) Inspection of nozzle exterior attachment welds may be performed using MT, PT, ET, or TECA. (13.5.2)

Note: The bolt-hole type ET probe would have a distinct advantage over conventional bobbin coils due to inspection speed and internal encoding that can narrow the zone containing any defects found.

14.6 Longitudinal Welds

14.6.1 Outer Layer Welds

(1) Assess layer count to determine whether a fracture mechanics analysis [3] (Section 8.3) can eliminate the need for inspection (loss of one layer of a vessel of many layers is far less significant than loss of one layer of a vessel that has fewer layers). ([1])

(2) If neither layer count assessment nor fracture mechanics analysis determine that inspection is not required, inspect using VT followed by TECA, MT, or PT for surface-connected defects, and PAUT for subsurface flaws if needed (especially in the case of thick layers, e.g. on autofrettage vessels). (12.1.1)

14.6.2 Inner Layer (Liner) Welds

(1) Inspection of inner shell welds is superseded by the inspection of vent holes for leakage, as fracture mechanics studies [3] have shown that probability of a catastrophic failure due to an inner shell flaw is highly unlikely prior to leakage. (13.9)

14.6.3 Intermediate Layer Welds

Intermediate layer welds are extremely difficult to inspect except for a very small portion adjacent to the circumferential welds; however, these welds do not need to be inspected because the structural report [3] demonstrates that they are not critical to LPV integrity (also see Sections 8.1 and 8.2). (8.1**,** 8.2)

14.7 Vent Hole Inspection

(1) Incorporate vent hole inspections in the Center pressure systems database or other preventative maintenance system for performance no less than annually. (13.10)

(2) Inspect each vent hole to verify that it is clear and functional in accordance with Section 13.10. (13.10)

(3) Protect each vent hole from extraneous matter and corrosion. Any means of protecting the vent holes should be tested and demonstrated not to retain sufficient pressure to overstress the outer layer in the event of a leak through the inner liner. (13.10)

(4) In the case of vessels with “vent hole closing plates” installed by the manufacturer, the vent holes may remain covered if analysis demonstrates that they present no risk of allowing sufficient pressure buildup to endanger the outer layer of the vessel. In this case, functioning of the vent holes is assumed effective for vessels in compressed gas service. (13.10)

14.8 Leakage Through Vent Holes

For all vessels, perform the following activities, in addition to the inspections specified for either gas or liquid service, as applicable:

(1) Permanently remove any existing threaded plugs or other devices or material that could diminish the venting function of vent holes (except that vent hole closing plates installed by the manufacturer and not capable of retaining excessive pressure may be retained). (13.10.2.2)

(2) Do not add welded covers over vent holes. (Welded vent hole covers are not permitted by the *ASME BPVC*.) (13.10.1.6)

(3) For vent holes covered by manufacturer-installed vent hole closing plates, carefully inspect the plate perimeter weld on a yearly (or shorter) basis to ensure that it is not compromised. (13.10.1.6, 13.10.2.2)

(4) Immediately remove from service any LPV showing signs of leakage, pending evaluation and disposition. (14.8)

(5) Do not replace vent hole covers if they fail in operation. (13.10.1.6, 13.10.2.2)

14.8.1 Gas Containing Vessels

For vessels containing gas, perform one or more of the following alternatives, taking appropriate cautions such as PPE and use of monitoring equipment for any vessels containing flammables, toxics, or asphyxiants:

(1) Listen for the sound of escaping gases while passing near all portions of the vessel. The listener should be a person without significant upper range hearing limitations. This should not be the sole technique used in areas of high noise. If a parabolic microphone is used for inspection of targeted areas from a distance, then each vent hole should be targeted with the microphone to ensure full coverage. (13.10.1.1)

(2) Perform ultrasonic or AE monitoring, either continuously or intermittently, for sound emissions resulting from flowing gas which are high amplitude and easily recognizable based on prior AE testing projects. The supplemental requirements provided in *ASME BPVC, Section V* [17], *Article 13, Mandatory Appendix VI Leak Detection Applications* may be used as guidance for those cases requiring continuous AE monitoring for leaks from the pressure boundary, though because of their service, continuous monitoring is not normally a requirement for NASA LPVs. (13.10.1.2)

(3) Perform a bubble leak test of all vent holes. It should be noted that a small amount of "breathing" (i.e., aspiration) may occur with changes in temperature and atmospheric pressure, making careful assessment necessary for small bubble indications. (13.10.1.3)

(4) Monitor vent holes for pressure increases, using pressure gauges or other pressure-activated indicators connected to each vent hole on a vessel. If this technique is used, consideration must be given to calibration requirements, verification of functionality over time, and maintaining the pressure relieving function of the vent holes. (13.10.1.4)

(5) Perform a careful inspection of any vent hole covers welded over the vent holes by the manufacturer. Such covers are shown on some AO Smith drawings and are currently in service at GRC, MAF, and possibly at other Centers. Such covers require careful monitoring, however, to identify any covers that have been compromised, and a cover with a cracked weld that leaks gas may not be visually obvious without careful screening. Covers over vent holes are not permitted by the *ASME BPVC*, and only those covers installed by the original manufacturer on these non-code vessels may remain. (13.10.1.6, 13.10.2.2)

(6) While it should not be used as a sole inspection technique, a significant leak will likely result in frost on the exterior of the vessel due to adiabatic cooling in the vicinity of the vent hole that is expelling gas. If such frost is visible, it should never be ignored, even if there is no audible indication of a leak. (13.10.1.7)

14.8.2 Liquid Containing Vessels

For vessels containing liquids, perform one or both of the following alternatives:

(1) Monitor vent holes for pressure increase, using pressure gauges or other pressure-activated indicators connected to each vent hole on a vessel. If this technique is used, consideration must be given to calibration requirements, verification of functionality over time, and maintaining the pressure-relieving function of the vent holes. (13.10.2.1)

(2) Perform a visual inspection for drips, rust, or product build up. (13.10.2.2)

Note: Many liquid-containing vessels will have gas or vapor ullage space at the top of the liquid space, in which case the techniques described for gas-containing vessels should also be applied.

14.8.3 Vessels Containing Lethal Fluids

Install a manifolded collection system encompassing all vent holes and monitor for pressure increase, using pressure gauges or other pressure activated indicators connected to each vent hole on a vessel. Consideration must be given to calibration requirements, verification of functionality over time, and maintaining the pressure relieving function of the vent holes. This approach is reported in industry literature but does not currently pertain to any in-service LPVs at NASA facilities.

14.9 Efficiency

This report uses the term “efficiency” as a brief way of referring to LPV expansion ratios during pressurization.

14.9.1 Circumferential growth measurement

(1) Measure circumferential growth of each LPV during pressurization, in accordance with *Appendix P* or an equivalent approved procedure. This measurement needs to be performed only once. (13.7)

(2) Due to the care required to obtain accurate and repeatable measurements with steel Pi Tapes (e.g., on vertical vessels, dirty vessels, large diameter vessels with easily non-orthogonal tape placement, etc.), out-of-family or incongruous data should be verified by remeasurement protocols. (13.8)

(3) Remove from service pending evaluation any LPV with a measured efficiency of less than 50%. (13.7.1.2)

14.9.2 Efficiency Calculation

(1) If the efficiency at MAWP is less than 50% based on verified measurements, the vessel must be removed from service or further investigation performed. (Such a value is out-of-family with respect to nearly all data collected during the study and indicates inadequate sharing of load among the layers.) (13.7.1.2)

(2) If the calculated efficiency is greater than or equal to 50%, the other prescribed inspections and assessments of the vessel must still occur, but no further efficiency evaluation is required. (13.7.1.2)

1. If the calculated efficiency is 40% or above, but less than 50%, and the pressurized Pi Tape measurement was taken at a pressure lower than MAWP, either the measurement can be retaken at a pressure closer to MAWP, or equation (2), can be used to extrapolate efficiency to MAWP. If the new calculated efficiency is greater than or equal to 50%, then no further efficiency evaluation is required. (13.7.1.2)

(1) If the calculated efficiency is less than 40%, the upper measurement pressure is already as close as possible to MAWP, and the measurement data was verified, then the measured efficiency must be assumed accurate. If this occurs, the vessel must be removed from service or further investigation performed. If the measured efficiency is less than 40%, and if the current pressure is not already close to or at MAWP, measurements at a pressure closer to MAWP should be taken, and the efficiency recalculated. Figure 14.9.2.1 shows the decision tree for understanding implications of the calculated efficiency and whether additional investigation is necessary. (13.7.1.2)

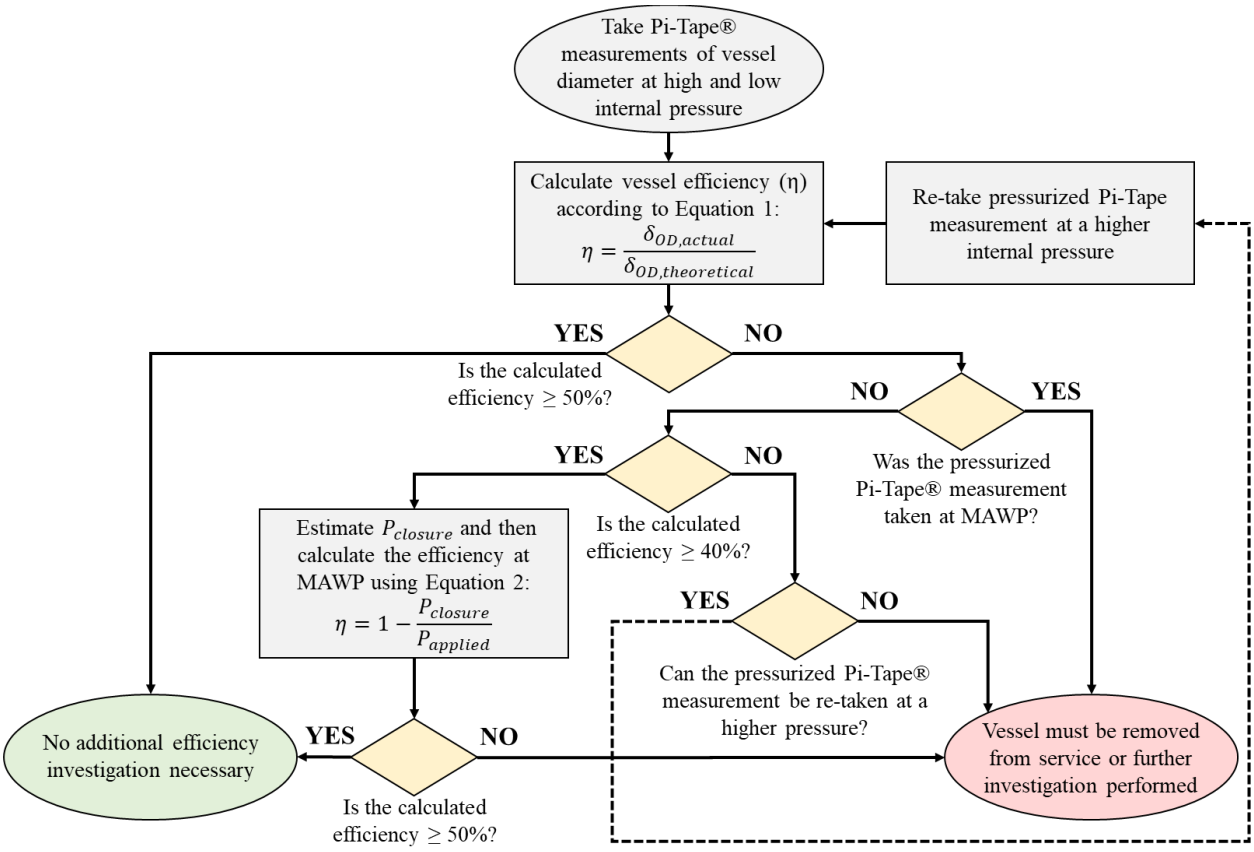


Figure 14.9.2.1: Efficiency calculation decision tree.

The decision tree graphically represents efficiency calculation recommendations 14.9.2 (1) through 14.9.2 (4) and can help determine whether additional investigation is necessary.

14.10 Acreage

(1) Perform a full visual inspection of all LPV surfaces no less than once every 10 years unless specific findings and assessments require more frequent inspection. (13.11)

(2) Perform NDE to characterize any cracks and a fracture mechanics assessment to determine acceptable crack size and remaining safe life in the parent material or repair the crack, regardless of location. (8)

14.11 Inspection for Loss of Layer

While loss of a weld in one or more layers reduces the effectiveness of that layer, because of friction effects this may not be obvious even in a careful Pi Tape inspection. Section 13.2 contains a further discussion of this phenomenon and Reference [3] also addresses it.

14.12 Visual on OD

(1) The initial inspection of LPVs should include all inspections normally included in an acceptance inspection for a pressure vessel, in addition to those items addressed in

periodic in-service inspections. This includes such items as weld contour and fill, head-to-shell transitions, quality of alignment and fit up, plus the in-service inspection items. (13.13)

(2) Regularly scheduled visual inspection of LPVs should include all aspects covered in an in-service visual inspection of a monolithic vessel, plus the vent hole inspection (13.10, 13.11, 13.12, 13.13***).***

15. Lessons Learned

(1) Prior to identification and qualification of appropriate NDE, it was necessary to determine what defect sizes and types needed to be reliably identified in order to ensure safety of LPVs. This resulted in an inevitable lag between the commencement of work on the materials and structures portions of the RMP and that of the NDE portion. This lag, combined with the natural tendency to put off paperwork and documentation, made completing this report difficult. Timely and complete documentation on future efforts will be facilitated by starting the writing effort earlier. Advantages of documenting both successful and unsuccessful work early include (1) Writing is easier when material is fresh in the writer's mind, (2) Less striking aspects of work are not forgotten or overlooked, (3) The effort to document the work accomplished brings to the forefront those aspects of work that are not yet complete, helping to bring resources to bear in these areas, (4) Overall document organization is facilitated by having write-ups available across the board, as important developments are more easily recognized in the broader context thereby provided.

(2) It is notable that long term OSMA leadership and funding was required to solve what is fundamentally a facility engineering problem. Sometimes it is not sufficient for Safety to simply identify problems and write risk/hazard assessments. This work is the culmination of a decade long system safety engineering effort that did not fit well within existing NASA organizations, but by which strong safety leaders were able to muster forces and obtain extended funding commitments to drive it to a successful and highly meaningful conclusion for both NASA and private industry.

(3) Be mindful of assumptions and the certainty that unknown unknowns do exist. This program started under the assumption that AE would quickly be proven all that was necessary and sufficient to qualify the fitness of service of these vessels, and in fact this technology had been used in that role for decades. In the end, AE does not even appear in the recommendations of this report for crack detection. Nonetheless, the lessons learned by the vendors who participated in this effort have spurred development in at least one case that may someday return to benefit LPV and other NASA pressure vessels.

(4) The goal of this effort has always been to "save" NASA's non-code LPVs which represent a billion-dollar replacement value and are single point failures for the continued operation of many critical facilities. However, at the time of this writing, it is not known what will be found at the Centers when the NDE techniques recommended herein are put

into practice by either NASA SMEs or outside NDE vendors. It is certain that PAUT is much more sensitive to finding crack-like defects than radiography. It is also clear that some of the critical CIFS and CCS are smaller than originally anticipated. It is therefore possible that application of these techniques to Center LPV will yield results that require extensive repairs or very frequent monitoring that may or may not be economically feasible. It is also noted that this work does not directly address repairs, and the effects of local repairs on weld residual stresses that were calculated specifically for this program may need to be considered. Ideally, these NDE methods would have already been applied to at least a random sampling of in-service vessels at each Center with LPVs, but resources and manpower constraints have precluded doing so. Consequently, it is possible that the results of this LPV program will not "save" every LPV at every Center.

16. Conclusion

This report documents the culmination of a multi-year effort to find and evaluate NDE technologies needed to identify critical flaws in LPVs. It provides recommendations for a credible inspection regime for such vessels.

The study assessed a number of techniques including AE, MAE, guided wave, TECA, UT, PAUT, 2D array PAUT, and circumferential growth measurement. Of the "new" techniques studied in this effort, TECA, PAUT, and 2D array PAUT stand out as particularly effective. Already accepted industry standard methods that were not assessed are sometimes also included in recommendations. Some techniques, such as MAE, show promise but are not recommended because of the greater current capabilities of PAUT.

With the exception of 2D array PAUT, each inspection technique that is included in the recommendations either represents a currently accepted process or has been validated during this effort. Formal validation of the use of 2D array PAUT for LPV inspection has not yet occurred, but vendor demonstrations as well as in-house tests have provided sufficient confidence that this technique is recommended for validation.

As noted at the beginning of the recommendations section, the NDE industry is not static. New capabilities are being discovered or invented, and older capabilities are being enhanced. Thus, while the recommendations included in this report are believed to provide the most appropriate currently available means of identifying critical defects in LPVs, it is expected that the industry will advance and new means of identifying these defects will become available. When new capabilities are developed, their effectiveness and cost should be assessed and they should be considered as potential replacements for current techniques. Only in this way will the best technology be used at the lowest cost.

17. Acronym list

AE	Acoustic Emissions Testing
ARC	Ames Research Center
ASME	American Society of Mechanical Engineers
BPVC	Boiler and Pressure Vessel Code
BTI	Bastion Technologies, Incorporated
CBI	Chicago Bridge and Iron Company
CCS	Critical Crack Size
CIFS	Critical Initial Flaw Size
CR	(NASA) Contractor Report
DIC	Digital Image Correlation
DWC	Digital Wave Corporation
ECA	Eddy Current Array
EDM	Electrical Discharge Machining
EFIT	Elastodynamic Finite Integration Technique
EM	Marshall Space Flight Center Materials and Processes Laboratory
ET	Eddy Current Testing
FMC	Full Matrix Capture
GRC	Glenn Research Center
HAZ	Heat Affected Zone
HMS	Health Monitoring System
ID	Inside Diameter (Dimension)
IP	Incomplete Penetration
IQI	Image Quality Indicator
KSC	Kennedy Space Center
LaRC	Langley Research Center
LPV	Layered Pressure Vessel
MAE	Modal Acoustic Emissions Testing

MAF	Michoud Assembly Facility
MONPAC	Monsanto/Physical Acoustics Technology for AE
MT	Magnetic Particle Testing
MSFC	Marshall Space Flight Center
NDE	Non-Destructive Evaluation (Examination)
NESC	NASA Engineering Safety Center
OD	Outside Diameter (Dimension)
OSMA	NASA Headquarters Office of Safety and Mission Assurance
PAUT	Phased Array Ultrasonic Testing
PT	Liquid Penetrant Testing
PV	Pressure Vessel
PVS	Pressure Vessels and Systems
RFI	Request for Information
RMP	Risk Mitigation Project
RT	Radiographic Testing
SSC	Stennis Space Center
SwRI	Southwest Research Institute
TECA	Tangential Eddy Current Array
TM	(NASA) Technical Memorandum
UT	Ultrasonic Testing
WFF	Wallops Flight Facility

18. References

Note: some references do not include dates because they are revised on a regular basis and the appropriate edition will be decided by the Pressure Systems Manager.

[1] *NASA Ground-Based Layered Pressure Vessels Fitness for Service Handbook*, NASA/TM-20210020974

[2] *NASA Ground-Based Layered Pressure Vessels Materials Report,* NASA/TM-20210019043

[3] *NASA Ground-Based Layered Pressure Vessels Structural Analysis Report,* NASA/TM-20210020972

[4] *American Society of Mechanical Engineers Boiler and Pressure Vessel Code, Section VIII Rules for Construction of Pressure Vessels*.

[5] Hudson, C. Michael, Newman Jr., J.C., and Lewis, Peter, *An Investigation of Fracture Toughness, Fatigue-Crack Growth, Sustained-Load Flaw Growth, and Impact Properties of Three Pressure Vessel Steels*, NASA, 1975.

[6] Hudson, Michael, *1975 Memo*, NASA LaRC Memo.

[7] *The Minutes of Meetings of the LaRC Pressure Systems Committee for November 19, 1974*, NASA LaRC.

[8] *The Minutes of Meetings of the LaRC Pressure Systems Committee for December 12, 1974*, NASA LaRC.

[9] *Discussion of Gaseous Helium LPV That Developed a Blowing Leak During Operation,* MMA-1884-80

[10] Welch, P.J., 1982, *Malfunction Investigation of a 6000 Psig Laminated Pressure Vessel*

[11] *Cyclic Crack Growth Testing of an A. O. Smith Multilayer Pressure Vessel with Modal Acoustic Emission Monitoring and Data Assessment*, NASA-CR-2014-218156 (https://ntrs.nasa.gov/citations/20140008836).

[12] *Multilayer Pressure Vessel Materials Testing and Analysis, Phase 1*, NASA-CR-2014-218157

[13] Multilayer Pressure Vessel Materials Testing and Analysis, Phase 2, NASA-CR-2014-218158

[14] *Evaluation of Agency Non-Code Layered Pressure Vessels Volume I* (corrected copy) and *Volume II*, NASA-TM-2014-218505

[15] *Hydrogen Gas Pressure Vessel Problems in the M-1 Facilities*, NASA CR-1305,

[16] *American Society of Mechanical Engineers Boiler and Pressure Vessel Code, Section IX Welding, Brazing, and Fusing Qualifications*

[17] *American Society of Mechanical Engineers Boiler and Pressure Vessel Code, Section V, Nondestructive Examination*

[18] *American Society of Mechanical Engineers Boiler and Pressure Vessel Code*, *Section X, Fiber-Reinforced Plastic Pressure Vessels*

[19] *National Board of Boiler and Pressure Vessel Inspectors, National Board Inspection Code NB-23*, 2019.

[20] Raude, Angelique; Sirois, Michael; Lemieux, Hugo; Crepeau, Joël; *Advances in Carbon Steel Weld Inspection Using Tangential Eddy Current Array*, Eddyfi Technologies.

[21] *API 579-1/ASME FFS-1 Fitness-for-Service*

[22] *ASTM E1025-18 Standard Practice for Design, Manufacture, and Material Grouping Classification of Hole-Type Image Quality Indicators (IQI) Used for Radiography,* ASTM International

[23] Y. Wang A.I. Soler, and G.L. Chen *Self-Rescue Capacity of Wrapped Vessels – A Theoretical and Experimental Analysis*, Transactions of the ASME, Volume 112, November, 1990

[24] *ASTM E-1419, Examination of Seamless, Gas-Filled, Pressure Vessels Using Acoustic Emission*, ASTM International

[25] *OSHRC Docket No. 93-0628*, Occupational Safety and Health Review Commission, 1997

[26] *NASA STD 8719.26 NASA Requirements for Ground Based Non-Code Metallic Pressure Vessels*

19. Appendices

A. A Synopsis of Known Catastrophic Failures of Layered Vessels
B. PVS-15-012 V0111 Inspection and Excavation
C. Demo Block and Ring Configurations 210726
D. PVS-16-004, MSFC Phased Array Ultrasonic Test (PAUT) for Layered Pressure Vessels
E. Request for Information (RFI) NNM17ZQD001L entitled “Feasible Technologies for Non-Destructive Evaluation (NDE) of Layered Pressure Vessels”
F. Simulation Work for Layered Pressure Vessels
G. Ultrasonic Testing Simulation Documentation
H. Detection of Transverse Flaw in a Root of Multi-Layered Vessel
I. Examination/Analysis of Acoustic Emission Waveform Data from Tensile Testing of Notched Curved Sample of LPV Steel
J. Tensile Testing of LPV Material at NIST Boulder
K. Far-Field Wave Propagation Signals from Pencil Lead Breaks on the Open End of a Thick-Walled Layered Cylinder, Part 1: Amplitudes and Frequency Content
L. Far-Field Wave Propagation Signals from Pencil Lead Breaks on the Open End of a Thick-Walled Layered Cylinder, Part 2: Modes of Wave Propagation
M. Summary of Zetec Inc. Dynaray System Demonstration, Document Number PVS-20-008
N. GRC UT Bore Probes, Dirienzo and Samuele, 2020
O. GRC Radiographic Specification for A.O. Smith PV
P. Circumferential Growth Measurement of Layered Pressure Vessels
Q. MPFR-16-016 Pi Tape Measurements of V0023
R. Efficiency Tables 20210325
S. PVS-19-011, Pi Tape Measurements of West Test Area (WTA) Hydrogen Bottles,
T. Test on Vessel V0023 MISTRAS Group AE Measurements and Analysis, September 13, 2016
U. Acoustic Emission Test Report for Vessel V0023, Report No. AE-V0023-2016
V. V0023 Vertical Multilayered Vessel Acoustic Emission Sensor Layout
W. Report on the Modal Acoustic Emission Testing of A.O. Smith Pressure Vessel V0023

Appendix A: A Synopsis of Known Catastrophic Failures of Layered Vessels

A SYNOPSIS OF KNOWN CATASTROPHIC FAILURES OF LAYERED VESSELS

SUBMITTED TO THE NASA LAYERED PRESSURE VESSEL TEAM

Maan Jawad
Global Engineering & Technology
July 13, 2017

Executive Summary

It is estimated that there are approximately 10,000 Layered Pressure Vessels in service worldwide. The service includes chemical processing, gas storage, hydrostatic presses, and other specialized services. Most of these Layered Pressure Vessels operate at a pressure above 1000 psi and temperatures up to 650^{o}F.

The following is a summary of recorded catastrophic failures in the chemical industry where corrosion and stress corrosion are a serious problem. Other failures may have occurred in this industry but are not recorded. It should be pointed out there are no known catastrophic failures recorded for Layered Pressure Vessels used in gas storage (such as the ones at the NASA facilities), hydrostatic presses, or other specialized services.

1. Hawkeye Chemical Company, Clinton, IA. March 30, 1969.
2. Chemical Construction Corporation, Louisiana. September, 1976.
3. Abocol in Cartagena, Colombia, SA. December 8, 1977.
4. Arcadian Corporation, Lake Charles, LA. July 28, 1992.
5. Qian'an, Hebei, China. October, 1995.
6. Pingyin [8], Shandong, China . March 2005.
7. Yichang [7], Hubei, China. June 2007.
8. Coffeyville Resources Nitrogen Fertilizers [9], LLC, (CVR), Coffeyville, Kansas. September 30, 2010.

March 30, 1969
Hawkeye Chemical Company [1], Clinton, IA

Failure Summary:

- A 34” Diameter by 34’ long vertical LPV failed at 5000 psi with 2/3 of the lower shell course blown away and fractured into several pieces.

Vessel Service:

- Placed in service: 1963.
- Service: Ammonia.
- Temperature: 30°F at bottom of vessel, 100°F at top.
- Pressure: 5000 psi.

General Description:

- Fabricator: Chicago Bridge and Iron Company.
- Approximate dimensions: 34" diameter x 34' long

Material of construction:

- Shell: Data matches A. O. Smith 1146 material.
- Heads: Not reported.

Construction Details:

- Vertical vessel
- Shell: Two courses.
- Liner: 1/2" thick.
- Shell construction: 11 layers of 1/4” plate.
- Bottom head: 2:1 ellipsoidal forging.
- Top head: Flanged with a flat cover.
- Nozzles: Five nozzles in bottom shell course.

Failure Details:

- Leakage noted in lower half of vessel about one month prior to failure (vessel was insulated, and frost was observed on the outside of the insulation).
- Catastrophic failure, with 2/3 of lower shell course blown away; shell fractured in several pieces.
- Some injuries to personnel, no fatalities.
- Extensive damage to surrounding plant.
- During reduced capacity operation the vessel is colder, and could have occasionally seen -29°F at operating pressure.

- Failure occurred at 4800 psi as vessel was being returned to service, and estimated temperature of 20°F to 30°F.
- Failed first at nozzle where stress was estimated to be approximately 75 ksi due to stress concentration at the nozzle area.

Source of Failure (Quoted from Reference [Cloud and Spiering, 1969]):

At the failure pressure of 4,800 psi the average hoop or circumferential stress in the vessel due to pressure was about 25,000 psi. This stress is well within the rated design stress of 29,551 psi, but there are other significant sources of stress. The most important additional sources are: (1) the general stress intensification in the area of the recirculation nozzle due to the opening; (2) thermal stresses due to both reduced temperature and differences in thermal expansion; (3) residual stresses due to weld shrinkage; (4) local stress concentration due to partial penetration welds of the internal stainless steel structure, and (5) cracks in welds in the recirculation nozzle.

September 1976
Chemical Construction Corporation [2], [3], Louisiana.

Failure Summary:

- Failure occurred in one of the longitudinal seams in the top two-thirds of the vessel.

Vessel Service:

- Placed in service: 1963.
- Service: Urea Autoclave.
- Temperature: 400^{o}F.
- Pressure: 4000 psi.

General Description:

- Fabricator: A. O. Smith Corporation.
- General Dimensions: 36" inside diameter x 32' T/T.

Material of construction:

- Shell: A.O. Smith 1135.
- Heads: ASTM A-105.

Construction Details:

- Vertical vessel
- 3/8 inch thick stainless steel inner liner.
- The shell consisted of three sections each about 10 feet long.
- 16 layers of 1/4 inch thick low strength steel.
- Top head is a reverse flange with a flat cover.
- Bottom head is a machined 2:1 surface in a flat disc.

Failure Details:

- The shell peeled opened between the top head seam and the seam between the bottom section and the middle section of the shell segments.
- The failure was ductile.
- No fatalities were reported.
- Vent holes were plugged with carbamate.

December 8, 1977
Abocol [3], [4], [5] in Cartagena, Colombia, SA

Failure Summary:

- The vessel broke into three sections during operation.

Vessel service:

- Placed in service: February 1963.
- Service: Urea Reactor.
- Temperature: 400°F.
- Pressure: 3600 psi.

General Description:

- Fabricator: A. O. Smith Corporation.
- General Dimensions: 41.375" inside diameter and an approximate length of 37'- 4" T/T.

Material of Construction

- Shell: A. O. Smith 1146 material.
- Heads: A. O. Smith 5002 material.

Construction Details:

- Vertical vessel
- Shell consists of four sections. Each section is 9'- 4" long.
- 1 inch thick lead liner.
- Shell has 1/2 inch steel inner shell, 0.1875 inch thick dummy wrap and 8 layers each 0.273 inch in thickness.
- Top head is a flange with flat cover.
- Bottom head is flat (inside and out).

Failure Details:

- Failure resulted in 30^{+} killed and 70^{+} injured.
- The vessel broke into three sections. The bottom section consisted of the bottom head plus 3'- 3" section of the shell. During the failure process the bottom section crushed the concrete ring girder which was supporting the vessel and rolled over its side.
    - The shell plates attached to the bottom section were sheared off in a ductile manner.
    - Investigation of the condition of the lead liner at a distance away from the sheared-off edge of the bottom section showed no signs of cracks.

    - Both vent holes in the bottom sheared off section of the shell were plugged.

- The middle section, which was about 15'- 4" long, split open longitudinally and then tore apart circumferentially 3'- 3" from the bottom head circumferential seam and at the middle circumferential seam of the vessel.
    - A piece measuring 63" x 40" was missing from the top section of the lead liner.
    - Areas adjacent to the missing piece showed a lead thickness of less than 0.25" as compared with the normal 1.0" thickness elsewhere in the vessel.
    - In the same vicinity, wraps 1, 2, 3, and 4 were corroded away in a small area. The plates thinned down from 0.273" at areas away from the corroded sections to less than 0.03" at the corroded sections.
    - The sheared areas of all plates had a ductile appearance.
    - Circumferential measurements indicated an approximate length of 123" to 124". Bulges due to excessive heating were not observed.

- The top section of the vessel, which was about 18'- 9" length of the shell plus the flange and top cover, weighed about 70,000 lbs. It moved upwards after breaking loose at the circumferential seam. It then came down, hit the roof edge of the staff building and then buried itself into the ground at a 45^{o} angle. The final location of this section was about 140' from the original vessel foundations.
    - Inspection of the failed section at the roundabout indicated ductile failure.
    - Inspection of the top cover and one of the studs did not reveal any stretch marks (no over pressurization).
    - Inspection of the lead liner did not reveal any erosion and/or corrosion.
    - One vent hole in the shell near the top flange was open while the other was plugged. Similarly, one vent hole in the shell near the bottom failed circumferential weld was open while the other one was plugged.

- Samples were taken from various plates for testing. All tensile and yield stresses were within the range for 1146 material. Charpy test values at 30^{o}F for some of the tested plates ranged between 13 ft-lbs and 15 ft-lbs. And while these Charpy values tend to be on the low side for this material, they were of no concern since the lowest average temperature in Cartagena, Colombia, is 81^{o}F in January.
- Plugged vent holes that led to corroded plates in a small area in the vicinity of the hole. Thus, the remaining uncorroded plates in the vicinity of the hole are overstressed due to internal pressure

July 28, 1992
Arcadian Corporation [6], Lake Charles, LA

Failure Summary:

- Failure occurred while the vessel was operating at full operating pressure and temperature.
- Failure occurred at a shell-to-shell seam.

Vessel Service:

- Placed in service: 1989.
- Service: Urea.
- Temperature: approximately 374°F.
- Pressure: 2,865 psi.

General Description:

- Fabricator: Schoeller Bleckmann (Austria).
- General Dimensions: 6' inside diameter x 90' long.

Materials of Construction

- Shell: Not reported.
- Heads: Not reported.

Construction Details:

- Vertical vessel
- Four shell courses each 20 ft long. The circumferential weld seams were designated as C1 (shell-to-bottom head), C3, C5, C7, and C9 (shell-to-top head).
- 1/2” inner stainless steel liner plus a dummy layer plus 13 layers of 1/4” plate.

Failure Details:

- Leak prior to failure, and one or more previous leaks had been repaired.
- Two employees hospitalized for several days.
- Failure occurred at circumferential weld seam C7. The top shell course and top head landed 650 feet south of the vessel while the remaining vessel sank in the ground 40 feet.
- Vent holes were plugged.

Oct. 1995
Qian'an [7], [8], [9], Hebei, China

Failure Summary:

- Failure similar to LPV in Cartagena where the middle section opened up longitudinally and then broke away at the end circumferential seams of the shell section.

Vessel Service:

- Placed in service: Not reported.
- Service: urea synthesis tower.
- Temperature: Not reported.
- Pressure: Not reported.

General Description

- Fabricator: Not reported.
- General Dimensions: Not reported.

Materials of Construction:

- Shell: Not reported.
- Heads: Not reported.

Construction Details:

- Not reported.

Failure Details:

- Failure resulted in 10 killed and 5 injured.
- Stress corrosion cracking.
- No mention of whether the failure is ductile or brittle.
- It is postulated that leakage in vent holes at various times resulted in the process product solidifying at various layers near the vent holes. The corrosive nature of the product may have produced stress corrosion cracking in the layers that facilitated crack initiation in various layers.

March. 2005
Pingyin [8], [10], Shandong, China

Failure Summary:

- Failure similar to LPV in Cartagena where the middle section opened up longitudinally and then broke away at the end circumferential seams of the shell section.

Vessel Service:

- Placed in service: Not reported.
- Service: urea reactor.
- Temperature: Not reported.
- Pressure: Not reported.

General Description:

- Fabricator: Not reported.
- General Dimensions: Not reported.

Materials of Construction:

- Shell: Not reported.
- Heads: Not reported.

Construction Details:

- Not reported.

Failure Details:

- Failure resulted in 4 killed and 32 injured.
- Stress corrosion cracking.
- No mention of whether the failure is ductile or brittle.
- It is postulated that leakage in vent holes at various times resulted in the process product solidifying at various layers near the vent holes. The corrosive nature of the product may have produced stress corrosion cracking in the layers that facilitated crack initiation in various layers.

June 2007
Yichang [7], Hubei, China

Failure Summary:

- Failure similar to LPV in Cartagena where the middle section opened up longitudinally and then broke away at the end circumferential seams of the shell section.

Vessel Service:

- Placed in service: Not reported.
- Service: ammonia synthesis reactor.
- Temperature: Not reported.
- Pressure: Not reported.

General Description:

- Build by: Not reported.
- General Dimensions: Not reported.

Materials of Construction

- Shell: Not reported.
- Heads: Not reported.

Construction Details:

- Not reported.

Failure Details:

- Failure resulted in 10 injured.
- Stress corrosion cracking.
- No mention of whether the failure is ductile or brittle.
- It is postulated that leakage in vent holes at various times resulted in the process product solidifying at various layers near the vent holes. The corrosive nature of the product may have produced stress corrosion cracking in the layers that facilitated crack initiation in various layers.

September 30, 2010

Coffeyville Resources Nitrogen Fertilizers [11], LLC, (CVR), Coffeyville, Kansas

Failure Summary:

- Fractured occurred at the weld between the top flange and layered shell (on the flange side).
- Fracture also occurred at the weld between the jacket and the flange.

Vessel Service:

- Placed in service: October, 2000
- Shell was fully jacketed. (Jacket removed during rework after failure, and not replaced.)
- Service: Urea.
- Temperature: 390^{o}F.
- Pressure: 3600 psi.

General Description:

- Fabricator: Hahn and Clay
- General Dimensions: 4' diameter x 88' long .

Materials of Construction:

- Shell: SA-724 Grade B.
- Jacket: SA-516 Grade 70.
- Heads.SA-508-4N Class 3.

Construction Details:

- Vertical vessel
- 1/4” inner stainless steel liner plus 14 layers of 1/4” plate.
- Outside jacket on the shell.
- Build in accordance with ASME VIII-1, 1995 edition.

Failure Details:

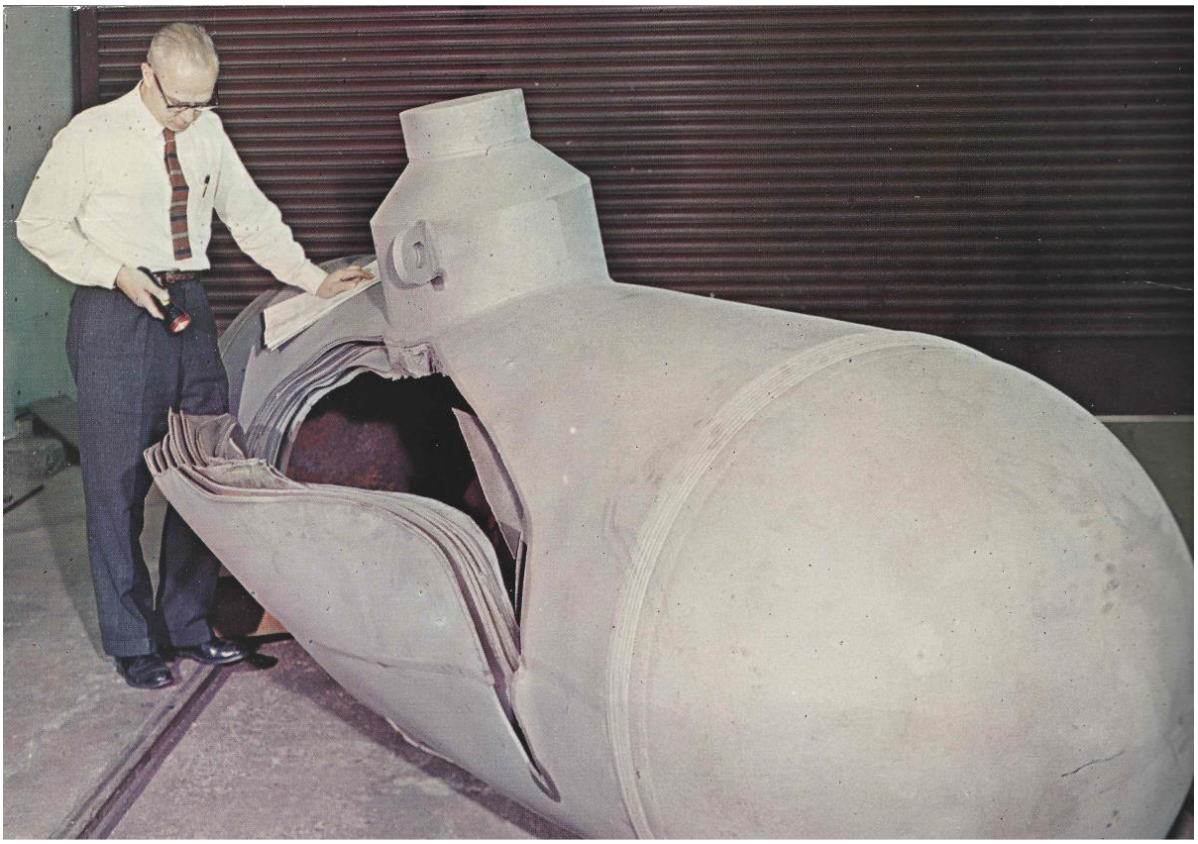
- Failure due stress corrosion cracking.
- Cracks in the heat effected zone of the weld between the flange and shell and also between the flange and jacket.
- Failure was ductile.

Some Observations on the Catastrophic Failure of Layered Vessels In the Chemical Industry

1. Because corrosion or stress corrosion cracking appear to have been involved in each case, plugged or otherwise non-functional vent holes were associated with most of the failures in this report.
2. Lack of monitoring and maintaining the vent holes seems to be a major contributor to catastrophic failures. Had the vent holes been adequately monitored and leaks not ignored, the presence of the vent holes would in most cases have prevented the mishap.
3. Corrosion in layers due to product leaks distributed through vent holes which are plugged near the outside surface of the vessel seems to be a serious problem in the chemical industry.
4. All reported failures were ductile in nature (the Chinese vessel reports did not indicate ductile or brittle failure). No carbonization or embrittlement of steel due to presence of H_2.
5. Because NASA operations differ significantly from those in the chemical industry, including not involving corrosive media, these cases provide little information regarding the likelihood of failure at NASA. They do, however, provide important information regarding how, once started, a crack may propagate to complete failure of an LPV.

Observation on some Experimental data

Most fabricators are reluctant to place large openings requiring reinforcement in Layered Pressure Vessel shells. However, the ASME Section VIII rules indicate that such reinforced nozzles are acceptable and the design procedure is the same as that for solid wall vessel. This policy stems from the results of failure tests made at various manufacturers showing that failure occurs at a pressure equal to or higher than the factor of safety for the vessel (4.0 when the rules were written). The following photograph indicated such a test.



References

[1] Cloud and Spiering, , March 30, 1969. “Failure of a High Pressure Vessel in Ammonia Service”, ASME, 81-PVP-8.

[2] A.O. Smith drawing MV-50781.

[3] Jawad, Maan. Private files.

[4] A.O. Smith drawing MV-50718.

[5] Toshio Jojima, Mitsui Toatsu Chemicals. “Urea Reactor Failure”. American Institute of Chemical Engineers, Symposium on Safety in Ammonia and Related Facilities, November 13, 1978, Miami Florida.

[6] Court Case, July 28, 1992”Arcadian Corp versus Olin Corp.” No 01-1066. 824So.2d 396 (2002).

[7] Xueqin Huang, Zhenhui Wang, Chunyan Ding, et al. “Energy estimation of materials in broken urea synthetic tower”, Journal of Hebei University of Science and Technology. 25, 1(2004) 69~72,76.

[8] Mingda Song, Weiqiang Wang, et al. “Multilayer Urea Reactor Safety Evaluation Based on Acoustic emission Examination”. PVP Conference July 15-19, 2012. Paper 78135.

[9] Mengli Li, Weiqiang Wang, et al. “Analysis of Layer Cracking in Urea Reactors”. PVP Conference July 18-22, 2010. Paper 25855.

[10] Weiqiang Wang, Aiju Li, Yanyong Zhu, et al. The explosion reason analysis of urea reactor of
Pingyin, Engineering Failure Analysis. 16, 3(2009)972~986.

[11] Mark Gilbertson (mmgilbertson@CVREnergy.com) and Daniel Benac (dbenac@BakerRisk.com), circa 2014. “Multi-Layered Secondary Urea Reactor Failure”.

Appendix B: PVS-15-012 V0111 Inspection and Excavation

Report # PVS-15-012

V 0111 Inspection and Excavation

Introduction:

During the summer of 2015, a Phased Array Ultrasonic Inspection of V111 revealed an indication in the weld volume that warranted further investigation. This indication was in excess of the Time Corrected Gain (TCG) investigation level and was sized according to the ASME Section VIII, Division II guidelines and compared to the charts in the aforementioned section for examinations using Fracture Mechanics based criteria to determine disposition. This evaluation yielded an indication that was rejectable and further manual scanning of the area reproduced the indication. The indication was marked on the weld surface and the vessel was removed from service to allow excavation and investigation of the indication.

Vessel:

The vessel under inspection (V-111) was built in 1957 and is a vertically oriented A.O. Smith layered pressure vessel consisting of a ½" inner shell liner and seven ¼" layers. These layers are formed from ASTM A225 Grade B Modified plate steel. The hemispherical heads are 33" diameter, 1- 3/16" thick nominal, and were required by the construction drawings to conform to A.O. Smith spec 11486. This vessel was designed with a safety factor of 2 to 1 based on material yield strength and constructed for a working pressure of 3500 Psi.



Figure A1: V- 111 at Bldg



Figure A2: V- 111 Data Plate

4619. **Inspection:**

The inspection of the head to shell welds was performed using the PAUT technique utilizing an Olympus Omniscan MX2, 5 MHz- 16 element transducer, and wedge that conforms to the outer diameter of the head. This combination was used to perform a sectorial scan from 35° to 70° in 0.5° increments (36 sound beams). Using this setup, 2 encoded line scans at separate indexes were required to provide complete coverage of the weld and heat affected zone. The acquisition of the inspection data was aided by the use of the Jireh Industries Navic vessel scanner, a remote controlled crawler held to the vessel outer wall magnetically. This allowed for a smooth scanning rate, and solid platform on which to mount the transducer/wedge combination. Coupling of the search unit to the vessel surface was provided by

an agricultural ATV sprayer fitted with a regulator. This enabled a steady flow of water and detergent to be applied through the irrigation holes in the transducer. Carbide pins built into the corners of the wedge set a water column between the wedge and part that is consistent throughout the scan. This also virtually eliminates any fluctuation of amplitude due to varied pressure applied to the transducer during the inspection.

Calibration of the UT instrument was performed using the Jacobs PAUT procedure P7401.1C, and was a standard ASME type calibration. Linearity for the unit was established using the IIW-2 (International Institute of Welding Type 2) block, and the TCG was established using an ASME compliant calibration block with holes located at ¼, ½, and ¾ of the block thickness. The response from the 2% notch on the block was then brought to 80% Full Screen Height and the gain setting was noted as the inspection sensitivity setting. This setup would be used for both index positions on the vessel.

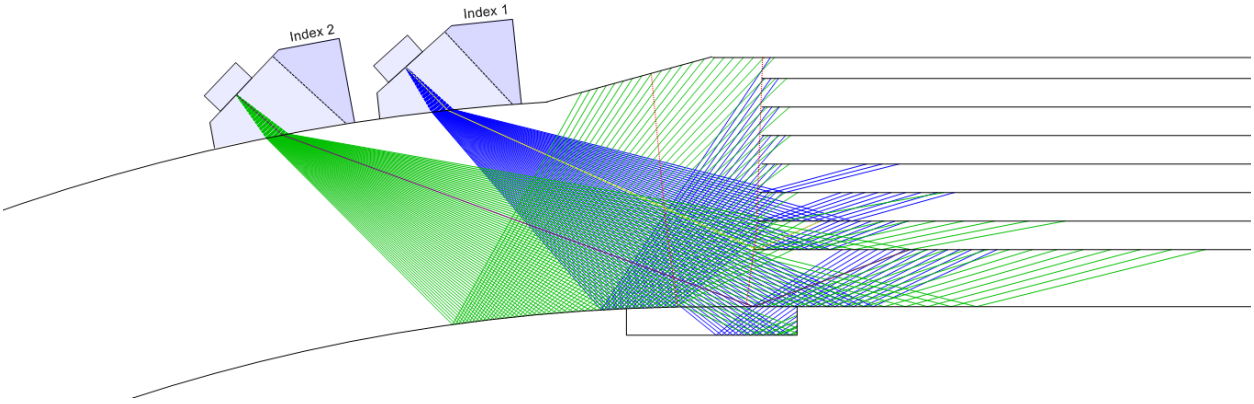


Figure A3: Pictorial rendering of Index 1 and Index 2 on a cross section of the weld.



Figure A4: Scanning a vessel using the Navic Crawler.

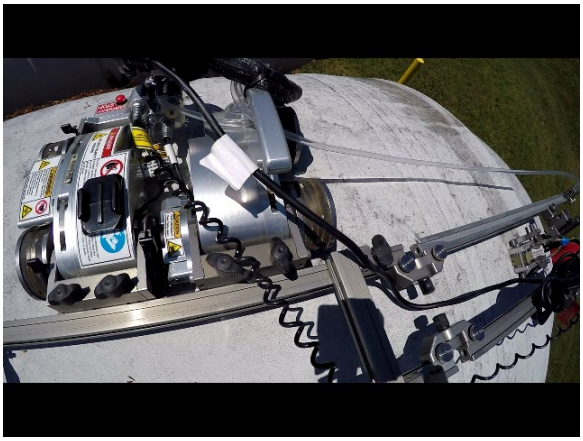


Figure A5: Navic Crawler during a scan of a vessel.

Evaluation of Inspection Data

Full length scan data was imported into the Olympus Tomoview program and both scans merged into one file. This allowed the data from both scans to be reviewed together. The data was reviewed using the A, B, S, C, and D scan representations. During this review, an indication was noted at 110.5” from the beginning of the scan that was indicative of a linear, crack like defect. Each view of the actual indication is shown in Figures A6 through A10. The indication exhibited a length of .236”, and a height of 0.200”. This was the only indication on the vessel noted in either scan that was found to be of any concern. Results of this examination were reported informally to management and the decision was made to immediately isolate this vessel from service until an evaluation of this indication could be performed.

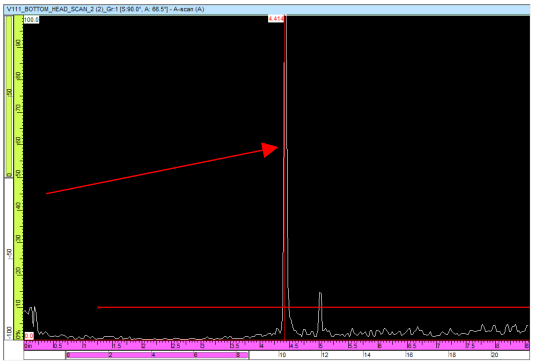


Figure A6: A- Scan representation

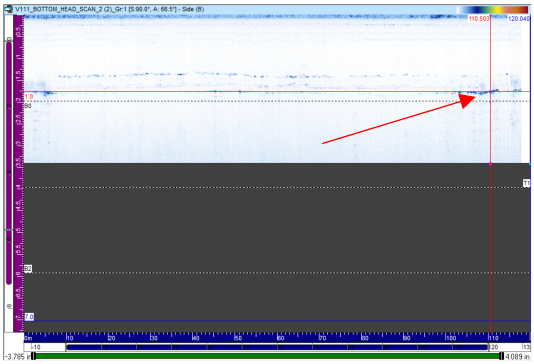


Figure A7: B- Scan representation

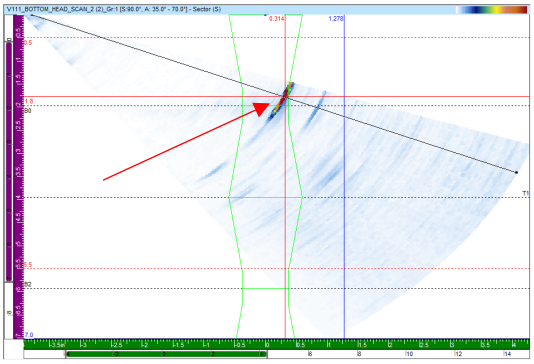


Figure A8: S- Scan representation

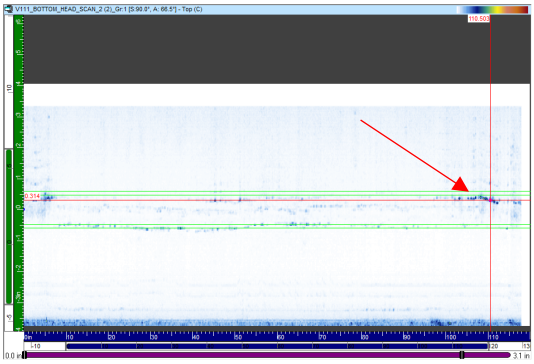


Figure A9: C- Scan representation

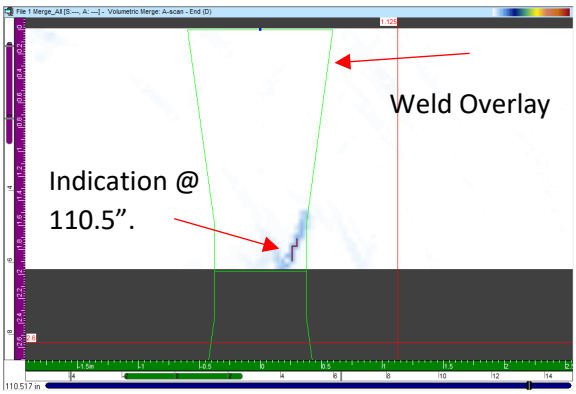


Figure A10: D- Scan Representation -18 dB.

The indication was evaluated for acceptance or rejection disposition using Table 7.10 from Section VIII Division II of the ASME Code- 2013 Edition. Using the height (h), length (l), remaining ligament to the nearest surface (S), and part thickness (t), the parameters in the table could be calculated for the flaw in question.

Flaw Height *(h)*: 0.200"
Flaw Length *(l)*: 0.236"
Part Thickness *(t)*: 1.950"
Remaining Ligament *(s)*: 0.100" from the inner wall

If *s* > 0.5h, defect is classified as subsurface
If *s* <= 0.5h, defect is classified as surface

In this case, the remaining ligament (S) is equal to one half the flaw height (h), therefore the finding is categorized as a surface flaw.

For a surface flaw, a = s + h = 0.100 + 0.200 = 0.300
a/l = 0.300/0.236 = 1.271
a/t = 0.300/1.95 = 0.154

The value of a/l exceeds the values in Section VIII Table 7.10 therefore the flaw is larger than allowed by code and was rejected. Due to the indication appearing crack like during the evaluation of the inspection data, a decision was made to expose the defect to validate the data interpretation. Given the construction of the vessel, an excavation from the OD was the only choice. The indication was interpreted to be 1.7" below the outer surface and metal was removed by grinding to this approximate depth at which point a crack indication was observed. Subsequent PT and MT examinations verified the existence of the crack. Photographs of the excavation area and the indication are shown in Figures 11 through 18. Actual visual measurements of this indication yielded dimensions very near that of the PAUT inspections.



Figure A11: Beginning excavation.



Figure A12: Excavation and ends of layers.



Figure A13: Excavation and ends of layers.

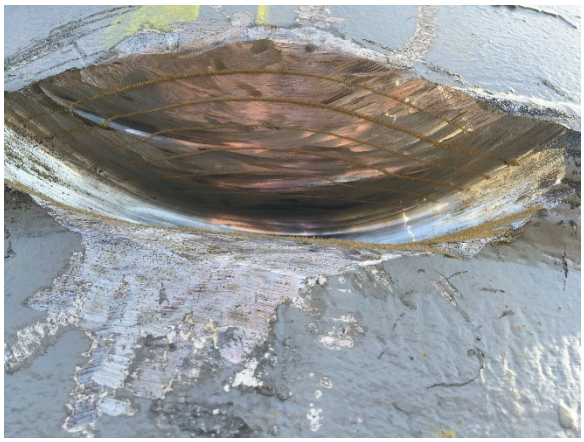


Figure A14: Excavation and ends of layers.

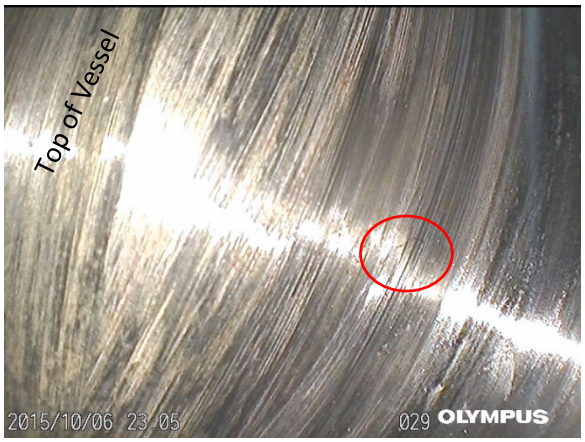


Figure A15: Indication discovered during excavation.

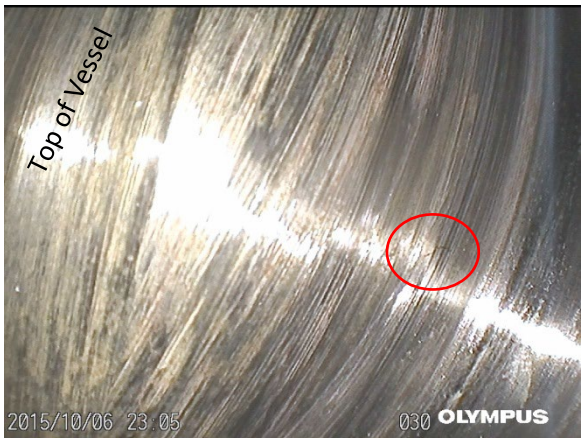


Figure A16: Indication discovered during excavation.



Figure A17: Indication discovered during excavation.



Figure A18: Indication discovered during excavation.

Disposition:

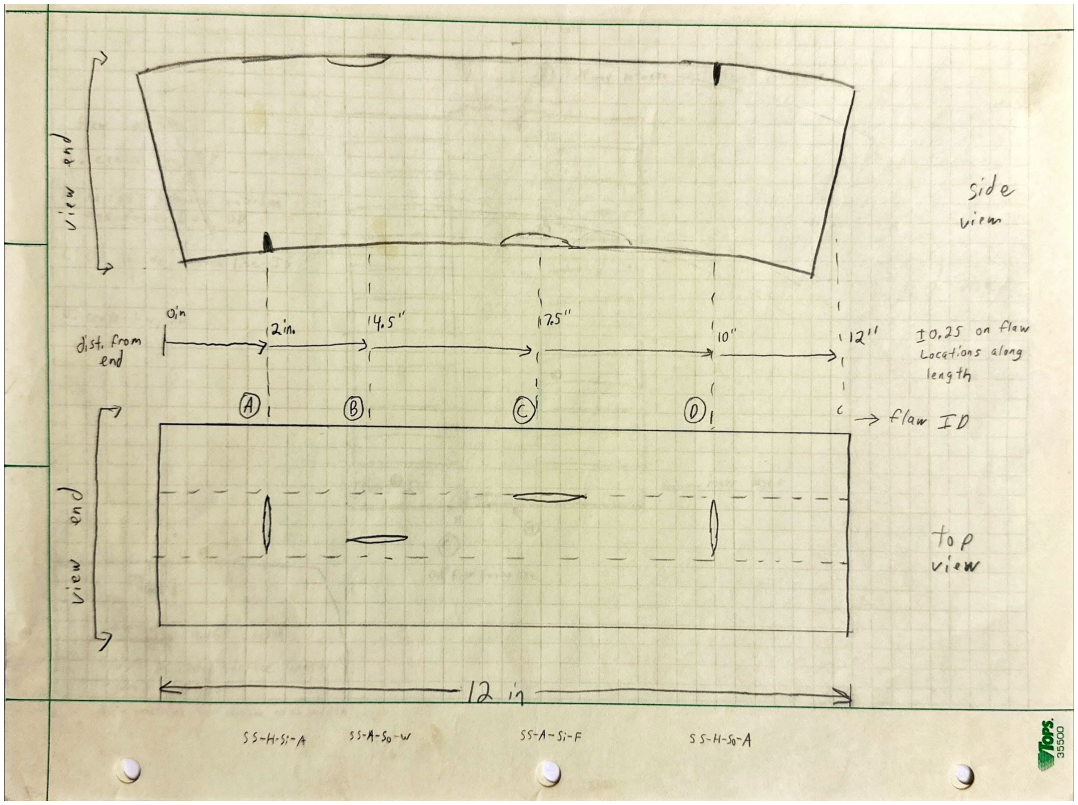
The indication that was discovered during this inspection and excavation still remains in the head, as well as the open excavation. A TPS has been issued and is currently in work to spray paint the open excavation to preserve the surface of the head should it be decided to repair this vessel in the future and return it to service. No further inspection of this vessel is planned at the time of this report.

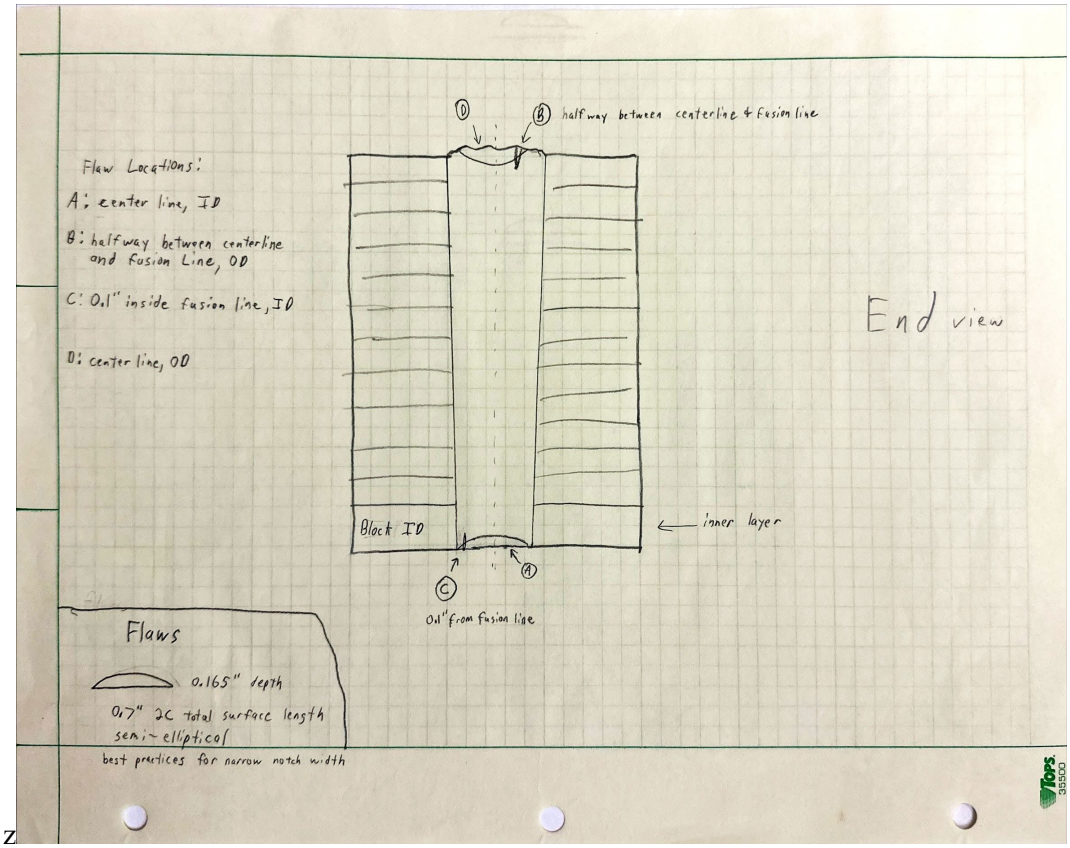
Appendix C: Demo Block and Ring Configurations 210726

Appendix C

Details of Demo Blocks and Rings

2018-03-30_10-41-09_081.jpeg

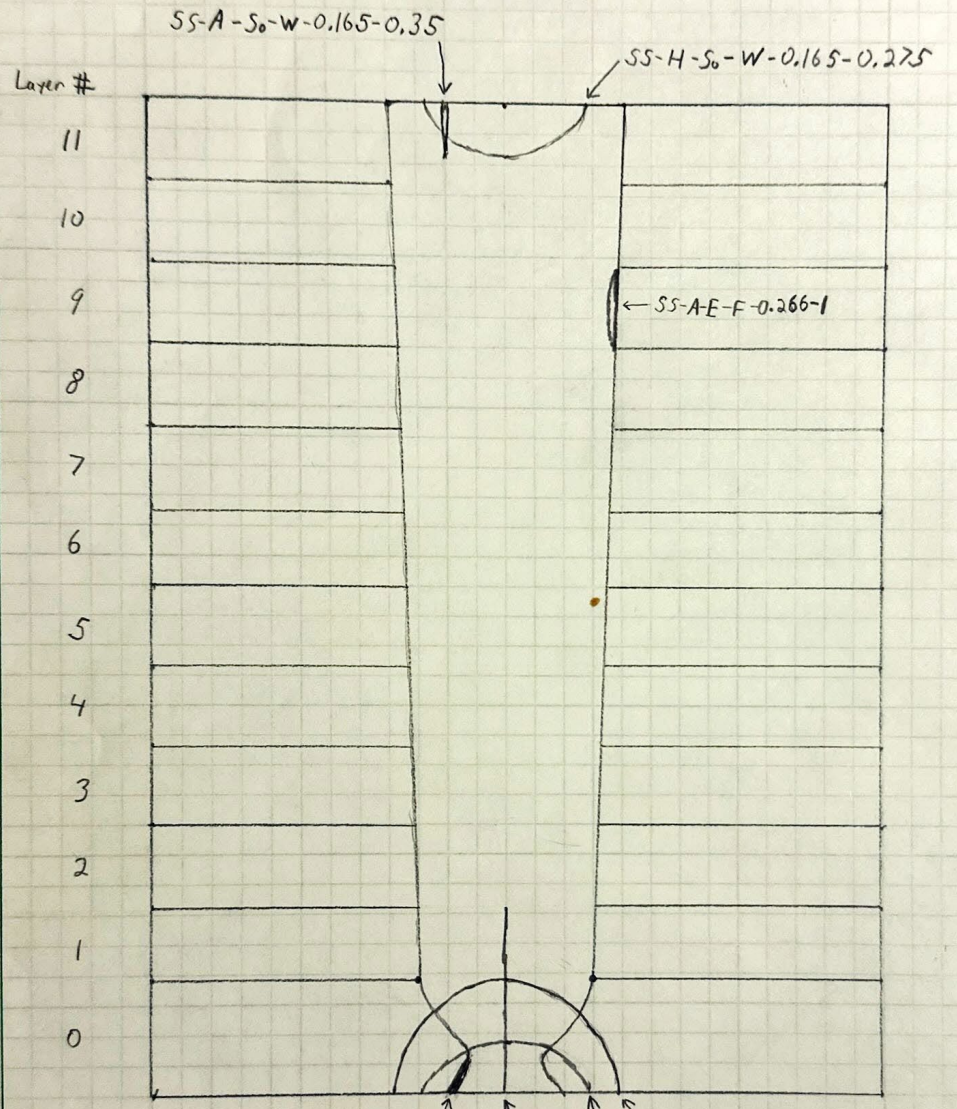




Demo Ring –

Flaw Map – Final.pdf

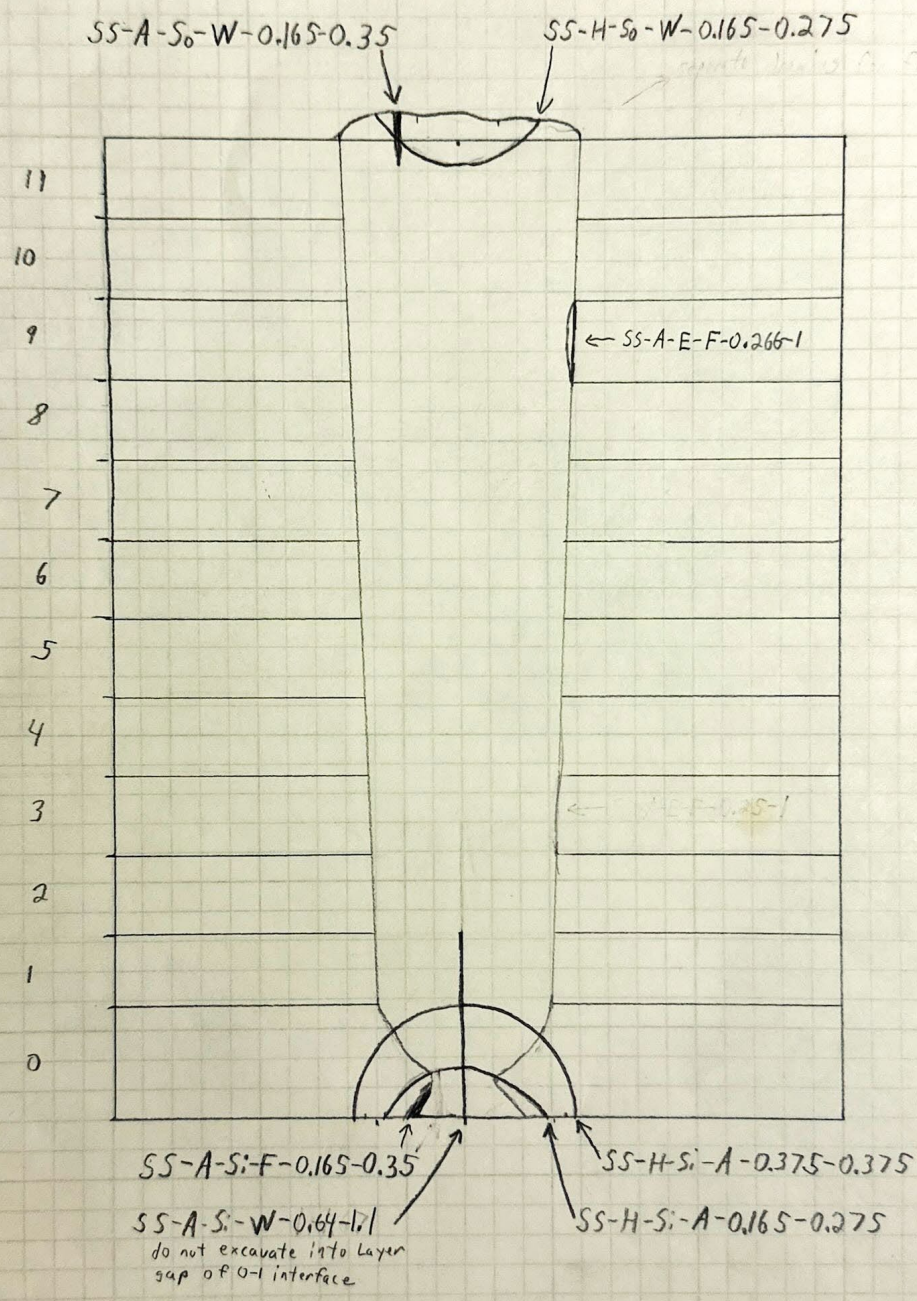
End View | Demo Ring | Weld B → Flat Top



t_{total} = 3.3" Layers 0-11
t_{inner} = 0.375" Layer 0
t_{wraps} = 0.266" Layers 1-11

TOPS. 35500

AS- Welded	Demo Rings	End View Weld A

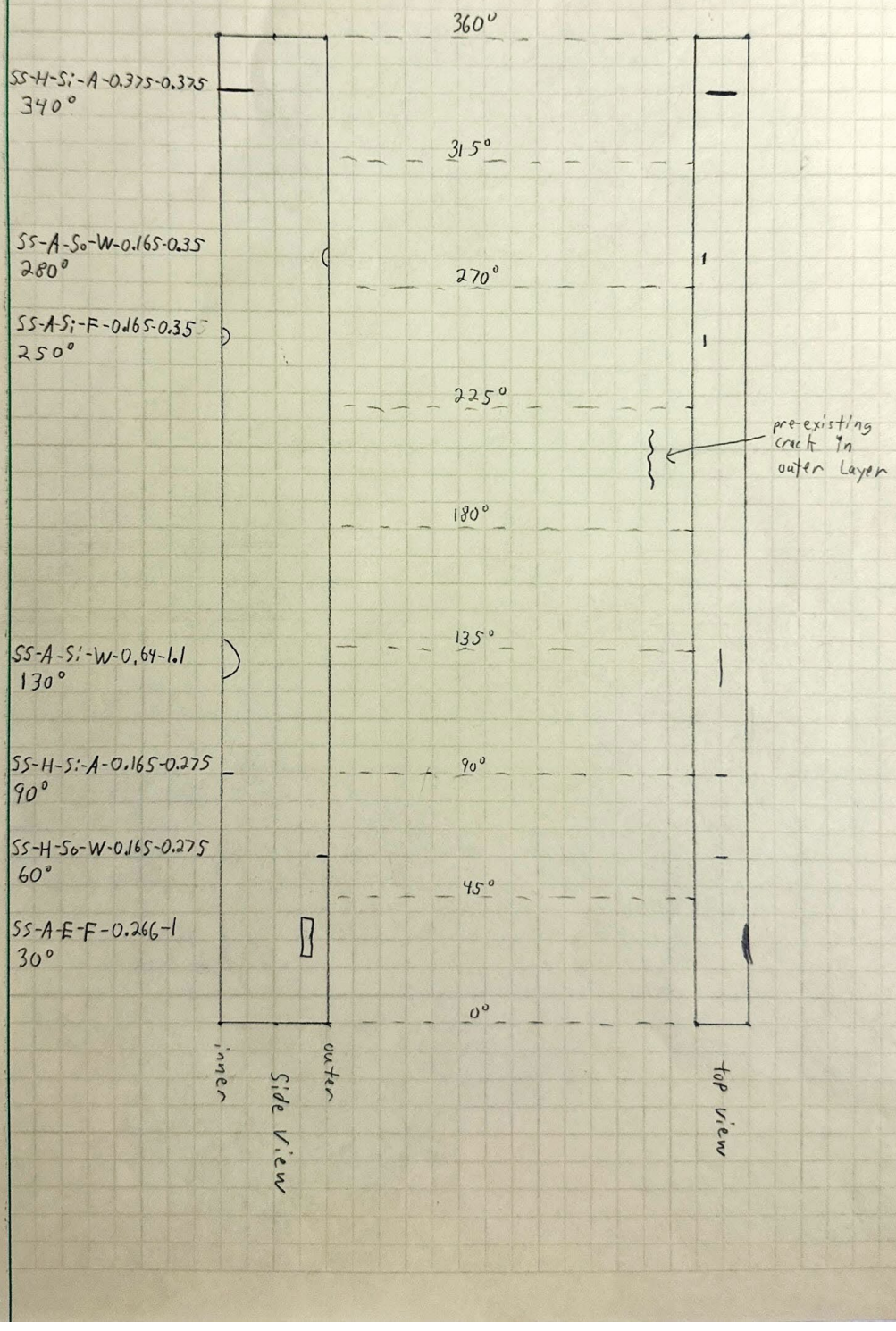


$t = 3.3''$ Layers 0-11

$t_{inner} = 0.375''$ Layer 0 $\quad t_{wrap} = 0.266''$ Layers 1-11

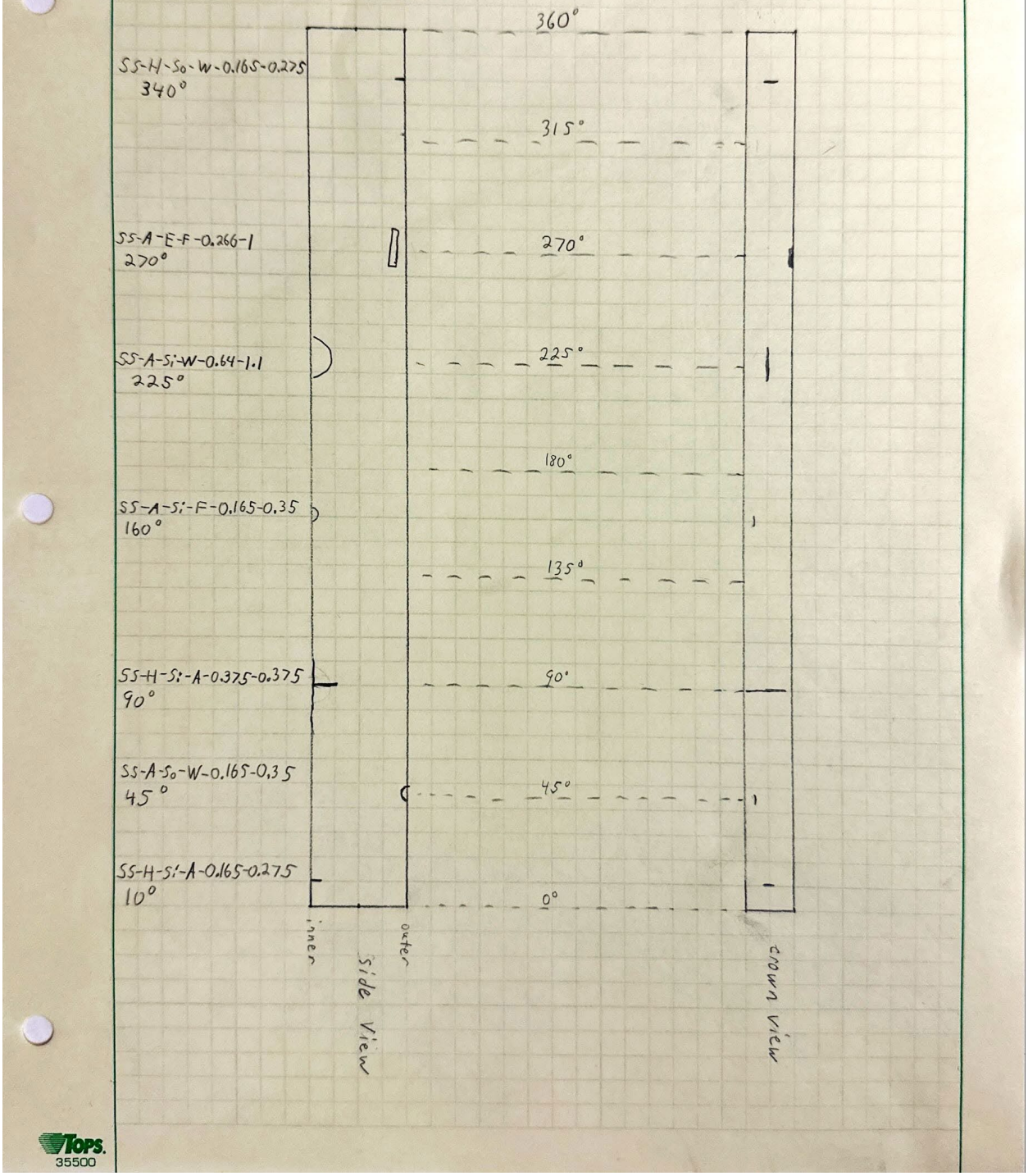
TOPS 35500

Demo Ring | Weld B – Flat top

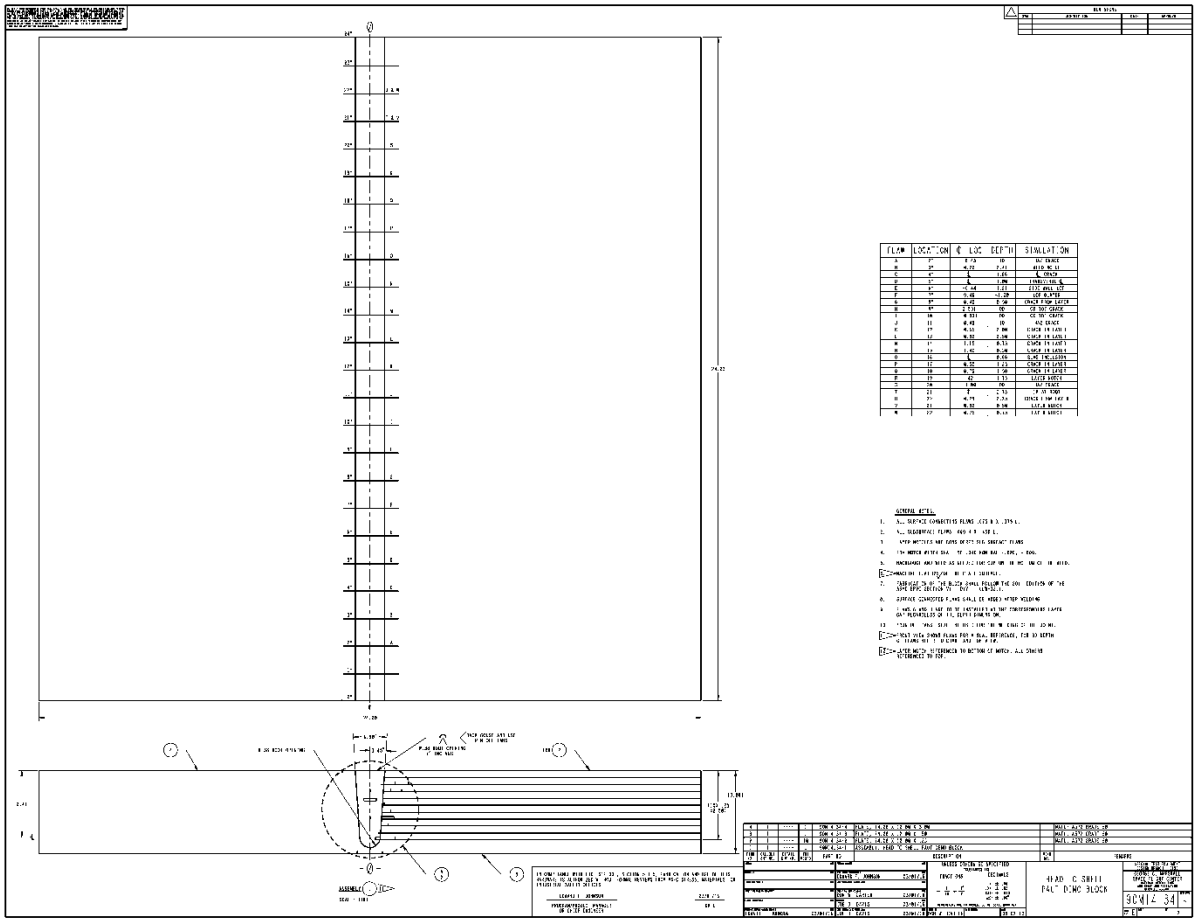


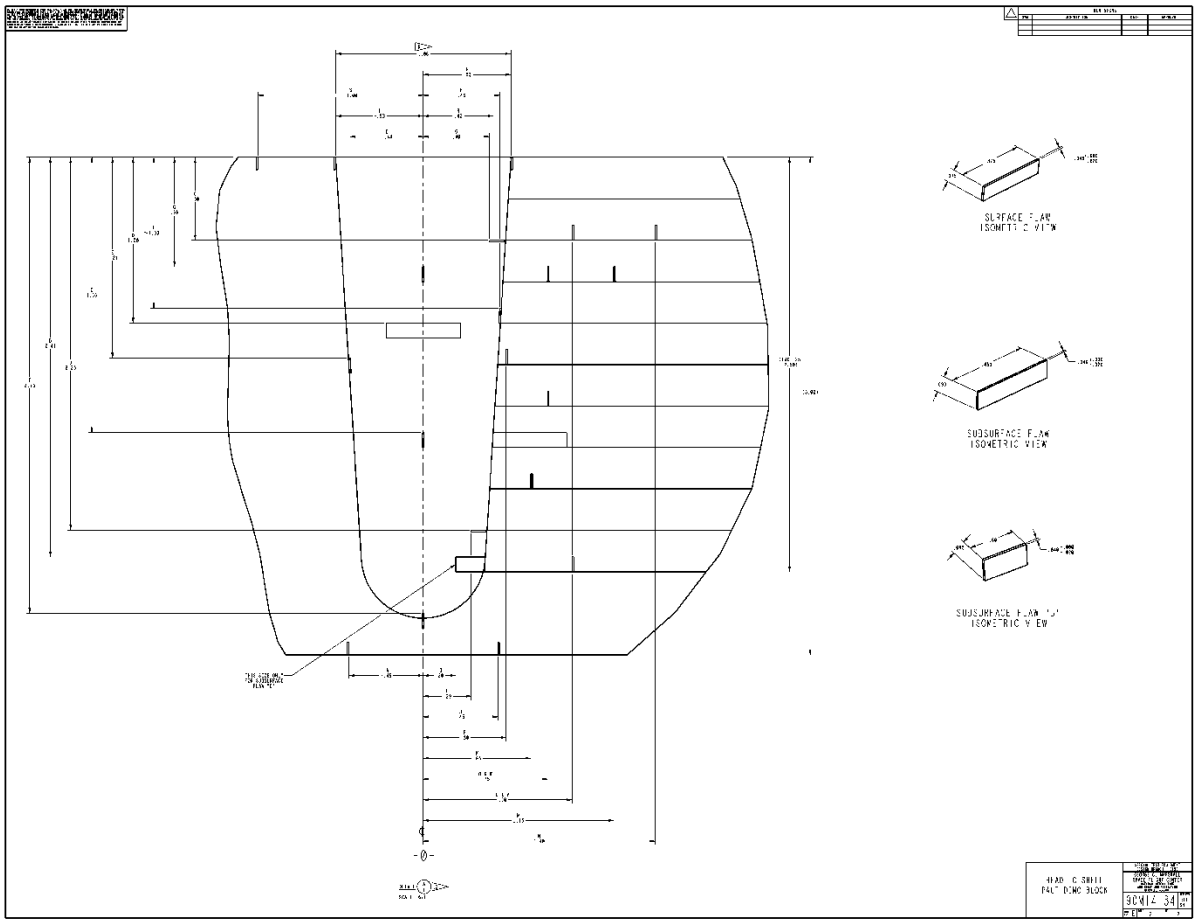
Demo Ring

Weld A – As-welded crown



Demo Block 90M14134 pdf d(03-01-2016) Final




SURFACE FLAW
ISOMETRIC VIEW
SUBSURFACE FLAW
ISOMETRIC VIEW
SUBSURFACE FLAW "A"
ISOMETRIC VIEW
HEAD C SHELL
FULL DIMENSION

Appendix D: PVS-16-004, MSFC Phased Array Ultrasonic Test (PAUT) for Layered Pressure Vessels

NASA Aeronautics and Space Administration

George C. Marshall Space Flight Center
Huntsville, AL 35812



MSFC Phased Array Ultrasonic Test (PAUT)

for

Layered Pressure Vessels

MSFC Pressure System Program Document

PVS-16-004

October 18, 2016

References

Note: In this document, the symbol " [ ] " denotes reference documents. Some of the references are attached as further denoted below.

1. "*Phased Array Ultrasonic Test (PAUT) Equipment Demonstration at MSFC*", MSFC Pressure System Program Report dated February 18, 2014 (Submitted to Dr. Bill Prosser/NESC in February 2014). (Attachment 1)

2. "*Davis NDE Statement of Work for Performance Demonstration Block*", MSFC Procurement Document dated December 24, 2013. (Attachment 2)

3. MSFC Drawing 90M14134 "*Head to Shell PAUT Demo Block*"

4. "*PAUT Demo Block Flaw Sizing for Layered Pressure Vessel Circumferential Welds*", MSFC Materials and Processes Laboratory Flash Report # MPFR-13-015, Joel R. Hobbs and Gilda Battista, July 1, 2013. (Attachment 3)

5. "*Final Report, NASA MSFC – Layered Vessel Demonstration Block*", Davis NDE final deliverable per contract: Bastion-BPO-140096-CO1, Parrish Furr, March 13, 2015. (Archived as Pressure System Program Document PVS-15-004)

6. "*Report # PVS-15-012, V111 Inspection and Excavation*", MSFC Pressure System Program document, Daniel Barrentine, December 2, 2015.

7. "*Report # PVS-15-013, V229 Inspection and X-Ray*", MSFC Pressure System Program document, Daniel Barrentine, 2015.

NOTE: Work described in this report was completed in 2014-2015. To ensure that all relevant information and documentation was captured and properly archived, this report was written providing a summary of MSFC PAUT activities referencing all relevant PAUT documentation which had not previously been archived or consolidated. This report, with all references and attachments, was provided to the Agency LPV Working Group in the summer of 2016 for review.

1.0 Background:

The objective of this report is to document the current process used at MSFC for examination of layered pressure vessels (LPVs) using phased array ultrasonic test (PAUT) methods. This report will also summarize previous PAUT activities at MSFC and serve as a means of consolidating and archiving documents which were created as part of these past efforts. MSFC began employing PAUT for inspection of LPV head-to-shell welds and head nozzle welds in 2015 after completing the performance demonstration effort discussed herein.

2.0 Previous MSFC PAUT Activities

MSFC began investigating the use of PAUT in 2013 in a collaborative effort with Stennis Space Center (SSC) and Glenn Research Center (GRC). The following information provides a brief timeline of events leading up to implementation of PAUT field inspection of LPVs at MSFC.

2.1 Initial PAUT Equipment Demonstration

Davis NDE personnel were invited to MSFC in April 2013 to provide a PAUT equipment demonstration. Davis NDE, a NDE training and consulting contractor located in Hoover Alabama, had previously reported some successes in detecting flaws in LPVs using PAUT. The equipment demonstration by Davis NDE included a weld scan in selected areas on an out-of-service MSFC LPV (vessel V0256). The conclusion drawn from this initial equipment demonstration was that PAUT appeared to offer an improvement over conventional ultrasonic test (UT) inspection methods providing much more weld volume detail. The report describing the initial PAUT demonstration effort is entitled "*Phased Array Ultrasonic Test (PAUT) Equipment Demonstration at MSFC*" dated February 18, 2014 [1]. This report was provided to the NASA Engineering Safety Center (NESC) LPV Working Group lead, Mr. Bill Prosser, in February 2014.

2.2 Performance Demonstration Block Evaluation

MSFC personnel began developing a concept for a more detailed evaluation of PAUT capabilities for LPV inspection in 2014. A statement of work (SOW) [2] was written for Davis NDE to fabricate a performance demonstration (PD) block with artificial flaws to be used for PAUT weld scans using guidance from ASME Section V Article 4 Appendix IX "Procedure Qualification Requirements for Flaw Sizing and Categorization". The SOW for construction of the PD block was reviewed by personnel at NASA headquarters Office of Safety and Mission Assurance (OSMA), the NASA Engineering Safety Center (NESC), Stennis Space Center (SSC) and Glenn Research Center (GRC) before being finalized and released for procurement.

Davis NDE was contracted to fabricate a 24" x 24" x 3" PD block using A572 Grade 50 material having a solid member (representing a LPV head) welded to a section consisting of 11 plates (representing a LPV shell section). The total thickness of the PD block and the number of individual layers were selected to represent a typical MSFC LPV. Twenty-three (23) artificial flaws of various orientation and location were either implanted into the weld volume or machined (EDM notches) between the layers in the PD block (unlike calibration blocks in which reflectors are typically represented by side-drilled holes). The flaws between the plate layers were intended to establish the distance into the shell section layers that

PAUT can detect flaws. The photos below show the completed PD block and also coupons cut from the PD block after fabrication to expose artificial flaws. The coupons served to demonstrate the level of dimensional control for flaw size and placement within the block during fabrication. (Note: The PD Block was initially fabricated to 32" raw length and contained 26 total flaws. After initial fabrication, 8" length was removed from the block and cut to provide NASA with three coupons showing exposed artificial flaws.)

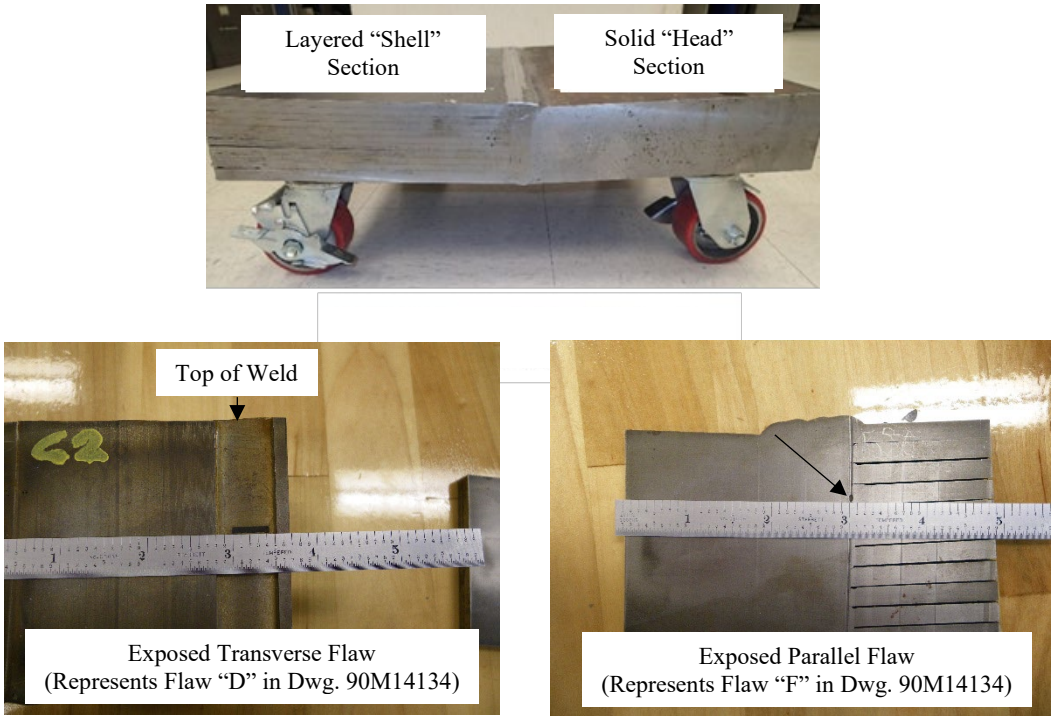


Figure 1: Performance Demonstration Block and Coupons Cut From Block

The specific flaw sizes selected for the PD block comply with demonstration block flaw sizing requirements of ASME Section V Article 4 Appendix IX which requires an aspect ratio (flaw height to length ratio) no larger than 0.25 for a material thickness of 1" or greater. As shown in MSFC drawing 90M14134 [3], the artificial flaws implanted in the PD block (surface and sub-surface flaws) have an aspect ratio of 0.2. The MSFC Material and Processes Laboratory (EM) concurred with the selection for the artificial flaw sizes by comparing the proposed PD block flaw sizes with estimated LPV limiting flaw sizes [4].

Note: The EM analysis references an artificial flaw size of 0.110" x 0.55" which was originally considered. The actual flaw sizes selected for the PD block for surface flaw (0.075" x 0.375") and sub-surface flaw (0.090" x 0.450") were smaller than the flaw assumed in the analysis which would not have changed the conclusion of the analysis and would make the artificial flaws even more difficult to detect.

Note: The EM report references ASME Code Case 2235 "Use of Ultrasonic Examination in Lieu of Radiography" which introduced flaw acceptance criteria for UT inspections based on location (surface or sub-surface) and size (length and through-wall height). These criteria are also included in ASME Section VIII Division 2 Part 7.

2.2.1 Conclusions from the PD Block Effort

The PD Block demonstration effort was completed in 2015 with Davis NDE submission of the final report, "NASA MSFC – Layered Vessel Demonstration Block" dated March 13, 2015 [5]. The three primary conclusions resulting from this effort included:

- The PAUT technique offers significant advantages over conventional UT for inspection of LPV head-to-shell welds when the heads are solid material. Scanning from the solid head allows the inspector to optimize the sound path incident angles to more fully evaluate the weld volume. Of the 23 weld flaws implanted in the PD block, 22 of the flaws were identified and characterized by PAUT using the head-to-shell weld scans. The one flaw which was not detected using the head-to-shell scan plan was a transverse flaw located between the plate layers (i.e., layer notch) and not physically located in the weld volume (flaw designation "R") [3]. This flaw was included to help determine whether PAUT could detect transverse flaws immediately adjacent to the weld volume. (It should be noted that the PAUT inspection of the PD block did detect flaws between the plate layers and even further from the weld centerline than flaw "R" but these other "layer notches" were oriented parallel to the weld direction and therefore more easily detected.)

- Code qualification of a PAUT procedure for the LPV head-to-shell weld appears promising for layered vessels with monolithic heads. ASME Section V Article 4 requirements for qualification of a PAUT procedure require that; 1) all flaws in the demonstration block be detected; 2) flaws produce an amplitude response greater than 20% reference level; 3) flaws are sized equal to or greater than actual size, and; 4) flaws be properly categorized (surface or subsurface). The number of implanted flaws in the PD block exceeded the number of flaws required by code and also included flaws placed in locations that would likely not be used in an actual procedure qualification block (for example, the "layer notches"). All artificial flaws in the PD block were identified and accurately characterized during the head-to-shell scan with the exception of the layer notch (flaw "R") discussed previously [5].

  Note: ASME Section V Article 4 Appendix IX requires a minimum of three flaws oriented parallel to the weld axis and major groove faces but does recommend consideration of additional flaws in the procedure qualification block for post-construction examination. The PD block had 23 artificial flaws with 12 of those being located in or immediately adjacent to the weld volume.

- The PD block effort further confirmed the difficulty and complexity of the shell-to-shell weld inspection. The restriction of having to scan welds from directly above the weld surface places significant limitations on the sound incident angles for ultrasonic flaw detection. During the performance demonstration block effort, the shell-to-shell PAUT weld scans detected the laminar and the transverse defects within the weld volume but did not detect parallel oriented flaws. In addition, because the shell-to-shell weld scan must be performed with the PAUT sensor located on the weld cap (directly above the girth weld), the surface of the weld must be relatively level and smooth to allow consistent and sufficient coupling between the PAUT sensor and the vessel (PD block weld was milled flat to facilitate sensor coupling). In reality, the surface of most pressure vessel weld caps are not level and smooth and would require weld cap preparation (e.g., grinding, machining) before a PAUT weld scan could be performed. Shell-to-shell weld surface preparation could be a substantial effort and cost especially for larger vessels and care would have to be taken to prevent damaging the vessel when removing metal from the weld surface. The effort and cost associated with preparing the LPV shell-to-shell weld surface for PAUT inspection is not currently justified.

3.0 Current MSFC PAUT Inspection Process

MSFC implemented PAUT inspection of LPVs during 2015 based on results of the performance demonstration block effort. The PAUT inspections are currently performed for the LPV head-to-shell welds and head nozzle welds but do not include inspection of the shell-to-shell welds for the reasons stated previously.

The PAUT procedure developed during the performance demonstration block effort has now been used at MSFC to inspect the head-to-shell welds of approximately 60 in-service LPVs. These inspections are considered both training for inspection personnel in PAUT data acquisition and interpretation as well as an opportunity to further assess the condition of the LPV head-to-shell welds. During these inspections, various indications have been observed with the most common indications being interpreted as slag or lack of fusion (manufacturing defects). Thus far, there have been very few instances of linear indications observed but in one case a vessel (V0111) was removed from service due to a defect which was interpreted to be crack-like and subsequently confirmed through weld excavation to be a crack (more details on this vessel below).

3.1 Defect Acceptance Criteria

A key feature of the PAUT equipment which aids in interpretation of data is the ability to accurately overlay indications into a ray tracing program along with a model of the specific weld detail as shown in Figure 2. This feature provides the inspector additional information to help interpret the indication based on weld geometry, flaw characterization and flaw location within the weld volume. It also aids the inspector in determining if there are weld geometry or part features that may act as reflectors potentially providing false indications. Recent improvements have been made in the inspection planning process that have yielded a more accurate inspection by the use of computer aided design (CAD) programs to sketch part features and then incorporating these into the PAUT ray tracing program.

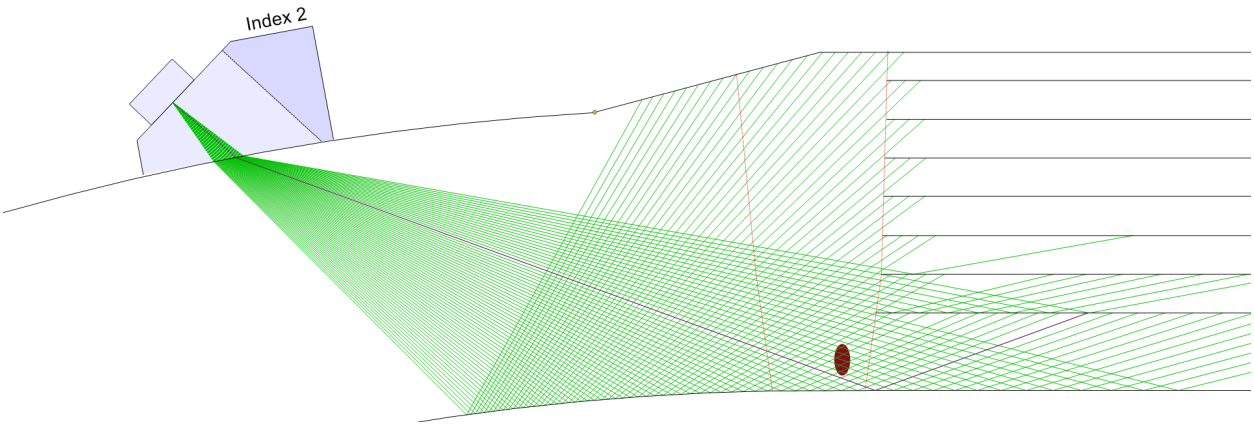


Figure 2: PAUT Scan of Head-to-Shell Weld on Vessel V0111

MSFC uses fracture mechanics based acceptance criteria in accordance with ASME code to determine criticality of defects found during PAUT inspection. The PAUT technique is able to more fully characterize flaws, as compared to UT shearwave or radiography for example, and therefore readily lends itself to a code based fracture mechanics inspection approach. ASME Section VIII Division 2 Part 7 provides the flaw acceptance criteria and Section V Article 4 and Appendix VIII provides the ultrasonic test (UT) examination requirements for a fracture mechanics based acceptance criteria. The fracture mechanics criteria takes into consideration the material thickness, the defect category (surface or sub-surface) and the defect size (length and through-wall height).

The current MSFC flaw evaluation process can be summarized as follows:

- Perform evaluation of any PAUT indications greater than 20% reference level
- Size indications for length and through-wall height and categorize indications as either surface or sub-surface (Note that a defect does not have to be surface connected to be classified as a "surface" defect" per Section VIII Division 2 Part 7)
- Evaluate defects using Section VIII Division 2 Part 7 "Ultrasonic Examination Used in Lieu of Radiographic Examination" based on defect aspect ratio and material thickness
- Indications which meet the acceptance criteria of Section VIII Division 2 Part 7 are generally accepted as non-critical (except for crack-like indications as further described below)
- Indications which do not meet the acceptance criteria are rejected and further evaluation is required (typically an API-579 analysis)

Because the PAUT effort at MSFC is still in its infancy and more technique validation work remains, indications classified as linear (i.e., crack-like) are currently rejected even if the flaw is determined to be acceptable using the flaw evaluation process described above. Follow up inspection and/or analysis is then performed on the rejected indication where possible. As mentioned previously, very few linear indications have been identified during the LPV PAUT inspections and two specific cases are cited below:

- A linear indication was observed in the lower head-to-shell weld on layered vessel V0111 which is a 120 cubic foot vessel manufactured in 1957 by A.O. Smith. The flaw evaluation process determined that the flaw was acceptable based on size and through-wall height. However, the indication was rejected (because it was crack-like) and a weld excavation was performed to help validate the accuracy of PAUT for characterizing the flaw. The excavation did expose the crack and confirmed the accuracy of the PAUT characterization of the flaw. The details and data from the inspection and excavation are documented in PVS-15-012 [6].

- A linear indication was observed in the lower head-to-shell weld on layered vessel V0229 which is a 35 cubic foot vessel manufactured in 1964 by Chicago Bridge and Iron (CB&I). In this case, the orientation of the linear indication did not allow flaw through-height to be measured therefore the defect evaluation process described above could not be used. The indication was rejected and follow-up inspection was performed using radiography and internal borescope inspection. Radiography did not reveal any indications but the borescope inspection did confirm the presence of a backing bar with stitch welds. The final conclusion was that the backing bar and intermittent welds created a false indication which was interpreted as a linear transverse weld volume defect (perpendicular to direction of weld). More details of this inspection are included in report PVS-15-013 [7].

4.0 Concluding Remarks

The MSFC PAUT inspection process and flaw acceptance methods can be further refined based on lessons learned, recommendations from the MSFC Materials and Processes Laboratory (EM) or guidance from the Agency LPV Working Group. EM is currently working to better characterize LPV materials through material testing and to develop analytical models to better define critical flaw sizes for LPVs. EM has also been requested to review the basis and assumptions for the fracture mechanics flaw acceptance criteria of ASME Section VIII in light of current LPV material test data.

One advantage of PAUT over more conventional shear-wave UT is that the weld scan data is electronically stored and indexed. If necessary, the weld scan data can be reevaluated (replayed) using different acceptance criteria without having to rescan the welds. This feature of PAUT has additional advantages for training personnel in evaluation of PAUT data and for in-service monitoring of flaws when necessary.

It should be noted that PAUT inspections at MSFC are not reserved strictly for layered vessels and have been used for solid wall vessel and piping system inspections as well. MSFC personnel have also performed PAUT inspections on solid wall vessels at SSC on two separate occasions.

Appendix E: Request for Information (RFI) NNM17ZQD001L entitled "Feasible Technologies for Non-Destructive Evaluation (NDE) of Layered Pressure Vessels"

ATTACHMENT 1

FEASIBLE TECHNOLOGIES FOR NON-DESTRUCTIVE EVALUATION (NDE) OF LAYERED PRESSURE VESSELS (LPVs)

Brief NASA Layered Pressure Vessel History

NASA has a large contingent of steel high pressure vessels fabricated using a layered construction technique. These vessels exist at eight NASA centers, though numbers vary from Center to Center. The design and manufacture of most of these vessels date to the late 1950s and early 1960s, acquired during the early stages of the Agency's infrastructural build-up for the Apollo missions. The fleet of layered vessels is aging, accumulating a half-century or more of cyclic fatigue and environmental exposure. NASA intends to establish a fitness-for-service (FFS) life extension methodology for continued use of these vessels to support the current and next generation of Agency missions. Figure 1 provides the LPV construction terminology and Figure 2 shows representative LPV installations at various NASA Centers.

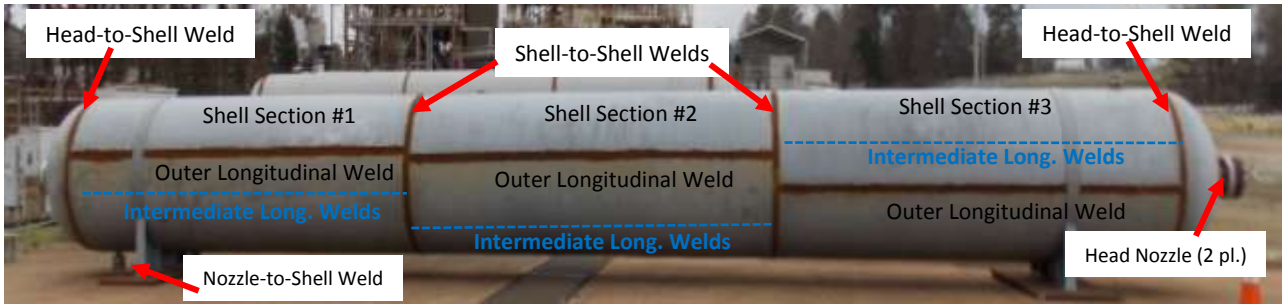


Figure 1. LPV Construction and Weld Nomenclature

Notes:
1) Not all NASA LPVs have shell-to-shell welds (depends on overall length of vessel)
2) All NASA owned LPVs have heads constructed of solid material (monolithic heads)
3) Intermediate longitudinal welds are covered by each overwrapping layer
4) Not all NASA vessels have a nozzle penetration through the layered section

The majority of layered pressure vessels in the Agency fleet were produced in the 1950's and 1960's, prior to the development of the OSHA regulations (early 1970's) and before the addition to the ASME Boiler and Pressure Vessel Code of provisions for such designs (1978) offered a means of achieving a "code-stamped" status. LPV construction consists of a thin inner cylindrical shell (typically ½") that is wrapped by additional thin shell layers (typically ¼") as needed to properly contain the hoop stress for the vessel's design pressure. Hemispherical (or elliptical) heads are then welded to the ends of the wrapped cylinder section to close out the vessel. The heads for all LPV's in the NASA fleet are solid sections (monolithic) and not of layered construction. The layered construction methodologies evolved during the 1940s and 1950s to include the following potential advantages or distinctions between their construction and a common thick-walled vessel: 1) the inner shell could be a different material (e.g., corrosion resistant steel) from the outer wrapping shells to offer more robust resistance to environments; 2) layering allows for easier metal forming construction by avoiding the need to form thick plates into cylinders; 3) layered design provides a health monitoring methodology via outer layer pressure relief vent holes allowing the vessel to present a detectable leak if a crack breaches the innermost layer; and 4) layered construction provides the potential to pre-stress the inner layers into compression as the outer layers are added, thus providing a more even distribution of through-wall stress under pressure relative to a solid-wall vessel. Despite these distinctions, layered construction presents a significant challenge regarding fitness-for-service (FFS) evaluation of aging vessels. Figure 3 shows LPV circumferential full penetration head-to-shell and shell-to-shell welds.



Figure 2: Examples of LPV at Various NASA Centers

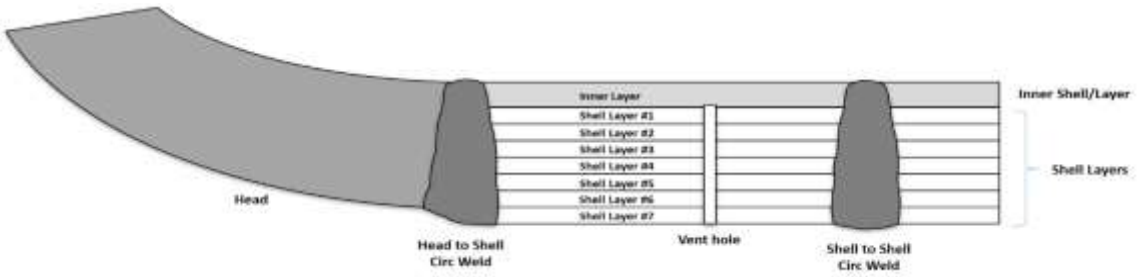


Figure 3. LPV Full Penetration Circumferential Welds

Notes:
1) Actual number of layers range from 2 to 31 with 6-14 layers being most typical
2) Total shell thicknesses range from 1" to 9" with 2"- 4" being most typical
3) Smaller NASA vessels do not have a shell-to-shell circumferential weld

Current Non-Destructive Examination (NDE) Methods Employed or Under Evaluation by NASA

NDE methods will play a crucial role in FFS evaluation of the NASA LPV fleet. NASA is seeking information on NDE technique capabilities to augment the limited NDE currently being performed within the Agency. The size and weight of the numerous NASA LPVs make transportation of the vessels impractical and costly therefore NDE techniques which can be performed at the vessel installation site are required.

The examination of LPVs can be largely broken into four distinct regions which require a thorough evaluation to ensure safe operation of the vessels. Current NDE techniques being employed by NASA for LPV examination are briefly described below. NDE techniques proposed in response to this RFI may supplement, improve or be substituted for NDE techniques currently being employed by NASA.

1) Head-to-shell circumferential welds: NASA is currently using phased array ultrasonic test (PAUT) methods to scan the head-to-shell welds with search units placed on the solid head surface. With the PAUT search unit placed on the solid head surface, the resulting ultrasonic sound incident angles are most favorable for detection of defects oriented parallel (or primarily parallel) to the weld centerline. Challenges remaining for a thorough volumetric examination of the head-to-shell weld are the ability to detect transverse defects and off-angle defects (i.e., those not oriented parallel or transverse to the weld centerline). Scanning from the head-to-shell weld crown presents challenges due to the rough and uneven weld surface, and in some cases, due to the transition from the vessel head to the vessel shell section as shown in the Figure 4 vessel cut-away section.



Figure 4: Head-to-Shell Transition Geometry

2) Shell-to-shell circumferential welds: Not all NASA LPVs have shell-to-shell welds however the larger vessels have multiple full penetration shell-to-shell welds (i.e., multiple layered shell courses - reference Figure 1). Currently NASA is not performing examination of the shell-to-shell welds due to; 1) the rough and uneven weld surface, on many but not all NASA LPVs, which make NDE ultrasonic transducer coupling difficult; and/or 2) difficulty getting sound, with

favorable sound incident angles, into the full weld volume due to the presence of layer gaps on both sides of the weld in combination with fairly narrow weld cap (narrow relative to the total thickness of the shell section).

3) Shell nozzles welds: Nozzles which are installed in the shell sections present similar challenges to those of the shell-to-shell circumferential welds. For ultrasonic-based techniques, the presence of the layer gaps makes data interpretation difficult because of sound wave reflections from the layer gaps.

4) Longitudinal welds/plate acreage: The LPVs can have numerous longitudinal welds within the layered sections depending on the vessel diameter and the number of individual layers comprising the shell section. The outermost layer longitudinal weld is accessible for examination but the intermediate and inner longitudinal welds are not directly accessible using conventional NDE techniques. (Note: The inner longitudinal weld is directly accessible from the vessel interior if the vessel has a manway, a feature lacking on most NASA LPVs.)

5) Vessel screening: Acoustic Emission (AE) Test is currently being evaluated by NASA as a technique that could potentially allow screening LPVs for defects. The primary challenges with AE on a LPV are potential extraneous acoustic signals (e.g., from layer movement or rubbing, corrosion between layers, slag cracking, etc.) during pressurization which could potentially mask relevant signals (indicative of a growing crack), the fact that AE may not in some cases fully characterize defects, and that other defect characterization techniques may not be available.

6) Radiography has been used for examination of many NASA LPVs but challenges remain with defect detection and film interpretation due to variability in the orientation of defects, the presence of layer wash (layer wash is defined in ASME Boiler and Pressure Vessel Code, Section VIII, Division 1 and 2), the overall thickness versus the layer thickness (which plays a role in determining critical defect sizes), and off-angle cracks. There are additional limitations using radiography for a FFS evaluation since flaws cannot be fully characterized as required to perform damage tolerance analysis. Even in light of these limitations, radiography and/or improvements in current radiography techniques, may still have relevant application when combined with other NDE techniques.

7) Weld surface examinations are performed on the NASA LPVs using a variety of conventional techniques including visual test (VT), dye penetrant test (PT), magnetic particle test (MT) and, to a lesser extent, eddy current test (ET). These examination techniques are fairly restricted for layered construction because only a limited number (small percentage) of LPV weld surfaces are directly accessible. A large number of longitudinal welds are located within the layered section but completely covered by each overwrapping layer rendering conventional surface NDE ineffective (reference intermediate longitudinal welds shown in Figure 1).

8) NASA performs periodic audible inspection of the LPV vent holes (reference Figure 3), or weep holes, which can provide an early indication that the inner shell layer (inner liner) has been compromised (i.e. listening for vent hole leakage). The current NASA audible inspections are performed without the use of any specialized equipment, instrumentation or audible aids.

RFI Respondent Evaluation

Responses to the RFI will be initially evaluated and those demonstrating merit will be selected for follow-up correspondence and further evaluation. Multiple phases will be required to complete this overall effort as follows:

Phase 1 – Initial evaluation of RFI responses using the general criteria described in the Synopsis and selection of NDE technologies for further assessment by the Government. To further expound on the general criteria, Government considerations made during this phase will include:

a. Overall technical feasibility for detection of likely LPV weld or heat affected zone (HAZ) defects
b. Identification of techniques that have potential application for multiple areas of interest on a LPV
c. Level of effort and cost to validate, improve or advance the technique for LPV applications
d. Level of effort and cost to procure packaged NDE or services and then implement the techniques for in-situ evaluation of LPVs
e. Level of effort and cost to procure health monitoring system, if proposed, and then implement for in-service monitoring of LPVs

Phase 2 – Government communication with vendors to discuss evaluation and assessment of technologies selected in Phase 1. Discussions may include opportunities for Government-vendor collaboration for validation, improvement or advancement of selected NDE techniques. Planning for Government visits to vendor locations or vendor visits to a NASA Center may occur during this phase.

Phase 3 – NDE technology capability evaluation and assessment. The Government may make limited funds available during Phase 3 depending on the complexity, rigor and level of effort required for the NDE technique demonstration and the specific pre-defined deliverables to the Government (reports, raw data, processed data, etc.). Activities during this phase may include one or more of the following:

a. Demonstration of the proposed NDE technique(s), either at the vendor location or at a NASA Center, using vendor owned and/or Government owned performance demonstration blocks, calibration blocks, test coupons or structurally similar items as the articles for examination. Government provided article(s) for examination will simulate specific LPV construction features and include known (documented) defects of various orientation, size and location within the weld volume.

b. For techniques that cannot be thoroughly evaluated using small scale examination articles, the Government may provide access to full scale LPVs, or large remnants of LPVs, as required for capability evaluation.

c. NDE data obtained from the technique demonstration(s) will be analyzed and compared with the known flaw characteristics of the examination article(s) to provide an objective assessment of NDE capability or limitation. Failure of a NDE technique to detect and/or characterize all known flaws in the examination article(s) will not necessarily result in rejection of the technique by the Government as the technique may still show merit for further assessment and/or development.

Phase 4 – The Government will select from the NDE techniques for potential investment which provide the most cost effective, timely and technically feasible options. Potential government investments would include packaged NDE systems (hardware/software), NDE services for examination and assessment of LPVs or some combination of both.

Appendix F: Simulation Work for Layered Pressure Vessels

Simulation Work for Layered Pressure Vessel

by
Elizabeth Gregory
Nondestructive Evaluation Sciences Branch

As part of the layered pressure vessel (LPV) project the in-house elastodynamic finite integration technique (EFIT) code was used to simulate two setups. The first setup was an attempt to simulate an acoustic emission that could occur during pressurization and indicate an internal delamination in the LPV. The questions to answer were: "Can an acoustic emission be detected if it occurs and can we detect where it occurs?" The second setup simulated a simple guided wave inspection to determine which types and orientations of damage could likely be detected with this inspection method.

We simulated various damage types and configurations in a layered material with variable contact. We found that for some configurations there is a resulting indication, meaning that the damage could be detected. However, the further the damage is away from the surface and the more disbanding that occurs between layers the less the corresponding signal results in significant indications.

EFIT is a staggered grid finite difference approach that was applied to elastodynamics in the 1990s [1,2]. Numerous mathematical approaches have been developed to model ultrasound behavior in solid media, including analytical and numerical methods [3]. Numerical methods are appropriate to use in cases with complex geometries, irregular defects, and/or complicated ultrasonic wave behavior as is often the case with guided wave ultrasound. Finite element analysis (FEA) is the most commonly used numerical approach for ultrasound modeling, with several packages that are commercially available. However, methods such as EFIT allow for easily parallelizable code that can be readily adapted to the latest computational architectures [4].

The custom code implementation used for this work, EFIT-CompCell, allows for diverse structural geometries with no changes to the computational parallelization scheme. EFIT-CompCell utilizes message passing interface (MPI) for parallelization. The user provides the basic parameters of the simulation and the software automatically performs an initial computational volume balancing based on anticipated computational loads and establishes the CPU communication patterns for any geometry.

KERNEL DESCRIPTION

The EFIT custom code, previously developed at NASA Langley Research Center by the Computational Nondestructive Evaluation (CNDE) team, was intended to provide a relatively fast, customizable, and versatile ultrasound simulation tool. The code was written in C++ with MPI for parallelization across processors. The previously developed code was not optimized and did not efficiently simulate complex geometries.

EFIT, and other numerical methods, become unstable when spatial and time step sizes are not properly selected, therefore implementing EFIT for realistically sized components requires that the technique be parallelized. The code must also be able to accurately simulate wave interaction with various boundary conditions and behavior in complex geometry

components. The previously developed code for isotropic EFIT was implemented in parallel and was validated against both experiment and theory [5-7].

The EFIT mathematical kernel is written in C++ with use of MPI. The EFIT equations for velocity are:

$$\Delta V_x = \frac{\Delta t}{\Delta n \frac{(\rho+\rho[x+1])}{2}}\left(S_x[x+1] - S_x + T_{xy} - T_{xy}[x-1] + T_{xz} - T_{xz}[x-1]\right) + F_x$$

$$\Delta V_y = \frac{\Delta t}{\Delta n \frac{(\rho+\rho[y+1])}{2}}\left(S_y[y+1] - S_y + T_{yz} - T_{yz}[y-1] + T_{xy} - T_{xy}[y-1]\right) + F_y$$

$$\Delta V_z = \frac{\Delta t}{\Delta n \frac{(\rho+\rho[z+1])}{2}}\left(S_z[z+1] - S_z + T_{xz} - T_{xz}[z-1] + T_{yz} - T_{yz}[z-1]\right) + F_z$$

S refers to normal stress and T refers to shear stress. ρ is density. Δn refers to spatial step size and Δt is the time step size. Finally, F refers to any external input, in this case the ultrasound excitation function converted into velocities. The square brackets refer to the parameter at the cell's x, y, or z neighbor.

The EFIT equations for normal stress are:

$$\Delta S_x = \frac{\Delta t(\lambda+2\mu)}{\Delta n}(V_x - V_x[x-1]) + \frac{\Delta t\lambda}{\Delta n}\left(V_y - V_y[y-1]\right) + \frac{\Delta t\lambda}{\Delta n}(V_z - V_z[z-1]),$$

$$\Delta S_y = \frac{\Delta t(\lambda+2\mu)}{\Delta n}\left(V_y - V_y[y-1]\right) + \frac{\Delta t\lambda}{\Delta n}(V_x - V_x[x-1]) + \frac{\Delta t\lambda}{\Delta n}(V_z - V_z[z-1]),$$

$$\Delta S_z = \frac{\Delta t(\lambda+2\mu)}{\Delta n}(V_z - V_z[z-1]) + \frac{\Delta t\lambda}{\Delta n}(V_x - V_x[x-1]) + \frac{\Delta t\lambda}{\Delta n}\left(V_y - V_y[y-1]\right),$$

The EFIT equations for shear stress are:

$$\Delta T_{xy} = \frac{4\Delta t}{\Delta n\left(\frac{1}{\mu}+\frac{1}{\mu[x+1]}+\frac{1}{\mu[y+1]}+\frac{1}{\mu[z+1]}\right)}\left(V_y - V_y[x-1] + V_x - V_x[y-1]\right),$$

$$\Delta T_{xz} = \frac{4\Delta t}{\Delta n\left(\frac{1}{\mu}+\frac{1}{\mu[x+1]}+\frac{1}{\mu[y+1]}+\frac{1}{\mu[z+1]}\right)}(V_z - V_z[x-1] + V_x - V_x[z-1]),$$

$$\Delta T_{yz} = \frac{4\Delta t}{\Delta n\left(\frac{1}{\mu}+\frac{1}{\mu[x+1]}+\frac{1}{\mu[y+1]}+\frac{1}{\mu[z+1]}\right)}\left(V_z - V_z[y-1] + V_y - V_y[z-1]\right),$$

where λ and μ are the first and second Lamé constants.

The EFIT code uses MPI to pass updated stress and velocity components between neighboring processors, as required. Therefore, the last two steps of the preprocessing phase are to ensure that each MPI process has approximately the same number of computational cells on which to operate (for computational load balancing) and that all cells are properly connected to their neighbors.

ACOUSTIC EMISSIONS SIMULATIONS

The initial AE simulations were sized to balance maximum volume and minimal solution time while maintaining numerical stability. Table 1 shows the baseline simulation parameters used for the initial simulations.

Table 1 Baseline Simulation Parameters

Description	Symbol	Value
Spatial step/cell size	Δn	0.0001 m
density	ρ	2780 kg/m^3
first Lamé constant	λ	51.75 GPa
second Lamé constant	μ	26.66 GPa
time step size	Δt	1.617 ns

The computational volume was 100 mm x 50 mm x 1.5 mm. The dipole was located at the center of the thickness at x = 15 mm x 25 mm. For the acoustic emissions (AE) simulation the source was simulated as a dipole force input. Each cell can only accept body-forces so the dipole had to be simulated as two separate forces on separate two cells, as shown in Figure 1. The number of elements between the input forces was shown to affect the results. If the forces were placed on adjacent cells, the simulation setup resulted in numerical instability as shown in Figure 2. The absolute distance between the forces had to be limited to 0.1 mm, so the cell size had to be reduced from an initial 1 mm value. Reducing the size of the elements increased the computational volume and therefore the computation time. For example, an 0.3 ms simulation took 4 hours.

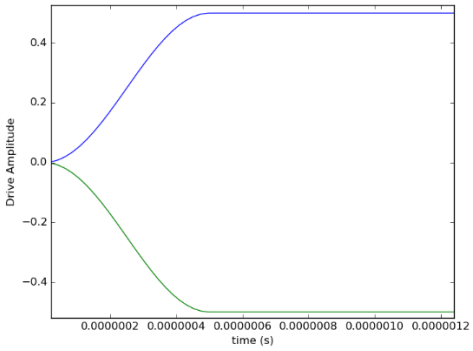


Figure 1 Dipole Amplitudes

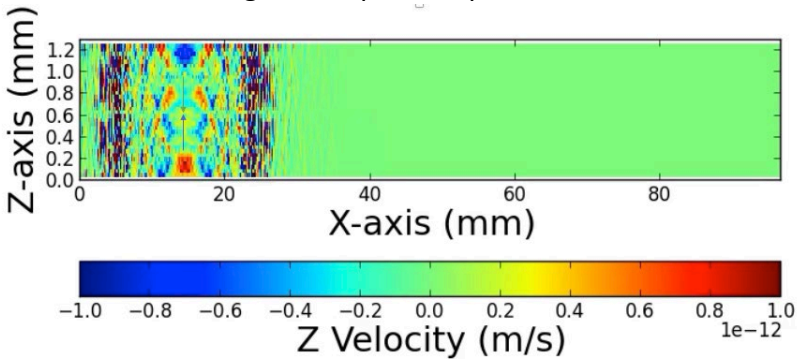


Figure 2 Example of instability due to the proximity of the dipole forces.

After some experimentation, the dipole sources were placed on adjacent cells but the simulation was split into two separate simulations, one for each source. Then the solution was found by adding the output together. This process still resulted in twice the simulation time.

The concern of the LPV project was observing AE signals in pressure vessels that have internal separation between layers as shown in Figure 3. The EFIT code was modified to incorporate variable boundary definitions that would could be activated or deactivated to allow or prevent wave transmission across layers. Contact surfaces were randomly generated in the spatial domain for 25%, 50%, 75% or 100% contact. Larger non-contact "patches" and higher percentage of non-contact both result in less pronounced indications of the flaw.

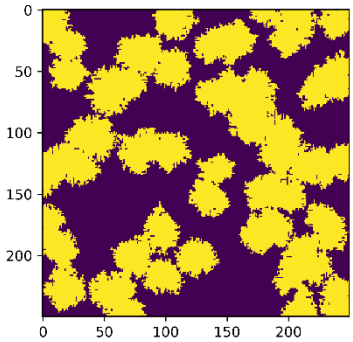


Figure 3 Example: 50% contact surface. Yellow pixels have no contact in the Z direction. 1 pixel has a size of 5 mm.

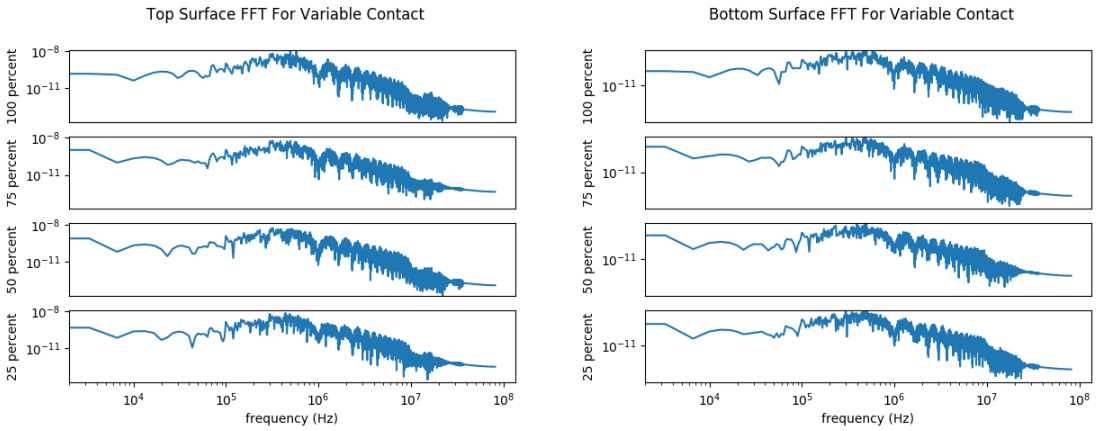


Figure 4 FFT's of signals acquired on the top and bottom surfaces 10 cm away from the X-Y location of the dipole sources for variable contact.

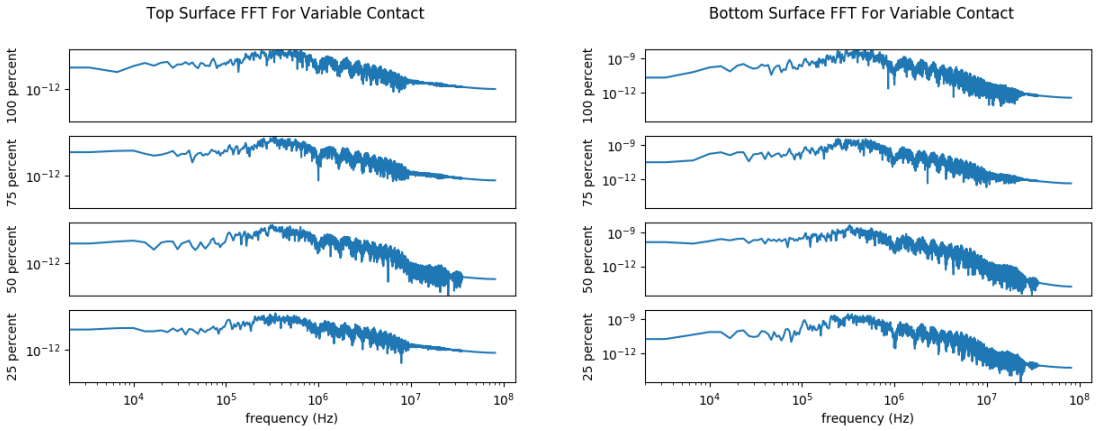


Figure 5 FFT's of signals acquired on the top and bottom surfaces 40 cm away from the X-Y location of the dipole sources for variable contact.

Even with variable contact the wave is observable on both surfaces.

GUIDED WAVE SIMULATIONS

Guided waves were also simulated in a layered volume meant to approximate a cross-section of a layered pressure vessel. Using the same modification described above for the variable contact, delaminations were introduced between the layers. A single transducer was used to approximate a UT signal and the results were analyzed. Similarly, "cracks" were simulated by placing surfaces of no-contact parallel to the input signal in a layer below the top layer (Figure 6). With a UT source specified (instead of the dipole) it was possible to increase the cell size. The material properties used for the layered simulations are shown in Table 2. The material properties are for aluminum. Absolute results will be different for different materials, however overall trends will be similar. The simulation is meant to be representative of different configurations (layers, contact, cracks, etc).

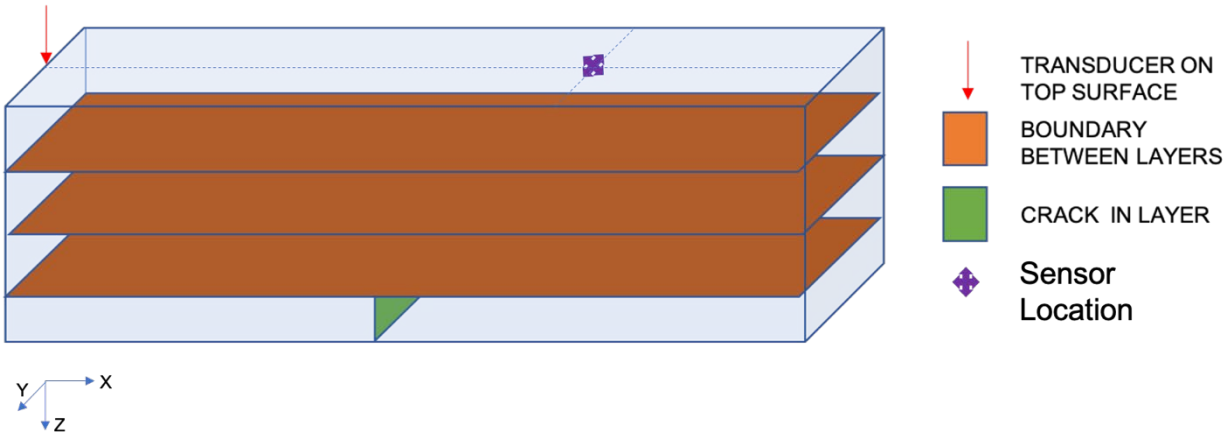


Figure 6 Example of the boundary definitions between layers and a simulated crack within the deepest layer.

Table 2 Layered Simulation Parameters

Description	Symbol	Value
Spatial step/cell size	Δn	0.005 m
density	ρ	2780 kg/m^3
first Lamé constant	λ	51.749939080 GPa
second Lamé constant	μ	26.664117020 GPa
time step size	Δt	30.672 ns

We observed that the less contact between layers led to less ability to see, or weaker indication of, the crack in a lower layer and that cracks that ran along the direction of the wave were nearly impossible to detect.

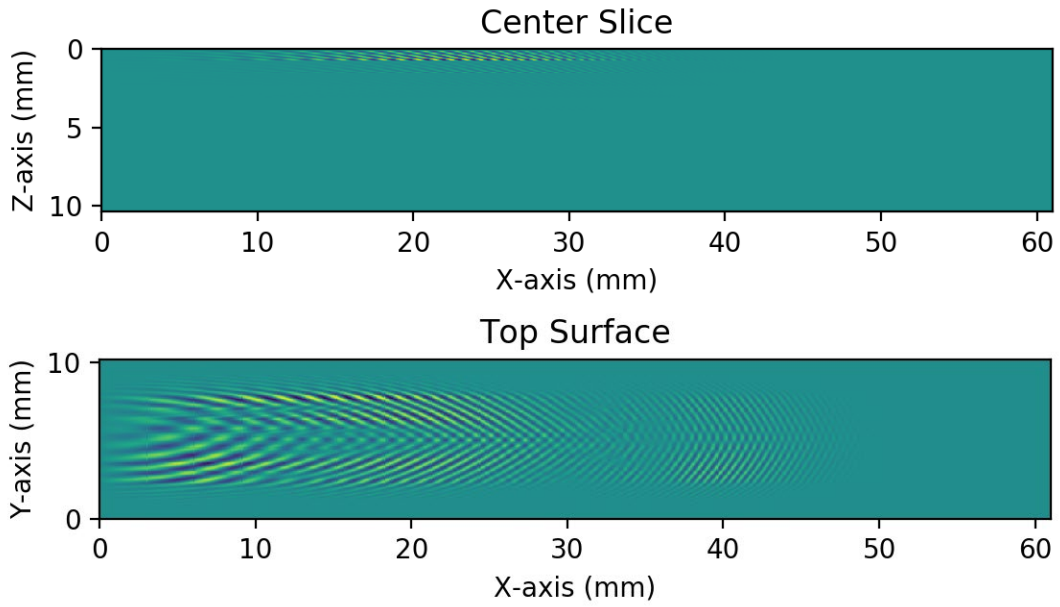


Figure 7 Results from the layered simulation, showing 2D slices taken from the 3D simulation for a case with a crack and 50% contact.

From the center slice in Figure 7 it is clear that the wave is not penetrating to the point where the crack is on the bottom surface. We then repeated the simulation with now variable boundary between layers (in reality eliminating the layers and making it a solid material). We still included a crack on the bottom surface, but its height was only 0.025 m or (1/4) of the 0.102m thickness of volume. The crack in the Y-Z plane spanned the entire width of the volume (0.102 m) and the crack in the X-Z plane was only 0.1 m of the 0.305 m length centered about the middle of the length. Example Results are seen in Figure 8.

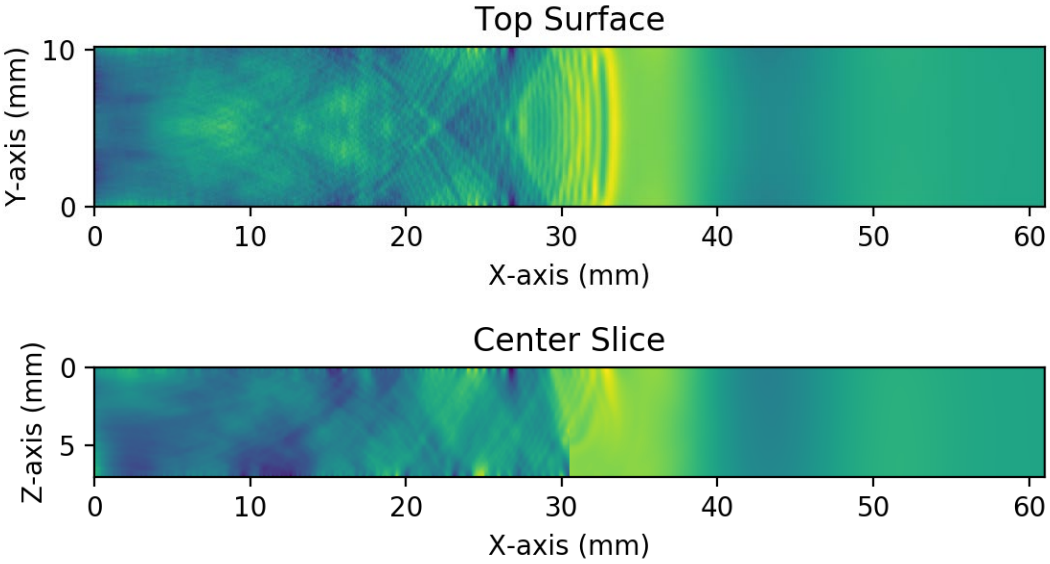


Figure 8 Results from the solid (unlayered) simulation.

Comparing the results to the case with no flaw makes it very clear how small the indications are for cracks parallel to the top surface (X-Z plane, Figure 9) and perpendicular (Y-Z plane, Figure 10). If we subtract a no-flaw solution from each we get the images below, showing there is a small indication from the opposite surface crack.

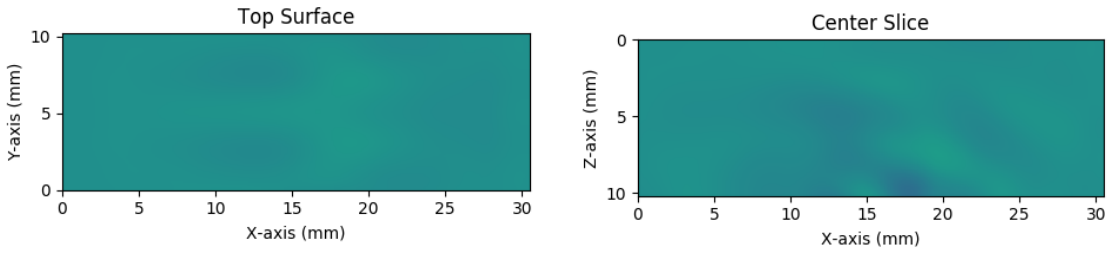


Figure 9 Simulation of crack in the X-Z plane with no-flaw solution subtracted.

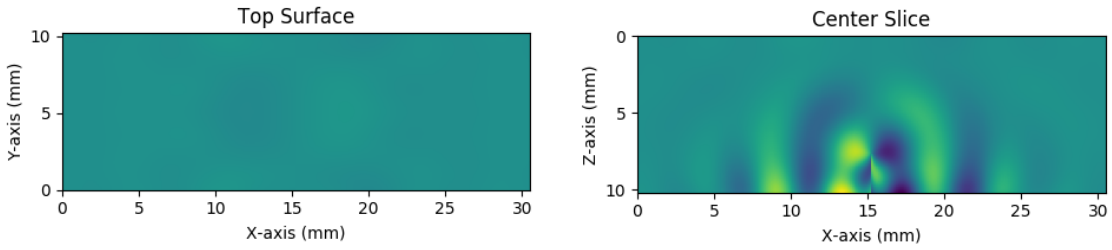


Figure 10 Simulation of crack in the Y-Z plane with no-flaw solution subtracted.

It is also important to realize that although there appears to be significant difference in the center slices of Figure 9 and Figure 10, all UT measurements will in fact be collected on the top surface where very little difference is observed in the simulation results. However, the simulation was limited in duration due to memory constraints. It is possible that a more significant indication would be seen on the top surface from the crack. Strong indications in the signal are limited by the dept of the flaw and imperfect contact between layers. The wave must penetrate to the flaw and then return to the sensor, anything that impedes this will cause the indication to be reduced or imperceptible.

We performed simulations with a variety of source types to approximate an acoustic source of a crack and to model a guided wave UT inspection. We also modelled "patchy" contact (like that in Figure 3) between layers to simulate disbonds between layers. There was some proof that a deep crack could be observed by a UT inspection but if there is significant disbond it is unlikely that a crack on the opposite side of the disbond will be easily detectable.

1. Fellinger, F. and Langenberg, K.J. "Numerical techniques for elastic wave propagation and scattering," Elastic Waves and Ultrasonic Nondestructive Evaluation (1990): 81-86.
2. Marklein, R. "The Finite Integration Technique as a General Tool to Compute Acoustic, Electromagnetic, Elastodynamic, and Coupled Wave Fields." Review of Radio Science (1999).
3. Schmerr, Lester W. "Fundamentals of Ultrasonic Nondestructive Evaluation: A modeling approach", New York: Plenum Press. (1998).
4. Leckey, Cara AC, Jeffrey P. Seebo, and Peter Juarez. "Challenges of NDE simulation tool validation, optimization, and utilization for composites." AIP Conference Proceedings. 1706.1 (2016)
5. Yu, Lingyu, and Cara AC Leckey. "Lamb wave–based quantitative crack detection using a focusing array algorithm." Journal of Intelligent Material Systems and Structures 24.9 (2013): 1138-1152.
6. Yu, Lingyu, Zhenhua Tian, and Cara AC Leckey. "Crack imaging and quantification in aluminum plates with guided wave wavenumber analysis methods." Ultrasonics 62 (2015): 203-212.
7. Leckey, Cara AC, et al. "Multiple-mode Lamb wave scattering simulations using 3D elastodynamic finite integration technique." Ultrasonics 52.2 (2012): 193-207.

Appendix G: Ultrasonic Testing Simulation Documentation

G. Ultrasonic Testing Simulation Documentation

G.1 Executive Summary

This document describes the efforts and results of the simulations of ultrasonic testing on layered pressure vessel (LPV) welds. The simulation software CIVA was selected to perform the simulations in the effort. Two types of LPV welds (head to shell and shell to shell) and two types of flaws (circumferentially and axially oriented cracks) were selected and simulated in the CIVA software. Simulations were able to show the sensitivity changes in flaw response due to variations in flaw size, location, and geometry, variations in inspection parameters and equipment, and variations in weld characteristics. Using simulated-guided inspection, novel inspection methodologies were discovered for detecting circumferentially oriented cracks in shell to shell welds.

G.2 Introduction

The unique geometry of layered pressure vessel (LPV) welds makes it an ideal candidate for iteratively simulating inspection scenarios to help understand, interpret, and identify flaws in low fidelity measurement data. Non-destructive evaluation (NDE) simulation can be used to demonstrate the feasibility of detecting flaws in structures, investigate new inspection methods and types of inspection equipment prior to investing in the hardware, enhance the inspector's ability to interpret inspection data, and assess how well we understand the material system and flaw characteristics by comparing simulation and inspection data.

To address the challenges associated with inspecting LPV welds, the computational simulation software CIVA was selected to simulate various inspection methods. CIVA is a semi-analytical and numerical multi-discipline NDE simulation software tool that was developed by CEA-LIST under the French Alternative Energies and Atomic Energy Commission. CIVA's modules are capable of simulating inspections using ultrasonic testing (UT), radiography, computed tomography, eddy current, and guided waves. For this case study, only CIVA's UT inspection module and UT beam simulation module were utilized. The UT inspection module is used to simulate real-world inspection cases using simulated equipment and flaws. The benefit of using CIVA's UT inspection module is that the data outputs in a format similar to real inspection data. The UT beam simulation is used understand how the generated acoustic energy interacts with the material and geometries, allowing the observation of focal points and dead zones in the acoustic

beam profile. Two parts of the LPV were studied: the head-to-shell welds and the shell-to-shell welds, highlighted in Figure G.2.1.

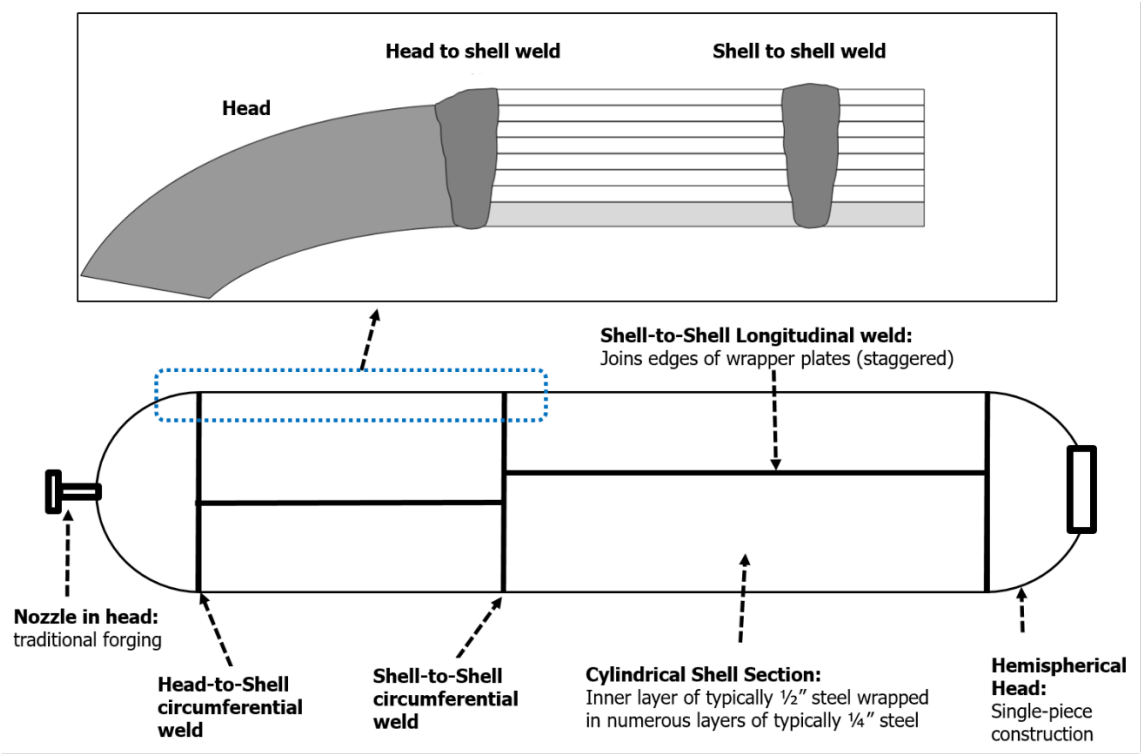


Figure G.2.1: Diagram of the layered pressure vessel, highlighting which parts of the structure were considered in this study

G.3 Verification Study

The first step of this investigation was to verify that CIVA could simulate an accurate representation of the LPV use case. To do this, two known flaws were selected from existing measurement data of a head-to-shell weld. These flaws were artificially created in the head-to-shell weld as part of a phased array ultrasonic testing (PAUT) demonstration block. The block

was 3 inch thick head plate welded to 11 stacked shell plates. The weld was a V-shaped multi pass weld approximately 1 inch wide. The block and selected flaws are shown in Figure G.3.1.

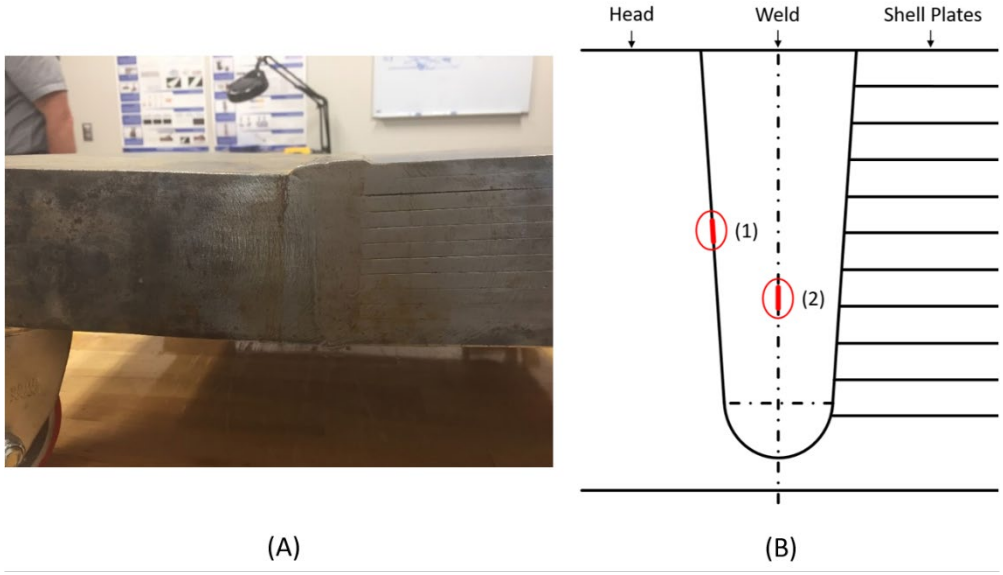


Figure G.3.1 (A) Photo of the head-to-shell weld PAUT demo block (B) Diagram of the head-to-shell weld and the selected flaws for the verification study.

Flaw 1 was a weld interface lack of fusion defect and flaw 2 was a centerline lack of fusion defect. Both flaws were 0.09 inches tall, 0.04 inches thick, and 0.45 inches long extending parallel to the weld. The head-to-shell weld was inspected using an Olympus 2.25L32-A11 PAUT probe, connected to an Olympus Omniscan performing a sectoral sweep between 20 degrees and 50 degrees. The demo block material properties, geometry, flaw characteristics, and inspection equipment were created virtually in CIVA and the inspections were simulated to create datasets comparable to the actual inspection data. The demo block material properties were imported from the build specifications, and the weld anisotropy was simulated using Olgivy's parameterized weld grain estimation [G1]. Specifically, the shell plates were modeled as isotropic steel with a longitudinal wave velocity of 5900 m/s and a shear wave velocity of 3230 m/s, and the weld was modeled as anisotropic steel with a transversely isotropic stiffness matrix, rotated according to the Ogilvy's parameter estimation. The stiffness constants are shown in Table G.3.1.

Table G.3.1 Stiffness matrix constant values for the transversely isotropic steel weld

Stiffness matrix constants	C_{11}	C_{12}	C_{22}	C_{44}	C_{55}
Value (GPa)	245	145	218	110	75

The verification was performed by comparing the relative dB drop between flaws 1 and 2 in the measurement data to the relative dB drop between the same flaws in the simulated inspection data. The real flaws showed a relative dB drop of 1.3 dB and the simulated flaws showed a relative dB drop of 0.8. The differences in these values are likely due to the assumptions inherent in the Ogilvy weld grain estimations, such as the uniformity of grains. Nonetheless, these values were considered close enough within the measurement error to be equivalent, and thus showed that CIVA was credibly representing the interaction between the energy and the material and flaws. Figures G.3.2 and G.3.3 show the side by side comparison of the simulated and real data. Amplitude values are scaled differently for each image to show flaw reflections more clearly.

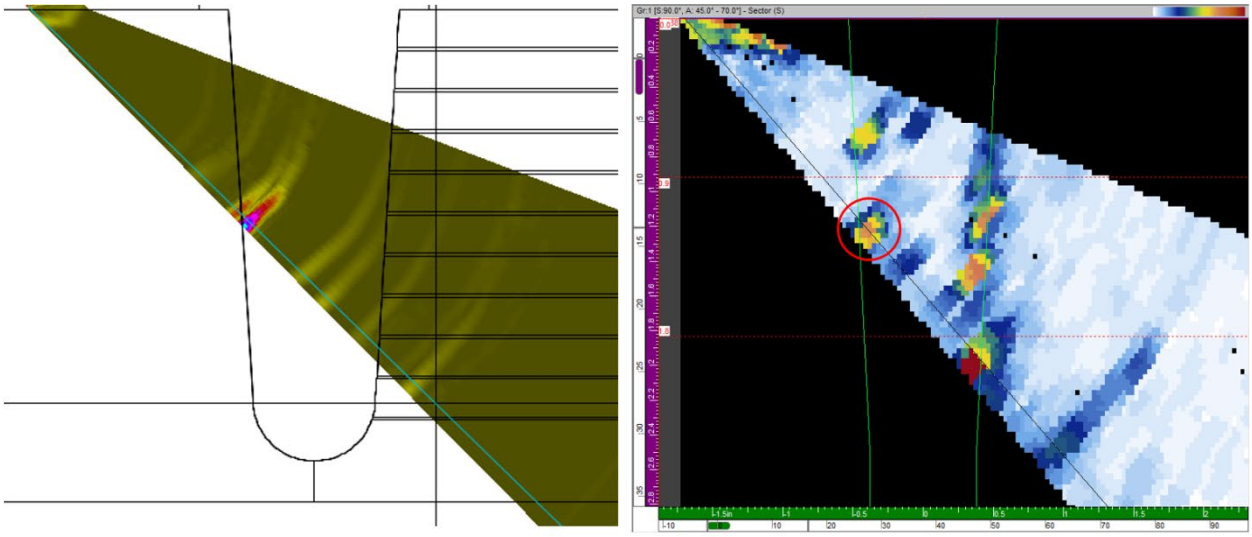


Figure G.3.2 (A) Flaw 1 simulated in CIVA (B) Flaw 1 in the PAUT inspection data of the demo block

While the verification study was considered successful in showing CIVA's applicability to this use case, there were still some aspects of the real inspection data that were still not represented in the simulation data. In particular, the reflections from the shell plate weld interfaces were absent, highlighted in Figure G.3.3B. After several iterations and model refining, these plate weld interface reflections were replicated in the simulation data. The solution was to change the specimen echo model to a specular solver, increase the gap spacing between the plates in the CAD model, and change the CAD geometry of the shell plate to weld intersections to more accurately represent the physical weld. The results are shown in Figure G.3.4, and it should be noted that the visual differences between the simulated and real data are due to the simulation having a higher number of data points and a higher resolution angular sweep than the measurement data.

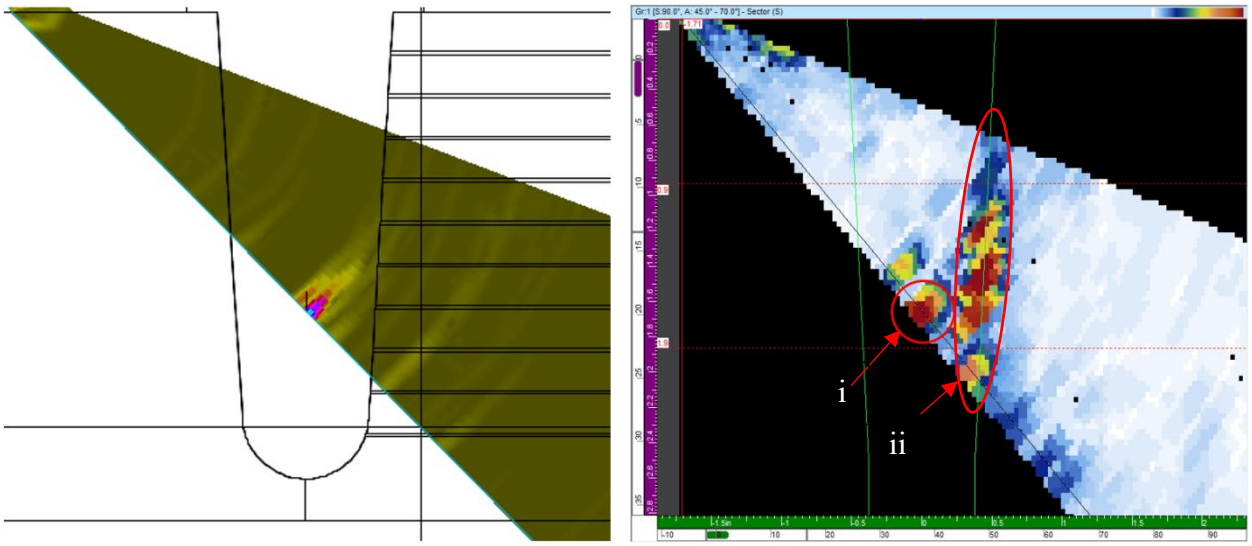


Figure G.3.3 (A) Flaw 2 simulated in CIVA (B) i: Flaw 2 in the PAUT inspection data of the demo block ii: highlight of the acoustic reflection from the shell plate weld interface in the real data, and the absence of this reflection on the simulated data

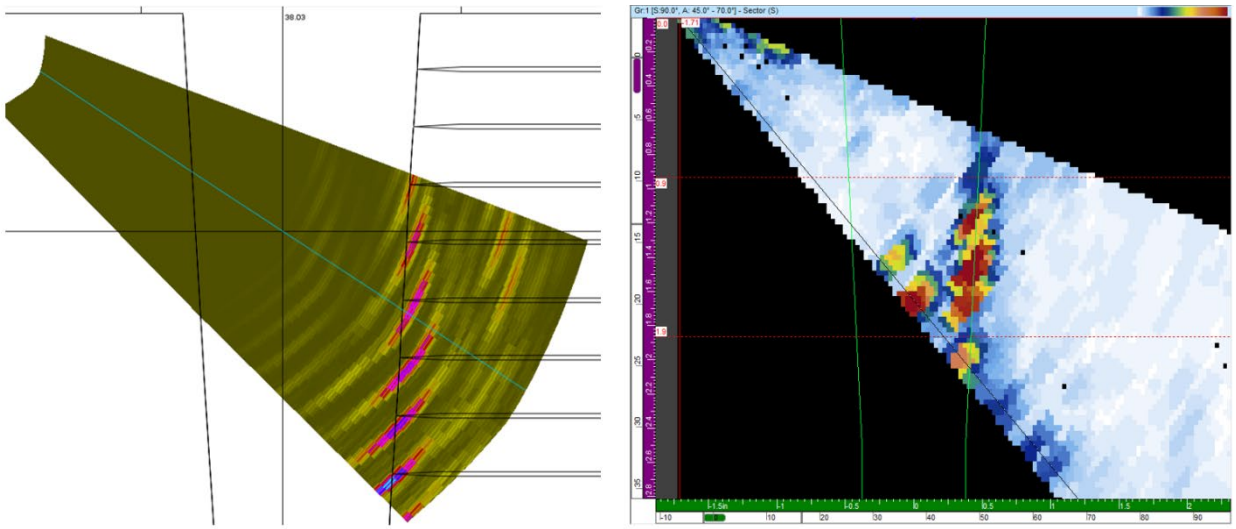


Figure G.3.4 (A) Simulated data showing the reflection of the shell plate weld interface (B) Real data showing the response of the shell plate weld interface.

G.4 Shell To Shell Weld Inspection Simulations – Axially Oriented Crack

With the verification study completed, the next task was to apply the CIVA simulations to more challenging inspection scenarios. While head-to-shell welds present a moderate challenge to inspectors, the challenge is not insurmountable; the entire depth of the weld can be interrogated through the head plate using PAUT. Welds between stacks of shell plates (known as shell-to-shell welds) present a much more difficult inspection case, since the only sound path to interrogate the entire weld is through the top of the weld itself. Because there is limited existing inspection data available for comparison, this effort is focused on examining feasible inspection methods and studying how flaw characteristics or geometry variations change detectability.

A CAD model was created using images of the cross section of real shell-to-shell welds. The model was simplified to represent the average variation in the weld profile, and the top of the weld was modeled as if it had been ground smooth (inspection through an as-welded surface will be presented in later sections). Characteristics of the weld, such as the root and the plate weld interfaces, were documented from the cross section images and represented in the final simulation model. This is highlighted in Figure G.4.1. The material properties of the LPVs varied from vessel to vessel, so the standard properties of steel found in the CIVA material library was used (longitudinal wave velocity of 5900 m/s and a shear wave velocity of 3230 m/s), and again Ogilvy's parameterized weld grain estimation was used to simulate the anisotropy in the weld. The transversely isotropic stiffness matrix constants are the same as the previous simulations, shown in Table G.3.1.

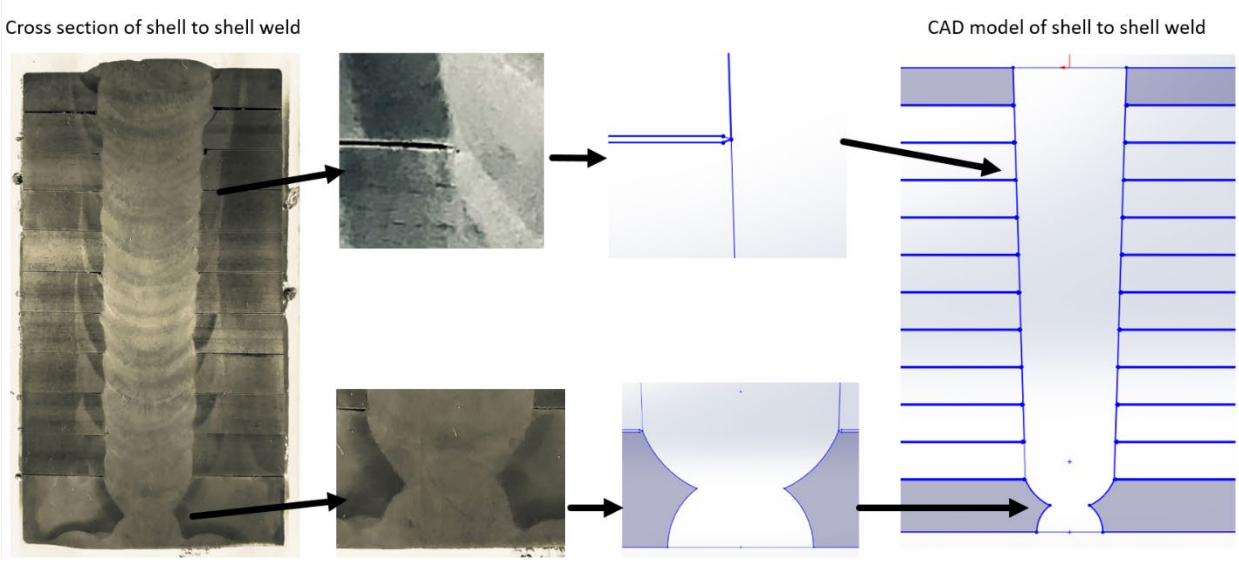


Figure G.4.1 Diagram showing how different characteristics of the real shell to shell weld were incorporated to the simulation model

The first flaw type that was investigated was the axially oriented crack (i.e. the length of the crack extends perpendicular to the weld) in the shell-to-shell weld. Figure G.4.2 demonstrates the orientation of this crack in relation to the weld. A contact 2.23 MHz transducer attached to a 40 degree wedge was simulated instead of the PAUT with sectoral sweep to simplify the simulations and decrease the run time. The probe was oriented and scanned parallel to the weld along the centerline. A 5mm tall straight notch was inserted near the bottom of the weld root which extended 5mm in each direction perpendicular to the weld. The simulation of this flaw was run twice, once with ideal surface conditions and again with simulated surface roughness on the inside of the vessel. CIVA simulates surface roughness by taking a user defined roughness parameter (Ra, or arithmetical mean height above the primary surface profile) and translates it into a frequency-dependent attenuation model that modifies the transmission/reflection coefficients at the surfaces. The roughness parameter used in this simulation was 250 µm, which is a typical surface finish seen in grinding and smoothing applications. These results are displayed in Figure G.4.3. The difference in signal response between the two simulations was -8.9 dB.

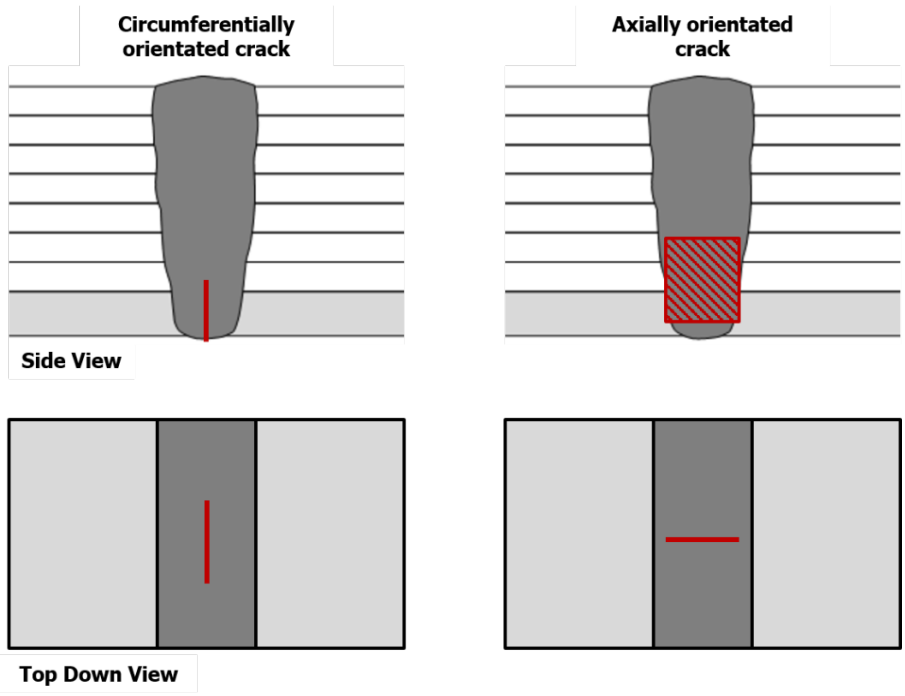


Figure G.4.2 Diagram of the two types of shell-to-shell weld cracks that were investigated. Displayed size of cracks were exaggerated for clarity and are not to scale of the cracks used in the simulations.

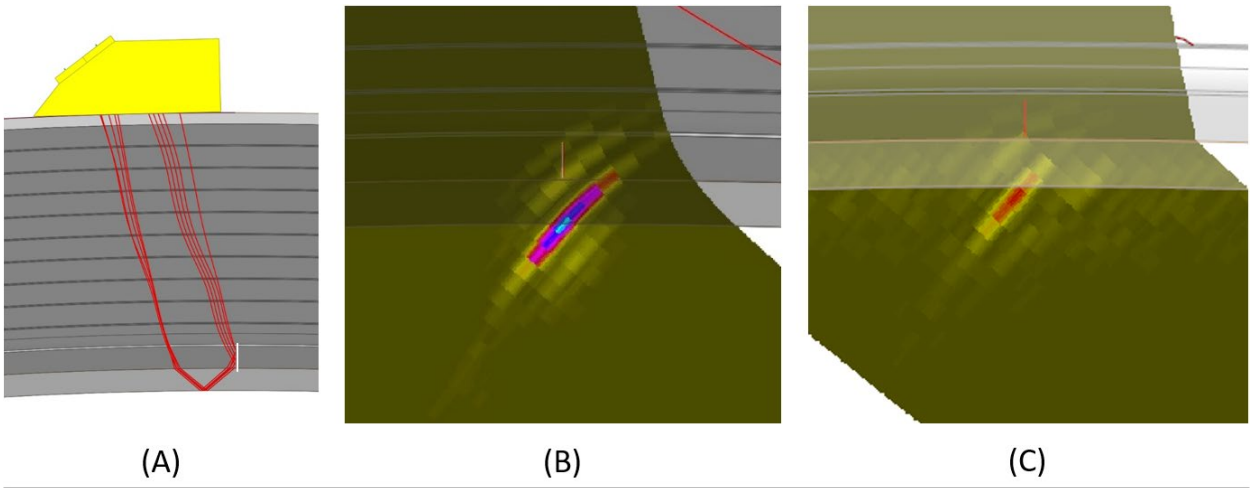


Figure G.4.3 (A) CIVA simulation model prior to running, showing the ray tracing of the ultrasound beam reflecting off of the defect (B) result of simulation using ideal surface conditions, (C) result of simulation using rough surface conditions. Image was calibrated to ideal scenario signal response.

Next, the effect of changes in the flaw characteristics were investigated. Simulations were created with the same straight line crack tilted +/- 10 degrees and +/- 20 degrees, and one

simulation was created using a branched (CIVA terminology) defect approximately the same height as the straight line defect. The branched crack is more representative of an actual crack as it has multiple facets at various inclinations along its height. The results in Figure G.4.4 were calibrated to the straight line crack of the previous simulation for a 0dB reference point to show the changes in signal response from this reference. All variations of the straight line crack showed significant drops in amplitude between -11.3 dB and -15.5 dB, while the branched crack showed higher signal response of +8.9 dB due to superposition of multiple reflections.

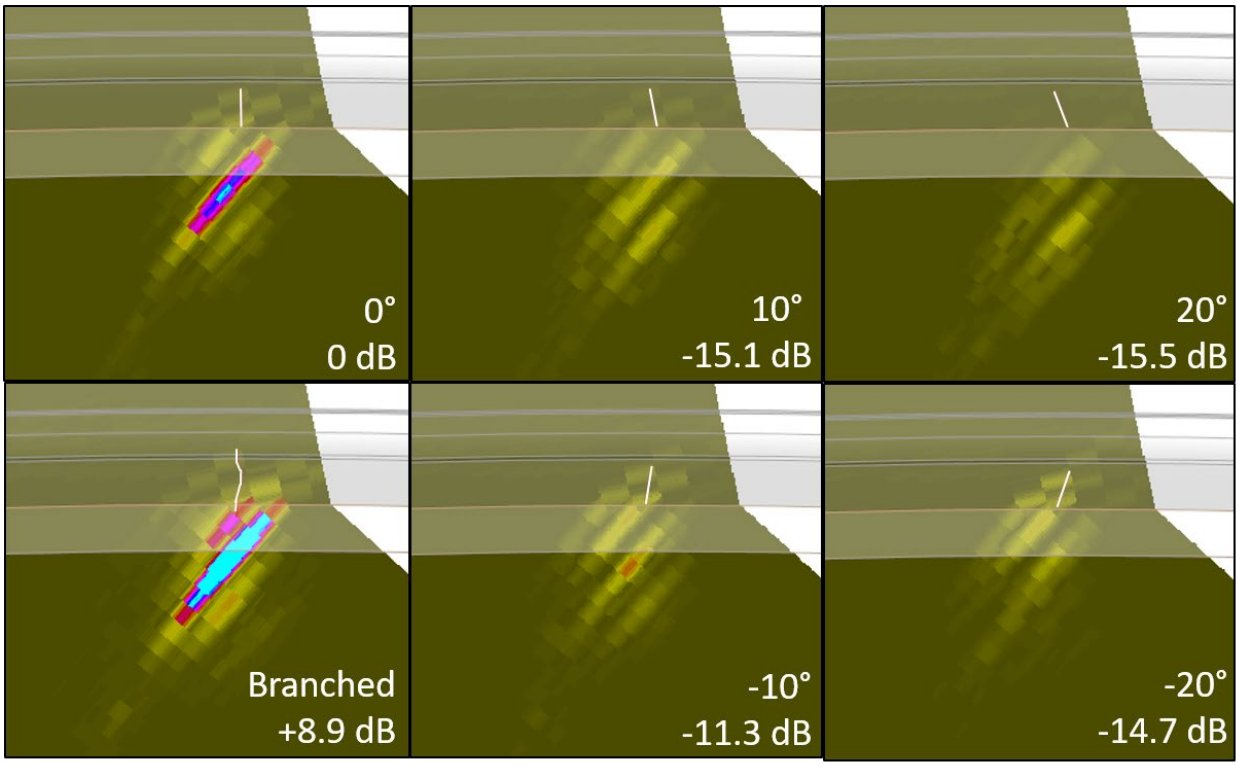


Figure G.4.4 Comparison in signal response to changes in flaw characteristics

G.5 Shell To Shell Weld Inspection Simulations – Circumferentially Oriented Crack

One of the most challenging shell-to-shell flaws to detect was the circumferentially oriented crack. This flaw has a length that runs parallel to the weld, as shown in the circumferentially oriented flaw in Figure G.4.2. If this crack is in the centerline of the weld, detection through direct or skipped reflection is almost impossible due to the angle of incidence. Depending on the width of the weld, detectability is only marginally better if the crack is located closer to the shell plate-weld interface. At the start of the project it was believed that a PAUT system using total focusing method and full matrix capture (FMC/TFM) could potentially image this defect. While

this technology was investigated through other efforts in the project, we were tasked with investigating alternative inspection methods using traditional technology.

Utilizing CIVA's ray tracing of ultrasonic beam profiles, it was discovered that when interrogating at the center of the weld at normal incidence, the anisotropy of the weld combined with its geometry created a complex modal coupling of the acoustic energy within the boundaries of the weld itself. Multiple modes of longitudinal and shear waves are steered and reflected from the changes in grain orientations and the weld to shell plate interfaces, keeping the majority of the acoustic energy within the weld until it was reflected off the bottom. It was theorized that a circumferentially oriented crack would act as enough of a discontinuity in the acoustic path that the energy would then be reflected out of the weld and into the shell plates. From an inspection perspective, this would present as a sudden and dramatic loss of signal from the back wall reflection.

CIVA's ray tracing of this scenario supported the hypothesis, shown in Figure G.5.1. In this figure, only modes that make it back to the probe are displayed. Figure G.5.1A is the ray trace of the ultrasonic beam in a pristine weld where each red or green line is associated with a path traveled by one of the ultrasonic modes. Figure G.5.1B shows the same ray trace in the presence of a 20mm tall circumferential crack, and shows a significantly lower density of ray traces returning to the probe. The red lines indicate longitudinal modes, while the green lines indicate shear modes.

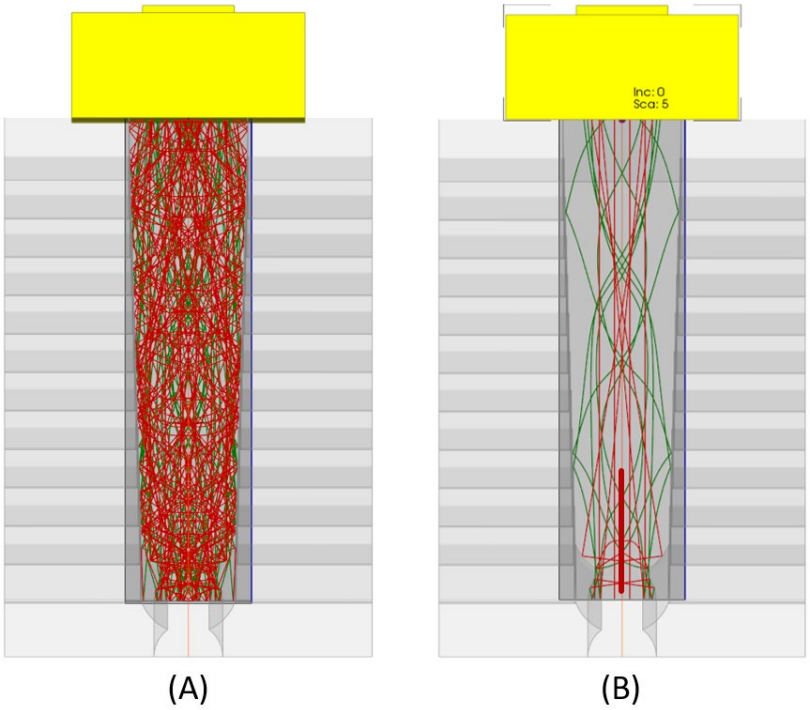


Figure G.5.1: Ray trace of the ultrasonic beam traveling from and returning to the inspection probe in (A) a pristine weld and (B) a weld with a 20mm circumferential crack in the centerline.

The results of the full simulation supported the results of the ray tracing. Figure G.5.2 shows the simulation of a 15mm circumferential crack in the weld centerline and the resulting abrupt and dramatic decrease in back wall reflection to the point that it is indistinguishable from the background noise. The simulation used a single element contact transducer on a normal incidence wedge. The single contact transducer was simulated in lieu of a PAUT to simplify the simulation. Given the results of this initial simulation supporting our hypothesis, several subsequent simulations were executed to investigate how variations in this flaw could influence detectability.

It should be noted that the run time on these simulations was considerably longer than the previous simulations (16-90 hours for the circumferential cracks compared to less than an hour for the axial cracks). Since this detection method is using the loss of signal as an indicator, the full extent of the existing back wall reflection must be realized in the simulations. This means there are fewer assumptions and fewer omitted modes in the simulations to simplify calculations, and thus longer computation time. This longer run time limited the number of iterations that were feasible in the time allotted.

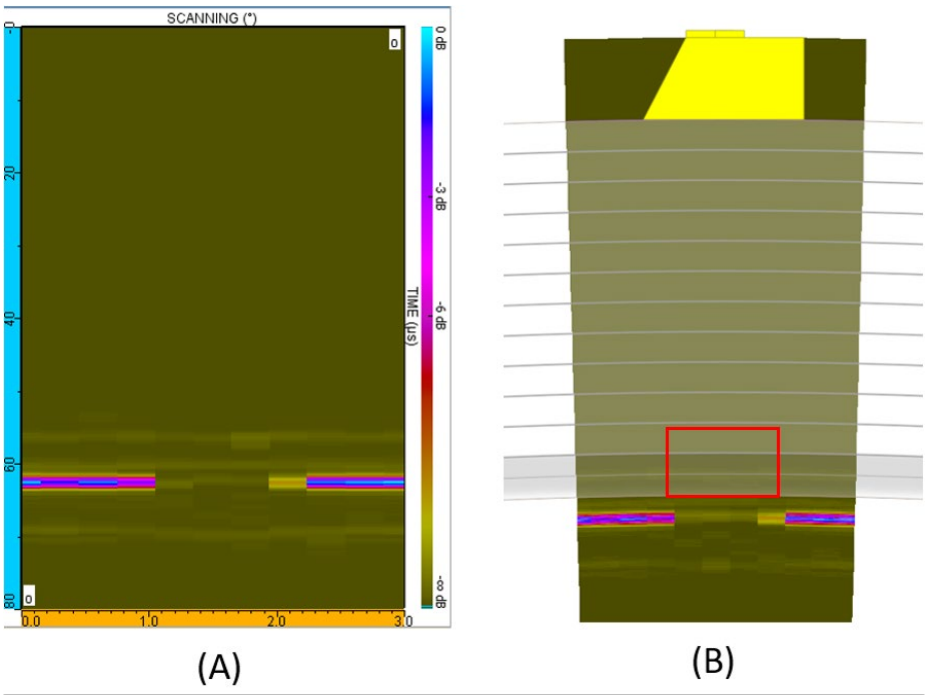


Figure G.5.2 (A) Results of simulating a 15mm circumferential crack at the weld centerline (B) the simulation results overlaid onto the CAD model. The red box outline shows the bounds of the simulated crack. (Weld runs left to right.)

A semielliptical shaped circumferential crack was simulated to determine the minimum size of the crack to become a noticeable loss of back wall signal. The results are shown in Figure G.5.3. A conservative threshold of 50% loss of back wall signal was selected as the detection criteria. With this threshold, it was determined that the minimum height for detectability was 6.18mm, demonstrated in Figure G.5.3B. For a threshold of 75% loss of back wall signal, the minimum crack height for detectability changes to 8.66mm.

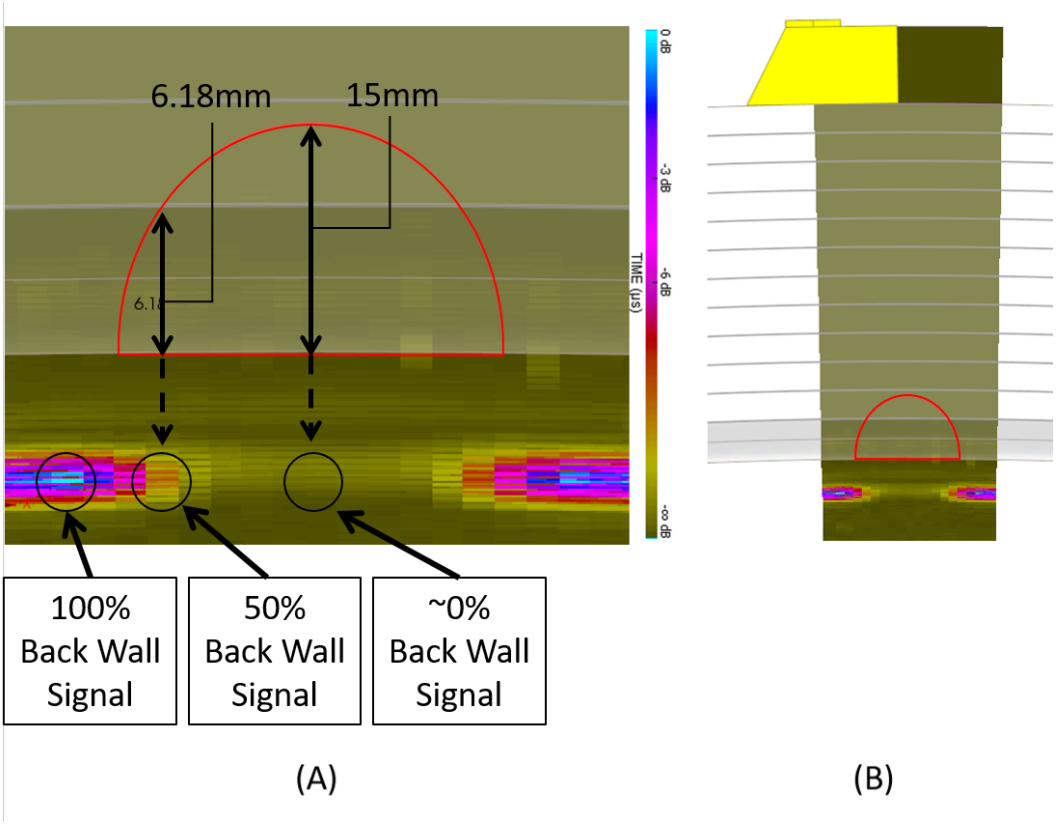


Figure G.5.3 (A) Results of simulating a semielliptical circumferential crack at the weld centerline (B) the simulation results overlaid onto the CAD model. The red box outline shows the bounds of the simulated crack. (Weld runs left to right.)

In all the simulations thus far the transducer and flaw have been located in the center of the weld, and each weld was modeled as if it were machined down to a flat surface. The next step was to investigate the effects on detectability when these parameters were not ideal (i.e. off center transducer, bumpy irregular weld surface geometry, etc.).

A set of simulations was run to model an inspection where the transducer was offset from the center of the weld. In these simulations, the transducer was positioned over a pristine region and scanned in a direction perpendicular to the weld for ten 0.4mm increments, to a maximum center offset of 4mm. Then, the transducer was positioned over a region with a circumferential crack at the weld centerline, and the same scanning pattern was executed. Since the goal of this simulation and the next simulation was to study the effect of inspection variability and not flaw size variability, the chosen crack height was larger than those used in previous simulations (25mm). This maximized the likelihood of observing changes in signal response over a larger number of inspection variabilities, because once the flaw signal disappears any additional simulations with more extreme inspection variability won't yield any more meaningful data points. Figure G.5.4 shows the results of these simulations, with Figure G.5.4A showing the B-scan of the pristine region and Figure G.5.4B showing the B-scan of the flaw region. Overall,

the loss of back wall signal between flaw and pristine regions at the same offset ranged from 55% loss to 96% loss. Table G.5.1 shows the changes in back wall signal loss as a function of offset from center. Incidentally, the smallest amount of back wall signal loss was not at the highest offset, but rather almost halfway between the center and the largest offset. The reason was later discovered when beam profile simulations were run to visualize where the acoustic energy was most dense and where there were blind spots. The beam profile simulations will be discussed in later sections.

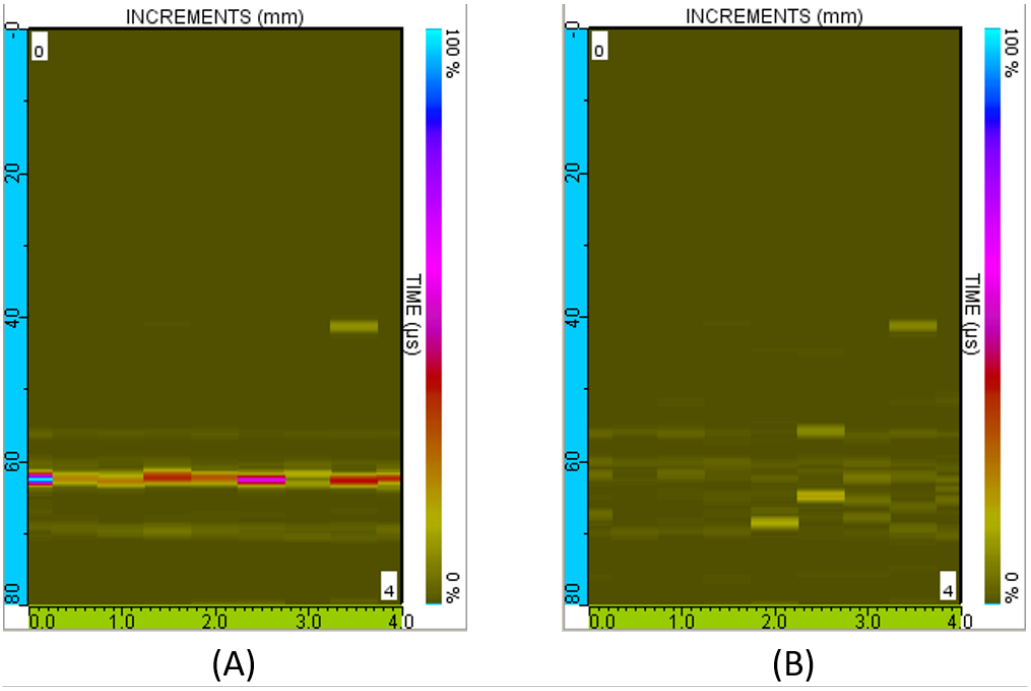


Figure G.5.4 B-scan results from a simulation of back wall signal reflection over variable probe offsets from center in (A) a pristine region and (B) a region with a 25mm circumferential crack in the weld centerline

As an extension of the previous exercise, a circumferential crack with variable offset from the center was investigated for changes in detectability. Due to the length of the simulation run time, only two offset distances were investigated: 3.5mm and 6.5mm from the weld centerline. The results of these simulations are shown in Figures G.5.5 and G.5.6. Both 3.5mm and 6.5mm offset simulations had similar losses in back wall signal reflection, 48.74% and 45.73% respectively.

Table G.5.1 Changes in loss of back wall signal as a function of probe offset from center

Distance from center (mm)	Percent loss of back wall signal
0	100%
0.4	96%
0.8	96%
1.2	92%
1.6	86%
2	94%
2.4	55%
2.8	68%
3.2	64%
3.6	81%
4	90%

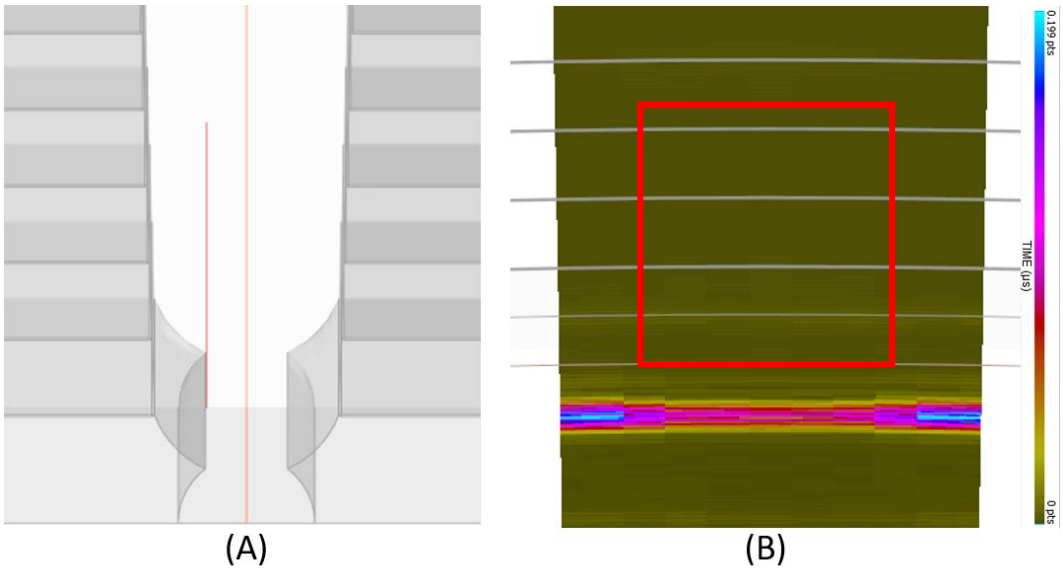


Figure G.5.5 (A) CAD model used in simulation a circumferential crack that was 3.5mm offset from weld centerline. The red line is the crack and the orange line is the weld centerline. (B) The result of the simulation showing a 48.74% drop in back wall signal. The red box outline shows the bounds of the simulated crack

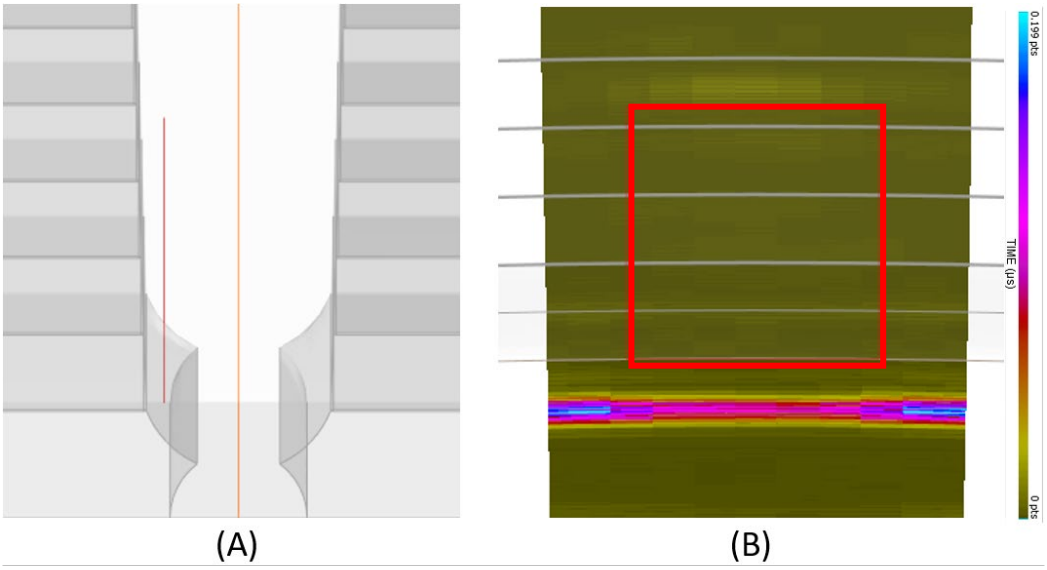


Figure G.5.5 (A) CAD model used in simulation a circumferential crack that was 6.5mm offset from weld centerline. The red line is the crack and the orange line is the weld centerline. (B) The result of the simulation showing a 45.73% drop in backwall signal. The red box outline shows the bounds of the simulated crack

To aid in the physical inspection of these LPVs, the plan was to machine the surface of the welds to be flush with the rest of the vessel. For some LPVs this will not be feasible, so the effects of the irregularities in an as-welded surface will need to be understood. The surface irregularities were simulated to two degrees of severity, shown in Figure G.5.6A and Figure G.5.6C. The irregularity was simulated using random spline curves along a semielliptical curve, with each spline having an aspect ratio of roughly the same magnitude. This inspection simulation was still focused on circumferential cracks at the weld centerline, but in this case both a semielliptical crack and a branched crack were inserted. As shown in Figure G.5.6B and Figure G.5.6D, the loss of back wall signal did not decrease any appreciable amount, and the only differences between these and the flat top simulations is a higher presence of noise artifacts.

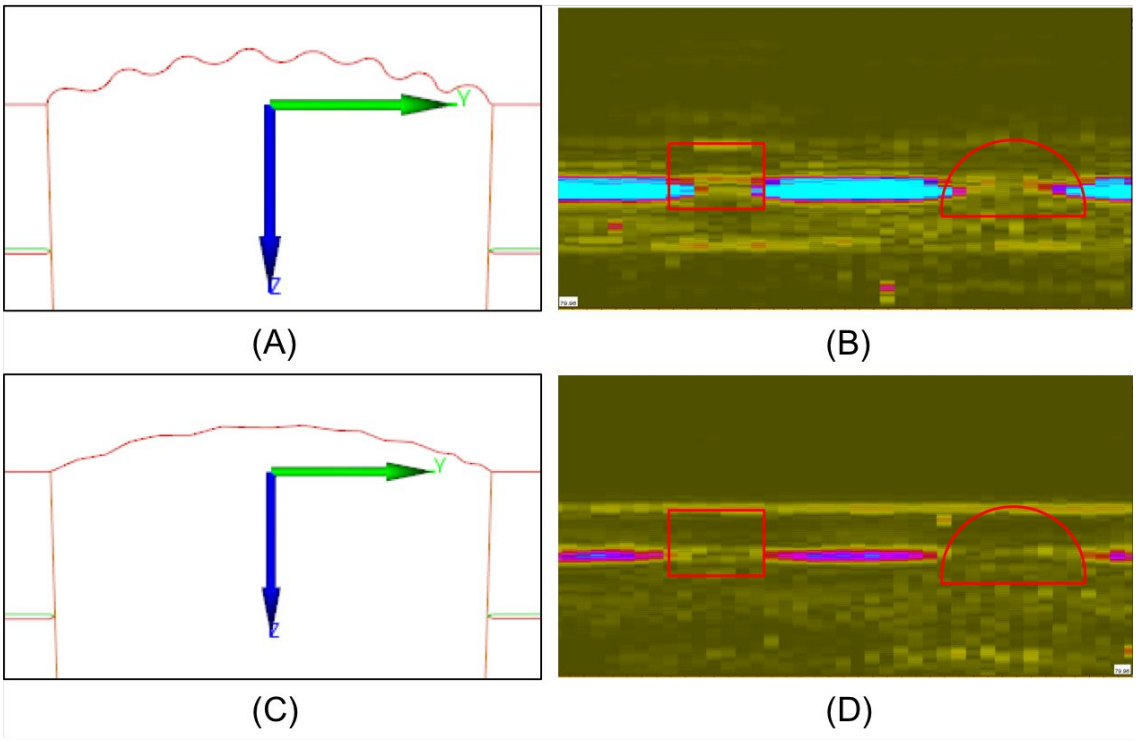


Figure G.5.6 Simulations of inspections over an irregular as-welded surface using two different surface profiles. (A) and (C) show the CAD models of the surface and (B) and (D) show their respective simulation results. The red box and semi circles show the bounds of the simulated cracks.

The final simulations run for the project utilized the beam simulation module of CIVA. This module allows for the visualization of the ultrasonic beam profile as it propagates through the material, revealing the focal points, dead zones, and side lobes that will influence the inspection results. The beam simulation module was used to study how uneven plate weld geometry affects the ability to detect defects. Figure G.4.1 shows an actual cross section of a shell to shell weld, and it can be seen that each plate weld interface is not always offset from the one below it in a

slope pattern defined by the V weld. In some cases the plates will protrude further into the weld than the layers below it, effectively shadowing any defects that might be present there.

Beam simulations were performed using a weld geometry that had a 3 mm plate offset on one side of the weld, and this case was run for a 2.25 MHz and 5 MHz simulation. The results displayed in Figure G.5.7 show how this shadowing can occur, as well as other dead zones in the beam profile that could hinder inspection capabilities. In this figure, the bright parabolic-shaped streaks represent the concentration of acoustic energy as it propagates through the material which is associated with a higher likelihood of detecting flaws in these areas. The areas in between have less focused acoustic energy and therefore a lower likelihood of energy-flaw interactions. Normally an acoustic beam will be scanned or swept along the material to ensure maximum coverage of the material, but in cases like Figure G.5.7 where the geometry blocks sound path there is no position we can inspect from that will cover this shadowed area (since we are limited to top surface inspections).

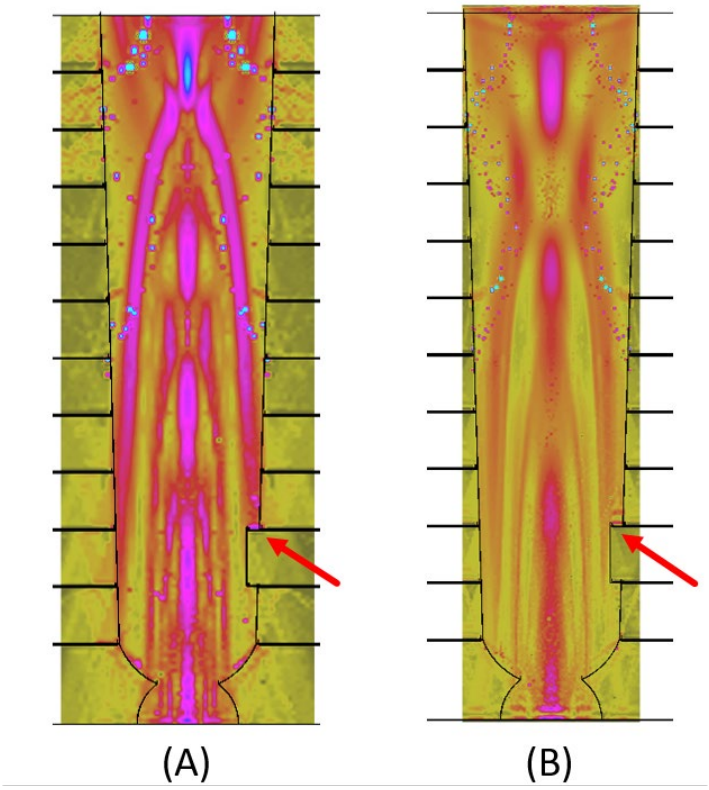


Figure G.5.7: Beam simulations showing how uneven plate weld geometry can shadow regions of the weld from inspections. Simulations run at (A) 5 MHz and (B) 2.25 MHz

G.6 Conclusions

The simulations in this study were able to show the sensitivity of the flaw signal response to various changes in the inspection cases. These changes include variations in flaw characteristics and locations, inspector error, and weld geometry and surface imperfections. The results of this sensitivity analysis will help guide the LPV inspection process by giving confidence to which flaw types are detectable and how much inspection/geometry variability changes this confidence. Additionally, this study helps inform inspectors of the behavior of the ultrasonic energy within these welds and how that energy interacts with the flaws.

Using simulated-guided inspection, novel inspection methodologies were discovered for detecting circumferentially oriented cracks in shell to shell welds. This technique revolved around the loss of signal caused by the vertical discontinuity in the acoustic path in the weld. This may prove to be a valuable inspection method in situations were other equipment or methods cannot reliably resolve this kind of flaw.

G.7 References:

[G1] J A Ogilvy, ‘Computerized ultrasonic ray tracing in austenitic steel’, NDT International, Vol 18, No 2, pp67-77, 1985.

Appendix H: Detection of Transverse Flaw in a Root of Multi-Layered Vessel

DETECTION OF TRANSVERSE FLAW IN A ROOT OF MULTI-LAYERED VESSEL

Prepared by:

Sergey Vinogradov

FINAL REPORT
SwRI® Project No. 18.24026

Prepared for

Bastion Technologies, Inc.
17625 El Camino Real, Suite 330
Houston, TX 77058

June 21, 2019



Clinton J. Thwing, Manager
Sensor Systems & NDE Technologies

TABLE OF CONTENTS

Section Page

1. INTRODUCTION....1
2. REPORTING AND DOCUMENTATION....1
3. MAGNETOSTRICTIVE SENSOR TECHNOLOGY....2
4. CIVA MODELLING....3
5. RESULTS OF MOCKUP TESTING....5
   - 5.1 Mockup....5
   - 5.2 Test procedure....6
   - 5.3 Assessment of energy distribution....6
   - 5.4 Detection of transverse anomalies....8
   - 5.5 Detection of transverse anomalies in a weld with a crown....10
   - 5.6 Alternative probe design....11
6. SUMMARY AND CONCLUSIONS....12
7. REFERENCES....12

1. INTRODUCTION

The inspection of the shell to shell circumferential welds for layered pressure vessels (LPV's) is challenging for current inspection methods. This is made difficult by three factors:

1. The intra-layer gaps on either side of the weld prevent the transmission of signals into the weld volume from areas adjacent to the weld. That means the only signal path is through the weld volume itself.
2. The welds are quite narrow.
3. The weld surface is typically rough due to the welded condition. Very few welds have had their outer surface machined to a smooth condition.

Inspection techniques that will facilitate evaluations in the as-welded condition are preferred.

Southwest Research Institute® (SwRI®) proposed utilization of low frequency transverse mode guided waves for detection of transverse anomalies on the root of the weld. Bastion Technologies, Inc. provided a test sample with machined transverse anomalies for the test. The test was conducted at SwRI facility during the time frame of April 3 – 5, 2019. Testing was conducted based on guidelines outlined in ASTM Standard E2929-13 [1].

2. REPORTING AND DOCUMENTATION

According to client request, this report shall contain the following:

- Results of any analytical modeling;
- Results of field testing for both welds over the variety of probe frequencies and positions used;
- If detection of flaw(s) is successful, characterization of location and size as best achievable;
- Characterization of signal with and without detected flaws;

- General findings, potential limitations, and recommendations for future development to increase guided wave's applicability for inspection of NASA layered pressure vessel shell to shell circumferential welds.

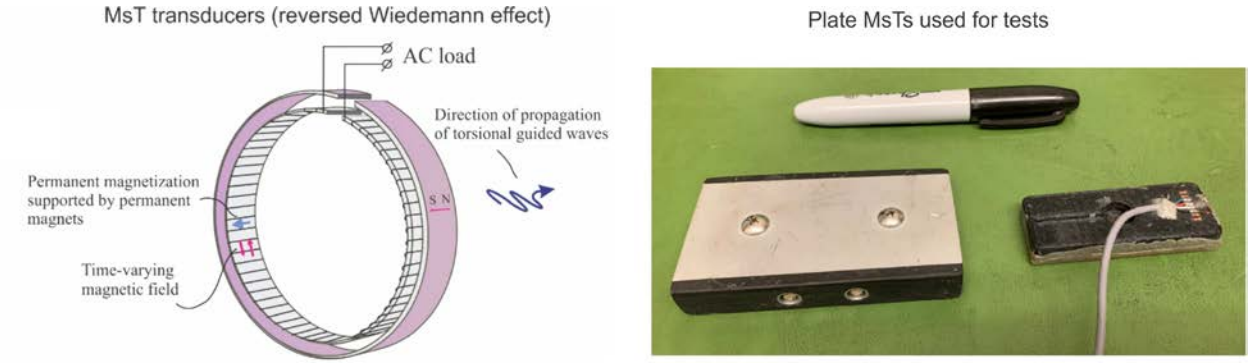
3. MAGNETOSTRICTIVE SENSOR TECHNOLOGY

Magnetostrictive transducers used for the test were invented in 2008 and utilize a reversed Wiedemann effect [2,3]. MsTs have the following major components:

- Toroidal AC coil wound around iron cobalt (FeCo) strip
- Array of small permanent magnets provides stable in-plane static magnetization of strip

Coil generates high amplitude AC magnetic field forcing domains in the FeCo strip to oscillate. Domain oscillation causes mechanical vibrations in the strip that can be transferred to the tested structure when the strip is acoustically coupled to the tested structure. Receiving guided waves is a reversed process when the mechanical vibrations result in magnetic domain oscillations that can be picked up by a coil.

The MsTs used for practical NDE have two transducers lined up one next to each other for direction control. Proper spacing between transducers cause a phase delay which allows for the sending of the guided waves in both a forward or backward directions. A fundumental shear horizontal mode was used in the frequency range 45 – 250 kHz. Figure 1(a) shows the MsT transducer design used for pipe inspection. Figure 1(b) shows a plate MsT transducers used for the test.



(a) (b)

Figure 1. MsT transducer design: a - MsT for pipe inspection; b – plate MsT Transducers used for the test

4. CIVA MODELLING

A commercially available CIVA software package delivered by Extende for simulation of guided wave propagation was used [4].

Initial modelling was done in a 101 cm (4 inches thick) carbon steel plate. The model simulated the thickness of the weld. The dispersion curves indicated that SH01 mode has even displacement through the thickness of the test article. SH02 mode has higher displacement near the top and the bottom of the plate. The same is correct about SH03 and SH04 modes. All calculated dispersion curves are shown in Figure 2. At higher frequencies (170 kHz) propagation of guided waves is constituted by a cluster of different modes (shown in circle).

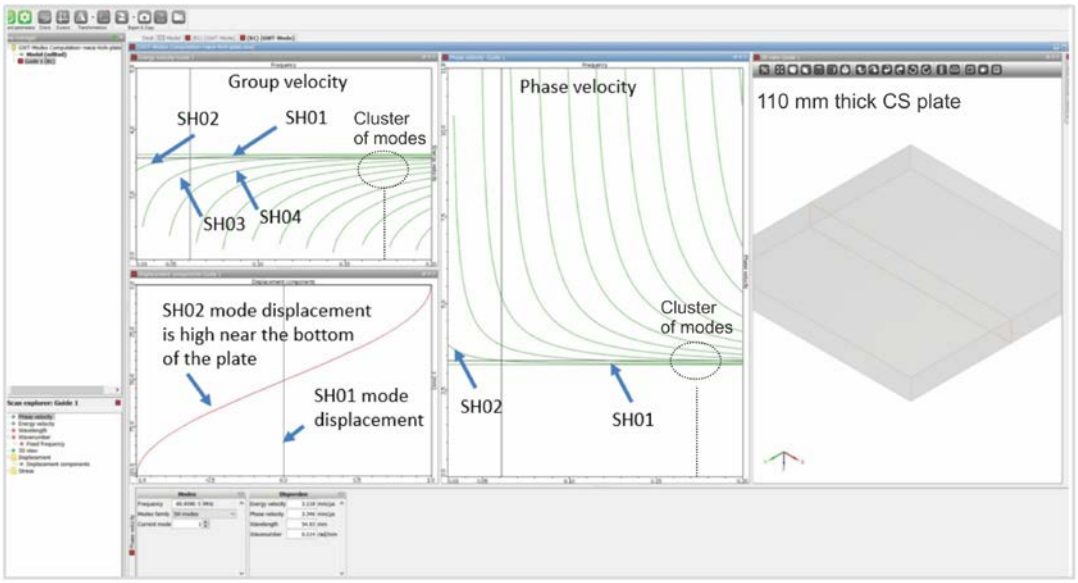
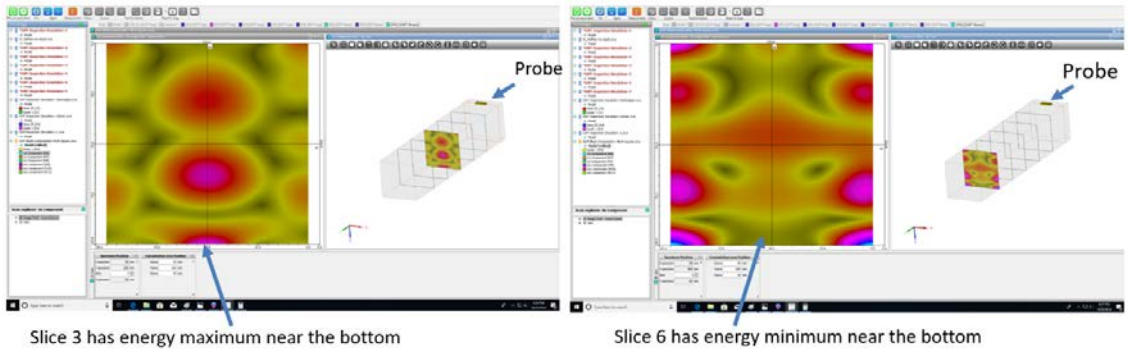


Figure 2. Dispersion curves for 4 inches thick carbon steel plate

Additional wave propagation simulation was done on 101 x 101 cm carbon steel bar. The results indicated that due to the presence of different modes there is an effect of uneven energy distribution through the bar cross section. These effects are shown in Figure 3(a) and (b) at 60 kHz center frequency. Local maximum and minimum of signal amplitude was observed in different bar crossections (shown as slices 3 and 6).



(a) **(b)**

Figure 3. Effect of uneven energy distribution in 101 x 101 cm thick bar at 60 kHz

The presence of this effect can result in variations of signal amplitudes produced by the anomaly as a function of distance between the probe and the anomaly. A few probe positions might be needed to normalize this effect.

Additional modelling was done in the structure simulating a weld with multi-layered attachments to see if any energy can penetrate to the root of the weld. For this model, CIVA supported only 30 mm thick specimen and was not able to process 100 mm thick model due to internal limitations (confirmed by CIVA support team). Figure 4 shows the results of modelling.

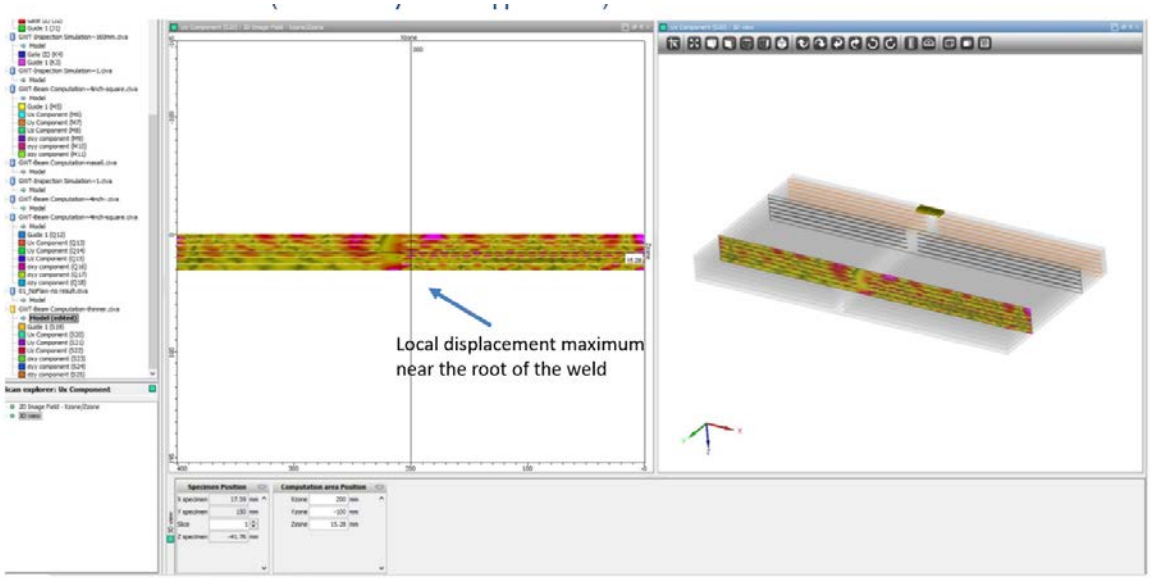


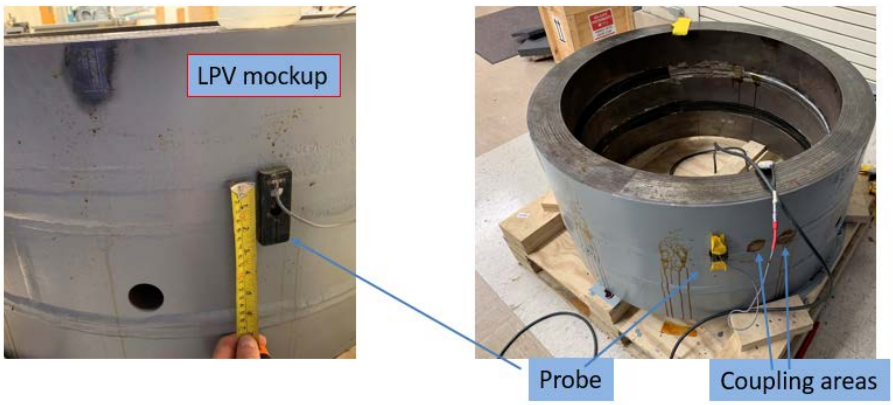
Figure 4. Results of modelling in 30 mm thick specimen simulating a guided wave propagation in a weld with multi-layered attachments at 90 kHz

Modelling in multi layered structure indicated that the energy can reach out to the root of the weld. However, due to the limited scale of this simulation, actual measurement of energy distribution near the weld root will be needed.

5. RESULTS OF MOCKUP TESTING

5.1 MOCKUP

The mockup delivered to SWRI is shown in Figure 5. Shear wave couplant was used for probe coupling. The probe was positioned on top of the weld with flat top as shown in Figure 5(a). The sides of the probe were covered with tape to prevent energy leakage to the areas outside of the weld crown. The magnets inside of the probe, help hold itself on top of the weld crown. A few different probe positions were used to verify relevant indications and at two coupling areas are shown in Figure 5(b).



(a) **(b)**

Figure 5. Mockup delivered to SwRI

5.2 TEST PROCEDURE

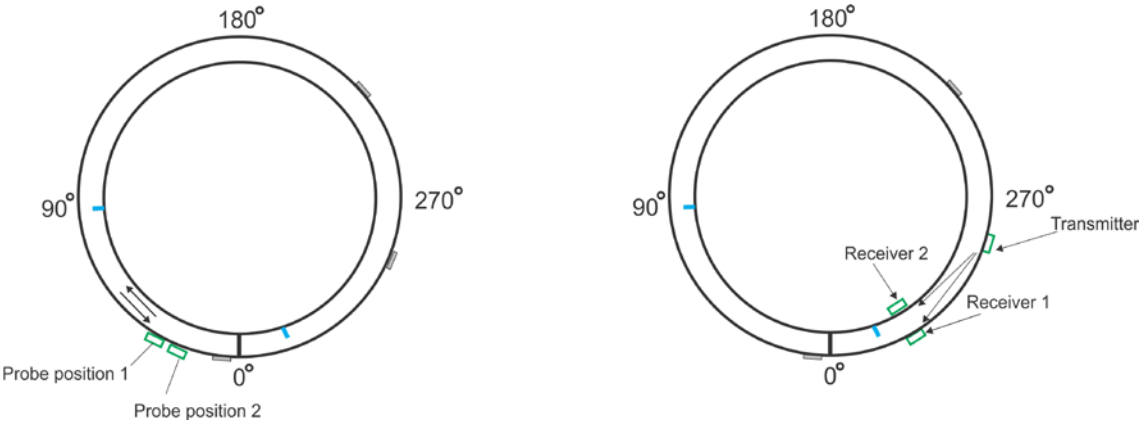
The test procedure followed these steps:

- Assessment of energy distribution of transverse guided wave through the weld thickness as a function of frequency (was measured in pitch-catch mode using one probe as a transmitter and another probe as a receiver). The first probe was coupled to the outer diameter (OD) surface and the second probe was coupled to both OD and inner diameter (ID) surfaces.
- Assessment of velocity of guided waves in the outer layer.
- Assessment of group velocity of guided wave modes reaching the weld crown.
- Ability of the method to detect known geometric features (vertical OD welds, a hole).
- Ability of the method to detect a tranverse anomalies (based on 1 – 4 different probe positions).

5.3 ASSESSMENT OF ENERGY DISTRIBUTION

The major method for the test is a pulse-echo probe operation using one probe and it is shown in Figure 6(a). For assessment of energy distribution, a pitch catch mode where two probes were utilized. The setup is shown in Figure 6(b). The transmitter was placed on the outer

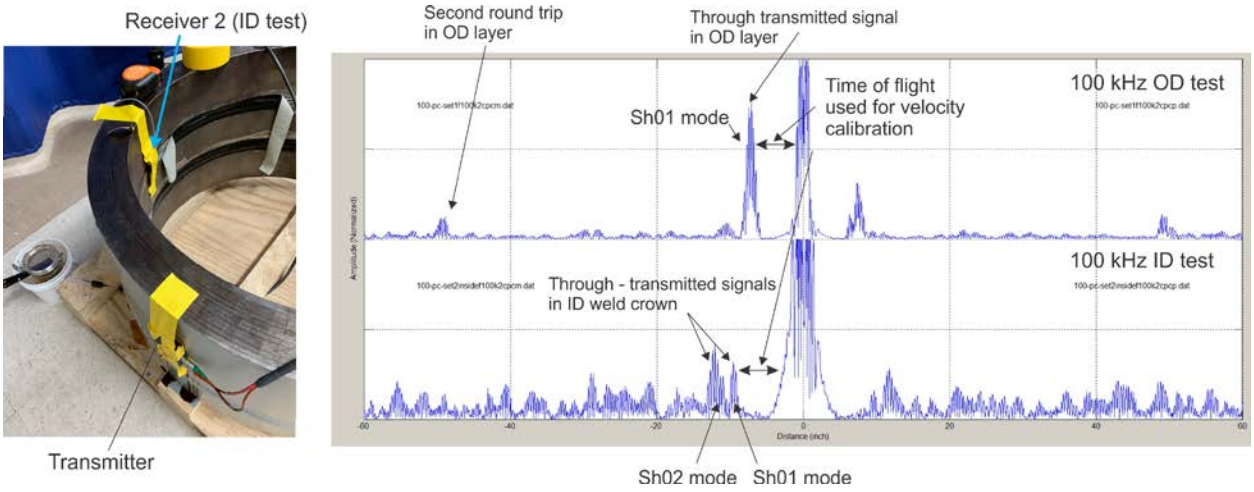
surface on top of the weld crown and a receiver was used in two positions – one on top of the weld crown and another on top of the weld root.



(a) **(b)**

Figure 6. Test modes: a – pulse-echo mode, b – pitch-catch mode

The actual probe layout used for the assessment of energy distribution is shown in Figure 7(a). Signals acquired with the receiving probe coupled to the OD surface and to the ID surface at 100 kHz center frequency are shown in Figure 7(b).



(a) **(b)**

Figure 7. Assessment of energy distribution: a – transmitter and receiver positions, b – signals acquired with receiving probe coupled to the OD surface (top) and to the ID surface (bottom)

Signal amplitude drop between OD and ID of the welds were found to be in the range of 9 –15 dB depending from frequency. The velocity of SH01 mode in the outer shell was

123 inches/msec. The velocity of SH02 mode in weld crown on the ID surface was calculated based on time of flight in the range 85 -90 inches/msec.

Figure 8 shows signal pattern acquired a range of frequencies from 45 to 135 kHz.

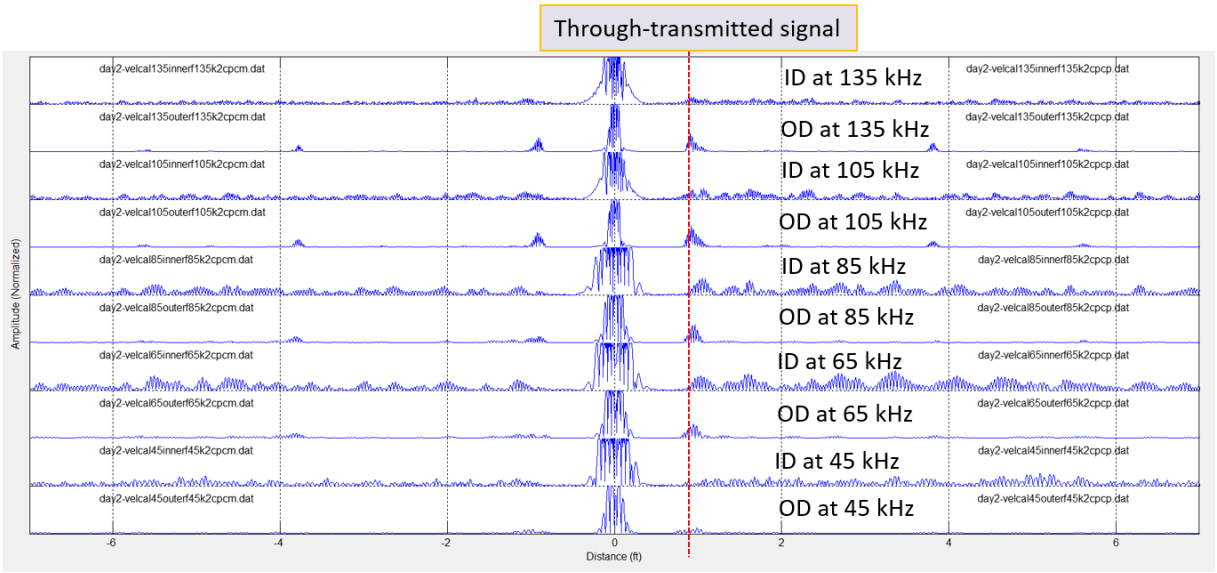
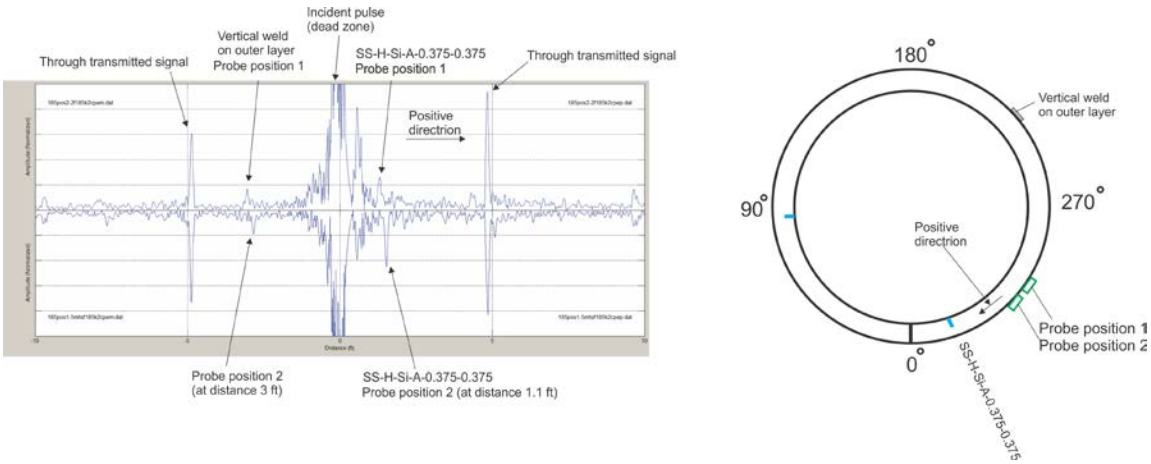


Figure 8. Signal pattern acquired in pitch-catch mode in a range of frequencies from 45 to 135 kHz

Based on these test results, energy penetration to the weld root was observed in the frequency range 45 – 135 kHz. Better signal to noise ratio was observed at higher frequencies – above 60 kHz. Essentially better amplitude of round trip signals were observed above 100 kHz frequency range.

5.4 DETECTION OF TRANSVERSE ANOMALIES

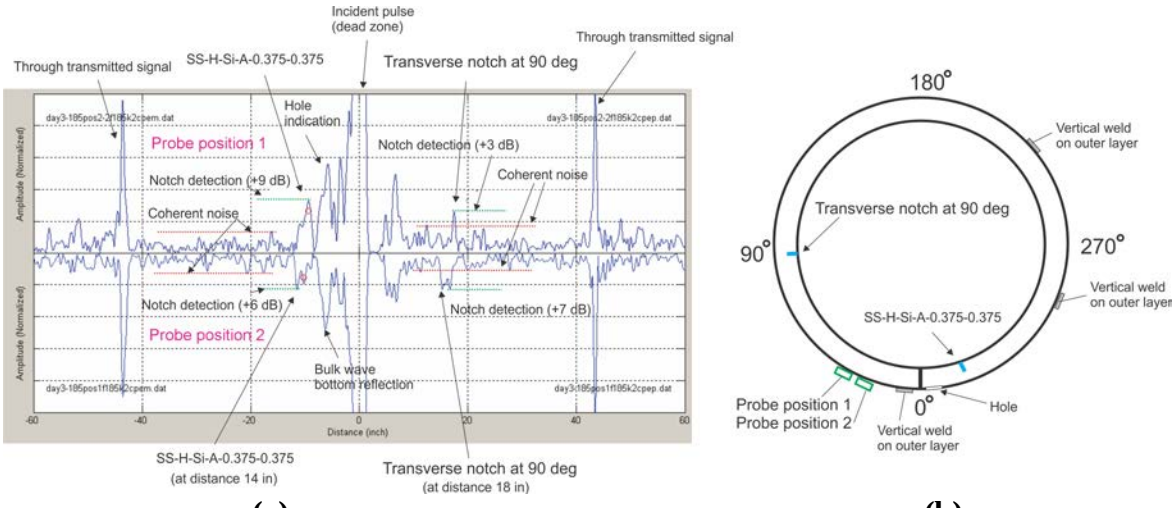
The detection of anomaly SS-H-Si-A-0.375-.0375 was accomplished at 185 kHz center frequency from test location at 292 degrees. The test utilized two probe positions with a distance between the two positions of about 6 cm were used. Figure 9(a) shows an A-sans acquired from probe position 1 (rectified positive) and from probe position 2 (rectified negative). The test location is shown in Figure 9(b) (290 degree test location). Other indications were observed such as through transmitted signal and reflections from vertical welds located on the outer layer.



(a) **(b)**

Figure 9. Detection of anomaly SS-H-Si-A-0.375-.0375 from two probe positions (at 292 degree test location)

To confirm detection of this anomaly another test location (at 15 dergee) was used. The results of the test are shown on Figure 10(a). The probe test location is shown on Figure 10(b). A-scans acquired from probe position 1 are (rectified positive) and from probe position 2 (rectified negative). From this second test location, a detection of the notch SS-H-Si-A-0.375-.0375 was also accomplished with SNR in the range 6 – 9 dB (the indications can be seen at distance mark -10 inches). Detection of a transverse notch located at 90 degrees was also accomplished from two probe positions with SNR in the range 3 – 7 dB (the indications can be seen at distance mark +18 inches).



(a) **(b)**

Figure 10. Detection of anomaly SS-H-Si-A-0.375-.0375 and a transverse notch located at 90 degree

Figure 11 shows a spectrogram of the acquired signals. Due to the broadband nature of the MsT probe, the actual frequency range can be evaluated based on a through transmitted signal. In this case, the frequency band was 100 to 250 kHz. Indication from notch produced the best response in the range from 100 to 150 kHz. Some indications forming a coherent noise had a slight upshift in frequency domain. This effect can be utilized for partial suppression of coherent noise indications by applying a frequency envelope in lower frequency range.

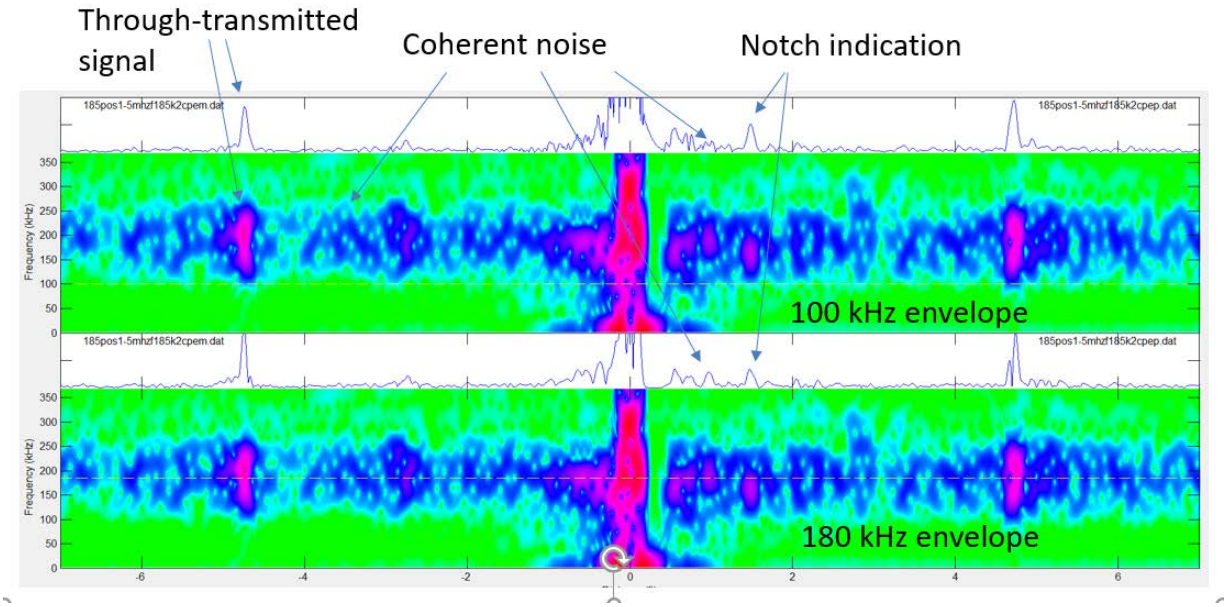


Figure 11. Spectrogram of acquired signals with 100 kHz (top) and 180 kHz frequency envelopes

5.5 DETECTION OF TRANSVERSE ANOMALIES IN A WELD WITH A CROWN.

Another test was conducted on the weld with a crown. Figure 12(a) shows a signal response with very weak through transmitted signal due to poor probe coupling. For comparison, a through- transmitted signal with a probe coupled to the shell on the side of the weld is shown in 12(b). As an option, a probe coupling from the side of the weld can be considered or, a flexible probe configuration has to be fabricated to fit the surface profile. As an example of a signal obtained with the probe coupled from the side of the weld but tilted towards the weld crown is shown in 12(c).

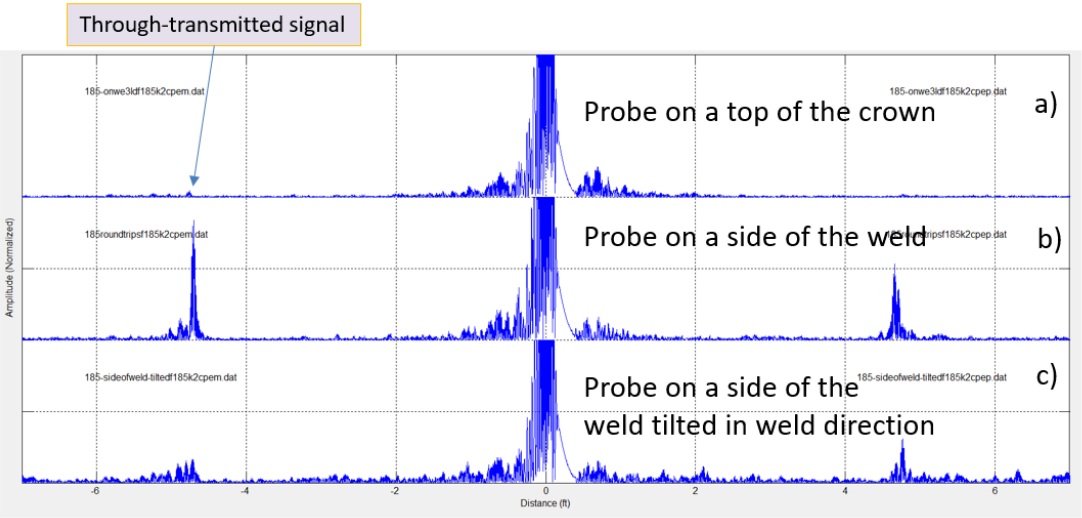


Figure 12. Performance of the probe on top of a weld with a crown

5.6 ALTERNATIVE PROBE DESIGN

A dual probe head configuration operating in pitch catch mode is recommended to accomplish a better acoustic coupling. The concept of such a probe is shown in Figure 13. In this probe configuration, two transmitting probes can be coupled to the outer shell on the two sides from the weld. If tilted towards the weld, good energy penetration can be expected at the root of the weld. The receiving probe will be positioned on top of the weld crown and should have the ability to conform to the weld profile.

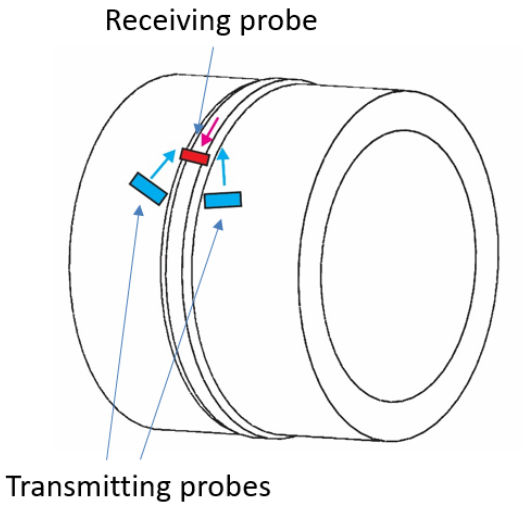


Figure 13. Dual probe head configuration operating in pitch catch mode

6. SUMMARY AND CONCLUSIONS

- 3-9 dB detection was accomplished on transverse notches from a distance up to 18 inches and at a center frequency 185 kHz
- Detection was confirmed with the probe located at different test locations on the mockup
- Also, the detection was confirmed from two slightly different probe positions at each test location
- On a weld with crown:
- Poor acoustic coupling did not allow reliable signal transmission
- A flexible probe would be needed
- Or, a dual probe coupled probe both sides of the weld used for transmission and a curved probe mounted on top of the crown for reception
- As an option, a flattened area would need to be machined on a weld

7. REFERENCES

[1] Standard Practice for Guided Wave Testing of Above Ground Steel Piping with Magnetostrictive Transduction, ASTM Standard E2929-13.

[2] Vinogradov S., 'Method and System for Generating and Receiving Torsional Guided waves in a Structure,' U.S. Patent 7,821,258, B2, October 26, 2010.

[3] Vinogradov S, Cobb A, and Light G, 'Magnetostrictive Transducers Utilizing Reversed Wiedemann Effect', AIP Conference Proceeding, Volume 36, 2016.

[4] CIVA website http://www-civa.cea.fr

Appendix I: Examination/Analysis of Acoustic Emission Waveform Data from Tensile Testing of Notched Curved Sample of LPV Steel

Examination/Analysis of Acoustic Emission Waveform Data from Tensile Testing of Notched Curved Sample of LPV Steel

by

M. A. Hamstad (mhamstad@du.edu)

Professor Emeritus, Mechanical and Materials Engineering Department

University of Denver, Denver, CO 80208

September 30, 2015

Work done under PO from Analytical Mechanics Associates, Inc.

21 Enterprise Parkway, Suite 300

Hampton, VA 23666

Introduction

Two notched tensile samples (labeled 106 and 107) made from a Layered Pressure Vessel (LPV) shell material were cycled several times to stress the center-notched region to high stresses. The purpose of the test was to determine characteristics of the acoustic emission (AE) generated from the notch tip regions. Two different AE systems were used (known as Digital Wave, [DW] and Physical Acoustics Corporation [PAC]) with each system monitoring a total of six sensors. This report is based on analysis of the parametric and waveform data files from the DW system. The report on the PAC data is found in reference 1. The sensors used for the DW system were model 1025. These sensors were mounted on both the front (convex side) and back (concave side) of the test sample. The sensors on the front and back were mounted so they were nearly back-to-back (or opposite from each other) from each other. This sensor arrangement was presumable made so that the out-of-phase character of the flexural mode could be identified, particularly for sensor sets being closest to back-to-back. One set of sensors (nearly back-to-back) was mounted on the top of the sample in the shoulder area, two similarly arranged sets were mounted one set near the notch region and one set near the bottom of the sample in the shoulder area (see **tables 1 and 2** for the reported coordinates of the locations of the centers of the sensors). **Figure 1** shows a schematic of the sensor arrangement (viewed from the front, convex side for sample 107) and the origin of the coordinate system relative to the data in **tables 1 and 2**. **Tables 1 and 2** also record the coordinates of the initial notch tips after the EDM machined through-thickness center notch of width 0.75 inches was created. The tensile specimen was nominally 0.250 inches thick and the reduced section was 3.5 inches wide with a reduced section length of 3.57 inches. The total length was 18 inches with a transition in the shoulder section to a 7.5 inch wide portion. Due to the nature of the curved sample, two machined backing pieces were made to account for this. These added to the total thickness in the grip region to increase the bearing area for the pin (1.75 in. dia.) loading. **Figure 2a** illustrates a schematic of the assembled sample with backing plates [1]. The backing pieces were screwed to the sample at four locations through the holes shown in **figure 2a**. Reference 2 provides dimensioned drawings of the test sample and backing pieces. **Figure 2b and 2c** show photographs of a sample installed in the hydraulic test machine with the clevis grips for the pin loading. In **figure 2c** it appears that the hole in the clevis grips is larger than the pin diameter thus possibly creating a stress concentration that could generate extraneous AE. Potential difference (PD) crack length monitoring equipment was connected to the test specimen in order to measure real-time crack length per reference 2. For this measurement two sets of probes were connected at the crack centerline and centered about the crack. The probes were spot welded to the test specimens using a dual pulse spot welder.

Loading Histories of the Samples and Waveform Files

Prior to the first AE monitored loading the notch tips were sharpened by fatigue cycling for a planned growth per reference 2. There were a total of five (106) or six (107) AE monitored load cycles to certain peak values for the test samples. For each sample the last load cycle was to complete failure of the sample. After reaching the peak values the loading (for the non-failure

cycles) was reduced at a constant rate. Between AE monitored load cycles, additional fatigue cycling at lower load levels was done to provide "marking" bands between the notch growth extensions that were generated during each AE monitored loading. This "marking" was successful as shown by an SEM photo (for 107) presented in **figure 3** [1] showing the initial notch, initial sharpening, sharpening "markers" between load cycles, and a part of the final failure surface. A table in the figure gives the growth extensions for each cycle (for one notch tip, which presumably were about the same on the other notch tip). Note that the scale of this SEM photo can be obtained by the knowledge of the 0.75 inch length of the EDM notch. The current author estimated the length of the initial sharpening shown in the table. **Tables 3 and 4** list the peak values of the loads (from the DW parametric files) during each of the monitored load cycles and the file names of the waveform files that were provided to the author for analysis of the AE. In some cases there were two data files for different portions of loading due to the DW wave system "locking up" (presumably due to being overloaded by a high event rate or a continuous event). Thus holds were introduced to allow a restart of the DW AE system. Fortunately these holds and possibly lost data occurred at lower load levels where extension of the notch region would be unlikely. Thus the AE data files were labeled by a "Test part" number and the load cycles are listed in the tables. In addition some of the data files were "cleaned up" prior to their transmission to the current author. Thus labels such as "cor" and "v1" were used to indicate such versions. The current author used "v0" to indicated data files in the original form and "vc" (so as to have a constant name length when individual event wave files were imported to a signal analysis package called FAMOS© [product of IMC in Germany]) which provided better visibility of results and allowed comparisons not possible with the DW software. The hydraulic test machine was run in stroke control (constant crosshead rate) during the loading, which resulted in a near constant loading rate of about 100 lbs/s [1] in the region of elastic response (after the initial portion of loading).

Setup of the Digital Wave AE System

Since a data base of AE information was not available for tensile testing of such samples, during the testing of the first sample, 106, a number of changes were made to the gains for both the recording of the waveforms from the six sensors and well as the gains for the threshold of the DW system. The goal here was presumably to determine optimal settings. As a result of the changes with sample 106, the gain settings were nearly constant for the second sample, 107. **Tables 5 and 6** show the gains used for both parts of the AE system. Since the DW system was operated with a constant threshold of ± 0.1 volt, the gain values for the trigger part of the system have been converted to dB_{AE}, which is the accepted approach in ASTM documents to report the threshold. The dB_{AE} value is based on a reference of 1 µV amplitude out of the AE sensor. A low gain for the threshold of the DW systems converts to a high threshold in dB_{AE} (low sensitivity). And a high gain for the threshold converts to a low threshold in dB_{AE} (high sensitivity). In addition, **tables 5 and 6** provide the frequency band information for both the trigger/threshold part and the waveform recording part of the DW system. Additionally, the DW system was setup

to record 8192 points of the signals from each sensor for each event at 5 MHz (0.2 μs between points). Of the 8192 points, 500 points were pre-trigger (i.e. 100 μs of data). Finally the operation of the DW system is such that when the trigger level is exceeded on one channel all the signals are recorded at once.

It is important to bring to the attention of the reader that the thresholds used for nearly all the load cycles were very high relative to typical values used for the AE monitoring of tensile testing of metal samples. In the author's experience, at the University of Denver, Denver, CO and NIST, Boulder, CO the thresholds typically attainable were much lower. This is also the case for tensile testing a various other locations that the author is familiar with. In fact, during the testing of sample 107 the typical threshold used was on the order of 20 dB that is ten times higher than the threshold reported in actual AE monitoring during pressure testing of a full sized LPV as reported in reference 3. Evidently the high threshold values were necessary due to the large amount of extraneous AE noise in the test environment as well as from the test fixturing. Even with the high threshold the analysis of the waveform data showed that noise signals dominated the total number of events recorded. A later section of this report will describe some of the noise characteristics which dominated during the test as well as some proposed approaches to determine the noise sources and possible ways to reduce the noise.

The high level of extraneous AE noise created two problems. First, it limited the dynamic range that could be observed in the AE data from notch-originated events. This was due to the fact of the ± 0.1 volt threshold and the saturation of the waveforms at just above ± 0.5 volts. Thus the dynamic range above the threshold, which was near the continuous noise levels, was only about 14 dB with the original digitized data. Thus, if a notch-based AE signal is saturated at the nearby sensors, then it is not possible to obtain relative attenuation data from the amplitude at more distant sensors. High-pass filtering could improve the dynamic range for future testing (by lowering the noise below the 0.1 volt level), but such filtering also removes the lower frequencies of the flexural mode of real AE signals. This is the mode that may be detectable at larger propagation distances in an actual test of a LPV. Second, the high threshold inhibits the ability to detect or identify signals originating from the notch region in two ways. For AE systems that use arrival times based on first threshold crossing to calculate the location of an event in a sample, the high threshold level means that the initial portion of the AE signal is below the threshold. Thus arrival times at the different sensors are inconsistent (since came from different propagation velocities) leading to false source locations being calculated. Further the high threshold means that some AE signals from the notch region would not be detected leading to a truncated database.

Insight from Analysis of the Load versus Time Data

The AE system recorded the load applied to the test sample (parametric data) at fixed intervals of typically 1 second. As an aside, the AE system did not record the increase in notch length during the test as measured presumable by the crack length measurement equipment. Hence, this report

does not take into account any such data. By converting the load versus time data to text files and then importing the data in the FAMOS© software, it was possible to compare these curves directly for the successive load cycles. **Figures 4 and 5** respectively show the plots of load versus time for the samples 106 and 107. The curves were arranged by changing the start times of the data so that the linear portion of the load versus time superimposed. As these two figures clearly show, the first load cycle for each sample became nonlinear at a much earlier load (compared to the peak load of the cycle) than in the subsequent load cycles. The typical value being a load of less than about 45 kips for each sample. By estimating the width of the notch after initial sharpening (from the SEM photo shown in **figure 3** for sample 107) at 0.82 inches, the net section material at the notch cross-section is about 0.67 in^2. Thus the nominal stress (ignoring the stress concentration) at a 45 kips load was about 60 ksi for the first load cycle and at the first cycle peak load of about 67 kips it is about 100 ksi. Since the yield and tensile strength of the 1146a steel material was given as 75 ksi and 101 ksi respectively in reference 4, it is conceivable that the whole cross-section at the notch region yields and strain hardens as the load increases. This possibility is based on the two actual strengths of the currently tested material being comparable to the values in reference 4. Since as shown in **figure 3** there is a growth of the notch length during this first load cycle, the nominal stress is even higher at the peak load. As a final point relative to the first load cycle, it is worth noting that the first cycle load curves for both samples could be laid directly on top of each other.

For the subsequent load cycles, the non-linearity starts at a load level not too much below the peak load of the previous cycle. This decrease is expected based on the fact of the growth of the notch length by the intervening fatigue cycles to "mark" the sample. Thus the notch length for each subsequent load cycle is longer than it was at the end of the previous one, leading to not reaching near the previous maximum load in a linear fashion. It is proposed that the non-linearity in these subsequent load cycles is in part due to the decrease in the net section at the notch as the notch extends, and it is possibly also indicative of additional strain hardening of the remaining cross-section at the notch section. It can be observed in **figures 4 and 5** that with additional load cycles the slope of the non-linear region progressively begins to exhibit behavior similar to a tensile test of an un-notched sample leading up to the beginning of necking (i.e. the curves are becoming "flatter"). These observations seem to support the possibility that during the first load cycle the whole cross-section at the notch yielded and progressively strain hardened over the significant increase in load starting at the deviation from linearity. Note, the growth of the notch (table in **figure 3**) during this first loading is not so different from that in subsequent load cycles for a much shorter load range of non-linearity. If the observations made here are correct, then the notch growth during later load cycles could be expected to generate more detectable AE since the material is not as ductile (leading to a more brittle failure) due to stronger material at the notch tip leading to a smaller "yield" radius. In future testing, it would be worthwhile to be able to monitor the strain field of the whole region ahead of the notch by a technique such as 3D digital image correlation (DIC). This approach is preferable since it does not involve contact with the sample or attaching by welding a crack length gage to the sample (during loading the

weld region could be a source of AE that seems to originate from the notch due to the proximity of the gage welds).

Procedure Adopted to Identify AE Events Originating from the Notch Region with High Extraneous Noise Being Present Throughout the Recorded AE Signals

The ability in the DW software to set up the screen of a computer monitor to view (in post processing) the waveforms from each event with a specific arrangement was used to organize the waveforms from top to bottom to correspond to the sensors from top to bottom of the test sample. Thus, the recorded waveforms were displayed as a row of two waveforms at the top of the screen from the two top sensors (left to right from front sensor to the back sensor) followed in a similar front to back sensor order by a row of the waveforms of the two sensors nearer the notch (often called the mid sensors in this report) and finally followed by a row of waveforms of the bottom two sensors. Considering the distances of the top and bottom sensors from the notch, the amount of pre-trigger time and the propagation velocities in a steel material, the total time displayed was selected to be 200 μs as ideal to display the waveforms so as to be able to identify signals coming from either the top or bottom grip/load-train regions or from the notch region. It is noted that the full length of the waveforms, 1.6 ms, did not contribute to this process. So in the future the data files could be obtained for a smaller number of waveform samples. So using the described display, by eye one could easily identify signals that originated from any of these three regions. Also, by eye one could identify a set of signals that originated from some other source that did not result in propagation between the rows of sensors, for example electromagnetic pulses. **Figures 6, 7 and 8** respectively show the views from the DW software on the computer monitor for a top grip/load-train source, notch region source and bottom grip/load-train source. These source origin regions are identified first of all by the progressive arrival in time of the signals and also to a lesser degree by the amplitude changes with distance of propagation. For smaller load cycle data files, the events could be viewed one at a time to determine the test sample source region or those not coming from a test sample source region. For larger files the software “Play” feature could be used to automatically go through the file and visually stop at events of notch region origin. In addition it was determined that playing through a data file that was high-pass filtered at 150 kHz or 200 kHz was also useful to recognize by eye notch-based signals. Due to time limits of the funding for this work and the wide variety of noise based events as well as the continuous noise in each signal, it was decided that it would not be productive to try to develop a software filter (and verify confidence in the required complicated filtering scheme based on various aspects in the signals) to identify notch-based events. Further it is expected that future tests will be done after a significant reduction of the extraneous noise so a filtering scheme with the current data would not be of use.

To be able to have a clearer view and do further analysis of the notch-region based signals (and also noise signals) some events from the data files were exported as text files and imported into the FAMOS© software. **Figure 9** (the same data as in **Figure 7**, the notch region source) shows an example, arranged slightly differently. From top to bottom of the figure, the sensor signals are

top front, top back, mid front, mid back, bottom front and bottom back. Several features of interest are illustrated in this figure. First, as can be observed by the **x** or **o** markers the out-of-phase aspect of the lower frequency flexural mode can be observed for the nearly back to back sensors. This result provides assurance that a real AE wave was propagating with Lamb mode characteristics even at the mid sensors which were quite close to the notch tips. Second, approximate arrival time differences can be examined in relation to the difference in propagation distances to the different sensors. Due to the large amount of continuous noise of significant amplitude, these values would only be approximate.

As an example of using arrival times, another notch event from load cycle 4 (at 71.83 kips) was selected. The approach was to obtain the differences of times of signal arrival between two sensors and with the propagation distances differences between these sensors make a rough calculation of the propagation velocities from both notch tips. Then with the calculated velocities determine which notch tip was most likely the one that emitted the event. To try to lessen the effects of the low frequency noise, the signals were high-passed filtered at 200 kHz before obtaining the arrival times as illustrated in **figure 10**. Using these delta time differences and the distance differences from the two different notch tips at the peak of this load cycle, the average velocities are about 0.161 in/μs if a left tip source (sample viewed from the front) and 0.066 in/μs for a right tip source. Comparing these two velocities with the group velocity results shown in **figure 11** at frequencies of 200 kHz and higher, the S0 mode is the best match with the left tip source.

Using the signals in the FAMOS© software, some aspects of the frequency characteristics can be demonstrated as well. **Figure 12** for the notch region source of **figure 9** shows the Fast Fourier Transform (FFT) results for the front sensor near (mid) the notch. In part (a) the FFT calculated using the whole recorded waveform (8192 points) is shown, and in part (b) the FFT was calculated using only the first 1024 points. Clearly the high frequency characteristics of the real AE are more distinctly present above about 340 kHz in part (b), since the continuous extraneous noise is not such a large part of the signal processed. To examine how the frequency characteristics potentially change at sensors further from the source, **figure 13** (for notch region source of **figure 9**) shows the FFT (1024 points) from the top and bottom front sensors as well as the mid front sensor. In the (b) part of the figure, the frequency scale was changed to focus on the region from 340 kHz to 800 kHz. Even with this change, it is not clear how the high frequency content changes from the near source sensors to farther sensors. It is expected that reflections are influencing the frequency content in this size test sample.

It is also potentially possible to determine arrival times by the use of frequency/time analysis with a Choi Williams Distribution calculation [5]. **Figure 14** illustrates the CWD results for three signals from **figure 9 (the three front sensors)**. Since the continuous noise is so strong, the data is shown first (on the left side) with only the original high-pass filtering at 20 kHz and also (on the right side) high-pass filtered at 140 kHz with an 8 pole Butterworth filter so as to eliminate the most intense region of the low frequencies where the continuous noise is prevalent.

The results show that the intense region is near 100 kHz, when no additional filtering was done and over a wide range of frequencies from 200 kHz and above after the 140 kHz filter. In this case the usefulness of the CWD is marginal due to the large amplitude of the low frequency noise and reflections. The CWD results do qualitatively show the arrival time differences between the mid sensor versus the top and bottom sensors by the intense portions (red) in both columns.

More Detailed Examination of Noise Signal Types and Frequency Characteristics

There were several noise signals that appeared in the recorded events that did not show propagation like that for grip/load-train related noise cases as shown earlier. **Figure 15** demonstrates one of these observed noise signals. Here there is a repeated set of noise spikes that arrive at the same time at all the sensors, and they do not show propagation. These signals were quite numerous and resulted in many triggers of the system that contribute to data that is not useful. **Figure 16** illustrates a noise signal that causes the system to trigger multiple times during the testing. In this case the high frequency noise source happens at the same time as a peak in the typical continuous low frequency noise. The superposition of the high frequency noise pulse then causes the signal to penetrate the threshold on one channel and the noise event is triggered.

To characterize the frequency content of the continuous noise a selection was made from sensor channels that were not hit by an electronic noise spike and had no propagating signal. **Figure 17** shows signals and the FFT results of a sampling of these signals from the same two sensors for two events. The potential issue shown by these results is the clouding of low frequency flexural mode results from real notch sources by this predominantly low frequency noise below about 125 kHz. This data illustrates one of the key reasons the threshold had to be set at such a high level. The same data (waveforms and FFT) for the first 1024 points (corresponds to the time period used for most of the examinations in this report) is shown in **figure 18**.

Figure 19 demonstrates two examples, columns (a) and (b), another noise source that at first view looks like a notch source, but in spite of reasonable amplitude at the mid sensors, there is no evidence of the signal arriving at the top and bottom sensors. Since this signal is only present on these two nearly back to back sensors, it is likely a source that occurs directly below these sensors having to do with the couplant adhesive or what appears to be Kapton© adhesive tape below the couplant adhesive (in photographs of **figure 2(b)**) locally de-bonding below one of the sensors due to the plastic deformation beneath the tape. The other possible option for this noise source is the sensor cables from these sensors sliding by each other due to movement during the test and thus generating a frictional source.

The biggest issue with rubbing noise sources that originate from the grip regions is the frequency content possibly being similar to that from the notch sources after some propagation distance. As **figures 20-22** show grip/fixture based noise sources can mimic the frequency content of the notch-based sources. In **figure 20** it takes a practiced eye to distinguish (based on propagation

arrivals at the sensors) the noise event (a) versus the notch event (b). After high-pass filtering at 200 kHz (6 pole Butterworth), the two origins of the sources are much clearer as shown in **figure 21**. But as the FFT results in **figure 22** demonstrate for the mid front sensors for these two events, simple high-pass filtering would not clearly distinguish these events as the noise signal actually has more high frequency signal strength above 200 kHz than the notch signal. This fact potentially complicates approaches to frequency filter data to eliminate non-notch sources.

Numbers of Events from the Notch Region

Due to the non-uniform settings of the gain for the threshold and the gain for the recorded waves for the load cycles of sample 106 as well as time constraints for this analysis, the main focus relative to notch-based AE signals was on sample 107. The two gains (for threshold and the waves) for this sample were much more consistent. **Table 7** shows the approximate number of notch-based events that were determined for the different load cycles applied to sample 107. The number is approximate since the high continuous extraneous noise likely made it not possible to clearly identify some notch-based events. The data in the table shows there were not many notch-based events. Also, that they did not appear until the latter load cycles. Finally, most of these events occurred during load cycle 4, which had the largest notch growth. Not shown by the table is the fact that all of these events occurred in the non-linear region of the load versus time curve and at load levels near the peak load of the cycle.

Figures 23 (a) and (b) and 24 (a) and (b) demonstrate the variety of notch-based events that were observed, all near the peak load of the cycle and at loads in the non-linear region of the load versus time curve. **Figure 23 (a)** illustrates a saturated notch source. **Figure 23 (b)** shows a low frequency notch based source. **Figure 24 (a)** demonstrates a higher frequency notch source. Finally, **figure 24 (b)** shows a notch source with a combination of high and low frequencies. It is important to note that the relative lower frequency portion of the flexural mode varies. Previous finite element modeling in aluminum plates by the author [6] shows that for in-plane dipole sources the relative contribution to the flexural mode amplitude varies as the depth of the source varies. There is a high flexural contribution for sources farther from the plate mid-plane and less for the source near the mid-plane. For real AE data, the amount of flexural signal that is present depends of the sensor frequency response characteristics.

Discussion of a Key Result and Other Aspects not addressed in this Experimental Data

The results shown in **figures 4 and 5** for the first load cycle demonstrate that at relatively low loads (by about 45 kips) relative to the final peak load (at about 67 kips) of that cycle, the load versus time curve deviated from a linear elastic response. In contrast for the subsequent loading cycles, the load versus time curves deviated from linearity at loads much closer to the peak load. The deviation from linearity of these following load curves is related at least in part to the "marker" fatigue cycles between load cycles that reduced the net notch region cross-sectional area. Since the measured extension of the notch tips was of the same order for the first and

subsequent load cycles, the question arises; did the whole specimen cross-section at the notch section yield and significantly strain harden during the long period of non-linearity in the first load cycle? Assuming for the moment that was the case, as the notch extended during subsequent load cycles, the notch extensions may be taking place into progressively strain hardened material rather than into material with the original yield strength. Thus the notch "tip-induced" plastic zone would have a smaller radius leading to higher stress concentrations at the notch tips. The result for AE would be increased likelihood of the generation of detectable AE from the growth process as it would take place at higher stresses in the region of generation of AE. If this was the case in the current experiments, then it is unlikely that the process would be the same for full scale LPV testing with AE monitoring. Since for the full scale testing, an individual shell layer with a fatigue generated flaw would not fully yield and strain harden. Thus the growth of the flaw during a monitored proof test would not be as likely to generate detectable AE. The reason is that the "tip-induced" plastic zone would be larger due to its extension into material with the original yield strength. A larger plastic zone would reduce the tip stress concentration resulting in a more ductile advance of the flaw and thus less likely to release detectable AE. The time period of the release of energy is directly related to amplitude of the resulting AE. A short time period (more brittle energy release) leads to higher amplitudes and vice versa. Since the early load cycles did not result in detectable AE from the notch region while the later load cycles did so, the data (the load cycles when notch-based events were present) from the current experiment tends to support the above ideas.

To move in a direction to resolve this key issue, it is suggested to carry out the following experiments (after resolving the excess extraneous noise in the current experiments). Deform in tension a test sample (that does not have a notch) well into the strain-hardening region (strain measured). Then create the EDM notch and then sharpen the notch by fatigue. Then carry out an AE monitored load cycle. Contrast the results with a repeat (with a non-strain-hardened sample) of the current AE testing (with the excess extraneous noise eliminated) where the sharpening results in a similar notch length as for the strain-hardened sample. If the strain-hardened sample does emit notch-based AE, while the non-strain-hardened sample does not, then the above analysis is supported. It may be useful to do tensile tests to characterize the yield and tensile strength of the base material to decide the strain level that can be developed in the strain-hardened case.

There are three other aspects to consider relative to AE monitored proof testing of real LPVs. First, the question arises, what is the effect of the biaxial stress field on the generation of AE? The current tensile testing only addresses an applied uniaxial stress field.

Second, does the steel material have a brittle inclusion content that may result in AE being generated by inclusion fracture or de-bonding in the notch tip plastic zone? Polishing samples (3D planes) without etching and obtaining micrographs may reveal the presence of inclusions that could generate AE as an alternate more brittle source that could be more easily detected.

Third, due to potential anisotropy of the LPV steel and the fact the current tensile test had the notch plane in the hoop direction rather than in an orientation of the notch in the more highly stressed longitudinal direction (i.e. perpendicular to the hoop stress in the pressure vessel), a question is would this orientation result in more detectable AE? The level of anisotropy of properties in the LPV steel would potentially answer this question.

Conclusions from Analysis

- The excessive extraneous noise resulted in an excess of events not of interest as well as the use of a threshold that is too high and thus makes it hard to detect the events of interest in a metal sample.
- The continuous noise is the most important one to eliminate or reduce as it leads to the need to use a threshold that is some 10 times higher that it should be.
- A future test with a sample strain-hardened prior to notching the sample is most critical to answering the question of the applicability of AE monitoring of real LPVs when it has a fatigue crack in a non-weld region.
- Future testing should address weld region test samples with notches.
- Simply applying a high pass frequency filter to data does not eliminate all extraneous AE events and may in fact eliminate notch-based events. The frequency content of the notch based sources varies.
- The notch-based AE events were most numerous in the later load cycles and always near the maximum load where the load versus time curve has deviated from linearity.
- In the first load cycle both samples showed an early deviation in the load versus time curve at the same load levels.

Recommendations for Subsequent Testing of Tensile Samples to Reduce the Extraneous Noise

Since the amount of background noise in the present tests makes it difficult to fully characterize (in particular the amplitudes) and detect the AE from the notch region, for similar testing and for potential future testing of welded samples, several recommendations are put forward to help to determine the noise sources and, in some cases, methods are presented to mitigate their amplitude.

1. Offset the noisy servo valve from the actuator by placing it on a manifold near the test machine and connect the servo valve outlets by reinforced rubber hoses to the actuator. This technique was discovered and implemented during work at Lawrence Livermore National Lab in the late 1970s. It was later successfully implemented for the same purpose at the University of Denver in the 1980s and at NIST in Boulder, CO in the 1990s.

2. To begin to trace the noise from the loading fixtures and other sources, machine a solid flat sample (with the thicker grip regions to match the final thickness of the sample with backing plates) without a reduced section and without a notch. This sample could be loaded with pinned clevises to loads above that present in proposed experiments. With proper construction of this sample (for example do not create the finished diameter of the loading-pin hole with a drill, but do it carefully with a reamer), it should emit relatively little or no AE, so that any observed AE only comes from the test environment and/or grip regions when monitoring at a threshold of about 32 dB_{AE}. Use the results of this test (loading and unloading as well as load and unload and uninstall the sample and then reinstall and reload again) to find and eliminate as many of the extraneous AE sources as is possible. Reference 7 may provide some ideas of possible noise sources that may be present.
3. After number 2, make a curved sample with the backing plates screwed in place, but without a notch and load to the highest load levels to determine the noise contribution from the fixturing in this setup.
4. Alternative to number 3, go immediately to a curved sample with the backing plates connected as described here. To manufacture this sample use press-fit pins to hold the sample and backing plates together prior to drilling **all at the same time** the large diameter loading pin hole (finished diameter not by drilling, but by reaming) and as required the screw holes through the backing plates and the sample. Again test this sample with no notch. Also, as a procedure before tensile testing preload the stress concentration region of the loading pin-hole region by the procedure (press on the end of the sample/backing plates while the pin is supported on either side) in reference 8. As a variation, examine whether using Teflon sheet material at the interfaces between the backing plates and the sample will help to control the noise that can be generated by these interfaces during loading. This approach may help since it has been observed that a curved sample tends to "flatten" when loaded in tension at NIST, Boulder, when tensile testing of samples taken from a pipe wall. The "flattening" likely induces the potential for rubbing of the interfaces between the backing plates and the test sample.
5. Also, consider final finishing of the hole (diameter just larger than the pin diameter) in the clevis, by reaming and use of new clean pins as surface imperfections and dirt particles lead to extraneous AE events.

Creating a less noisy test environment will allow much better determination of whether the AE from a notch region (be it typical material, welded or heat affected zone material) will be feasible. A primary reason is to have a wider dynamic range. For example, if a sharpened notch AE event from a weld region saturates (due to the high extraneous AE noise and use of a high threshold) the signal at the near sensors then it will not be possible to characterize the attenuation to further sensors. Further, with saturated signals the frequency content of the signals cannot be correctly calculated by an FFT. Note that the gain for the wave recording should be decreased to reduce the potential for saturation.

As already indicated the use of non-contact DIC measurements during the test is potentially a better solution to determine crack advance, as well as, how far beyond the current notch tips the plastic deformation extends. Further the noncontact DIC method is less likely to create potential AE noise events.

References

1. "Multilayer Pressure Vessel tensile coupon test (106-107)".pdf, Contact James Walker at NASA Huntsville, AL.
2. "Layered Pressure Vessel (LPV) Acoustic Emission (AE) Laboratory Test Plan," Matthew Adler, EM20, August 27, 2014.
3. "Cyclic Crack Growth Testing of an A.O. Smith Multilayer Pressure Vessel with Modal Acoustic Emission Monitoring and Data Assessment," Digital Wave Corporation. 13760 East Arapahoe Road, Centennial, Colorado, 80112.
4. Hudson, M.C., Newman, J.C., & Lewis, P.E., An Investigation of Fracture Toughness, Fatigue-crack Growth, Sustained Load Flaw Growth, and Impact Properties of Three Pressure Vessel Steels, NASA Technical Memorandum X-3315, Langley Research Center, December, 1975
5. AGU-Vallen Wavelet software, version R2010.0202, Vallen Systeme GmbH, Icking, Germany (2010). Available at http://www.vallen.de/downloads.
6. "Examination of the Application of a Wavelet Transform to Acoustic Emission Signals: Part 1. Source Identification," M. A. Hamstad, A. O'Gallagher and J. Gary, J. of Acoustic Emission, Vol. 20, 2002, pp.39-61.
7. "Wideband and Narrowband Acoustic Emission Waveforms From Extraneous Sources During Fatigue of Steel Samples," M. A. Hamstad and J. D. McColskey, Journal of Acoustic Emission, Vol. 15 No. 1-4, 1997, pp. 1-18.
8. "Fracture Analysis by Use of Acoustic Emission," H. L. Dunegan, D.O. Harris and C.A. Tatro, Engin. Fract. Mech., vol. 1, p. 105, 1968.

Tables

Table 1 Location of Sensors and Original Notch Tips for Sample 107 (Source E. Madaras)

Sensor no.	x-coordinate, in.	y-coordinate, in.
1	1.35	2.28
2	2.78	-0.47
3	1.1	-2.28
4	1.35	2.1
5	2.65	-0.35
6	1.2	-2.16
Left tip notch	2.125	0
Right tip notch	1.375	0

Table 2 Location of Sensors and Original Notch Tips for Sample 106 (Source E. Madaras)

Sensor no.	x-coordinate, in.	y-coordinate, in.
1	1.25	2.38
2	1	0.5
3	1.27	-2.35
4	1.12	2.35
5	0.9	0.37
6	0.9	-2.35
Left tip notch	2.125	0
Right tip notch	1.375	0

Table 3 Loading Levels and Data File Names (supplied) for Sample 107 (Source E. Madaras)

Load Cycle	Peak load, kips	Data file names
1	69.5	Test part 1 11-5-14 S380-107; Test part 1 11-5-14 S380-107-v1
2	70.9	Test part 2 11-6-14 S380-107; Test part 2 11-6-14 S380-107-v1
3	71.6	Test part 3 11-6-14 S380-107 cor; Test part 3 11-6-14 S380-107-v1 Test part 4 11-6-14 S380-107; Test part 4 11-6-14 S380-107-v1
4	72.3	Test part 5 11-6-14 S380-107; Test part 5 11-6-14 S380-107-v1
5	71.7	Test part 6 11-6-14 S380-107 cor; Test part 6 11-6-14 S380-107-v2 Test part 7 11-6-14 S380-107
6 (to fail)	71.1	Test part 8 11-6-14 S380-107; Test part 8 11-6-14 S380-107-v1

Table 4 Loading Levels and Data File Names (supplied) for Sample 106 (Source E. Madaras)

Load Cycle	Peak load, kips	Data file names
1	68.0	Test part 1 11-4-14 S380-106 cor; Test part 1 11-4-14 S380-106-v1 Test part 2 11-4-14 S380-106 cor
2	69.5	Test part 3 11-5-14 S380-106; Test part 3 11-5-14 S380-106-v1
3	70.8	Test part 4 11-5-14 S380-106 cor Test part 5 11-5-14 S380-106; Test part 5 11-5-14 S380-106-v1
4	72.2	Test part 6 11-5-14 S380-106; Test part 6 11-5-14 S380-106-v1
5 (to fail)	72.7	Test part 7 11-5-14 S380-106; Test part 7 11-5-14 S380-106-v1

Table 5 Thresholds, Gains and Filtering for Sample 107 (Source E. Madaras)

Load Cycle	Part of test	Threshold gain, dB and (dB_{AE})	Threshold filter, kHz	Waves gain, dB	Waves hi-pass filter, kHz
1	1	51 (49)	50 to 750	54	20
2	2	51 (49)	50 to 750	54	20
3	3	51 (49)	50 to 750	54	20
3	4	48 (52)	50 to 750	54	20
4	5	48 (52)	50 to 750	54	20
5	6	48 (52)	50 to 750	54	20
5	7	48 (52)	50 to 750	54	20
6 (to fail)	8	48 (52)	50 to 750	54	20

Table 6 Thresholds, Gains and Filtering for Sample 106 (Source E. Madaras)

Load Cycle	Part of test	Threshold gain, dB and (dB_{AE})	Threshold filter, kHz	Waves gain, dB	Waves hi-pass filter, kHz
1	1	56 (44)	50 to 750	48	20
1	2	44, 50 (56, 50)	50 to 750	36, 42	20
2	3	47, 50 (53, 50)	50 to 750	42	20
3	4	77 (23)	50 to 750	60	20
3	5	77 (23)	50 to 750	60	20
4	6	51 (49)	50 to 750	54	20
5 (to fail)	7	51 (49)	50 to 750	54	20

Table 7 Number of events originating from the notch part 107

Load cycle	Peak load, kips	Notch growth one side, in.	Number of notch events
1	69.5	0.0121	0
2	70.9	0.0077	0
3	71.6	0.0104	2*
4	72.3	0.0241	13
5	71.7	0.0161	3
6	71.1	--------	1**

* One of these was the highest amplitude source event observed in all the analysis, and it saturated at all but one of the six sensors.

** In addition, after the peak load while the sample was pulled to failure several notch events occurred.

Appendix J: Tensile Testing of LPV Material at NIST Boulder

Tensile Testing of LPV Material at NIST Boulder

Final Report

September 2018

By

M.A Hamstad

(Work done at NIST Boulder under contract to PROTIRO, INC

8354 Northfield, Denver, CO, 80238)

Support from J. D. McColskey and T. S. Weeks

National Institute of Standards and Technology (NIST)

Applied Chemical and Materials Division (647)

325 Broadway

Boulder, CO 80305-3328

Contract to NIST from

National Aeronautics and Space Administration

Marshall Space Flight Center

Huntsville, AL 35812

This report presents the results of research based on the following ***edited*** (to correspond to changes as the testing developed, intermediate results were obtained and additional NASA input was received) statements of work/technical approach.

Scope of Work and Technical Approach

Task 1 - Evaluation of loading/gripping methods for suppression of acoustic emission (AE) noise emanating from the grip regions during uniaxial testing.

Two distinctly different loading approaches (clevis grips and hydraulic grips) will be addressed:

- For clevis grip experiments: A pin loading method (as was used before at NASA) with a modification to minimize movement between the specimen and the backing plates by match drilling and adding four press fit pins. In addition, to reduce noise from the loading-pin hole, the final hole diameter will be reamed to match the load pin and clevis hole diameters. NASA will provide samples for this grip-testing effort. Two samples will have Teflon™ sheets inserted between the specimen ends and backup plates to eliminate direct metal to metal contact between the backing plates and the test specimen. One sample will not have Teflon™ inserted between the specimen ends and endplates.

- For hydraulic grip experiments, NASA shall provide an additional sample fabricated as described above, but without Teflon™ sheets.

Each of the relevant acoustic emission sensor/preamps (4 different types, used on vessel 023 test) will be used for each specimen and testing will be conducted on a 220-kip capacity servo-hydraulic fatigue tester with 110-kips capacity hydraulic wedge grips. The machine has an acoustically isolated service manifold to minimize continuous extraneous AE noise from the servo valve. The tensile force will be applied to the sample until macroscopic yielding occurs. The AE system for Tasks 1, 3 and 4 will be setup such that when one channel is triggered all the channels will be simultaneously triggered to capture the digitized signals from each sensor/preamp. In addition, the tensile force at each trigger/hit will be recorded from the parametric input.

Goal: Determination of best specimen grip design and loading method to suppress extraneous noise emanating from the grip regions.

Task 2 - For all four of the "end sensor" types, use pencil lead breaks (PLBs) to make a rough estimate of how much the direct to sensor signals from the crack-tip regions are reinforced by reflections from the side edges of the narrow specimens used in the tensile tests of samples with cracks.

Carry out in-plane PLBs on a series of different 0.25-inch-thick flat steel plates with the following width by length dimensions in inches: 24 by 36, 12 by 36, 6 by 36, 3.5 (width of reduced section of notched samples) by 36. The PLB (on the sample width edges) monopole force will be directed parallel to the 36-in. direction and will be located with offsets from the center line of each sample's width at distances that correspond to the expected locations of the sharpened notch tips in the tensile samples. The four "end sensors" used one at a time, will be located at the planned positions for the actual test specimen, relative to the notch plane and notch tips. The small diameter trigger sensor (PICO) will be located near the sample end and close to the PLBs to provide a correlated time base. The pencil lead breaks (pencil held parallel to the surface of the plates) will be located on the plate width edge about 1/16 inch below the top surface of the plates. Several PLBs waveforms will be averaged for each PLB location and then analyzed for peak amplitudes and frequency content (primary comparisons for the 24 inches versus the 3.5 inches wide sample) for comparison between the sensor/preamp types as a function of the two distances from the pencil break positions and the changing distances to the width-edges of the plates. To attempt to obtain the reflected signals as a function of the changing distance and sensor/preamp type, the averaged waveforms from the largest sample (assumed to have no side edge reflections) will be subtracted from the averaged waveforms of the other samples. This attempt may not work due to deviations in the PLBs.

Goal: Determination of a rough estimate of the potential reinforcement to the peak amplitude at the "end sensors" of AE signals originating from notch tip regions due to reflections from the side edges of the tensile specimen as a function of the different sensor/preamps for the smallest width plate sample (corresponds to the width of the tensile sample reduced section).

Task 3 - Tensile testing of NASA-supplied base-material samples with sharpened cracks will be carried out while monitoring acoustic emission (AE) with a multi-channel AE system and the strain field with Digital Image Correlation (DIC).

Loading will be carried out to 10% above the maximum cycling loads used during the notch sharpening procedure. This approach follows typical AE testing of pressure vessels to 10% above the operating pressure. If tip region events are not detected during the load increment of 10%, then continue loading to the yielding of the full cross-section at the notch plane. The NASA-provided samples will be prepared in the grip regions as per the Task 1 results above and will be EDM notched and sharpened by fatigue at NASA. Two specimens, along with a backup specimen will be provided by NASA, for a total of three base-metal, fatigue-sharpened samples. The peak fatigue loads and number of fatigue cycles used for notch sharpening will be provided along with the samples. Four sensor/preamps (of all the types being used) will be located vertically with their centers at approximately 2.9 inches from the crack tips. Two small diameter PICO sensors will be located very close to the crack tips to provide a convenient way to reduce the amount of extraneous AE data recorded and to possibly provide a means to determine the AE energy release from subcritical crack advance events without edge reflections (base material

versus task 4 with planned crack in the heat affected zone of weld region material). The minimum loads at which notch tip events are detected will be determined for each sensor/preamp. Also, analysis will determine the peak AE signal amplitudes and their frequency content as well as their energy, for events from the notch tip region for each of the sensor/preamp types. The strain field at the crack tip regions will be documented with DIC. If the whole notch section does not yield on the first load cycle, continue loading two or three more similar load cycles (10% overload), with fatigue sharpening between each load cycle. After testing the first sample adjust the test plan.

Goals: Determine if AE events from the base-metal fatigue-sharpened notch are generated before the sample yields at the notch section. Characterize and contrast the minimum loads at which notch tip events are detected by each sensor/preamp. Determine the peak AE amplitudes, frequency content and energy of notch tip AE events as well as the loads at which they occurred for each sensor/preamp type. Since sets of waveforms are gathered from each sensor/preamp simultaneously, the waveform data will provide the amplitudes and signal-to-noise levels for each sensor/preamp for each event. Thus, the effects of different AE thresholds on assumed crack advance detection can easily be examined and compared for each sensor/preamp.

Task 4 - Tensile testing of NASA-supplied samples with sharpened cracks planned for the heat affected zone of a weld will be carried out while monitoring acoustic emission (AE) with a multi-channel AE system and the strain field by Digital Image Correlation (DIC).

Loading of four samples will be carried out to 10% above the maximum loads used during the notch sharpening procedure or to the yielding of the full cross-section at the notch plane. Location of notch relative to planned heat affected zone in the weld region to be determined by NASA in consultation with NIST. The NASA-provided samples will be prepared in the grip regions as per the Task 1 results and will be EDM notched and sharpened by fatigue at NASA. The test procedure, including the possibility of termination of testing due to whole section yielding will be as for Task 3. The data analysis will also be per the process for Task 3.

Goals: Determine if AE events from the fatigue-sharpened notch in the planned heat affected zone are generated before the sample yields at the notch section. Characterize and contrast the minimum loads at which these notch tip events are detected by each sensor/preamp. Also, determine the peak AE amplitudes, frequency content and energy of these notch tip AE events as well as the loads at which they occurred for each sensor/preamp type. Since sets of waveforms are gathered from each sensor/preamp simultaneously, the waveform data will provide the amplitudes and signal-to-noise levels for each sensor/preamp for each event. Thus, the effects of different thresholds on assumed crack advance detection can easily be examined and compared for each sensor/preamp.

Report on Task 1: Evaluation of loading/gripping methods for suppression of AE noise emanating from the grip regions during uniaxial testing.

Introduction

Past tensile testing of steel samples [1, 2] with sharpened cracks in base material were carried out with a relatively high acoustic emission (AE) threshold due to the large amount of extraneous noise that was observed during the loading of the first tensile sample. The resulting high threshold resulted in minimal detection of crack-region AE sources at reasonable overloads (above the prior cycling peak load). This minimal detection was due to the fact that crack region sources do not have large amplitudes when they originate from base material (as will be observed later in this report in Task 3). The extraneous noise in the past work was due to both the test machine and the specimen design. The noise from a typical hydraulic tensile machine emanates from the servo valve mounted on the actuator. This noise is continuous AE that superimposes on the continuous electronic noise that originates in the preamplifier electronics. The extraneous test specimen noise is burst type AE that comes from relative motion in the grip regions of the specimen. Since the test specimen requires backer plates in the grip region outside of the reduced section, the previous design using screws to hold the backer plates on each side of the end sections did not provide sufficient support to minimize the relative motion between the backer plates and the test specimen (results in frictional noise sources). The testing at NIST Boulder was configured to significantly reduce both types of noise sources.

Test Specimens, Test Machine/Grips and AE sensors/system

Several changes (relative to the previous NASA tests) were made to the test specimens for the work at NIST. First, NASA adopted a procedure to roll the plates from the curved material of a layer extracted from the teardown of layered pressure vessel 023 (material A. O. Smith 1146a). This change resulted in flat plates from which the tensile specimens were machined. This change potentially reduced extraneous noise sources, since it has been observed during tensile testing at NIST that samples with curvature perpendicular to the load direction tend to flatten as the load is increased. Such flattening would potentially result in relative motion between the backing plates and the tensile sample that would generate frictional noise. Second, the steel backing plates and the test specimen were match-drilled and then assembled together using four press-fit pins on each end of the grip regions. This “tighter” fit was expected to reduce relative motion between the test specimen and the backing plates. In addition, the large loading pin holes were drilled undersize and then reamed to full size to create a smoother surface and closer fit for the loading pins. Third, some of the tensile samples had a layer of Teflon^{TM} inserted between the backing plates and the test sample. This low friction material was expected to mitigate interfacial friction-based AE noise. All the tensile samples for Task 1 did not have an electrical discharge machined (EDM) notch so no AE was expected to be generated from the reduced section of these test

samples until the whole section began to yield. Figure 1 shows a NASA-supplied drawing of the sample and backing plate regions (note the actual backing plates extended further shown in figure 2). Figure 1 also shows locations of the centers of the positions of the six numbered AE sensors. Figure 2 provides a photo of the tensile samples with and without the Teflon™ layers. This figure also shows the thickness of the specimens, backing plates and Teflon™ layers.

The test machine used at NIST for this work had been configured in the late 1990s with a remote manifold upon which the servo valve was mounted as shown in figure 3. The connection of the servo valve to the actuator was made by wire braided flexible hydraulic hoses. This connection method significantly reduces the continuous AE generated by the servo valve due to attenuation in the hoses. Thus, less noise reached the test specimens and a AE lower threshold could be used during the AE testing. Two different standard types of grips were used for the tests as shown in figure 4. Typical clevis grips provided pin loading for some of the tensile samples and hydraulic wedge grips were used to grip and load the ends of a test sample.

Two categories of AE sensors used. The first category consisted of four different sensor designs (DW modal, Mist modal, WD and R15), which will be referred to as "end sensors" throughout this report. These four sensor types were selected since they duplicated the sensors used in the AE monitored pressure test conducted in September of 2016 with layered pressure vessel 023. The four "end sensors" each had integral preamplifiers with differing gains and filtering. The second category consisted of two sensors (PICO), which will be referred to as "tip sensors" throughout this report, of another design were chosen to act as trigger sensors for crack-tip AE sources. These "tip sensors" were connected to external preamplifiers. The centers of these two sensors were located at about 0.25 inches from where the EDM notch tips would be in the later experiments with cracks. Due to their very small diameter (5 mm) they could be located at such a position, and due to their location near the crack tips the AE waves arriving from tip region sources at these sensors would have high amplitudes since very little geometric spreading of the waves would occur in the propagation from the source to these sensors. Thus, in the case of crack-tip AE sources, the AE system would be triggered with these early arrivals, and the crack tip where the AE originated could easily be determined. The identities of the sensors are shown in table 1 along with other characteristics. Note that the sensor model names and manufactures are provided, not to recommend any of these, but due to the unique frequency response of different AE sensor designs. Figure 5 shows a photo of all six sensors mounted on a dummy test specimen. To consistently mount the sensors as close as possible to the same positions for each test, a template was used.

The six-channel AE system (Vallen AMSY-6) used for all experiments was setup such that when the signal on any channel penetrated the set voltage threshold, all the channels simultaneously triggered to record at 10 MHz all the waveforms (8192 points each with 16 bits) on the same time scale. This setup effectively meant that for the extraneous noise studies in this task, the trigger came from one of the "end sensors" located nearest the ends of the reduced section of the tensile samples, and for the later tasks with cracks, the trigger came from one of the small "tip

sensors" located near the crack tips or from one of the "end sensors" for an extraneous noise source. In addition, the AE system also recorded standard AE parameters (trigger time, peak amplitude, counts, duration, energy and load etc.) for each of the channels where the individual channel set voltage threshold was exceeded. Additional setup conditions of the AE measurement system are given in table 2. Since the different AE sensors and their preamplifiers had different characteristics, the thresholds were altered for the different channels. Comparison of these thresholds with those previously used [1, 2] showed they are significantly lower as was expected due to the isolated servo valve. Also, the AE system uses the gains for each channel to convert all the outputs for each channel to a gain of one. Thus, for example the peak amplitudes are presented as dB_{AE} (referred to 1 μV out of the sensor active element). The above conditions were used throughout all the AE testing of tensile samples, except for the first noise test sample which was used as a pathfinder to determine the best setup conditions for the AE measurement system. In addition, prior to each tensile loading pencil lead breaks (PLBs) were conducted on the test specimen to verify AE system operation, sensor function and proper acoustic coupling of the sensors. It should be noted that the exact output circuitry of the preamps and the input circuitry of the AE measurement system are not revealed by the manufactures. Thus, details of the impedance matching cannot be ascertained other than the standard 50 ohm termination used at the input to the AE measurement system.

Grip Noise Testing Plan/Results

The four "end sensors" were coupled with Apiezon M vacuum grease and were held in place by clamps as shown in figure 6 (Note separate experiments using a pencil lead break source showed the clamping did not change signals compared to a sensor mounted without a clamp on a horizontally oriented dummy specimen). The two "tip sensors" were coupled and held in place by Tacky wax. Again, not to recommend coupling materials, specific names are provided since couplant materials also have unique characteristics and different couplant film thickness. The tensile samples were loaded in displacement control at 0.01 inches/minute to provide a force loading rate of about 100 lb/s. After the pathfinder test, three distinct cases were tested: (i) clevis grips with pin loading of a sample with Teflon™ layers, (ii) clevis grips with pin loading of a sample without Teflon™ layers and (iii) hydraulic wedge grips to load a sample without Teflon™ layers. The wedge grips had serrated faces that made direct contact with the backing plates. The samples were loaded to a few kips above 80 kips, which approached the macroscopic yielding of the samples (measured by NASA for vessel 023 layers at 90 to 92 ksi). The sample stress in the reduced section (3.5 by 0.28 inches or 89 by 7 mm) at 80 kips was 81.6 ksi. These loads were well beyond those used in later tasks with cracks where the maximum loads were 44 to 48 kips (which provided nominal stresses (ignoring the crack) near higher working stresses of LPVs).

Figures 7 and 8 show the peak amplitudes of detected events from the AE sensors (where the voltage signal exceeded the set threshold values for the different channels) versus tensile load for the different load transfer methods and different grip designs. In each figure, a vertical red line

shows the maximum load of 44 kips that was attained for the samples with cracks in base material. The results in figure 7 are for hits with peak amplitudes greater than or equal to 35 dB_{AE} which is near the lowest thresholds used during the test. Figure 8 shows the results for amplitudes greater than or equal to 45 dB_{AE}. This figure, which more clearly shows the noise signal peak amplitudes, was selected since the expectation is that peak amplitudes of crack-based events in the small tensile samples (in Tasks 3 and 4) must be well above the lowest thresholds used to be detectable in full scale layered pressure vessels. There are two primary reasons why large amplitude sources will be necessary for detection in the full scale LPVs. First, the wall thickness of a LPV is considerably thicker (up to 3 inches or more) so more signal energy will be lost in the near field as the waves spread through the greater thickness, and second, the sensors will be further away in the real LPV case so geometric spreading and dispersion will further reduce the wave amplitudes. Note in these two figures, most of the peak amplitude hits come from sensor # 6 since it has the lowest resonant frequency of 150 kHz, and thus, it is expected to be more sensitive to the lower frequencies of grip-noise AE events. Using the arrival sequence in time at the six sensors for the different events, they were all verified to originate in either the top or bottom grip regions. A typical set of waveforms from all six sensors from both a top-grip and bottom-grip noise source are shown in figure 9. Figure 10 shows the corresponding fast Fourier transform (FFT) spectra results for each sensor for both the grip noise sources. Examination of the arrivals of the signals in figure 9 clearly shows the arrival sequence from the top end sensors (# 1 and # 4), to the middle tip sensors (# 2 and # 5) and then to the bottom end sensors (# 3 and # 6) for the top-grip source and the reversed sequence for the bottom-grip source. The FFT results show a dominance of low frequencies except for the PICO sensors (#'s 3 and 5) which have a very strong resonance at about 500 kHz. The FFT results (delta frequency step of 1.2 kHz) were calculated for the signal lengths shown in figure 9.

Based on the results in figures 7 and 8, the choice of a grip design with Teflon^{TM} layers and clevis pin loading is superior to reduce the grip noise. Hence, this specimen design/load transfer was used for all testing in Tasks 3 and 4 for samples with cracks. Reduction of the grip noise has three beneficial effects. First, the thresholds of the AE channels can be set to lower values so more crack-based signals can potentially be obtained. Second, the amount of data to be analyzed is reduced (important relative to the waveform data). Third, there is less likelihood that a grip-noise event will be present when a crack-based source operates.

Task 1 Conclusions

- *The isolated servo valve allowed significantly lower thresholds to be used due to the reduction in the amplitude of continuous noise from this valve.*

- *The combination of clevis/pin loading, Teflon™ interfaces, press-fit pins (for backing plates) and reamed loading pin holes resulted in the generation of a minimal number of grip-based AE signals.*

- *The loading with hydraulic wedge grips or clevis/pins loading without Teflon™ generated more grip noise AE signals.*

Report on Task 2: For all four of the "end sensor" types, use pencil lead breaks (PLBs) to make a rough estimate of how much the direct to sensor signals from the crack-tip regions are reinforced by reflections from the side edges of the narrow specimen used in the tensile tests of samples with cracks.

Introduction

Since AE waves reflect from boundaries of test samples, the question arises as to whether the AE waves from the crack tips in the tensile samples will reflect from the side edges (of 3.5-inch-wide samples in the reduced section) such that the signals at the end sensors will have significantly higher amplitudes due to reinforcement of the direct signals. A previously published paper [3], showed significant amplitude reinforcement (up to 12 dB) with finite element modeled (FEM) results from in-plane buried dipole sources. It should be noted that the sample width in this reference was only 1 inch. Ideally, the current tensile sample case should be examined by FEM modeling with buried dipoles. As an interim method to obtain an estimate, the approach in this task used in-plane PLBs on the edges of plates of different widths with the various "end sensors" located one at time at their typical location relative to the PLB edge and notch tips that represents the notch/crack plane of the tensile samples.

Test Specimens and Test Setup

A series of steel plates of widths of 24, 12, 6 and 3.5 inches were provided by NASA with a thickness of 0.25 inches (similar to the thickness of the tensile samples with cracks). The lengths of the plates were 36 inches to prevent early reflections from the plate end (opposite the end of the PLBs) that would confuse the results. It should be pointed out that the edges of these plates were laser machined so there were some variations that would not be present with normal machined edges. Figure 11 shows a typical setup for both the widest plate and the narrowest plate. In this figure, the edge for the PLBs represents the plane of the planned crack in Tasks 3 and 4. This figure also shows the PLB points (0.3 mm diameter, 2H lead, lead extended about 2 mm) located at the ends of the planned electrical discharge machined (EDM) notch (at "minus" 3/8 inch, the left side and "plus" 3/8 inch, the right side; these distances are relative to the centerline of the sample widths). The figure also shows a single sensor located at the 2.9-inch distance from the plate edge, as it is in a tensile sample relative to the EDM notch. The center of

this sensor is located at 0.75 inches from the center line of the plate width, so again as in the tensile sample. A trigger PICO sensor (to provide time correlation between plates of different sample widths) was located as shown (at 0.25 inches from the edge of the PLBs) to again represent its position on the typical tensile sample. By use of PLBs at the two positions and rotating the four-end sensor types all the cases could be examined. To record signals from the AE sensors during these experiments a waveform recorder was used with digitization at 10 MHz of 12-bit data. All the signals in this task were not corrected for the gain of the preamps. Table 3 shows calculated propagation distances both for the direct distances to the center of the end sensor at the position shown in figure 11 from each of the two PLB points and the reflected distances for the two PLB locations versus the different plate widths. These calculated distances were to the centers of the planned (experimental placement is not perfect) locations of the four end sensors. The PLBs were done at about $1/16^{th}$ inch distance below the top surface of the plates so as to generate some flexural mode. Since it is not physically possible to locate the PLB at an exact repeatable distance below the top surface (as can be done with FEM modeling), variations were expected in the amount of the flexural mode generated as different PLBs were done. It should be noted for each PLB location, there are two reflection paths corresponding to the two plate sides (of the width dimension). Also, in table 3 it can be observed that the differences in the distances of the two reflection paths (shorter and longer) for the minus 3/8-inch position are larger than for the plus 3/8-inch position. Thus, it was expected that it would be possible to more easily distinguish the different reflection arrivals for this case. In contras for the plus position, the two reflections would likely superimpose. Also, it is important to note that for each reflection path there are two distinct wave mode reflections present when considering the two fundamental modes of propagation in a plate. These are one reflection from the extensional wave mode and one reflection from the flexural wave mode. The velocities of the initial arrivals of these modes in steel were taken respectively at 5.42 mm/μs and 3.22 mm/μs. In addition, another complication is the presence of higher modes that can confuse the results depending on the velocity of these modes.

The current “end sensors” do not have a response that is flat with frequency. This may result in reflected wave arrivals with different frequencies and different velocities than the initial arrival of a particular mode. Additionally, and more importantly, they are not point contact sensors. Thus, to check the calculations for the reflection paths a NIST Boulder designed FHWA conical point-contact sensor [4] with near flat response with frequency over a wide frequency range was used. Also, to allow the potential reflections to be identified this verification experiment was done on a 12-inch wide plate so that the reflections would not be present during the direct arrival signal. In addition, to provide the best possible separation of the reflections the PLB was located at the minus 3/8-inch position for the reason pointed out above. Figure 12 (a) with an unfiltered waveform and a 15-kHz high pass waveform (to provide some reduction of the flexural mode amplitude) shows several distinct direct mode arrivals. These direct arrivals are (i) extensional mode, S0, both an initial low frequency part (left red cursor) and later (in time) a higher frequency [labeled “reversal part,” based on the shape of the group velocity curve for this mode];

(ii) flexural mode, A0, (right red cursor); (iii) "mingled" S0 and S2 modes and just a small amount later in time "mingled" S0 and S1 modes. In part (b) of this figure the same two waveforms are shown, but here the four calculated reflection times of the two fundamental modes are marked with red cursors. The calculated times from S0 (reflections from both sides) and A0 (reflections from both sides) are shown to closely match small indications in the signals. In these figures and in other figures in this task report, the cursor positions for reflection arrivals were placed based on the difference in propagation time from the initial direct extensional mode arrival to the calculated reflection arrival time. This approach was determined to be a more accurate approach rather than using differences from arrivals at the PICO sensor. Thus, these results provide a verification of the calculations. In contrast, figure 13 shows for a PLB at the minus 3/8-inch position for the 12-inch wide plate that with the Mist modal sensor (not a point contact sensor and not as flat frequency response as the NIST FHWA sensor) some of these fundamental mode reflections do not as clearly appear at the calculated times.

Results for the End Sensors

The results for the four "end sensors" located as shown in figure 11 relative to both PLB positions (-3/8 and +3/8) and all four plates are presented in two series of four figures. Figures 14 through 17 show the results for the four end sensors for each plate width (respectively 24 in. to 12 in. to 6 in. and 3.5 in.) with typical waveforms and red cursors at the earliest reflection arrival times calculated for the fundamental modes (again for the "end sensors" located as shown in figure 11). These typical waveforms were selected based on waveform shape/features, and they were not based on typical peak amplitudes. Figures 18 through 21 show the typical waveform results for the sequence of end sensors (respectively DW to Mist to WD to R15, located as shown in figure 11) with each figure showing the four plate widths for a single sensor type. In this set of figures, the cursors are arranged on the left at the original extensional mode direct arrival and on the right at the signal peak amplitude for the 24-inch wide plate (its arrival time varies for the different sensors). Several aspects are clear from these two sets of figures. First, the reflected wave arrivals, as expected, move towards the direct arrivals as the plate width decreases. Second, as the plate width decreases, the duration of the signals increases as the reflections merge with the direct signal. This increase in duration is accompanied by an increase in the energy of each signal even though the source has not changed significantly. Third, from figures 18 through 21, an estimate can be made of the time after the initial extensional arrival to the peak amplitude using the 24 inch information. This time interval respectively for minus 3/8th and plus 3/8th is about 8 to 10 μs , 20 to 13 μs, 10 to 17 μs and 16 to 20 μs respectively for the DW, Mist, WD and R15 sensors. These approximate intervals can be compared to the results in tasks 3 and 4 to ascertain if the peak amplitudes are clearly in the region of reflections. Finally, it is not apparent as to how to extract the amplitude increase for the smaller plate widths of 6 inches and 3.5 inches. This aspect is indicated in the set of figures 18 through 21 for the different plate widths by the labels "no effect" on peak amplitude and "potential effect" on peak amplitude. The "potential effect" cases are those where the reflection arrivals are well within the direct signal portion. There are several difficulties in trying to extract the information on

potential amplitude reinforcement. First, there are variations in placement of the sensors as plate width changes. Second, there are variations in the PLB positions both in the in-plane direction (along the plate width) and most important the thickness direction. Third, there are variations in the edge conditions from one plate to the next due to the laser cutting rather than standard machining. Finally, there are variations in the force release magnitude from one PLB to the next. Even though all these are all small variations, they add up and make determination of peak amplitude differences difficult. These variations also interfered with the original plan to attempt to average the complete waveforms and subtract the averaged waveforms for the largest width sample from the averaged waveforms of the other widths. Despite these issues, the average peak-to-peak amplitude differences between the 3.5-inch wide plate relative to the 24-inch wide plate was obtained for five or six PLBs for each sensor type and the two PLB locations. To obtain these averages the peak-to-peak amplitudes were normalized based on a single value of the amplitude of the very first arrival of the direct extensional wave. This arrival was verified to not be influenced by reflections even for the smallest width plate. This normalization removed nearly all the variation in the magnitude of the PLB force release. Table 4 provides the results from this analysis. The largest reinforcement is on the order of 4 to 5 dB. To provide some perspective, in ASTM standard, E2661, the results from different sensors/channels are required to be within ± 4 dB of the average of all the channels in a multi-channel test. Thus, it appears that the potential reinforcement is not significantly above what is the case with a ASTM-based AE test with multiple AE sensors of the same type. Also, it should be pointed out again that the monopole PLB source is different from a buried dipole source, which itself is only a representation of a real crack-advance of a full thickness crack source advance. In retrospect, it seems that a finite element modeling approach would provide the clearest results since all locations (sensor and PLB point) can be precisely located and the PLB force is constant, but even this approach is not perfect as it is not easy to model the different sensor types. Considering the small potential reinforcement, it seems that it would not be worthwhile to do a FEM study at this time.

The effect of edge reflections on the FFT results of the signals were also examined for each end sensor and the 3.5-inch plate case was compared to the 24-inch plate for the plus and minus PLB points. Figures 22 through 25 show the FFT differences respectively for the DW, Mist, WD and R15 sensors. To make this comparison, a shorter segment of the waveforms was used based on the desire to not include reflections in the 24-inch plate, which was used as a reference case. Thus, the actual signal segment for each case was typically the first 90 μs of signal for both the 3.5-inch and 24-inch wide plates. The FFT results for the 3.5-inch wide plate exhibit a more complicated spectrum than the 24-inch wide plate. The largest changes are for the non-resonant DW and Mist sensors where the FFT becomes much more complicated.

Task 2 Conclusions

Calculated reflection distances were verified using a point contact near-flat-with-frequency sensor and a 12-inch wide plate. Such verification was not as clear with a modal sensor that is not a point contact and is not as flat response with frequency.

Cursors placed in the signals for the various plate widths show in the case of the 6-inch and 3.5-inch plates that reflections do arrive within the direct signals.

Based on the PLB results of peak-to-peak amplitudes for the 3.5 inch versus 24 inch plate widths, the reinforcement in the peak signal amplitude at the end sensors in the tensile tests with cracks could be up to about 4 to 5 dB.

This difference in peak to peak amplitudes due to reinforcement is slightly above the range for allowed differences between same type sensors per ASTM requirements for multi-sensor AE tests.

The results from FFT analysis of the minimum plate width signals versus the maximum plate width signals show the reflections result in more complicated spectra due to reflections arriving within the direct signal. This is particularly the case with the modal sensors.

A more exact analysis of reflections can be made with finite element analysis, but the current results indicate that this may not be necessary.

Report on Task 3: Tensile testing of NASA-supplied base-material samples with sharpened cracks will be carried out while monitoring acoustic emission (AE) with a multi-channel AE system and the strain field with Digital Image Correlation (DIC).

Introduction

The current potential application of AE to layered pressure vessel (LPV) testing is to detect and locate growing cracks. There are four reasons why the AE signals from growing cracks will need to have a sufficiently large magnitude. First, since the thickness of the layered pressure vessel

can be a large as 3 inches or more, the energy emitted in the form of acoustic waves from a crack advance will spread over this thickness in the immediate region of the source. Thus, the wave amplitude that starts to travel to the sensors is reduced. Second, the traveling waves will lose additional amplitude due to geometric spreading as the waves travel to the sensors. Third, as the waves travel they will experience dispersion with the attendant reduction in amplitude. Finally, it is to be expected that the layered structure of the vessel walls will add additional attenuation as compared to a monolithic vessel wall. These four effects will result in lower wave amplitudes that reach the AE sensors. Thus, the level of acoustic energy release from sub-critical crack advances in the current relatively thin specimens (0.28 inches nominal thickness) will need to be large enough so that the waves can be detected with sufficient signal-to-noise ratio at reasonable propagation distances from the source.

A key purpose of this task is to determine the numbers of tip events and more importantly the amplitudes of the AE signals from sources at crack tip regions when the crack is in base steel material. This task contrasts with Task 4 where the crack is planned to be in the heat affected zone of the weld region. In addition, this task will examine the relative peak amplitudes, FFT spectra, as well as signal-to-noise information for the detected AE signals at the four different "end sensors" that were used in the full-scale pressure test of vessel 023. This data will be distinctively different from that examined to date from the full-scale test in that the AE signals from crack-tip events from the same individual events will be compared at the four different "end sensors" located at approximately the same distance from the sources.

Specimens/Test Plan

A total of three tensile specimens were provided for this task by NASA (labeled as "shakedown", AE final 1 and AE final 2). The plates (material A.O. Smith 1146a) for these samples (typical thickness of 0.280 in.) were obtained by rolling to flatten material taken from vessel 023. The axial direction of these samples was in the original rolling direction of the plates. These specimens were prepared with the Teflon^{TM} layer design along with a center EDM notch (length of 0.75 inches) that had been sharpened by fatigue cycling. The fatigue cycling was started with a maximum load of 20 kips and then the load was shed down to 16 kips at the end of cycling. All the cycling was conducted with a load ratio R = 0.1. Table 5 shows the measured crack growth on the two faces of the reduced section at the two different tips. Note that tips A and B were on one side and C and D were on the opposite side. Also, A and D were for the same tip and B and C were from the same tip. The AE sensors were mounted on the side with A and B tips and the DIC speckle pattern was on the opposite side. The "shakedown" sample provided an opportunity to develop the testing plan for the two AE final samples. For all the tensile samples, the test machine was operated in load control to simulate the typical loading during a pressure test of a LPV. The testing approach followed the established ASTM procedure E1419 where the sample is loaded to 10% above the prior cycling/operating level while recording the AE. To examine the potential effect of different crack lengths after the initial 10% overload was applied, the samples were cycled to sharpen and grow the crack at the level of the 10% overload. This cycling also

serves as a mark to later determine the potential crack growth during the overload. Then the process was repeated, but in this case the sample was loaded well beyond a new 10% overload to reach high tensile stresses that might be the case for some LPV applications. This approach was based on results from the "shakedown" sample that did not show a significant increase in crack tip region source amplitudes at this much higher load level. For this larger overload, only the 10% overload (above the sharpening level) was the focus of the primary AE analysis. Followings this test additional cycling was done to mark, extend the crack and sharpen it. Then a final added 10% overload was applied with AE monitoring. After this loading, additional cycling was done to mark the end of the potential crack extension during the final 10% overload. The samples were sent back to NASA to break apart and determine from the crack surfaces the history of crack tip positions during the stages of tensile testing. The details of the loadings, cycling and some expected cyclic crack growth increments for each sample are given in table 6.

Instrumentation/AE/DIC

The same set of AE "end sensors" (positioned at the same locations relative to the crack plane) and AE measurement system with the same settings was used as in Task 1. In addition, a 3D digital imaging correlation (DIC) system was used to capture the strain field in the crack tip regions as a function of the applied loads. The DIC system cameras were focused on the opposite face from the mounted sensors on the 3.5-inch-wide reduced section of the sample. This face had been prepared with white paint where a speckle pattern was applied. Prior to each tensile loading the DIC instrument was calibrated. In addition both before and after each AE monitored load cycle, PLBs were conducted on each test specimen to verify proper sensor operation and acoustic coupling. Figure 26 (a) and (b) shows photos of both faces of an installed tensile specimen.

Results

Since the PICO sensors were located very close to the crack tips, the acoustic waves arrive there first from crack tip region sources. Thus, first arrivals in time at these sensors were used to identify events that originated from the crack tip regions. Figure 27 shows the peak amplitudes from the PICO sensor nearest the emitting crack tip as a function of load (applied in load control at 25 lb/s) for the 10% overload to 17.6 kips for AE final 1 (left side) and 2 (right side). The range of loads used was from 90% to 110% of the cyclic peak loads. The choice to use the peak amplitudes from these sensors was made due to the fact they are very close to the crack tips and far enough for the sample edges so that reflections from these edges do not impact the values of the peak amplitudes. Thus, this data will also provide a database to compare with similar data without potential reinforcement effects when the samples with cracks in the weld region are tested in Task 4. In addition, as will be shown later, the peak amplitudes of the PICO sensor(s) were typically above those from the end sensors. As the horizontal red cursors in these figures show most of the events had peak amplitudes below 50 dB_{AE}. Also, the total number of tip region events (sum for both tips) was respectively 22 and 27 for AE final 1 and AE final 2. Similar results for 10% overloads to 19.36 kips and 44 kips are shown in figures 28 and 29 respectively. Figures 27, 28 and 29 show that within each 10% overload the peak amplitudes did

not progressively increase as the load increased. Thus, the detectability by the different sensor/preamps will depend on their signal-to-noise (S/N) ratio and not the load level. Clearly, as the load levels of the 10% overload load range increased in magnitude (to 16.6, to 19.36, to 44 kips), the number of tip region events increased and the crack lengths were longer after sharpening, but the typical peak amplitudes did not substantially increase. When the average number of tip events per ksi of load increase was calculated, that number was more similar over the different overload ranges. A summary of the total numbers of tip region events and total number greater than 50 dB_{AE} are given in table 7 (also includes some results from the shakedown sample for comparison). For AE final 1 and final 2 for the load range beyond 110% after the cycling at17.6 kips the numbers of tip events with peak amplitude greater than 50 dB_{AE} was respectively 7 and 34 events. These numbers contrast with 0 and 7 respectively for AE final 1 and 2 for the 90% to 110% for all three loadings. Thus the number of higher amplitude tip events also differs between these two samples.

Without some extensive research beyond the scope of this work the specific source type(s) of the observed AE from the crack tip regions cannot be identified. A list of possible source types includes:

1. Fracture of inclusions/precipitates particles
2. Separation of boundaries of inclusions/precipitates
3. Micro-crack growth of the existing crack
4. Grain boundary separation
5. Void nucleation
6. Dislocation motion/slip lines
7. Failure of “bridge” between voids
8. Possibly from crack face interaction if strong stick-slip behavior. Typically, this behavior does not generate higher frequencies.

Since for the 10% overloads the range of peak amplitudes from the PICO sensors for tip region events varied from 34 dB_{AE} up to 64 dB_{AE} (a total of 30 dB or a factor of 31.6), it may be that the sources were due to changes in the size of particles that fractured rather than this wide range of crack increment advances.

To begin to characterize the differences between the four “end sensors” a series of four figures 30 through 33 are provided as a function of increasing signal amplitude as measured by the PICO sensor (# 5) nearest the originating crack tip region. These figures show the waveforms (low pass filtered at 800 kHz and corrected to remove the gains of the preamplifiers) of all the sensors from individual events for a signal length from 85 μs to 155 μs (from before the initial wave arrival to show approximate signal-to-noise (S/N) through a portion of the direct arrival signal duration without a large portion of the extended arrivals due to reflections). The peak amplitudes of each sensor are shown as well in each of these four figures. In each case, the fast Fourier transform (FFT) is also presented for each signal shown. The FFT results were calculated by extending

with zeros so the delta frequency increment was 9.8 kHz. Figure 30 is for an event with low peak amplitude of 37.6 dB_{AE} (measured from sensor # 5) from AE final 1 at a load of 16.58 kips during loading to 10% above the cycling load of 16 kips. Figure 31 is for a higher amplitude event of 44.7 dB_{AE} at sensor # 5. This event was obtained from AE final 1 at 39.25 kips on the loading well above the load cycling at 17.6 kips. Figure 32 is for an even higher amplitude event of 54.9 dB_{AE} at sensor # 5. This event is from AE final 1 at 39.25 kips during loading that also was well above cycling load of 17.6 kips. Finally, figure 33 is for the highest amplitude event at 68.4 dB_{AE} at sensor # 5 from AE 2 at 38.60 kips during loading also well above the cycling load of 17.6 kips. These figures show many significant aspects. First, the signal arrival sequence is clearly first at PICO # 5, then shortly after at PICO # 2 (note PICO # 2 was found to have a lower sensitivity than PICO # 5 during PLB testing) and finally at the "end sensors" all at nearly the same time. Second, in the case of the lower amplitude events the S/N ratio was such that the initial extensional mode arrivals could not be clearly observed at sensor # 1 and just barely at sensor # 3. In such low S/N cases the tip event would likely not be detected when the PICO sensor signals are not present to identify that a tip region event has occurred. Thus, these sensors require a higher amplitude source event for detection than the other two end sensors (resonant type) even though the peak amplitudes are similar in magnitude. Third, the FFT results mirror the resonant frequencies of the resonant sensors (#'s 2, 5, 6 with single resonances and # 4 with at least two resonance regions). Fourth, the two modal sensors demonstrate the presence of higher frequencies above about 300 kHz to about 700 or 800 kHz (present for the higher amplitude event). Fifth, the FFT results for the crack tip region source of figure 32 clearly show the higher frequencies present when the FFT data is compared in figure 34 for a lower grip noise (steel grips without Teflon^{TM}) AE source. Sixth, the PICO # 5 sensor (near the emitting tip region) has peak amplitudes above all the end sensors, except in one case (figure 31) where it is lower by only about one dB. The frequency FFT results from tip events are compared further in figure 35 for the modal sensors (DW # 1 and Mist # 3) as a function of four increasing PICO peak amplitudes (37.6 dB_{AE} to 68.4 dB_{AE}). The same comparison for the resonant sensors (WD #4 and R15 # 6) is shown in figure 36. Both these figures further illustrate both the resonant characteristics as well as the higher frequencies in the modal sensor results. The WD sensor shows differences for the four events relative to the intensity of the low frequency region from 100 to 300 kHz and the high frequency region greater than 500 kHz. The cases where the low frequency region is more intense are likely due to a source that generates more flexural mode. In the modal sensor results, it is also apparent that the DW sensor loses this characteristic frequency pattern when the S/N ratio is low (for example when the peak PICO amplitude was 36.5 dB_{AE}) where the background noise dominates. Thus, this sensor/preamp requires a higher amplitude source to be able to detect the signal. A final observation from figures 30 – 33 relates to the time increment from the first extensional arrival to the peak amplitude. This time increment varies from values near the increments pointed out in task 2 to larger values. In the cases with larger values, the peak amplitude is not much larger than earlier times in the signals, except for the R15 sensor.

The data obtained in these experiments also can provide information to quantitatively study the AE detection capabilities of the four different end sensors, but the process to do this in a quantitative fashion is not straightforward. First, due to wave reflections that superimpose in a relatively random fashion for the different end sensors with their differing frequency response characteristics, the peak amplitudes from these sensors for the different source events are not representative of the real source strength for these tip region AE sources. Second, the background noise (typically from the preamplifier electrical components) varies for the different preamps in the sensors. Table 8 characterizes the variation of the root mean square (RMS) voltage values observed during these cracked sample tests. The data in this table represents the RMS over a signal length of about 40 ms. The data summarized in this table also showed some variation (due to unknown causes) from the equivalent data during the grip-noise testing as indicated in the table. Due to the above reasons, a different approach (rather than simply peak amplitudes) was taken to characterize the S/N behavior of the four end sensors. This alternative approach evaluated S/N by a ratio (A/B) of two "energy" increments as illustrated in figure 37. The "energy" for this analysis was obtained by the integral of the square of the sensor voltage for a signal interval from 0 to 150 μs, where the first approximately 110 μs of data came from the region before the arrival of the tip event AE signal (background noise region) and the second approximately 40 μs came from a portion at the beginning of the tip event AE signal. The result is that a large ratio indicates an excellent S/N ratio relative to detection of the AE signal. The results of this approach for the four different sensors are shown in table 9 as a function of the event peak amplitude from PICO # 5 sensor, which was nearest the emitting tip region. For a given event measured amplitude (at PICO # 5) the table shows the ratio increasing from DW to Mist to WD to R15 sensors. As expected, the ratio for a given sensor tends to increase as the source event increases, but for the two resonant sensors the increase is not steady. This may be a result of the frequency characteristics of these resonant sensors as compared to the frequency characteristics of the particular source events. Also it is clear, that the ratio is not a consistent pattern relative to the differences between sensors for the different tip region events, but in general, the ratio is considerably larger for the resonant sensors.

Since PLBs have long been used in AE experimental work to demonstrate the ability to locate AE sources as well as to determine appropriate spacing of sensors in an array on a test object, it is of interest to compare PLB signal amplitudes in these experiments versus the crack tip region AE signal amplitudes. Figure 38 shows a photo of the PLB location chosen for in-plane lead breaks (0.3 mm, 2H with extended length of about 3 mm (0.12 inches)). The lead was broken very close to the mid-plane of the tensile sample thickness. This figure includes a table of the typical average PLB amplitude in dB_{AE} for each of the six sensors. In summary, the average amplitude varied from 76 to 83 dB_{AE} (ignoring PICO # 2, which was not as sensitive as PICO # 5). For the crack tip region AE events in the current experiments with the crack in the base material, figure 39 shows the PICO maximum peak amplitude events along with peak amplitudes

of all the end sensors for that event for the loadings of 10% above the cycling levels of 16 kips, 17.6 kips and 40 kips are all well below the PLB amplitudes. This result is the case, even with the in-plane loading used for these PLBs (does not generate the high amplitude flexural mode to the same degree at an out-of-plane loading). To provide a statistical sample of peak amplitudes of the four end sensors versus the peak amplitude of PICO # 5, a total of 42 higher amplitude events as measured by PICO # 5 sensor (varied from 41.2 to 70.6 dB_{AE} with an average value of 51.3 dB_{AE}) were examined. These events included some events beyond the 10% overload levels. In figure 40 the results are presented for the PICO sensor amplitude after the amplitude of each end sensor had been subtracted. Clearly the PICO # 5 sensor peak amplitudes generally exceed the amplitudes of the end sensors when the averages are considered. The maximum amount it exceeds can be quite large up to 15 dB in the case of the R15 sensor, but even the other end sensors can be lower than the PICO sensor by a significant amount. Based on the averages the PICO sensor exceeds respectively by 5.4, 2.7, 6.3 and 7.9 dB for the DW, Mist, WD and R15 sensors. These lower amplitudes of the end sensors, despite some possible small reinforcement from side-edge reflections) are due to geometric spreading and dispersion.

The DIC results were used to verify the similarity of the concentrated strain field at the two crack tips, to document the increase in size of this field at higher load levels and to show the shape of this field versus that expected from analytical calculations. Figure 41 for both AE final 1 and 2 at a load of 17.6 kips shows the similarity and the shape of the concentrated strain fields are as expected. Figure 42 for both AE final 1 and 2 at 40 kips shows how the region of high strain intensity increases at this higher load (note same intensity scale as figure 41) and that the tip regions are similar for both tips of a sample as well as the two different samples at this load.

Task 3 Conclusions

- *During the 10% overloads, the peak amplitudes of the PICO sensor signals (no reinforcement from specimen edge reflections) from tip region sources were typically less than 50 dB_{AE}, with only seven events having peak amplitudes ≥ 50 dB_{AE}.*

- *The range of the peak amplitudes measured from tip region events did not increase progressively as the load increased within each 10% overload. Thus detection of tip region events did not depend on the load/stress level, instead it depends on the S/N ratio of the different sensor/preamps.*

- *Further, as the load range for the 10% overloads increased to higher loads the range of peak amplitudes did not increase.*

- *When the 10% overload took place at higher loads, the number of tip region events increased.*

- *In all the various measures of numbers of tip region events, the AE final 2 sample was more active than AE final 1. This result indicates there were some significant differences in the plate regions that the tensile samples were extracted from.*

- *The PICO # 5 sensor signals peak amplitudes from tip events were found to be both typically and statistically higher than those of the end sensors, which were reduced due to geometric spreading and dispersion.*

- *Spectra results for tip events demonstrated higher frequencies in the two modal sensor signals with values well over 300 kHz. Further, the spectra mirrored the resonant or non-resonant characteristics of the sensors.*

- *A signal-to-noise (S/N) examination using an "energy" approach demonstrated that the resonant sensors had a significantly larger S/N ratio than the two modal sensors for tip region AE signals. Also, one modal sensor was significantly better than the other. Further, from only a detection point of view, rather than also source identity, the resonant sensors were superior.*

- *Grip noise spectra, with modal sensor signals, were shown to be lower frequency with the dominant peak frequency typically less than 200 kHz compared to spectra from tip region events with dominant frequencies well above 300 kHz.*

- *The peak amplitudes of PLBs (range of 76 to 83 dB_{AE}) conducted on the tensile samples were well above the peak amplitudes (only seven events with range 50 to 64 dB_{AE}) measured from crack tip region events for the 10% overloads.*

- *DIC results demonstrated the expected shapes of the high strain intensity at the crack tips and that the shape was of similar size and shape at the two crack tips for each tensile specimen.*

- *The size of the region of high DIC intensity at the crack tips increased as the load/stress increased.*

Report on Task 4: Tensile testing of NASA-supplied samples with sharpened cracks planned for the heat affected zone of a weld will be carried out while monitoring acoustic emission (AE) with a multi-channel AE system and the strain field by Digital Image Correlation (DIC).

Introduction

Since, as was expected, the cracks in base material did not emit large amplitude AE signals due to the ductility of the material and large fracture toughness [5], Task 4 involved tensile samples with the fatigue-sharpened cracks planned for the heat affected portion of the weld region material. It was expected that this material would be more brittle, and thus it would more likely emit higher amplitude AE signals compared to base material cracks. Such higher amplitude events may be detected in the full thickness material at reasonable propagation distances to the AE sensors.

Testing/Samples

Four tensile samples were received from NASA with sharpened fatigue cracks planned for the heat affected zone of the welds. For convenience, until the actual locations of these cracks with respect to the heat affected zone can be verified by posttest examination, all the cracks in this task will be referred to as "weld region cracks" and the samples will be referred to as "weld region" or "weld material samples." All the conditions for the specimen design were the same as for Tasks 1 and 3 with one exception. Rather than rolling to flatten the samples, the samples were machined flat out of the 15/16 -inch inner layer of vessel 023 (tested September 2016). The resulting thickness of the different samples in the reduced section varied from 0.251 to 0.255 inches. Figure 43 shows photos of the specimens. On the right side of this figure, at the very edge region of the grip region (on the side where the sensors would be installed) the original outer portion of the layer could be observed. The location of this did not have any impact on the testing and results. In contrast to the base material cracked samples, the axial direction of the 1146a material specimens was transverse to the rolling direction of the original plates. It should be noted that the inner layer had been stress relieved after welding during the vessel fabrication

at a temperature of 1150 ^{0}F. Since these samples had cracks in the weld region contrary to those in Task 3 in base material, and they had been sharpened at lower peak loads in fatigue at 5 or 8 kips (versus 16 kips for the base material case), one sample (C1_1_4) was chosen to use as a "pathfinder" for the weld samples to gain experience as to both the AE generation and fatigue crack growth characteristics at different load levels. All the conditions for the instrumentation (AE and DIC), instrument settings, sensor positioning, sensor clamping, pencil lead breaks before and after each loading (to verify proper coupling and operation of the AE equipment) were the same as for Tasks 1 and 3 with two minor exceptions. First, after the initial loading cycle of the "pathfinder", the PICO sensor # 2 was replaced by one with sensitivity closer to that of PICO sensor # 5. Second, the threshold was adjusted to a slightly higher value (42.6 versus 40.6 dB_{AE}) for the DW # 1 channel to reduce triggers from that channel from background electrical noise spikes. In the case of the pathfinder, the loading rate in load control varied from 5 lb/s for the lowest peak loads to 30 lb/s for the highest peak loads. After the data from the pathfinder had been analyzed, all subsequent loadings were done at a fixed rate of 20 lb/s to minimize potential superposition of events and still have a reasonable test duration. Table 10 provides the measured final growth of the crack tips on both faces for the four samples during the fatigue cycling at NASA. Note that tips A and B were on the same side and C and D were on the opposite side. Also, A and D were for the same tip and so were B and C. As before in Task 3, the AE sensors were mounted on the side with A and B labeled tips. The cycling at NASA was started at either 11 or 12 kips (R = 0.1) and then stepped down as tip growth proceeded. Table 10 also shows the final peak load for each sample during the cycling as well as the total number of cycles completed at NASA. The test plan varied for the other three samples due to different perspectives on AE generation from subcritical crack growth. The two main perspectives were fatiguing at the peak load of the previous AE monitored load cycle and fatiguing at lower loads than the previous load cycle peak load. For one case, sample C4_2_2, this meant fatiguing at one half the previous load cycle peak.

Results Weld Samples

During testing the root mean square (RMS) voltage of the background noise was checked to compare with the same information measured during the cracked base material studies in Task 3. The results are shown in table 11. The results were essentially the same as before. In this table, the dB difference (with reference to the R15 sensor/preamp with the lowest background noise) for the weld sample tests of the electronic noise level has been added as well as the threshold levels selected. The highest noise levels are for the modal sensors, as expected due to the larger frequency range of sensitivity. The noise increase for these sensors is 11 dB and 18 dB for the Mist and DW respectively. There is not a direct transfer from RMS noise levels to threshold settings as the amplitude distribution of the background electronic noise is a part of what leads to the selection of threshold settings. This noise amplitude distribution is beyond the scope of this work. As was done with the base material work in Task 3, the arrival sequence was used to determine which recorded events originated from the crack tip regions and which originated

from the grip regions. Figures 44 and 45 respectively for a crack tip region source near PICO # 5 and a bottom grip region source show how this sequence of arrivals appears on the waveforms taken with the pool triggering (all channel waveforms taken when the threshold is exceeded on one channel). In these figures, vertical red lines mark the trigger time. Since the loading and cycling varied for each of the four samples, the results and specific test loading history are examined individually below.

Table 12 shows the loadings, number of cycles between loadings, crack extensions for tips A and B (due to the DIC speckled pattern it was not possible to make measurements for tips C and D) as well as the AE tip region events for the "pathfinder" sample C1_1_4. The statistics of numbers of tip region events were divided into three load regions for all four samples. These divisions were made when it became clear that the load regions with significant numbers of tip events in the weld samples differed from than in the base material samples. First, the number of tip events detected at loads less than 90% of the just prior cycling peak load. Second, the number of tip events detected at loads between 90% and 110% (sometimes referred to as plus 10%) of the previous peak cycling load. Third, the number of tip events beyond 110% (beyond plus 10%) of the previous cycling peak load. This table also shows the number of tip events with peak amplitudes (all peak amplitudes refer to the nearest PICO sensor to the emitting tip region, which as has been pointed out before is typically higher than the amplitudes at the end sensors and its amplitude is not impacted by reflections) less than 40 dB_{AE} and $\geq$ 50 dB_{AE}. As can be observed in the table, almost no tip region events were detected in all three load ranges for the loadings to 5.5, 12, 13.2 and 24 kips. After the cycling at 24 kips peak load for 10,000 cycles, the subsequent three loadings to 26.4, 32 and 40 kips resulted in more tip region events being detected. This situation may have been, in part, a result of the large growth (grew faster than anticipated) during the 10,000 cycles (all cycling at NIST for the weld samples was done at R = 0.1) at 24 kips peak, which led to the total extensions at tips A and B respectively to be 0.389 in and 0.388 in. For the three highest peak loadings for the three load regions described above, the largest number of tip region events (55 of 92) was detected at loads below the 90% value of the previous cycling peak (see blue background). Considering all the detected tip events of all the loadings for this sample, nearly 50% had peak amplitudes of less than 40 dB_{AE}. On the other hand, 12 of the total of 92 events had amplitudes $\geq$ 50 dB_{AE} and all but three of these events were in the load region < 90%. As will be discussed later, tip region sources that result in peak PICO amplitudes $\geq$ 50 dB_{AE} typically provide the most reliable frequency spectra at good signal-to-noise (S/N) ratios to characterize the frequency properties of the tip region sources using the waveforms from the two modal sensors.

Table 13 shows the same categories of information for sample C1_1_2. The selection of cycling loads differed for this sample as the cycling loads were chosen to be significantly lower than the peak load of the previous load cycle. For this sample most of the tip events, about 79%, came from the loads beyond 110% of the previous cycling peak load (see blue background). As with the previous sample, a large number (about 62%) of the tip region events had peak amplitudes of

less than 40 dB_{AE}. It is also important to note that no tip events were detected in the range from 90% to 110%, which is a key region for AE testing of pressure vessels, since loading of pressure vessels during proof tests with AE monitoring is typically limited to 10% above the previous levels of operation of the vessel. For this sample only 3 tip region events had peak amplitudes ≥ 50 dB_{AE}. There was one issue that slightly complicated the analysis of the data from the loading to 24 kips (after the NASA cycling at 5 kips peak load) of this sample. During this loading about 270 extraneous events were detected on either PICO # 2 or PICO # 5 between 6.28 kips to 6.38 kips. These events were identified as extraneous since each did not propagate to the adjacent PICO senor or to any of the end sensors. Figure 46 shows examples of these events hitting one of the PICO sensors but not the adjacent one. In this figure above the red line, the two PICO waveforms and FFT results are shown for an event recorded only on PICO #2 channel. Below the red line, similar results are illustrated for an event only recorded on PKICO # 5. Most of these events hit PICO # 2 and had higher amplitudes on that channel, and they had low frequency peaks (less than 100 kHz as shown in figure 46) on the spectra of the hit PICO channel. The events occurred over a period of about 4 seconds, at an average rate of about one event every 4 milliseconds. This rate was well within the capabilities of the AE recording system, and thus it is expected that no crack tip events were missed. Since similar PICO waveforms were generated by sliding the cable from the PICO sensor to the preamp against the clevis (in a separate experiment), it is speculated that the very thin sensor cables of the PICO sensors came in contact with the clevis grips during this short time period. It is suggested that the sensor cables can act as waveguides. As a precaution, for the subsequent testing these cables were taped so they would not slide during testing.

Table 14 shows the same categories of information for sample C4_2_4. The loading and cycling schedule for this sample was chosen differently to better model typical field AE testing of pressure vessels. Thus, the cycling peak loads at NIST were done at the previously AE monitored peak loads, which were 16, 32 and 42 kips. For this sample most of the tip region AE events were detected at loads beyond 110% of the previous cycling load (see blue background) similar to the previous sample C1_1_2. The second most active load region of tip events was at loads below 90%, and only a few tip events were generated during the important 90% to 110% overload region. Again, of the total tip events, about 82% had peak amplitudes of less than 40 dB_{AE}. Also, only two events had peak amplitudes of ≥ 50 dB_{AE}.

Table 15 shows the same categories of information for the fourth sample C4_2_2. The loading and cycling schedule for this sample was altered such that the cycling after a peak loading was done at one half of that peak load. Again, in this case, most of the detected tip events came for loads beyond 110% of the previous cycling level (see blue background), and by far this region had the most tip events for any of the samples (a total of 242 for all the loadings). Like all the previous samples, a large percentage of about 79% of all the tip events had peak amplitudes less than 40 dB_{AE}. In total, there were only three tip events with amplitudes ≥ 50 dB_{AE}.

A potential issue arose during the final two loadings of sample C4_2_2 to the peaks of 42 kips and 48 kips, after respectively cycling at peak loads of 16 kips and 21 kips. During these loadings the grip regions generated considerable extraneous noise over a portion of the loading. These AE events were verified to come from either the upper or lower grips by the arrival times at the sensors and/or the sequence of arrivals in the set of waveforms for each event. Further, these events typically had high peak amplitudes (up to 90 to 100 dB_{AE}) and resulting long durations. Figure 47 shows this concentration of grip-generated AE events (top for the loading to 42 kips and bottom for the loading to 48 kips). These results are in contrast to that shown in figure 48 where there was no extra concentration of grip events for the prior loading of this sample to 32 kips. In figure 47 (top) for the loading to 42 kips (cycled at 16 kips before), the excess grip noise extends from about 5.5 kips to about 20 kips, and in figure 47 (bottom) for the loading to 48 kips (cycled at 21 kips before), it extends from about 6 to 26 kips. The total number of grip and tip events that were recorded during these two intervals was respectively 162 and 492. In spite of these grip-noise events, searching through the sets of waveforms for the noisy load region for the loading to 42 kips, a total of seven tip events were found starting at 16.7 kips up to 20 kips, where the grip noise events subsided. Similarly, for the loading to 48 kips, a total of 28 tip region events were found starting at 20.8 kips up to 26 kips where the extra grip noise subsided. These results provide some evidence that tip events could be found in these regions. Considering the rate of all events in these regions respectively, the 42 kips loading had on average an event about every 4.2 s, and for the 48 kips loading this number was one event about every 2 s. Since the AE system records events at a much faster rate, at most only a very few low amplitude tip events might have been lost if they occurred simultaneously with a high amplitude grip event. It is possible a few tip region events could be lost during the approximately 2 ms rearm period (time period after an initial event before the AE system is ready to detect a new event). The AE system for each channel records the number of hits that were detected during these rearm periods, but it does not record characteristics that would allow determination of whether they were from a tip region. For the worst case, the loading to 48 kips; it was found that about 7% of the original AE events had additional hits during the rearm period. Hence, it is possible some tip region events were lost during these rearm periods. Considering all the other loadings of this sample and the other three test samples, there was no indication that large numbers of tip events with amplitudes ≥ 50 dB_{AE} would be expected during these load intervals. It is surmised that the reason for these grip related events might be associated with the reaction of the Teflon^{TM} layers to the many total cycles applied to this sample. A summary of cycles showed that prior to the loading to 42 kips a total of 254,863 cycles (114,500 fatigue cycles (from 8 to 11 to 8 kips peak) at NASA, 102,000 cycles (8 kips peak) at NIST and 38,363 cycles (16 kips peak) at NIST) had been accumulated. It is expected that a future disassembly of this sample may define the nature of this problem.

Contrasts or Similarities of Tip Region Events of Weld Samples versus Base Material Samples

To facilitate the comparison, table 16 shows the base material cracked samples results in the same format as the cracked weld samples tables above. There are six distinct contrasts or similarities. First, for the base material samples very few events prior to 90% were present, only 5 (see magenta background) versus 83 (most from weld sample C1_1_4) in total for the weld samples. This difference may be related to the shape of the crack front both in the thickness direction and the in-plane direction as it grew. A more complex shape may result in friction based AE sources and/or stick slip behavior. This potential difference from the base material case may require a computed tomography characterization in three dimensions. Second, for the region from 90 to 110%, the total of 41 for the weld samples was much less than the 234 (see green background) for the base material samples. Third, for the load range beyond 110%, the base material samples (see blue background) had more than 2.7 times more tip region events. Fourth, the two base material samples had a total of 48 events (41 of these beyond + 10%) $\geq$ 50 dB_{AE} while the four weld samples only had 20 (12 of these in the load range less than 90%). Fifth, more than one-half the tip region events with peak amplitudes $\geq$ 50 dB_{AE} (at the PICO sensors) in the weld samples occurred in the load range less than 90% of the prior cycling level, whereas in the base material there weren't any in this load region. In the base material most were in the > 110% load region. Sixth, for tip region events less than 50 dB_{AE} in the load region less than 90% of the prior cycling peak there was a total of 71 in the weld material and only 5 in the base material. In the 90% to 110% load region this result was reversed with a total of 227 in the base material and only 36 in the weld material. Except for the weld sample C1_1_4, the largest number of tip region events less than 50 dB_{AE} were generated in the load region beyond 110%. Seventh, one partial similarity for both material types was present with some exceptions. This characteristic was that as the peak loading level increased for each of the three loading regions the number of tip region events generally increased. This was always the case for the base material samples. The exceptions were for weld samples C1_1_2 and C4_2_4. In the load range beyond 110% were the general trend was opposite for these samples. In these cases the largest number of events was for the two lowest loadings.

To further examine characteristics of tip region events from base material cracks as compared to weld region cracks, frequency analysis was carried out. The approach was based on three criteria. First, the modal sensors (DW and Mist) were used since they have a less resonant and wider frequency response band, so they provide better distinctions of frequency content. Second, only events with peak amplitude at the first hit PICO sensor signal greater than 50 dB_{AE} peak amplitude were used so an excellent signal-to-noise (S/N) ratio in the modal sensor signals provided the most accurate frequency characteristics of the sources. Figures 49 and 50 provide input to illustrate why this amplitude restriction can be important. These two figures show modal sensor waveforms for two events in weld material with PICO amplitudes less than 50 dB_{AE}. To

reduce as much as possible high frequency noise in the AE signals of the modal sensors, the signals were low-pass filtered at 800 kHz for these figures. In figure 49, the PICO # 5 signal peak amplitude was 47.6 dB_{AE}, and the DW and Mist modal sensors had significantly lower (than the PICO signal) peak amplitudes respectively of 40.8 and 37.4 dB_{AE}. From top to bottom, the waves and FFT results are PICO #5, DW # 1 and Mist # 3. The FFTs was calculated using the 40 μs "window" as shown in the waveform curves. Due to the relatively low S/N ratios as can be observed by the signal levels before the "widows" in the modal sensor signals, the frequency content in the FFT result may be misleading. A similar conclusion can be made with respect to figure 50 for a tip event in weld material with peak amplitude of 46.6 dB_{AE} at PICO # 5. In this case, the DW and Mist modal sensor signals had significantly lower peak amplitudes (than the PICO signal) respectively of 37.1 and 35.8 dB_{AE}. Thus, again the results for the FFTs would be under question due to the poor S/N ratios (signal levels before the "widows") for the modal sensor signals. Third, calculate the FFT for a region of about 40 μs at the beginning of the signals so there is potentially less frequency distortion from reflections. These two figures 49 and 50 illustrate the poor S/N ratio cases, whereas figure 31 for base material illustrates a case of slightly lower PICO # 5 peak amplitude of 44.7 dB_{AE} where the modal signals peak amplitudes DW and Mist were respectively not much different than the PICO at 45.3 and 45.9 dB_{AE}. In this case, the S/N in the modal signals was higher and resulted in more reliable FFT results. Thus, the requirement of signals with PICO amplitude greater than 50 dB_{AE} is not a universal requirement, but to be conservative in the comparison here the cases were selected with this requirement on the PICO amplitude. As will be observed below in a few cases for sources that have significant high frequency content well above the 500 kHz resonance of the PICO sensors, the modal sensors signals can have amplitudes greater than the PICO signal at the emitting tip region even after the waves experience geometric spreading and dispersion. This result is due to the better high frequency response of the modal sensors.

Hence, to conservatively obtain the best tip-region-source frequency characterization, only tip events with peak amplitudes (from near PICO sensors) > 50 dB_{AE} were used to examine FFT results for cracked weld versus cracked base material. Thus the S/N ratios in the modal sensor signals would be very good. A total of eight figures based on signals low-pass filtered at 800 kHz were created to do the comparison. In each figure, the top waveform and (to its right) associated FFT result are for a typical tip region source in cracked weld material, and the bottom waveform and associated FFT are for a typical crack tip region source in the base material. The eight figures should be viewed as four sets of two figures for the same two material AE sources with the first figure of the set being for the Mist sensors and the second figure of the set being for the DW sensor. Thus in what follows, the two material classes of samples and their source frequency content are examined by FFT characteristics using the modal sensor spectra. In each case, the signal waveform shows a window of 40 ms width of the time portion that was used for the FFT calculation. The first set in figures 51 and 52 shows for typical cases that both crack material types had high frequency content; defined in this work as well over 200 to 300 kHz. In all these figures, it can be observed that the two modal sensors did not have the same spectra due to their

different frequency response, but the presence of high frequency content was there. Also, note that the modal sensor signals for the weld material source had larger peak amplitudes (by about 2.5 dB) than the PICO sensor, due to the presence (as discussed above) of very high frequencies well above the resonance (500 kHz) of the PICO sensor. In contrast, the modal sensor peak amplitudes for the base material were some 4 dB less in peak amplitude than the PICO sensor. This reduction in the base material cases examined in the following sets of figures was also the case. The peak amplitudes at the modal sensors for the base material tip events were less than the PICO sensor signals by up to about 7 dB. The second set of figures 53 and 54 for typical sources in the two materials also shows the tip region events from both materials had the high frequency signal content. Again in the weld material case the very high frequency content lead to peak amplitudes at the modal sensors some 3 to 5 dB above the PICO sensor. Beginning with the third set of figures 55 and 56, a different frequency character is present in the typical signals/FFTs from the two different crack material cases. In these figures, the typical weld crack tip event signal now shows low frequency (<200 kHz) dominant behavior for both sensor types, while the base material is still characterized by high frequency content since that is more typical for base material cracks. Likewise, for the fourth set figures 57 and 58, the base material typical case has the high frequency content while the typical for the weld material crack has low frequency content. There were not enough cases of the weld material tip region events to conclude that the sources with high frequency content always extended will beyond the 500 kHz resonance of the PICO sensors. Hence, the bottom line of the FFT comparisons is currently limited to the presence of both low and high frequency content sources in weld material and nearly all cases of the base material having high frequency content.

The WD sensor with its lower background noise and both high and low frequency resonant response potentially offers an alternative with better S/N ratios to determine the frequency characteristic of tip event sources as compared to the modal sensors. It may provide signal frequency content (and thus source characteristics) for source signals with peak amplitudes at the near PICO of less than 50 dB_{AE}. The FFT results from the WD sensor signals were examined for several tip events with high frequency content in the modal sensor signals. The results showed two classes: (i) clear dominance of high frequency dominance and (ii) some examples where the WD sensor signal showed a primary dominance of low frequency content as well as less intense high frequency content. It is suspected that this behavior was due to these sources generating a significant flexural mode. Thus, the WD sensor can provide source frequency information to identify sources with high frequency content, when the modal sensors suffer from poor S/N ratios. Care in analysis of the FFT results must be exercised due to the potential for the lower frequency resonance of the WD sensor to be excited by a strong flexural mode.

For tip region events in the base material, it was shown (see figures 27, 28 and 29) that the peak amplitudes of the tip region signals measured with the PICO sensors did not show an increase in amplitude as the applied load/stress increased. Making use of the data from specimen C1_1_2 for the loading to 24 kips after cycling at 5 kips, the peak amplitudes of the near PICO sensor were

plotted as a function of load in figure 59 (a). In figure 59 (b) similar results were plotted for weld sample C4_2_2 for the loading to 32 kips after cycling at a peak load of 8 kips. This figure shows that there was no progressive increase in amplitudes for the weld region events as the load level increased. Thus, as was concluded for the base material case, the detectability of tip region events by the different sensor/preamps will depend on signal-to-noise (S/N) ratio and not the load level for both material cases. The detectability characteristics of the different sensor/preamps have already been examined in Task 3, so it will not be repeated here.

To complete the contrast relative to the highest amplitude sources in both cracked material types, events with amplitudes above 60 dB_{AE} peak amplitude (PICO sensor) were examined as to the load region where they occurred (relative to the prior cycling peak load), the frequency content they had using modal sensor data, the load of event occurrence and the prior cycling level. It is such high amplitude source signals that might be most likely to propagate to further distances in a LPV and still be detectable. Lower source amplitude signals such as those greater than about 50 dB_{AE} but less than about 60 dB_{AE} might be expected to be detectable at shorter distances in a LPV (Conclusions about the detectability of such sources will in the end depend on modeling results). Table 17 shows the results for all nine such events from the weld samples and all four such events from the base material samples. Of the nine from the weld material only three had high frequency content, and for the base material samples all four had high frequency content. The load range and actual load where these highest amplitude signals were generated is also provided in the table as well as the peak cycling load just prior to the loading. In the case of weld material two of those with high frequency content occurred at less than 90%, while in the base material case three of the four with high frequency content were generated at greater than 110%.

DIC information was obtained for each of the four cracked weld samples. Figure 60 illustrates with sample C4_2_2 how the plastic zone size changes with an increase in the peak load of the cycling. In this figure, the DIC views were taken at a load of 8 kips. The far right view shows the larger plastic zone due to the cycling at 16 kips peak load as compared to the other two views that were cycled at 8 kips peak load. In figure 61, the DIC view was taken at a load of 40 kips for sample C1_1_4. This view is interesting since load versus crosshead displacement indicated this sample experienced macroscopic yielding at about 38 kips. The figure shows the plastic zone has extended to the edges of the 3.5-inch width of the reduced section, and it shows where this plastic deformation is concentrated, which is away from the region immediately ahead of the crack. Figure 62 compares the DIC view at a load of 38 kips for sample C1_1_2 with that for C4_2_4. This load in both cases is beyond the cycling peak load. The tip A values at the start of the load cycles for each sample were respectively 0.251 inches and 0.208 inches. These values would imply that C1_1_2 should have greater stress intensity (about a factor of 1.1). This conclusion is opposite to what is observed in figure 62. The fact that the DIC view is on the opposite side of tip A (tip D in the notation adopted at NASA) confuses the attempt to explain the differences. Thus, it is only possible to point to potential causes. First, the crack may be located in a different position within the weld region in the two specimens. Figure 63 shows a

micrograph of a weld region. Clearly, through cracks can encounter different material conditions depending on where it actually is located within this region. This fact leads to a recommendation to examine the actual crack paths for the four weld samples tested. Second, the crack has grown a different amount at the tip D, which could not be measured during the test due to the DIC painted/speckled area. Third, the plates inherently differed in material properties.

Task 4 Conclusions

- *In base material, nearly all tip region events have significant high frequency content well above 200 kHz, with modal sensors data. In contrast, the weld samples tip region events, with the same modal sensors; less often had high frequency content. Limited to results from events ≥ 50 dB_{AE}.*

- *During loading after cycling, almost no AE events were generated from the tip regions of base material prior to reaching 90% of the prior cycling peak load. In contrast, some weld samples C1_1_4 and C4_2_4 generated significant numbers of events in this load region.*

- *For the loading region from 90% to 110% of the previous cycling peak load, the base material samples generated a significant number of events. In contrast, considerably fewer events were generated in the weld samples in this load region, where AE typically is applied.*

- *For the loading region greater than 110% of the previous peak cycling load, the base material samples generated nearly three times the number of tip region events than the weld samples.*

- *For both crack material types, the large majority of tip region events had peak magnitudes below 40 dB_{AE} at the nearby PICO sensors.*

- *In addition, for both material types the peak amplitudes did not progressively increase as the load/stress increased. Thus detectability of tip events depends on S/N of the different sensor/preamps and not on the load for a particular sensor/preamp.*

- *Considering the generation of AE tip region events with magnitudes of ≥ 50 dB_{AE} for all three load regions, the base materials generated a total of 48 for the two samples with the maximum amplitude high frequency source being 68.8 dB_{AE}. In contrast, the four weld samples generated a total of 20 events with the maximum amplitude high frequency source being 69.4 dB_{AE}.*

- *In order to assure good S/N ratios in both modal sensor signals, the peak amplitudes at the PICO sensors generally needed to be at least 50 dB_{AE}. For these event amplitudes the good S/N ratios at the modal sensors resulted in the most reliable results for source frequency characterization. Due to the lower background electronic noise of the Mistras modal sensor, the PICO peak amplitude could be a few dB less to obtain reliable results. In some cases, the frequency content of the tip region source was such that the falloff from the PICO signal amplitude to the modal sensors was less, likely due to the source having very high frequency content that the PICO sensor did not respond to. In these cases, the S/N ratio at the modal sensors was good for near tip PICO signals down to the mid-40s dB_{AE}.*

- *Even though the WD sensor has both high and low frequency resonances and a lower background noise, it requires a more sophisticated analysis to identify sources with high frequencies when they were generated in the tip regions. This may be due to the amount of flexural mode generated by the particular tip event.*

- *The grip design with the Teflon^{TM} layers did not perform well for one sample (weld sample C4_2_2). This test specimen generated multiple large amplitude grip-originated sources for some load ranges. It is suggested that this behavior was brought about by the large number of fatigue cycles 114,500 (from 8 to 11 to 8 kips peak) at NASA, 102,000 (8 kips peak) at NIST and 38,363 (16 kips peak) at NIST. The grand total of 254,863 cycles seems to have created this situation. It is expected that a future disassembly of this sample will define the nature of this problem.*

- *Pencil lead breaks had peak amplitudes ranging from 78 to 82 dB_{AE} in the weld samples for all the sensors after changing the PICO # 2 sensor to one with more sensitivity.*

- *Including both sample types, a total of 13 AE tip region events had PICO amplitudes above 60 dB_{AE}, five of the nine in weld samples did not have high frequency content while all four in the base material had high frequency content. There was no evidence that significantly higher peak amplitudes were generated in the weld material specimens as compared to the base material specimens.*

- *DIC results showed some expected behavior and also some evidence of different plate materials or different locations of the cracks relative to the weld material samples.*

- *It is suggested that the microstructure be examined for the region (from the center of the weld across to base material) of crack propagation to define what the cracks propagated through. Further, to determine the historical crack front paths in the weld samples computed tomography may be used to provide 3D results.*

- *An added suggestion is to examine the sizes and distribution of particles in the base material and weld material regions.*

Overall Conclusions

- *The number of tip region events during loading differed substantially when the base material specimens were compared to weld material specimens. Also, the load regions where the largest number of such events was generated differed.*
- *For tip events with PICO signal amplitudes ≥ 50 dBAE, most events from weld samples came from less than 90% of the previous cyclic peak load (dominated by C1_1_4), while for the base material most came from greater than 110%. On the other hand for tip events with PICO signal < 50 dB_{AE}, the order from most to least events for weld material was > 110%, < 90% and 90% to 110% and for base material > 110%, 90% to 110% and < 90%.*
- *The tip region source peak amplitudes from the PICO sensor signals was substantially the same for both materials types, ranging from 34 dB_{AE} to just less than 70 dB_{AE}.*
- *In the relevant 90% to 110% load range (based on peak loads in prior cycling), for testing of LPVs with AE, there were substantial differences between the two different material types in the numbers of tip events ≥ 50 dB_{AE}. There were a total of five for all the weld samples including all loadings. In contrast for the base material, the same number was seven for two less specimens.*
- *For events less than 50 dB_{AE}, the numbers respectively for weld and base material were 36 and 227.*
- *Except for two loadings of one weld sample (C4_2_2) the Teflon™ layered specimen design functioned well in reducing grip noise.*
- *By use of pencil lead breaks on progressively less wide samples, it was estimated that the 3.5 inch wide tensile samples would not experience large reinforcements of peak amplitudes during the tensile tests.*
- *It was shown using FFTs of modal sensor signals that tip events in the base material nearly all had dominant high frequency content well above 200 kHz, while the tip events in weld material had some events with similar dominant high frequency content while others had dominant low frequency content.*
- *A very small number of events had PICO signal amplitudes greater than 60 dB_{AE}. The four from base material all had a dominance of high frequencies, while of the nine in weld crack material only three had high frequency dominance.*
- *Detection of tip events was shown to depend on the S/N characteristics of the different sensor/preamps and not on load/stress levels. The background noise levels varied substantially for the different sensor/preamps. The highly resonant sensors have the least while the modal sensors had the most. From the point of view of source identification the modal sensors provide more information while the resonant sensors provide less. For only signal detection the resonant sensors have the advantage.*
- *Since no evidence was found that significantly higher amplitude signals were generated in the weld cracked samples, it is important to verify where the actual cracks were located in these samples.*

References

1. "Multilayer Pressure Vessel tensile coupon test (106-107)".pdf, Contact James Walker at NASA Huntsville, AL.

2. M. A. Hamstad report 9/31/2015, submitted to Dr. Eric Madaras at NASA Langley. VA.

3. M. A. Hamstad, A. O'Gallagher and J. Gary, "Effects of Lateral Plate Dimensions on Acoustic Emission Signals from Dipole Sources," J. of Acoustic Emission, Vol. 19, 2001, pp. 258-274.

4. M.A. Hamstad "Improved Signal-to-Noise Wideband Acoustic/Ultrasonic Contact Displacement Sensors for Wood and Polymers,", Wood and Fiber Science, 29 (3), 1997, pp. 239-248

5. Levi Shelton, "V0023 1146a Parent Material Inner vs. Wrapper Layer Properties," MPFR-17-003, 2017.

Tables

Table 1 Acoustic emission sensor information

Channel no., Sensor ID	Manufactures frequency electronic bandpass, kHz	Preamp: location and gain, dB	Electrical connector sensor to AE system	Resonance characteristics; manufacturers information	Outer diameter, mm
1. Digital Wave, B454 – IPP, modal	20 - 1500	Internal 20	BNC to BNC	Not strongly resonant; broadband	14
2. Mistras, PICO	None (preamp)	External 34	Internal to BNC	Resonant at 500 kHz	5
3. Mistras, PKBBI, modal	20 - 600	Internal 26	SMA to BNC	Not strongly resonant; broadband	18
4. Mistras, WDI	200 - 900	Internal 40	BNC to BNC	Resonant at about 130 kHz and 320 kHz and some higher frequencies	27
5. Mistras, PICO	None (preamp)	External 34	Internal to BNC	Resonant at 500 kHz	5
6. Mistras, R15I	50 - 400	Internal 40	BNC to BNC	Resonant at 150 kHz	26

Table 2 Setup of AE system for tensile loading

Channel no., sensor ID	Threshold, dB_{AE}	Filter for waveforms digitized at 10 MHz	Filter for AE features	Waveform trigger and pretrigger points	Duration discrimination, µs and Rearm time, ms
1. DW, modal	40.6	FIR; 18 kHz HP	40 to 800 kHz	Pool; 1000	250; 2
2. PICO	34	FIR; 18 kHz HP	40 to 800 kHz	Pool; 1000	250; 2
3. Mist, modal	38.1	FIR; 18 kHz HP	40 to 800 kHz	Pool; 1000	250; 2
4. WDI	36	FIR; 18 kHz HP	40 to 800 kHz	Pool; 1000	250; 2
5. PICO	34	FIR; 18 kHz HP	40 to 800 kHz	Pool; 1000	250; 2
6. R15I	36	FIR; 18 kHz HP	40 to 800 kHz	Pool; 1000	250; 2

Table 3 Calculated distances from PLB points to center of AE sensor located as in figure 11

Plates; 36 in. long	PLB at minus 3/8 inch		PLB at plus 3/8 inch	
Plate width, in.	Shorter reflection distance, mm	Longer reflection distance, mm	Shorter reflection distance, mm	Longer reflection distance, mm
24	585.7	642.4	604.6	623.8
12	285.9	341.4	304.3	322.8
6	144.1	195.4	160.8	177.9
3.5	95.2	138.7	108.3	122.9
Direct distance to sensor, mm	74.3		79.0	

Table 4 Average peak-to-peak amplitude for 3.5-in.-wide plate relative to that from 24-in.-wide plate

Sensor/PLB point	PLB at minus 3/8 inch	PLB at plus 3/8 inch
DW	-1	1
Mist	4	5
WDI	3	4
R15I	2	2

Table 5 Growth of crack tips from EDM notches of base material during cycling at NASA Marshall

Specimen	Tip A, in.	Tip B, in.	Tip C, in.	Tip D, in.	Cycles at loads, kips
AE final 1	0.050	0.075	0.026	0.023	36,000 @ 20 to 16
AE final 2	0.051	0.063	0.022	0.023	30,000 @ 20 to 16

Table 6 Loading procedures used for AE final 1 and 2 from base material

Test step	Description of step
1	Load to 17.6 kips (10% above last cycling peak of 16 kips) at 25 lb/s. Unload at same rate.
2	Cycle (R = 0.1) at 17.6 kips to mark ends of potential crack growth after step 1 and re-sharpen crack tips. Total about 10,000 cycles
3	Load to 40 kips at 30 lb/s. AE analysis concentrated on load up to 19.36 kips (10% above last cycling peak of 17.6 kips). Unload at same rate.
4	Cycle (R = 0.1) at 40 kips to mark ends of potential crack growth after step 3, re-sharpen crack tips and grow tips about 0.1 in. Typically, about 3,000 cycles
5	Load to 44 kips (10% above last cycling peak of 40 kips) at 30 lb/s. Unload at same rate
6	Cycle (R = 0.1) to 44 kips to mark ends of potential crack growth after step 5. AE final 1 for 778 cycles and AE final 2 for 5000 cycles

Table 7 Summary of number of crack tip events for the plus 10% loadings including the number with peak amplitude greater than 50 dB_{AE}

Loading	AE final 1 (≥ 50 dB_{AE})	AE final 2 (≥ 50 dB_{AE})	Shakedown (≥ 50 dB_{AE})
To 17.6 kips (10% above 16 kips)	22 (0)	27 (1)	16 (2)
To 19.36 kips (10% above 17.6 kips)	27 (0)	37 (2)	Not done
To 44 kips (10% above 40 kips)	34 (0)	73 (4)	36 (0)

Table 8 Root mean square voltage (RMS) background noise level (primarily from the electronics of the different preamps) versus sensor (taken over periods of about 40 ms)

Sensor ID	Approximate RMS background noise level during tensile test of cracked base material tests, μV	Approximate RMS background noise level during grip noise tests, μV
DW	19	14
Mist	9.6	6.6
WDI	3.7 to 5.0	5.5 to 6.5 (with a different WD sensor)
R15I	2.7	2.7
PICOs	2.9 (#2) and 3.1 (#5)	2.9 (#2) and 3.1 (#5)

Table 9 Measure of signal-to-noise of tip events in cracked base material versus peak amplitude of AE

Event peak amplitude at PICO # 5 (from source at tip nearest PICO #5), dB_{AE}	DW ratio*	Mist ratio*	WDI ratio*	R15I ratio*
37.8	0.057	0.88	3.0	7.2
44.7	3.13	8.94	85.9	214
54.9	4.13	18.5	53.2	53
68.8	80.3	1580	2600	8800

* Ratio = (Event “energy” increment beyond extended background noise “energy”)/ Extended noise “energy”)

Table 10 Final crack growth at tips of EDM notch for weld samples during cycling at NASA Marshall

Specimen	**Tip A, in.**	**Tip B, in.**	**Tip C, in.**	**Tip D, in.**	**Cycles at loads, kips**
C1_1_2	**0.076**	**0.050**	**0**	**0**	**173,000 @ 12 to 5**
C1_1_4	**0.071**	**0.053**	**0.019**	**0.013**	**320,000 @ 12 to 5**
C4_2_2	**0.068**	**0.040**	**0.002**	**0.038**	**114,500 @ 11 to 8**
C4_2_4	**0.065**	**0.063**	**0.023**	**0.037**	**120,000 @ 11 to 8**

Table 11 RMS noise from preamplifier electronics during tensile tests compared for weld *cracks versus base material cracks. Also, the dB increase in noise compared to the lowest noise case R15 for* weld *cracks*

Sensor ID	Weld samples, RMS noise, µV (dB difference vs. R15)	Weld sample, AE Threshold, dBAE	Base material samples, RMS noise, µV	Base material samples, AE Threshold, dBAE
DW Ch. # 1	≈ 19.5 (18)	42.3	≈ 19	40.6
PICO Ch. # 2	≈ 3.1 (2.2)	34.0	≈ 2.7	34.0
Mist Ch. # 3	≈ 8.5 (11)	38.1	≈ 9.6	38.1
WD Ch. #4	≈ 3.7 (3.8)	36.0	≈ 3.7 to 5.0	36.0
PICO Ch. # 5	≈ 3.1 (2.2)	34.0	≈ 3.1	34.0
R15 Ch. # 6	≈ 2.4 (0)	36.0	≈ 2.7	36.0

Table 12 Loadings, cycles between loadings, crack growth and statistics of tip region events for Pathfinder, sample C1_1_4

Statistics for Sample C1_1_4 for tip region events						
Cycles @ Peak load, kips	Load to, kips	No. of tip region events below 90 % of cycling load (no. < 40 dB)	No. of tip region events 90 % to plus 10 % above cycling load (no. < 40 dB)	No. of tip region events in range beyond 10 % above cycling load (no. < 40 dB)	Tip A added extension from cycling, in.	Tip B added extension from cycling, in.
320,000 @ 12 to 5	5.5	0	0	NA	0.071	0.0523
30,000 @ 5.5	12	0	0	2 (2)	Not measured	Not measured
25,000 @ 12	13.2	2 (1)	0	NA	Not measured	Not measured
18,000 @ 13.2	24	1	0	1 (0)	Not measured	Not measured
10,000 @ 24	26.4	18 (10)	5 (2)	NA	Total Tip A = 0.389 (most from this cycling)	Total Tip B = 0.388 (most from this cycling)
2,000 @ 26.4	32	22 (9)	6 (2)	6 (4)	0.073	Not measured
150 @ 32	40*	12 (5)	7 (4)	10 (5)	0.048	Not measured
Results on amplitudes ≥ 50 dB to right (Total of 12)	* Section yielded at about 38 kips	Loads to 5.5, 12 & 13.2 none; load to 24 one @ 62.0; load to 26.4 four, max. 61.8 ; load to 32 two, max. 65.9; load to 40 two, max. 68.0 (dB)	Loads to 5.5, 12, 13.2, 24, & 26.4 none; load to 32 two, max. 69.4; load to 40 one @ 56.2 (dB)	Loads to 5.5, 12, 13.2, 24, & 26.4, 32 & 40 none	Final total extension A = 0.51 and B = 0.509	

Table 13 Loadings, cycles between loadings, crack growth and statistics of tip region events for sample C1_1_2

Statistics for Sample C1_1_2 for tip region events						
Cycles @ Peak load, kips	Load to, kips	No. of tip region events below 90 % of cycling load (no. < 40 dB)	No. of tip region events 90 % to plus 10 % above cycling load (no. < 40 dB)	No. of tip region events in range beyond 10 % above cycling load (no. < 40 dB)	Tip A added extension from cycling, in.	Tip B added extension from cycling, in.
173,000 @ 12 to 5	24	0	0	23 (17)	0.076	0.05
4,800 @ 24 and 14,000 @ 12	34	0	0	3 (2)	0.1	Not measured
18,000 @ 20	40	1 (1)	0	1 (1)	0.074	Not measured
1,800 @ 32	48*	8 (4)	0	1 (1)	0.05	Not measured
Results on amplitudes ≥ 50 dB to right (Total of 3)	* Section yielded at about 47 kips	Loads to 24, 34 & 40 none; load 48 two, max. 60.5 (dB)	All loadings none	Loads to 34, 40 & 48 none; load to 24 one @ 50.4 (dB)	Final total extension A = 0.301 and B = 0.265	

Table 14 Loadings, cycles between loadings, crack growth and statistics of tip region events for sample C4_2_4

Statistics for Sample C4_2_4 for tip region events						
Cycles @ Peak load, kips	Load to, kips	No. of tip region events below 90 % of cycling load (no. < 40 dB)	No. of tip region events 90 % to plus 10 % above cycling load (no. < 40 dB)	No. of tip region events in range beyond 10 % above cycling load (no. < 40 dB)	Tip A added extension from cycling, in.	Tip B added extension from cycling, in.
120,000 @ 8 to 11 to 8	16	0	1 (1)	11 (10)	0.065	0.063
16,000 @ 16	32	1 (1)	3 (2)	25 (22)	0.053	Not measured
3,000 @ 32	42	7 (5)	2 (2)	4 (3)	0.09	Not measured
1,400 @ 42	48*	11 (7)	0	NA*	0.145	Not measured
Results on amplitudes ≥ 50 dB to right (Total 2)	* Section yielded at about 43 kips; terminated at 46.4 kips	Loads to 16, 32 & 48 none; load to 42 one @ 54.8 (dB)	Loads to 16, 42, & 48 none; load to 32 one @ 58.2 (dB)	All loadings none	Final total extension A = 0.301 and B = 0.265	

Table 15 Loadings, cycles between loadings, crack growth and statistics of tip region events for sample C4_2_2

Statistics for Sample C4_2_2 for tip region events						
Cycles @ Peak load, kips	Load to, kips	No. of tip region events below 90 % of cycling load (no. < 40 dB)	No. of tip region events 90 % to plus 10 % above cycling load (no. < 40 dB)	No. of tip region events in range beyond 10 % above cycling load (no. < 40 dB)	Tip A added extension from cycling, in.	Tip B added extension from cycling, in.
114,500 @ 8 to 11 to 8	16	0	2 (2)	5 (3)	0.068	0.04
102,000 @ 8	32	0	0	54 (46)	0.035	Not measured
38,363 @ 16	42	0	*2 (2)	89 (67)	0.085	Not measured
30,000 @ 21	48	0	*13 (11)	94 (73)	0.12	Not measured
* Possible loss of some tip events due to grip noise. Results on amplitudes ≥ 50 dB to right (Total 3)		All loadings none	Loads to 16, 32 & 40 none; load to 48 one @ 50.8 (dB)	Loads to 16 & 42 none; load to 32 one @ 54.5; load to 48 one @ 61.8 (dB)	Final total extension A = 0.326 and B = 0.204	

Table 16 Loadings, cycles between loadings, crack growth and statistics of tip region events for AE final 1 and 2, base material samples

Statistics for AE final 1						
Cycles @ Peak load, kips	Load to, kips	No. of tip region events below 90 % of cycling load; (no. less than 40 dBAE)	No. of tip region events 90 % to plus 10 % above cycling load; (no. less than 40 dBAE)	No. of tip region events in range beyond 10 % above cycling load; (no. less than 40 dBAE)	Tip A added extension from cycling, in.	Tip B added extension from cycling, in.
36,000 @ 20 to 18 to 16	17.6	0	22 (15)	NA	0.076	0.05
≈ 10,000 @ 17.6	40*	0	28 (21)	421 (303)	Not measured	Not measured
≈ 3,000 @ 40	44	2 (2)	36 (27)	NA	≈ 0.1	≈ 0.1
Results on amplitudes ≥ 50 dB to right (Total of 7)	* plus 10 % from cycliing level = 19.36	All loadings none	All loadings none	Load to 40 kips 7 , max. 55.1 dB	Final total extension A = 0.301 and B = 0.265	
Statistics for AE final 2						
Cycles @ Peak load, kips	Load to, kips	No. of tip region events below 90 % of cycling load; (no.	No. of tip region events 90 % to plus 10 % above cycling load; (no. less than 40 dBAE)	No. of tip region events in range beyond 10 % above cycling load; (no. less than	Tip A added extension from cycling, in.	Tip B added extension from cycling, in.
30,000 @ 20 to 18 to 16	17.6	0	27 (17)	NA	0.051	0.027
≈ 10,000 @ 17.6	40*	2 (1)	44 (21)	> 421 (est.)	Not measured	Not measured
≈ 3,000 @ 40	44	1 (1)	77 (53)	NA	≈ 0.1	≈ 0.1
Results on amplitudes ≥ 50 dB to right (Total of 41)	* plus 10 % from cycliing level = 19.36	All loadings none	Load to 17.6 kips one @ 51.5 dB; load to 40 kips two, max. 63.6 dB; load to 44 kips four, max @ 55.0 dB	Load to 40 kips 34, max. 68.8 dB	Final total extension A = 0.301 and B = 0.265	

Table 17 Characteristics of tip region events with peak amplitude greater than 60 dB_{AE}

Sample	Peak, dBAE (load at event, kips)	Load Range	Load to, kips (cycling peak, kips	Frequency character
C1_1_4	62.0 (8.318)	< 90 %	24 (13.2)	Low
C1_1_4	61.8 (13.207)	< 90 %	26.4 (24)	High
C1_1_4	65.9 (4.840)	< 90 %	32 (26.4)	Low
C1_1_4	64.1 (8.167)	< 90 %	32 (26.4)	Low & High
C1_1_4	69.4 (26.675)	90 % to 110 %	32 (26.4)	High
C1_1_4	68.0 (3.692)	< 90 %	40 (32)	Low
C1_1_4	64.9 (7.714)	< 90 %	40 (32)	Low
C1_1_2	60.5 (16.136)	< 90 %	48 (32)	Low
C4_2_2	61.8 (47.073)	> 110 %	48 (32)	Low
AE final 2	63.6 (17.545)	90 % to 110 %	40 (17.6)	High
AE final 2	60.9 [est. from #5, hit #2 1st] (26.675)	> 110 %	40 (17.6)	High
AE final 2	61.5 (27.053)	> 110 %	40 (17.6)	High
AE final 2	68.8 (38.603)	> 110 %	40 (17.6)	High

Figures

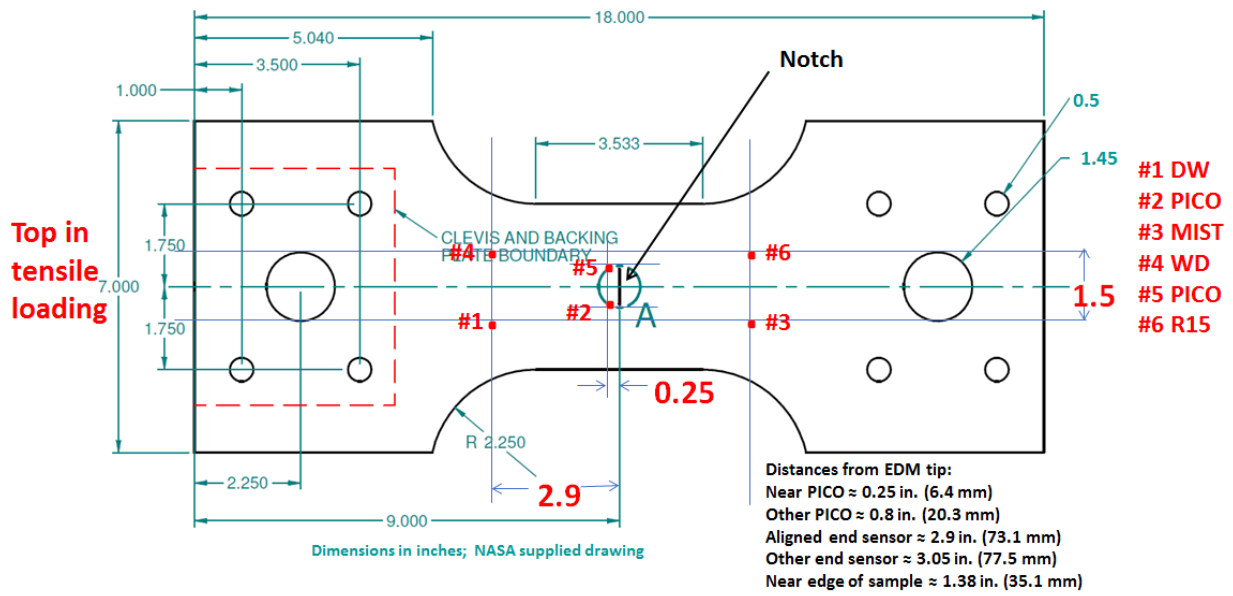


Figure 1 Drawing of test specimen and backing plate regions. Also, shows distances from the notch tips to the locations of centers of the six numbered AE sensors

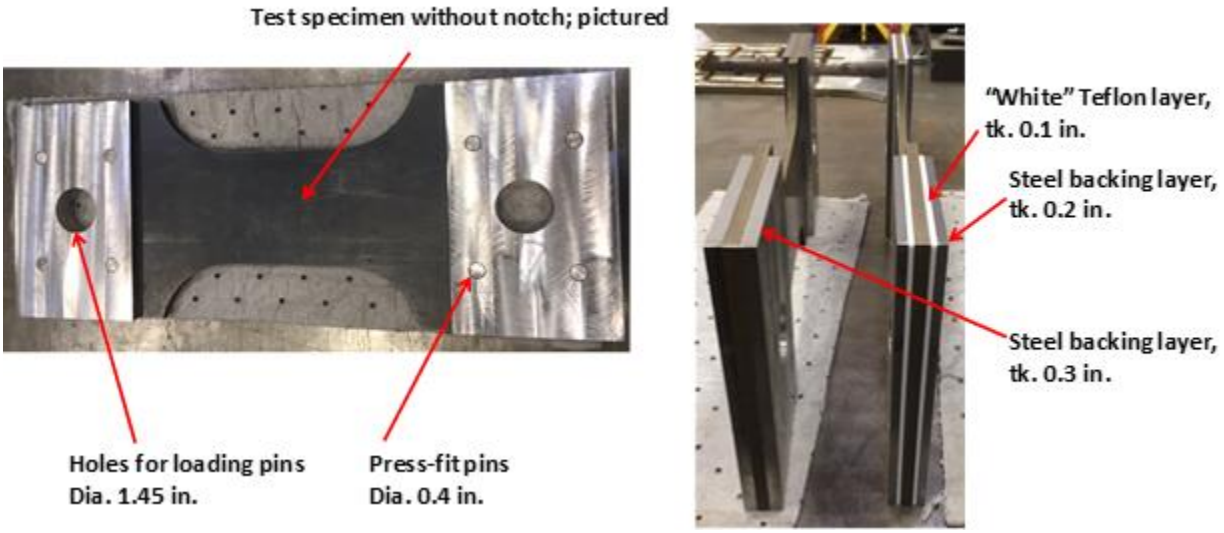


Figure 2 Photo of tensile samples of the nominal 0.28 inches thickness. Specimens on right shown with and without Teflon layers

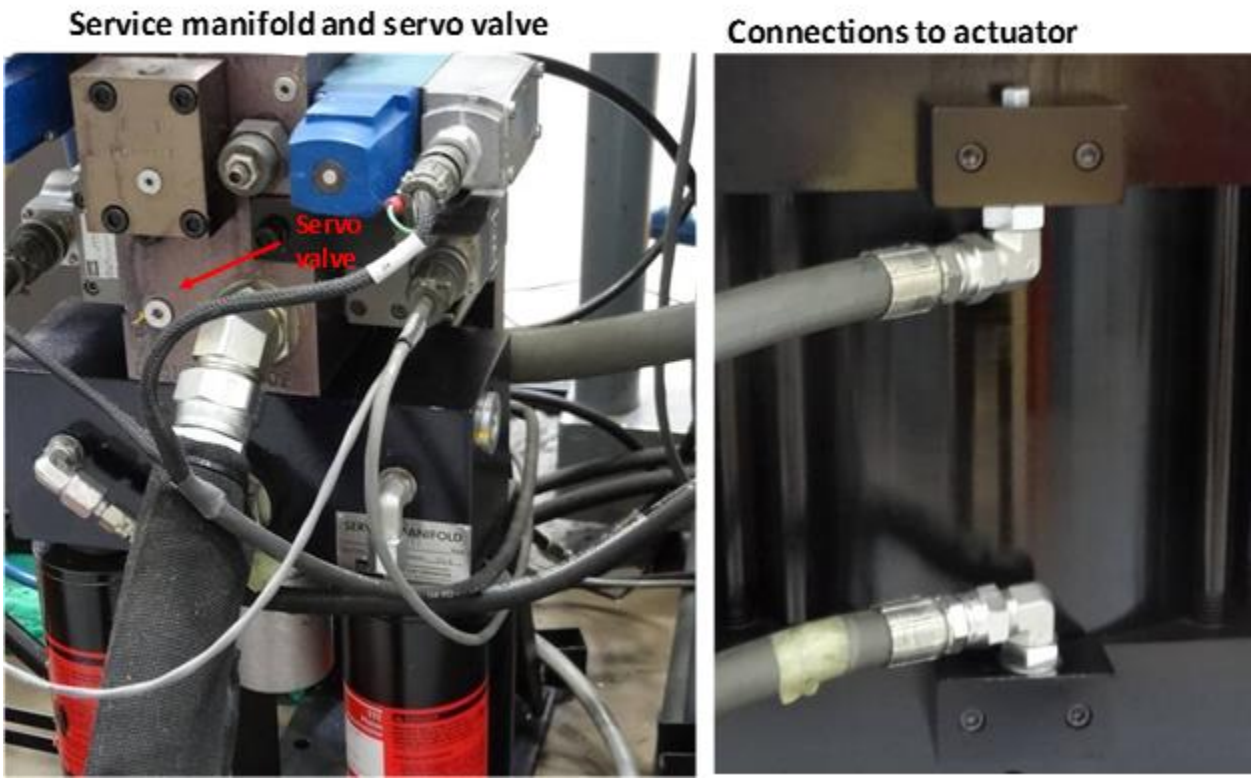


Figure 3 External mounted servo valve and hydraulic hose connections to actuator

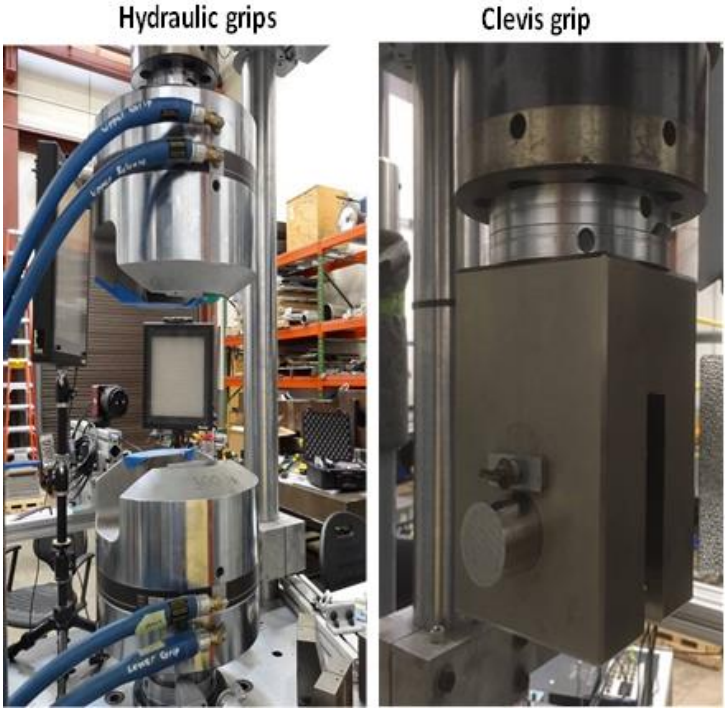


Figure 4 Photos of NIST hydraulic wedge grips and top clevis grip

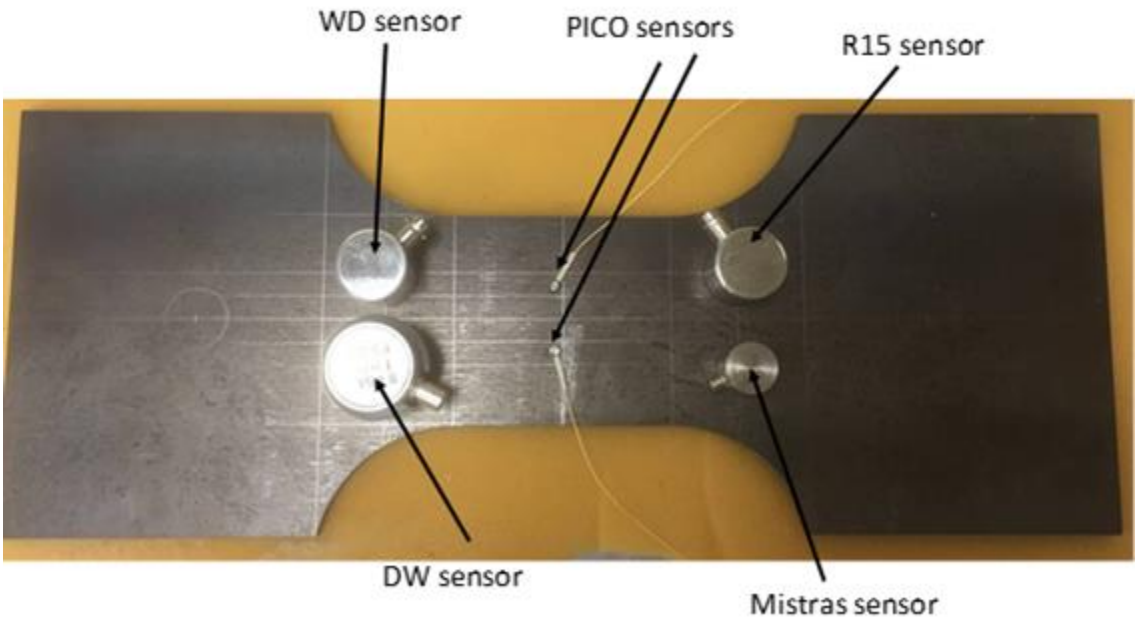


Figure 5 Photo of all six AE sensors mounted at their positions on a dummy test sample

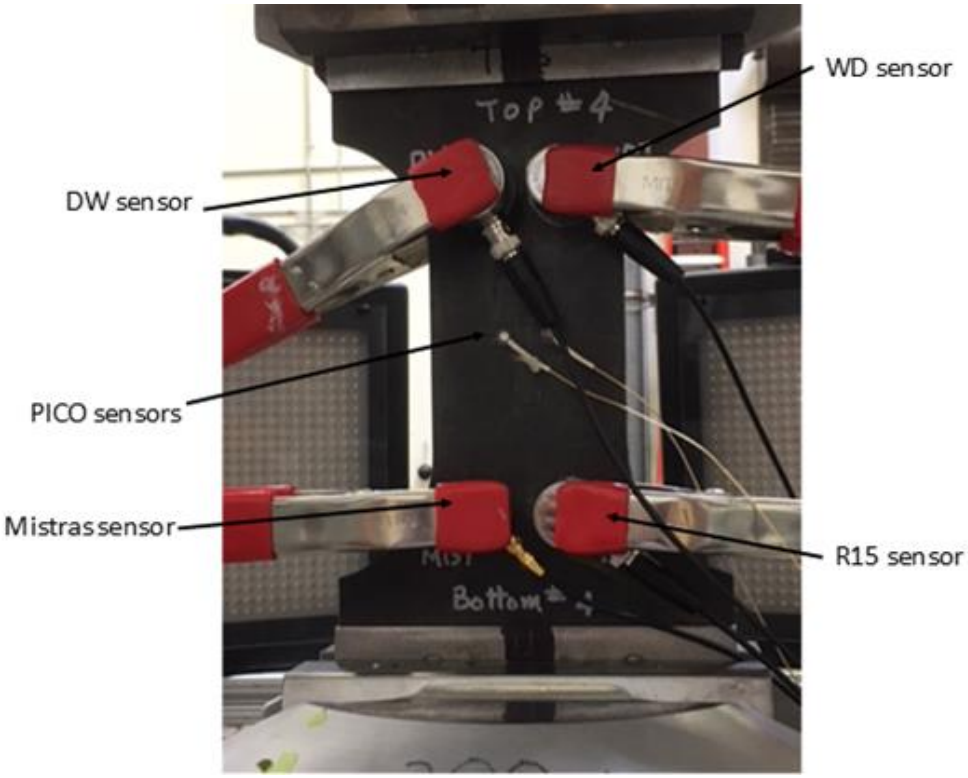


Figure 6 Photo of a grip-noise tensile sample, without a notch, with all six sensors mounted

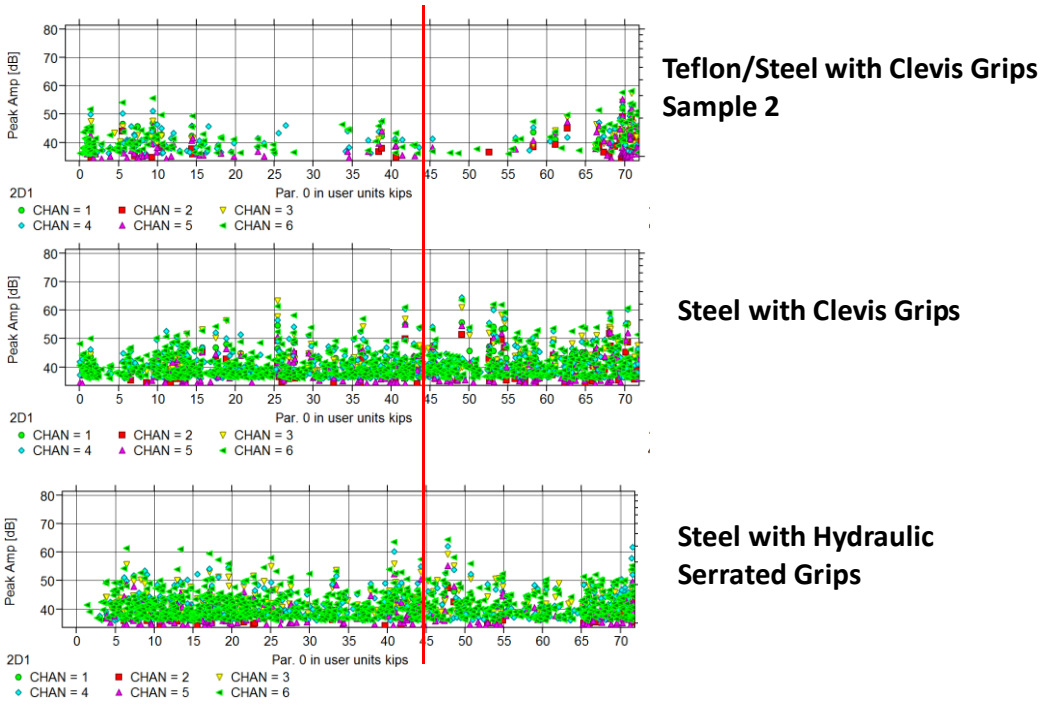


Figure 7 Peak amplitudes of grip noise AE for peak amplitudes ≥ 35 dB_{AE} versus load scale of 0 to 70 kips for different designs. Vertical red line maximum load reached in tests of cracked samples of base material

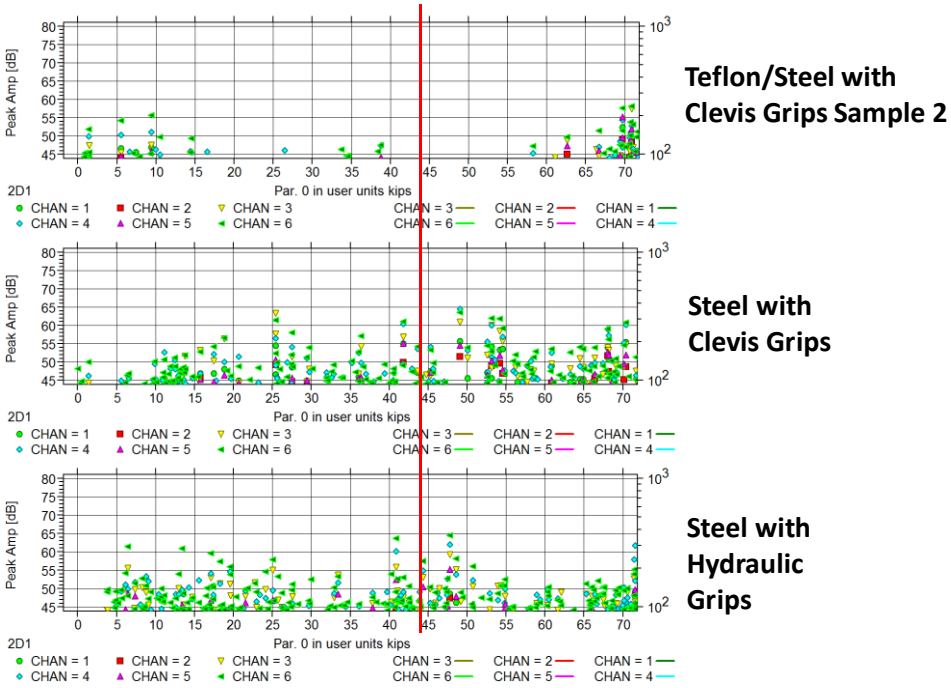


Figure 8 Peak amplitudes of grip noise AE for peak amplitudes ≥ 45 dB_{AE} versus load scale of 0 to 70 kips for different designs. Vertical red line maximum load reached in tests of cracked samples of base material

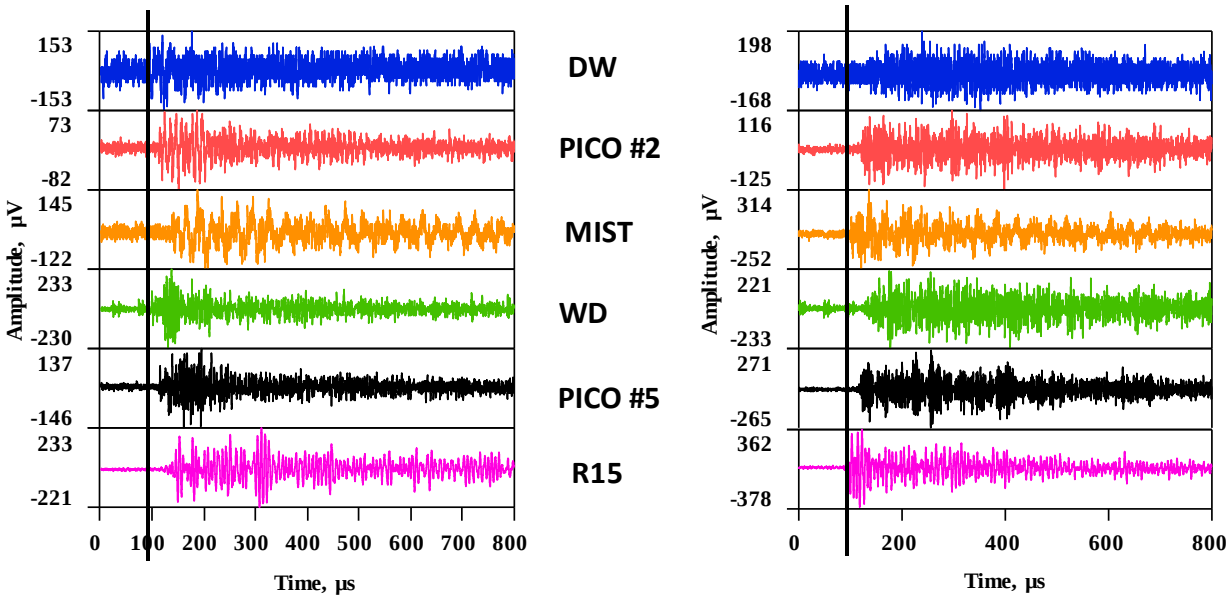


Figure 9 Typical waveforms for grip noise events in a Teflon layer sample. Left-side top grip event and right-side bottom grip event. Vertical line shows first arrival for each case

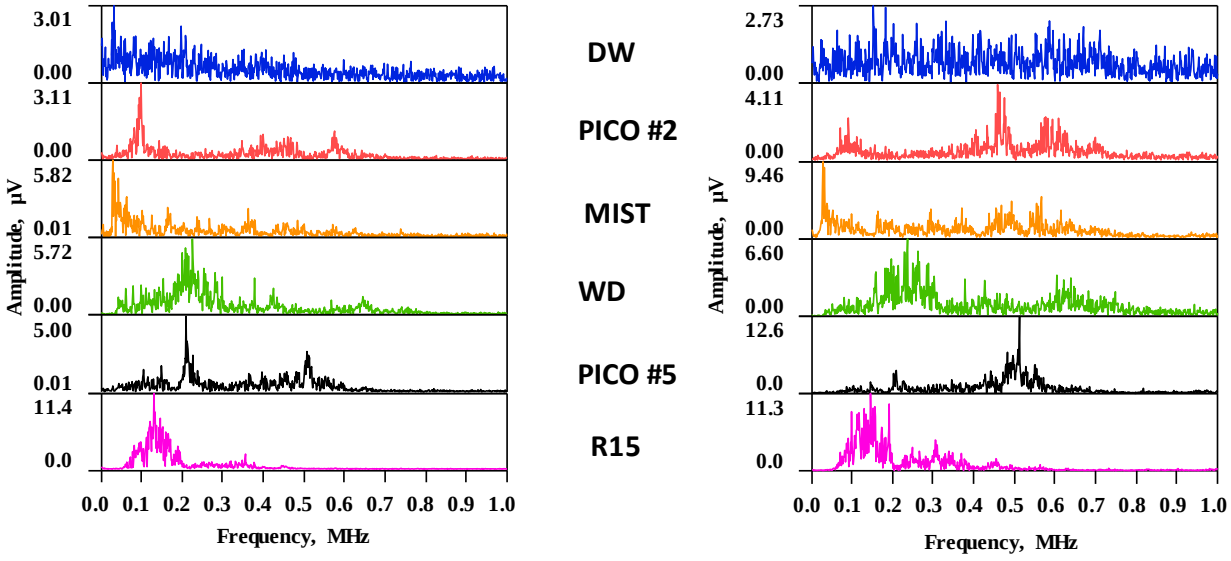


Figure 10 Corresponding FFT results respectively for signals shown in figure 9

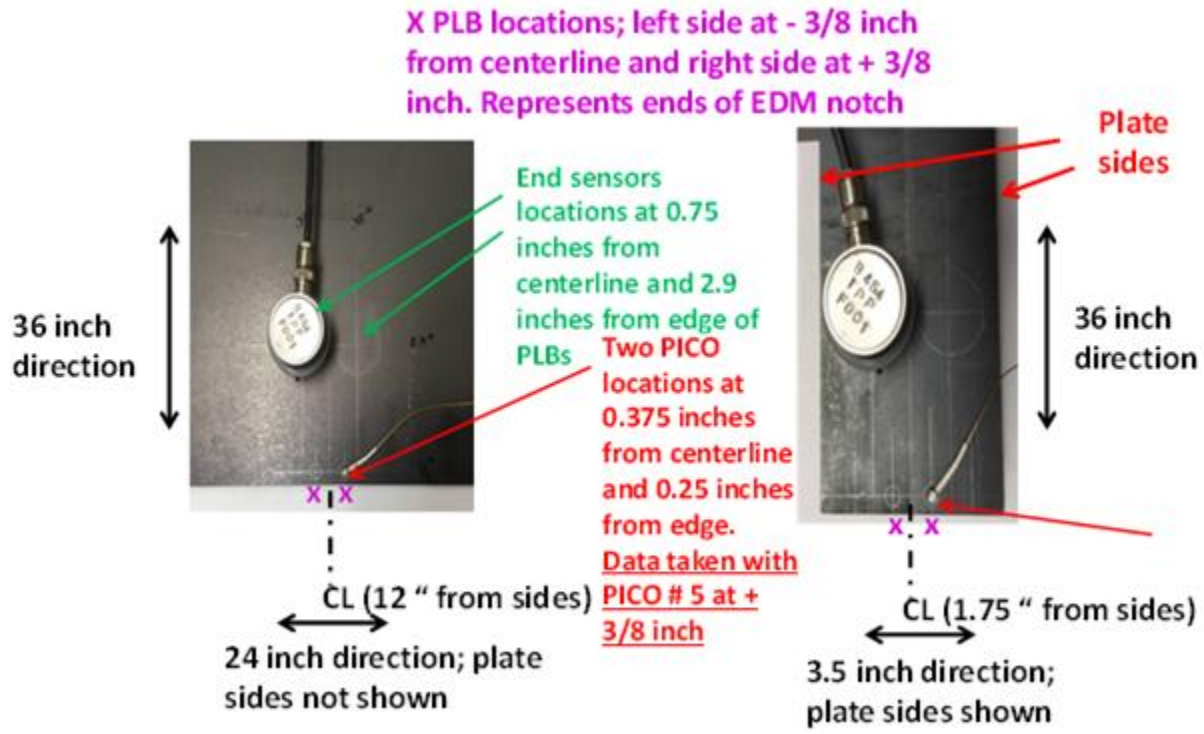


Figure 11 Typical setup for PLBs on edge of plates with different widths. Left side largest width (24 inch) plate (edges not shown) and right side smallest width (3.5 inch) plate (edges shown)

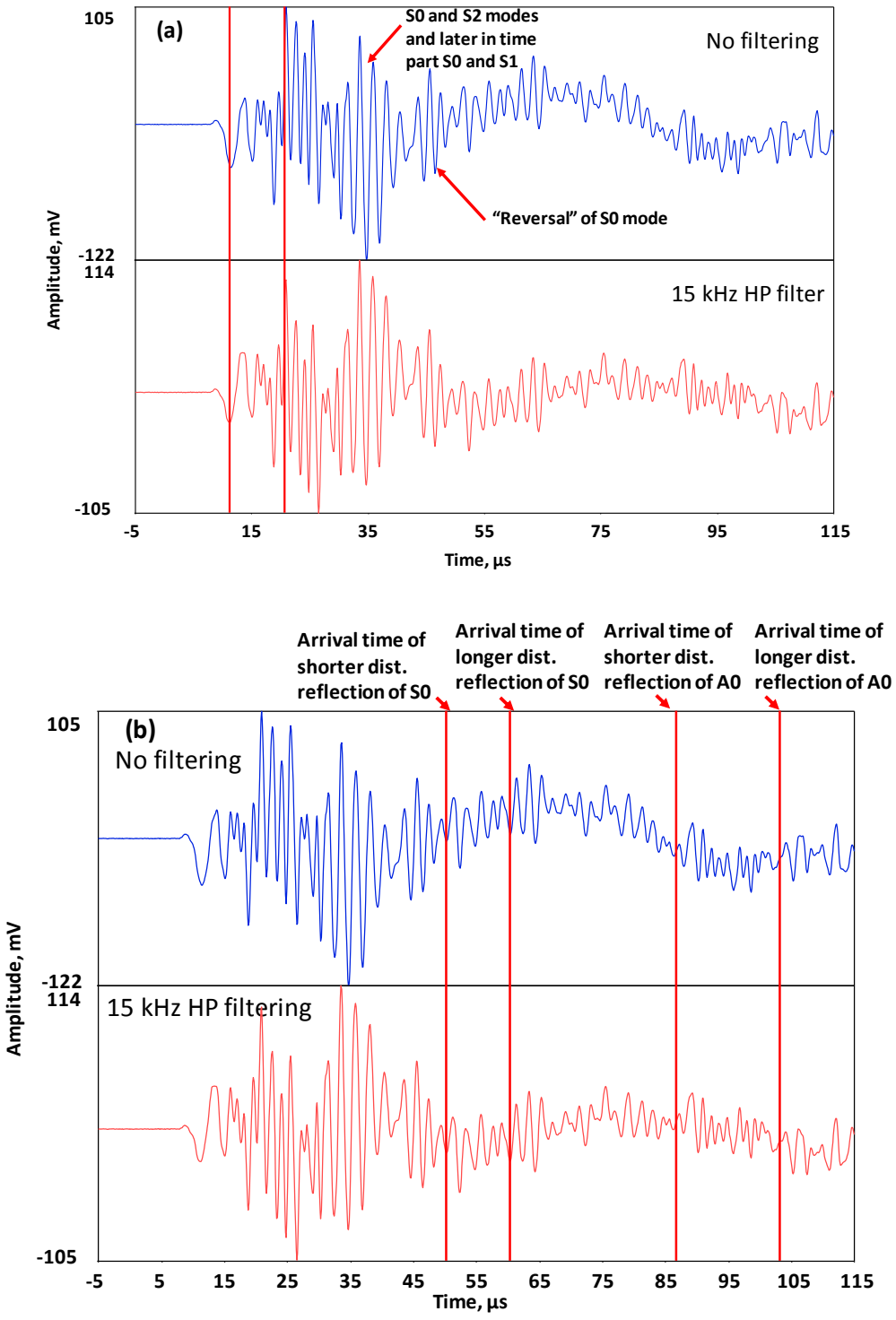


Figure 12 Shows the waveforms (without and with 15 kHz HP filtering) from a PLB at the minus 3/8-inch position using the NIST FHWA point-contact sensor on the 12-inch-wide plate. Part (a) shows first arrivals (red cursors) of the fundamental modes S0 and A0 as well as added mode arrivals that are not reflections and part (b) shows the potential correspondence of the calculated arrivals of the four reflections of the fundamental modes

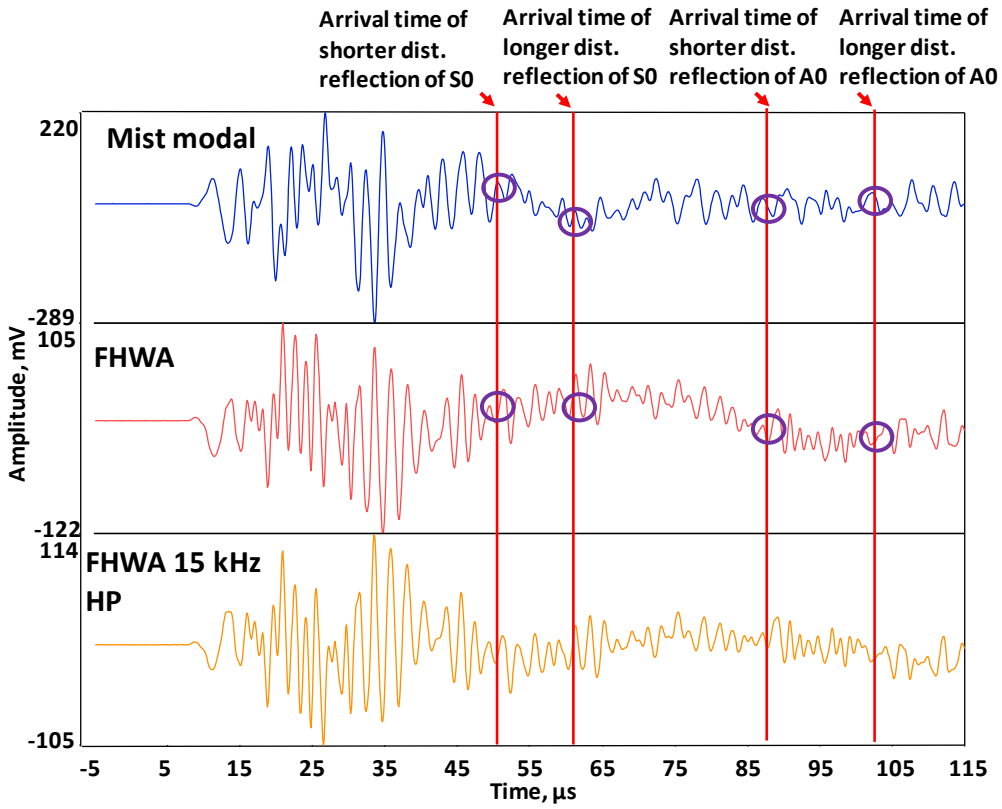


Figure 13 For the same setup as figure 12, but with the Mist modal sensor waveform added. Shows the expected calculated reflection arrivals (cursors with circles) of the fundamental modes are not as easily recognized with the Mist sensor

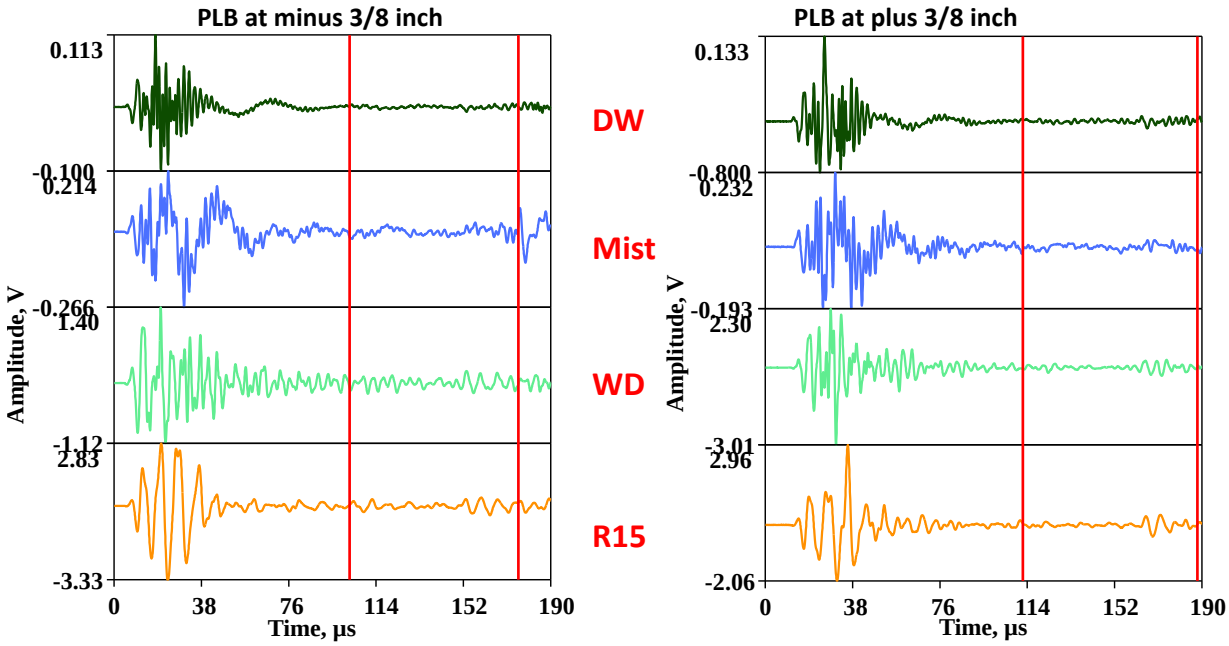


Figure 14 Shows typical signals from each of the four end sensors from PLBs at the minus 3/8-inch position (left side) and plus 3/8-inch position (right side) using the 24-inch-wide plate. Red cursors at earliest calculated reflections, left for extensional mode and right for flexural mode

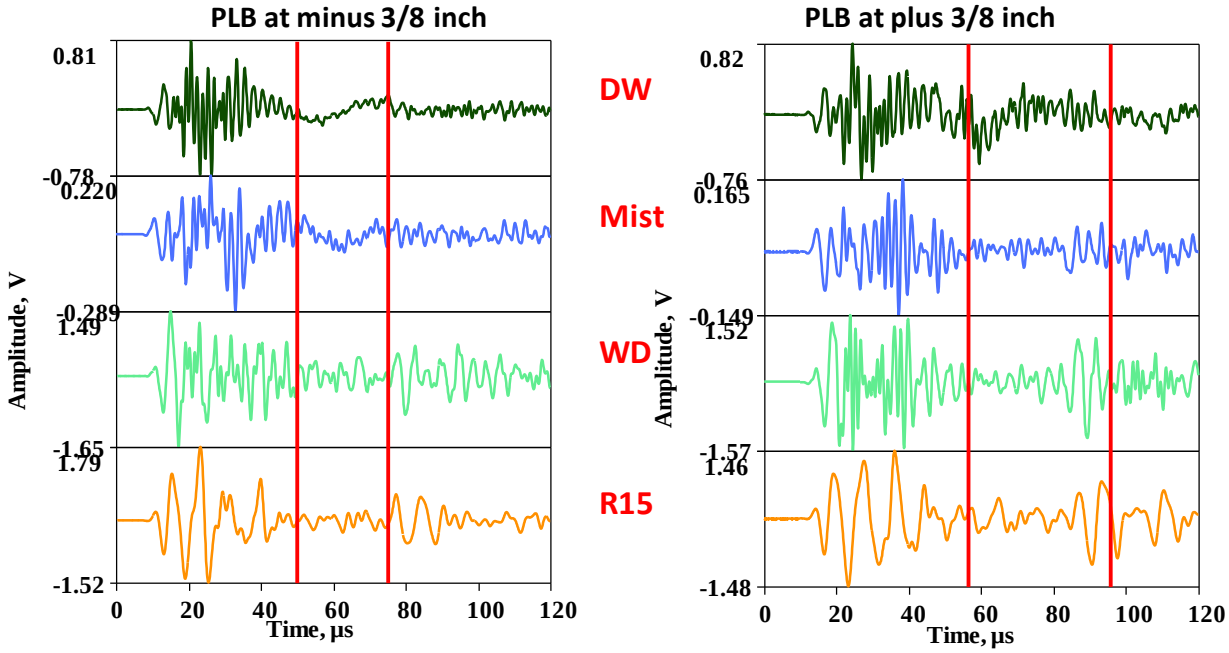


Figure 15 Shows typical signals from each of the four end sensors from PLBs at the minus 3/8-inch position (left side) and plus 3/8-inch position (right side) using the 12-inch-wide plate. Red cursors at earliest calculated reflections, left for extensional mode and right for flexural mode

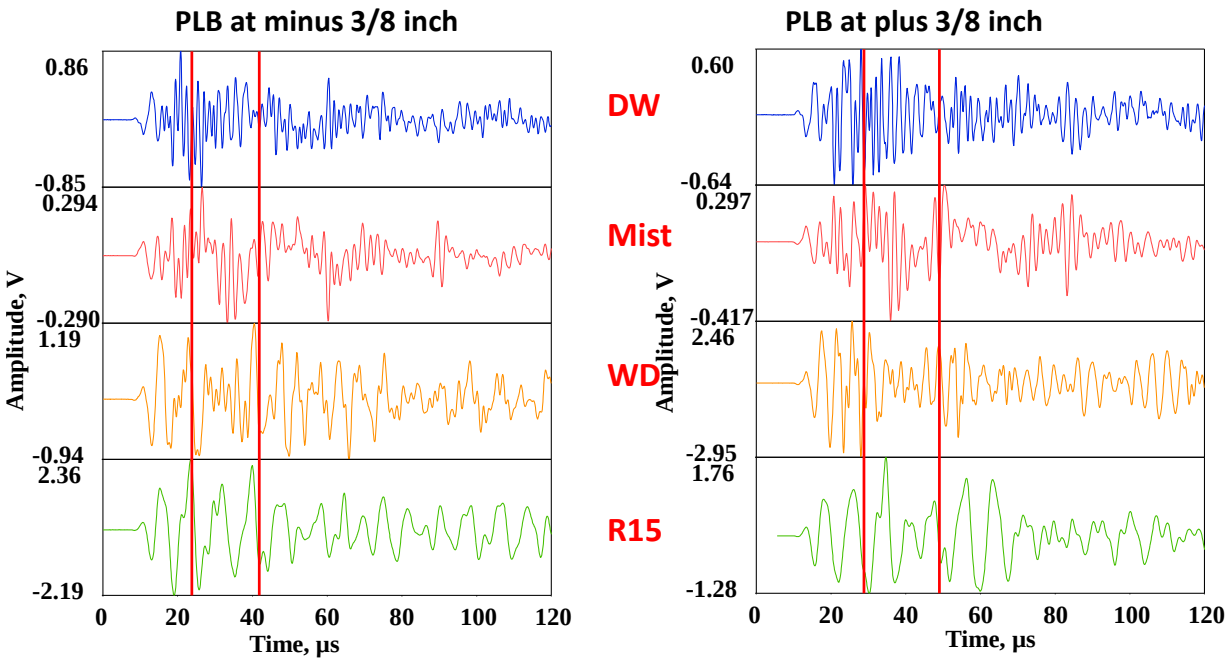


Figure 16 Shows typical signals from each of the four end sensors from PLBs at the minus 3/8-inch position (left side) and plus 3/8-inch position (right side) using the 6-inch-wide plate. Red cursors at earliest calculated reflections, left for extensional mode and right for flexural mode

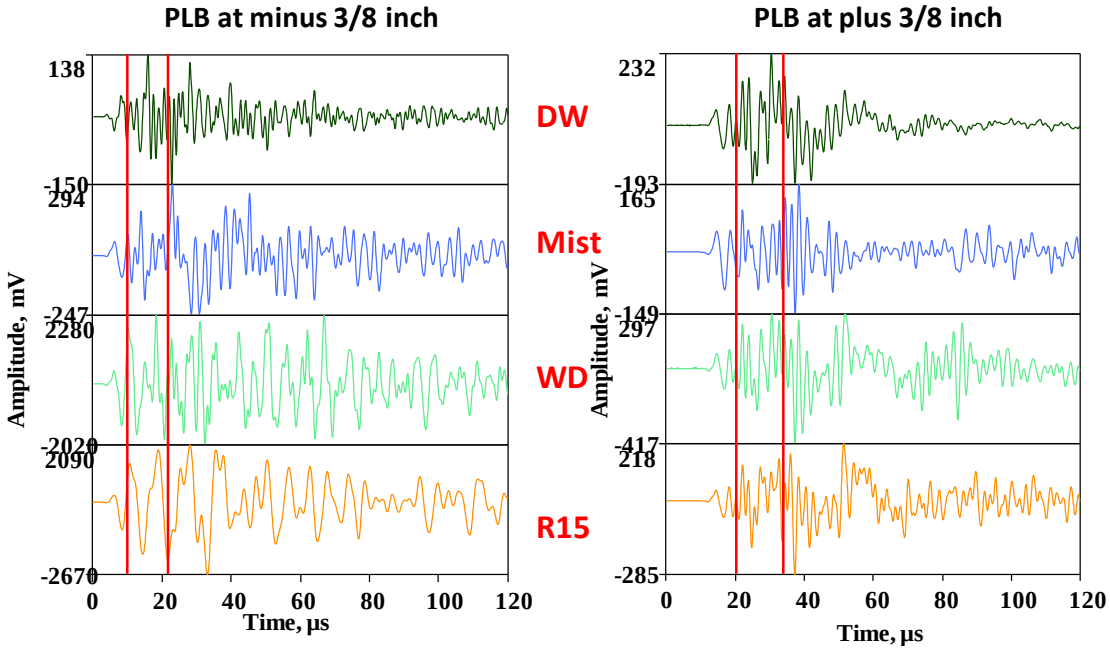


Figure 17 Shows typical signals from each of the four end sensors from PLBs at the minus 3/8-inch position (left side) and plus 3/8-inch position (right side) using the 3.5-inch-wide plate. Red cursors at earliest calculated reflections, left for extensional mode and right for flexural mode

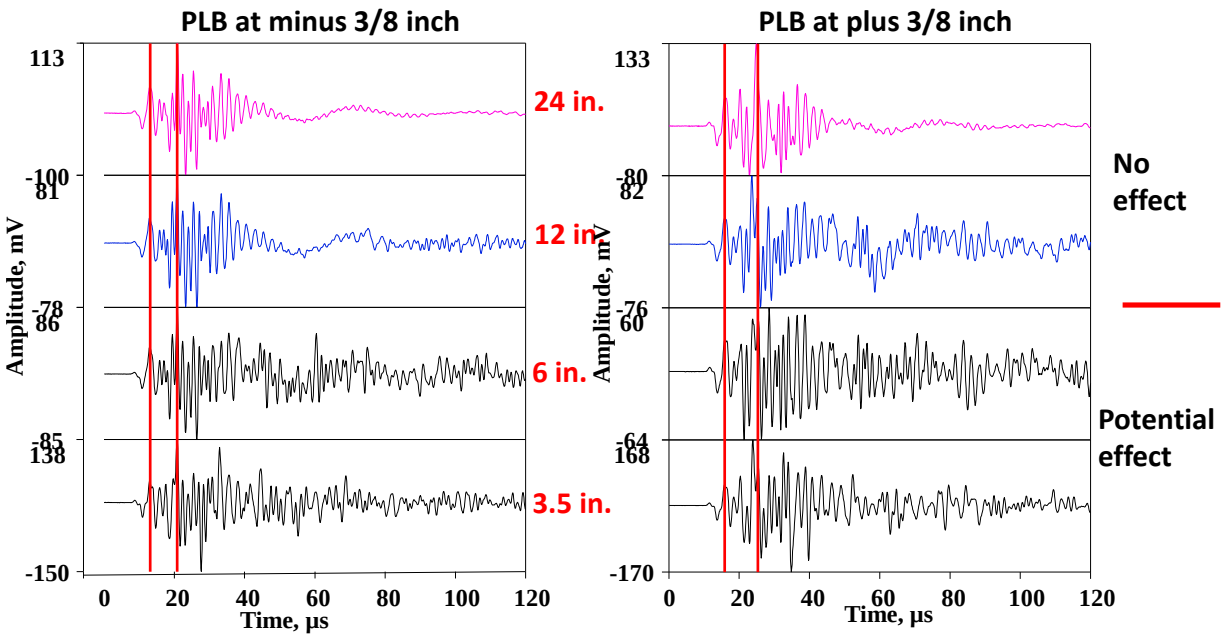


Figure 18 Shows typical signals from DW sensor from PLBs at the minus 3/8-inch position (left side) and plus 3/8-inch position (right side) using all four plate widths. Cursors left at initial direct extensional arrival and right at peak amplitude for the 24-inch plate

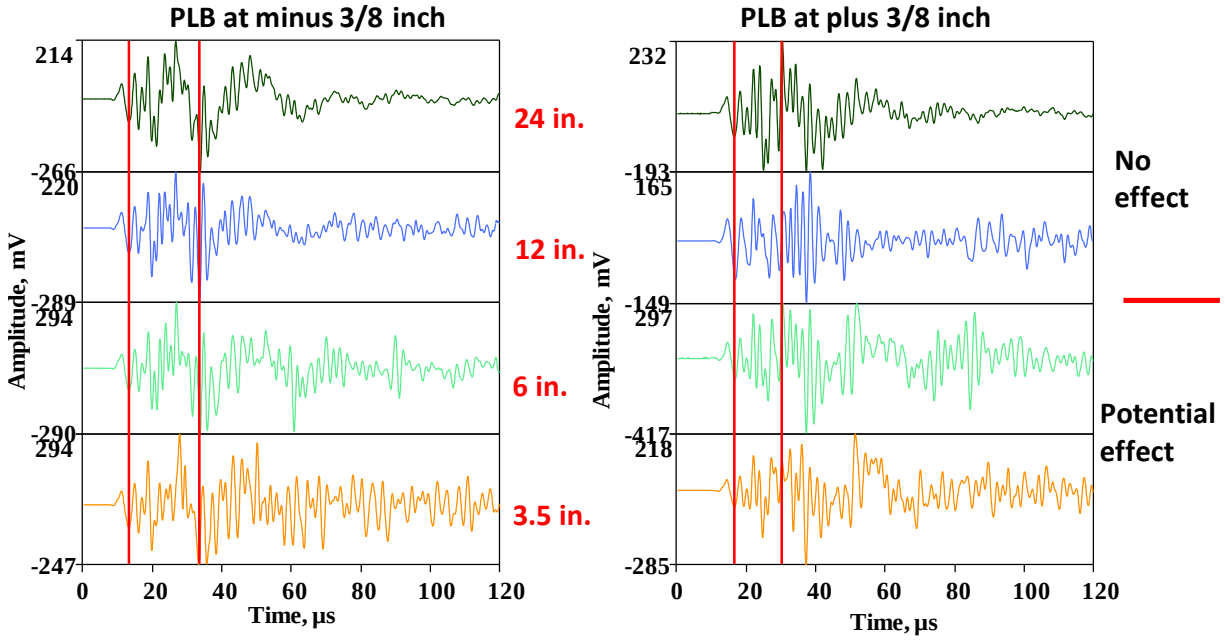


Figure 19 Shows typical signals from Mist sensor from PLBs at the minus 3/8-inch position (left side) and plus 3/8-inch position (right side) using all four plate widths. Cursors left at initial direct extensional arrival and right at peak amplitude for the 24-inch plate

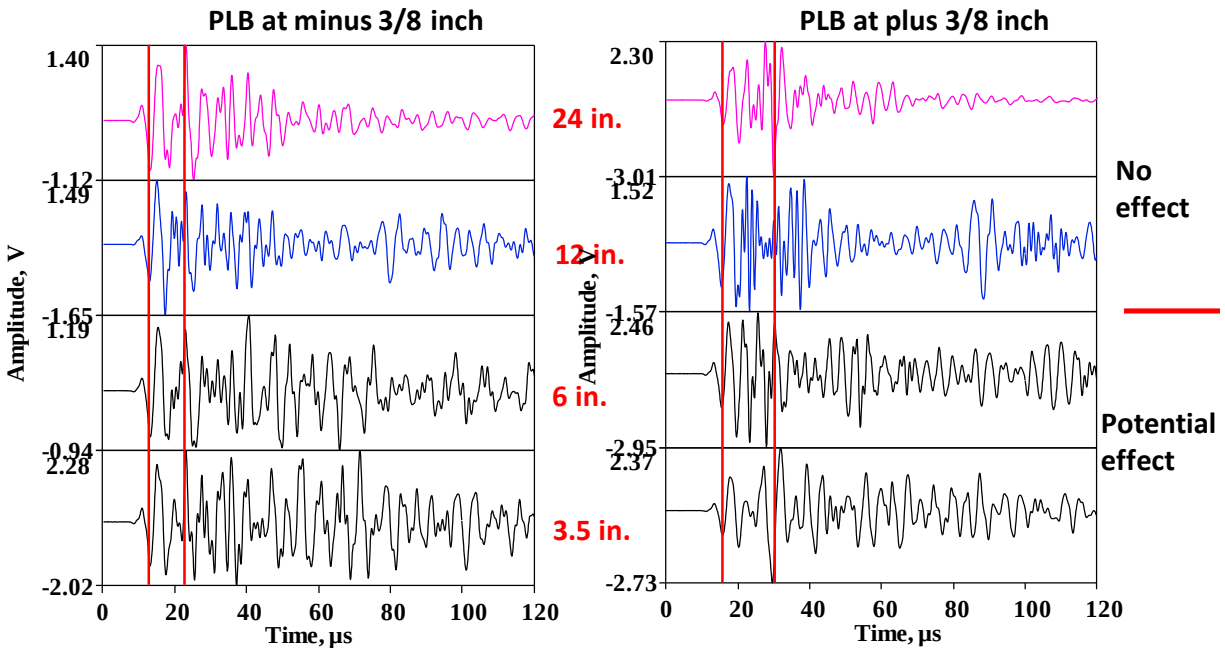


Figure 20 Shows typical signals from WD sensor from PLBs at the minus 3/8-inch position (left side) and plus 3/8-inch position (right side) using all four plate widths. Cursors left at initial direct extensional arrival and right at peak amplitude for the 24-inch plate

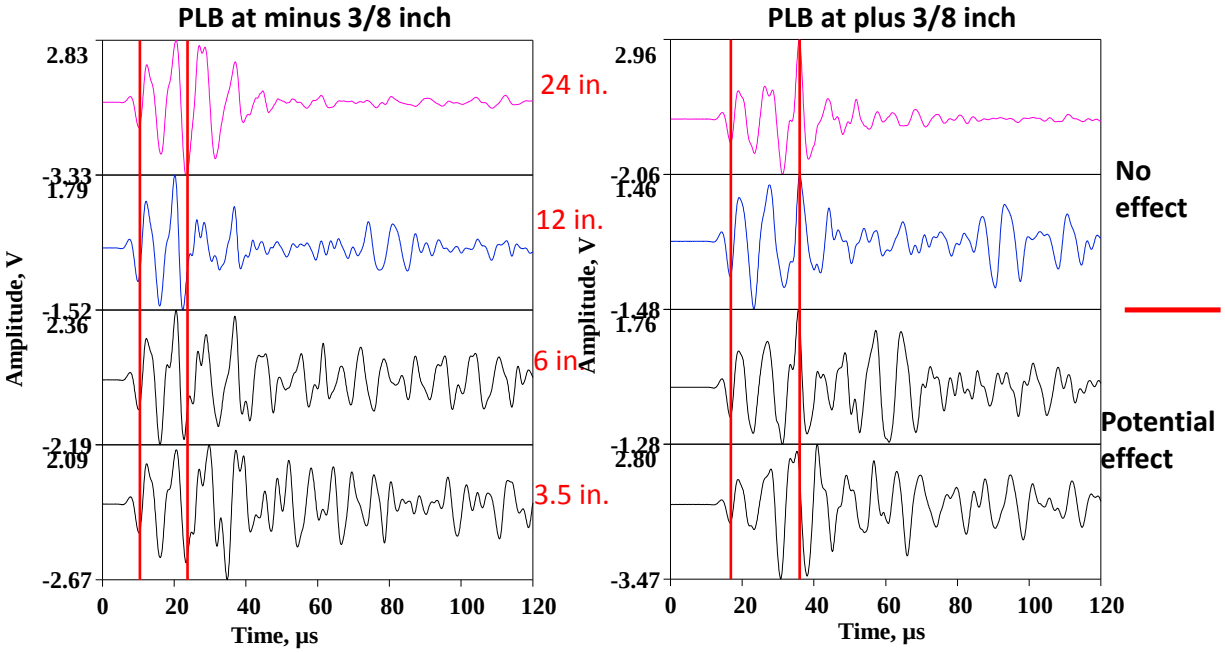


Figure 21 Shows typical signals from R15 sensor from PLBs at the minus 3/8-inch position (left side) and plus 3/8-inch position (right side) using all four plate widths. Cursors right at initial direct extensional arrival and left at peak amplitude for the 24-inch plate

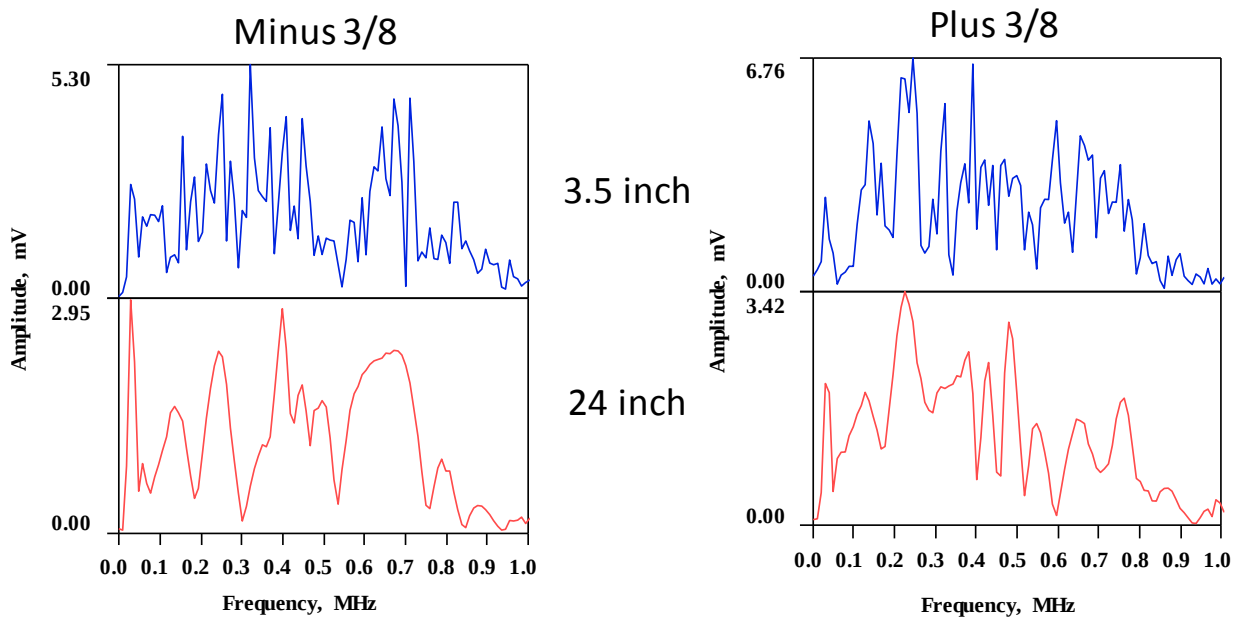


Figure 22 FFT results compared for DW sensor on 24-inch versus 3.5-inch plates for both PLB positions

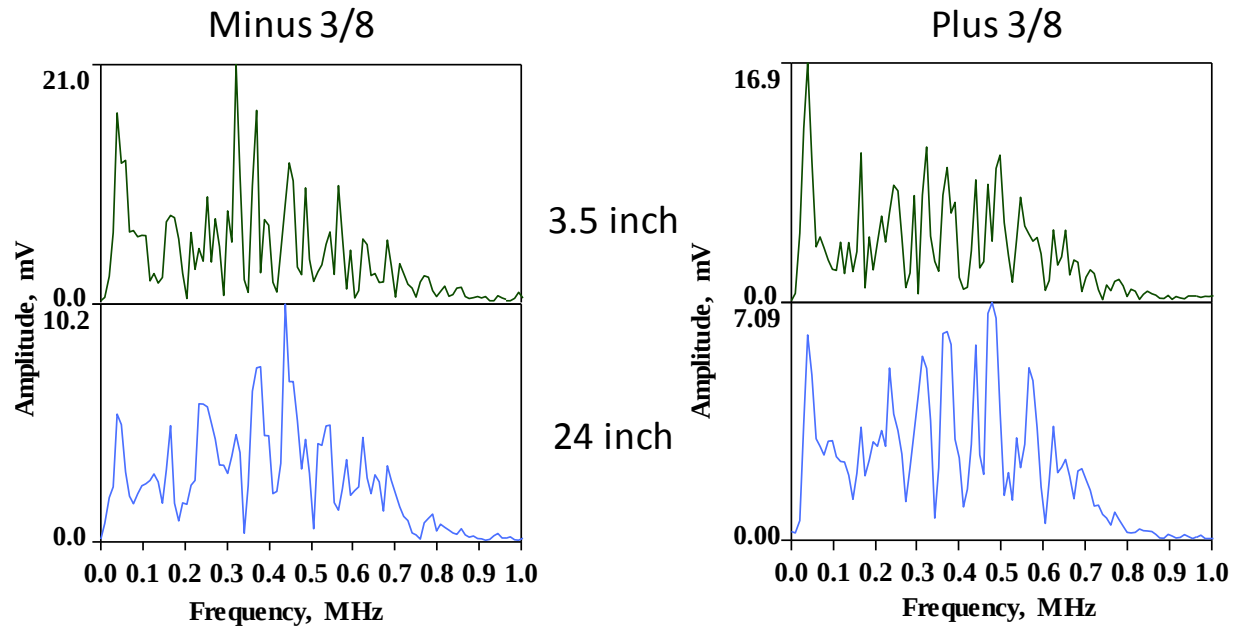


Figure 23 FFT results compared for Mist sensor on 24-inch versus 3.5-inch plates for both PLB positions

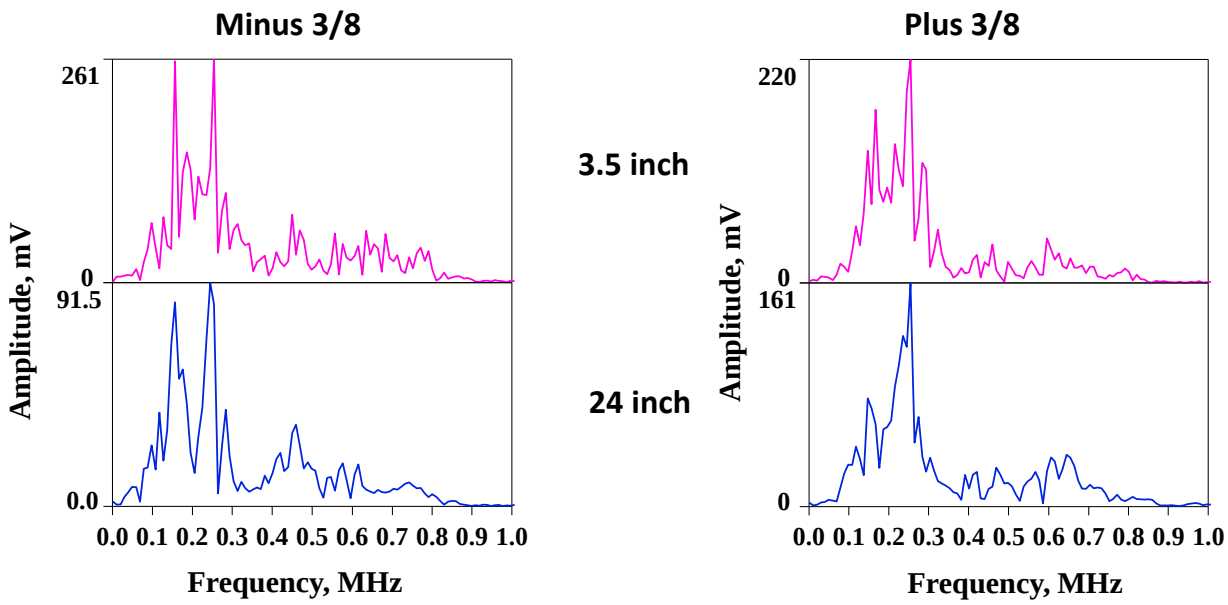


Figure 24 FFT results compared for WD sensor on 24-inch versus 3.5-inch plates for both PLB positions

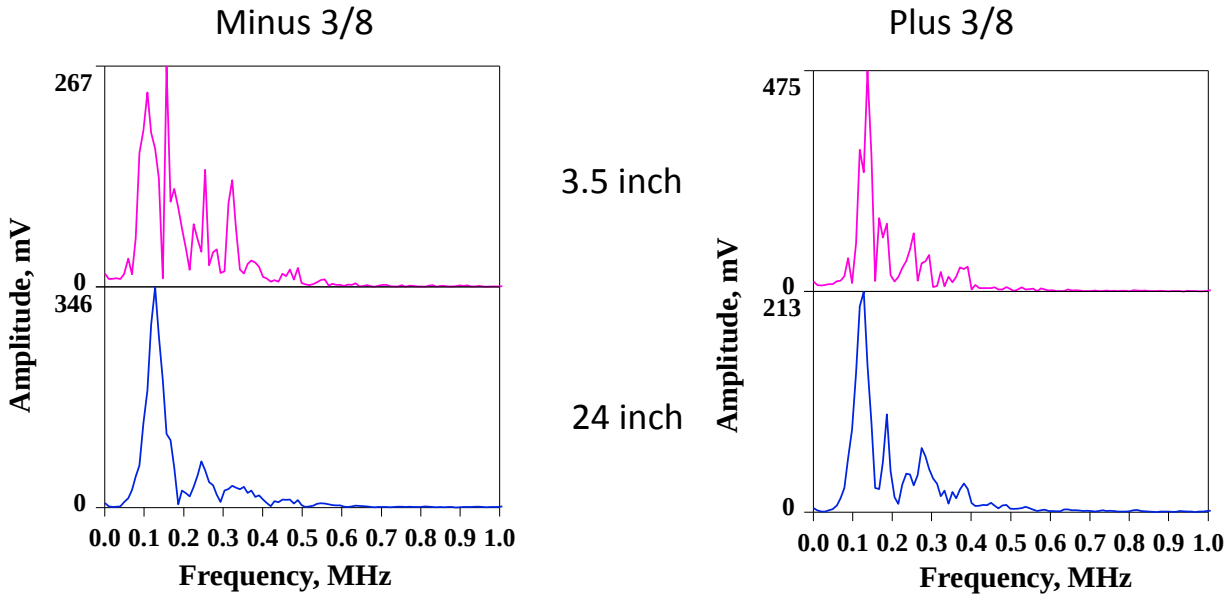


Figure 25 FFT results compared for R15 sensor on 24-inch versus 3.5-inch plates for both PLB positions

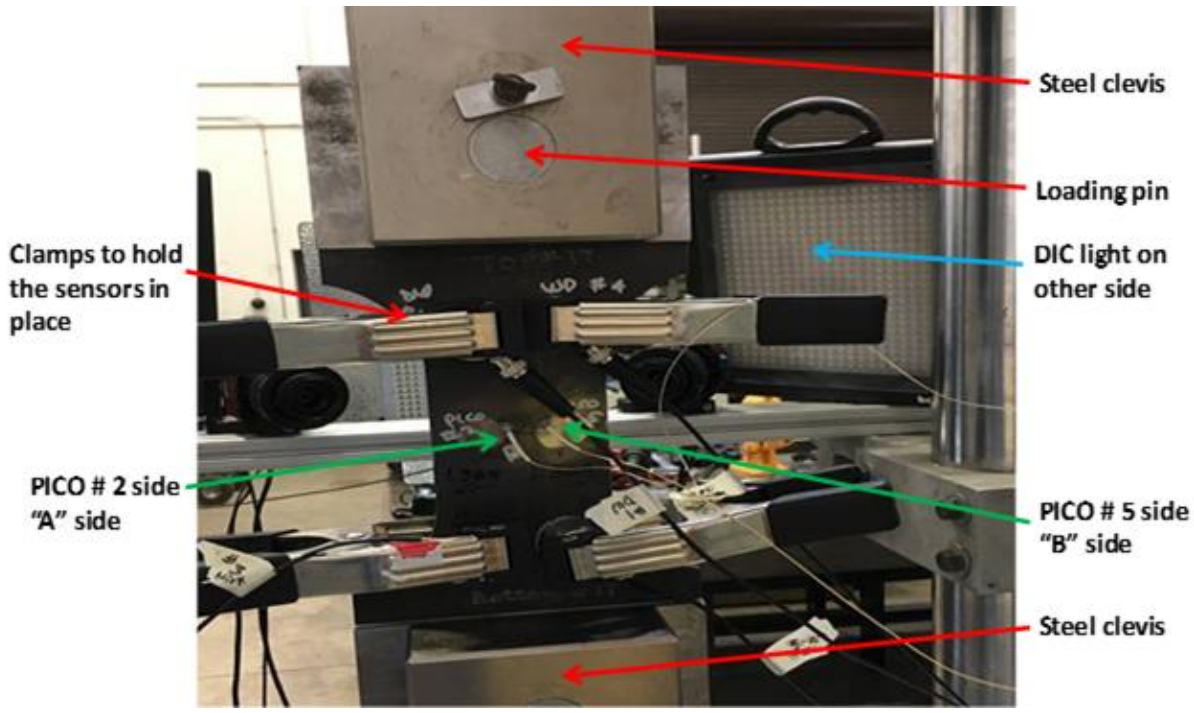


Figure 26a Instrumented tensile specimen with crack; showing sensor side

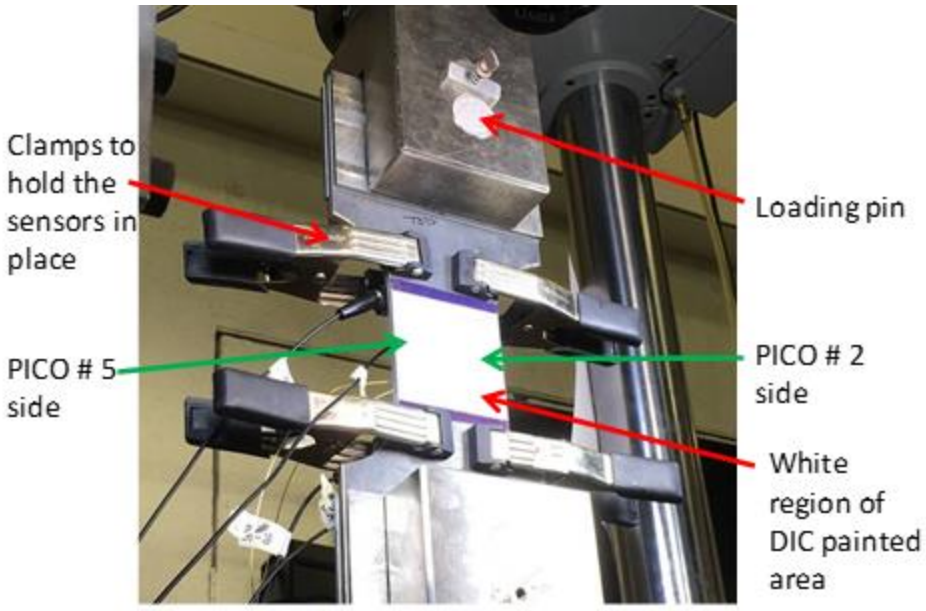


Figure 26b Instrumented tensile specimen with crack; showing side for DIC measurements

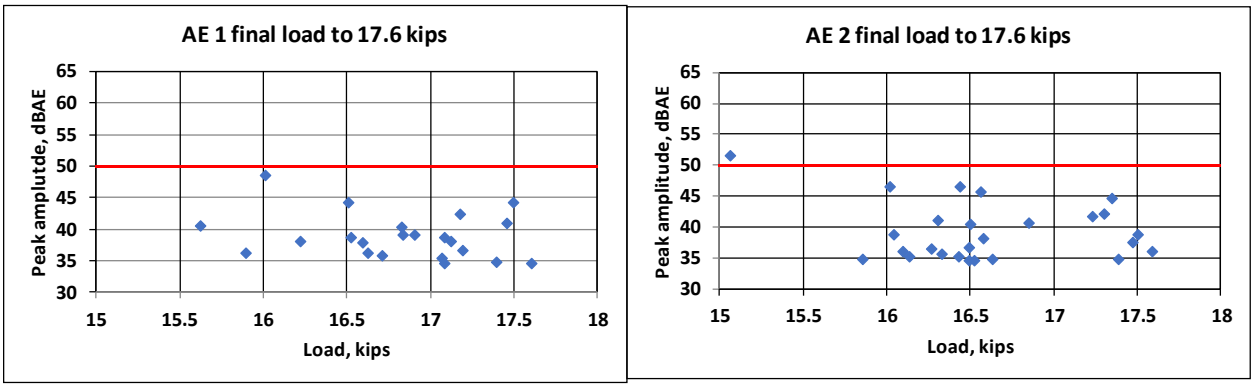


Figure 27 Peak amplitudes of crack-tip-region AE events in cracked base material from PICO sensor nearest crack tip for 10 % overload after cycling at 16 kips.

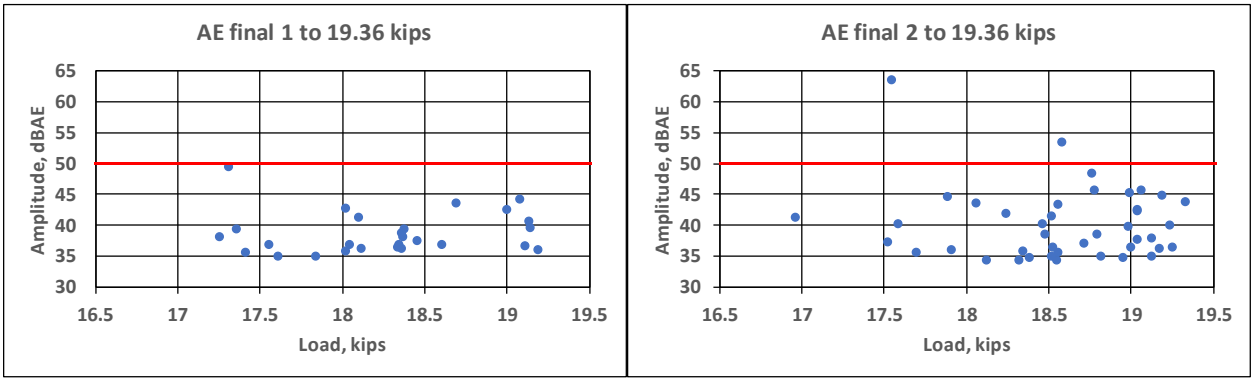


Figure 28 Peak amplitudes of crack-tip-region AE events in cracked base material from PICO sensor nearest crack tip for 10 % overload after cycling at 17.6 kips

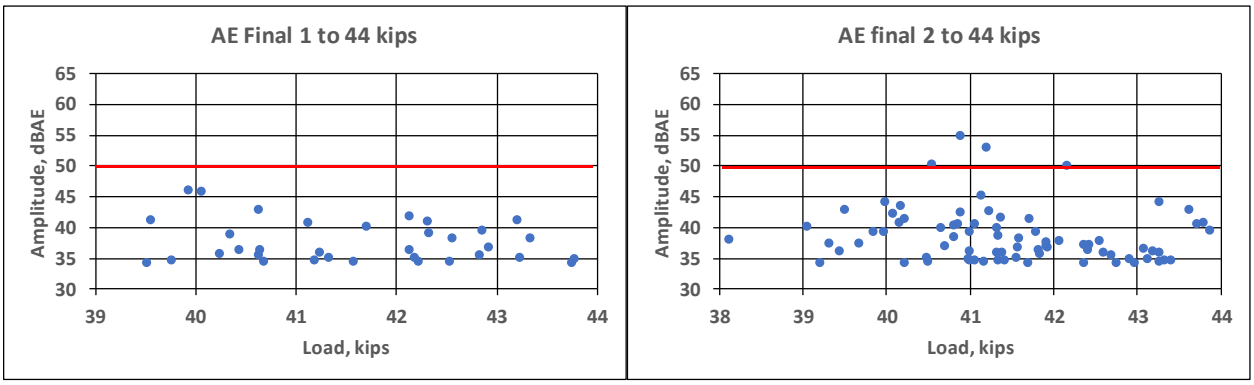


Figure 29 Peak amplitudes of crack-tip-region AE events in cracked base material from PICO sensor nearest crack tip for 10 % overload after cycling at 40 kips

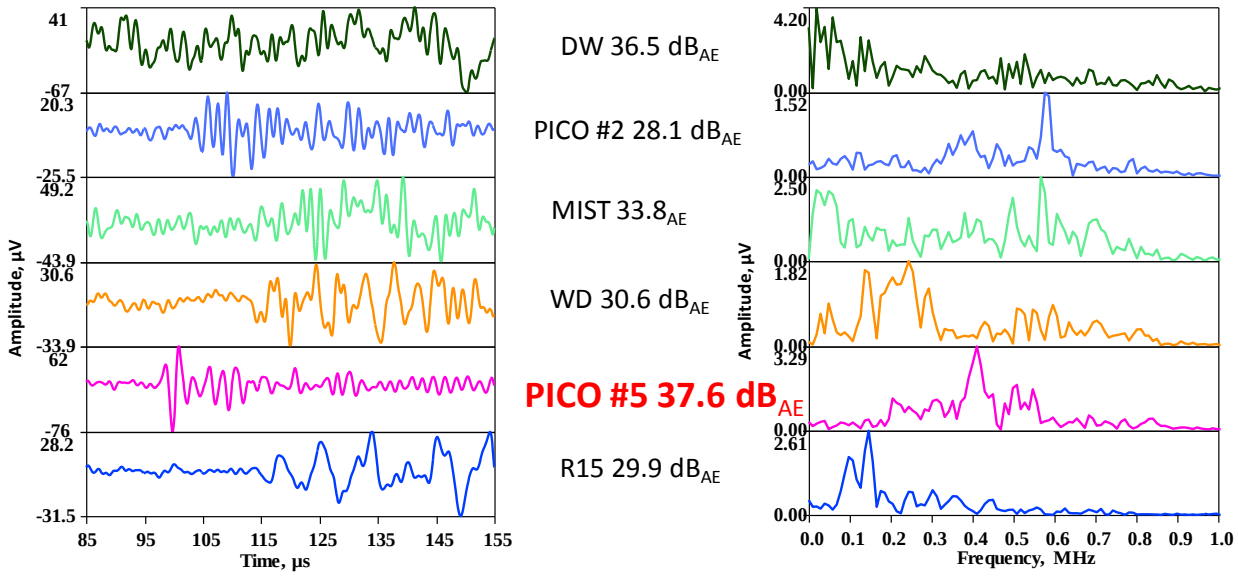


Figure 30 Signals, LP 800 kHz, from all six sensors along with their respective FFT results for a lower peak amplitude event in cracked base material as measured by PICO #5 at 37. 6 dB_{AE}. Peak amplitudes of each sensor shown

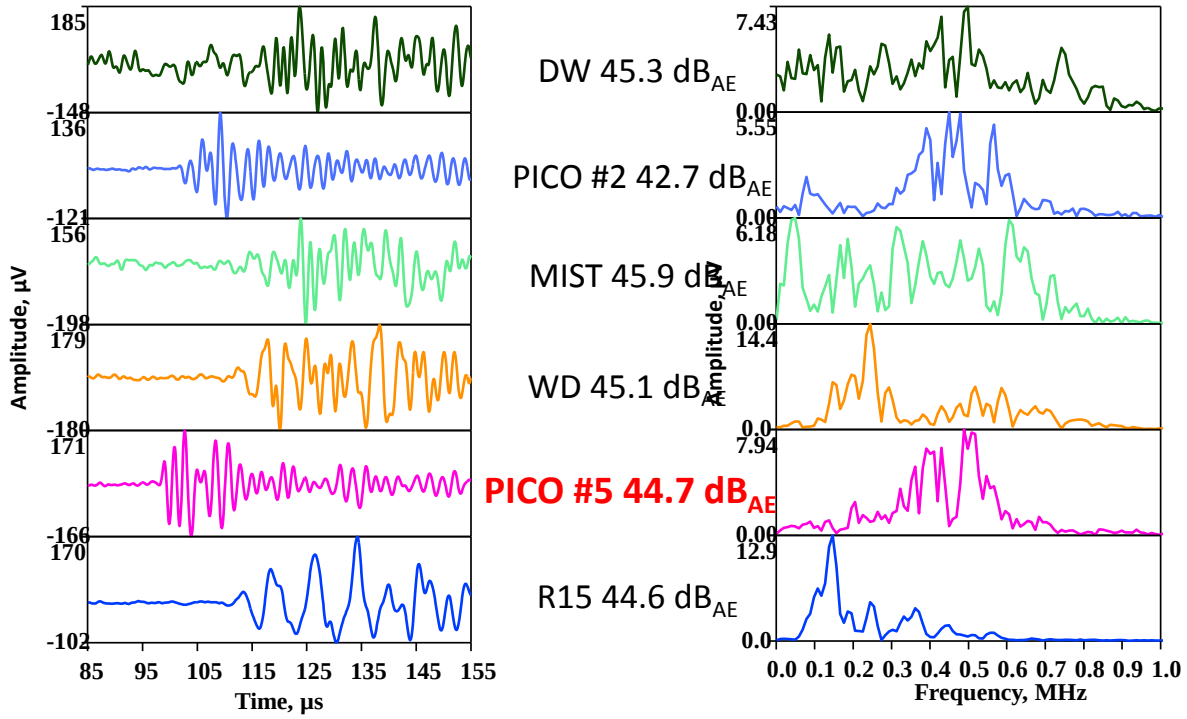


Figure 31 Signals, LP 800 kHz, from all six sensors along with their respective FFT results for a lower peak amplitude event in cracked base material as measured by PICO #5 at 44.7 dB_{AE}. Peak amplitudes of each sensor shown

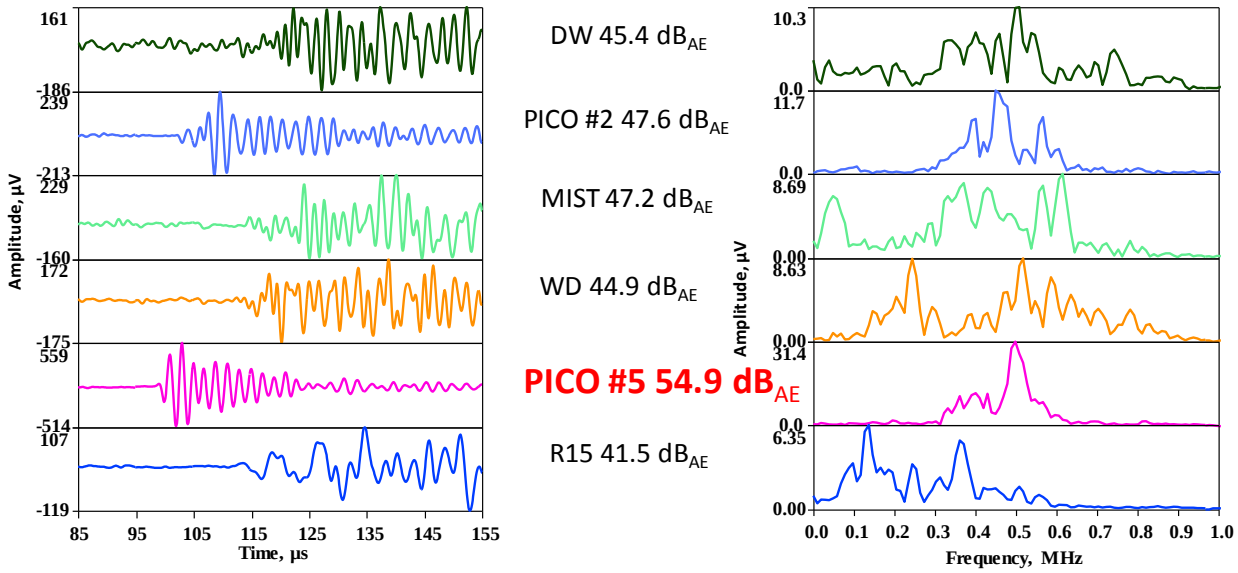


Figure 32 Signals, LP 800 kHz, from all six sensors along with their respective FFT results for a larger peak amplitude event in cracked base material as measured by PICO #5 at 54.9 dB_{AE}. Peak amplitudes of each sensor shown

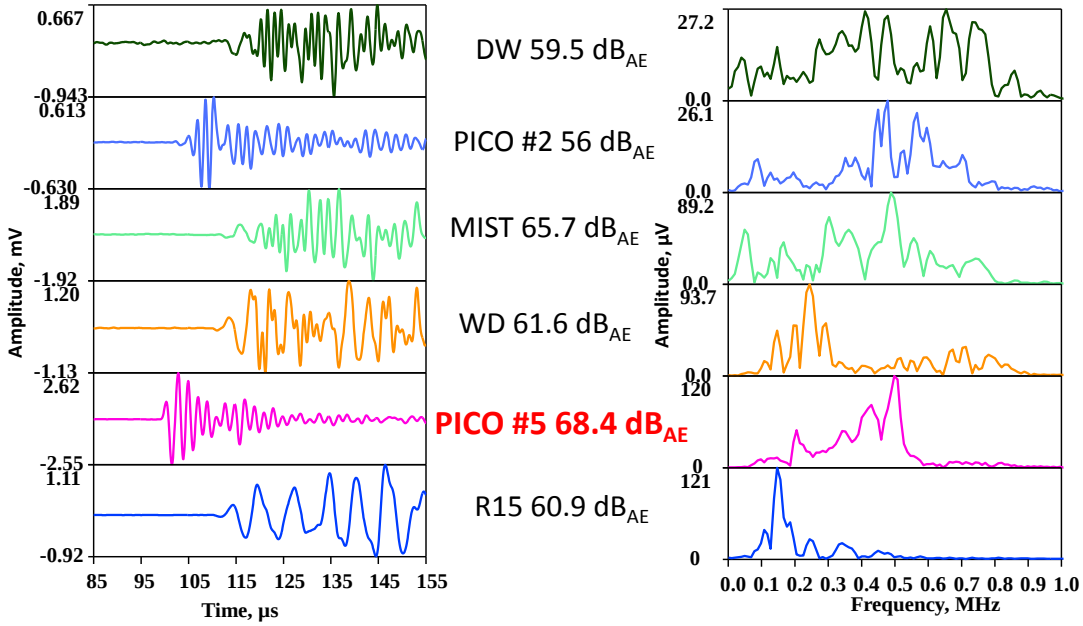


Figure 33 Signals, LP 800 kHz, from all six sensors along with their respective FFT results for a larger peak amplitude event in cracked base material as measured by PICO #5 at 68.4 dB_{AE}. Peak amplitudes of each sensor shown

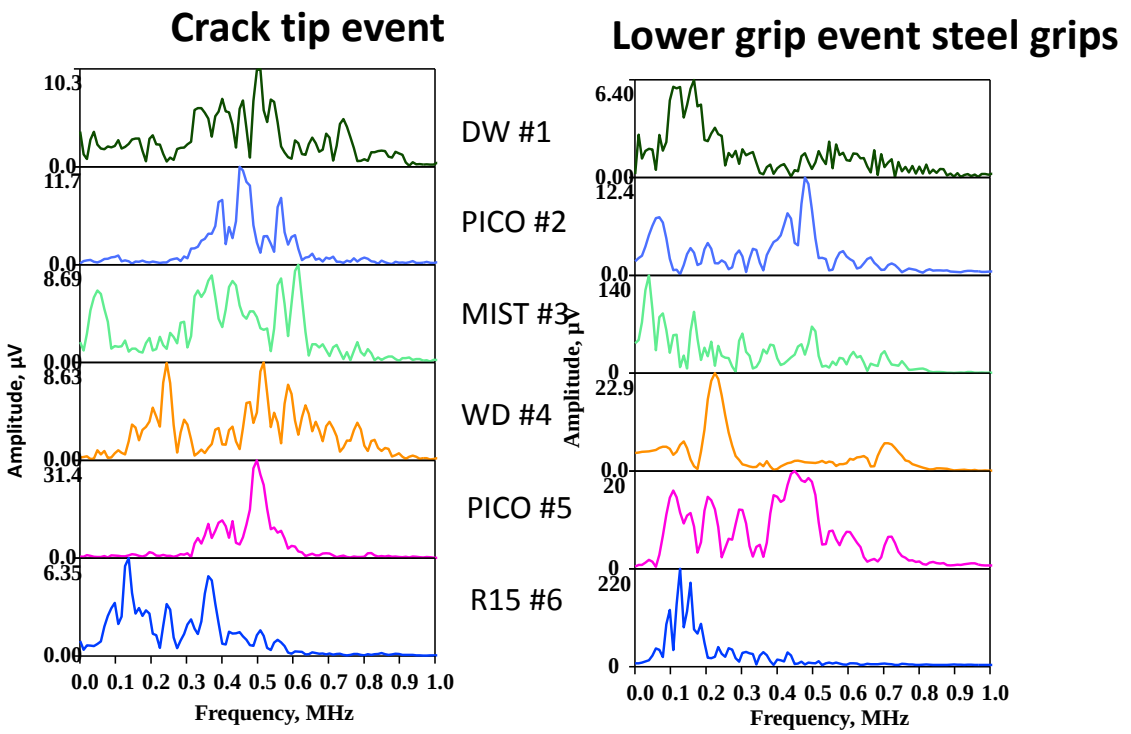


Figure 34 Comparison of FFT results from grip noise AE event versus the crack-tip region AE event of figure 32 from base material

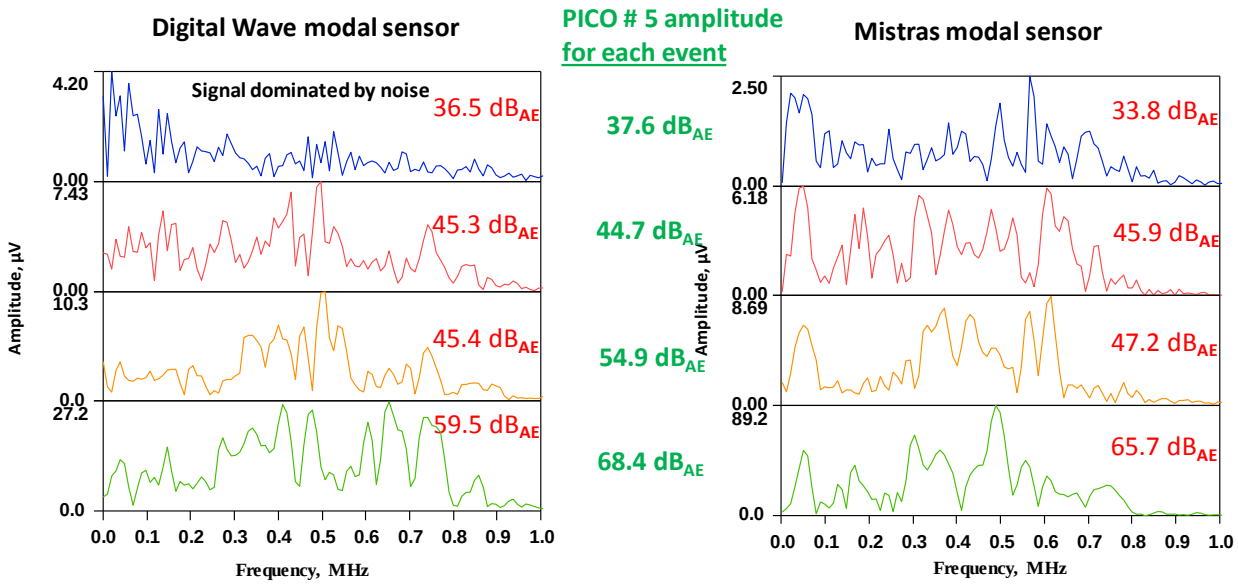


Figure 35 For the two modal sensors, comparison of FFT results as the AE event amplitude in base material changes (measured by PICO #5 sensor). Peak amplitudes for the modal sensors shown for each case

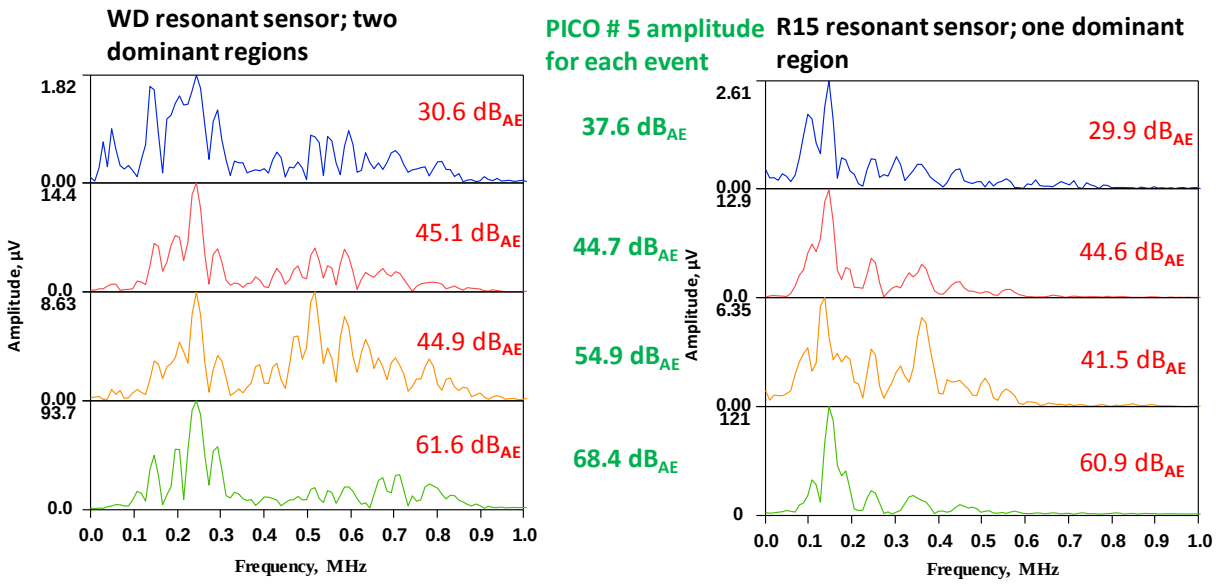


Figure 36 For the two resonant sensors, comparison of FFT results as the AE event amplitude in base material changes (measured by PICO #5 sensor). Peak amplitudes for the modal sensors shown for each case

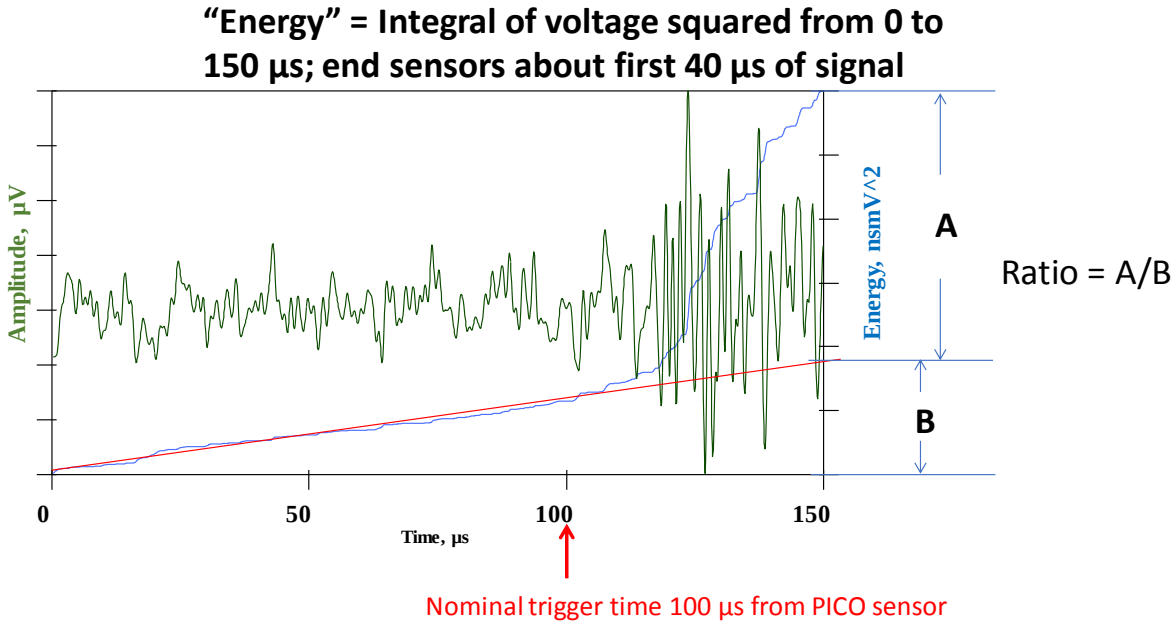


Figure 37 Example of calculation of ratio of "energy" for initial portion of AE event versus background noise

Sensor	Typical average peak amplitude, dB_{AE}
Digital Wave Modal # 1	79.6
PICO # 2	71.4
Mistras Modal # 3	80.5
Mistras WD # 4	82.7
PICO # 5	76.8
Mistras R15 #6	81.3

Summary 76 to 83 dB_{AE}, ignoring less sensitive PICO #2

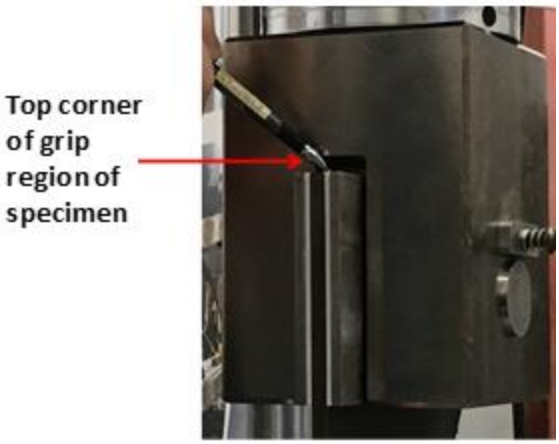


Figure 38 PLB location on tensile specimen and typical peak amplitudes with base material specimens

Loading 10 % above cycling at 16 kips:

AE final 1 (22 events)

a) Max. amplitude of a PICO sensor = 48.5 dB_{AE}
b) This event amplitude of non-PICO sensors
   i. DW = 42.3 dB_{AE}
   ii. MIST = 46.3 dB_{AE}
   iii. WD = 38.9 dB_{AE}
   iv. R15 = 39.9 dB_{AE}

AE final 2 (27 events)

a) Max. amplitude a PICO sensor = 51.5 dB_{AE}
b) This event amplitude of non-PICO sensors
   i. DW = 48.1 dB_{AE}
   ii. MIST = 47.5 dB_{AE}
   iii. WD = 44.7 dB_{AE}
   iv. R15 = 42.8 dB_{AE}

Loading 10 % above cycling at 17.360 kips:

AE final 1 (27 events)

a) Max. amplitude of a PICO sensor = 52.6 dB_{AE}
b) This event amplitude of non-PICO sensors
   i. DW = 45.6 dB_{AE}
   ii. MIST = 51.8 dB_{AE}
   iii. WD = 50.4 dB_{AE}
   iv. R15 = 45.6 dB_{AE}

AE final 2 (37 events)

a) Max. amplitude a PICO sensor = 63.6 dB_{AE}
b) This event amplitude of non-PICO sensors
   i. DW = 55.8 dB_{AE}
   ii. MIST = 58.8 dB_{AE}
   iii. WD = 54.9 dB_{AE}
   iv. R15 = 54.0 dB_{AE}

Loading 10 % above cycling at 40 kips:

AE final 1 (34 events)

a) Max. amplitude of a PICO sensor = 46.0 dB_{AE}
b) This event amplitudes of non-PICO sensors
   i. DW = 42.3 dB_{AE}
   ii. MIST = 44.3 dB_{AE}
   iii. WD = 41.5 dB_{AE}
   iv. R15 = 40.4 dB_{AE}

AE final 2 (73 events)

a) Max. amplitude of a PICO sensor = 55.0 dB_{AE}
b) This event amplitudes of non-PICO sensors
   i. DW = 51.3 dB_{AE}
   ii. MIST = 54.3 dB_{AE}
   iii. WD = 52.3 dB_{AE}
   iv. R15 = 49.8 dB_{AE}

Figure 39 Data showing the maximum peak amplitudes (for cracked base material events) of the PICO and end sensors are considerably lower than the range of PLB peak amplitudes of 76 to 83 dB_{AE}

Sensor	DW	MIST	WD	R15
Minimum, dB	- 0.5	- 3.6	1.6	1.3
Maximum, dB	10.5	8	13.7	15.3
Std. Dev., dB	2.7	2.9	2.9	3.5
Ave., dB	5.4	2.7	6.3	7.9

Figure 40 Statistical data of peak amplitude of PICO # 5 sensor minus each end sensor for 42 crack tip region events in base material. Shows the maximum peak amplitudes of the PICO sensor # 5 is nearly always larger relative to the end sensor amplitudes and at worst is a small amount less for DW and Mist (negative values)

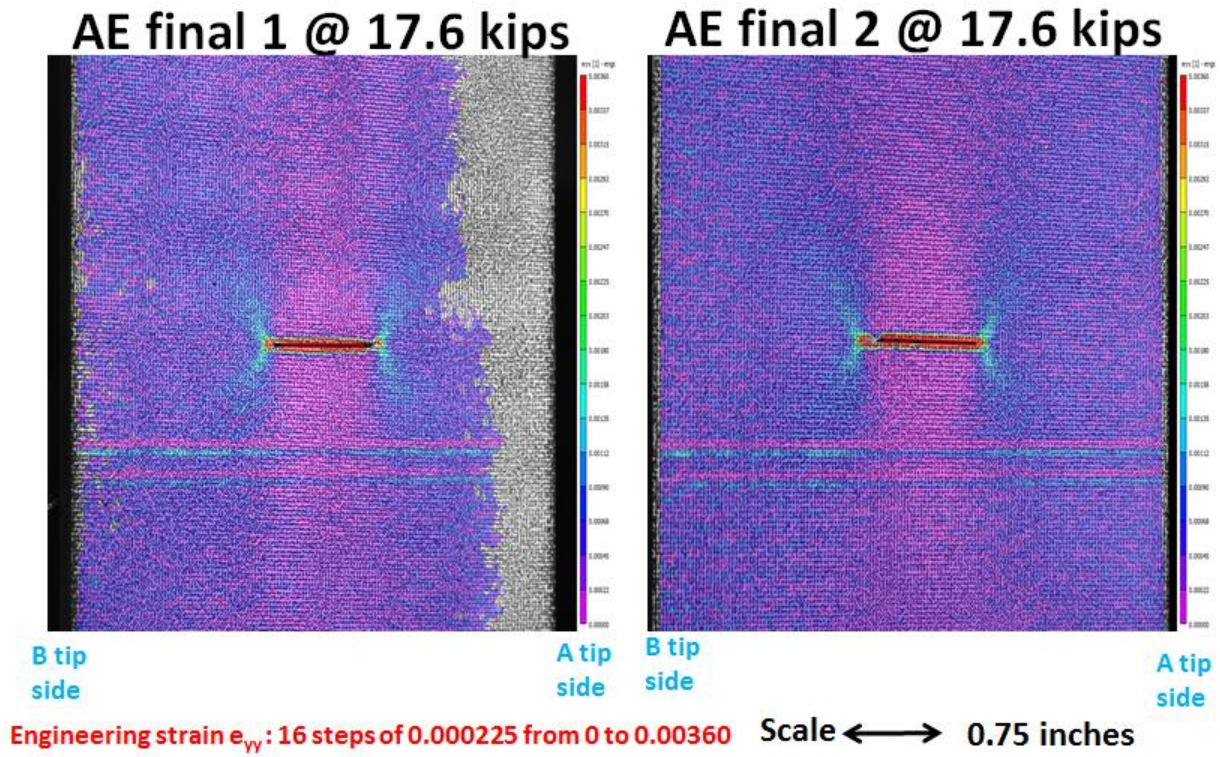


Figure 41 DIC results for AE final 1 and 2 at lower load of 17.6 kips. Note horizontal lines are camera artifacts and not material responses. Strain scale same as figure 42

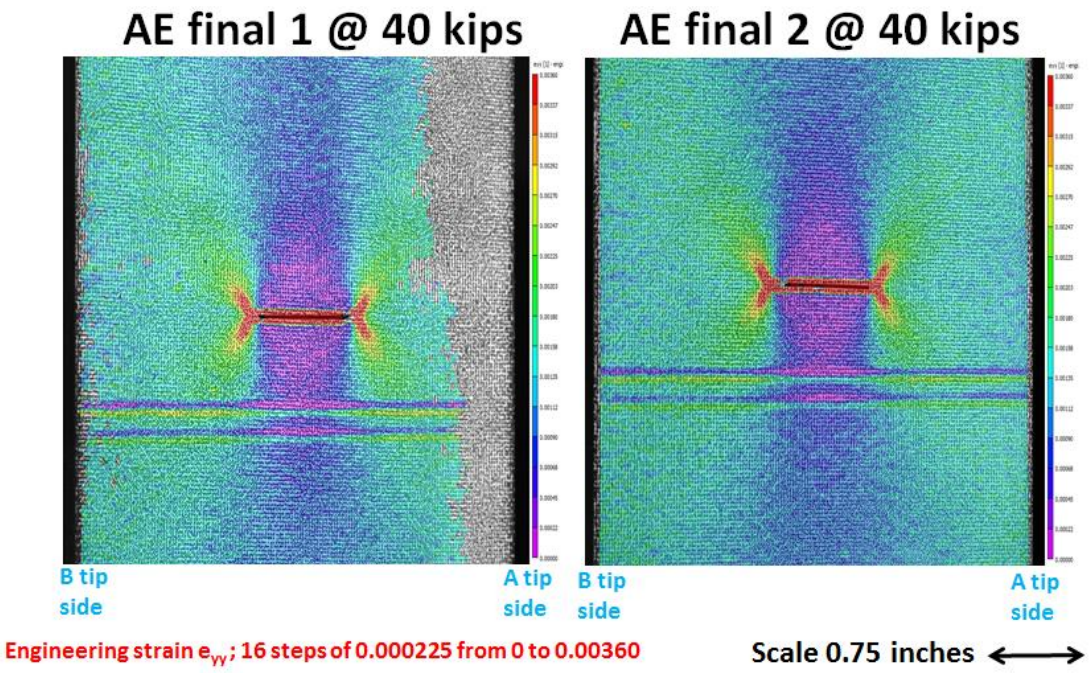


Figure 42 DIC results for AE final 1 and 2 at higher load of 40 kips. Note horizontal lines are camera artifacts and not material responses. Strain scale same as figure 41

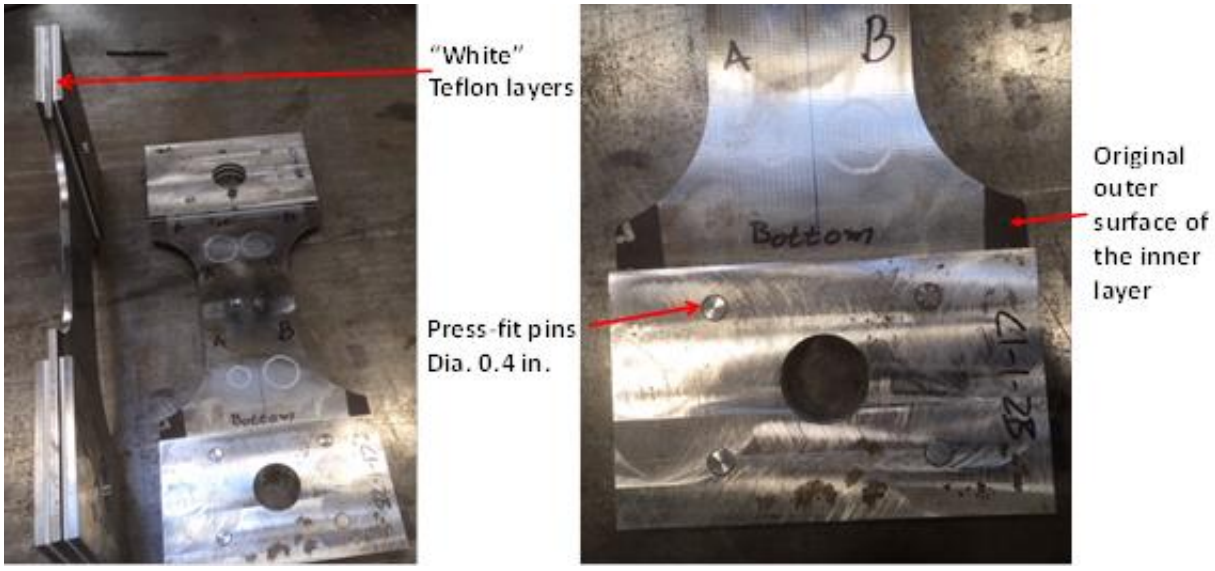


Figure 43 Photos of weld samples showing the specimen design, with Teflon™ layers, and the original outer surface of the inner layer of vessel 023 in the grip region

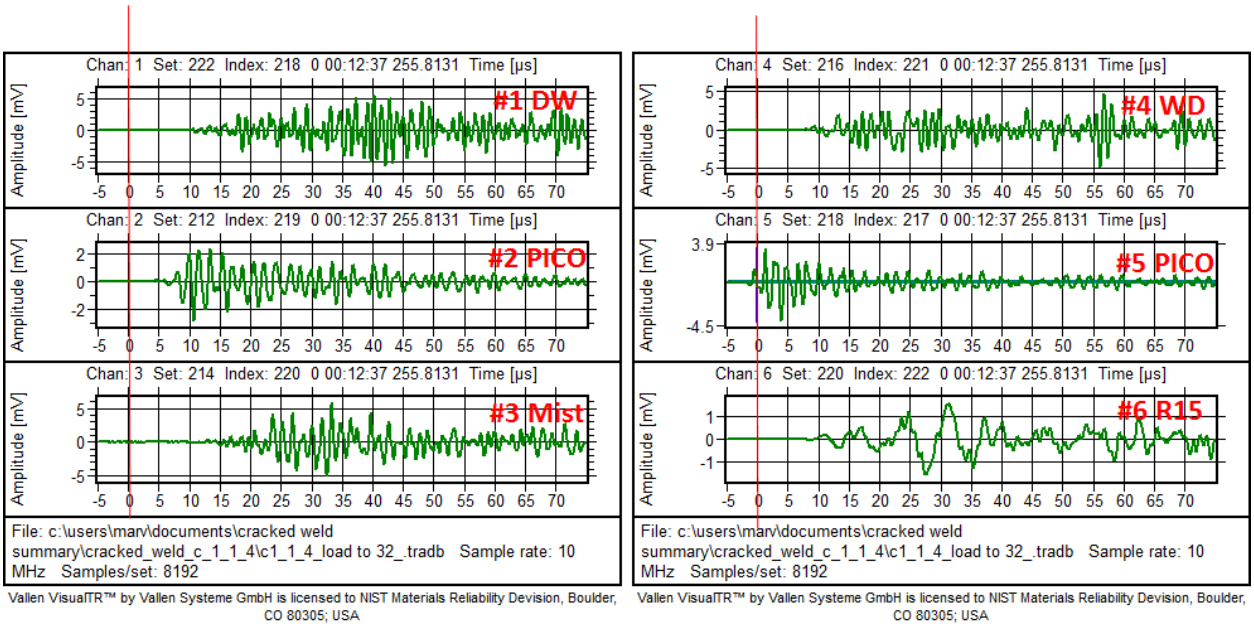


Figure 44 Illustration of use of arrival sequence at the different sensors to identify a crack tip region event in weld material, in this case from the tip near PICO # 5. Vertical red lines mark zero trigger time. Horizontal scale in µs

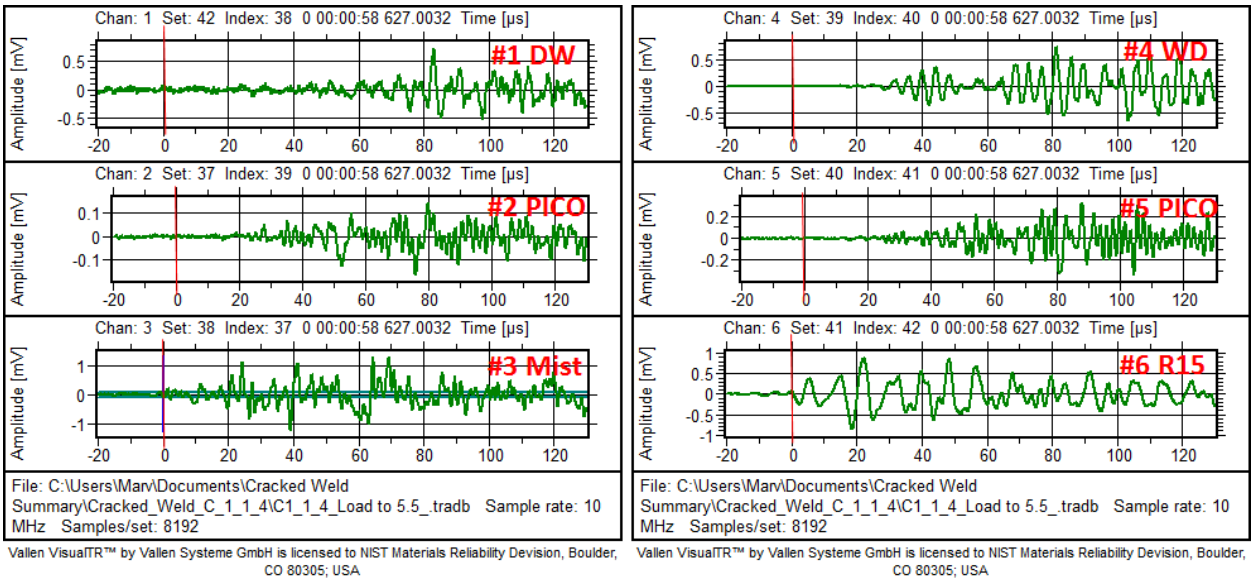
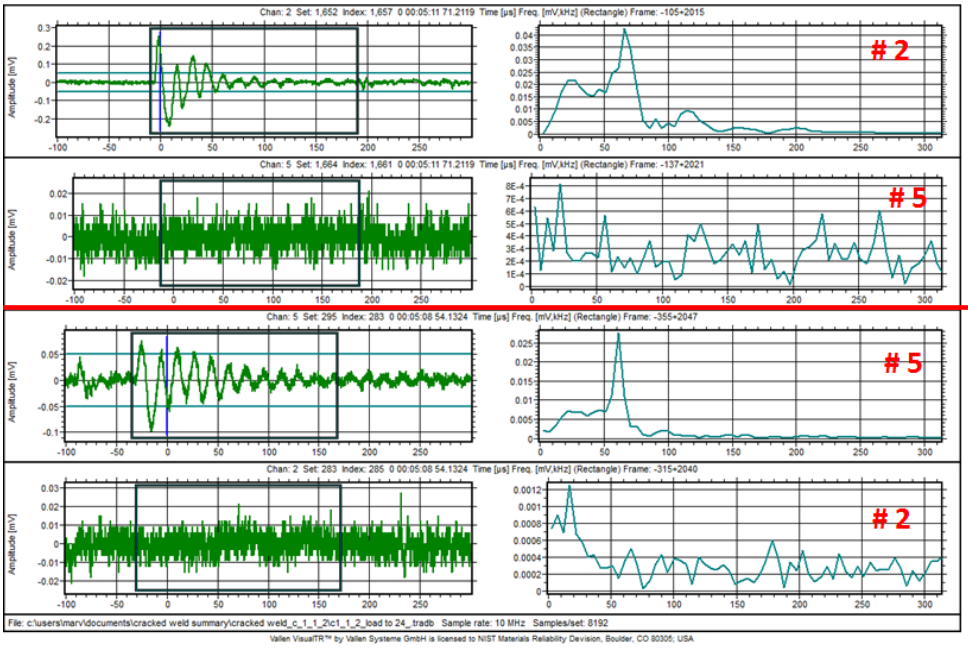


Figure 45 Arrival sequence for a bottom grip source in weld material sample, Mist and R15 first arrivals (note offsets of 0 µs time in figure, could not be corrected). Vertical red lines mark zero trigger time. Horizontal scale in µs



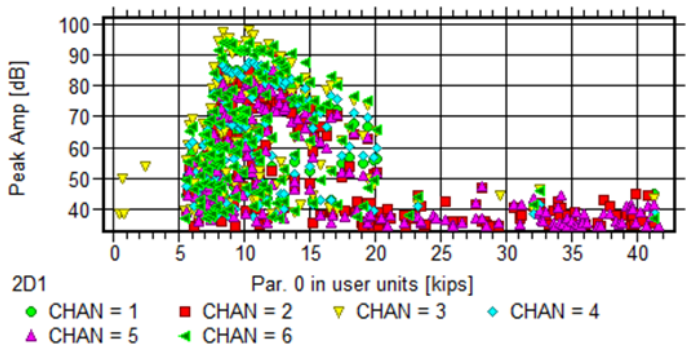
Event 1657 PICO # 2, 47.2 dB_{AE}, at 6.352 kips; peak frequency at 65 kHz

Event did not propagate to PICO # 5

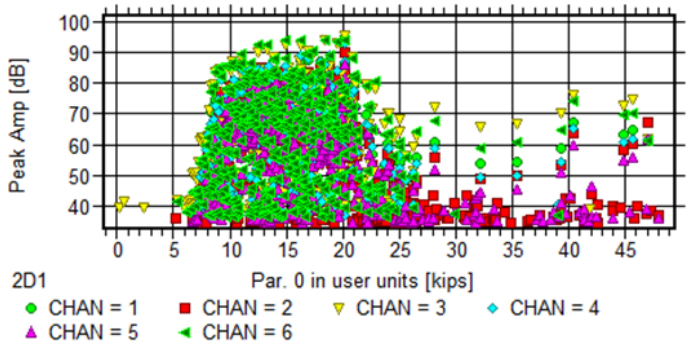
Event 283 PICO # 5, 37.5 dB_{AE}, at 6.291 kips; peak frequency at 61 kHz

Event did not propagate to PICO # 2

Figure 46 Typical extraneous noise events in weld sample C1_1_4 during loading to 24 kips. Horizontal scale in microseconds on left and kHz on right

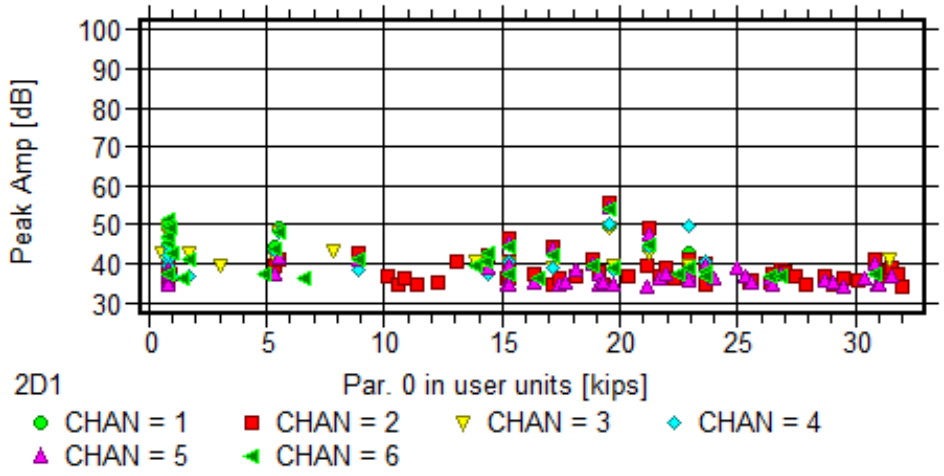


Loading to 42 kips C4_2_2 after cycling for 38,363 cycles at 16 kips peak, excess grip noise from about 5.5 kips to about 20 kips. A total of about 162 grip and tip events, on average about 1 per 4.6 seconds



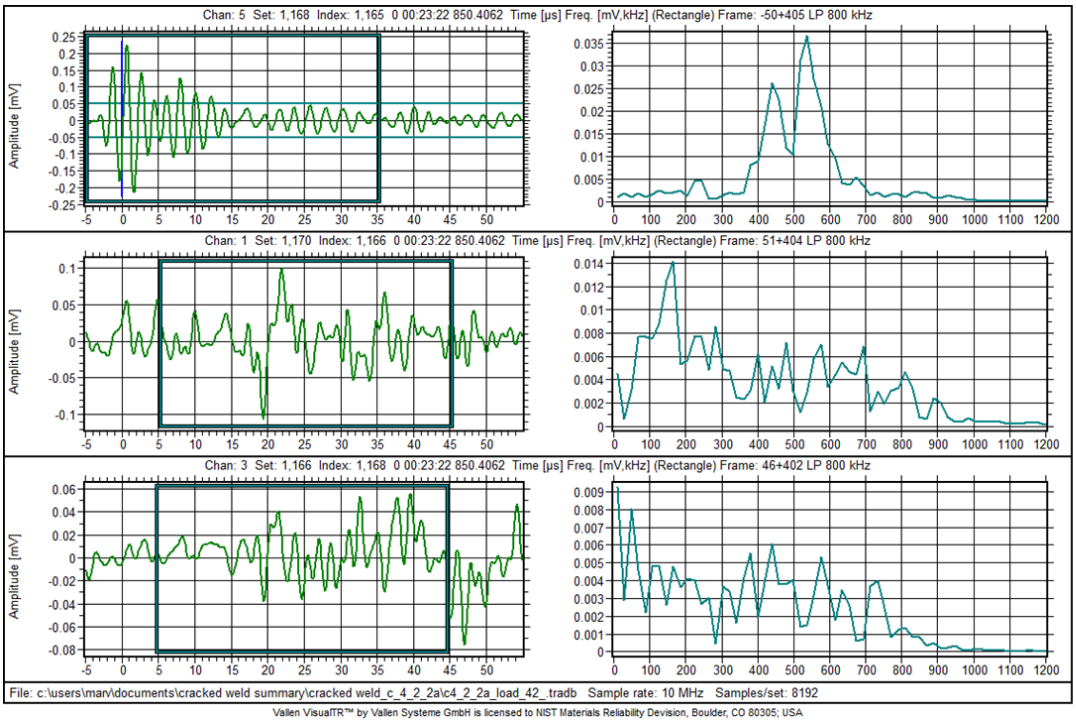
Loading to 48 kips C4_2_2 after cycling for 30,000 cycles at 21 kips peak, excess grip noise from about 6.0 kips to about 26 kips. A total of about 492 grip and tip events, on average about 1 per 2 seconds

Figure 47 Shows the large number of extraneous grip-originated events during two loadings of weld sample C4_2_2



Loading to 32 kips C4_2_2 after cycling for 102,000 cycles at 8 kips peak, no excess grip noise

Figure 48 Contrast of few events, when no extra grip generated events were present at an earlier loading of 32 kips for weld sample C4_2_2



C4_2_2,load to 42 kips, cycled at 16 kips, Evt. 1165 @ 28.201 kips, 47.6 dB_{AE}, # 5

DW channel 1

Mist channel 3

Figure 49 Tip region event (LP 800 kHz) in weld material near PICO # 5 with peak amplitude of 47.6 dB_{AE}. Peak amplitudes DW 40.8 dB_{AE} and Mist 37.4 dB_{AE}. Horizontal scale in µs

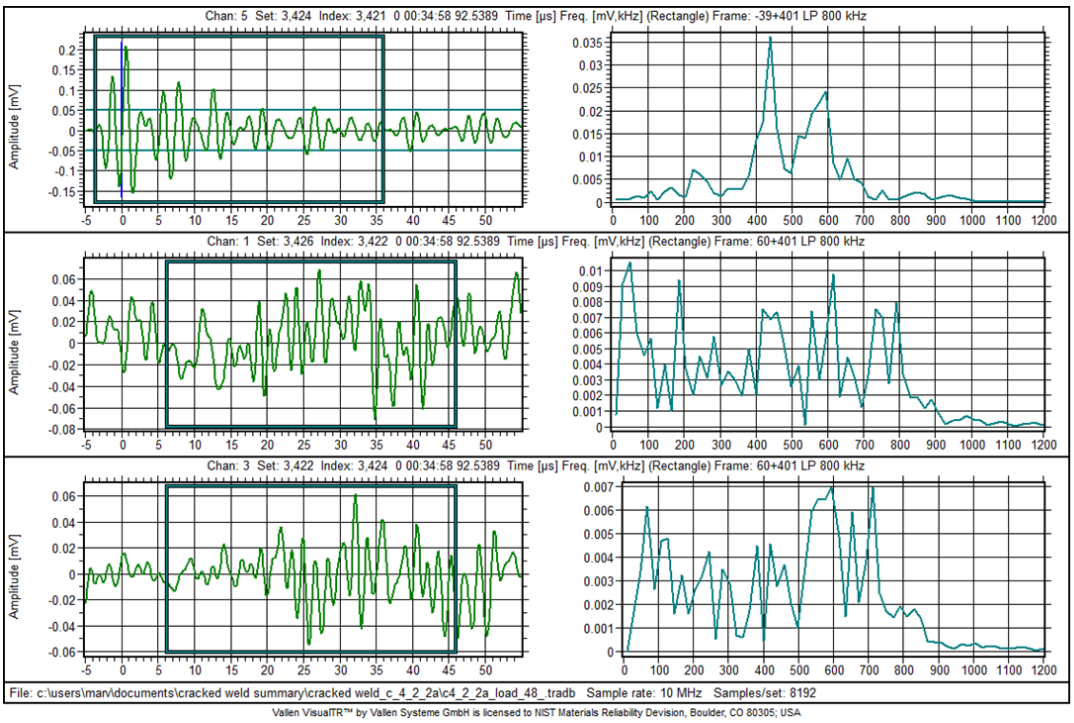


Figure 50 Tip region event (LP 800 kHz) in weld material near PICO # 5 with peak amplitude 46.6 dB_{AE}. Peak amplitudes DW 37.1 dB_{AE} and Mist 35.8 dB_{AE}. Horizontal scale in µs

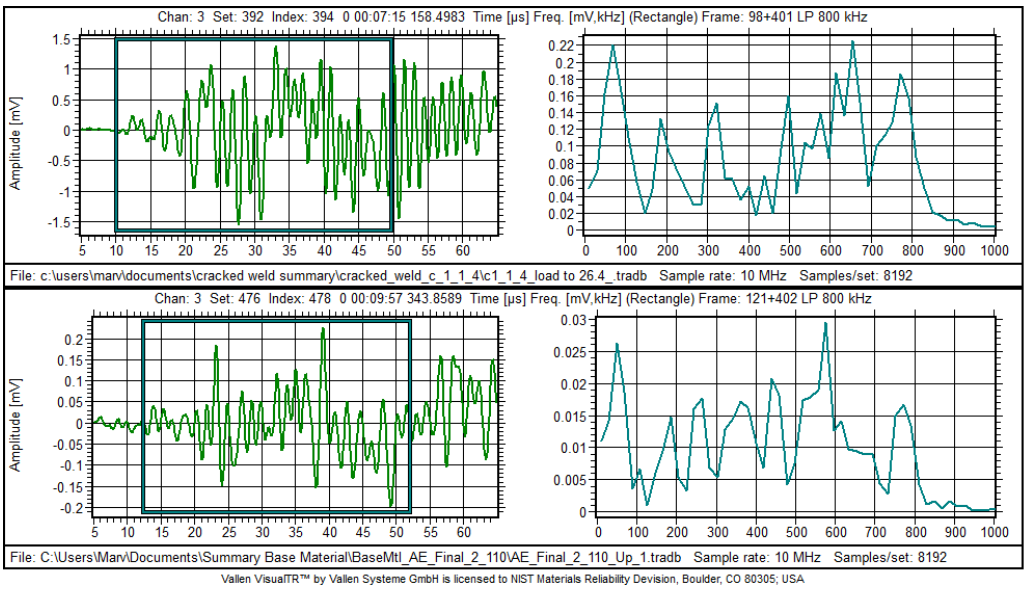
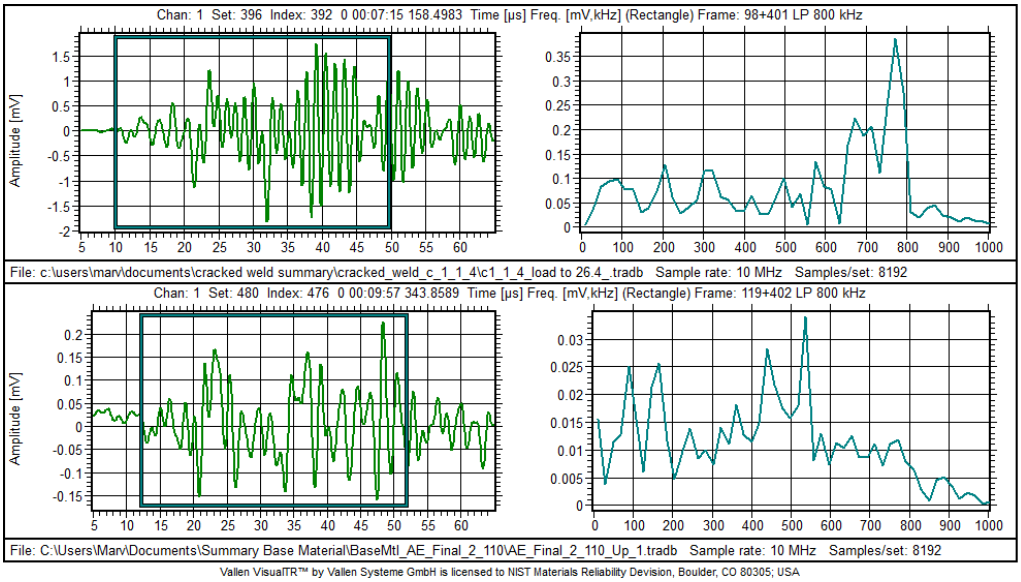


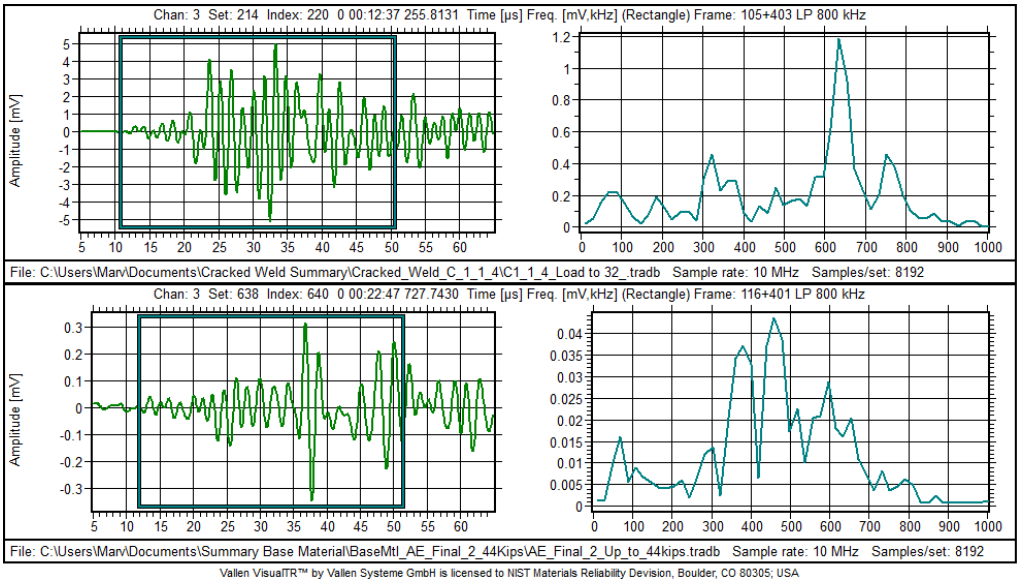
Figure 51 First set of different cracked materials with Mist sensor results (LP 800 kHz). Peak amplitudes of Mist sensors cracked weld 64.2 dB_{AE} and base material 47.5 dB_{AE}. Horizontal scale in µs on left and kHz on right



Cracked weld **C1_1_4, load to 26.4 kips, Evt. # 391 @ 12.006 kips, # 5 @ 61.8 dB_{AE}**

Cracked base material AE final 2, load to 17.6 kips, Evt. # 475 @ 15.070 kips, # 5 @ 51.5 dB_{AE}

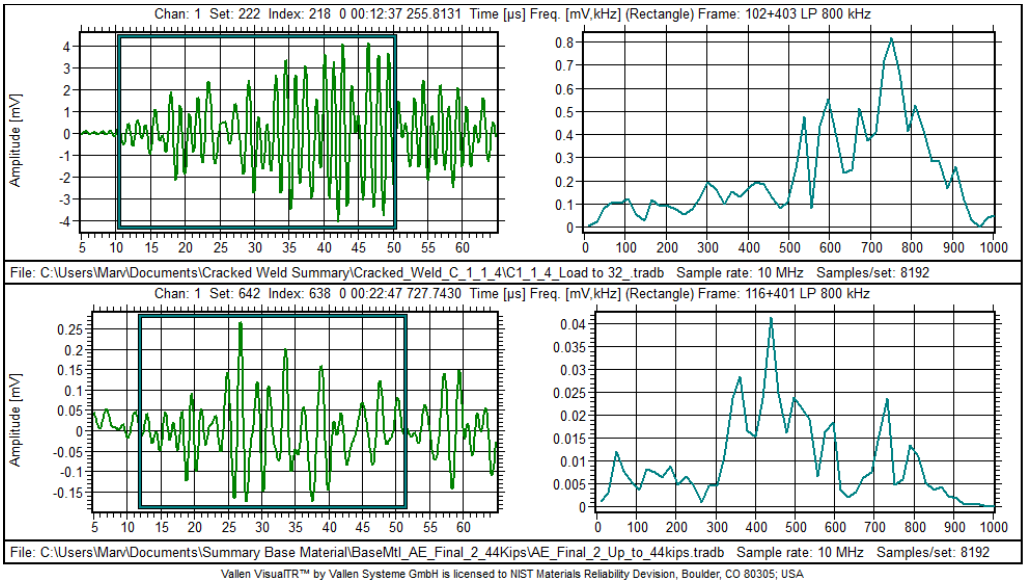
Figure 52 First set of different cracked materials with DW sensor results (LP 800 kHz). Peak amplitudes of DW sensors cracked weld 64.4 dB_{AE} and base material 47.2 dB_{AE}. Horizontal scale in µs on left and kHz on right



Cracked weld **C1_1_4, load to 32 kips, Evt. # 217 @ 26.675 kips, # 5 @ 69.4 dB_{AE}**

Cracked base material AE final 2, load to 44 kips, Evt. # 637 @ 41.888 kips, # 5 @ 53.1 dB_{AE}

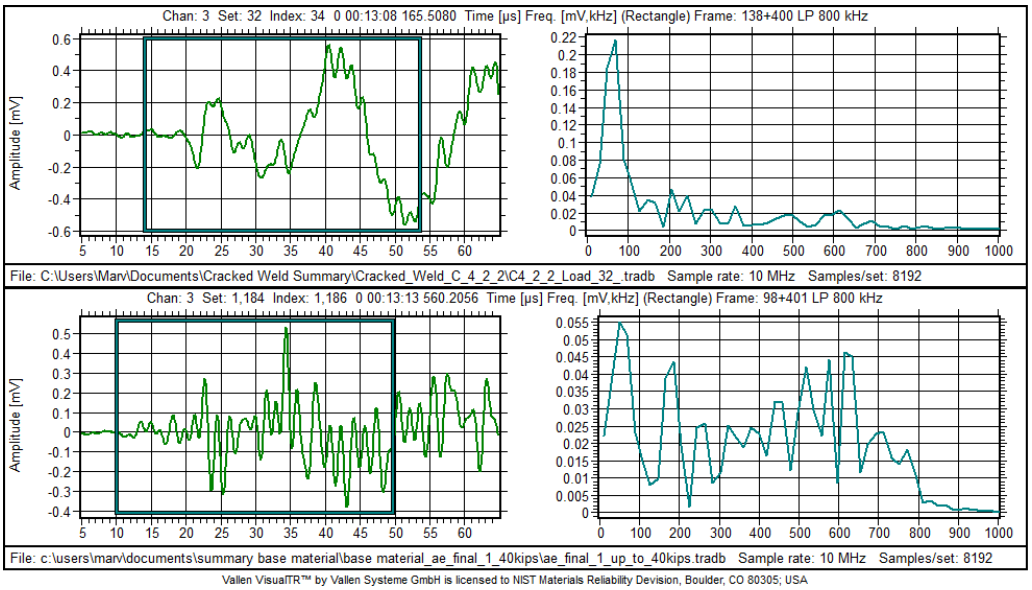
Figure 53 Second set of different cracked materials with Mist sensor results (LP 800 kHz). Peak amplitudes of Mist sensors cracked weld 74.8 dB_{AE} and base material 50.8 dB_{AE}. Horizontal scale in µs on left and kHz on right



Cracked weld C1_1_4, load to 32 kips, Evt. # 217 @ 26.675 kips, # 5 @ 69.4 dB_{AE}

Cracked base material AE final 2, load to 44 kips, Evt. # 637 @ 41.888 kips, # 5 @ 53.1 dB_{AE}

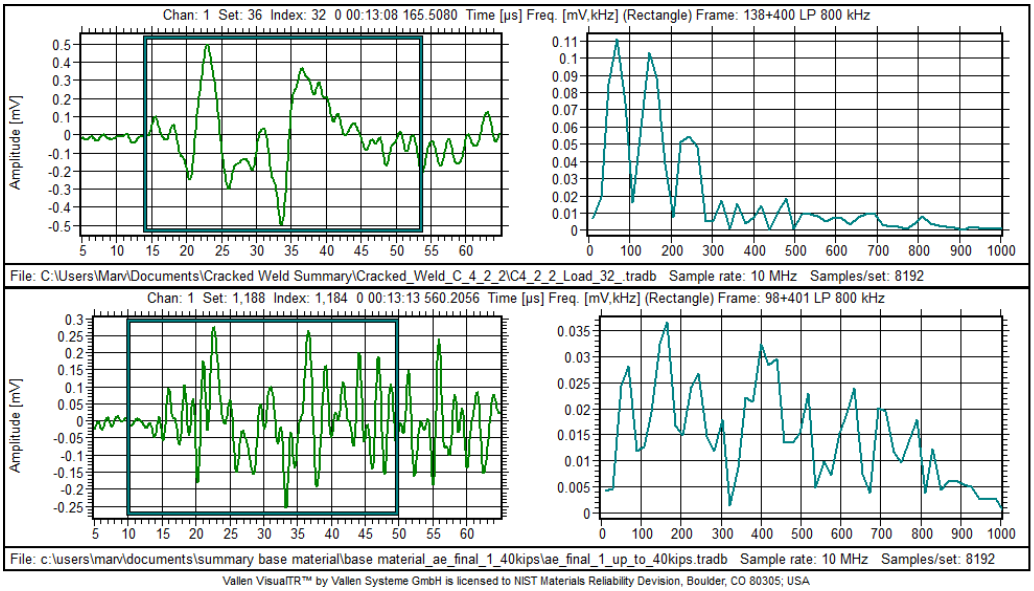
Figure 54 Second set of different cracked materials with DW sensor results (LP 800 kHz). Peak amplitudes of DW sensors cracked weld 72.6 dB_{AE} and base material 47.8 dB_{AE}. Horizontal scale in µs on left and kHz on right



Cracked weld C4_2_4, load to 32 kips, Evt. # 31 @ 15.888 kips, # 5 @ 58.2 dB_{AE}

Cracked base material AE final 1, load to 40 kips, Evt. # 1183 @ 23.952 kips, # 5 @ 54.5 dB_{AE}

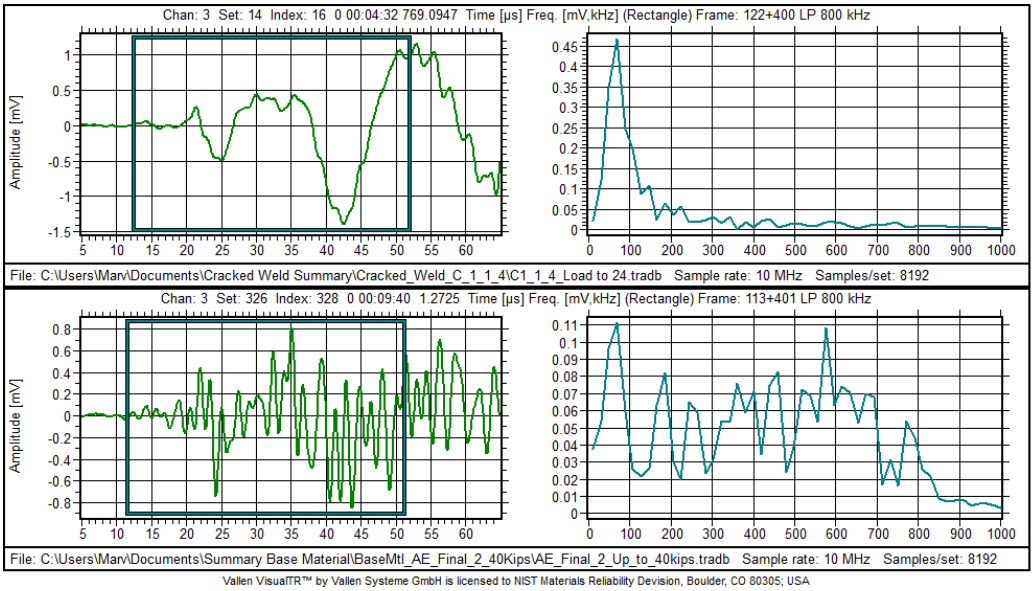
Figure 55 Third set of different cracked materials with Mist sensor results (LP 800 kHz). Peak amplitudes of Mist sensors cracked weld 53.0 dB_{AE} and base material 52.2 dB_{AE}. Horizontal scale in µs on left and kHz on right



Cracked weld C4_2_4, load to 32 kips, Evt. # 31 @ 15.888 kips, # 5 @ 58.2 dB_{AE}

Cracked base material AE final 1, load to 40 kips, Evt. # 1183 @ 23.952 kips, # 5 @ 54.5 dB_{AE}

Figure 56 Third set of different cracked materials with DW sensor results (LP 800 kHz). Peak amplitudes of DW sensors cracked weld 51.8 dB_{AE} and base material 50.1 dB_{AE}. Horizontal scale in µs on left and kHz on right



Cracked weld C1_1_4, load to 24 kips, Evt. # 13 @ 8.319 kips, # 5 @ 62.0 dB_{AE}

Cracked base material AE final 2, load to 40 kips, Evt. # 325 @ 17.545 kips, # 5 @ 63.6 dB_{AE}

Figure 57 Fourth set of different cracked materials with Mist sensor results (LP 800 kHz). Peak amplitudes of Mist sensors cracked weld 58.6 dB_{AE} and base material 58.8 dB_{AE}. Horizontal scale in µs on left and kHz on right

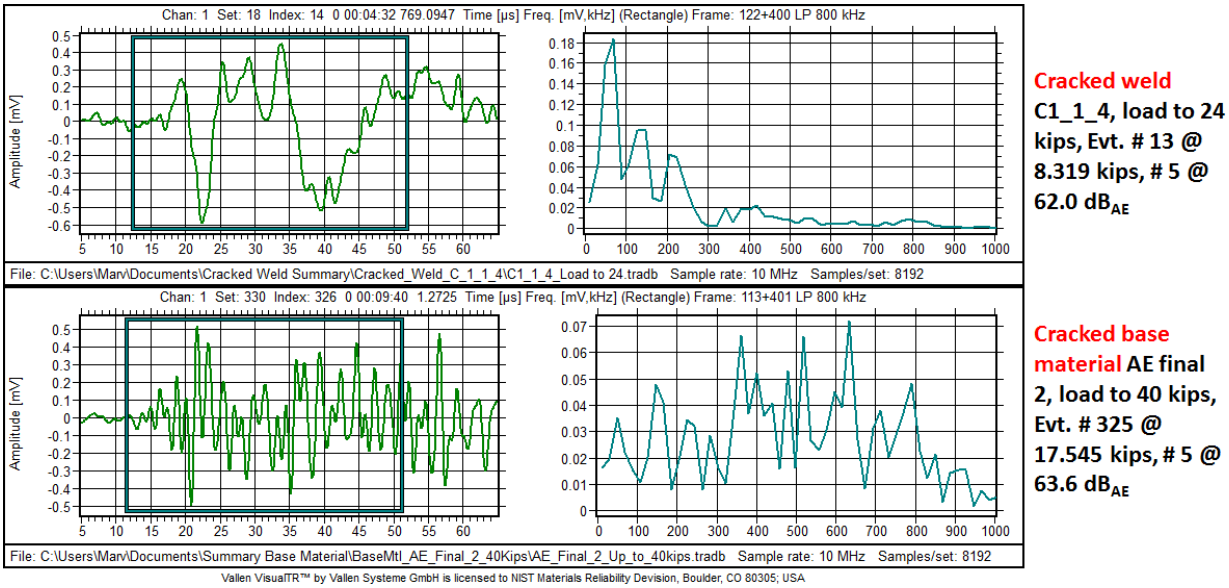


Figure 58 Fourth set of different cracked materials with DW sensor results (LP 800 kHz). Peak amplitudes of DW sensors cracked weld 54.6 dB_{AE} and base material 55.8 dB_{AE}. Horizontal scale in µs on left and kHz on right

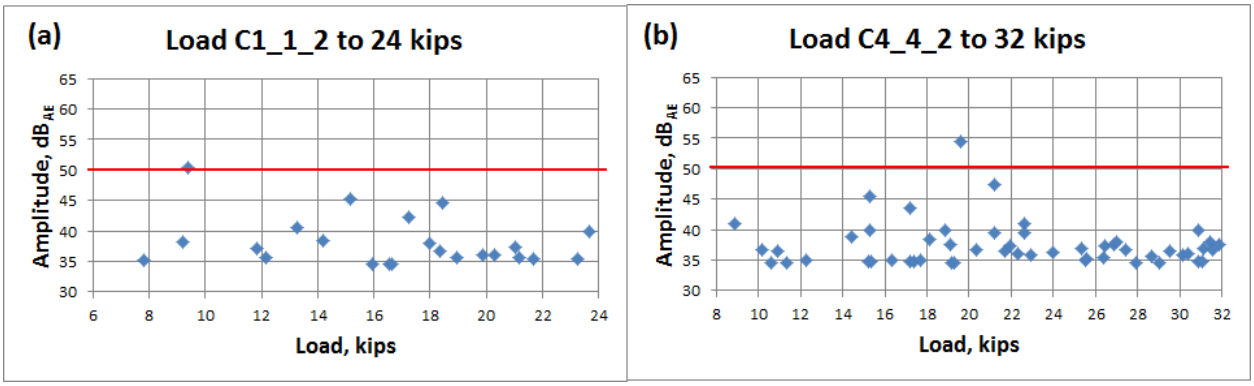


Figure 59 Amplitude versus load for tip events in weld sample (a) C1_1_2 and (b) C4_4_2 with no systematic increase in peak amplitude with load increases

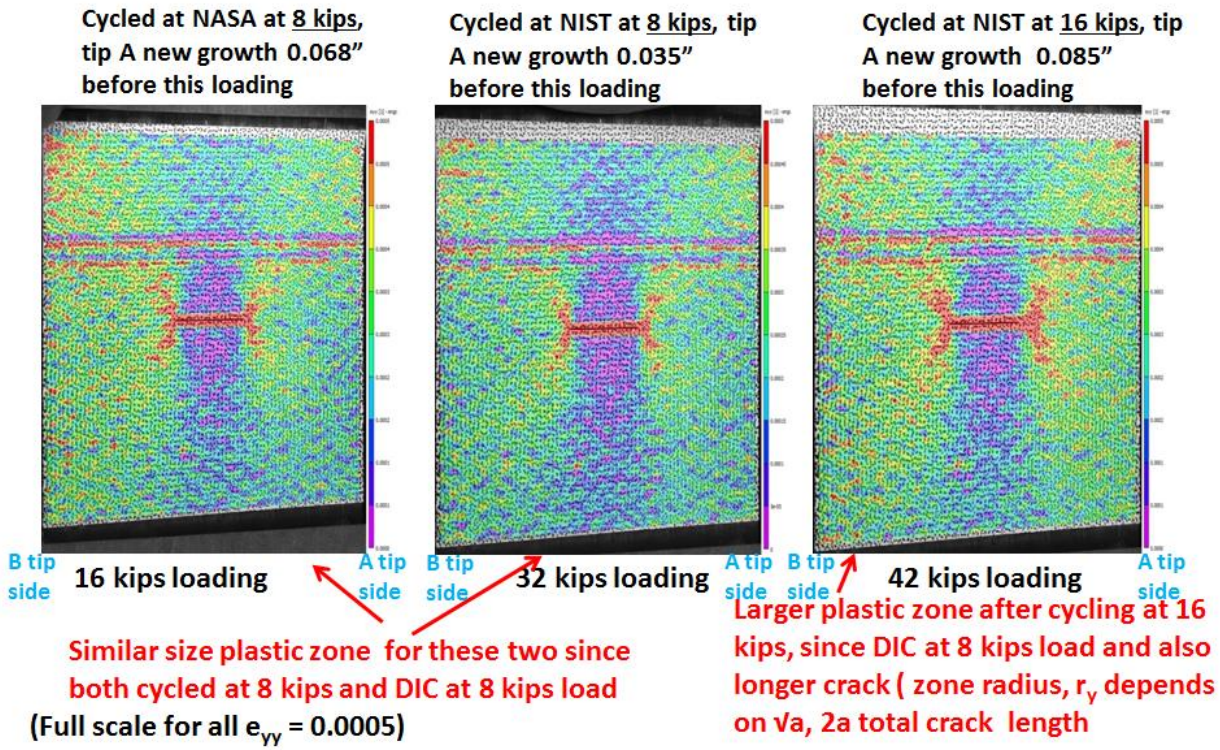


Figure 60 Weld sample C4_2_2 shows change in plastic zone size when the cycling level was increased from 8 to 16 kips. Horizontal lines are camera artifacts and not material responses

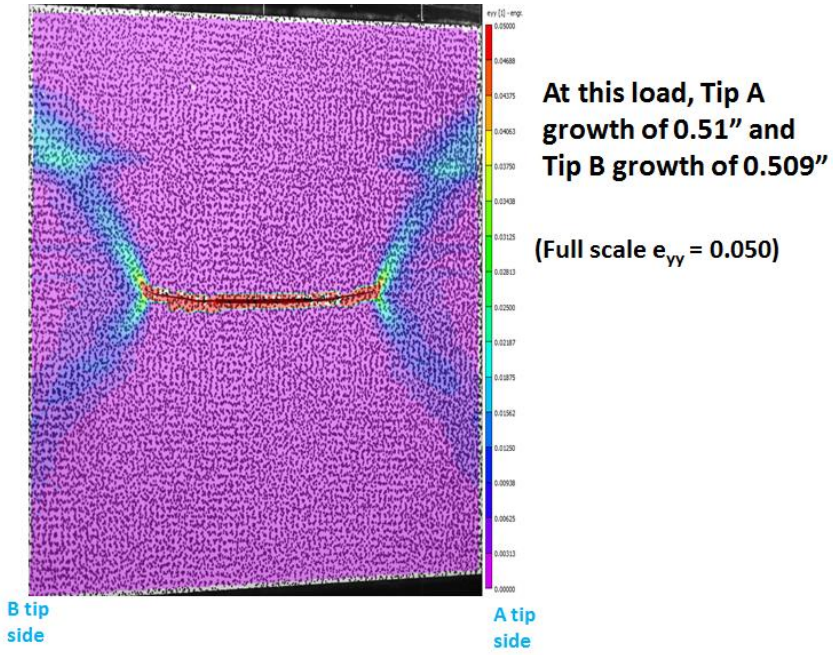


Figure 61 DIC view of weld sample C1_1_4 at 40 kips showing plastic region extending to edges of reduced section

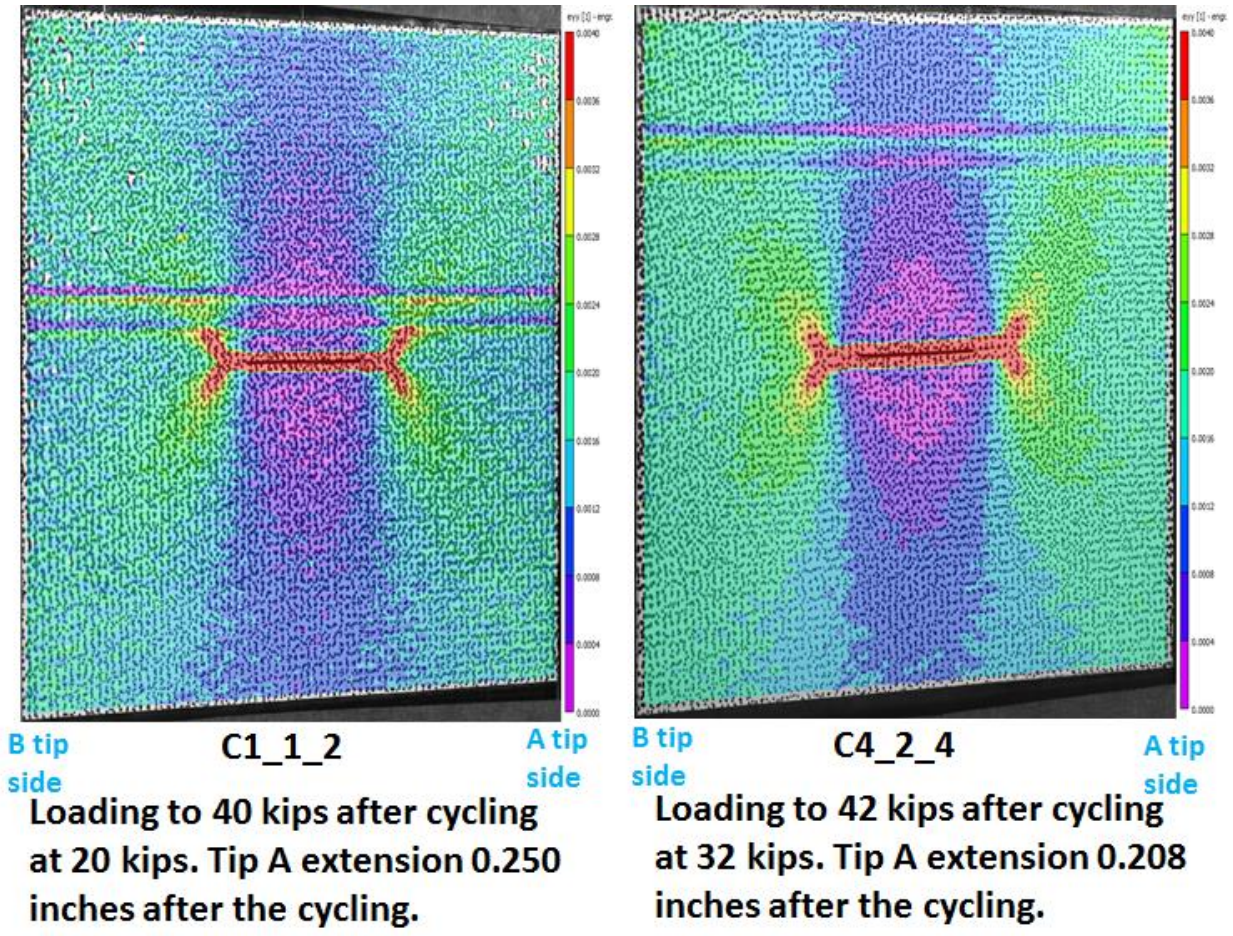


Figure 62 Comparison of DIC high stress regions at 38 kips loading from two different weld samples from different plates showing evidence of material differences or differences from DIC view to sensor side where the tip A extensions were measured. Horizontal lines are camera artifacts and not material responses (Full scale for both $e_{yy} = 0.0040$)

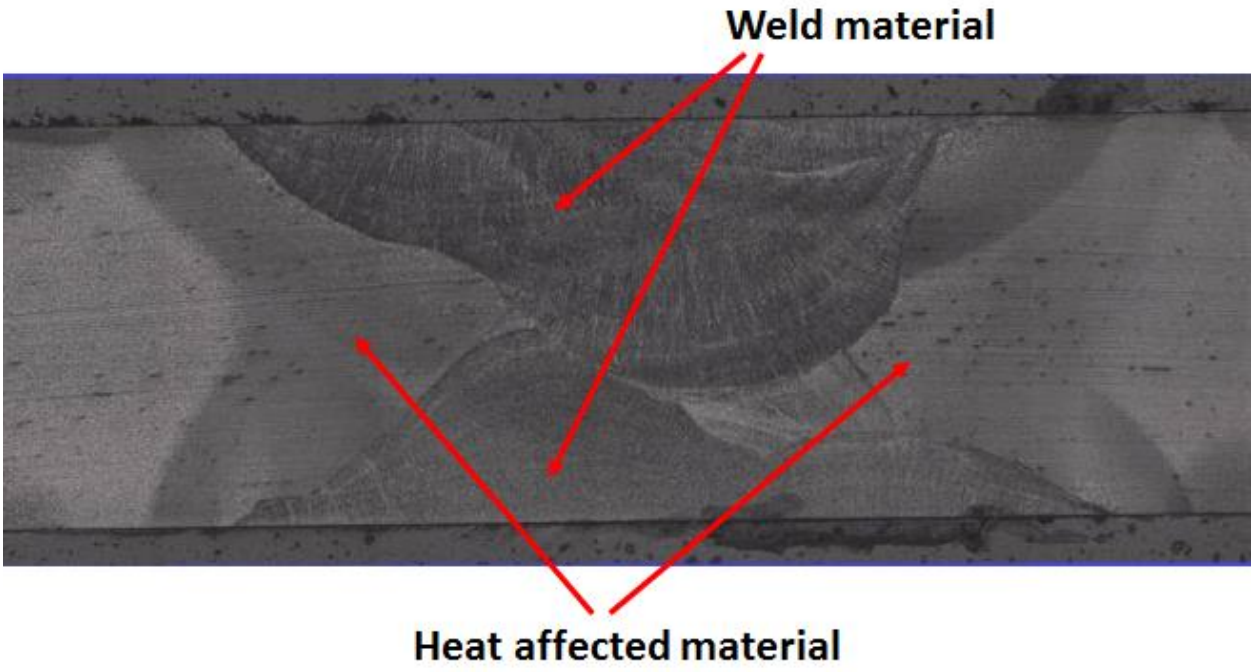


Figure 63 For a crack in the weld region, approximately vertically oriented, a variety of different material conditions could be encountered depending on its actual location

Appendix K: Far-Field Wave Propagation Signals from Pencil Lead Breaks on the Open End of a Thick-Walled Layered Cylinder, Part 1: Amplitudes and Frequency Content

Far-field Wave Propagation Signals from Pencil Lead Breaks on the Open End of a Thick-Walled Layered Cylinder: Part 1 Amplitudes and frequency content

M. A. Hamstad
Department of Mechanical and Materials Engineering
University of Denver, Denver, CO, 80208 USA

Abstract

Relative to potential use of acoustic emission (AE) to monitor pressure testing of large steel pressure vessels, in-plane pencil lead breaks (PLBs) were carried out on the open end of a remnant of such a vessel. This remnant had an inner diameter of 58 in. (1473 mm), a wall thickness of 3.3 in. (84 mm) and a total cylindrical length of 125 in. (3175 mm) ending in a head welded to the cylindrical section. The cylindrical section did not have a monotonic wall, but instead it was made of 11 layers (10 at about 0.277 in. [7 mm] thick, and the inside one of about 0.47 in. [11.9 mm] thick) to create a layered pressure vessel (LPV). Due to the presence of the multiple interfaces between layers, a question arose as to whether a sensor mounted on the outer layer was relatively less sensitive and had different frequency content for sources on the inner layers compared to sources on the outer layers? The PLB study used four pairs of different types of AE sensors. The sensor types included: i) strong resonance at a single frequency region; ii) multiple resonance frequencies; iii) and iv) broadband response with different frequency responses. Each sensor pair was acoustically coupled, one on the outside surface and one directly below on the inside surface. The sensor pairs were located at 66 in. (1676 mm) (20 times the wall thickness) from the PLB points. This distance was considerably less than the helical path of about 214 in. (5436 mm). Considering PLBs on the ends of the different layers, Part 1 focused on changes in the character of the AE signals from the four sensor types. Comparisons for each sensor type were made of the amplitudes of the outside sensor relative to those of the inside one. In addition, as the PLB was moved to different layers, the changes in the signals and frequency content of the different sensor signals were studied. Except for one sensor type, the outer sensor peak signal amplitudes relative to the inner sensor peak signal amplitudes changed significantly as the PLB layer moved from the outer layers to the inner layers. In addition, the signals and frequency content also varied with changes in the PLB layer. The results represent a lower bound due to the potential for some increased transmission between layers when an LPV is pressurized to significant levels.

Keywords: Thick-walled layered cylinder, pencil lead breaks, four sensor types, inside and outside sensors, acoustic emission wave propagation, amplitudes and frequency content.

Introduction

Acoustic emission (AE) testing has been used for many years to monitor pressurization of pressure vessels as evidenced by the ASTM standards (E569 first version 1976 and E1419 first version 1991 [1]). These standards do not specifically address the steel vessel of current interest, namely a type of vessel made up of layers of steel rather than a monotonic vessel wall. Several hundred similar layered vessels were manufactured starting in the late 1950's and early 1960's for use by the National Aeronautics and Space Administration (NASA) and other commercial organizations. In the current time frame, to enhance the analysis of AE results from a monitored pressure test of such a vessel, an important step is to understand the wave propagation of AE-like waves. An opportunity was available to carry out wave propagation studies on a remnant of such a vessel, which had been cut from a large layered pressure vessel (LPV). Thus, the overall goal of this study was to examine far-field AE signals from in-plane pencil lead breaks (PLBs) using four different AE sensor types as the PLB layer was changed. The specific goal in Part 1 was to examine the sensor signals as a function the four sensor types to determine the amplitudes, frequency content and propagation characteristics resulting from PLBs on different layers

 ©2019 Acoustic Emission Group

of the exposed open end of the remnant. In addition, the results may guide the best choice of sensor type(s). Besides the uniqueness of the layered construction, a further unique aspect was the use of pairs of like AE sensor types located back-to-back on the outside and inside of the vessel wall.

Wave Propagation Specimen

An overall view of the LPV remnant is shown on the left side of Fig. 1. On the right side the sensor location on the inside is shown. The remnant has a total length of about 157 in. (3990 mm) (note in this paper all dimensions are first given in their measured units and then converted to S.I. units, if they were not originally measured with those units) and an inside diameter of 58 in. (1470 mm). It is made up of a layered cylindrical section of about 125 in. (3175 mm) in length, which was welded to a steel head with a monotonic wall. Based on the manufacturer's fabrication data, the wall thickness is about 3.3 in. (84 mm), and it is made up of 11 layers. The inner layer was about 0.47 in. (11.9 mm) thick, and the remaining layers were about 0.277 in. (7 mm) thick. The open end where the PLBs were carried out was locally machined where the PLBs were done to smooth out the roughness resulting from water jet cutting. At the 66 in. (1676 mm) distance (20 times the wall thickness), where the sensors were located, flats were machined/ground on the inside and outside so that good contact could be made between the sensor faces and the vessel wall. These flats were about 0.01 in. (0.3 mm) deep. The inside flat was of the most



Fig. 1. Showing the remnant on the left and the inside sensor on the right, along with the trigger sensor (PICO) on the open end. The arrowhead pointing to PICO sensor is the region of close-up in Fig. 3.

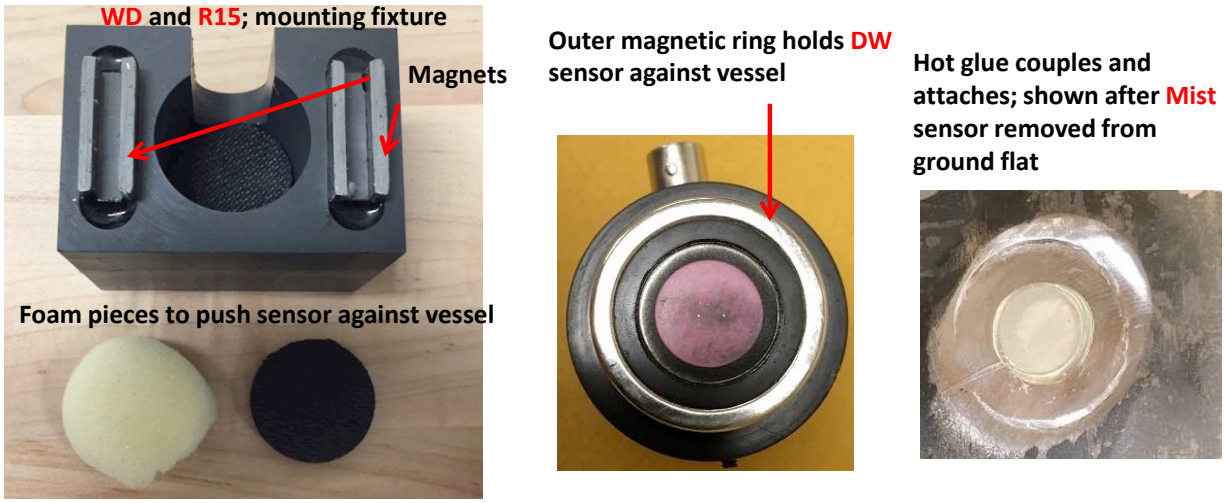


Fig. 2. Showing attachment fixtures and methods of attachment for the sensors.

importance due to the curvature of the vessel wall, which would have offset the central part of the sensor face from the wall. The paint on the outer surface had been removed. The alignment of the wave propagation path from the PLB location to the sensors was selected so that no nearby axial welds were present.

Acoustic Emission Sensor Types/Attachment/Coupling

Four different types of AE sensors were used; a pair of the same type at a time. Each sensor had an internal DC powered preamp. The manufacturer's information about the sensors/preamps is shown in Table 1. As shorthand for the rest of this paper, from the first column of the table moving down, the shorthand labels are: DW, Mist, WD and R15. One sensor the R15 has a strong resonance in a single frequency region. Another resonant sensor, the WD has more than one resonance due to its design with more than one sensing element. The other two sensors Mist and DW are broadband, but the frequency response characteristics of the Mist sensor were altered due to the couplant used, as will be shown later in this paper. Three of the sensor types were held in place by the force from a magnetic fixture or magnetic ring on the sensor's outer diameter, as shown in Fig. 2. The other sensor type, Mist, was both held in place and acoustically coupled by hot melt glue (residual glue layer shown in Fig. 2 was about 0.03 in. [0.8 mm] thick). The other three sensor types were acoustically coupled by Apiezon M grease.

Table 1. Sensor characteristics

Sensor ID	Mfr. electronic frequency specification, kHz	Preamp gain, dB	Resonance characteristics from mfr.	Outer diameter, mm
Digital Wave, B454 - IPP	20 - 1500	20	Broadband, not strongly resonant	14
Mistras, PKBBI	20 – 600	26	Broadband, not strongly resonant	18
Mistras, WDI	200 – 900	40	Resonant at several frequencies	27
Mistras, R15I	50 - 400	40	Resonant at about 150 kHz	26

Experimental Details

The PLBs were generated by the fracture of about a 3 mm length of 2H lead held in contact with the open end of the remnant. The lead diameter was selected to be 0.7 mm to create better signal-to-noise (S/N) ratios so that the wave propagation characteristics could be determined with greater confidence. To provide a nearly constant trigger time (relative to the time of the PLB) for waveform recording a small diameter (5 mm) PICO sensor (resonant at about 500 kHz) was coupled and held in place by Tacky Wax on the same layer where the different PLBs were made. The center of this sensor was only about 0.48 in. (12 mm) from the PLB points. It was attached to a standard external preamp with 40 dB gain and a high pass 100 kHz filter. The use of the trigger sensor allowed all the sensor signals resulting from the PLBs on different layers to be correlated to the same time base. Figure 3 shows a close-up photograph of the location of the PICO sensor on layer 10 as well as the red labeling of the layer numbers. The PLBs were carried out near the middle of the end of each layer. Figure 3 also shows by black marks the top and bottom of the different layers. At least five PLBs were done for each selected layer. Most of the selected layers were from near the outer or inner layers, since the comparative transfer of the waves to sensors farther or nearer the PLB layer was of the most interest. All sensor preamps were powered using a decoupling circuit. After the decoupler the signals from the back-to-back sensors were high pass filtered with a five-pole passive Butterworth filter at 10 kHz. The inputs at the waveform recorder were terminated by 50 ohms. All testing was done inside at nominal room temperatures.

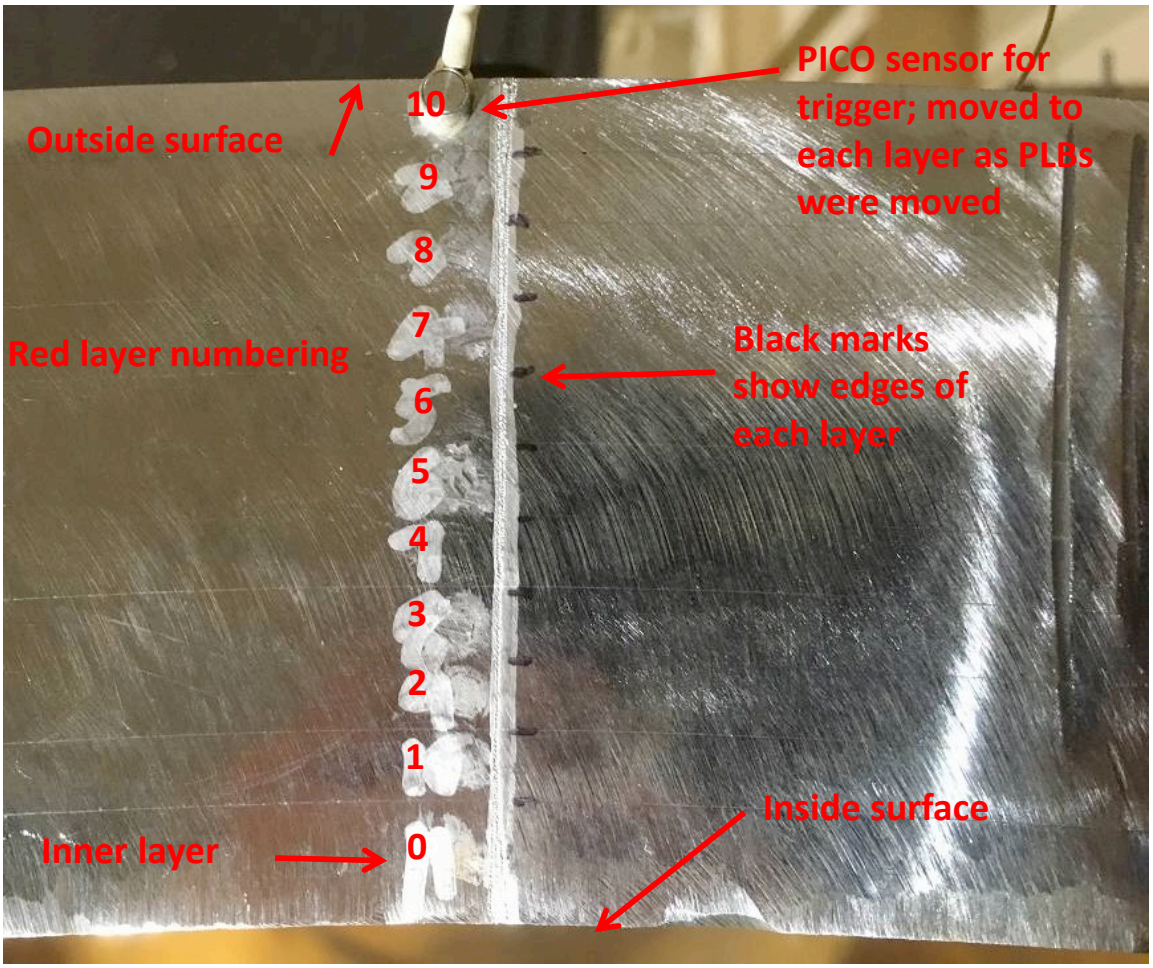


Fig. 3. Shows close-up of layers and position of PICO sensor for PLBs on layer 10. Faint lines are the layer interfaces as marked in black.

The waveforms from the trigger sensor as well as those from the back-to-back sensor pair were simultaneously recorded by a PicoScope at 5 MHz when the voltage threshold for the PICO channel was exceeded. A 500 μs pretrigger was used along with a total digitized length of 25000 points for each of the three signals. The waveforms were recorded with 12 bits resolution. The recorded signals were exported as txt files and then imported to a software package for processing. In the presentation of the results, the figures and discussion are biased towards the outer sensor signals, since those are the only sensor signals available in a real AE test of an LPV.

Experimental Results

A. Contrasts in the outer sensor signals between sensor types for PLBs on the same layer

Since there were four significantly different sensor types, it is of interest to compare the signals from the different types for PLBs on the same layers. From the five or more PLBs on each selected layer for each sensor type, typical signals were selected. The choice of the typical signals was not made based on peak amplitudes; instead it was made on visually viewing the waveform characteristics (all five waveforms at once for each case) in the signal time increment prior to any arrival of helical path signals. Figure 4 shows the selected typical outer sensor signals from the four sensor types for PLBs on the middle of the ends of the outer layer 10 and inner layer 0. Unless stated, all the signals in this paper were not altered by the gains of the various preamplifiers. In Fig. 4 and subsequent figures of signals, two vertical red reference lines (or partial lines for clarity) are included. These lines are the calculated first

arrival times of fundamental extensional (S_0) and flexural (A_0) modes of Lamb waves. Initially, the time of arrival of the peak of the first positive half cycle in the PICO trigger signal was obtained. From this time the propagation time from the PLB point to the center of the PICO sensor location was subtracted. This calculation provided the PLB time. To this time, the propagation times of the extensional and flexural first arrivals to the sensors were added. The velocities from Kolsky [2] used for these calculations were bulk velocity 5.94 mm/μs to the PICO sensor and 5.42 mm/μs and 3.22 mm/μs respectively for the extensional and flexural modes to the distant sensors. The calculated times are an extensional mode first arrival at about 813 μs and a flexural mode first arrival at about 1024 μs. The presented signals (Fig. 4) are shown from 0.75 ms (to provide some signal representing background noise prior to the AE signal arrival) to 1.45 ms, which corresponds to 3500 points. The termination at 1.45 ms was before the extensional wave first arrival time from the two helical paths which was calculated to be about 1.50 ms. For the Mist and R15 sensors, the signals were low pass software filtered respectively at 500 kHz and 400 kHz with a eight-pole Butterworth filter to remove some of the background electromagnetic noise that was unavoidably present at certain times due to other activities going on in the test facility building. The Mist sensor signals were most affected by this noise due to the use of the sensor manufacturer supplied 1 m sensor cable that had the required SMA connector to attach to the sensor. This cable did not have high shielding. After this sensor cable, a well shielded RG58 50 ohm cable with BNC connectors was used. This cable type was used to directly connect to the other three sensors. The above low pass filtering did not alter the key results with these sensors, as will be shown later, since the primary frequency content was well below these low pass frequencies.

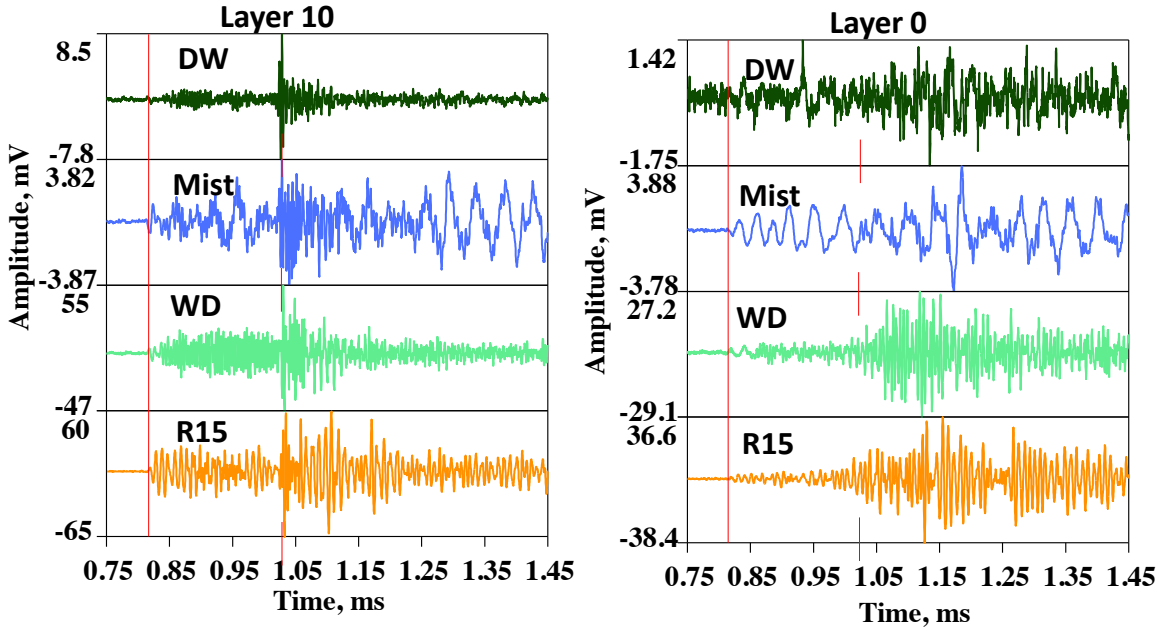


Fig. 4. Typical signals from all four sensor types located outside for PLBs on the ends of the outer layer 10 and inner layer 0.

Some clear observations can be made from Fig. 4. First, for the PLBs on layers 10 and 0, the first arrivals of the signals correspond reasonably well with the calculated first extensional arrival for all the sensors, except one sensor type, when viewed with a shorter time scale and more sensitive vertical scale in Fig. 5. In the case of the DW sensor, for a PLB on layer 0, there was no correspondence. This result seems to be related to a poor S/N ratio. The poor S/N ratio can be the result of either less low frequency response and/or higher preamp noise. Since these layers represent the extremes, as expected for PLBs on all the intermediate layers, for all the sensor types except the DW, the sensor signal arrivals were found to correspond to the calculated extensional arrival (this result is not shown here, but some results are shown in later figures in part E). In the case of the DW sensor only for PLBs on layers 10 and 9 was a correspondence present. Second, for all of the sensor types for PLBs on the end of layer 10 (the outer

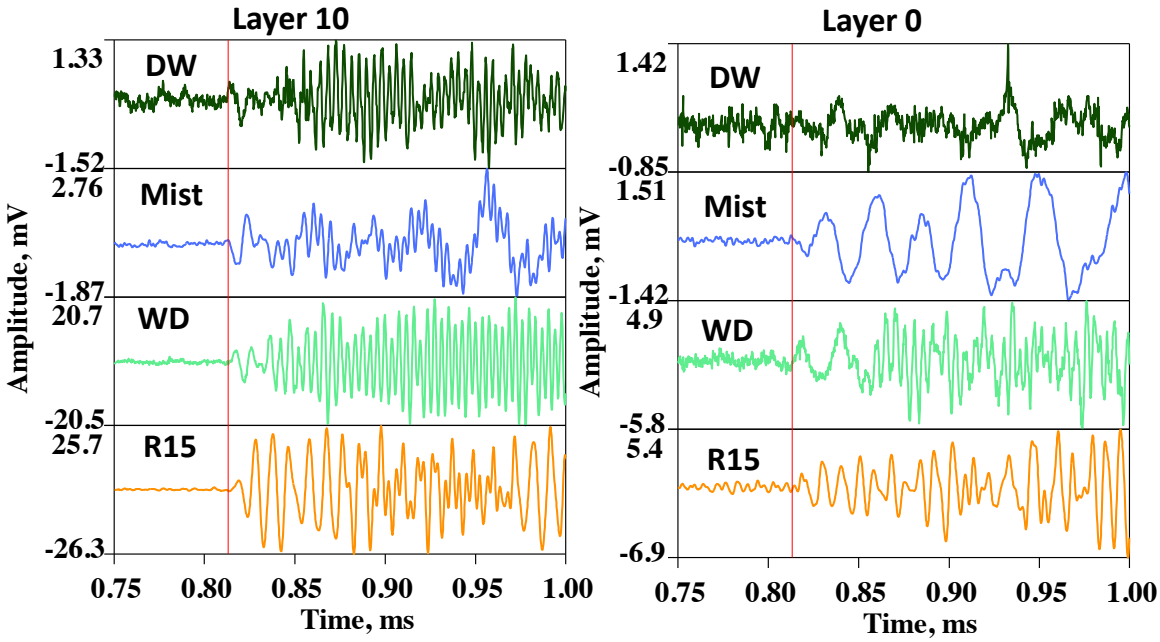


Fig. 5. The same waveforms as in Fig. 4 with a shorter time scale to better define the first arrivals of the extensional mode.

layer) there are clear indications in the signals of the flexural first arrival near the calculated value. The presence of higher frequencies at the initial arrival of the flexural mode is as expected. Third, for the PLB on the end of the inside layer 0 the correspondence of the signals to the calculated flexural mode arrival is not clear for all of the sensor types. Fourth, there are large differences in the character of the signals for the different sensor types for both PLB layer cases shown. The signals from sensor types WD and R15 were the most similar to each other, and the boadband sensor signals DW and Mist differed substantially from each other in their low frequency character.

B. Contrasts in the outer sensor frequency content between sensor types for PLBs on the same layer

Figure 6 illustrates the differences in the frequency content in the signals shown in Fig. 4 for the PLBs on the ends of layers 10 and 0. These results were developed using the same time portion of the signals from 0.75 ms to 1.45 ms. The fast Fourier transform (FFT) was calculated with a fill with zeros routine that extended the number of points from 3500 to 4096 to provide the results with increments of 1.22 kHz. Clearly, there are very significant differences even though the source is essentially the same for the results from the different sensor signals. Both the frequency range of content and the peak regions differ. The differences between the sensor types are the largest for the PLBs on the outer layer 10. In this case, the DW sensor results show that a very wide range of frequencies were excited as would be expected for a broadband sensor. The Mist sensor results also show a broad range, but the frequency content is dominated by very low frequencies. This dominance, which is related to the use of hot melt glue as the couplant, will be discussed later in this paper. The resonant outer sensors for the PLBs on layer 10 show some differences related to their resonant behavior. The R15 signals have a dominant peak at about 100 kHz, while the WD signals have more than one dominant region with content up to even about 600 kHz due to the design with two different sensing elements. Turning to the frequency content in the signals for the PLBs on the inner layer 0, there is a shift to lower frequency content particularly for the DW and WD sensors. On the other hand the peak regions for the Mist and R15 sensor signals remains quite similar to the frequency content for the PLBs on layer 10.

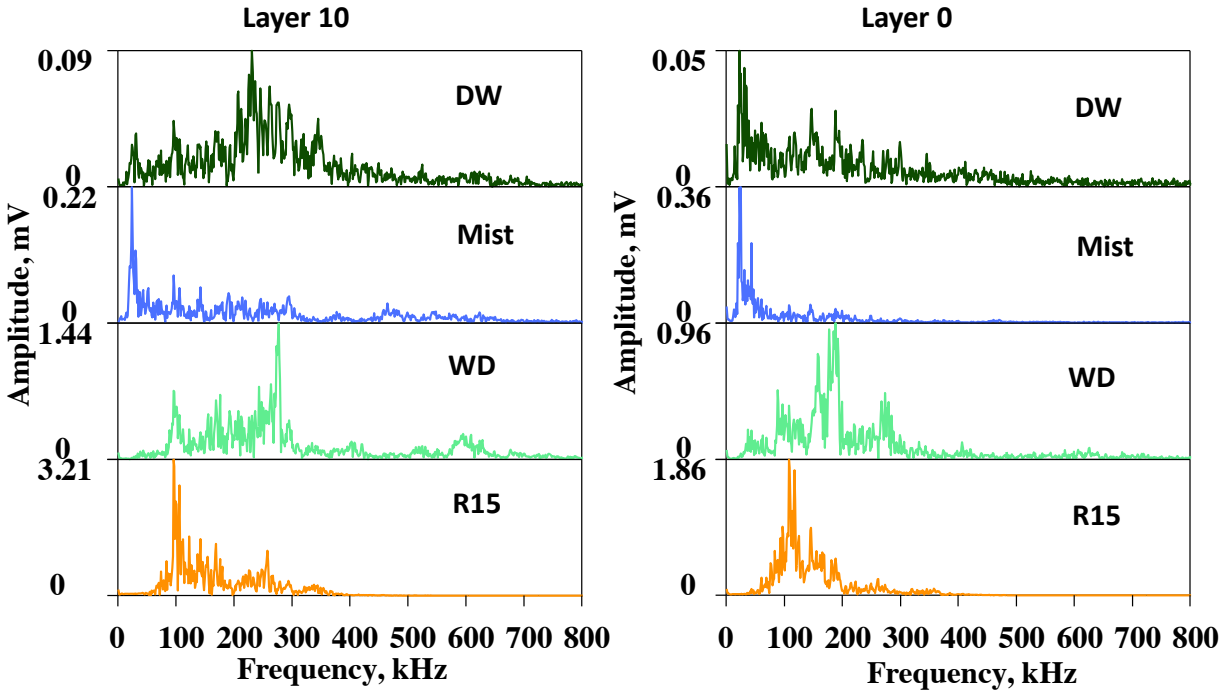


Fig. 6. Frequency content results for the signals in Fig. 4 for all four sensor types located outside for PLBs on the ends of the outer layer 10 and inner layer 0.

C. Changes in the signals from the individual outer sensors types as the PLB layer changes

The observations in this section are confined to the flexural arrivals as the correspondence to the extensional arrivals has already been presented in the previous section. In Fig. 7, the outer sensor signals as a function of the PLB layer are shown for the two broadband sensors, DW (left) and Mist (right). The DW sensor signals for the PLBs on layers 5, 2, 1 and 0 (sequence of layer numbers will be ordered from the outer to inner in this paper since the outer sensor is the only one that can be used in an actual test) have a different character than the signals from the PLBs on the outer layers 10, 9 and 8. For the PLBs on the outer three layers, the signals show a clear first arrival of the flexural mode and correspondence with the calculated value, and the signals are similar to each other in both modal regions ("extensional region" from first arrival to the arrival of the flexural mode with the following "flexural region"). For the PLBs on the four layers (5, 2, 1, 0) some distance further below the outside, the outside sensor signals are similar to each other, but the flexural mode first arrival is not clearly defined and does not clearly correspond to the calculated arrival. Also, for these four PLB layer cases, it seems the high amplitude portion of the flexural region extends for a longer time period than for the three PLB layers (10, 9, 8) close to the outer surface. This difference is primarily due to the scaling for the three outer PLB layer cases, as a result of the large initial amplitude of the flexural arrival. The peak amplitude of the signals in all the PLB layer cases is either the flexural mode first arrival or at a later time in the region of dominant flexural mode.

As shown on the right side of Fig. 7, the Mist sensor signals again show that the signals from the PLBs on the outer three layers are reasonably similar to each other, and the arrival of the flexural mode, indicated by a short region of higher frequency, corresponds to the calculated value. This correspondence for the flexural mode is not clear for the four lower layer PLB cases. The four lower layer signals are quite similar to each other in character with mostly low frequency content. In contrast to the DW sensor signals, the Mist sensor signals have some similarity to each other for all the PLB layer cases. This similarity is in their lower frequency content in both the extensional mode region and the latter part of the flexural mode region.

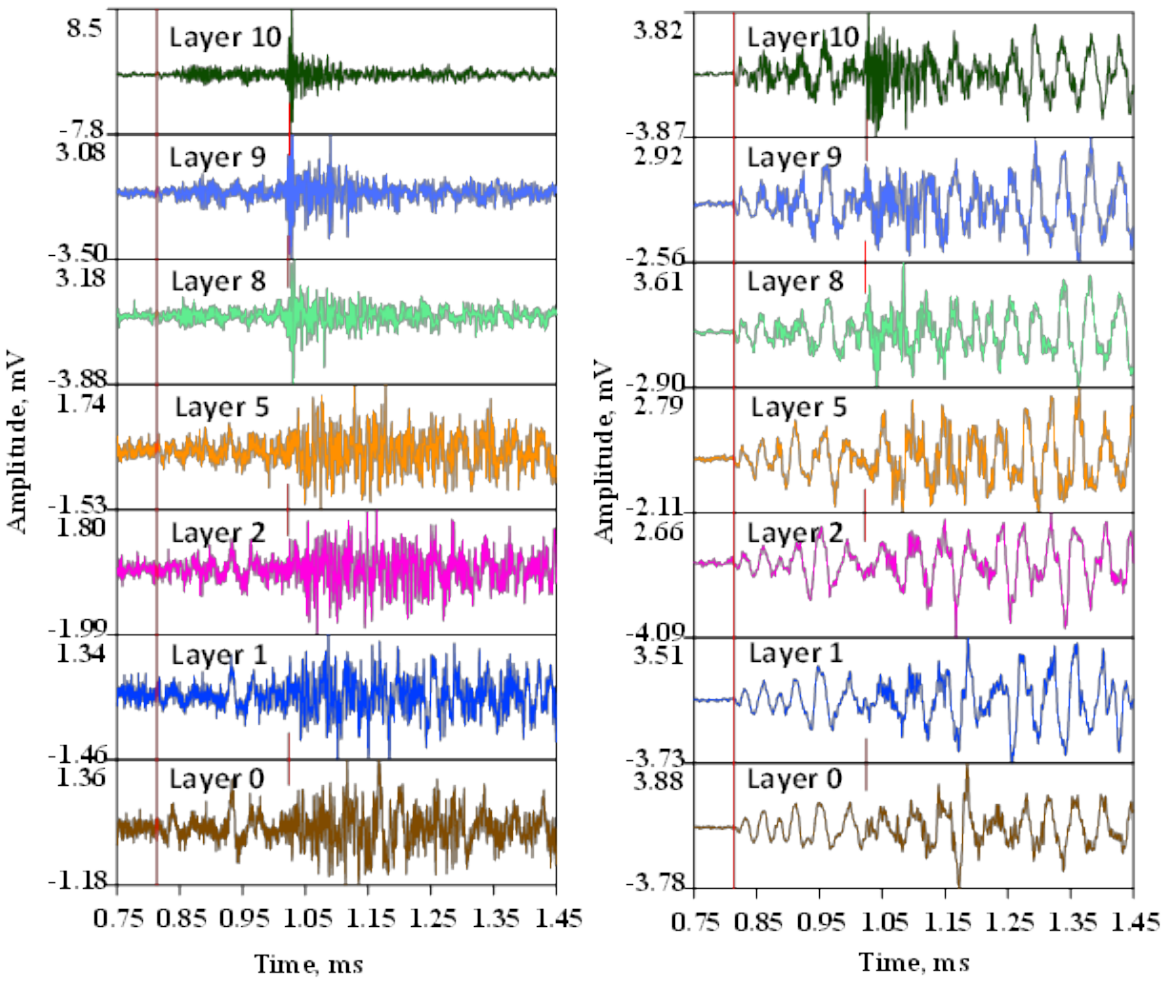


Fig. 7. Signals versus end of PLB layer for DW sensor (left) and Mist sensor (right).

In Fig. 8, the outer sensor signals are shown for the two resonant sensors the WD (left side) and R15 (right side) for PLBs on the same set of seven layers. For both sensors types the first arrivals of the flexural mode correspond reasonably well with the calculated values for PLBs on the ends of layers 10, 9 and 8. In the case of the WD and R15 sensors, this behavior possibly also extends to some of the layers 5, 2 and 1. Also, for both sensor types, the flexural mode's distinct first arrival seems to be missing for PLBs on layer 0. As with the Mist sensor signals, there is some signal similarity for each sensor type as the PLB layer changes. For both of these sensor types, the signals for PLBs on layers 5, 2, 1 and 0 also have an extended portion of high amplitude in the flexural region. This difference is again primarily due to the scaling for the three outer layer cases as a result of the large initial amplitude of the flexural arrival. Again for both of these sensor types, the location of the peak amplitude is in the flexural region.

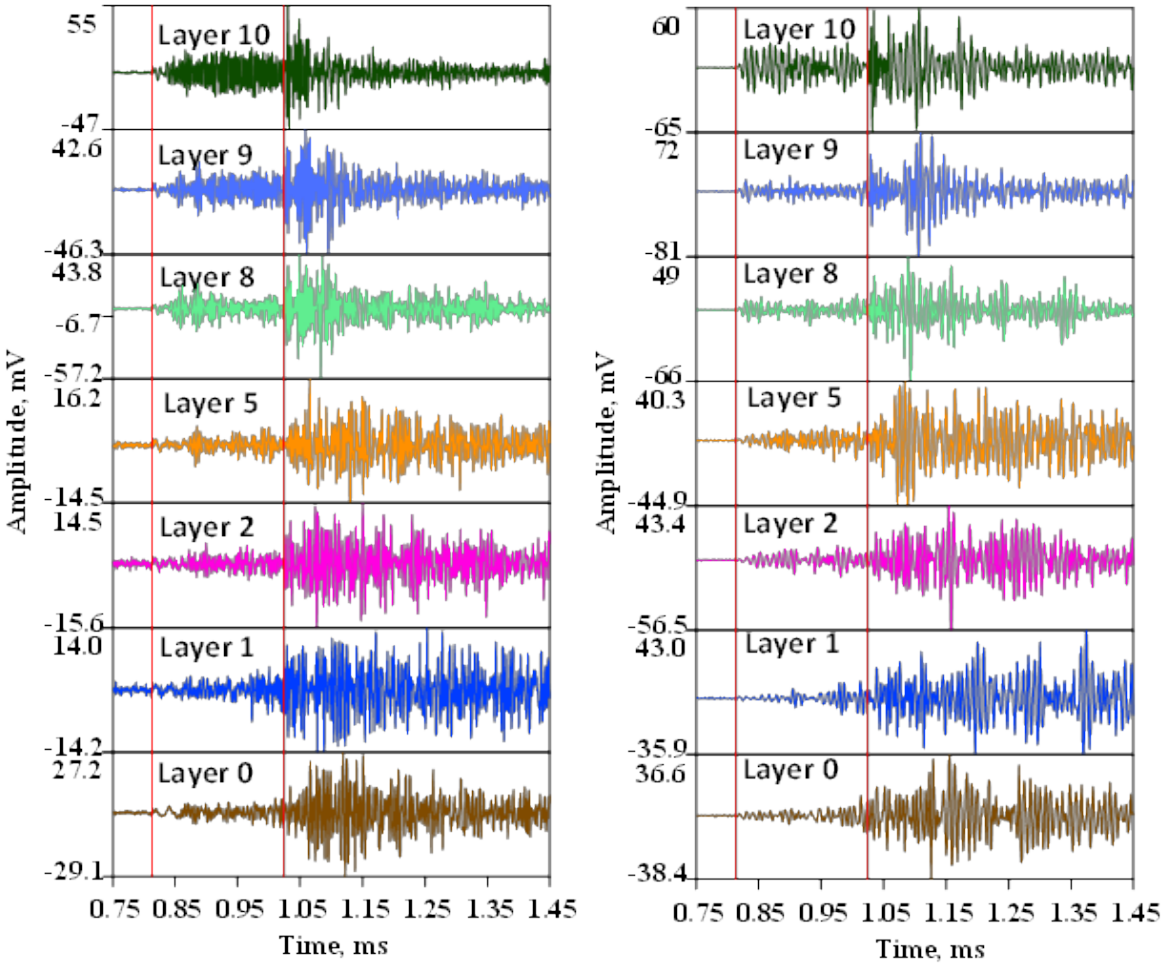


Fig. 8. Signals versus end of PLB layer for WD sensor (left) and R15 sensor (right).

D. Changes in frequency content of the individual signals of the outer sensor types as the PLB layer changes

The same approach for the calculation of the frequency content was used as described previously. Figure 9 for the DW and Mist outer sensor signals and Fig. 10 for the WD and R15 outer sensor signals show the FFT results as a function of the PLB layer. To show a similar frequency region for all four sensor types, the FFT results are shown out to 800 kHz even though that range is not applicable to all the sensor/preamp types and to the previously described low pass filtering. Several aspects are clearly observed in these figures. First, as the PLB layer moves closer to the inner layer, there is a reduction in the presence of higher frequencies. This is particularly evident in the signals from the DW and WD sensors. Second, it is now clear that the Mist sensor signals have been altered by the use of the hot melt glue as the couplant, which acts as a filter to prevent high frequencies from reaching the sensing element. The primary frequency content of this sensor's signal is low at less than 200 kHz, and the peak intensities are well below 100 kHz. A reference that examined this material as a coupling agent [3] showed a drop-off in sensitivity at frequencies above 200 kHz. Additional work with the same type sensor, showed much higher frequency content up to about 600 kHz [4] in the signals from PLBs on a steel plate using vacuum grease couplant. Third, the sensors that primarily have low frequencies in their FFT results, R15 and Mist, do not show a large change in the FFT frequency region of highest intensity, as the PLB layer moves from the outer layers to the inner layers. Fourth, for the DW and WD sensors with significant high frequencies present, there is a distinct change in the peak frequency region for PLBs on inner layers as

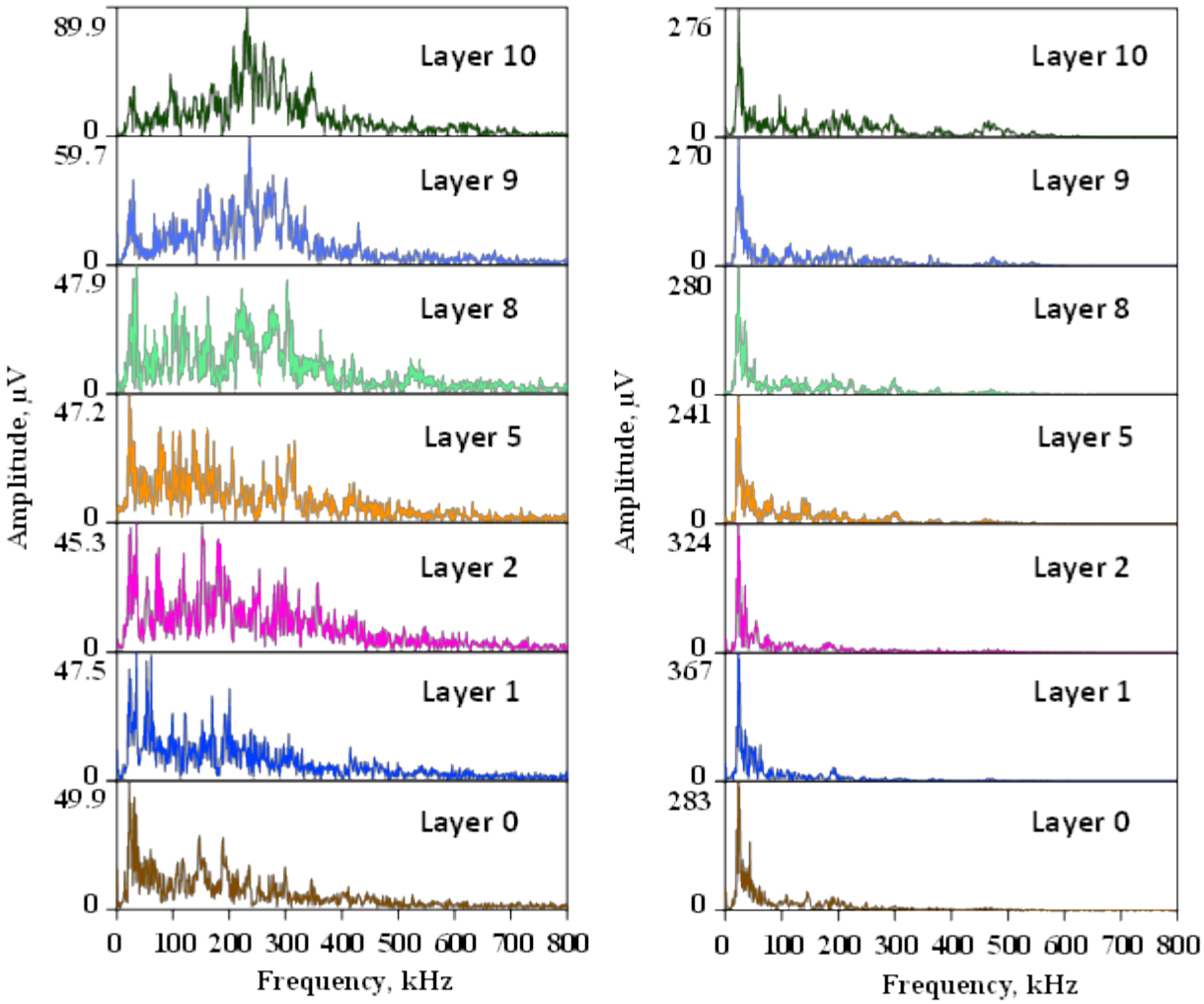


Fig. 9. Frequency content versus end of PLB for DW left and Mist right.

compared to the PLBs on the outer layers. For example, the DW sensor signal has a peak at about 230 kHz for the outer layer 10 PLB, and already for the PLB on layer 8 the peak region is centered at about 35 kHz. For the PLBs on the remaining lower layers the peak region remains somewhat similar, along with less and less intensity above 100 kHz. The peak frequency of the WD sensor signals changes from about 270 kHz for PLBs on layers 10, 9 and 8 to about 180 kHz for PLBs on layers 5, 2, 1 and 0. The peak frequency of the Mist signals is about 25 kHz for all the PLB layers shown. Similarly for all the PLB layers shown, the peak frequency for the R15 sensor signals varies from about 100 kHz to 120 kHz.

E. Comparisons of the outer and inner sensor signals for PLBs on the same layers

Since the PLBs were done with the same type sensor coupled on the inside as on the outside, direct comparisons could be made of the signals from PLBs on the layers. Rather than show a comprehensive set of figures, representative cases were selected for each sensor type. Thus, the figure for each sensor type shows the outer and inner sensor signals as a direct comparison of PLBs on layers 10 and 8 near the "level" of the outer sensor and on layers 2 and 0 near the "level" of the inner sensor. In each of these comparisons of the signals, a shorter time increment from 0.75 ms to 0.85 ms is shown as an inset to focus on the initial arrival of the extensional region with more sensitive scales. As before in these figures vertical red lines (for the flexural mode in the longer time increment signal and for the extensional mode in the shorter time increment signal) show the calculated first arrival times of the fundamental modes. Also, the two sensor locations are labeled out and in. It should be kept in mind when viewing these comparisons, that the thicknesses of the layers on which the two sensors are mounted are different. The

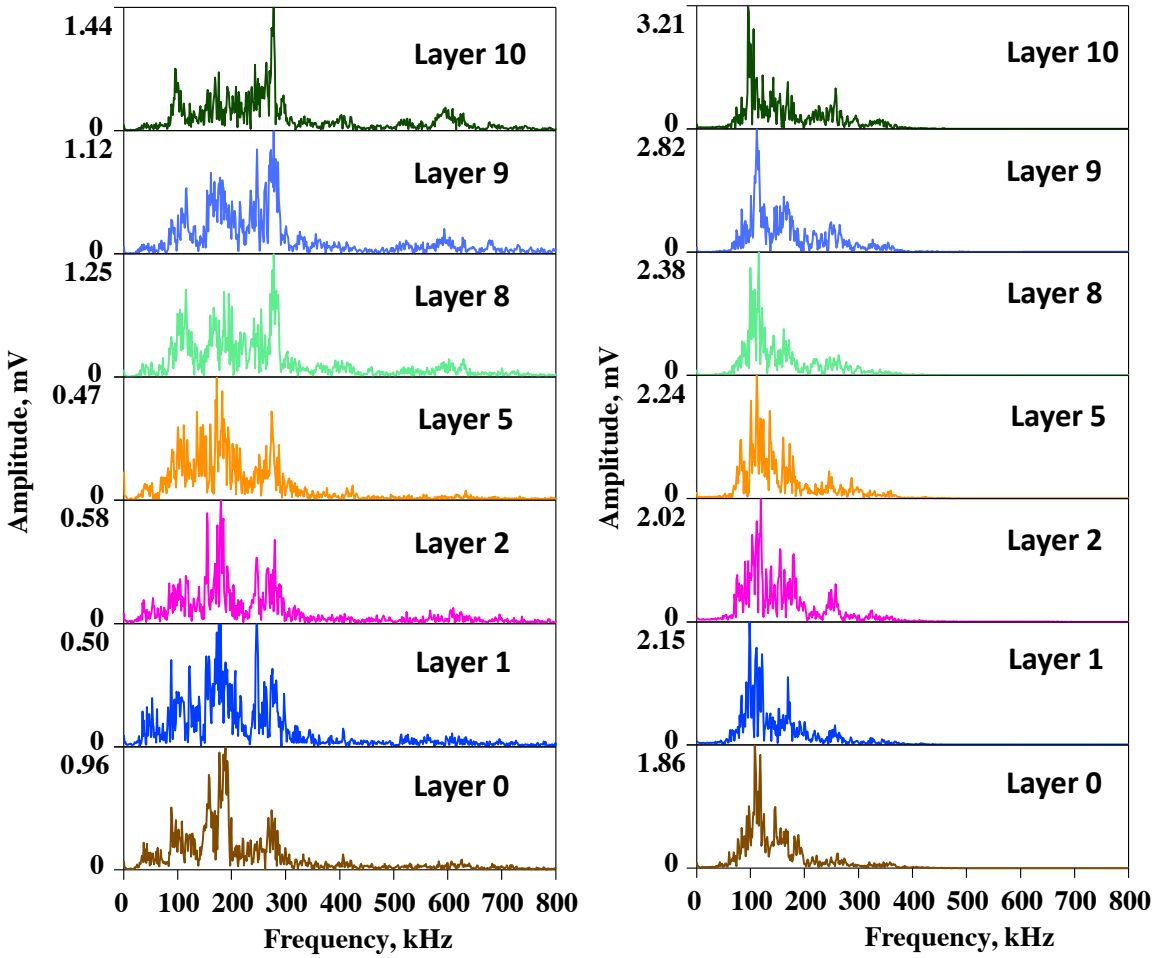


Fig. 10. Frequency content versus end of PLB for WD left and R15 right.

outer sensor is mounted on a layer with thickness of about 7 mm thickness while the inner sensor is mounted on a layer of thickness of about 11.9 mm thickness. Thus, if the signals are dominated by or in part made up of Lamb wave propagation confined to just the layers upon which the sensors are mounted, the frequency content in the waves will vary due to the thickness differences. Figures 11 – 14 show the comparisons respectively for the DW, Mist, WD and R15 sensor pairs.

From examination of the insets in the figures, it is clear, as has been pointed out earlier, that the calculated extensional first arrival corresponds quite well with the signal arrivals for both the outer and inner sensors for all four PLB layers and for all the sensors except the DW sensors. For the DW sensors, the figures imply that the primary issue is the S/N ratio. Also, an important observation of this correspondence is the relatively low frequencies at the initial extensional arrivals, which corresponds to the theory of Lamb waves.

Next the potential correspondence of the calculated first arrival of the flexural mode is examined relative to the signal characteristics of the outside and inside sensor signals for the PLBs nearest the layers the sensors are mounted on. First, for all four sensor types, the outer sensor signal corresponds to the calculated flexural mode arrival time for PLBs on the ends of the outermost layers 10 and 8. By eye, this correspondence is due to identifying a small time increment of “dense” high frequency at the calculated arrival time. This behavior is consistent with the theory-based expectation that the initial arrival frequencies of the flexural mode are from higher frequencies. Second, contrary to the observation for the flexural mode arrivals for PLBs on layers near the outer sensors, the correspondence to the calculated flexural arrival time of the inner sensors signals for PLBs on the nearby layers 2 and 0 does not apply. In fact, what the inner sensor signals show in some sensor cases is a delayed “dense” high frequency time

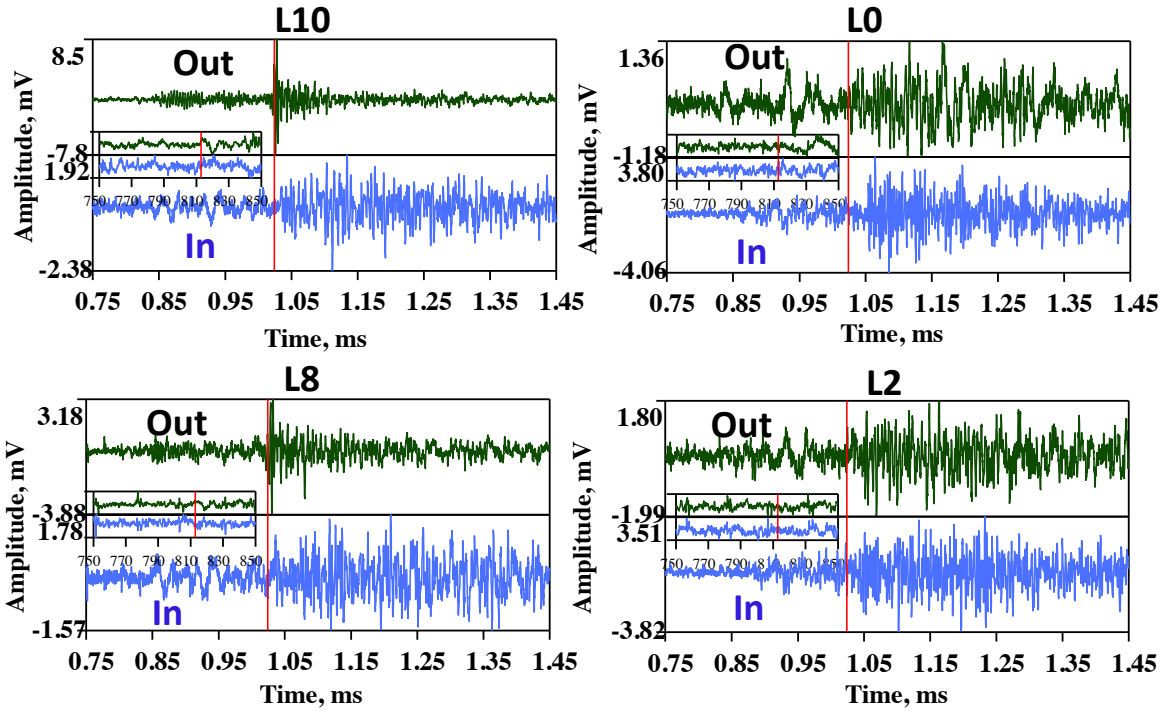


Fig. 11. Comparisons of signals from the outside and inside DW sensors versus end PLBs on different layers.

increment that is best shown in the signals from the DW and Mist inner sensor signals (less for the Mist case for the PLB on layer 2). The delay is typically about 70 μs, which at a bulk shear velocity of 3.22 mm/μs corresponds to a distance of about 225 mm. This distance is much greater than any small measurement error made in locating the inner sensor flat directly below the outer sensor flat. A possible explanation for this delay may be the presence of a full-thickness inner layer circumferential weld located about 9 in. (230 mm) prior to the center of the inner sensor flat. The width of this weld was on the order of 0.8 to 1 in. (20 to 25 mm). Other than this possible explanation, the author is not aware of any other possible explanation. For the WD and R15 inner sensor signals from PLBs on layers 2 and 0, the signals do not clearly show even these delayed arrivals, except possibly the WD sensor for the PLB on layer 0.

When the potential correspondence of the calculated flexural mode arrival time was compared to the signals from the sensors located at a "level" well away from the PLB "level," the correspondence of the calculated flexural arrival is not clearly apparent in all the PLB cases and all the sensors. The potential reason for this fact may be a loss of transfer of higher frequencies between the layers due to imperfect contact (asperity-to-asperity) between the layers. Some work has been published relative to the transfer of ultrasonic signals between layers with imperfect contact. For example reference 5, shows decreasing transfer between two aluminum plates as the frequencies increased from about 2 or 3 MHz to 7 or 9 MHz and increasing transfer of frequencies as the compressive load between the plates increased from 9 MPa to 79 MPa (1305 psi to 11460 psi). The surfaces of these plates had been machined to a root-mean-square (RMS) finish of 0.68 μm. This study included both normal incidence and oblique incidence as well a model that was fitted to the experimental results. No references were located for the kHz frequency range relevant to this work. Also, no references were found that addressed the very large number of interfaces that are encountered in full-thickness propagation of waves in an LPV. Further, the roughness of the interface surfaces of the steel layers in the LPV is unknown. Since it is the higher frequencies that are present at the first arrival region of the flexural mode, this potential loss of higher frequencies with their smaller wavelengths seems to be a plausible explanation. This imperfect contact did not create an issue with the extensional mode since low frequencies with their larger wavelengths make up the initial portion of the arrival of this mode.

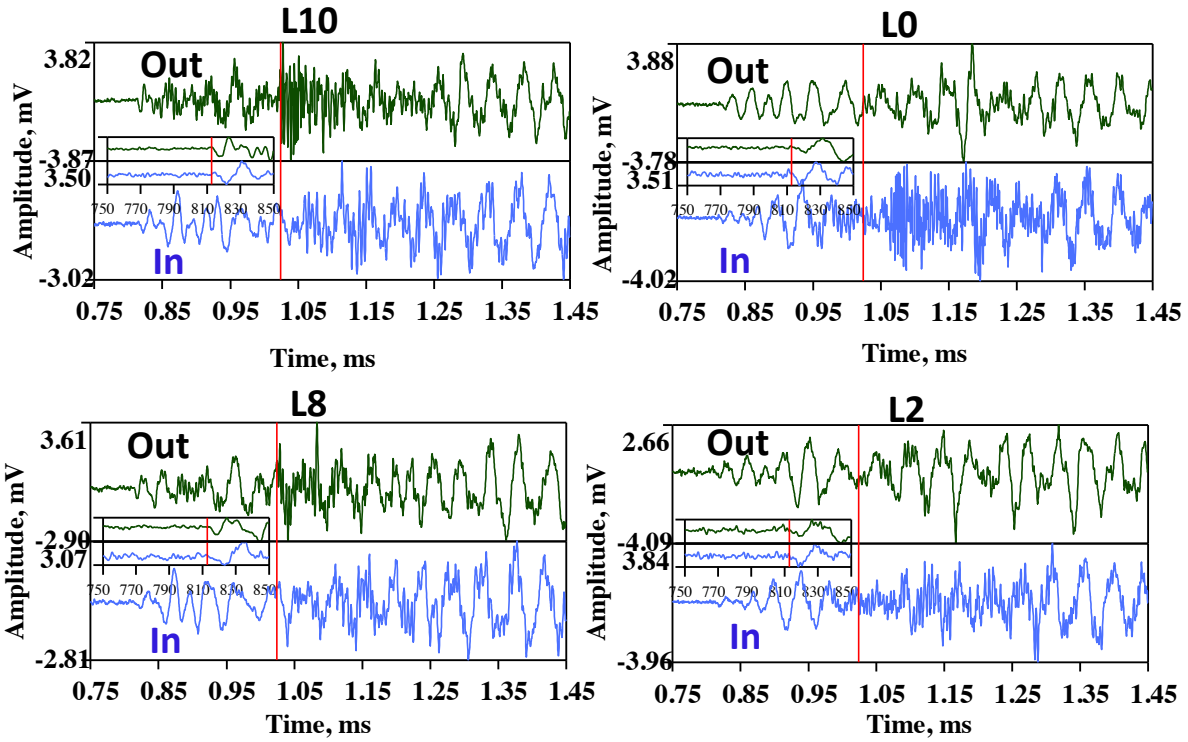


Fig. 12. Comparisons of signals after low-pass 500 kHz from the outside and inside Mist sensors versus end PLBs on different layers.

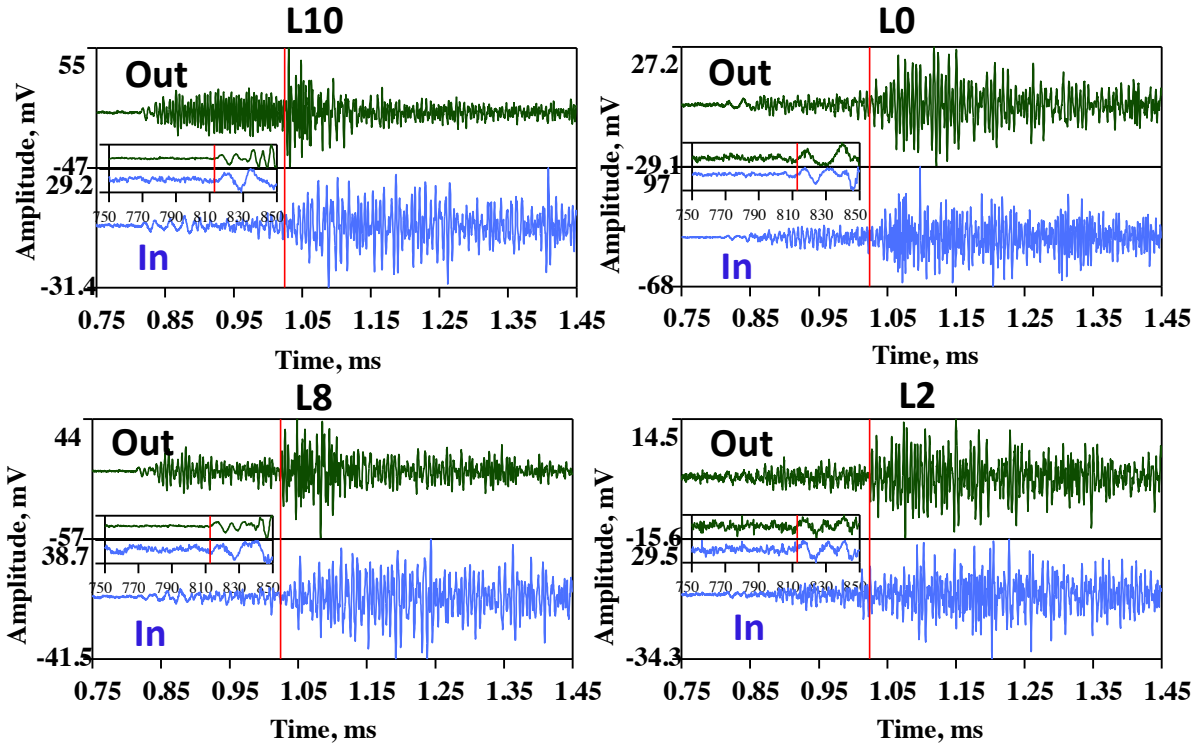


Fig. 13. Comparisons of signals from the outside and inside WD sensors versus end PLBs on different layers.

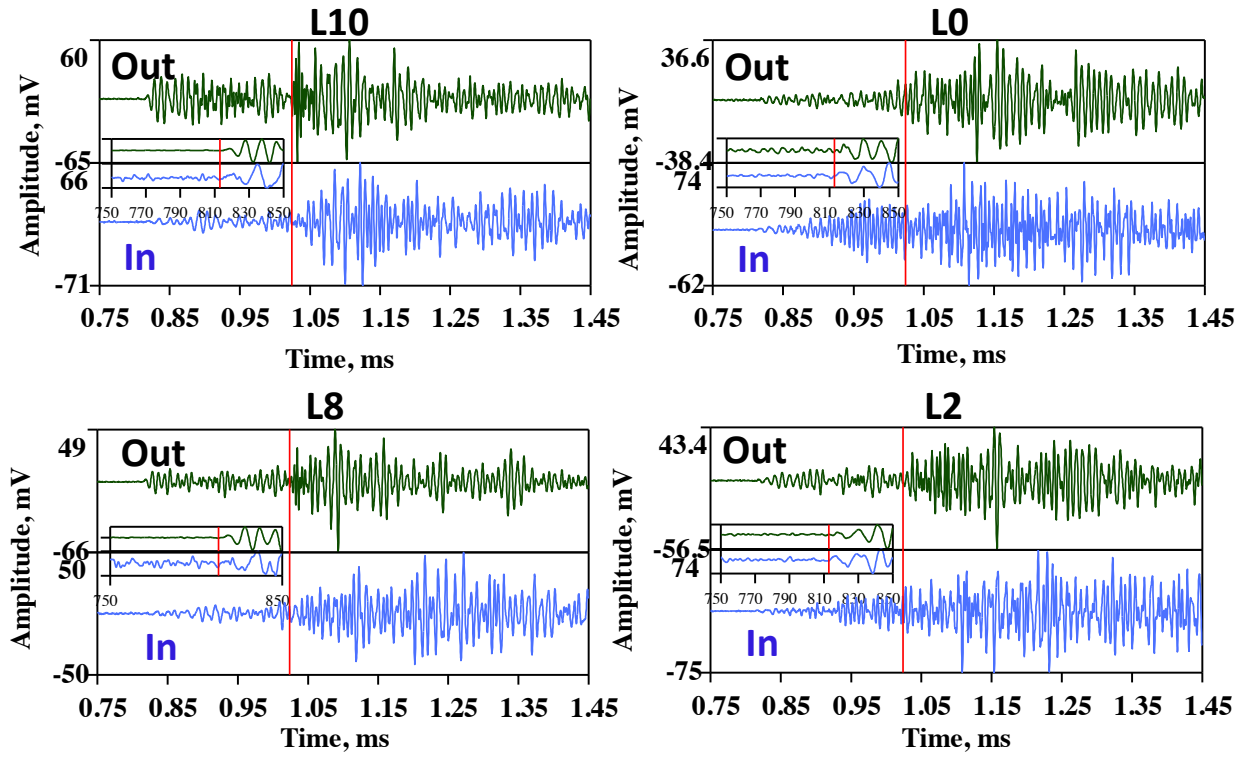


Fig. 14. Comparisons of signals after low-pass 400 kHz from the outside and inside R15 sensors versus end PLBs on different layers.

F. Comparisons of the outer and inner sensor FFT results for PLBs on the same layers

The direct comparisons of outer sensor signal FFT results with inner sensor signal FFT results were also done for these same four PLB layers for each sensor type. Figure 15 shows these FFT results for the DW sensor signals shown in Fig. 11. Using above 200 kHz as a comparison frequency range, it is clear for PLBs on layers 10 and 8 that the nearer outer sensor has a larger portion of the signal above this frequency compared to the inner sensor. For PLBs on layers 2 and 0, the nearer inner sensor signal is dominating with a larger portion of the signal above 200 kHz.

Figure 16 provides results for the Mist sensor signals for PLBs on the same set of layers as in Fig. 12. Again using the frequency range above 200 kHz, a single result applies. Namely the nearby sensors have comparatively more signal in this higher frequency range, and the far sensors have less. Due to the strong loss of high frequencies as a result of the couplant the difference is not as large as with the DW sensor signals.

Figures 17 and 18 respectively for the WD and R15 sensors (waveforms respectively in Figs. 13 and 14), also show similar results with respect to higher frequencies. In the case of the WD sensor the results are similar to the DW sensor, and in the case of the R15 sensor the results are similar to those from the couplant-modified Mist sensor, since both (Mist and R15) primarily are sensitive to frequencies below 200 kHz. Thus, as a general conclusion for all four sensor types, the frequency range above 200 kHz has more intensity from the sensor signal on the closer layer to the PLB layer and less from the sensor signals that are farther away from the source PLB layer.

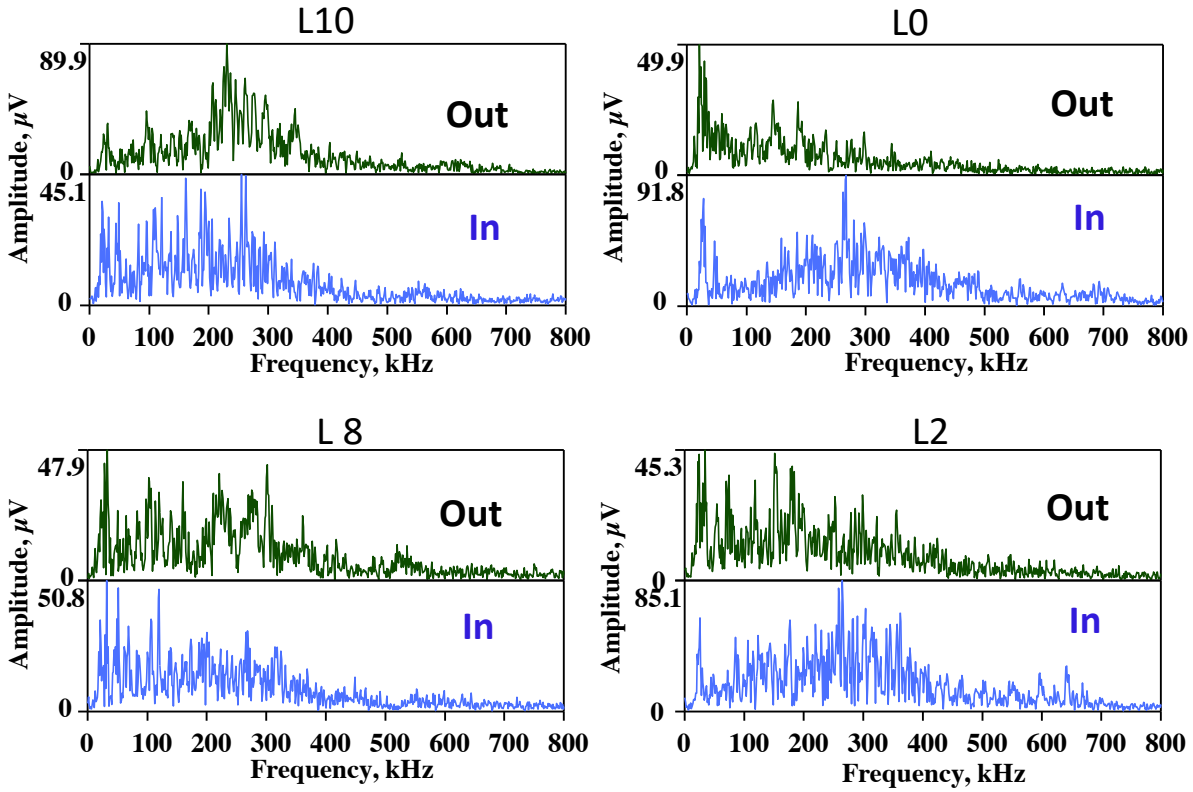


Fig. 15. Comparisons of FFTs of signals from the outside and inside DW sensors versus end PLBs on different layers. Sensor signals shown in Fig. 11.

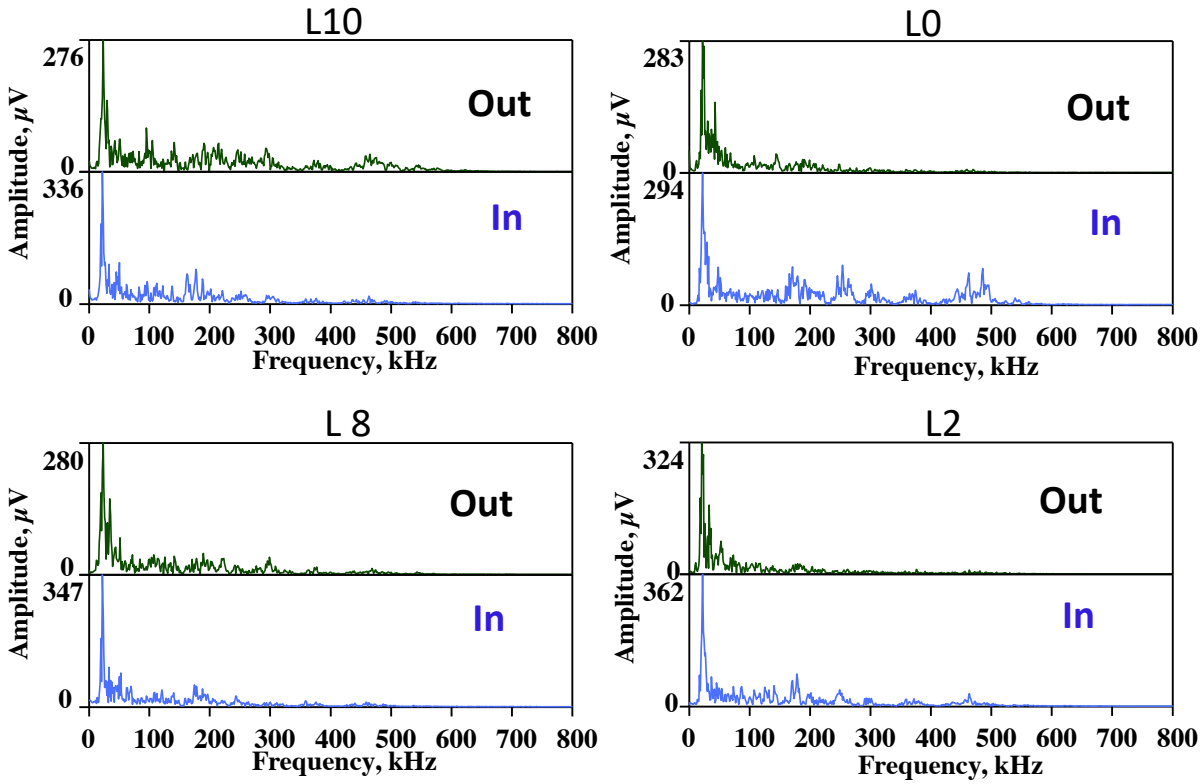


Fig. 16. Comparisons of FFTs of signals from the outside and inside Mist sensors versus end PLBs on different layers. Sensor signals shown in Fig. 12.

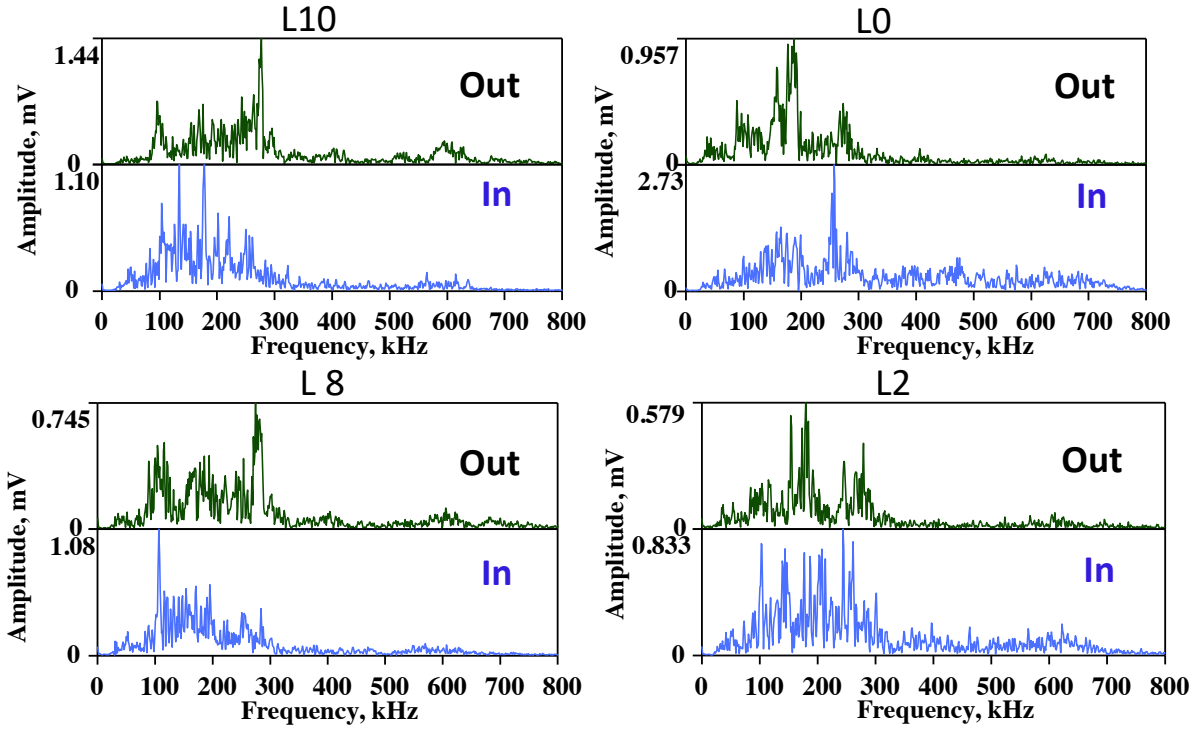


Fig. 17. Comparisons of FFTs of signals from the outside and inside WD sensors versus end PLBs on different layers. Sensor signals shown in Fig. 13.

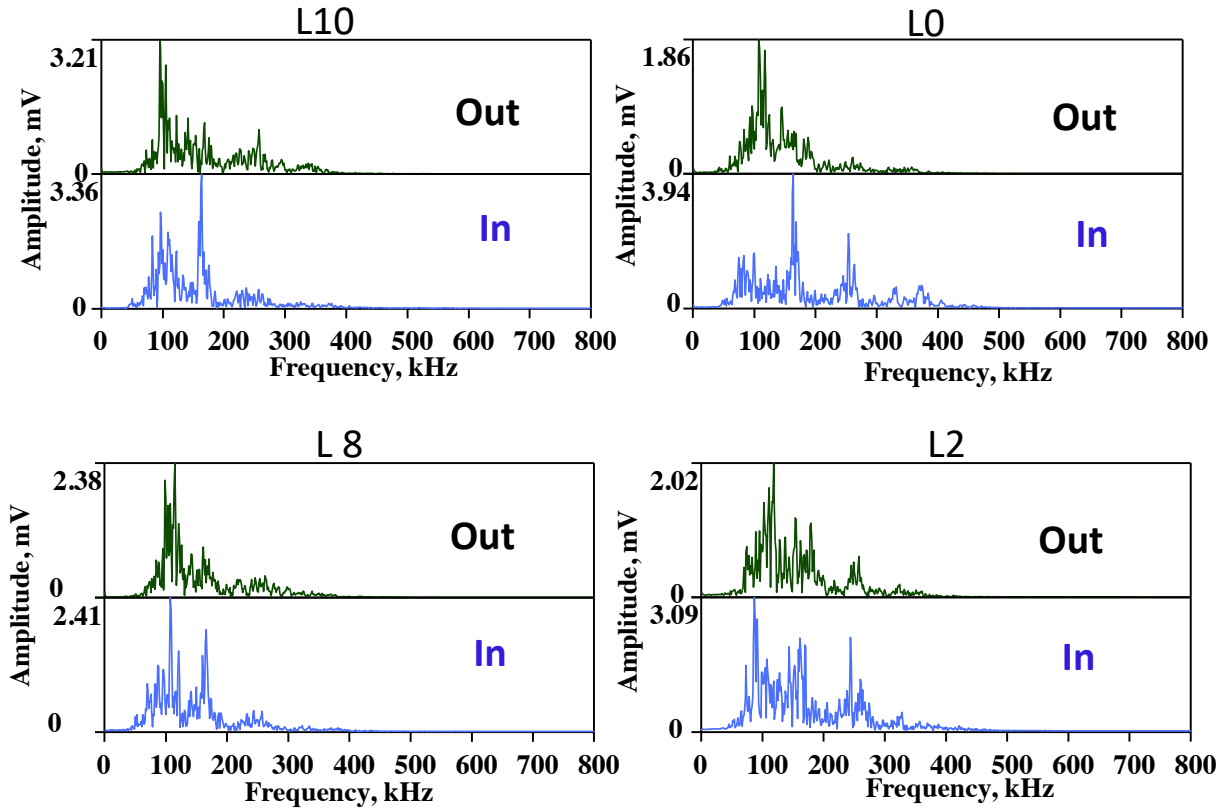


Fig. 18. Comparisons of FFTs of signals from the outside and inside R15 sensors versus end PLBs on different layers. Sensor signals shown in Fig. 14.

G. Peak amplitudes of outer and inner sensor signals versus the PLB layer

In an application of AE to monitor pressurization of LPVs, it is important that the sensitivity of the outer sensor not be heavily biased toward sources that originate in the outer layers. Thus, an examination of the relative peak amplitude difference of the outer sensor signal was obtained relative to the inner sensor peak amplitude for the same PLB layer. All the peak amplitudes occurred in the flexural region. To provide this comparison the ratios of the peak amplitude of the outer sensor signal to the peak of the inner sensor signal were averaged for five PLBs on each relevant layer and expressed as a dB difference relative to the inner sensor signal. This analysis is not a perfect one, since the thickness is different for the two layers the sensors are mounted on. Thus, as mentioned before, the frequency content will change to the extent there is propagation that is confined to those individual layers. Table 2 provides these results with positive values when the outer sensor peak average is larger than the inner peak average for the different PLB layers and vice versa for negative values. For this table the DW and WD sensor signals were also low pass filtered at 500 kHz to provide a better comparison to the filtered Mist and R15 results. Clearly, the Mist sensor provides the most uniform sensitivity as a function of the PLB layer. This outer sensor varies by at most 2.3 dB (ignoring signs) from the inner one. As mentioned before, this desirable aspect of the Mist sensor signals is due to the loss of higher frequencies as a result of the hot melt glue used for attachment and couplant. The expectation is that, if this sensor was coupled by vacuum grease, the relatively uniform sensitivity would not be maintained. On the other hand the maximum differences for the other three sensors, respectively for the DW, WD and R15 sensor signals, are (ignoring signs) 10.6 dB, 10 dB and 6.3 dB. Thus, except for the Mist sensor, there is a lack of uniform sensitivity in the outer sensor signals as the PLB layer changes.

Table 2. Average peak amplitude of outer sensor with reference to inner sensor peak amplitude.

Layer of PLB/Sensor	DW LP @ 500 kHz, dB	Mist LP @ 500 kHz, dB	WD LP @ 500 kHz, dB	R15 LP @ 400 kHz, dB
10, outer	10.6	-0.2	5.9	-0.9
9	5.5	-1.0	2.2	3.5
8	5.4	1.7	2.9	2.2
2	-5.0	-1.2	-5.8	-3.0
1	-5.8	-2.3	-8.8	-4.6
0, inner	-9.4	-0.1	-10	-6.3

H. Comparisons of the outer sensor peak amplitude at zero gain for PLBs on different layers

After subtracting the relevant gains from the signals from each sensor/preamp type, the average peak amplitude (five PLBs on each layer) of the different outer sensor signals as a function of the PLB layer was obtained. These results are expressed in dB_{AE} in Table 3. Clearly, except for the Mist sensor, the trend is a decrease in peak amplitude as the PLB moves further below the outer layer where the sensors were mounted. The Mist sensor shows very small changes until the PLB was done on layer 0. For this case there is an unexpected increase in the amplitude. An explanation for this behavior is not apparent. The next to last row of the table provides the difference in peak amplitude from the PLB on layer 10 relative to the value from PLB on layer 0. The large value of 14.1 dB for the DW sensor is due to the high amplitude of the Rayleigh wave for the PLB on layer 10. From PLBs on layers 9 to 0, the difference for the DW sensor is about 8 dB. As a potential measure of relative outer sensor response sensitivity for PLBs on the layers near the inside, the average peak amplitude values for the PLBs on layers 2, 1 and 0 were calculated. The values respectively for the DW, Mist, WD and R15 sensors in dB_{AE} are 42.3, 45.8, 46.1 and 53.1 as shown in the last row of Table 3.

Table 3. Average peak amplitude in dB_{AE} for the different outer sensors versus PLB layer.

Layer of PLB/Sensor	DW LP @ 500 kHz, dB_{AE}	Mist LP @ 500 kHz, dB_{AE}	WD LP @ 500 kHz, dB_{AE}	R15 LP @ 400 kHz, dB_{AE}
10, outer	56.2	43.6	54.7	55.2
9	50.4	42.8	52.7	56.9
8	50.7	43.6	52.6	57.1
2	42.3	45.6	46.1	55.1
1	42.6	44.7	44.4	53.2
0, inner	42.1	47.0	47.7	51.0
Amplitude peak difference in dB from outer to inner layer PLBs	14.1	-3.4	7.0	4.2
Average peak in dB_{AE} for PLBs on layers 2, 1 and 0	42.3	45.8	46.1	53.1

Relative to the approach of using the first arrival of the extensional mode to obtain an arrival time, the average peak amplitude (for five PLBs) for the outer sensor signals was determined for the PLBs on the same set of layers, and it is shown in Table 4. All the determinations of the location in time of the first arrival were done by "eye" when viewing each individual waveform. These results are shown in dB_{AE} after correcting the values by the relevant gains of the preamps. The choice of the amplitude to use was based on the amplitude of the first half cycle above the background noise level. This first half cycle amplitude was negative for all the sensor signals. In the case of the DW sensor, the poor S/N ratio only allowed determination of these amplitudes for PLBs on layers 10 and 9, and even in these cases knowing where the arrival was supposed to be in time helped determine a value. Clearly, as with peak amplitude, the Mist sensor provides the most uniform results as the layer of the PLB varies, as can be observed in the next to last row of Table 4. As a potential measure of relative outer sensor response sensitivity for PLBs on the layers near the inside, the average peak amplitude values (first half cycle) for the PLBs on layers 2, 1 and 0 were calculated. The values in the last row are respectively for the Mist, WD and R15 sensors were in dB_{AE} 26.7, 20 and 18.7.

Table 4 Average peak amplitude of the first arrival (half cycle peak) of the extensional mode for outer sensor signals

Layer of PLB/Sensor	DW LP @ 500 kHz, dB_{AE}	Mist LP @ 500 kHz, dB_{AE}	WD LP @ 500 kHz, dB_{AE}	R15 LP @ 400 kHz, dB_{AE}
10, outer	32.7	30.4	30.3	30.6
9	29.7	29.6	28.9	28.1
8	-	27.5	26.4	24.8
2	-	25.7	21.6	18.0
1	-	26.5	18.0	18.6
0, inner	-	27.9	20.4	19.4
Amplitude peak difference in dB from outer to inner layer	-	2.5	9.9	11.2
Average peak in dB_{AE} for PLBs on layers 2, 1 and 0	-	26.7	20	18.7

In order to obtain an estimate of the S/N ratio relative to the peak amplitude (for the flexural region) and the extensional first arrival (half cycle) amplitude for the different sensor/preamps, the time increment from 0 to 750 μs (before the signal arrival) was used for the outer sensor signals for 30 different PLBs to obtain a noise estimate. This choice meant that a total time of 22.5 ms was examined. Choosing 30 different cases was expected to provide a more representative value than one for a continuous time period of the same length. Since peak amplitudes of noise are what is important in

choosing an AE threshold, the maximum observed peak amplitude over the 22.5 ms was used. Then, using the respective preamp gains the dB_{AE} peak noise estimates were obtained. Table 5 shows the noise results in the first row. It should be noted that the noise level for the Mist sensor is a few dB higher due to the noise spikes (previously mentioned) that were not completely eliminated by the low pass filtering.

The S/N examination was based on using the average amplitude for PLBs on the inner layers 2, 1 and 0. From the second row of the table, the S/N ranking can be observed of the average flexural region peak amplitude from highest to lowest to be R15, WD, Mist and DW. The same process was repeated for the average peak amplitude of the first half cycle extensional arrival. The final row of Table 5 shows the extensional S/N ranking from highest to lowest to be R15, WD and Mist. It is important to note that all the values in the last row are negative meaning that a threshold based on the peak noise amplitudes would not have detected the first arrival of this mode for PLBs on the inner layers. Thus, the use of the "eye" technique to determine the location of the time of the first half cycle was a key.

Table 5 Electronic noise peak amplitude estimates for the different sensor/preamps and S/N estimates

Sensor/preamp	DW LP @ 500 kHz	Mist LP @ 500 kHz	WD LP @ 500 kHz	R15 LP @ 400 kHz
Electronic noise level in dB_{AE}	35.9	31.6	24.4	22.1
Peak amplitude difference in dB from average peak in flexural region for PLBs on layers 2, 1 and 0	6.4	14.2	21.7	31
Peak amplitude difference in dB from average peak (half-cycle) first extensional arrival for PLBs on layers 2, 1 and 0	-	- 4.9	-4.4	-3.4

I. Discussion of current results relative possible sensor choices for the potential application of AE monitoring during pressurization of LPVs

Three aspects need to be discussed: (i) detection of AE signals; (ii) locating AE sources and (iii) identification of the source type of located sources.

(i) In typical AE testing, detection of AE signals fundamentally depends on the amplitude of a particular signal compared to a set voltage threshold. Thus, based on the current S/N results, one might conclude that the best choice is the R15 sensor, but there is another important consideration. That consideration is that sensors mounted on the outer surface should have near equal sensitivity to sources no matter what "level" in the wall thickness the AE source originates. Relative to this requirement, the Mist sensor with the hot melt glue coupling is the best at having the most uniform amplitudes versus the layer region where the source originates.

(ii) With the background view that typically the calculation of a source location depends on the determination of signal arrival times that correspond to the same propagation velocity for each of the sensors in an array of at least three sensors, three location calculation approaches are considered relative to the results of this investigation. First, in typical commercial-service AE testing of pressure vessels the propagation velocity used is the Rayleigh velocity or the close-by shear velocity. Ignoring the possibility of arrival times being obtained from the extensional region before a potential Rayleigh wave arrival, the current results indicate a possible problem in that as the layer of the PLB moved to inner layers the distinct Rayleigh wave/flexural mode arrival no longer appeared in the case of each of the four sensor types. This aspect, due to a loss of higher frequencies transmitting to the outer surface, would result in errors when using the assumption of the mentioned single velocity for the location calculations when the

layer of the AE source changes. Second, another technique used for determination of arrival times at a fixed velocity is to detect the very first arrival of the extensional mode and use that velocity for the calculation of the source location. The current results indicate that three of the four sensor types do have a correspondence of the first arrival with the calculated arrival based on the extensional velocity for all the different PLB layers. Further and more important, when this correspondence was examined in detail, it was found that the background noise level would preclude this determination with the standard approach of using a fixed threshold to determine arrival times. Thus, a more sophisticated approach would be required (discussion of this is beyond the scope of this work) for the detection of the time of the first arrival of this mode. Alternatively, a significant reduction in the propagation distance to the sensors would increase the S/N ratio and potentially allow detection of the first extensional arrival. Third, the cross-correlation technique of determining an arrival time at a fixed frequency of a particular mode is also a possible approach provided the frequency is relatively low so that sources located in the inner layers can be located. This technique does depend of the use of a broadband sensor without strong resonances. For the current considerations that would mean the DW sensor or the Mist sensor, in the latter case depending on the selected correlation frequency alternate coupling may be necessary.

(iii) There are at least two primary AE source types that are present during an AE monitored pressurization of an LPV. These two are crack-tip region sources and friction-based sources at the interfaces between layers. Thus, successful AE testing requires the identification of these two types so that the irrelevant friction events can be eliminated. Friction-based sources tend towards lower frequencies, while crack-tip region sources during an overload beyond the maximum loads of prior cycling have a frequency range that extends to higher frequencies. Testing of LPV steel base material with sharpened cracks demonstrated that crack tip region events during a 10% overload had frequency content well above 200 kHz and up to at least 600 kHz with the same types of broadband sensors used in this study (with vacuum grease coupling), while friction extraneous sources had frequency content below 200 kHz with these same sensors [4]. Since, in the current work, the PLBs on the ends of the lower layers did not produce these higher frequencies at the outer sensors, this frequency distinction between the source type of interest and the source type that is extraneous presents a problem. Potentially, under pressure the frequencies transmitted to the outer surface may show some increase. To determine the increase in higher frequencies transmitted under pressure requires other experiments that are beyond the scope of this work.

Conclusions

- At the outer sensors, the calculated first arrival of the extensional mode corresponds to the signal arrival for all but one sensor type for all PLB layers. For the calculated flexural mode arrival, only for PLBs on the outer three layers does the actual signal arrival correspond for all the outer sensor types.
- Two outer sensor types (DW and WD) experienced significant loss of higher frequencies for PLBs on layers lower than layer 8, while two types (Mist and R15) that do not have higher frequency sensitivity did not show this significant change.
- As the PLBs moved to the inner layers the peak amplitudes of the outer sensor signals decreased significantly relative to the peak amplitudes of the inner sensors for all the sensor types, except for the couplant/modified Mist sensor.
- In dB_{AE} the average peak amplitudes (flexural region) of the different outer sensor types for PLBs on the inner three layers ranged from 53.1 to 42.3, and for the extensional first arrival from 26.7 to 18.7.
- The background electronic noise levels of the different sensor/preamps varied significantly.
- For PLBs on the inner three layers the S/N ratios of the outer sensors for the peak amplitude and the first half cycle peak amplitude are influenced by the differences in background noise levels of the different sensor/preamps as well as the differences in response of the different sensor types.

- The choice of the appropriate sensor type is not straightforward, as there were significant differences in the signals, frequency content and S/N ratio of the four different sensor types.
- The current results might be considered a lower bound relative to the lack of transfer of higher frequencies to outer-surface mounted sensors. The upper bound being the case of a monotonic wall of the same total thickness. The situation during a pressurization with imperfect interfaces will be somewhere in between and may be "tilted" towards the lower bound as the surfaces with asperity-to-asperity contact will remain imperfect to a large degree. Further, the waves must interact with the imperfect interfaces a very large number of times in the development and propagation of full-thickness Lamb waves to distant sensor positions.

Acknowledgements

The author gratefully acknowledges project funding, facilities and excellent experimental support, as well as purchasing of sensors and instrumentation, provided by NASA Marshall Space Flight Center, Huntsville, AL, USA.

References

1. ASTM Standard E569, "Acoustic Emission Monitoring of Structures During Controlled Simulation," 2013 and ASTM Standard E1419, "Examination of Seamless, Gas-Filled, Pressure Vessels Using Acoustic Emission," 2015a, ASTM International, West Conshohocken, PA.
2. Kolsky, H., *Stress Waves in Solids,* Dover, New York, 1963.
3. Wu, Bill S. and Gregory C. McLaskey, "Broadband Calibration of Acoustic Emission and Ultrasonic Sensors from Generalized Ray Theory and Finite Element Models," Journal of Nondestructive Evaluation, Vol. 37, No. 8, pp. 1 – 16, 2018.
4. Hamstad, M. A., personal communications, NIST, Boulder, CO, January 2019.
5. Baltazar, Arturo, Stanislav I. Rokhlin and Claudio Pecorari, "On the Relationship between ultrasonic and Micromechanical Properties of Contacting Rough Surfaces," Journal of Mechanical and Physics of Solids, Vol. 50, pp. 1397 – 1416, 2002.

Appendix L: Far-Field Wave Propagation Signals from Pencil Lead Breaks on the Open End of a Thick-Walled Layered Cylinder, Part 2: Modes of Wave Propagation

Far-field Wave Propagation Signals from Pencil Lead Breaks on the Open End of a Thick-walled Layered Cylinder: Part 2 Modes of wave propagation

M. A. Hamstad
Department of Mechanical and Materials Engineering
University of Denver, Denver, CO 80208, USA

Abstract

Relative to potential use of acoustic emission (AE) to monitor pressure testing of large steel pressure vessels, in-plane pencil lead breaks (PLBs) were carried out on the open end of a remnant of such a vessel. This remnant had an inner diameter of 58 in. (1473 mm), a wall thickness of 3.3 in. (84 mm) and a total cylindrical length of 125 in. (3175 mm) ending in a head welded to the cylindrical section. The cylindrical section did not have a monotonic wall, but instead it was made of 11 layers (10 at about 0.277 in. [7 mm] thick, and the inside one of about 0.47 in. [11.9 mm] thick) to create a layered pressure vessel (LPV). Due to the presence of the multiple interfaces between layers, a question arose as to whether a sensor mounted on the outer layer was relatively less sensitive and had different frequency content for sources on the inner layers in comparison to sources on the outer layers? The PLB study used four pairs of different types of AE sensors. The sensor types included: i) strong resonance at a single frequency region; ii) multiple resonance frequencies; iii) and iv) broadband response with different frequency responses. Each sensor pair was acoustically coupled, one on the outside surface and one directly below on the inside surface. The sensors were located at 66 in. (1676 mm) (20 times the wall thickness) from the PLB points. This distance was considerably less than the helical path of about 214 in. (5436 mm). Considering PLBs on the ends of the different layers, Part 2 focused on identification of Lamb modes of wave propagation in the AE signals from the four sensor types. In addition, by use of superimposed group velocity curves on frequency versus time results, the peak intensity in the frequency versus time domain for the outside sensor types was studied relative to determination of the presence of dominant full thickness propagation or dominant single layer propagation. For PLBs on the outer most layers, both single layer propagation and full thickness propagation were present in some of the outer sensor signals.

Keywords: Thick-walled layered cylinder, pencil lead breaks, four sensor types, inside and outside sensors, acoustic emission wave propagation and Lamb modes

Introduction

Acoustic emission (AE) testing has been used for many years to monitor testing of pressure vessels as evidenced by ASTM standards (E569 first version 1976 and E1419 first version 1991) [1]. These standards do not specifically address the steel vessel of current interest, namely a vessel made up of layers (11 in this research) of steel rather than a monotonic vessel wall. Several hundred similar layered vessels were fabricated starting in the late 1950's and early 1960's for use by the National Aeronautics and Space Administration (NASA) and other commercial organizations. In the current time frame to more knowledgeably examine AE results from potential pressure testing of such vessels, an important step is to understand the wave propagation of AE-like waves in such a vessel. An opportunity was available to carry out wave propagation studies on a vessel remnant, which had been cut from a large layered pressure vessel (LPV). Thus, the overall goal of the study was to examine pencil lead break (PLB) AE signals in the far field using four different AE sensor types as the layers of the PLBs changed. Besides the uniqueness of the layered construction a further unique aspect was the use of pairs of like AE sensors located back-to-back on the outside and inside of the vessel wall.

In Part 1 of this research, analysis was done of the waveforms and fast Fourier transform (FFT) spectra of the signals received in the far-field at 66 in. (1,676 mm; in this paper, the first listing of units

refers to the actual measured value, if not in S.I. units then the converted units are added), which is 20 times the vessel wall thickness. Four different types of AE sensors were used for in-plane PLBs on the open ends of different layers. As described in Part 1, the large remnant was of sufficient size so that the signals from the direct path could be examined prior to the arrival of the waves from the two helical paths.

In the research reported here in Part 2, the purpose was to determine, for the outer sensor position, the dominant region present in the intensity of frequency versus time data and the possible modes of Lamb wave propagation that were present. An additional goal was to determine if dominant Lamb-wave propagation was full-thickness (like for a monotonic wall) or single-layer propagation for the layer the sensor was mounted on. The variables were: (i) the PLB layer and (ii) sensor type. Four approaches were used. First, the intensity of frequency versus time plots of the signals was examined by use of the Choi Williams distribution (CWD) [2] along with superposition of the appropriate group velocity curves (transformed to frequency versus time for the current propagation distance) as a function of the layer on which the PLB was done and the sensor type. Second, the same CWD data was used to compare the four different sensors types for PLBs on the same layers. This comparison examined the area patterns of the intensity. Third, the waveforms from one sensor with good non-resonant low frequency response were used to compare the phase relationships of the signals for PLBs on layers near the outside and near the inside of the remnant wall. Fourth, the CWD results were considered at the very beginning of the outside sensor signals as a function of the PLB layer. In the application of these approaches, two regions of the signals were examined. The first region was the so-called "extensional region" for the portion of the signal from just before the first arrival of the fundamental extensional mode (lowest symmetric Lamb mode) to an end shortly before the arrival of the fundamental flexural mode (lowest antisymmetric Lamb mode). The second region the so-called "flexural region" added the additional portion of the signal beyond the arrival of the flexural mode to the examination. It is worthwhile to note that the peak amplitudes of the signals were always in the "flexural region."

Group Velocity Curves, Choi Williams Distribution and Experimental Conditions

The primary required group velocity (GV) curves were calculated using freeware software from Vallen [3]. The GV results are shown in Fig. 1 respectively (left to right) for the outer layer of nominal thickness 0.277 in. (7 mm) and the full nominal thickness of 3.3 in. (84 mm). The thickness values are from the original manufacturing information. Note all the layers except the inner one had this same nominal thickness. The inner layer had a thickness of 0.47 in. (11.9 mm). The properties used for the GV calculations were for steel using the bulk velocities from Kolsky [4] (longitudinal at 5.94 mm/μs and shear 3.22 mm/μs). The group velocity curves are shown to 500 kHz for the smaller thickness (based on a preliminary analysis of frequency versus time results) and 120 kHz for the full nominal wall thickness (also based on a preliminary analysis of frequency versus time results). These limitations on the maximum frequency range facilitate viewing the GV results that correspond to Lamb waves most appropriate for each potential thickness. The modes shown in these figures are limited to those most likely to be present in the signals. When these two thickness cases are compared, it is clear that the frequencies are much lower for the 84 mm case at similar velocities. Further, in the 84 mm case upon approaching 120 kHz, the A_0, S_0 and A_1 curves are all becoming asymptotic to the Rayleigh velocity for steel. In contrast, for the 7 mm case at 500 kHz only the A_0 mode is approaching the Rayleigh velocity.

The frequency versus time intensity was obtained by use of Vallen freeware, specifically using the CWD [3]. These calculations were made using the default values for the number of terms in the damping summation and the exponential damping parameter along with choosing of a frequency increment of 1.22 or 2.44 kHz. In addition, the out-of-plane intensity (color scale) of the CWD results used the default 100 % range based on the peak value.

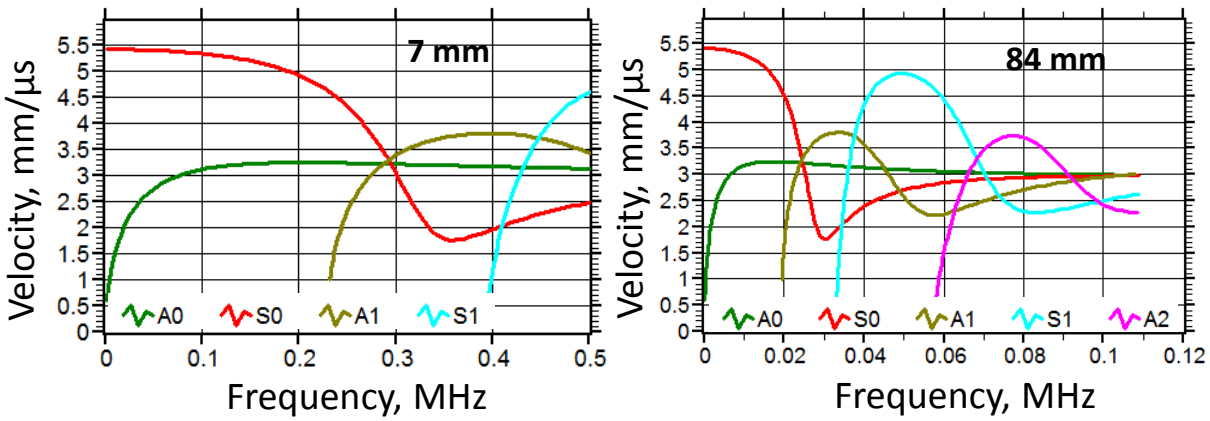


Fig. 1. Group velocities for steel plate thicknesses of 7 mm left and 84 mm right.

The reader of Part 2 is referred to Part 1 [5] for the experimental details including: remnant specimen details, sensor types, layer numbering, trigger sensor (relocated to be very close to the PLB points on the different layers), sensor attachment, instrumentation and acoustic coupling, etc., so as to not unnecessarily repeat this lengthy information. The shorthand notation for the four sensor types remains the same, as used in Part 1: Digital Wave (DW) broadband sensor; Mistras (Mist) broadband sensor; Mistras WD (WD) resonant sensor and Mistras R15 (R15) resonant sensor. Due to unidentified intermittent electromagnetic noise from other activities in the test building, as in Part 1, when certain sensor types were being used, low pass software filtering was used for the Mist and R15 sensor signals respectively at 500 kHz and 400 kHz. This filtering did not alter the key range of frequency response for these sensors. All the original data was taken using a passive high pass filter at 10 kHz.

A. Modal examinations by use of the CWD as the PLB layer changes for each sensor type

All the analysis of the sensor signals in Part 2 used the same 700 µs signal increment used in Part 1. For convenience in the multiple steps to import the signals into the CWD software and setting up the computations there, the 700 µs time increment was extracted, and the initial time was set to zero µs. The key result to keep in mind with this adjustment is that the calculated first arrival times (from Part 1) of the fundamental Lamb modes changed to 63 µs for the extensional mode and 274 µs for the flexural mode. Also, it is important to keep in mind that the initial portion of up to 63 µs represents background noise, and the termination of the signal at 700 µs is about 50 µs before the initial signal arrivals of the two helical paths to the sensors. Note that the peak amplitudes of the signals occurred prior to the end of this 700 µs time increment.

Before specific results for each sensor type are presented, the layout of the pairs of figures, for all the sensor types in this section, needs some explanation. First, since the superposition of the GV curves tends to "hide" the maximum intensity region (red color) when the GV curve closely matches the intensity data, the relevant GV results are shown above (7 mm case) and below (84 mm case) the CWD results. This placement facilitates the reader's comparisons GVs versus CWD results. In order to align the transformed GV curves in time, an offset time is required. The value selected was based on the following considerations. The 7 mm S_0 mode GV was aligned with the initial intense portion of the CWD result to 500 kHz in the extensional region for the outer DW sensor for a PLB on the end of outer layer 10, which resulted in an offset value of –245.2 µs. Then, the 11.9 mm S_0 mode GV was aligned with the initial intense portion of the CWD result to 250 kHz in the extensional region for the inner DW sensor for a PLB on the end of inner layer 0, which resulted in a value of –246.2 µs. The average offset value of –245.7 µs was used for all cases. This value is very close to the value based on the PLB time, which was –246.6 µs. Since this value (based on assumed propagation velocities) did not result from an actual comparison with CWD results, it was not used. Figure 2 illustrates (using the selected offset) with the DW sensor the close "fit" of the S_0 mode with the outer sensor for a PLB on layer 10 on the left and a PLB on layer 0 with the DW inner sensor on the

right. Second, the most relevant GV curves are shown in each case as a minimum, and in some cases for reference, some not relevant are shown to demonstrate they are not relevant. Third, the left column in each figure provides frequency results to 120 kHz to more clearly show cases where the intensity at low frequency potentially corresponds to the GVs for 84 mm thickness case. The far-right column provides frequency results to 500 kHz to give a better view of potential correspondence to the GVs for the 7 mm thickness case. Also, the color scale, provided in the figures, shows the range of colors of the out-of-plane intensity. In each case, the peak of the color scale, red color, represents the maximum intensity. Fourth, in the middle column, the waveforms on which the CWD results were based are shown along with vertical red cursors at the calculated first arrival times of the fundamental modes. The PLB layers are also indicated in these waveform plots. Fifth, for each sensor type there is a pair of figures. The first is for a time increment to 260 µs to allow a focus on the "extensional region," and the second figure for a time increment to 700 µs to provide a focus additionally on the "flexural region." Sixth, frequencies and time values that are provided in the text and tables were determined from the large size view on the computer monitor. These values were based on results using a computer mouse in conjunction with the software to point to key regions. Seventh, in this section, the focus is on determining the correspondence of the GV mode curves with the most intense portion in frequency and time within the CWD results. Finally, for this section of the paper, all the data is for the outer sensors, since the results for that sensor are of the most importance. The obvious reason is that the outer sensor is the only sensor position that is available in a typical pressure test of an LPV with AE monitoring.

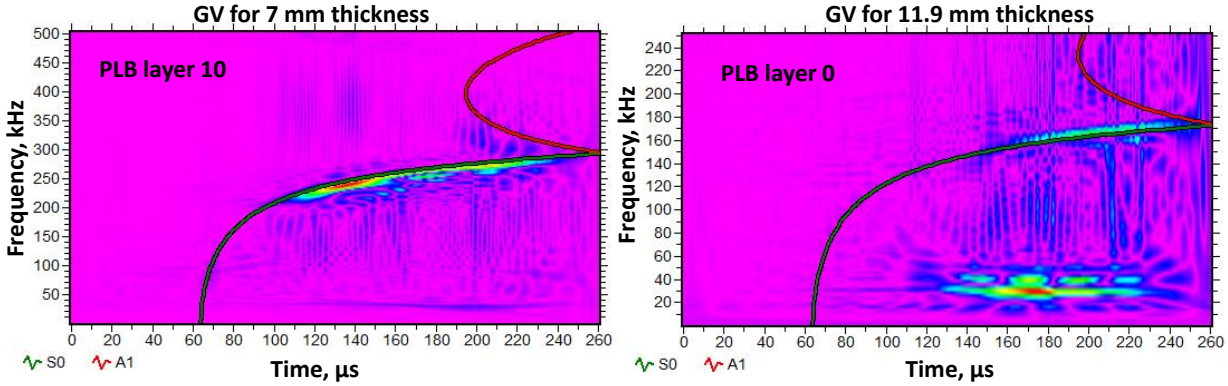


Fig. 2. Illustration of the "fit" of CWD in the intense portion with the S_0 mode for the two relevant GV curves using the outer DW sensor on the left and the inner DW sensor on the right.

i) DW sensor signal CWD results

In Figs. 3 and 4, the CWD results are shown for the DW sensor signals (note in this paper, as shorthand, "sensor signals" is shortened to "sensor" in some cases). When the DW sensor CWD results are examined in the extensional region (Fig. 3) for the range up to 120 kHz, the most intense region, for all the PLB layer cases, is close to the S_0 mode from the 84 mm GV thickness. The peak intensity arrival time varies for the different layers from about 188 µs to 210 µs. The frequency at the peak intensity varies for the different layers from about 28 kHz to 32 kHz. When the focus for the extensional region changes to a frequency range up to 500 kHz, the layer 10 PLB most intense region corresponds very well to the 7 mm S_0 mode. This long-time region of intensity is above 200 kHz. The peak intensity arrives at about 136 µs with a frequency of about 239 kHz. As the PLB source moves to layers further into the wall thickness, the most intense region moves to the frequencies and arrival times already discussed above for the frequency range to 120 kHz and the 84 mm GVs.

In Fig. 4, when the time range is extended to 700 µs to include the flexural region for the frequency range to 120 kHz, the peak intensity varies from about 100 kHz to 107 kHz for PLBs on layers 10, 8, and 5 (as in Part 1 of this paper, the sequences of layers are numbered as Layer 10 for the outside and Layer 0 for the innermost layer, while the sensor is on the outer surface) corresponding to the 84 mm GVs for the A_0, S_0 and A_1 modes as the PLB layer changes. It is worth noting that the frequencies from 100 kHz to 107 kHz may be as high as they are due to some contribution from single layer propagation for 7 mm GVs.

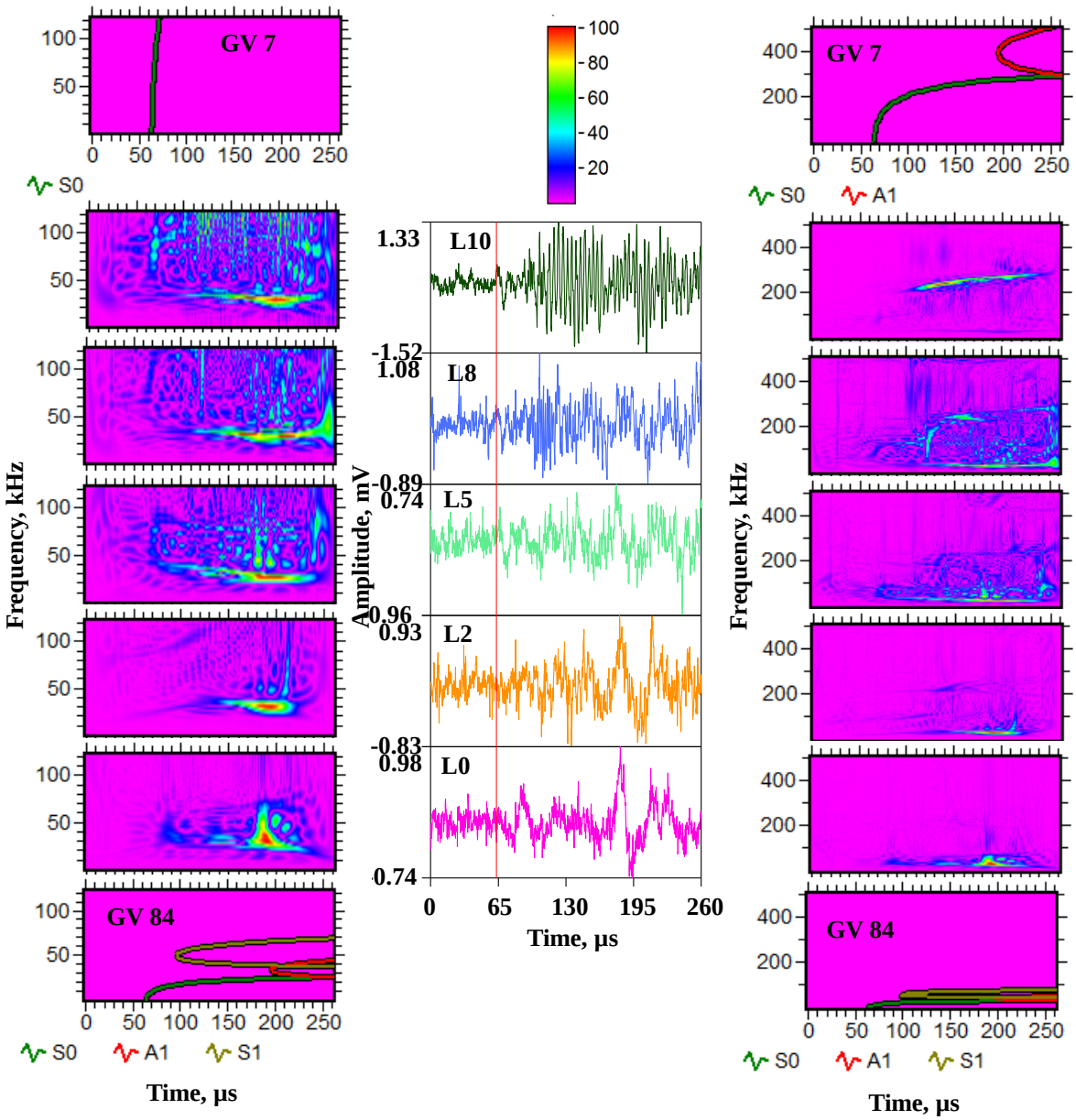


Fig. 3. Shows the CWD results for the DW outer sensor signals for a time increment of 0 to 260 µs (extensional region). Left column frequencies to 120 kHz and right column frequencies to 500 kHz. Middle column shows the signals used. GV results for two thicknesses shown.

For the layer 2 PLB, there is no direct match with 84 mm GV modes due to a scatter in the most intense points in the frequency range of about 78 kHz to 120 kHz for the above three modes. In the case of layer 0 PLB, it is clear that the 84 mm S_0 modes corresponds with peak intensity at both 31 kHz and 45 kHz with respective arrival times of about 428 µs and 436 µs.

When the frequency range for the CWD increases to 500 kHz, it is clear that the peak intensity corresponds to 7 mm A_0 for PLBs on layers 10 and 8 for respective frequencies at about 248 kHz and 254 kHz with arrival times at about 277 µs and 280 µs. For the PLB on layer 5, the peak intense region drops to about 122 kHz arriving at about 322 µs and the modes are for 84 mm GV S_0 and A_0 modes. For PLBs on layers 2 and 0 the comments are the same as for the frequency range to 120 kHz, except that the scattered points for layer 2 PLB cover a frequency range from 156 kHz to 203 kHz. Again the previous comment about the frequencies in the broad 100 kHz range potentially having some contribution from the single layer propagation may apply.

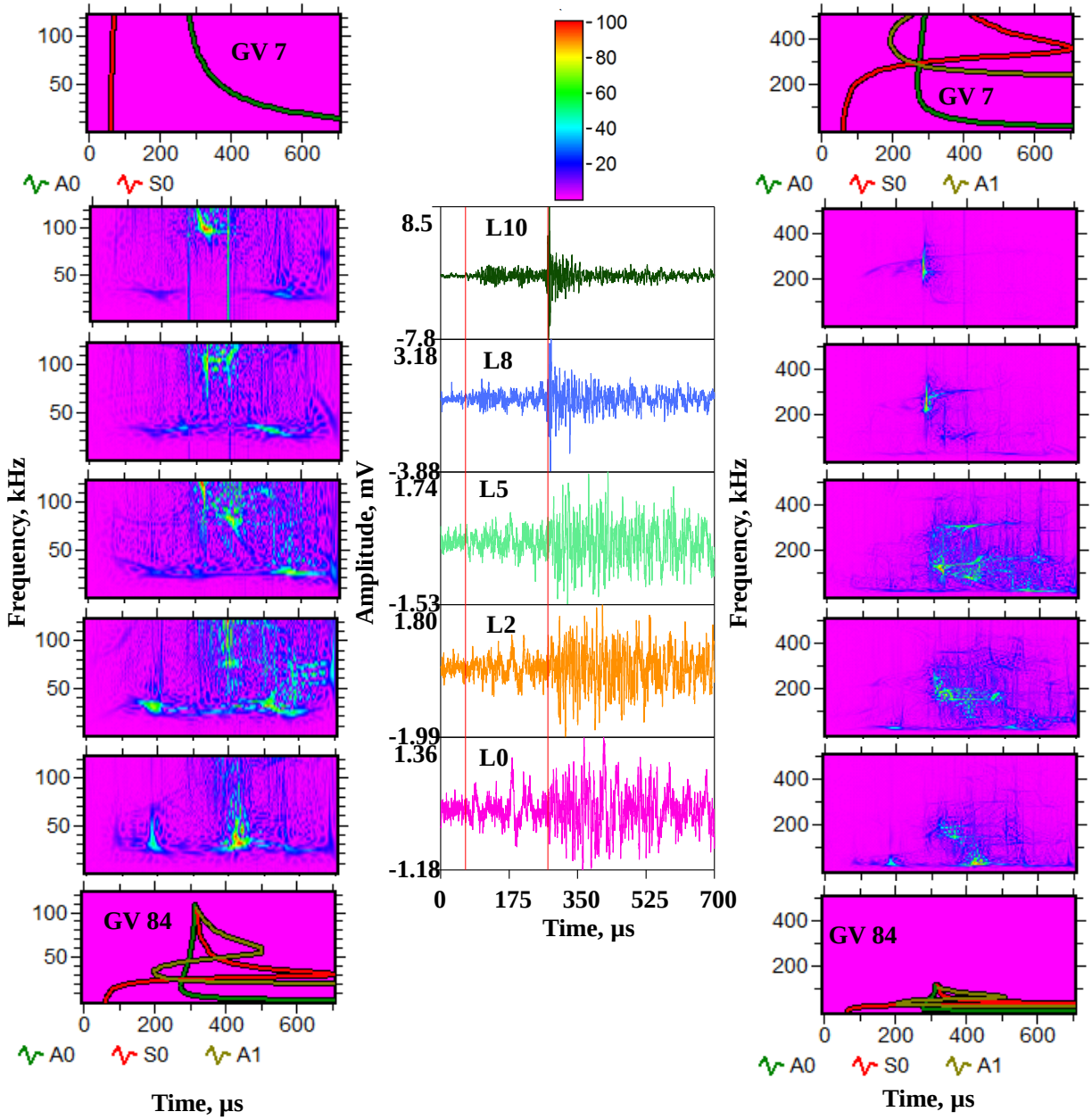


Fig. 4. Shows the CWD results for the DW outer sensor signals for a time increment of 0 to 700 µs (flexural region). Left column frequencies to 120 kHz and right column frequencies to 500 kHz. Middle column shows the signals used. GV results for two thicknesses shown.

ii) Mist sensor signal CWD results

Figure 5 provides the CWD results up to 120 kHz for the Mist sensor signals in the extensional region. For this frequency range, the correspondence of the peak intensity is with the 84 mm S_0 mode for PLBs on layers 10, 8, 2 and 0. The frequency range varies from about 26 to 27 kHz with arrival times varying from about 196 µs to 215 µs. In the case of the PLB on layer 5, the peak intensity correspondence is with 84 mm S_0 mode with the peak frequency at about 32 kHz with an earlier arrival time (possibly influenced by the S_1 mode) at about 160 µs as compared to the other layers. When the CWD frequency range is increased to 500 kHz, the most intense region for all the PLB layers continues to be the same as for the 120 kHz results. When the CWD time range is extended in Fig. 6 to include the flexural region, the 84 mm GV modes again dominate for both the 120 kHz and 500 kHz frequency ranges. The peak frequencies are in the range of

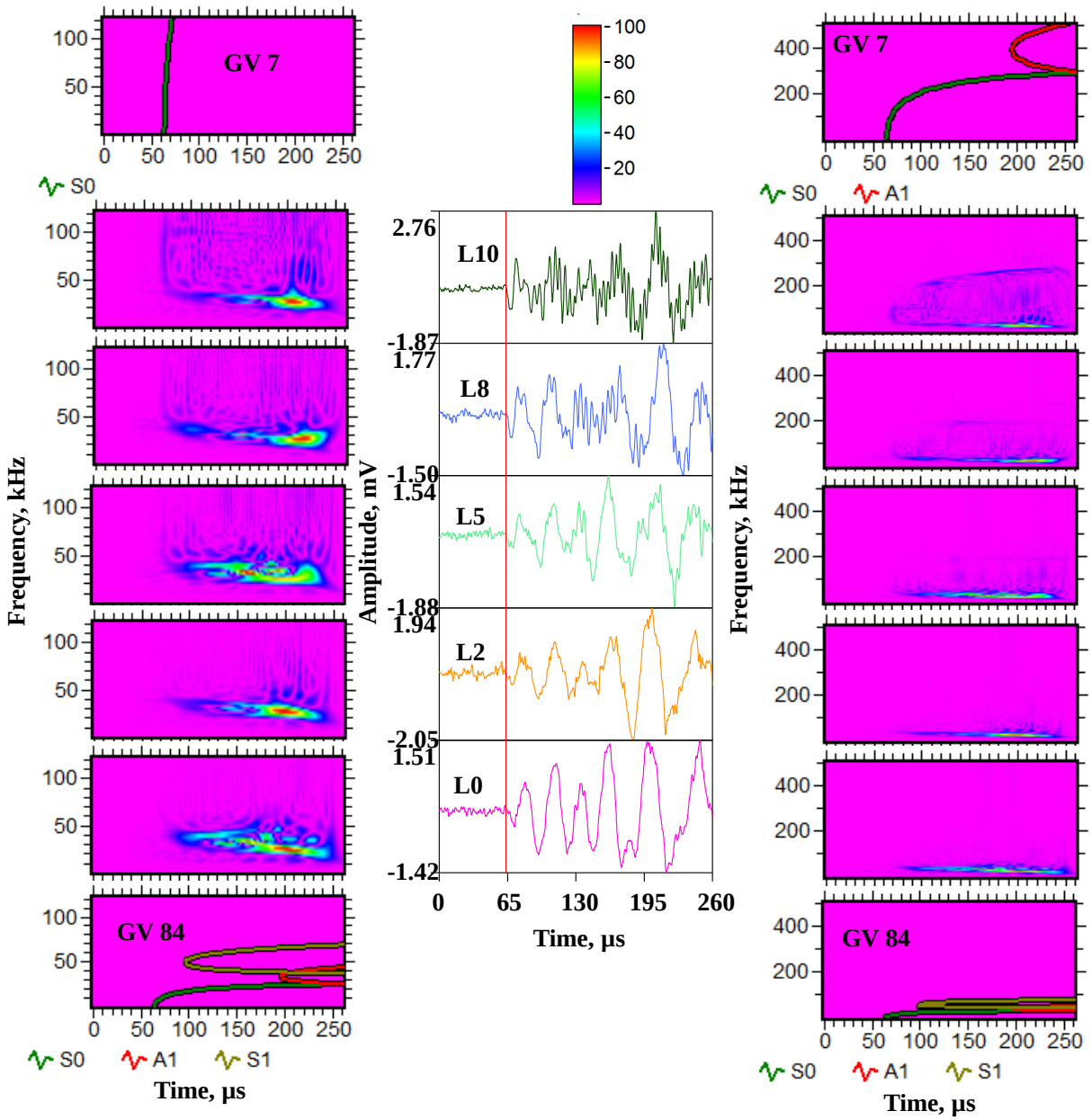


Fig. 5. Shows the CWD results for the Mist outer sensor signals for a time increment of 0 to 260 µs (extensional region). Left column frequencies to 120 kHz and right column frequencies to 500 kHz. Middle column shows the signals used. GV results for two thicknesses shown.

24 to 32 kHz, and the arrival times of these peaks varied from 571 to 619 µs (well into the flexural region) for layers 10, 8, 5 and 2 PLBs. The mode is S_0 for these layers. For layer 0 PLB, the peak time is earlier at about 426 µs, and the modes seem to be a combination of S_0, A_1 and S_1 with a peak frequency of about 32 kHz. As was pointed out in Part 1, the dominance of low frequencies for the Mist sensor is a result of the use of hot melt glue to couple the sensor, which resulted in significant attenuation of the higher frequencies prior to reaching the sensor's sensing element.

iii) WD sensor signal CWD results

In the case of the WD sensor, due to the resonant behavior, only limited CWD peak intensity matches to the GV curves were observed. Figure 7 shows the results for the extensional region. For the CWD frequency range up to 120 kHz, there are no clear matches of the CWD intensity and the GV curves.

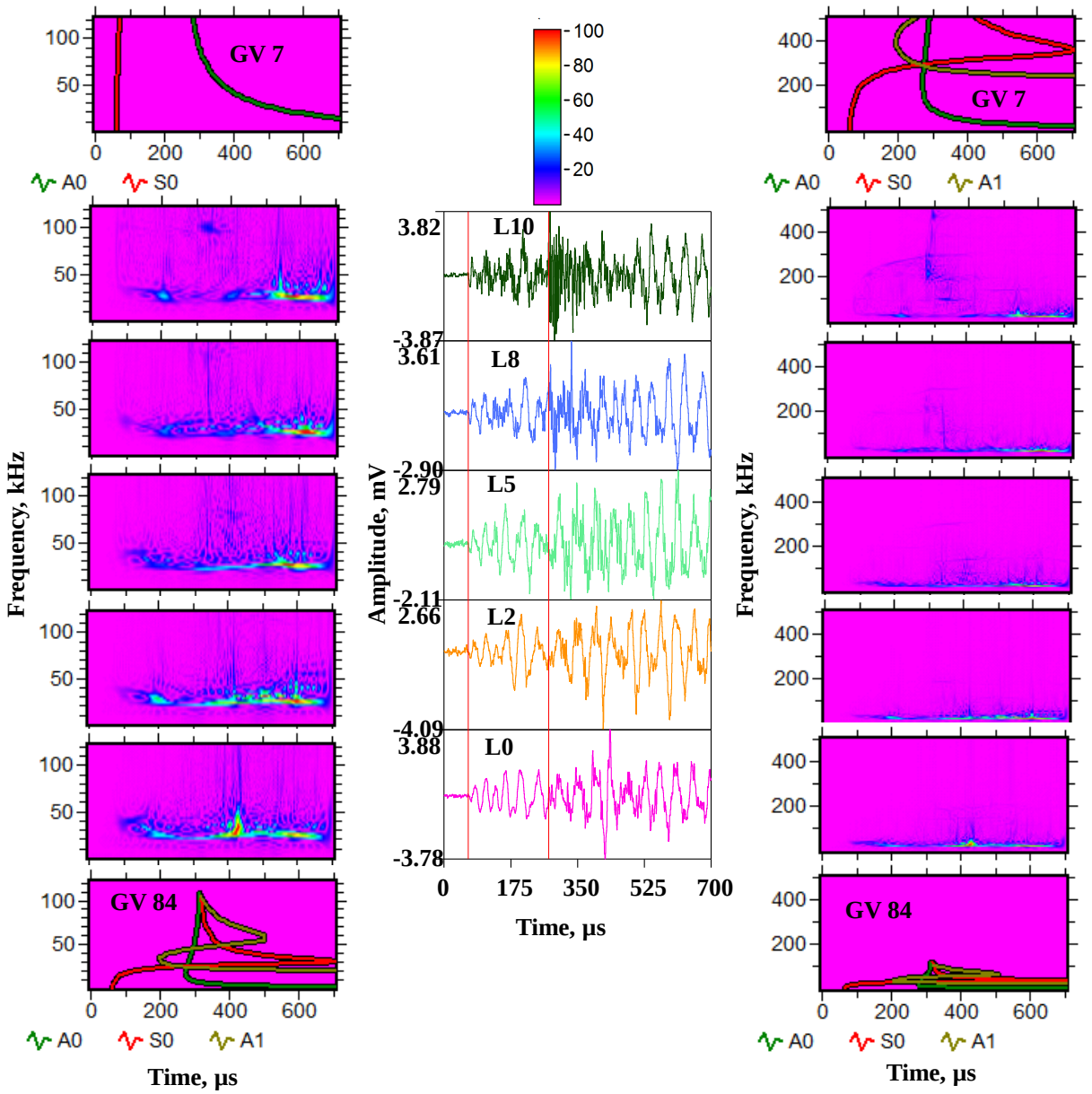


Fig. 6. Shows the CWD distribution results for the Mist outer sensor signals for a time increment of 0 to 700 µs (flexural region). Left column for frequencies to 120 kHz and right column for frequencies to 500 kHz. Middle column shows the signals used. GV results for two thicknesses shown.

When the frequency range was expanded to 500 kHz, a correspondence of the peak intensity was found for 7 mm S_0 mode at a peak frequency of about 269 kHz for layer 10 PLB with an arrival time of 203 µs.

For the other PLB layers no clear matches were found. Upon expansion of the time range (0 to 700 µs) to include the flexural region, as shown in Fig. 8, there seems be correspondence of the GV curves with the peak intensity regions for the PLBs on layers 10 and 8 in the CWD results up to 120 kHz for 84 mm where modes A_1 and A_2 cross each other at frequencies of about 100 kHz and 107 kHz with respective times of 344 µs and 335 µs. For PLBs on layers 5, 2 and 0 the peak intensities are in the 84 mm GV region, but there are no apparent matches of the CWD peak intensity to the GV curves.

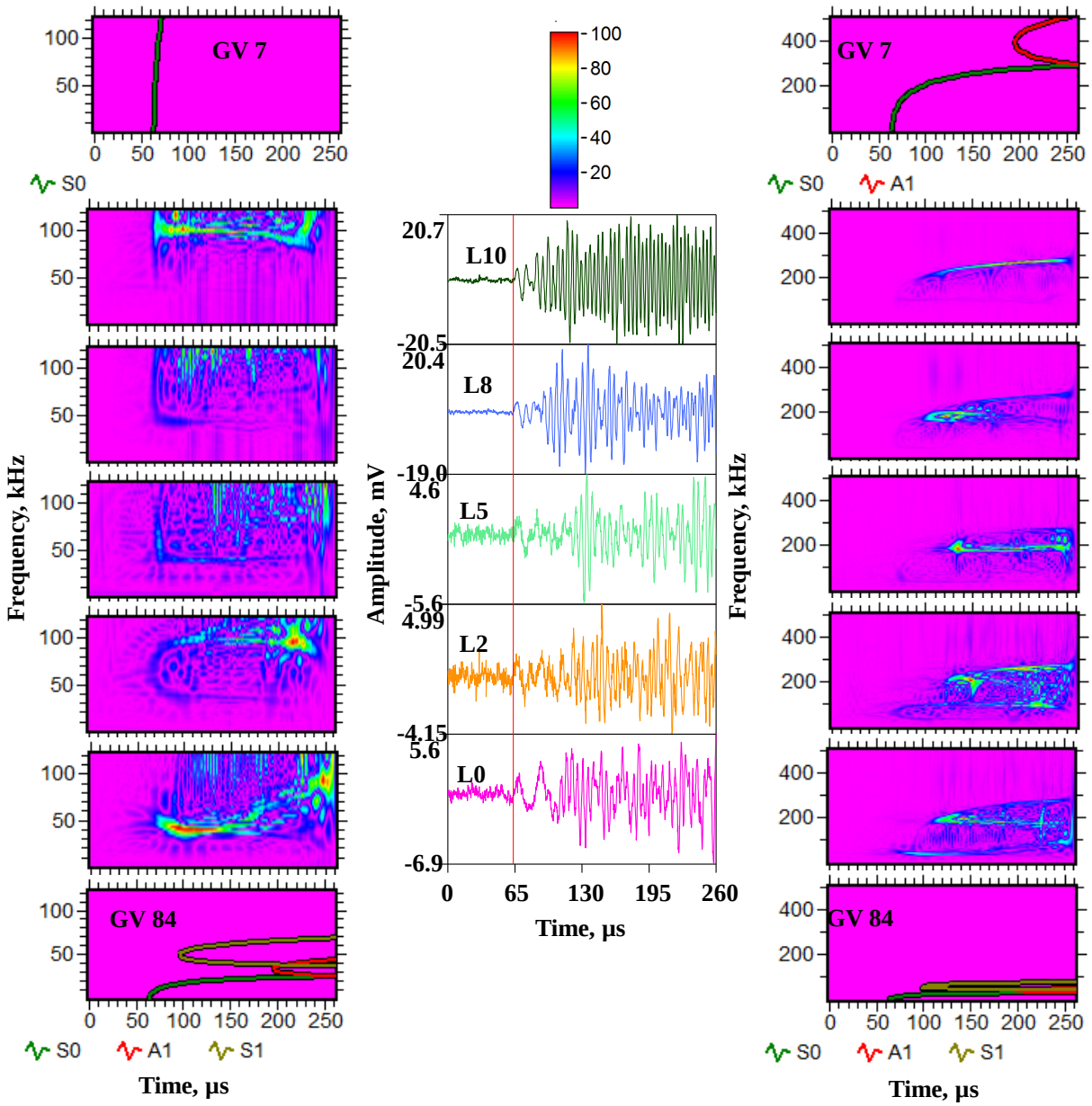


Fig. 7. Shows the CWD results for the WD outer sensor signals for a time increment of 0 to 260 µs (extensional region). Left column frequencies to 120 kHz and right column frequencies to 500 kHz. Middle column shows the signals used. GV results for two thicknesses shown.

When the CWD results in the flexural region are expanded to 500 kHz, there is close correspondence of peak intensity for layer 10 PLB where modes A_0 and A_1 cross each other for the 7 mm GV curves. The peak frequency and time is 278 kHz and 281 µs. For layer 8 PLB there is a potential correspondence to 7 mm GVs with a peak frequency of 283 kHz between the close-by S_0 and A_1 curves at a time of about 337 µs. When the PLBs are on the ends of layers 5, 2 and 0, the intense peaks are approximately in the range of 178 to 186 kHz. These are above the frequencies of the 84 mm GV modes, but they do not match the 7 mm modes. In summary, for this resonant sensor, the matches that were observed may be happenstances of sensor resonant frequency ranges corresponding to certain intense modal regions for the current thicknesses, but these matches may not be present for these modes when other thicknesses are present.

iv) R15 sensor signal CWD results

Figure 9 shows the CWD results for the R15 sensor in the extensional region up to 260 µs. There does not seem to be any matches for the CWD intense regions and the GVs for either thickness 7 mm or 84 mm

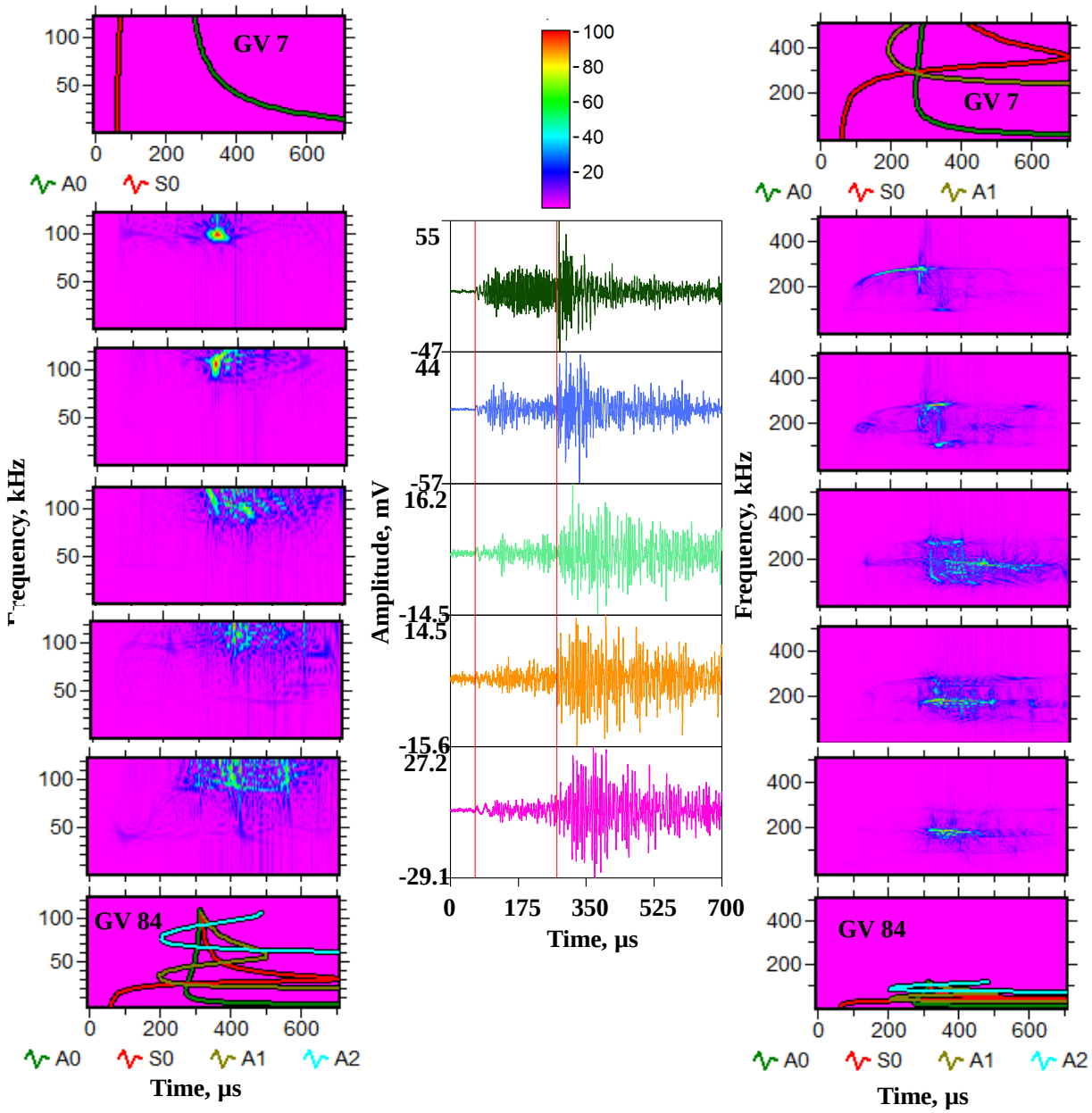


Fig. 8. Shows the CWD distribution results for the WD outer sensor signals for a time increment of 0 to 700 µs (flexural region). Left column for frequencies to 120 kHz and right column for frequencies to 500 kHz. Middle column shows the signals used. GV results for two thicknesses shown.

and for either frequency range to 120 kHz or to 500 kHz. This result is not unexpected, since this sensor has a relatively strong resonance at about 150 kHz, according to the manufacturer. The interesting fact is that all the peak intensity frequencies occur in the frequency range of about 101 to 127 kHz (checked by expanding the frequency range to 150 kHz), which is below the manufacturer's value. The time range of the peak frequencies varies over a wide range from 112 µs to 245 µs. Likewise, in Fig. 10, when the time increment is increased to 700 µs to include the flexural region, even when both CWD frequency ranges are considered, only one correspondence was found for PLBs on layer 5. In this case, the GVs for 84 mm and modes A_0 and S_0 matched the peak intensity for both CWD frequency ranges at about 117 kHz and a time of 338 µs. For the PLB layers 18, 8, 2 and 0, the peak frequencies ranged from101 kHz to 112 kHz with no matches to GV curves.

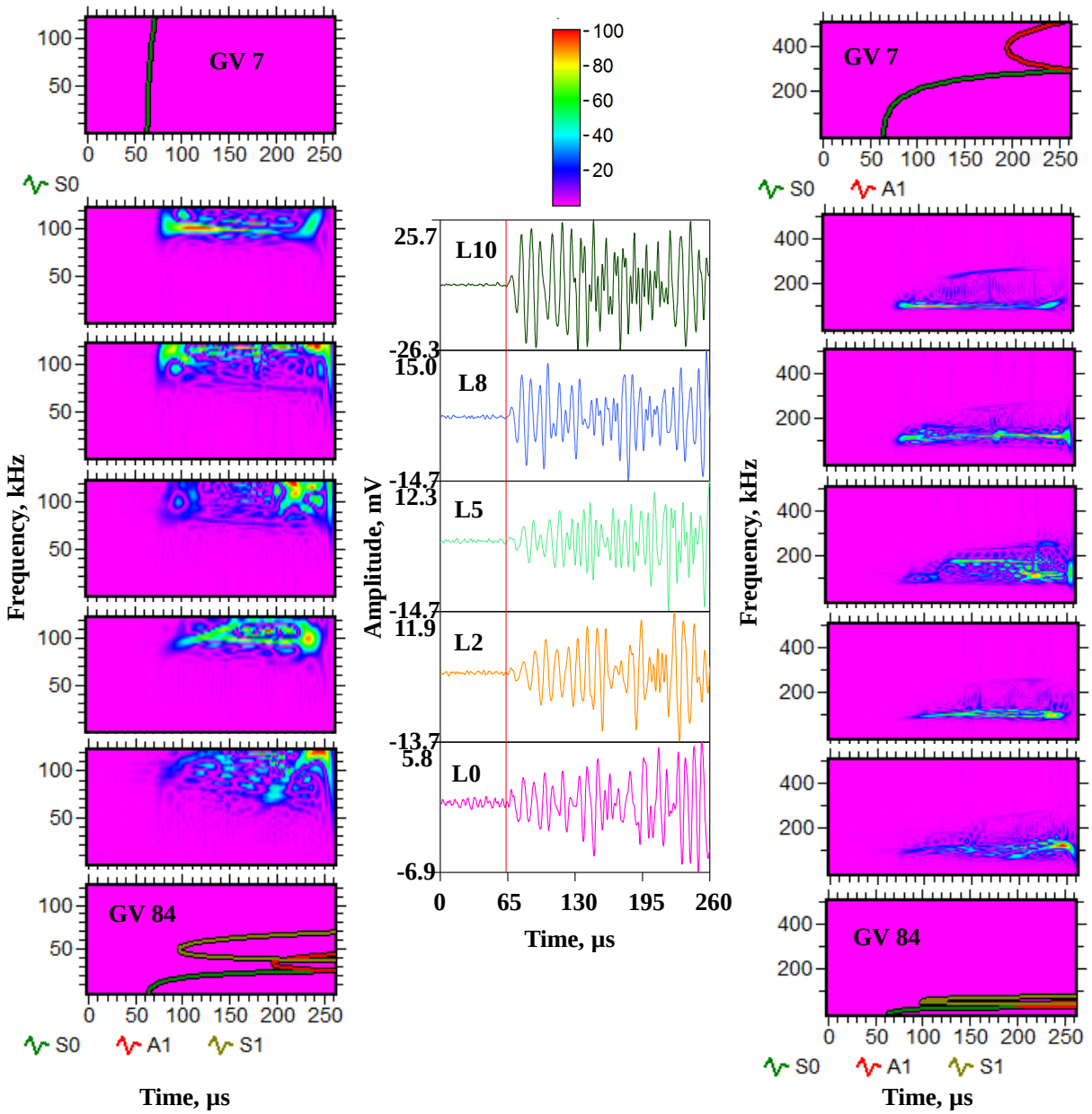


Fig. 9. Shows the CWD results for the R15 outer sensor signals for a time increment of 0 to 260 µs (extensional region). Left column frequencies to 120 kHz and right column frequencies to 500 kHz. Middle column shows the signals used. GV results for two thicknesses shown.

To provide the reader with a convenient summary of the CWD peak intensity data for the different sensors and the different PLB layers, two tables are provided. Each "cell" of these tables shows consecutively the most intense frequency, the arrival time of that most intense frequency and, where applicable, the thickness in mm and GV mode(s) that reasonably correspond to that peak intensity. Table 1 shows the CWD peak intensity results for the ranges to 120 kHz and 500 kHz for the extensional region. Table 2 shows the CWD peak intensity results for the ranges to 120 kHz and 500 kHz for the extensional region and flexural region signals.

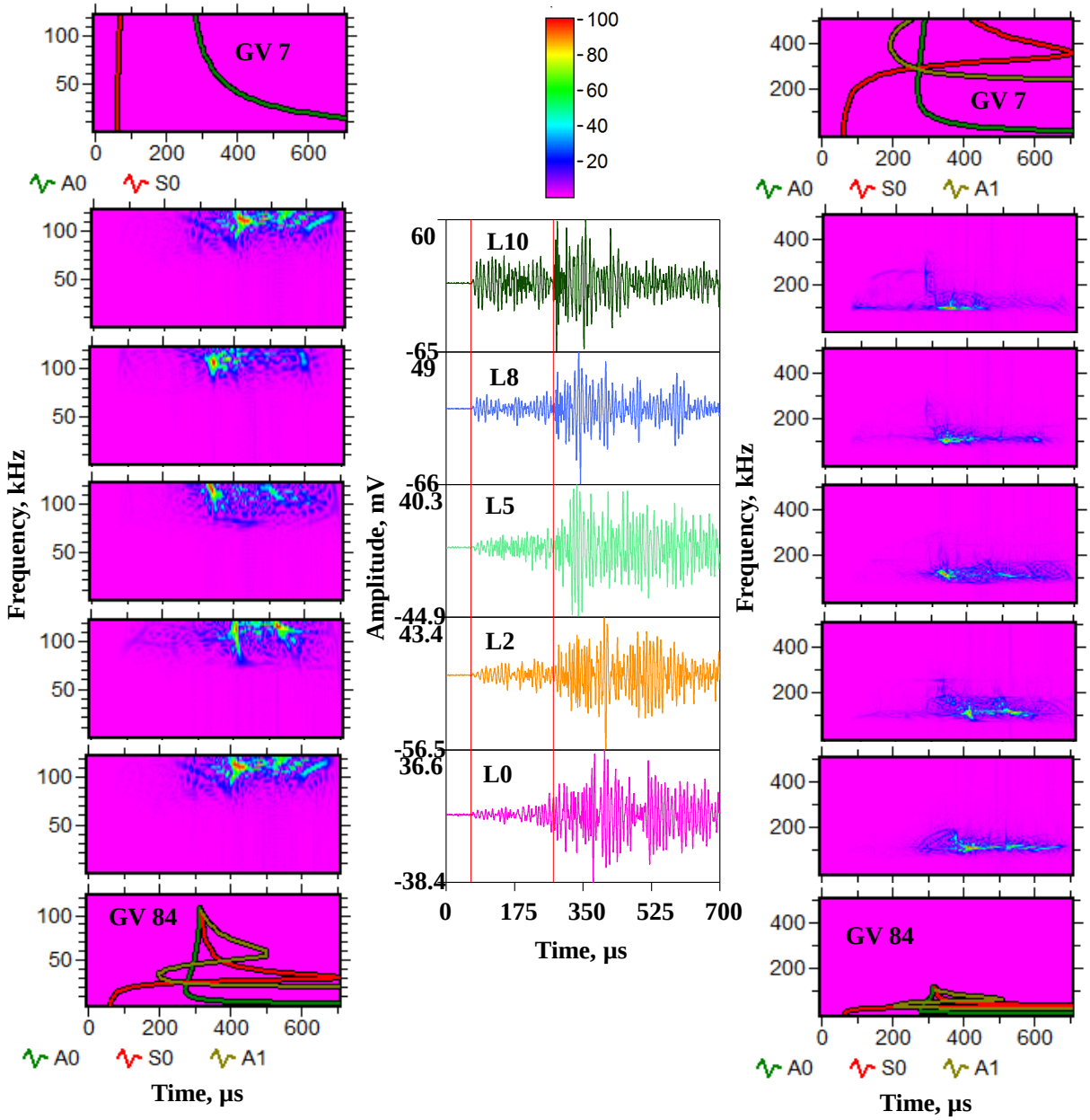


Fig. 10. Shows the CWD distribution results for the R15 outer sensor signals for a time increment of o to 700 µs (flexural region). Left column for frequencies to 120 kHz and right column for frequencies to 500 kHz. Middle column shows the signals used. GV results for two thicknesses shown.

From the two tables, the general trend for both broadband sensors was most often correspondence of the highest intensity CWD results with the GVs for the 84 mm full-thickness propagation in both the extensional and flexural regions for all the PLB layers and the two CWD frequency ranges. This result applied to all 20 cases for the Mist sensor. The exceptions for the DW sensor were for PLBs on the outer layers 10 and 8 (only layer 10 in the extensional region). In these cases, the peak intensity CWD correspondence in both the extensional and flexural regions was to the 7 mm GVs when the frequency range was extended to 500 kHz. The general results for the WD and R15 sensors were no correspondence of the intense CWD results and the GV curves. Exceptions for the WD sensor were for PLBs on layers 10 and 8 (only layer 10 in the extensional region). The only peak CWD intensity correspondence for the R15 sensor was in the flexural region for a PLB on layer 5 in the flexural region.

Table 1 Most intense frequency, arrival time and mode(s) in extensional region 0 to 260 μs

Frequency range, kHz	PLB layer and sensor	DW: frequency, kHz; time μs; GV thickness, mm and mode(s)	Mist: frequency, kHz; time μs; GV thickness, mm and mode(s)	WD: frequency, kHz; time μs; GV thickness, mm and mode(s)	R15: frequency, kHz; time μs; GV thickness, mm and mode(s)
0 to 120	10	29, 197, 84: S_0	27, 205, 84: S_0	101, 99, No match	101, 112, No match
	8	28, 210, 84: S_0	26, 215, 84: S_0	118, 131, No match	121, 243, No match
	5	28, 195, 84: S_0	32, 160, 84: S_0	120, 250, No match	121, 218, No match
	2	32, 188, 84: S_0	27, 198, 84: S_0	98, 217, No match	107, 191, No match
	0	29, 190, 84: S_0	26, 196, 84: S_0	42, 94, No match	121, 245, No match
0 to 500	10	239, 136, 7: S_0	27, 205, 84: S_0	269, 203, 7: S_0	101, 112, No match
	8	28, 210, 84: S_0	26, 215, 84: S_0	183, 121, No match	127, 180, No match
	5	28, 195, 84: S_0	32, 160, 84: S_0	186, 134, No match	121, 218, No match
	2	32, 188, 84: S_0	27, 198, 84: S_0	212, 147, No match	107, 191, No match
	0	29, 190, 84: S_0	26, 196, 84: S_0	195, 143, No match	123, 245, No match

Table 2 Most intense frequency, arrival time and mode(s) in flexural region 0 to 700 μs

Frequency range, kHz	PLB layer and sensor	DW: frequency, kHz; time μs; GV thickness, mm and mode(s)	Mist: frequency, kHz; time μs; GV thickness, mm and mode(s)	WD: frequency, kHz; time μs; GV thickness, mm and mode(s)	R15: frequency, kHz; time μs; GV thickness, mm and mode(s)
0 to 120	10	100, 325, 84: S_0, A_0	24, 581, 84: S_0	100, 344, 84: A_1, A_2	101, 349, No match
	8	107, 331, 84: A_0, A_1	24, 612, 84: S_0	107, 335, 84: A_1, A_2	107, 342, No match
	5	100, 322, 84: S_0, A_0	27, 571, 84: S_0	120, 422, No match	117, 338, 84: A_0, S_0
	2	78 to 120, scattered in time	24, 593, 84: S_0	117, 401, No match	112, 329, No match
	0	31 and 45, 428 and 436, 84: S0	32, 426, 84: S_0, A_1, S_1	109, 486, No match	112, 407, No match
0 to 500	10	248, 277, 7: A_0	24, 612, 84: S_0	278, 281, 7: A_0, A_1	101, 349, No match
	8	254, 280, 7: A_0	24, 619, 84: S_0	283, 337, 7: S_0, A_1	107, 342, No match
	5	122, 322, 84: S_0, A_0	27, 612, 84: S_0	178, 458, No match	117, 338, 84: A_0, S_0
	2	156 to 203, scattered in time	24, 593, 84: S_0	183, 324, No match	112, 407, No match
	0	31 and 45, 428 and 436, 84: S_0	32, 426, 84: S_0, A_1, S_1	186, 383, No match	112, 421, No match

B. Comparisons of sensor types based on CWD area-patterns of intensity for PLBs on the exposed end of the same layer

To provide input as to how all the various intense frequency(s) and time(s) area-patterns relate to each other as a function of the sensor type for PLBs on a single layer at a time, Figs. 11 and 12 were created. These figures used the same CWD results for the outer sensors presented in Figs. 3 through 10 arranged in a different fashion. The layout in these figures is as follows. Figure 11 has the results for the extensional region time from 0 to 260 μs for both frequency ranges, and Fig. 12 has the results for the time from 0 to

700 μs to include the flexural region for both frequency ranges. In both figures, the top four rows include all four sensor types for the CWD results over the range to 120 kHz, and the bottom four rows include all four sensor types the for the CWD results to 500 kHz. Also, in both figures, the PLB layers are in columns from left to right labeled 10, 8, 5 and 0. The CWD results for layer 2 were not included as they did not appreciably add to the sequence of layer-related changes as the PLB source moved from layer 5 to the inner layer 0. Again, the analysis of the results in these figures is centered on area-patterns of the intensity within the frequency versus time results, not the peak intensity, since that was already covered in section A. Further, since area-patterns are the key emphasis, the specific modes are not discussed. It is noted that area-patterns of intensity in frequency versus time results can relate to certain source characteristics (for example rise time [6] with broadband sensors).

From an overall perspective, several results are apparent when the potential area-patterns of intensity in the CWD results are examined for PLBs on a single layer at a time and comparisons of the results are made for the four sensor types. This overall discussion is divided into two parts, first for the extensional region (Fig. 11) and then for the flexural region (Fig. 12).

In the following the comparisons are between the two broadband sensors and between the two resonant sensors. The discussion starts in the extensional region with the frequency of the CWD results limited to 120 kHz, so as to focus on the primary region of GV curves for the full thickness propagation. The results show the broadband sensors do not have similar area-patterns individually by layer for PLBs on layers 10, 8 and 5. In the area-patterns for these layers, the DW results show intensity at higher frequencies not present with the Mist sensor. Both sensors do have intensity at similar low frequencies. Only for PLBs on layer 0 do the intensity area-patterns remain reasonably the same for both sensors. For the resonant sensors in the extensional region to 120 kHz, the two sensors have similar area-intensity patterns only for PLBs on layer 10. For the other three layers, the pattern differs, although both have similar higher frequency regions. The R15 sensor lacks the low frequency region of the WD that increases in intensity as the PLB layer moves from 8 to 0. When the frequency range in the extensional region expands to 500 kHz, the broadband sensors only have matching area-patterns of intensity for PLBs on layers 10 and 0. For the in-between PLBs on layers 8 and 5, the Mist sensor lacks a higher frequency region present in the DW result. In the case of the resonant sensors for this case, there does not seem to be any clear area-pattern matches.

Turning to the flexural region (Fig. 12) and again starting with the maximum frequency to 120 kHz, the broadband sensors are considered first. The area-pattern match is present for PLBs on layers 10 and 8, but the relative intensity of the intense areas varies between the two different broadband sensors for PLBs on these layers. For the other two PLB layers 5 and 0, the pattern similarity is not present due to the DW sensor having a higher frequency region not present with the Mist sensor. When the results for the resonant sensors are compared as a function of the PLB layer for the 120 kHz range, there is some reasonable area-pattern similarity for PLBs on layers 5 and 0. For PLBs on layers 10 and 8, the WD sensor does not have the extended in time intensity region that is present in the R15 case. After extending the frequency range to 500 kHz in the flexural region, the broadband sensors have areas that result in a pattern match for layer 8 PLB with relative intensity differences in the two sensor results. For PLBs on layers 5 and 0, due to the high frequency region in the case of the DW sensor and lower frequency regions for the Mist sensor, there are no area-pattern matches. In the case of the resonant sensors, there are relatively poor area-pattern matches for PLBs on layers 8, 5 and 0. Only for PLBs on layer 10 do the areas have some common intense regions in the results for these two sensors.

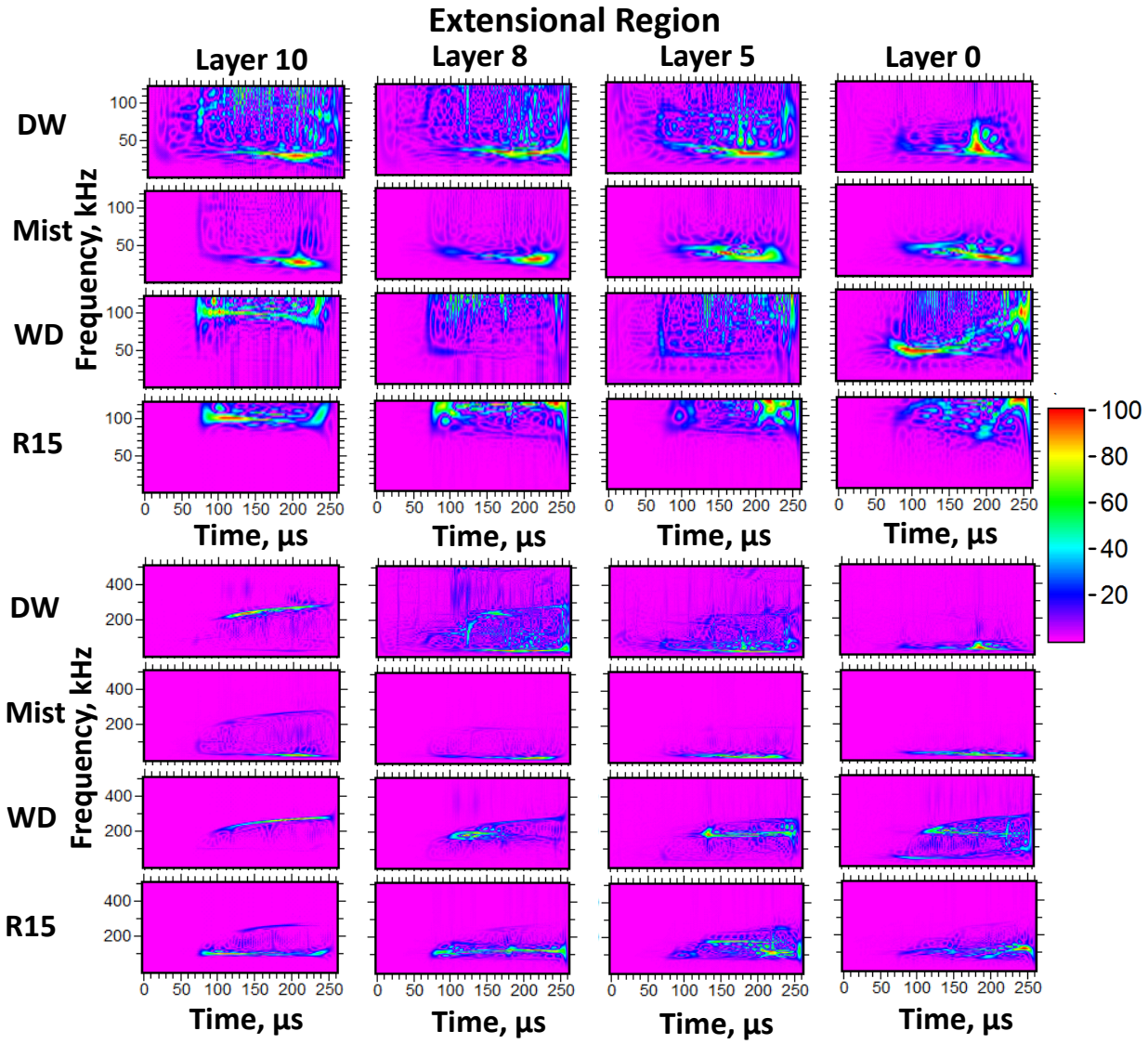


Fig. 11. For the extensional region (0 to 260 µs), the CWD results are shown in columns for PLBs on layers 10, 8, 5 and 0 for the four sensor types as labeled on the left for the frequency to 120 kHz in the top four rows. The bottom four rows show the same arrangement of information when the frequency is extended to 500 kHz. A color scale of intensity is shown on the right side.

To provide an explicit summary of the area-pattern similarities in each region, two tables are presented. Table 3 shows both frequency regions of the extensional part, and Table 4 shows for the flexural part of both frequency regions. In the tables, PS stands for area-pattern similarity and IS for incomplete area-pattern similarity. For the broadband sensors, a total of seven area-pattern matches of the CWD results were found. Overall the lack of area-pattern matches (total of 9 out of a possible 16) for the broadband sensors is driven by the relatively higher frequency response of the DW sensor and the relatively lower frequency response of the Mist sensor as a result of the couplant used. If vacuum grease or an equivalent had been used, it is likely that the Mist and DW would be much more similar in all the regions considered. Overall for the resonant sensors, the four area-pattern matches (out of a possible total of 16) were limited by the differences in their resonant frequencies.

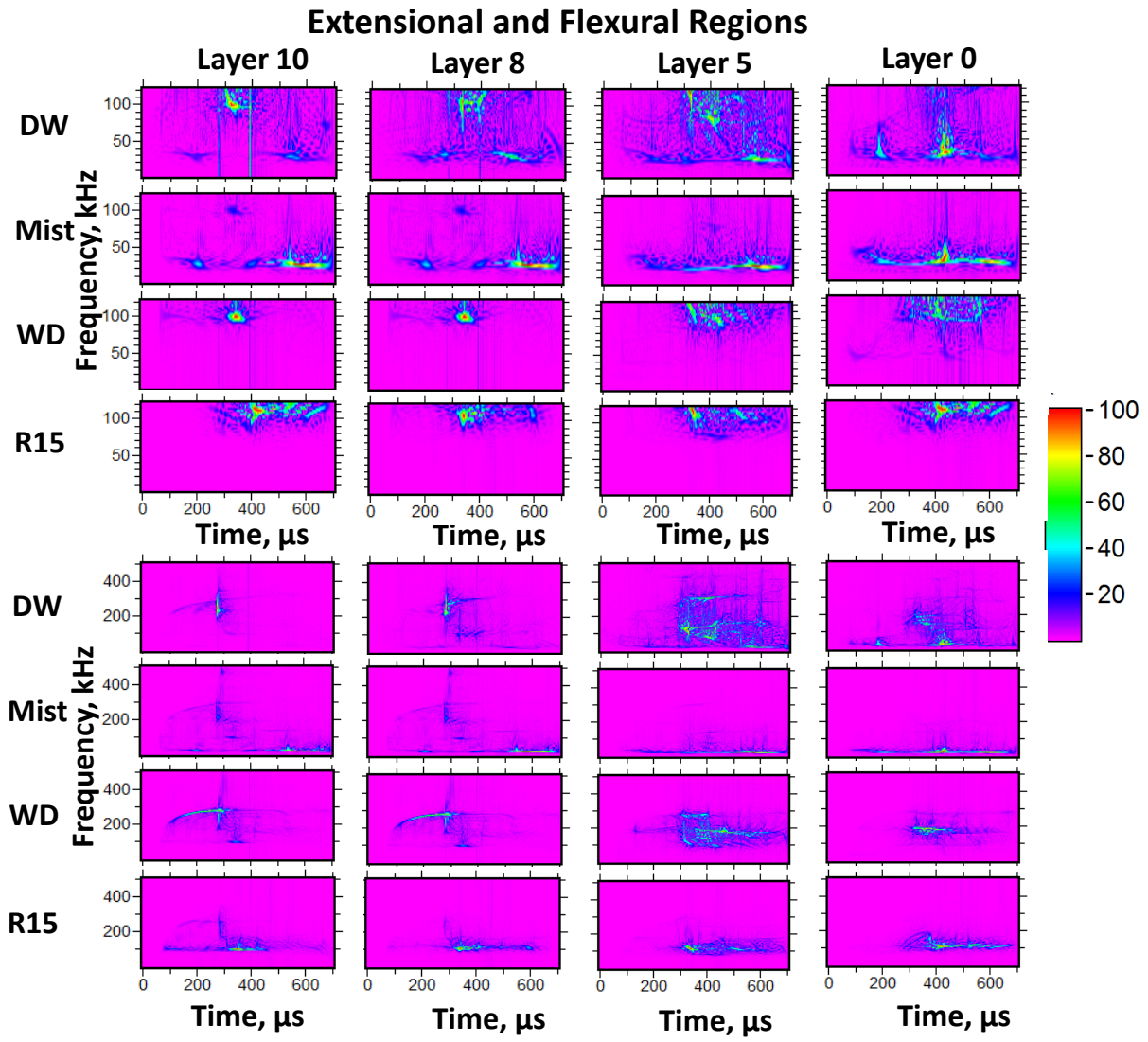


Fig. 12. For the extensional and flexural regions (0 to 700 µs), the CWD results are shown in columns for PLBs on layers 10, 8, 5 and 0 for the four sensor types as labeled on the left for the frequency to 120 kHz in the top four rows. The bottom four rows show the same arrangement of information when the frequency is extended to 500 kHz. A color scale of intensity is shown on the right side.

Table 3 Summary of CWD area-pattern matches in extensional region

Sensors/PLB Layer	10	8	5	0
DW and Mist to 120 kHz	IS	IS	IS	PS
WD and R15 to 120 kHz	PS	IS	IS	IS
DW and Mist to 500 kHz	PS	IS	IS	PS
WD and R15 to 500 kHz	IS	IS	IS	IS

Table 4 Summary of CWD area-pattern matches in flexural region

Sensors/PLB Layer	10	8	5	0
DW and Mist to 120 kHz	PS	PS	IS	IS
WD and R15 to 120 kHz	IS	IS	PS	PS
DW and Mist to 500 kHz	PS	PS	IS	IS
WD and R15 to 500 kHz	PS	IS	IS	IS

C. Additional observations relative to full thickness and/or single layer propagation.

i) Waveforms of Mist sensor signals

Due to the strong lower frequency sensitivity of the Mist sensor as a result of the use of hot melt glue coupling, this sensor's waveforms show some clear indications at lower frequencies of the presence of full-thickness Lamb wave propagation due to a contrast in the extensional and flexural regions for PLBs on the ends of layers near the outside and near the inside. Thus, as shown here, these results complement the modal results. Figure 13(a) shows the outer Mist sensor signal (top) for a PLB on layer 9, which is near the layer of the outer sensor, and it also shows the outer sensor signal (bottom) for a PLB on layer 1, which is near the inner layer of the wall. As illustrated in this figure by the vertical red cursor at about 627 μs in the flexural region at about 24 kHz A_1 mode (per the CWD results for 84 mm GVs), there is a complete reversal of phase for the signal from the near outer layer PLB compared to the near inner layer PLB signal (Note that for the 84 mm thickness the flexural mode is A_1, since the frequency at this time for the A_0 mode of about 2 kHz is well below the capability of the Mist sensor and is also below the high pass 10 kHz filter used). In contrast, the red vertical cursor at about 121 μs in the extensional region at about a frequency of 35 kHz S_0 mode (per the CWD results for 84 mm GVs), shows the signals from PLBs on both the layers are in phase. This phase behavior (same in extensional region and reversed in the flexural region) in the signals from PLBs on the edge near the top of the LPV remnant wall compared to the PLB on the edge near the bottom of the wall thickness is the same as that previously obtained for a sensor on the top surface of a 3.1 mm thick aluminum plate, in unpublished work [7] for Lamb waves in the far-field (full-thickness propagation). By use of a broadband conical sensor located on the top surface at 127 mm from the PLB edge, the results shown in Fig. 13(b) were obtained. The top waveform was for an in-plane edge PLB near the top surface and the bottom waveform for an in-plane edge PLB near the bottom surface of the plate. In Fig. 13(b), the cursors again show in the flexural region at 54 μs at a frequency of 50 kHz A_0 mode (per CWD results for aluminum 3.1 mm GVs), the phase reversal is present, while in the extensional region at 11 μs at a frequency of 100 kHz S_0 mode (per CWD results for 3.1 mm GVs), the signals are in phase. The ability to show behavior similar to Fig. 13(a) with the other three sensor types is hindered by different factors. With the WD and R15 sensors the resonant behavior as well as a lack of lower frequency response precludes such an illustration. For the DW sensor less low frequency response and higher electronic noise does not allow such an illustration.

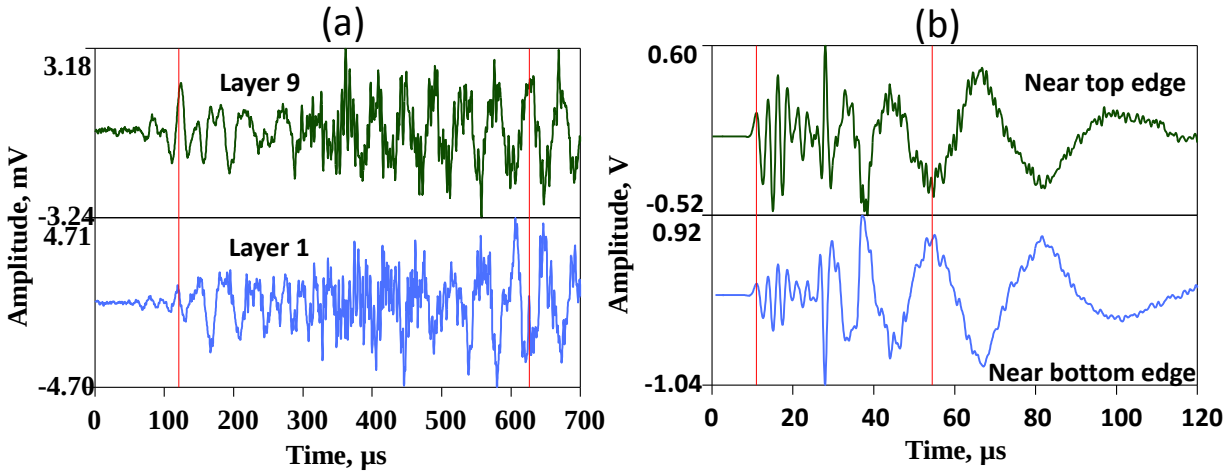


Fig. 13. (a) Example with the remnant for a low frequency portion in Mist outer sensor signals of reversal in phase in flexural region and no reversal of phase in extensional region. (b) Top surface broadband conical sensor signals for PLBs on end of large aluminum plate showing reversal in flexural region and no reversal in extensional region.

ii) Mist sensor CWD in the region of the initial arrival of the extensional mode

By use of Mist sensor results at the very first arrival portion of the extensional mode for a signal portion from 0 to 100 µs, a changeover of mode dominance can be observed in the CWD results in Fig. 14. In this figure, the 84 mm GVs S_0 and S_1 modes are shown in the left column for PLBs on layers 10, 9, 8, 5, 2 and 0 with the CWD results, and the S_0 mode GV for 7 mm thickness is shown along with the same CWD results in the right column for PLBs on the same set of layers. The initial match for the 7 mm S_0 mode can be observed for layer 10 PLB (viewing both columns for these comparisons) and a partial shift to 84 mm GV for layer 8 PLB. Then, the dominance of 84 mm GV for S_0 and S_1 can be seen in the lower layers.

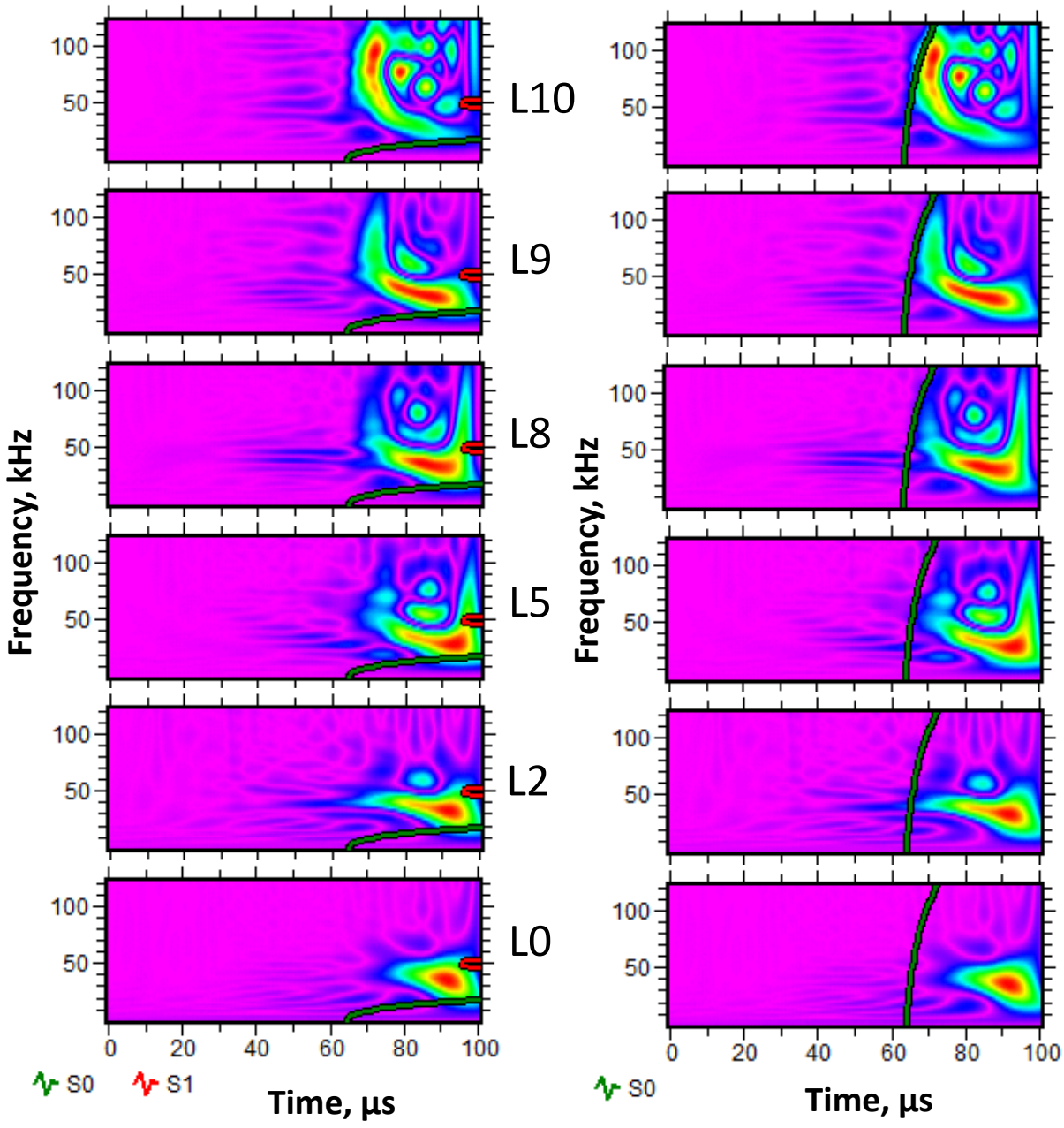


Fig. 14. Mist sensor CWD results very first portion of extensional mode as a function of the PLB layers and with GVs to 120 kHz shown for both the 84 mm thickness (left) and the 7 mm thickness (right).

Overall Perspectives of the Research Results

When the most intense regions in the CWD results for the outer Mist sensor signals were examined for PLBs on layers 10, 8, 5, 2 and 0, the correspondence of the CWD results was with the 84 mm GVs for full-thickness dominant wave propagation with the peak frequencies ranging from 26 kHz to 32 kHz in all 20 cases in Tables 1 and 2.

For the outer DW sensor signals, the correspondence differed. Out of the 20 cases, the correspondence of the most intense CWD results was with the 84 mm GVs for 15 cases with peak frequencies ranging from 28 kHz to 107 kHz. It is noted that the higher frequencies 100 kHz to 107 kHz may have been influenced in part by single-layer propagation corresponding to 7 mm GVs. For three cases the CWD peak intensity results for the DW sensor signals showed correspondence with the 7 mm GVs for PLBs on the outer layers 10 and 8 when the CWD frequency range extended to 500 kHz.

In summary, the high intensity CWD results for the different broadband outer sensor signals provided evidence of both single-layer and full-thickness propagation when the frequency region of the CWD calculation was extended to 500 kHz for the PLBs on the outer layers 10 and 8. The Mist sensor signals showed peak intensity correspondence with 84 mm GVs (full-thickness propagation), and the DW sensor signals showed peak intensity correspondence with 7 mm GVs (single-layer propagation). Thus, correspondence with the two different modes of propagation depended on both the sensor frequency response characteristics and the frequency range used for the CWD calculation for these outer layer PLBs. For inner layers, the CWD peak intensity for both broadband sensors generally had correspondence with the 84 mm GVs representing full-thickness propagation for most of the PLB layers.

For the outer resonant sensor signals only a very few cases resulted in correspondence of the intense regions with the GV curves, and these were cases of either single-layer or full-thickness Lamb wave propagation. The WD sensor had five out of possible 20 cases (three for 84 mm GVs and two for 7 mm GVs). The R15 sensor had two out of possible 20 cases (both for 84 mm GVs).

Due to the couplant-modified frequency response of the Mist sensor, two other illustrations of full-thickness propagation were observed at low frequencies with this sensor:

- Waveform results at low frequencies (about 24 to 35 kHz) for the outer sensor when compared for PLBs on a near outer layer to those from a near inner layer showed no phase change in the extensional region and a phase reversal in the flexural region. These results are a characteristic of full-thickness propagation.
- At the very first arrival region of the extensional mode, the CWD results showed a transition from correspondence to single-layer propagation for 7 mm GVs to full-thickness propagation for 84 mm GVs as the PLBs moved from the outer layer to lower layers.

Comparisons of the two classes of different outer sensor types for PLBs on the same layer by CWD frequency/time areas of intensity showed some limited area-pattern intensity matches (seven out of possible 16) when the two broadband sensor signal results were compared to each other. For cases where there were such area-pattern matches for the same frequency/time regions, the relative CWD intensities were ordered differently for these two sensors. The key reason for the lack of matches was the couplant modified response of the Mist sensor. The limited CWD area-pattern matches (four out of a possible 16) for the resonant sensors, when compared to each other, were due to the different resonant frequencies of the two sensors.

Conclusions for Sensors Mounted on the Outer Layer

- The fact that GV curves for 84 mm superimposed on top of the intense CWD results for the Mist sensor signals for all the cases demonstrated that full-thickness Lamb wave propagation was present for PLBs on all the layers when a broadband sensor with only lower frequency response was used.

- For outer layer PLBs, the DW sensor signals showed the presence of single-layer dominant Lamb wave propagation when the frequency range was extended to 500 kHz. For lower layer PLBs, the result was full-thickness propagation similar to the Mist results.
- The peak frequencies that corresponded to 84 mm GVs in the CWD results with the broadband sensor signals were primarily low frequencies ranging from 24 kHz to 32 kHz, with a few possible cases as high as 100 kHz to 107 kHz for peak frequencies in the flexural region.
- The CWD results from the resonant sensor signals along with the GV curves did not conclusively show full-thickness or single layer propagation for nearly all the PLB layers.
- Waveform results at low frequencies (about 24 to 35 kHz) for the Mist outer sensor when compared for PLBs on the ends of a near outer layer to those from a near inner layer showed no phase change in the extensional region and a phase reversal in the flexural region. These results are a characteristic of full-thickness propagation.
- For PLBs on the same layer, area-intensity pattern matches of the CWD frequency/time areas of intensity were limited for both sensor types. For the broadband sensors, it was due to different frequency ranges of response. For the resonant sensors, it was due to the different resonant frequencies of the two sensors.

Acknowledgements

The author is grateful for the funding, purchase of equipment, facilities and excellent experimental support provided by NASA Marshall Space Flight Center, Huntsville, AL, USA.

References

1. ASTM Standard E569, "Acoustic Emission Monitoring of Structures During Controlled Simulation," 2013 and ASTM Standard E1419, "Examination of Seamless, Gas-Filled, Pressure Vessels Using Acoustic Emission," 2015a, ASTM International, West Conshohocken, PA.
2. Choi, R., and Williams, W. J., “Improved Time-Frequency Representation of Multicomponent Signals Using Exponential Kernels," IEEE Transactions in Acoustics, Speech, and Signal Processing, Vol. 37, pp. 862-871, 1989.
3. Vallen Systeme Gmb, Icking, Germany, http://www.vallen.de/downloads/, Vallen Freeware for AGU-Vallen Wavelet version R2010.0202 and Vallen Dispersion version R2010.0202.
4. Kolsky, H., *Stress Waves in Solids*, Dover, New York, 1963.
5. Hamstad, M. A., “Far-field wave propagation signals from pencil lead breaks on the open end of a thick-walled layered cylinder: Part 1 Amplitudes and frequency content,” J. Acoustic Emission, Vol. 36, pp. 30 – 50, 2019.
6. Hamstad, M. A., “On Lamb Modes as a Function of Acoustic Emission Source Rise Time,” J. Acoustic Emission, Vol. 28, pp. 41 – 58, 2010.
7. Hamstad, M. A, Unpublished work at the University of Denver, Denver, CO, 2007.

Appendix M: Summary of Zetec Inc. Dynaray System Demonstration, Document Number PVS-20-008

Summary of Zetec Inc. Dynaray System Demonstration

Document Number PVS-20-008

December 03, 2020

As a result of the NASA Request for Information (RFI) NNM17ZQD001L released in 2017, Zetec Incorporated was chosen by the NASA Layered Pressure Vessels Working Group (LPVWG) as a vendor whose inspection technique offered high probability of detection and characterization of defects in shell to shell welds. Zetec proposed utilizing two dimensional phased array probes driven by their Dynaray system and their Ultravision software. The proposed inspection would employ a large, custom designed, 5 MHz, 252 element array probe in combination with a custom wedge for shear wave inspection for the detection of axial flaws, and another custom longitudinal wave wedge for the detection of circumferential flaws. The second probe in the proposed inspection solution would be a commercially available 5 MHz 64 Element array probe with a custom shear wave wedge optimized for detection of flaws near the OD surface.

The proposed solution had been partially demonstrated previously on the original MSFC 24" layered performance demonstration block but needed further optimization for the shell to shell weld application. During the RFI process, NASA provided to Zetec, a smaller layered vessel weld sample (519-180) with only 2 ID and 2 OD flaws implanted. Details of the blocks and flaws contained in each may be found in drawing Attachment 1, 2018-03-30_10-41-09_081.jpeg. For both the ID and the OD flaws, one flaw was oriented axially and the other circumferentially to the weld direction. Detection and characterization, (length and flaw height) would serve as justification to move forward with building and optimizing probes for the NASA application of this system. Favorable inspection results were reported back to the LPVWG as indicated in Zetec report NASA Solicitation NNM17ZQD001L_Inspection Zetec_20181023, and the decision was made by the working group to move forward with 2D probe development.

In an effort to evaluate the newly developed Zetec 2D probes, a layered section harvested from MSFC Vessel 0125 was selected to be cut into 3 pieces, weld prepped, and sub arc welded back together in very similar fashion to the vessel fabrication typically found in all NASA layered vessel shell to shell welds. This layered vessel ring section was then sent to Flawspec in Edmonton, Alberta, Canada to have a total of 14 actual flaws implanted into the welds. Each of the two weld contained the same 7 flaws, but the flaws were rotated (clocked) about the circumference so as to not have identical flaw locations. This sample could be used as the test bed for weld flat top machining, Tangential Eddy Current Array (TECA), and the newly developed PAUT probes. It was also intended as a teaching and training aid for others not familiar with the techniques for inspection of layered vessels. Details of the flaws including dimensions and location in this block can be found in Attachment 2, Flaw Map- Final.



Figure 1- Demonstration Ring "As Welded" packaged for shipment to Flawspec.

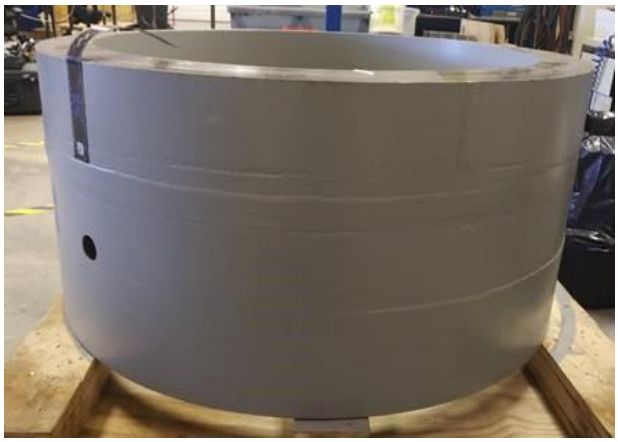


Figure 2- Demonstration Ring "Flat Topped and Painted" as Sent to Zetec

The layered demonstration ring was shipped to Zetec in Quebec City, Canada for demonstration of the Dynaray System/2D probe capability after the two shell to shell welds were machined flat to allow PAUT sensor coupling. The NASA owned Jireh Navic Crawler was also provided to Zetec for use during the demonstration effort to closely simulate the ultrasonic sensor configuration which would eventually be used for PAUT examination of vessels. Zetec provided an initial pro bono demonstration of the system on Weld 1 of the layered ring section although this was not a blind test. NASA had provided Zetec with details of the Weld 1 flaw orientation, size and location to allow Zetec to determine how best to configure and optimize the PAUT system. Results of the first demonstration (Weld 1) were reviewed by members of the LPVWG during a virtual demonstration by Zetec on August 20, 2020. A separate virtual demonstration on Weld 2, for which NASA had released a purchase order to Zetec, was held on September 1, 2020. Results from both these inspections were presented to NASA as PowerPoint files, and can found in Bastion PO142305_Demonstration_update20200818 and Bastion PO142305_Inspection Demonstration Report_Final 20200910_Part 2 (Attachment 1 of this report). The inspection data and analysis from weld 2 further proved that the two dimensional array technique was in fact very capable of the detection and sizing of defects of interest in a shell to shell weld section; provided that the weld presented a suitable surface for probe coupling.

During the first demonstration, evaluation of inspection data was performed using the industry standard 6 dB drop method. This technique provided adequate results in detection, but refinement was needed to accurately define both flaw orientations. In an effort to further define the capabilities of the system to size both orientations of flaws, the data from Weld 2 was evaluated using the standard 6 dB drop method, as well as the -14 dB drop from the primary reference level recommended by the ASME BPVC in Section V, Article 4. The detailed results of this comparison can be found in the Zetec weld 2 data analysis slides. Through comparison of these evaluation levels, it was determined that the increased evaluation level of -14 dB from the primary inspection reference level proved more accurate in the length sizing of defects in both orientations.



Figure 3- Demonstration Ring With Crawler and Two Dimensional Array Probe Fitted on Flat Topped Weld.

The results from these two demonstrations were considered to be very successful due to the detection and sizing of defects oriented in both the transverse and circumferential axes with a single method in both welds. Inspection data from these weld demonstration scans displayed the indications quite clear, and defect sizing was within the limits set forth in the ASME BPVC Section V for a code qualified technique. These results prompted NASA to move forward with the procurement of the Zetec Dynaray system, as well as perform the flat topping operation on the first set of vessels. Further refinement of the primary reference level used during the data acquisition and sizing of defects may need to be performed, but has not been evaluated fully at this time. Primary reference levels used during inspections should be based on thickness rather than number of vessel layers, and the degree of sensitivity required to accurately detect and size the required indications. This can easily be accomplished by the fabrication of different thickness reference blocks similar to those described in the ASME BPVC Section V, Article 4 corresponding to a range of part thicknesses; but using a reflector size corresponding to a specific flaw size. It is expected at the time of this report that NASA will refine the primary reference level as needed, document the procedure for data acquisition and analysis, and employ this inspection method for the evaluation of shell to shell welds on all Agency layered pressure vessels as well as head to shell welds and nozzles.

Appendix N: GRC UT Bore Probes, Dirienzo and Samuele

Pressure Vessel Nozzle UT Bore Probes

Calogero Dirienzo and Vince Samuele

This appendix describes development and testing efforts and results for ultrasonic nozzle bore probes used to examine non-code PV nozzles at NASA Glenn Research Center since the 1980s. GRC developed two bore probes to perform UT examinations on PV nozzle full penetration welds from the Inside Diameter (ID) of the nozzle.

- First Generation Bore Probe

The first bore probe was developed to perform UT examinations on PV nozzle full penetration welds from the ID of the nozzle. Developed in the 1980s by UTX for NASA under a contract with General Physics, it is pictured in Figure 1.



Figure 1. First Generation Bore Probe, developed 1980's

The first generation bore probe was developed specifically to examine A.O. Smith LPV head nozzles and other similar non-code PV nozzles at GRC. Figure 2 depicts a typical head nozzle penetration weld joint with a 3/4" wide square joint configuration.

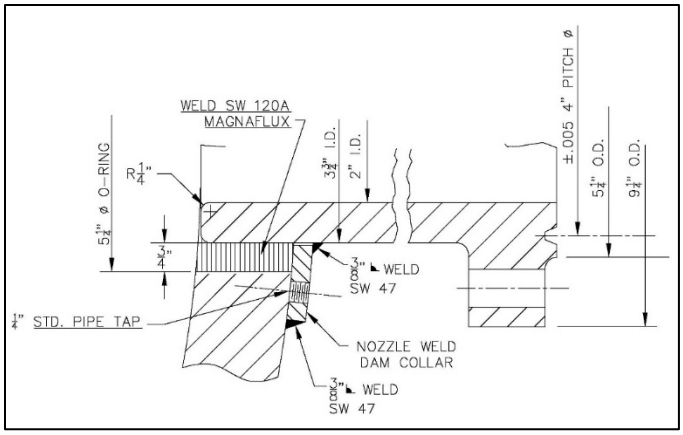


Figure 2. Two inch Nozzle N-1 and N-2 2500# R.T.J. L.W.N.

Couplant is manually applied to the probe's face prior to its insertion into a nozzle. The bore probe shaft's flexible design allows for ease in manipulating and a 360 degree weld inspection by manually rotating the probe inside the nozzle. The probe heads containing the UT transducers are spring loaded to provide continuous contact with the nozzle interior surfaces. The probe's spring loaded heads are designed to accommodate examination of 1-1/2" to 2" ID nozzles (Figure 3).

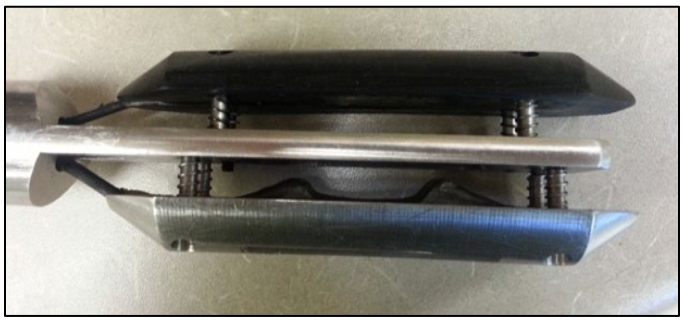


Figure 3. Spring Loaded Probe

The first generation probe heads contained a single straight beam transducer at 0 degrees (Figure 4) and two 45 degree shear wave transducers (Figure 5). Each transducer is directed longitudinally to the nozzle bore, angled forward or backward.



Figure 4. Single 0 degree Transducer



Figure 5. Two 45 degree Transducers

The first generation probe was developed primarily to detect flaws oriented parallel to the nozzle weld (e.g. lack of fusion and incomplete penetration, as shown in Figure 6, flaw "A") and flaws oriented perpendicular to the nozzle's longitudinal axis (flaw "B" in Figure 6). The capabilities of this probe were limited. It was found to be incapable of detecting nozzle corner cracks (flaw "C" in Figure 6) and flaws oriented parallel to the nozzle longitudinal axis (flaw "D" in Figure 6).

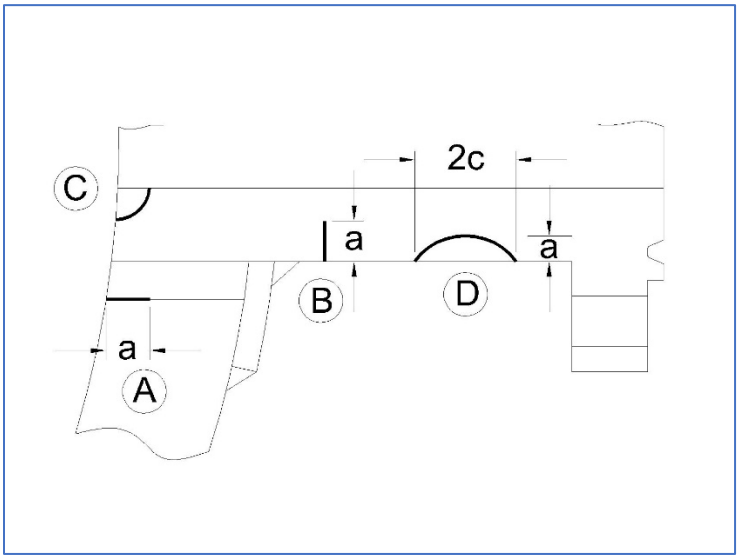


Figure 6. Cracks at Nozzles and Piping Branch Connections. Crack-Like Flaws A and B Represent the Detectible Flaw Orientations. Crack-Like Flaws C and D Represent the Additional Desired Detectible Flaw Orientations.

A calibration standard was designed and fabricated in accordance with ASME BPVC, Section V, Article 4 [19]. The specifically designed calibration standard contains two 1/8" inch diameter holes (Figure 7). The side drilled holes are located 3/4 inch and 1-3/4 inches from the inside diameter hole, representing the

nozzle weld front and back fusion zone locations. The standard also contains 6 machined planar flaws (Figure 8). Three planar flaws are located within the sidewall of the hole and are 0.250, 0.375 and 0.500 inches long by 0.125 inch wide and 0.0625 inch deep to simulate 3 internal nozzle surface breaking flaws. Three additional 0.065 inch wide planar flaws with radiuses of 0.090, 0.100, and 0.135 inches are located at the outer surface of the standard to simulate 3 corner crack-like flaws.

While the details of this calibration standard were considered acceptable at the time, recent review of the planer flaws indicates that they may be valid for verification of capability to detect slag or lack of fusion, but have called into question their validity for demonstrating capability to detect surface cracks.

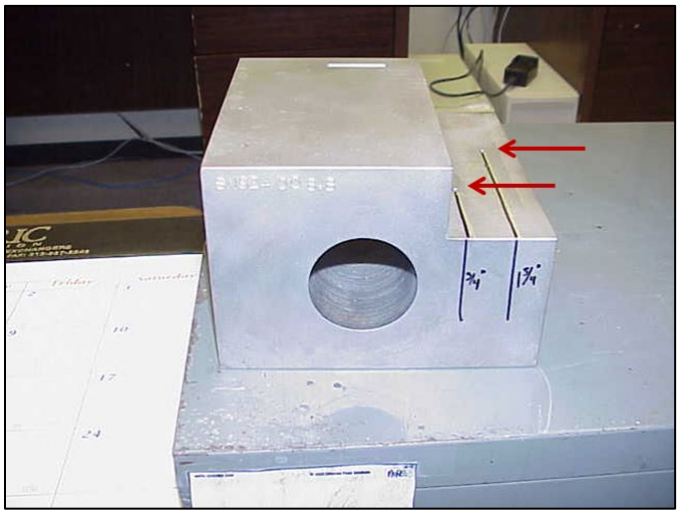


Figure 7. View of Calibration Standard Side Drill Holes

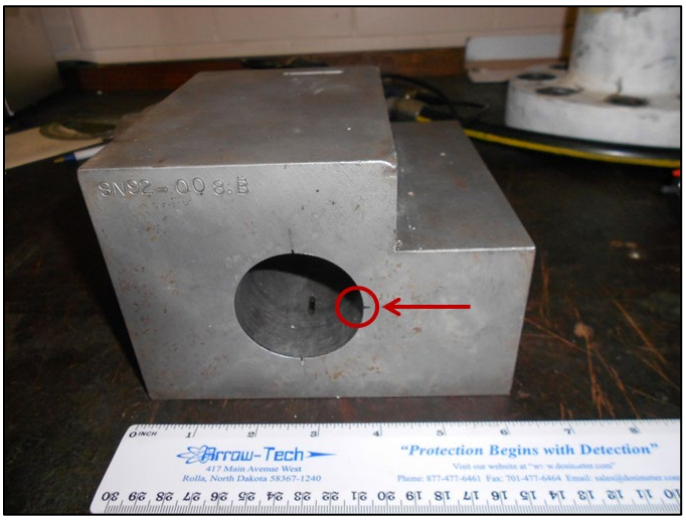


Figure 8. View of Calibration Standard Planar Machined Flaws

- Advantages

The first generation probe has successfully detected Incomplete Penetration (IP) and Incomplete Fusion (IF) using the straight beam at 0 degrees in A.O. Smith PV nozzle welds for more than 20 years. Length

(around the nozzle circumference) and flaw depth (from the outside of the weld surface) of IP and IF are determined by measuring angle of rotation and depth of insertion into the nozzle face.

- Limitations

The weld joint design configuration must be known. The straight beam transducer can only detect planar flaws oriented within the circumferential plane of the nozzle weld. The two 45 degree shear wave transducers can only detect planar flaws oriented perpendicular to the nozzle's longitudinal axis (flaw "A" in Figure 2) in the nozzle wall and weld. The probe was unable to detect nozzle corner cracks (typically the highest stressed region) and flaws oriented parallel with the nozzle longitudinal axis due to the transducer orientations. Indication detection on the nozzle wetted surfaces was not feasible due to the indication location within the dead zone of the transducer (Figure 9). (In contact ultrasonic testing, the dead zone is that region just below the surface of a test object that cannot be inspected because the signal returns while the transducer is still ringing down and is not yet ready to receive signals.) Detection of wetted surface flaws on the second leg was also not feasible in the portion of the nozzle wall full penetration welded to the head due to loss of signal because of the lack of a sound reflector (Figure 9).

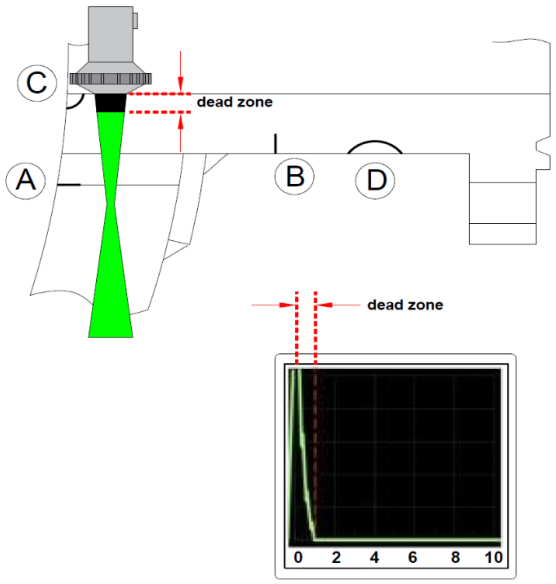


Figure 9. UT Probe Dead Zone and Beam Path

- Second Generation Bore Probe

A second generation probe was developed in 2011 to address the limitations of the first probe. Specifically, the second probe was designed to detect flaws in the radial plane (flaw "D" in Figure 6), and corner cracks (flaw "C" in Figure 6) in addition to flaws oriented parallel to the nozzle weld (e.g. lack of fusion and incomplete penetration, see flaw "A" in Figure 6). It was not intended to detect flaw "B", and could not do so. It was also not fully successful in detecting flaw "C".

The second generation probe was developed by GRC and fabricated by General Electric Technologies in 2011 (Figure 10). This bore probe contains interchangeable heads for 1 inch through 2 inch inside nozzle diameters Figure 11 and Figure 12). The new probe heads contain a single straight beam transducer at 0 degrees located in the middle of the bore probe head and two 45 degree shear wave transducers oriented in each by the circumferential direction of the nozzle. The first 45 degree transducer is angled clockwise while the second 45 degree transducer is angled counter-clockwise. Unlike the first generation bore probe, the couplant is injected through holes in the probe's head.



Figure 10. Profile View of 2nd Generation Bore Probe

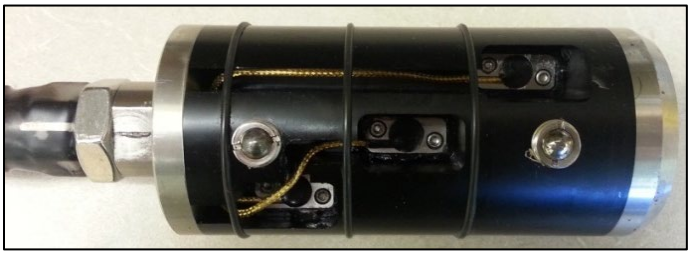


Figure 11. Transducer 45 degrees - 0 degrees - 45 degrees



Figure 12. Interchangeable Heads

The second generation probe has also successfully demonstrated the ability to detect flaws oriented parallel to the nozzle weld (e.g. lack of fusion and incomplete penetration) as well as detecting flaws in the radial plane (e.g. longitudinal cracks in the nozzle wall and weldment), although it proved

unsuccessful in detecting corner cracks. The difficulty in corner crack detection within the first leg is attributed to the crack being located within the dead zone of the transducer, while at the same time the lack of a back wall reflector prevents detection in a second leg reflection (Figure 9).

- Issues involved in use of both bore probes:
  1. The PV must be taken out of service.
  2. Mating piping and flanges must be removed.
  3. Must have sufficient clearance outside nozzle to allow insertion of probe into the nozzle bore.
  4. ID surface of nozzle must be relativity free of corrosion.
  5. Contamination issues of vessel wetted surface due to the UT couplant.

- Conclusions:

Although the bore probes have a successful detection history for limited defect types, namely those located within vessel nozzles and nozzle welds addressed above, there are inherent limitations when using conventional UT. Therefore, the bore probe and calibration standard advancement work was suspended as a result of the work performed by the Agency LPV team using Phased Array Ultrasonic Testing. PAUT provides numerous technical advantages over conventional UT, including the ability to sequentially scan at multiple angles and the ability to display detailed, accurate cross-sections of the weld which aids in interpretation of indications. It is also useful in situations with less mechanical scanning room because it is able to sweep the beam without moving the probe. For nozzles in heads, PAUT can be performed from outside vessel surfaces. If fully successful, this will eliminate the need to take the vessel out of service and remove piping, and it eliminates contamination issues for these nozzles. The technique has successfully identified a corner crack on one occasion. Consistent effectiveness in detecting this type of flaw remains to be demonstrated. Nozzles in layered shell sections will still require internal access for bore probe inspections.

Use of Eddy Current techniques would also be effective in the detection of corner cracks and wetted surface flaws, but like the UT bore probe, would require vessels to be removed from service to gain access to the nozzle ID.

Appendix O: GRC Radiographic Specification for A.O. Smith PV

GRC Radiographic Specification for A.O. Smith PV

- Scope:

This section details the minimum requirements that NASA GRC utilizes to perform radiography for multilayer weld flaw detection in accordance with the 2019 Edition of ASME B&PV Section VIII Division 1, Part ULW or Division 2 Part 4, Paragraph 4.13, and ASME Section V.

11.1.1.1.1 All radiography shall be performed by qualified and certified NDE technician(s) and supervised by an experienced American Society for Nondestructive Testing (ASNT) NDE level III Examiner. The NDE level III examiner interprets the final results of the radiography. The NDE Level III Examiner shall have a minimum 10 years of experience in multilayer PV radiography.

11.1.1.1.2 All radiography shall be performed in accordance with the latest edition of ASME Section V, Article 2, Radiographic Examination.

11.1.1.2 Radiography Preparation Requirements

This specification requires that the PV to be examined is safely de-pressurized and open to atmosphere.

NOTE: This specification does not address oxygen cleanliness requirements.

11.1.1.2.1 The radiographic test set-up shall be dependent on vessel orientation, location, diameter, accessibility to the vessel ID, and the number of welds to be radiographed.

11.1.1.2.2 Lead identification markers (number belt) shall be placed on the vessels outside diameter (OD), adjacent to the weld, with spacing not to exceed the length of the film (typically 14"). Identification markers shall be placed on the thicker member of the weld.

11.1.1.3 Radiation Source Selection/Placement

11.1.1.3.1 Source selection shall be dependent on vessel dimensions, weld thickness, source strength, and radiographic technique.

11.1.1.3.1.1 Typical recommended isotopes include Iridium-192 and Cobalt-60.

11.1.1.3.2 Panoramic technique shall be used.

11.1.1.3.3 Head to Shell Welds shall:

11.1.1.3.3.1 Have a certified American National Standards Institute (ANSI) shooting rod long enough to reach alignment with the center of the circumferential weld from the vessel ID.

11.1.1.3.3.2 Have a shooting rod centered within the vessel to prevent accidental superimposing of indication(s) in the weld onto the film (i.e. layerwash). The direction of the beam of radiation shall be centered on the area of interest.

11.1.1.3.4 Shell to Shell Welds shall:

11.1.1.3.4.1 Contain a 3/32" wire cable strung through the vessel's centerline and pulled tight using jigs bolted to the vessel's head nozzle flanges.

11.1.1.3.4.2 Have a source tube attached to the wire cable and pulled into place. The source shall be aligned at the center of the circumferential shell-to-shell weld of interest.

11.1.1.3.4.3 Have a source tube that does not exceed the crank cable limit.

11.1.1.4 Penetrameter Selection or Image Quality Indicator

11.1.1.4.1 Penetrameters shall be selected in accordance with American Society for Testing and Materials (ASTM) E1025.

11.1.1.4.2 Penetrameter material shall be of the same alloy material group or grade as the vessel material.

11.1.1.4.3 Source side penetrameter shall be used when possible. Film side penetrameter can be used, but must be identified on the radiographic image with the letter "F".

11.1.1.4.4 Penetrameters size shall be determined by the nominal single-wall thickness plus the estimated weld reinforcement, not to exceed the maximum permitted by the referencing the 2019 Edition of ASME Section V, Article 2, Table T-276 Code Section.

11.1.1.4.5 Placement of the penetrameter shall be on the thicker of the two adjacent sides of the circumferential weld.

11.1.1.4.6 Shim(s) shall be placed between the vessel and the penetrameter. Shim thickness shall be selected to match the weld thickness, including weld reinforcement. Shim materials shall be of the same alloy material group or grade of the vessel material.

11.1.1.4.7 When multiple penetrameters are used, the requirements of the 2019 Edition of ASME Section V, Article 2, Section T-277 shall be met.

11.1.1.4.8 The radiographic technique shall be sufficient to display the penetrameter hole-type (IQI), essential hole, identifying number, and letters.

11.1.1.5 Technique

11.1.1.5.1 Film Selection

11.1.1.5.1.1 Film selection shall be based on the best means of achieving radiographic sensitivity which includes many factors (i.e. radiographic contrast and radiographic definition).

11.1.1.5.1.2 A technique shot shall be used to evaluate the radiographic sensitivity and adjustments should be made for all further exposures.

11.1.1.5.1.3 Film shall cover the entire weld being radiographed including 1 – 2 inches of base material on either side of the weld. This helps facilitate identification of crack-like flaws adjacent to the weld.

11.1.1.5.1.4 Film technique shall be single film viewing.

11.1.1.5.1.5 Radiographic film shall be placed on the vessel OD, centered directly on the weld of interest.

11.1.1.5.2 Geometric Unsharpness (Ug)

11.1.1.5.2.1 Radiograph Ug shall be in accordance with the 2019 Edition of ASME Section V, Article 2, Paragraph T-274 :

$$U_g = Fd / D$$

Ug = geometric unsharpness
F = source size: the maximum projected dimension of the radiating source (or effective focal spot) in the plane perpendicular to the distance *D* from the weld or object being radiographed.
D = distance from source of radiation to weld or object being radiographed.
d = distance from source side of weld or object being radiographed to the film.
D and *d* shall be determined at the approximate center of the area of interest.

11.1.1.5.3 Radiographic technique

11.1.1.5.3.1 Single wall exposure technique shall be used for radiography.

11.1.1.5.3.2 An adequate number of exposures shall be made to demonstrate that the required coverage has been obtained.

11.1.1.5.4 Intensifying screens

11.1.1.5.4.1 Intensifying screens 0.010" thick shall be used in the front and back of the radiographic film.

11.1.1.5.5 Film Density

11.1.1.5.5.1.1 The transmitted density through the radiographic image shall be between 2.0 and 4.0 and measured with a calibrated densitometer.

11.1.1.5.6 Film Processing

11.1.1.5.6.1 Film processing shall be performed in accordance with the Standard Guide for Controlling the Quality of Industrial Radiographic Film Processing ASME Section V, Article 2, SE-999, or Paragraph 23 through 26 of Standard Guide for Radiographic Examination SE-94.

11.1.1.5.7 Backscatter Radiation

11.1.1.5.7.1 Film shall be protected from backscatter radiation per the 2019 Edition of ASME Section V, Article 2, Paragraph T-223.

11.1.1.5.8 Quality of the Radiograph

11.1.1.5.8.1 All radiographs shall be free from mechanical, chemical, or other blemishes to the extent that they do not mask or cause any confusion with the image of any discontinuities in the area of interest of the object being radiographed in accordance with the 2019 Edition of ASME Section V, Section T-280.

11.1.1.5.9 Documentation

11.1.1.5.9.1 Documentation that records the radiographic technique details in accordance with the 2019 Edition of ASME Section V, Paragraph T-290 (Figure 11-15) shall be prepared.

11.1.1.6 Film Interpretation

11.1.1.6.1 The interpretation of the film shall be performed by an ASNT certified Level II or Level III film interpreter with a minimum 10 years of experience interpreting multi-layer PV welds.

11.1.1.6.2 Interpretation shall be performed in accordance with the 2019 Edition of ASME Section VIII Div. 1, Part ULW-54 or VIII Div. 2, Section 7.4.11, whichever is applicable.

RADIOGRAPHIC EXAMINATION TECHNIQUE

Part Description			
Item Description	A.O. Smith Pressure Vessel		
Referencing Code:	ASME Section VIII, Div. 1, Part ULW		
Part #	MV50563-1 & MV50563 -B2	Model No.:	MV50563
Weld Thickness	5.507"	Part Diameter:	70.5"
Joint Type	Butt	Material	Carbon Steel
Source Type			
Radiation Source:	Co-60	Focal Spot Size:	
Source Strength:		Ug (Geometric unsharpness)	< 0.070
Exposure Time:			
Penetrameter Type			
Penetrameter Type:	ASTM E1025	Penetrameter Size	50 (2T)
Penetrameter Material:	Carbon Steel	Penetrameter Location:	Film Side
Shim Material:	Carbon Steel	Shim Thickness:	0.125"
Location Marker Placement:	OD - shell side	ID Placement:	OD - shell side
Technique			
Film Type	DuPont 55	Film Technique:	Single
Film Size	7" X 17"	Screens Lead	.010"
Source to Film Distance	35.25"	Source to Film Object:	30"
Film Processing	Manual	Viewing	Single
Backing Lead Thickness:		Backing Lead Location:	Behind cassette
Surface Condition	As welded		
Technique Used:	B		

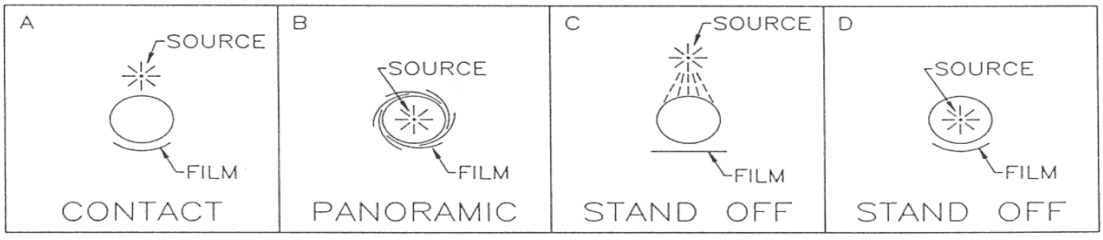


Figure 11-1 Sample Radiography Technique Sheet

Appendix P: Circumferential Growth Measurement of Layered Pressure Vessels

Circumferential Growth Measurement of Layered Pressure Vessels

May 5, 2021

The following procedure is intended to ensure that circumferential growth (typically referred to as Pi-Tape®) measurements of LPV shells are correct and consistent:

1.1.1 Pi Tape® measurement procedure.

The following procedure is recommended, with results recorded at both zero pressure and at near design pressure for the LPV:

The operation should be planned in advance so as to permit efficient operations and minimize both measurement and other errors.

(1) Identify the vessels to be measured, including designations to be used in marking and recording measurements.
(2) Determine the approximate pressures at which measurements will be taken.
    a. A low pressure and a high pressure measurement must be taken. The greater the difference in pressure of these two measurements, the greater will be the accuracy of the efficiency calculation.
    b. The lower pressure should be as close to zero as possible. It must be below the closure pressure for a 99% efficient vessel.
    c. The higher pressure should be as close to MAWP as possible. It must be above the closure pressure for an assumed 40% efficient vessel.
(3) Determine marking conventions, including shell course numbering and markings regarding measurements. Shell course numbering conventions should normally be consistent with other documentation for the vessel(s) in question. In Figure 36, the plus sign with the elongated horizontal line is used to mark the midpoint of the shell course, the double dashed lines indicate tape location, and the vertical arrow indicates the location at which the measurement was read.
(4) Arrange for sufficient personnel to permit efficient and accurate measurements. Two to three people will often be sufficient for horizontal vessels in the range of 5-6 feet in diameter, while 4-5 persons will likely be needed for the same vessel oriented vertically.
(5) Identify planned measurement locations.
    a. Unobstructed shell courses should be measured within six inches of the middle.
    b. If the middle half of the a shell course is accessible, a single measurement should be taken in the middle of the accessible section (in Figure 36, marked by the plus sign with the long horizontal line).
(6) If the middle of a shell course is obstructed, or if a nozzle exists in a shell course, any accessible length greater than one fourth of the length of the shell course should be measured within six inches of its midpoint. (Shell sections of less than one fourth of the course length need not be measured.) Arrange for access to the vessels, if needed.
    a. Some horizontal vessels are accessible from the ground, while others may require ladders, scaffolding, manlifts, etc.
    b. Vertical vessels will typically require scaffolding or manlifts, though for smaller vessels ladders may be sufficient.
(7) Measure and record the vessel wall temperature, in case temperature adjustments are, or will be, needed for comparison with past or future measurements.

(8) Wrap the tape and tension it around the vessel in accordance with the manufacturer's instructions, and with the measuring portion of the tape (vernier or digital) located on the surface of the vessel and away from of surface discontinuities such as weld crowns.

(9) With the tape tensioned around the vessel, the assisting personnel move the tape back and forth (horizontal vessel) or up and down (vertical vessel) slightly at intervals around the vessel to ensure that it seats snugly and flat around the vessel, in a plane perpendicular to the vessel axis, so as to achieve the minimum dimension.

(10) Using a permanent marker, mark the tape location on the vessel, on both sides of the tape, at intervals of one to two feet (dual dashed lines in Figure 36) (to allow comparison measurements to be taken at the same location).



Figure 36. Marking of Pi-Tape® Location – Plus sign with the long horizontal line indicates the middle of the shell course (i.e., target measurement location). Double dashed lines indicate actual tape location. Vertical arrow indicates location at which measurement is read.

(11) Make sure that the scale on the tape is away from any significant surface irregularities such as welds, large paint drips, etc., and mark this measurement location as well (The vertical arrow in Figure 36) .

(12) Mark the following information on the vessel or on a label in a location that will be visible in a photograph of the measurement: Vessel identification, shell course identifier, current pressure state.

(13) Read the Pi-Tape® following manufacturer's guidance.



Figure 37. Reading a Pi-Tape®

(14) Record the Pi-Tape® measurement.

(15) Photograph the tape reading to permit later review (Figure 37).

(16) Release the tape, then, starting fresh, take a new measurement in the same location, repeating steps 8-15, adjusting the tape back and forth as needed to achieve the minimum dimension, except that the tape will generally follow the marks already applied to the vessel to indicate the tape location. (This is to account for variabilities that can occur when working on a vessel shell with hand marked locations.) If possible, have a different person take the second reading.

(17) If there is a chance that repeat measurements may be wanted at a later time for comparison, the location markings on the vessel may be enhanced with low-stress stampings to minimize the risk that environmental degradation will obliterate them.

Appendix Q: MPFR-16-016 Pi Tape Measurements of V0023

Pi Tape Measurements of V0023

Author:	Org:	Phone:	email:
Brian Stoltz	EM21	256-544-5153	Brian.Stoltz@nasa.gov

Date:	Supported Element/System:
October 21st, 2016	Layered Pressure Vessel

Keywords: Pi Tape, Layered Pressure Vessels (LPVs), acoustic emission, V0023

Executive Summary: (Purpose and Result)

On September 14th MSFC Layered Pressure Vessel (LPV) V0023 was pressurized to 3100psig, and depressurized while obtaining acoustic emission (AE) data and Pi Tape measurements for the duration of the test.

During the depressurization, AE data collected indicated a pressure at which the frequency, amplitude, and duration of acoustic events began to occur. The data strongly suggests that the outermost layer began to slide at that pressure and gapping/sliding increased for the remainder of the depressurization. This reduction of layer efficiency at low pressure is slightly noticeable in the relatively coarse Pi Tape data.

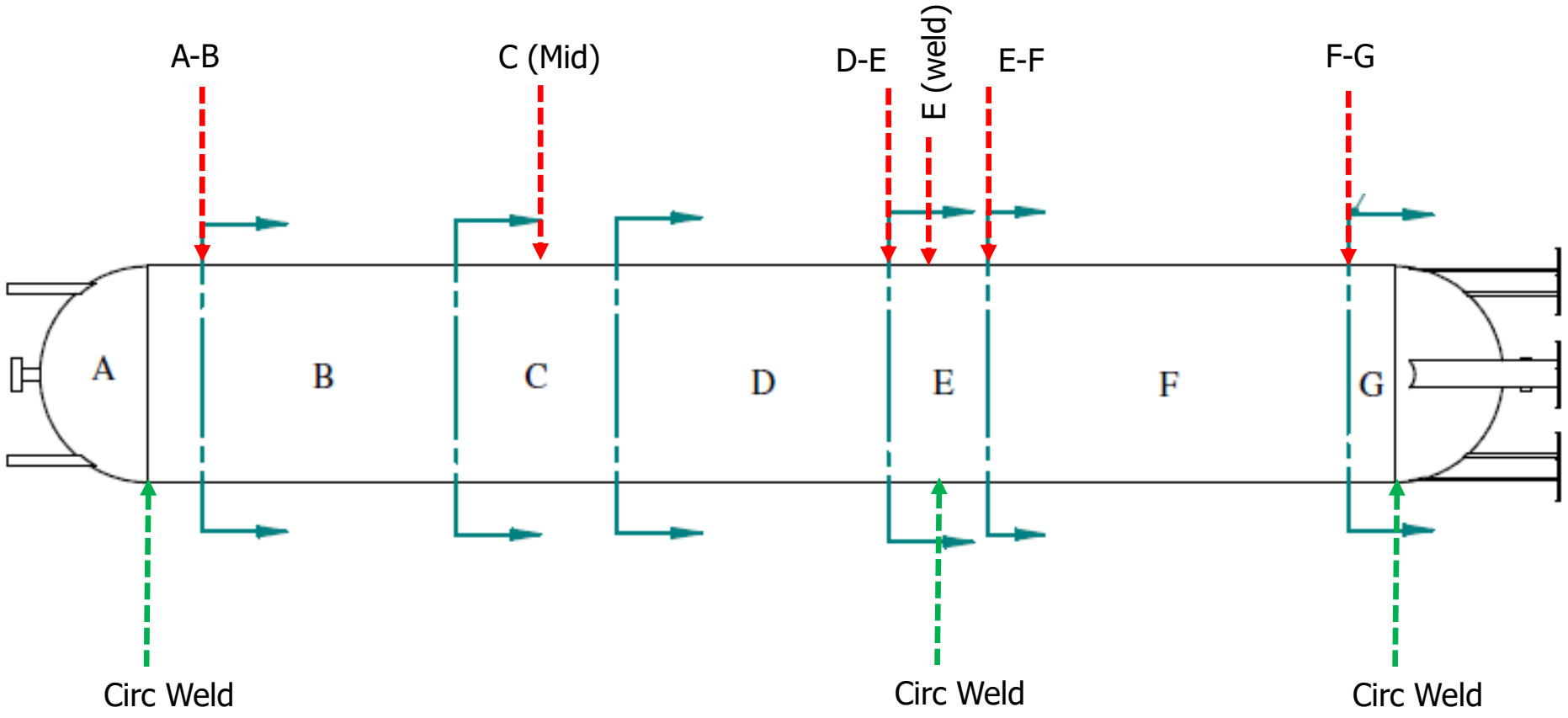
This AE-indicated pressure of "first sliding" was input into the LPV Gap Closure Tool (LPVGCT), and an analytical value for expected diametrical expansion/layer efficiency was calculated independently from the AE data.

The Pi Tape results for expansion range from 82.4-94.1% layer efficiency (0.042-0.048") with an average of the 6 locations calculated as 89.5% (0.046"). The LPVGCT analytical results based off AE calculated a "vessel average" of 87.4% efficiency (0.045"). Monolithic vessel prediction for 100% efficiency is 0.051" expansion.

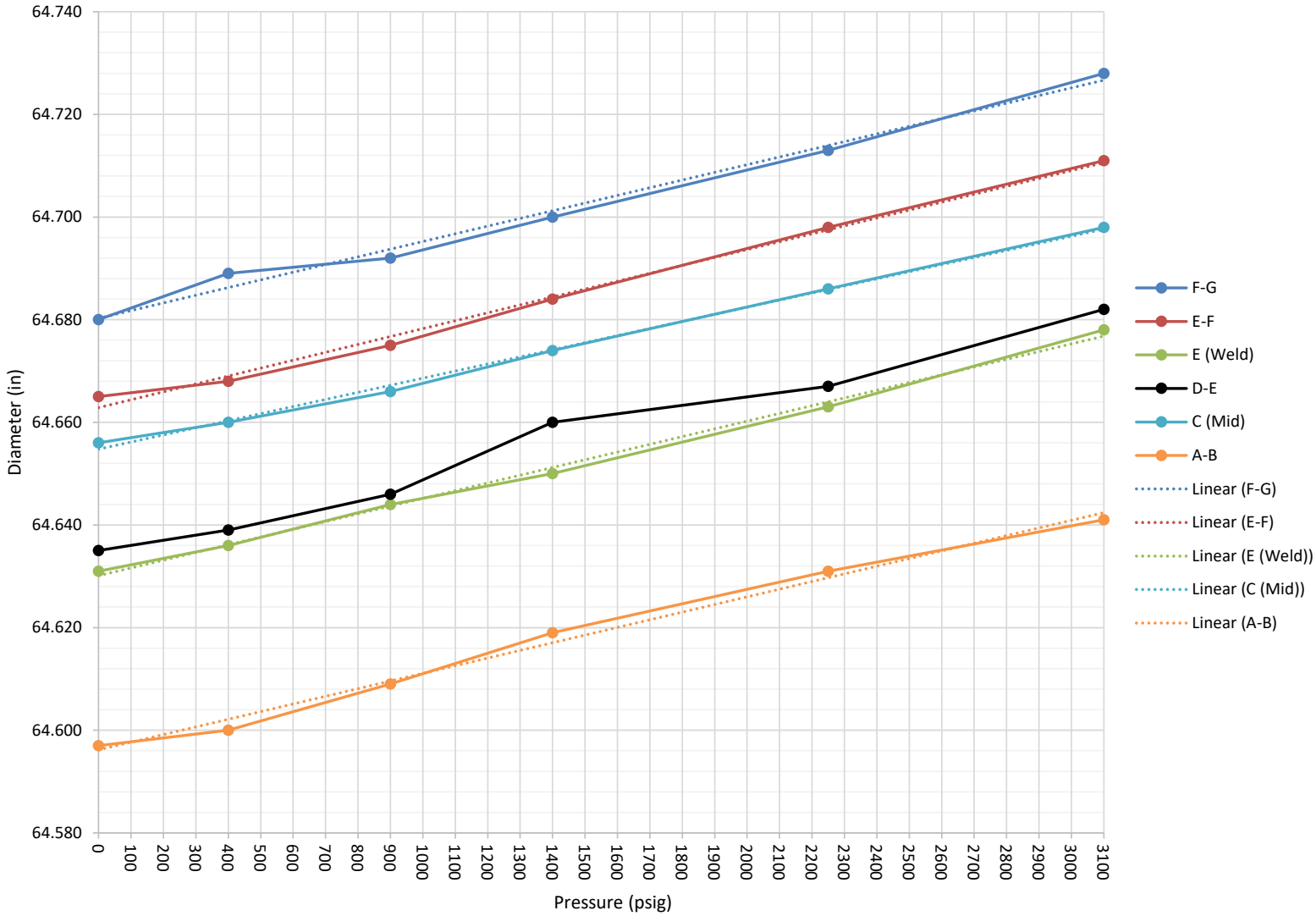
References: (work orders, reports, etc.)

N/A

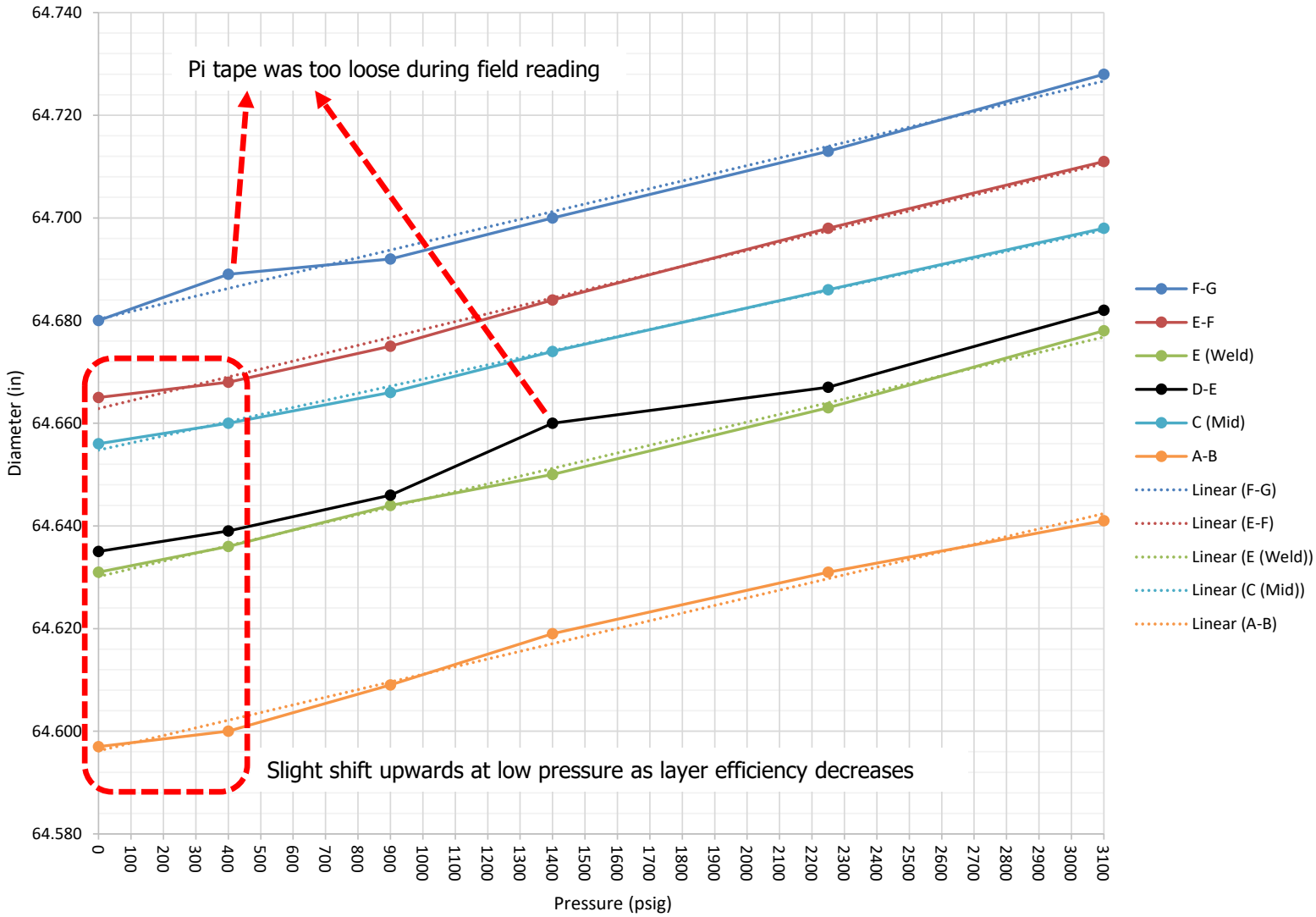
Pi Tape Measurement Locations




message
For
From
Time
Phone
URGENT!
Date
Weld 400
64 636
Post-it



Title:	SBU Controlled?	Number:	Page 4
Pi Tape Measurements of V0023	NO	MPFR-16-016	

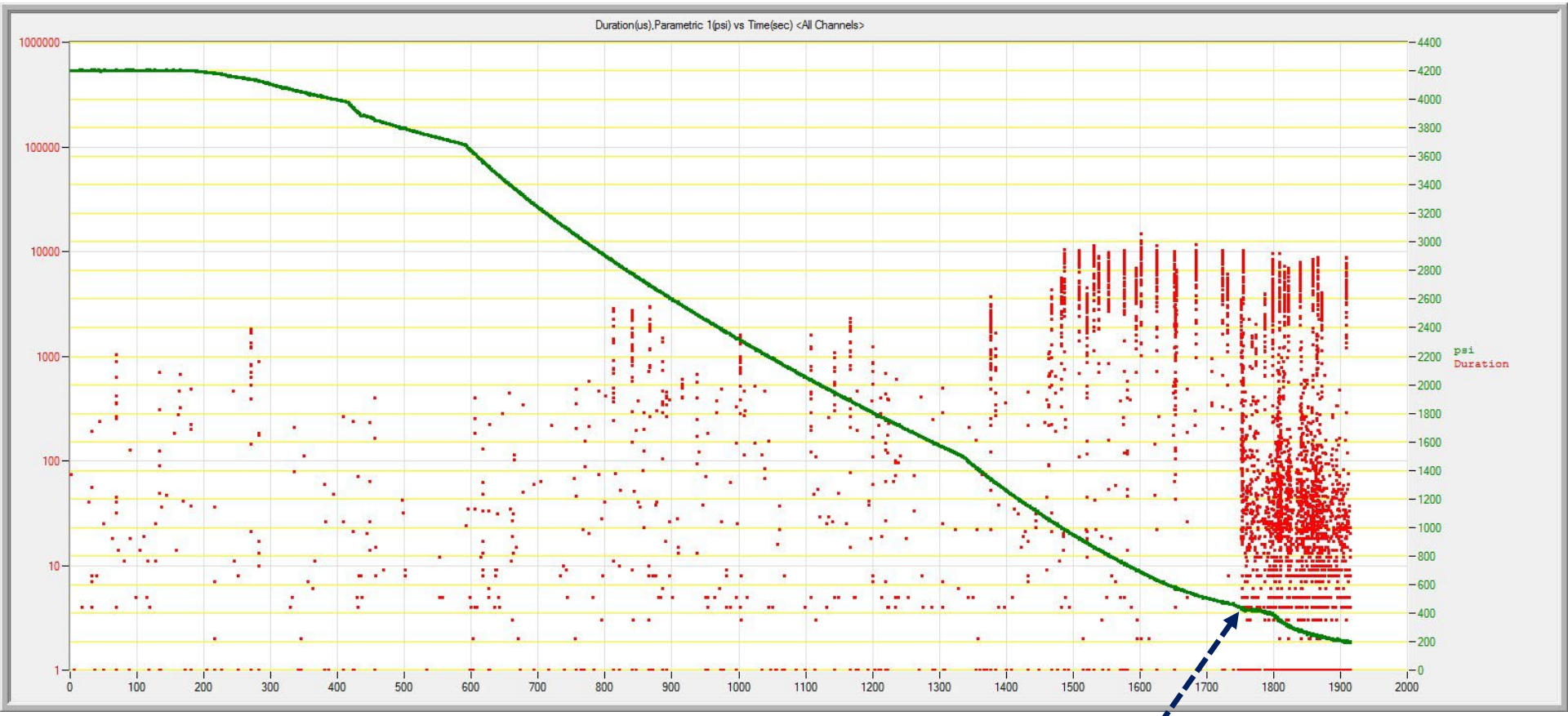


Title:	SBU Controlled?	Number:	Page 5
Pi Tape Measurements of V0023	NO	MPFR-16-016	

Pi Tape Raw Data

Pressure (psig)	Diameter at Location (in)							
	F-G	E-F	E (Weld)	D-E	C (Mid)	A-B	Average (Pi Tape)	LPVGCT (AE)
0	64.680	64.665	64.631	64.635	64.656	64.597		
400	64.689	64.668	64.636	64.639	64.660	64.600		
900	64.692	64.675	64.644	64.646	64.666	64.609		
1400	64.700	64.684	64.650	64.660	64.674	64.619		
2250	64.713	64.698	64.663	64.667	64.686	64.631		
3100	64.728	64.711	64.678	64.682	64.698	64.641		
Delta	0.048	0.046	0.047	0.047	0.042	0.044	0.046	0.045
Efficiency	94.1	90.2	92.2	92.2	82.4	86.3	89.5	87.3

AE Data: Pressure & Signal Duration vs Time



Significant layer sliding begins, ≈400psig

LPVGCT Screenshot

Vessel					Mono Response		Layered Response			
d inner	58	in.		P (psi)	σ (ksi)	D (in)	D (in)	Efficiency		
t total	3.27	in.	Initial	0	0	64.54	64.54			
E	29500000	psi	Final	3100	29.04235	64.59127	61.7412			
					delta:	0.0513	0.0448	87.4		
										P actual
Layer #	T layer	Gap	R Layer	T closure	P closure	Sig closure	R Mono	C closure	D Closure	0
0	0.47	0.0006	29.235	0.470	11.451	712.281	29.235	185.169	58.941	11.45107
1	0.28	0.0006	29.610	0.750	18.099	708.886	29.375	186.929	59.501	29.55029
2	0.28	0.0006	29.890	1.030	24.621	705.524	29.515	188.688	60.061	54.17131
3	0.28	0.0006	30.170	1.310	31.019	702.193	29.655	190.447	60.621	85.19045
4	0.28	0.0006	30.450	1.590	37.296	698.893	29.795	192.206	61.181	122.4867
5	0.28	0.0006	30.730	1.870	43.455	695.625	29.935	193.966	61.741	165.9414
6	0.28	0.0006	31.010	2.150	49.497	692.387	30.075	195.725	62.301	215.4387
7	0.28	0.0006	31.290	2.430	55.426	689.179	30.215	197.484	62.861	270.865
8	0.28	0.0006	31.570	2.710	61.244	686.000	30.355	199.244	63.421	332.1089
9	0.28	0.0006	31.850	2.990	66.953	682.851	30.495	201.003	63.981	399.0616
10	0.28	0.0224	32.130	3.270	2708.714	25376.588	30.635	202.899	64.585	3107.775

Equivalent uniform concentric gap if distributed between all gaps

Significant layer sliding begins/ends, ≈400psig

Pi Tape measurements are confirmed to be a simple method of measuring LPV layer efficiency. Additionally, it was demonstrated that a depressurization AE test can also be used to accurately evaluate layer efficiency when combined with the LPV Gap Closure Tool (LPVGCT).

Using either the Pi Tape data or AE data, the LPVGCT can be used to determine a distribution of uniform concentric layer gapping which would result in the measured layer efficiency.

Future work should include a similar test on another vessel to confirm the observed correlations. A smaller vessel is recommended, such as a V0032 sister vessel.

Appendix R: Efficiency Tables 20210325

Table 1. Pi-Tape measurement data and efficiency at factor of safety of 3 (MAWP = 2946 psi) for sixteen LPVs at NASA's Ames Research Center at N250A.

		Pressurized Measurement			Unpressurized Measurement						
Vessel ID	**Shell Course (Circ Welds)**	**Vessel Pressure (psig)**	**Vessel Temp (°F)**	**Pi-Tape® Reading (in)**	**Vessel Pressure (psig)**	**Vessel Temp (°F)**	**Pi-Tape® Reading (in)**	**Temp. Corrected $\delta_{OD,actual}$ (in)**	**$\delta_{OD,theoretical}$ (in)**	**Closure Pressure (psi)**	**Efficiency at 2946 psi (%)**
1	1 (C1-C2)	3000	49.4	65.607	0	35.5	65.556	0.045	0.062	826.45	71.9
	2 (C2-C3)	3000	49.3	65.614	0	37.0	65.560	0.049	0.062	648.20	78.0
	3 (C3-C4)	3000	50.6	65.629	0	37.1	65.575	0.048	0.062	674.03	77.1
	4 (C4-C5)	3000	51.5	65.588	0	39.1	65.534	0.049	0.062	649.24	78.0
	5 (C5-C6)	3000	50.9	65.570	0	39.2	65.518	0.047	0.062	731.17	75.2
	6 (C6-C7)	3000	50.6	65.581	0	40.1	65.525	0.052	0.062	513.97	82.6
	7 (C7-C8)	3000	51.1	65.630	0	40.1	65.575	0.050	0.062	575.52	80.5
	8 (C8-C9)	3000	51.4	65.607	0	40.3	65.555	0.047	0.062	721.65	75.5
	9 (C9-C10)	3000	51.6	65.594	0	40.1	65.544	0.045	0.062	825.51	72.0
2	1 (C1-C2)	3000	51.4	65.574	0	32.5	65.520	0.046	0.062	781.77	73.5
	2 (C2-C3)	3000	51.4	65.624	0	32.0	65.572	0.044	0.062	892.40	69.7
	3 (C3-C4)	3000	51.6	65.648	0	32.5	65.593	0.047	0.062	742.27	74.8
	4 (C4-C5)	3000	51.1	65.640	0	32.4	65.589	0.043	0.062	926.41	68.6
	5 (C5-C6)	3000	50.8	65.615	0	32.7	65.561	0.046	0.062	769.50	73.9
	6 (C6-C7)	3000	51.4	65.580	0	32.4	65.533	0.039	0.062	1123.62	61.9
	7 (C7-C8)	3000	50.9	65.673	0	32.6	65.621	0.044	0.062	873.41	70.4
	8 (C8-C9)	3000	51.5	65.680	0	32.7	65.630	0.042	0.062	981.57	66.7
	9 (C9-C10)	3000	51.5	65.647	0	32.7	65.595	0.044	0.062	882.79	70.0
3	1 (C1-C2)	3000	50.3	65.655	0	33.1	65.601	0.047	0.062	753.06	74.4
	2 (C2-C3)	3000	50.0	65.661	0	33.2	65.605	0.049	0.062	647.84	78.0
	3 (C3-C4)	3000	51.4	65.633	0	36.9	65.578	0.049	0.062	646.62	78.1
	4 (C4-C5)	3000	51.6	65.608	0	33.8	65.555	0.045	0.062	809.04	72.5
	5 (C5-C6)	3000	51.7	65.605	0	33.7	65.550	0.047	0.062	717.34	75.7

Vessel ID	Shell Course (Circ Welds)	Pressurized Measurement			Unpressurized Measurement			Temp. Corrected $\delta_{OD,actual}$ (in)	$\delta_{OD,theoretical}$ (in)	Closure Pressure (psi)	Efficiency at 2946 psi (%)
		Vessel Pressure (psig)	Vessel Temp (°F)	Pi-Tape® Reading (in)	Vessel Pressure (psig)	Vessel Temp (°F)	Pi-Tape® Reading (in)				
	6 (C6-C7)	3000	50.9	65.607	0	33.6	65.554	0.046	0.062	798.69	72.9
	7 (C7-C8)	3000	49.7	65.551	0	34.1	65.500	0.044	0.062	857.28	70.9
	8 (C8-C9)	3000	50.2	65.565	0	34.7	65.514	0.044	0.062	856.25	70.9
	9 (C9-C10)	3000	51.2	65.610	0	34.0	65.550	0.053	0.062	459.76	84.4
4	1 (C1-C2)	3000	51.1	65.648	0	34.2	65.594	0.047	0.062	747.38	74.6
	2 (C2-C3)	3000	51.0	65.615	0	35.5	65.569	0.039	0.062	1100.24	62.7
	3 (C3-C4)	3000	51.2	65.645	0	35.2	65.592	0.046	0.062	775.89	73.7
	4 (C4-C5)	3000	51.5	65.600*	0	35.4	65.600	-0.007	0.062	3329.53	-13.0
	5 (C5-C6)	3000	51.6	65.665	0	35.8	65.610	0.048	0.062	675.85	77.1
	6 (C6-C7)	3000	51.5	65.642	0	35.5	65.695**	-0.060	0.062	5872.31	-99.3
	7 (C7-C8)	3000	51.5	65.598	0	35.3	65.556	0.035	0.062	1307.67	55.6
	8 (C8-C9)	3000	51.6	65.652	0	35.6	65.600	0.045	0.062	823.62	72.0
	9 (C9-C10)	3000	51.0	65.574	0	35.3	65.540	0.027	0.062	1683.42	42.9
5	1 (C1-C2)	2950	40.0	65.608	0	38.4	65.555	0.052	0.061	427.20	85.5
	2 (C2-C3)	2950	39.6	65.593	0	38.4	65.544	0.048	0.061	612.07	79.2
	3 (C3-C4)	2950	40.1	65.578	0	38.5	65.525	0.052	0.061	424.78	85.6
	4 (C4-C5)	2950	40.4	65.548	0	39.0	65.493	0.054	0.061	322.47	89.1
	5 (C5-C6)	2950	39.5	65.625	0	39.4	65.573	0.052	0.061	446.04	84.9
	6 (C6-C7)	2950	40.2	65.601	0	38.9	65.548	0.052	0.061	421.50	85.7
	7 (C7-C8)	2950	40.6	65.572	0	39.4	65.520	0.051	0.061	465.45	84.2
	8 (C8-C9)	2950	40.6	65.602	0	38.9	65.550	0.051	0.061	477.08	83.8
	9 (C9-C10)	2950	39.6	65.556	0	40.0	65.510	0.046	0.061	721.49	75.5
6	1 (C1-C2)	2950	44.0	65.590	0	38.4	65.538	0.050	0.061	557.31	81.1
	2 (C2-C3)	2950	44.1	65.672***	0	38.2	65.520	0.149	0.061	-4265.32	244.8
	3 (C3-C4)	2950	44.1	65.604	0	38.6	65.552	0.050	0.061	555.32	81.1
	4 (C4-C5)	2950	44.5	65.560	0	39.0	65.516	0.042	0.061	939.78	68.1

Vessel ID	Shell Course (Circ Welds)	Pressurized Measurement			Unpressurized Measurement			Temp. Corrected $\delta_{OD,actual}$ (in)	$\delta_{OD,theoretical}$ (in)	Closure Pressure (psi)	Efficiency at 2946 psi (%)
		Vessel Pressure (psig)	Vessel Temp (°F)	Pi-Tape® Reading (in)	Vessel Pressure (psig)	Vessel Temp (°F)	Pi-Tape® Reading (in)				
	5 (C5-C6)	2950	43.7	65.575	0	40.5	65.526	0.048	0.061	650.81	77.9
	6 (C6-C7)	2950	43.8	65.586	0	39.6	65.532	0.052	0.061	431.56	85.4
	7 (C7-C8)	2950	44.6	65.582	0	39.8	65.531	0.049	0.061	588.58	80.0
	8 (C8-C9)	2950	43.6	65.573	0	39.4	65.525	0.046	0.061	720.59	75.5
	9 (C9-C10)	2950	44.4	65.608	0	40.2	65.564	0.042	0.061	915.20	68.9
	1 (C1-C2)	2950	44.6	65.519	0	38.4	65.469	0.047	0.061	658.92	77.6
	2 (C2-C3)	2950	44.1	65.620	0	38.6	65.567	0.051	0.061	509.32	82.7
	3 (C3-C4)	2950	44.1	65.600	0	38.7	65.548	0.050	0.061	552.96	81.2
	4 (C4-C5)	2950	44.4	65.604	0	39.4	65.558	0.044	0.061	834.81	71.7
7	5 (C5-C6)	2950	44.0	65.602	0	39.5	65.555	0.045	0.061	776.11	73.7
	6 (C6-C7)	2950	44.8	65.640	0	38.6	65.594	0.043	0.061	860.90	70.8
	7 (C7-C8)	2950	44.7	65.638	0	39.5	65.589	0.047	0.061	695.52	76.4
	8 (C8-C9)	2950	44.2	65.650	0	38.5	65.600	0.048	0.061	658.44	77.6
	9 (C9-C10)	2950	44.4	65.640	0	39.2	65.595	0.043	0.061	888.60	69.8
	1 (C1-C2)	2950	44.5	65.580	0	38.3	65.528	0.049	0.061	567.84	80.7
	2 (C2-C3)	2950	44.7	65.602	0	38.5	65.550	0.049	0.061	569.55	80.7
	3 (C3-C4)	2950	44.3	65.628	0	39.0	65.576	0.050	0.061	553.09	81.2
	4 (C4-C5)	2950	44.1	65.648	0	39.0	65.603	0.043	0.061	888.11	69.9
8	5 (C5-C6)	2950	44.8	65.598	0	39.2	65.549	0.047	0.061	701.83	76.2
	6 (C6-C7)	2950	44.2	65.593	0	39.2	65.542	0.049	0.061	592.51	79.9
	7 (C7-C8)	2950	44.0	65.589	0	38.5	65.556	0.031	0.061	1471.79	50.0
	8 (C8-C9)	2950	44.6	65.595	0	38.4	65.542	0.050	0.061	520.69	82.3
	9 (C9-C10)	2950	44.4	65.561	0	39.0	65.516	0.043	0.061	888.42	69.8
	1 (C1-C2)	2950	45.0	65.605	0	38.3	65.557	0.045	0.061	773.24	73.8
9	2 (C2-C3)	2950	44.9	65.664	0	38.5	65.614	0.047	0.061	674.88	77.1
	3 (C3-C4)	2950	45.4	65.621	0	38.6	65.571	0.047	0.061	679.90	76.9

Vessel ID	Shell Course (Circ Welds)	Pressurized Measurement			Unpressurized Measurement			Temp. Corrected $\delta_{OD,actual}$ (in)	$\delta_{OD,theoretical}$ (in)	Closure Pressure (psi)	Efficiency at 2946 psi (%)
		Vessel Pressure (psig)	Vessel Temp (°F)	Pi-Tape® Reading (in)	Vessel Pressure (psig)	Vessel Temp (°F)	Pi-Tape® Reading (in)				
	4 (C4-C5)	2950	45.4	65.602	0	38.9	65.550	0.049	0.061	574.69	80.5
	5 (C5-C6)	2950	45.4	65.584	0	39.3	65.548	0.033	0.061	1340.06	54.5
	6 (C6-C7)	2950	45.7	65.594	0	39.2	65.551	0.040	0.061	1010.86	65.7
	7 (C7-C8)	2950	45.5	65.635	0	38.8	65.595	0.037	0.061	1161.22	60.6
	8 (C8-C9)	2950	45.6	65.584	0	38.3	65.534	0.047	0.061	687.42	76.7
	9 (C9-C10)	2950	45.6	65.523	0	38.9	65.474	0.046	0.061	717.92	75.6
	1 (C1-C2)	2950	44.5	65.633	0	50.2	65.581	0.054	0.061	328.48	88.8
	2 (C2-C3)	2950	45.0	65.620	0	50.2	65.580	0.042	0.061	914.90	68.9
	3 (C3-C4)	2950	45.5	65.607	0	50.9	65.560	0.049	0.061	573.07	80.5
	4 (C4-C5)	2950	45.2	65.586	0	49.6	65.540	0.048	0.061	641.41	78.2
10	5 (C5-C6)	2950	45.3	65.625	0	50.5	65.581	0.046	0.061	724.29	75.4
	6 (C6-C7)	2950	45.7	65.639	0	48.7	65.600	0.040	0.061	1011.53	65.7
	7 (C7-C8)	2950	45.1	65.510	0	49.9	65.461	0.051	0.061	481.34	83.7
	8 (C8-C9)	2950	45.8	65.535	0	49.6	65.480	0.057	0.061	214.40	92.7
	9 (C9-C10)	2950	45.1	65.586	0	50.4	65.575	0.013	0.061	2312.08	21.5
	1 (C1-C2)	2950	47.7	65.550	0	50.5	65.498	0.053	0.061	380.41	87.1
	2 (C2-C3)	2950	47.2	65.536	0	50.0	65.502	0.035	0.061	1251.19	57.5
	3 (C3-C4)	2950	48.2	65.610	0	49.5	65.557	0.054	0.061	367.78	87.5
	4 (C4-C5)	2950	48.2	65.575	0	50.5	65.521	0.055	0.061	296.00	90.0
11	5 (C5-C6)	2950	47.8	65.570	0	49.5	65.515	0.056	0.061	258.53	91.2
	6 (C6-C7)	2950	48.2	65.545	0	50.5	65.493	0.053	0.061	390.28	86.8
	7 (C7-C8)	2950	48.0	65.596	0	50.7	65.545	0.052	0.061	434.50	85.3
	8 (C8-C9)	2950	48.2	65.624	0	50.0	65.572	0.053	0.061	407.96	86.2
	9 (C9-C10)	2950	48.7	65.608	0	50.3	65.551	0.058	0.061	168.22	94.3
12	1 (C1-C2)	2950	48.2	65.695	0	50.0	65.640	0.056	0.061	268.12	90.9
	2 (C2-C3)	2950	48.2	65.675	0	50.5	65.620	0.056	0.061	255.13	91.3

Vessel ID	Shell Course (Circ Welds)	Pressurized Measurement			Unpressurized Measurement			Temp. Corrected $\delta_{OD,actual}$ (in)	$\delta_{OD,theoretical}$ (in)	Closure Pressure (psi)	Efficiency at 2946 psi (%)
		Vessel Pressure (psig)	Vessel Temp (°F)	Pi-Tape® Reading (in)	Vessel Pressure (psig)	Vessel Temp (°F)	Pi-Tape® Reading (in)				
	3 (C3-C4)	2950	48.0	65.609	0	50.3	65.555	0.055	0.061	297.82	89.9
	4 (C4-C5)	2950	48.6	65.602	0	49.8	65.549	0.054	0.061	368.15	87.5
	5 (C5-C6)	2950	48.4	65.559	0	49.7	65.506	0.054	0.061	364.63	87.6
	6 (C6-C7)	2950	47.9	65.594	0	50.8	65.540	0.055	0.061	286.29	90.3
	7 (C7-C8)	2950	48.5	65.575	0	50.0	65.520	0.056	0.061	263.06	91.1
	8 (C8-C9)	2950	48.3	65.598	0	50.7	65.545	0.054	0.061	345.22	88.3
	9 (C9-C10)	2950	48.5	65.625	0	49.6	65.565	0.060	0.061	34.08	98.8
	1 (C1-C2)	2950	50.2	65.596	0	38.5	65.545	0.046	0.061	730.43	75.2
	2 (C2-C3)	2950	50.0	65.608	0	38.9	65.556	0.047	0.061	670.70	77.2
	3 (C3-C4)	2950	50.0	65.606	0	38.3	65.556	0.045	0.061	780.49	73.5
	4 (C4-C5)	2950	50.5	65.618	0	38.5	65.554	0.059	0.061	110.38	96.3
13	5 (C5-C6)	2950	50.4	65.624	0	39.5	65.570	0.049	0.061	572.28	80.6
	6 (C6-C7)	2950	50.4	65.638	0	38.5	65.586	0.047	0.061	689.41	76.6
	7 (C7-C8)	2950	49.3	65.657	0	38.3	65.605	0.047	0.061	671.34	77.2
	8 (C8-C9)	2950	50.7	65.632	0	38.8	65.572	0.055	0.061	301.77	89.8
	9 (C9-C10)	2950	50.5	65.632	0	38.6	65.578	0.049	0.061	593.46	79.9
	1 (C1-C2)	3000	51.5	65.600	0	38.5	65.543	0.051	0.062	517.56	82.4
	2 (C2-C3)	3000	51.2	65.608	0	39.2	65.552	0.051	0.062	545.99	81.5
	3 (C3-C4)	3000	51.5	65.595	0	38.3	65.539	0.050	0.062	568.56	80.7
	4 (C4-C5)	3000	51.5	65.577	0	38.8	65.525	0.047	0.062	751.23	74.5
14	5 (C5-C6)	3000	51.7	65.587	0	38.3	65.536	0.045	0.062	814.70	72.3
	6 (C6-C7)	3000	51.5	65.578	0	38.4	65.525	0.047	0.062	711.18	75.9
	7 (C7-C8)	3000	51.6	65.620	0	39.0	65.564	0.051	0.062	559.29	81.0
	8 (C8-C9)	3000	51.7	65.603	0	39.4	65.547	0.051	0.062	551.74	81.3
	9 (C9-C10)	3000	51.9	65.605	0	38.6	65.550	0.049	0.062	619.74	79.0
15	1 (C1-C2)	3000	51.6	65.600	0	39.5	65.545	0.050	0.062	594.68	79.8

Vessel ID	Shell Course (Circ Welds)	Pressurized Measurement			Unpressurized Measurement			Temp. Corrected $\delta_{OD,actual}$ (in)	$\delta_{OD,theoretical}$ (in)	Closure Pressure (psi)	Efficiency at 2946 psi (%)
		Vessel Pressure (psig)	Vessel Temp (°F)	Pi-Tape® Reading (in)	Vessel Pressure (psig)	Vessel Temp (°F)	Pi-Tape® Reading (in)				
	2 (C2-C3)	3000	51.6	65.469	0	39.0	65.408	0.056	0.062	305.31	89.6
	3 (C3-C4)	3000	51.9	65.585	0	39.0	65.530	0.050	0.062	609.91	79.3
	4 (C4-C5)	3000	51.8	65.565	0	38.9	65.510	0.050	0.062	608.31	79.4
	5 (C5-C6)	3000	51.7	65.584	0	38.5	65.529	0.049	0.062	617.03	79.1
	6 (C6-C7)	3000	51.6	65.581	0	39.1	65.525	0.051	0.062	553.02	81.2
	7 (C7-C8)	3000	51.7	65.621	0	39.5	65.568	0.048	0.062	696.01	76.4
	8 (C8-C9)	3000	51.5	65.632	0	39.2	65.576	0.051	0.062	555.14	81.2
	9 (C9-C10)	3000	51.7	65.528	0	38.9	65.471	0.052	0.062	507.45	82.8
16	1 (C1-C2)	3000	52.5	65.625	0	38.4	65.570	0.049	0.062	638.79	78.3
	2 (C2-C3)	3000	52.1	65.600	0	38.7	65.548	0.046	0.062	766.32	74.0
	3 (C3-C4)	3000	52.4	65.616	0	39.5	65.561	0.050	0.062	613.42	79.2
	4 (C4-C5)	3000	52.6	65.648	0	38.5	65.591	0.051	0.062	545.16	81.5
	5 (C5-C6)	3000	52.7	65.596	0	39.7	65.540	0.050	0.062	566.58	80.8
	6 (C6-C7)	3000	52.6	65.572	0	39.1	65.515	0.051	0.062	525.51	82.2
	7 (C7-C8)	3000	52.6	65.591	0	38.5	65.535	0.050	0.062	587.76	80.0
	8 (C8-C9)	3000	52.4	65.600	0	39.2	65.543	0.051	0.062	522.70	82.3
	9 (C9-C10)	3000	52.2	65.566	0	38.8	65.508	0.052	0.062	473.55	83.9

* Transcription error, in which the unpressurized Pi-Tape® reading was repeated for the pressurized reading (data not used in analysis)
** Likely a misread error (data not used in analysis)
*** Likely a misread error (data not used in analysis)

Table 2. Pi-Tape® measurement data and efficiency at factor of safety of 3 (MAWP = 3678 psi) for nineteen Hydrogen LPVs at NASA's Marshall Space Flight Center.

		Pressurized Measurements				Unpressurized Measurements							
Vessel ID	**Shell Course**	**Vessel Pressure (psig)**	**Vessel Temp (°F)**	**Pi-Tape® Reading #1 (in)**	**Pi-Tape® Reading #2 (in)**	**Vessel Pressure (psig)**	**Vessel Temp (°F)**	**Pi-Tape® Reading #1 (in)**	**Pi-Tape® Reading #2 (in)**	**Temp. Corrected $\delta_{OD,actual}$ (in)**	**$\delta_{OD,theoretical}$ (in)**	**Closure Pressure (psi)**	**Efficiency at 3678 psi (%)**
V0009	Lower	2950	41	64.729	64.729	0	43	64.696	64.695	0.035	0.049	822	77.7
	Upper	2950	41	64.740	64.740	0	43	64.712	64.709	0.032	0.049	1002	72.8
V0010	Lower	2950	41	64.663	64.663	0	43	64.619	64.619	0.045	0.049	222	94.0
	Upper	2950	41	64.750	64.745	0	43	64.708	64.710	0.038	0.049	642	82.5
V0011	Lower	2950	41	65.200	65.200	0	43	65.170	65.173	0.031	0.049	1062	71.1
	Upper	2780	75	65.234	65.233	50	70	65.199	65.200	0.032	0.046	832	77.4
V0012	Lower	2950	41	64.795	64.789	0	43	64.745	64.750	0.045	0.049	222	94.0
	Upper	2780	75	64.745	64.748	50	70	64.713	64.714	0.030	0.046	952	74.1
V0013	Lower	2950	41	64.698	64.697	0	43	64.665	64.664	0.034	0.049	882	76.0
	Upper	2780	75	64.675	64.676	50	70	64.639	64.639	0.034	0.046	712	80.6
V0014	Lower	2950	41	64.795	64.793	0	43	64.750	64.750	0.044	0.049	282	92.3
	Upper	2780	75	64.754	64.755	50	70	64.720	64.720	0.032	0.046	832	77.4
V0015	Lower	2950	41	64.707	64.705	0	43	64.675	64.673	0.033	0.049	942	74.4
	Upper	2780	75	64.730	64.730	50	70	64.692	64.693	0.036	0.046	592	83.9
V0016	Lower	2950	41	64.694	64.694	0	43	64.650	64.650	0.045	0.049	222	94.0
	Upper	2780	75	64.670	64.670	50	70	64.632	64.632	0.036	0.046	592	83.9
V0017	Lower	2950	41	64.670	64.669	0	43	64.626	64.629	0.044	0.049	282	92.3
	Upper	2780	75	64.700	64.700	50	70	64.657	64.660	0.041	0.046	292	92.1
V0018	Lower	2950	41	65.231	65.231	0	43	65.183	65.184	0.049	0.049	-18	100.5*
	Upper	2780	75	65.219	65.217	50	70	65.182	65.178	0.037	0.046	532	85.5
V0019	Lower	2950	41	64.726**	64.725**	0	43	64.700	64.695	0.031	0.049	906	75.4
	Upper	2780	75	64.745	64.740	50	70	64.703	64.705	0.035	0.046	652	82.3
V0020	Lower	2950	41	64.760	64.760	0	43	64.716	64.716	0.045	0.049	222	94.0

		Pressurized Measurements				Unpressurized Measurements							
Vessel ID	**Shell Course**	**Vessel Pressure (psig)**	**Vessel Temp (°F)**	**Pi-Tape® Reading #1 (in)**	**Pi-Tape® Reading #2 (in)**	**Vessel Pressure (psig)**	**Vessel Temp (°F)**	**Pi-Tape® Reading #1 (in)**	**Pi-Tape® Reading #2 (in)**	**Temp. Corrected $\delta_{OD,actual}$ (in)**	**$\delta_{OD,theoretical}$ (in)**	**Closure Pressure (psi)**	**Efficiency at 3678 psi (%)**
	Upper	2780	75	64.700	64.702	50	70	64.665	64.665	0.033	0.046	772	79.0
V0021	Lower	2950	41	64.637	64.637	0	43	64.607	64.600	0.038	0.049	642	82.5
	Upper	2780	75	64.665	64.665	50	70	64.623	64.624	0.040	0.046	352	90.4
V0022	Lower	2950	41	64.710	64.710	0	43	64.669	64.665	0.046	0.049	162	95.6
	Upper	2950	41	64.691	64.691	0	43	64.650	64.650	0.042	0.049	402	89.1
V0024	Lower	2950	41	64.675	64.675	0	43	64.639	64.635	0.041	0.049	465	87.4
	Upper	2950	41	64.636	64.635	0	43	64.595	64.596	0.041	0.049	465	87.4
V0025	Lower	2950	41	64.768	64.768	0	43	64.720	64.725	0.049	0.049	-18	100.5*
	Upper	2780	75	64.731	64.731	50	70	64.695	64.695	0.034	0.046	712	80.6
V0026	Lower	2950	41	65.250	65.250	0	43	65.212	65.211	0.040	0.049	522	85.8
	Upper	2950	41	65.321	65.325	0	43	65.280	65.277	0.045	0.049	222	94.0
V0027	Lower	2950	41	64.670	64.670	0	43	64.625	64.626	0.046	0.049	162	95.6
	Upper	2950	41	64.652	64.650	0	43	64.613	64.613	0.038	0.049	642	82.5
V0028	Lower	2950	41	64.765	64.765	0	43	64.730	64.728	0.038	0.049	642	82.5
	Upper	2950	41	64.755	64.755	0	43	64.715	64.712	0.044	0.049	282	92.3

* Very unlikely for efficiency to be greater than 100% based on friction between layers (data not used in analysis)

** Pressurized Pi-Tape® readings were originally reported as 64.716 and 64.715 inches, however the measurement team identified there to be a misread error after reviewing photos of the Pi-Tape®. Based on the photos, the correct Pi-Tape® measurements are 64.726 and 64.725 inches respectively.

Appendix S: PVS-19-011, Pi Tape Measurements of West Test Area (WTA) Hydrogen Bottles

TO: Memo for the Record

FROM: Edward Johnson/QD10

Doc. #: PVS-19-011

Date: December 16, 2019

Re: Pi-Tape Measurements of West Test Area (WTA) Hydrogen Bottles

---

One requirement of the Layered Pressure Vessel (LPV) Alternate Standard, which is currently in draft, will be to calculate layer gap efficiency as part of the overall evaluation of layered vessel structural integrity. Calculating layer gap efficiency requires measuring the diameter of the vessel in its pressurized and unpressurized states and calculating the diameter difference. The Alternate Standard will furthermore recommend that the pi-tape measurements be made at approximately the mid-point of each shell course. Precision pi-tapes, which wrap around the outside vessel wall, are the most typical tool for obtaining accurate vessel wall diameter measurements. Although the tool is rather simple in its design, the process of using the pi-tape accurately can become complicated due to variables such as vessel size, vessel installation orientation (horizontal or vertical) and vessel access.

This memo focuses specifically on the pi-tape measurements for the WTA hydrogen bottles which were the first MSFC vessels on which pi-tape measurements were made for certification purposes. These specific vessels are also considered the most difficult group of MSFC LPVs to measure due to vessel size (over 5 foot diameter) and physical access issues. This memo addresses only the pi-tape measurement process and not the resulting efficiency calculations which will be addressed in the vessel certification/qualification report to be prepared at a later date. The pi-tape measurement process will eventually be performed on other LPVs certified or qualified in accordance with the Alternate Standard.

In late November 2019, the Pressure System Certification Team was notified that the 19 vertical LPVs located at B4699B would be converted from high purity air (HPA) to hydrogen service by end of December to support hydrogen test requirements in the West Test Area. The conversion of the vessels from HPA to hydrogen requires that the vessels be depressurized, purged to remove residual air and then re-pressurized with hydrogen. The conversion of these vessels was an opportunity to take pi-tape measurements of the vessels in both a pressurized and de-pressurized condition. Once refilled with hydrogen, the vessels may not be vented to low pressure for many years to come as these vessels are maintained at high pressure even when no test operations are being performed. Therefore, this was an opportunity to obtain pi-tape data which may not be available again for many years.

Taking the pi-tape measurements was complicated by the large diameter of these vessels, close proximity of one vessel to another and the height at which the measurements were made due to the vessel vertical orientation. A decision was made that measurements on all lower shell courses could be obtained with one two-man team working in a man-lift and two additional personnel working from ladders placed between the vessels (see Photo 1). However, it was decided that getting upper shell course measurements from all 19 vessels was too difficult and inherently unsafe unless other costly measures were undertaken to facilitate access (e.g., removing upper catwalk from vessels). Upper shell course measurements would only be taken from vessels which could be accessed by personnel working from two man-lifts to reach around the perimeter of the vessels (see Photo 2).

The pi-tape readings obtained for each of the vessels are shown in the attachment.



Photo 1. Taking Lower Shell Course Measurements

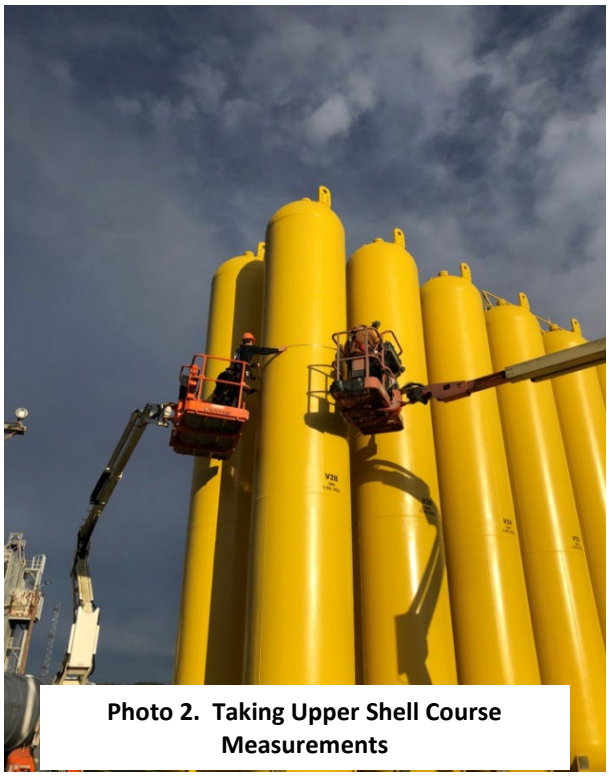


Photo 2. Taking Upper Shell Course Measurements

For these specific vessels, the first pi-tape measurements were made with the vessel fully pressurized (~2950 psig) and the second measurements made after the vessels had been vented to 0 psig. Figure 1 shows the WTA hydrogen bottle configuration. The timeline for obtaining the measurements was as follows:

November 20, 2019: Pi-tape measurements were made on the lower shell courses for all 19 vessels with the vessels pressurized to ~2950 psig (approximately 4 hours to complete work).

November 21, 2019: Pi-tape measurements were made on the upper shell courses for 9 vessels with the vessels pressurized to ~2950 psig. Upper course measurements attempted on V9, V10, V27, V28, V25, V26, V24, V21 and V22 as these vessels allowed some access around full circumference using two man-lifts (approximately 4 hours to complete work). Note that vessel V23 had been removed previously allowing better access to the surrounding vessels than would otherwise have been available (see Figure 1).

November 26, 2019: Pi-tape measurements repeated with the vessels vented to 0 psig (19 lower course and 9 upper course) (approximately 4.5 hours to complete work).

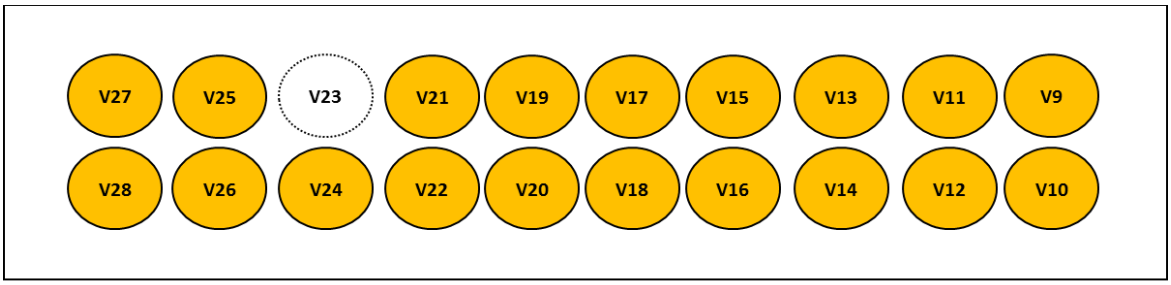


Figure 1. Configuration of WTA Hydrogen Bottles

Note: V23 was removed from the bottle bank in 2017 to be used in an Acoustic Emission capability demonstration project. V23 had been out of service since the 1990s due to an AE indication identified during inspection and certification.

The basic procedure used to take the pi-tape measurements for each vessel is as follows:

1) A dry run was performed at ground level to determine how many personnel were required to extend the pi-tape around the full circumference of the vessel and hold it flat and square as necessary to get an accurate and repeatable measurement. This dry run indicated that a minimum of four (4) personnel were necessary to properly deploy the pi-tape on vessels of this diameter.

2) The pi-tape was placed around the circumference of each shell course at approximately the mid-point between the head-to-shell and shell-to-shell weld avoiding any particularly rough surface areas. With one person pulling on the ends to place tension on the pi-tape, the other three personnel would slightly move the edges of the pi-tape up and down to ensure it was sitting square to the vessel axis and flat against the vessel surface. The diameter measurement was recorded and a marker was used at multiple circumferential locations to mark the specific location of the pi-tape. Once a measurement was obtained and recorded, the tape would be relaxed and the process repeated to ensure a consistent diameter reading was obtained. Deviations of a few thousandths of an inch were regularly observed between the two readings and deemed acceptable.

a) In general, having a second person read the pi-tape would be preferable to avoid human error in reading the scale, however, accessibility difficulties and tight quarters with two personnel working inside the man-lift basket did not facilitate having two different personnel read the scale. The alternative in this case was to relax the pi-tape and then take the pi-tape measurement again. Repeatable measurements would help ensure that there was no error in reading the scale and would indicate the pi-tape was indeed flat and square during the first reading.

b) The process of marking the vessel wall to indicate the location of the pi-tape was as follows (see Photo 3): The mid-point between head-to-shell and shell-to-shell weld was located and marked with an elongated plus sign. The pi-tape was then pulled around the vessel and settled into a stable location within 2-3 inches (+/-) of the mid-point. The tape location was marked with parallel lines above and below the tape at multiple locations around the circumference of the vessel. An arrow was also drawn on the vessel pointing to the location where the tape reading was taken (i.e., where the pi-tape scale is located when reading the measurement) taking care to locate this in a region of smooth flat surface away from any significant surface irregularity (e.g., longitudinal welds, paint runs, foreign matter on vessel wall).

3) Photos of the pi-tape readings were made in case there were questionable measurements upon further review of the data or the subsequent calculation results (see Photo 4).

4) An IR thermometer was used to measure the vessel wall temperature (although the layer gap efficiency calculation does not require wall temperature as an input).

5) Steps 2-4 were repeated once the vessels were vented to 0 psig. For these measurements, the marks made previously on each vessel (step 2b) were used to position the pi-tape thereby ensuring that measurements for the pressurized and unpressurized states were made at the same location.



Photo 3. Marking the Vessel Wall to Indicate Pi-Tape Placement

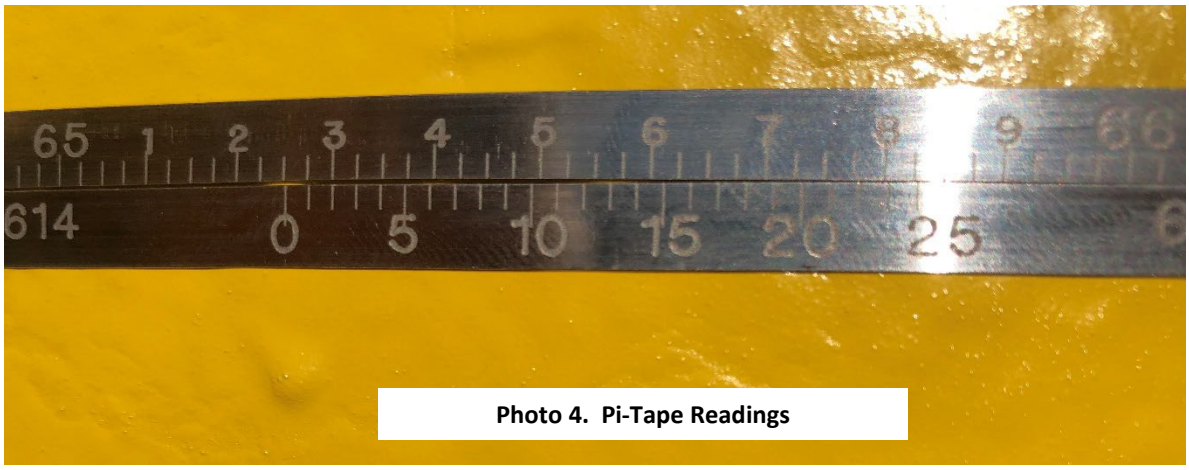


Photo 4. Pi-Tape Readings

Pi-Tape Data Obtained from WTA Hydrogen Vessels

	High Pressure Readings				Low Pressure Readings				
Vessel Number	**Vessel Pressure (psig)**	**Vessel Wall Temp (F)**	**Pi-Tape Reading #1**	**Pi-Tape Reading #2**	**Vessel Pressure (psig)**	**Vessel Wall Temp (F)**	**Pi-Tape Reading #1**	**Pi-Tape Reading #2**	**Comments/Notes**
V9	2950	36	64.729	64.729	0	61.7	64.696	64.695	
V9 Upper	2950	52	64.74	64.74	0	36.3	64.712	64.709	
V10	2950	43	64.663	64.663	0	39.9	64.619	64.619	
V10 Upper	2950	58	64.75	64.745	0	39.7	64.708	64.71	
V11	2950	37	65.2	65.2	0	46.4	65.17	65.173	
V12	2950	50	64.795	64.789	0	39.1	64.745	64.75	
V13	2950	35	64.698	64.697	0	46	64.665	64.664	
V14	2950	51	64.795	64.793	0	39.8	64.75	64.75	
V15	2950	40	64.707	64.705	0	46.7	64.675	64.673	
V16	2950	53	64.694	64.694	0	42.3	64.65	64.65	
V17	2950	38	64.67	64.669	0	46.9	64.626	64.629	
V18	2950	44	65.231	65.231	0	42.3	65.183	65.184	
V19	2950	33	64.716	64.715	0	36.6	64.7	64.695	High-pressure measurements believed to be in error--should be 64.726 and 64.725 based on photo of pi-tape reading
V20	2950	44	64.76	64.76	0	45.1	64.716	64.716	
V21	2950	39	64.637	64.637	0	32.4	64.607	64.6	
V21 Upper	2950	49	64.668	64.668	0	32.9	64.616	64.614	Measurement not believed to be accurate which may be explained by the vessel location in the bottle bank and resulting difficult access for maintaining pi-tape flat and square against vessel wall
V22	2950	41	64.71	64.71	0	42.6	64.669	64.665	
V22 Upper	2950	48	64.691	64.691	0	55.2	64.65	64.65	
V24	2950	49	64.675	64.675	0	58.4	64.639	64.635	
V24 Upper	2950	47	64.636	64.635	0	48.2	64.595	64.596	
V25	2950	46	64.768	64.768	0	38.3	64.72	64.725	
V25 Upper	2950	51	64.745	64.745	0	41	64.732	64.732	Measurement not believed to be accurate which may be explained by the vessel location in the bottle bank and resulting difficult access for maintaining pi-tape flat and square against vessel wall
V26	2950	48	65.25	65.25	0	52.7	65.212	65.211	
V26 Upper	2950	51	65.321	65.325	0	46.4	65.28	65.277	
V27	2950	38	64.67	64.67	0	43.4	64.625	64.626	
V27 Upper	2950	51.4	64.652	64.65	0	40.5	64.613	64.613	
V28	2950	49	64.765	64.765	0	48.6	64.73	64.728	
V28 Upper	2950	52.5	64.755	64.755	0	49.6	64.715	64.712	
Note: "Upper" refers to upper shell course measurement									

Appendix T: Test on Vessel V0023 MISTRAS Group AE Measurements & Analysis, September 13, 2016

Test on Vessel V0023, September 13, 2016

MISTRAS Group AE Measurements and Analysis

Report to

Jacobs Engineering / NASA at MSFC

by

Dr. Adrian. A. Pollock, MISTRAS Group

Second Submission, October 21, 2016

A Deliverable Submitted under Jacobs PO # 16N0471

TABLE OF CONTENTS

1. Background 1
2. Test 2
3. Post-Test Activities 3
4. Data Analysis 4
   - 4.1 Outside Information; Stages of Analysis 4
   - 4.2 Stage 1: Preliminary Analysis - Transcript from On-Site Report (9/16) 5
   - 4.3 Stage 2: Adjusted Location – Reported 9/19 7
   - 4.4 Stage 3: Additional (MAE) Analysis of Linear Cluster – Current Report 9
     - 4.4.1 Illustrative Waveforms, Waveform Interpretation and Source Discrimination 9
     - 4.4.2 Calculating Source Locations using a Lowered Threshold 10
     - 4.4.3 Calculating Source Locations using a Specific Mode 10
     - 4.4.4 Estimation of Source-Sensor Distance using MAE; Dispersion Curves 11
     - 4.4.5 Comparison between Measured and Theoretical Waveforms 12
     - 4.4.6 Wave Propagating as in a Single Layer 13
   - 4.5 Discussion 16
5. Summary and Conclusions; Addendum 17

TABLE OF FIGURES

Fig. 1 Vessel V0023 in Test Position 1
Fig. 2 Bank from which V0023 Came 1
Fig. 3 File pf1: All Data 6
Fig. 4 File pf2: Area of Interest Selected 6
Fig. 5 Amplitude > 50dB Selected 6
Fig. 6 Expanded View 6
Fig. 7 Waveforms from Three Events, All with Channel Hit Sequence 1-4-3 9
Fig. 8 Cluster Processed at 10,700 ft/s after Adjusting Hit Timings to F-wave Arrivals 11
Fig. 9 Dispersion Curves (Group Velocity, m/s vs Frequency, MHz) for a 0.277” Steel Plate 12
Fig. 10 Signal from Channel 1, Event at 4973 s. 13
Fig. 11 Theoretical Out-of-Plane Surface Movement for 55.3” Source-Sensor Distance 13
Fig. 12 Axial Position of Events in Cluster, Calculated Two Different Ways 15

ABSTRACT

This report describes MISTRAS participation in the hydrotest with AE monitoring, that took place on September 13, 2016 on multilayer vessel V0023 at MSFC Huntsville.

NASA's total test program for this vessel included pi-tape measurements, radiographic testing (RT) and destructive testing in an area thought to contain a significant AE source that had been very active in a test in 1983. As a result of this high-level AE, the vessel had been removed from service. Now, it became a testbed. MISTRAS participation was limited to acoustic emission (AE) testing. For this component of the program, we were assigned some oversight responsibilities; and we also brought to site eight channels of our latest-generation AE equipment, that is suited for both conventional feature-based AE and for the newer technology of Modal Acoustic Emission (MAE). Most of this report deals with the results obtained with this latest-generation equipment, especially some applications of MAE technology.

On site, high priority was assigned to source location in order to give maximum support to the RT measurements that were scheduled to begin immediately after the AE pressurization activities were completed. However, time was also devoted to wave propagation measurements (not reported here), taking advantage of the ready access to this vessel and to the opportunity to record the effect of water fill on acoustic wave propagation.

Source location results were delivered, a first version before leaving site, a second version (adjusted) on the next business day, and a third version (further refined) herein. An addendum in this second submission includes information on the double-cluster nature of the source, which had been observed but not documented or reported on in the first submission.

MAE results described in this report include source location refinements, source-sensor distance measurements used to validate the linear nature of the discovered source cluster, and the demonstration that wave propagation characteristics (at least for the discovered cluster) were like those of an unrestrained plate having the same thickness as a single layer of the multi-layer vessel.

It is recommended that close attention be paid, in the ongoing destructive tests and associated material examination, to the condition of any surfaces that could be involved in oxide breaking in tension, compression or shear; rubbing between vessel layers; rubbing between crack surfaces; and actual crack growth. Correlation between the visual testing results and the AE results can be of much value in the ongoing learning process of AE source discrimination in this particular kind of vessel.

1. Background

This test on vessel V0023 was undertaken as an unusual opportunity to develop techniques for requalifying the large number of multi-layer pressure vessels in service across numerous NASA locations. The unique feature of V0023 is that it was taken out of service in 1983 after an unusual finding during an acoustic emission inspection. Acoustic emission (AE) is a prime candidate for use as requalification technology for the multi-layer vessel inventory, but it is not considered at this time to be fully validated. So demonstrating AE capability was an important prospect for this test. Other kinds of NDT were also part of an integrated, multi-method agenda.

Vessel V-0023 is a multi-layered pressure vessel, one of a bank of 20 (Figs. 1, 2). Full details of the 1983 inspection are no longer accessible. However there is a written record of the overall requalification process undertaken on this bank of vessels, showing that this particular one did not pass inspection. There is also clear oral narrative to the effect that:

(a) The vessel became exceptionally active at 2750 psi (cf working pressure 3100 psi). The operator called a halt to the test at that pressure.
(b) The source of the activity was located, an estimated 10'-12' below the upper closure weld. It was close to a longitudinal weld. Signals were said to have classic crack-like characteristics. The source was assigned to the most severe category, "Grade A" (note that this terminology differs from today's), and the vessel was removed from service.
(c) Radiographic testing using a cobalt source was conducted in an effort to get more information about the apparent flaw, but did not reveal anything further. (Comments have been made in the Subteam that with such a large thickness of steel between RT source and film, radiographic contrast would necessarily have been limited.)
(d) A limited amount of further AE testing, for which no documentation is available, was performed in the few years after the vessel was removed from service. The maximum pressure attained is not known.
(e) These vessels were built in 1960 by A. O. Smith, to an allowable working pressure of 4400 psi and a hydrostatic test pressure of 7475 psi. After an extended period in hydrogen service they were downrated to a maximum allowable working pressure of 3345 psi on consideration of the deleterious effect of hydrogen on steel. The actual normal working pressure (of the vessels remaining in service) was 3100 psi.

Fig. 1 Vessel V0023 in Test Position



Fig. 2 Bank from which V0023 Came



MISTRAS was contracted primarily to supply consultation to the overall effort and to assist in the Level II recertification of Wyatt Hunter. Among other contributions to the test planning, we participated actively in the determination of the loading schedule and in technical discussions about crack growth, etc. Also as part of our engagement in this test, the opportunity was taken to monitor the supposed flaw area with our latest generation of AE equipment. This included broadband sensors suitable for modal acoustic emission MAE testing, and an 8 channel "Express" signal measurement and data storage system that has significantly enhanced performance compared with previous generations of AE hardware. MAE technology is distinct from the feature-based MONPAC technology that was delivered to Jacobs in 2012 along with their multi-channel DiSP (Digital Spartan) system.

2. Test

V0023 was pressurized with water on 2016, September 13 while being monitored for AE by three independent teams: Jacobs (Wyatt Hunter), Digital Wave (Steve Ziola and Brian Burks) and MISTRAS Group (Adrian Pollock). The test plan, developed by Jacobs in consultation with the NASA AE Sub-Team, was Document # PVS-16-009. This test plan includes important details of vessel construction, etc.

The 8-channel Express system was deployed to cover a 14 ft. axial length of the vessel centered on the reported location of the 1983 AE source. The Jacobs and Digital Wave systems had many more channels and were deployed to cover the entire vessel. Sensor configurations were somewhat different but in the end the sensor density was similar for all three systems.

The Jacobs system was installed during the week preceding the actual test. The Digital Wave and MISTRAS systems were installed and checked out using pencil lead breaks on Monday, September 12. On that same day after installation and checkout, two preliminary pressurizations were performed, to 1000 psi. These preliminary pressurizations served several purposes: (a) giving the team practice in coordination and communication around the pressurization and AE recording processes; (b) checking all systems including connection of the pressure signal to the NASA and MISTRAS AE systems; (c) familiarizing with the general AE behavior of this vessel and in particular to get preliminary data regarding AE from interaction between vessel layers, a major topic of interest in the effort to validate AE for applicability to this class of vessels.

The main test took place on Tuesday, September 13 following a pressure schedule that had been thoroughly discussed with in the AE Subteam. After much discussion it was finally agreed to have a series of rising loads with MONPAC-style pressure holds at 90%, 100% and 110% of the normal operating pressure of the vessel bank. Given a normal operating pressure of 3100 psi, these holds would be at 2790 psi, 3100 psi and 3430 psi. This would allow an AE assessment of the condition of the vessel with recommendations for follow-up action, had it been a candidate for continuing service. In fact, this vessel was not a candidate for continuing service because it was designated for radiographic inspection followed by destructive examination of the flaw area (assuming that the 1983 flaw could be found again). Nevertheless, a MONPAC-style test would provide an excellent cross-reference between MONPAC results and the results of other NDT and destructive examination, something that has not been

available for multi-layered vessels. Such a comparison is entirely in the spirit and style in which MONPAC procedure was developed.

At the end of the 90%, 100% and 110% holds the vessel was depressurized by 250 psi then immediately repressurized and on to the next hold. This was a supplement to the normal MONPAC pressurization schedule. It would not be considered for single-layered vessels but it might be valuable for multi-layer vessels because it could provide additional data for discriminating between inter-layer movement and any flaw growth that might be present.

In order to expedite the test it was agreed that the final (110%) hold would be curtailed to 10 minutes instead of the MONPAC-standard 30 minutes. After the final pressure hold (3410 psi) the pressure was raised towards the original allowable working pressure, 4400 psi. It was getting close to that, 4317 psi, when the pressurization system ran out of capacity. Depressurization was monitored, recording to a fresh data file, and the AE test was terminated.

3. Post-Test Activities

The immediate goal of the upcoming data analysis was to provide maximal information, in the time available, to assist the radiographic and destructive testing that was to be carried out in the very near future. Confirmation, precise location and any possible characterization of the 1983 source were of paramount interest.

But also, because of the easy access and the water filling and emptying that was going on, this test also provided an unusual opportunity to study other points of technical interest. It was desired also to take advantage of this opportunity. These points of interest, secondary in relation to the immediate goal but potentially useful in the longer term, were:

(a) wave propagation in the multi-layer construction, as a function of internal pressure that would tend to bring the layers into more intimate contact;

(b) wave propagation in the multi-layer construction, making use of the weepholes to get access to mid-thickness excitation points;

(c) wave propagation influences coming from water contents as opposed to gas contents.

Prospectively these points could be examined simultaneously with the broadband Express system and the resonant-sensor Jacobs DiSP system, allowing comparison of the two systems' performance and capabilities.

We therefore made wave propagation measurements during depressurization of the vessel after the main test, and then while the vessel was being drained, and finally after it was fully empty. These were performed with pencil lead break (PLB) and automatic sensor test (AST, an electronic pulsing technique) at convenient moments. The Express system and broadband sensors were then taken down and packaged for shipment. These activities took most of Wednesday September 14th and Thursday September 15th. After that, we turned to data analysis.

4. Data Analysis

4.1 Outside Information; Stages of Analysis

In this project, the communication of analysis information is being carefully controlled by Jacobs/NASA. This is being done in order to (a) optimally pursue the major purpose of validating/qualifying AE as an NDT method for these vessels; (a) maintain independence between the AE testing organizations and avoid “cross-contamination” of their results; (b) provide timely interchange of information with the other test activities, for mutual benefit and efficiency. As is typical with NDT, the use of multiple sources of information is very important for an operator trying to reach the best possible conclusions about the structure under test. Therefore in this section, a full account is given of the information that we were receiving from other sources along the way, and the stages in which the analysis was conducted and reported.

At the outset, we were guided by the information that the 1983 source was estimated to be 10’-12’ below the upper closure weld (see Test Plan). We therefore placed our eight sensors with four on either side of that 2’-wide band, in diametrically opposed pairs, with axial spacing 4’ 6” between pairs. The sensors thus covered a total spread of 13’ 6” along the axis of the vessel. During system checkout, Sensor 5 was found to have failed, probably because it was dropped during mounting. Since the overall layout was robust from the standpoint of source location capability, we proceeded with the remaining seven sensors, without altering their positions.

Circumferentially, we did not have advance information about the expected location of the 1983 source so our sensor placement was indifferent in that respect. We simply started at the twelve o’clock position, with the thought that there might be an opportunity to measure wave propagation measurements above and below the waterline, before the test when there would be was just a small air space left at the top of the vessel.

We did receive an indication of the expected circumferential location of the 1983 source during setup, when Wyatt Hunter gestured towards the upper quadrant on the east side of the vessel (as it lay), near the end, and said “that’s where the flaw is”.

Data analysis was conducted in three stages. All three were directed at locating the 1983 source as closely as possible, in support of the upcoming radiographic and destructive examination. In brief, the stages were as follows; further details of each are given below.

1. A preliminary analysis, from which the results were presented to Ed Johnson (NASA) late morning on Friday September 16th. The purpose of this was to provide results as soon as possible for guidance of the radiographic testing that was scheduled to begin that evening and continue through the following week.
2. An adjusted location result was furnished on the evening of Monday September 19th, after it was discovered that the preliminary analysis had been less than satisfactory and had been affected by confusion over sensor co-ordinates. A different data filtering approach was used and there was greater confidence in the results. A different cluster was reported, about 4’ distant from the location reported in stage (1).
3. A final analysis, to characterize more closely the source reported in (2), is reported here for the first time. This includes further use of modal acoustic emission (MAE) techniques. The decision to focus on this source alone, rather than spend time

comparing it with others, was based on three reasons. First was the good quality of the actual filtered data and general confidence in the path by which it had been obtained. Second was a remark in an e-mail from Ed Johnson on September 20, acknowledging receipt of (2): “Your data and Wyatt’s data appear to have close correlation”. Third was material discussed during the AE Subgroup telephone call on October 3. In this telephone call, Wyatt Hunter gave an oral report to the effect that he had identified a one foot square area, that it had been radiographed, and that a crack had been found. It was also reported that the crack appeared to be in one of the outer layers, and was close to or in a longitudinal weld seam. The length of the crack as observed by radiographic testing was 1½ inches, but it was possible that this was just part of a tight crack that was actually much longer. This material discussed on October 3 was very interesting; however the actual location reported by Wyatt Hunter was not disclosed.

4.2 Stage 1: Preliminary Analysis - Transcript from On-Site Report (9/16)

The pressure profile went well to plan (until 4317 psi) and the inflow and outflow of fluid did not generate significant background noise.

The MISTRAS broadband system detected 43,310 hits (detected signals on individual channels). This tally includes the center punch that was performed before pressurization to permit synchronization of data between the three AE systems. Within this set of 43,310 hits there were 1747 events. (Using this location software, any groups of 3-5 hits that occur within about one millisecond are treated as a single physical event in the structure, whose location is then calculated).

This preliminary analysis proceeded as follows:

(a) First, the center punch hits and the hits from seven low-pressure inter-layer slides or rubs were removed from the original file p.dta to produce file pf-1.dta. This left 1541 events as shown in Fig. 3.

(b) Looking at file pf-1.dta, several highly concentrated sources were noted as well as a diffuse area of activity in the general area of the suppose 1983 source.

(c) Given that the immediate goal was to support the upcoming radiograph and destructive testing, attention was focused on the diffuse area of activity in the general area of the 1983 source. A further filtered file was generated containing only events in the area 4<x<11, 18<y<27.5 (coordinates in feet using the agreed coordinate system). This reduced the tally of events from 1541 to 239 (Fig. 4, file pf2.dta).

(d) The hits in these events were reviewed using a duration/amplitude crossplot. Many of the lower-amplitude events appeared to have the nature of friction or corrosion product breaking, and were not considered to be such good candidates for accurate source location. The larger events, those with amplitudes in the range 50 to 75 dBae, were in the region of the crossplot associated with crack activity and were considered better candidates for source location. So a further filtered file was generated containing just these events. This reduced the tally of events from 239 to 78 (Fig. 5, pf3.dta).

(e) Modal AE technique was applied to the 78 events of file pf3. It was noted on the location plot that there was a tight cluster near the bottom of the selected area.

Looking at the waveforms associated with the locations in and around that cluster, it was noted that for the events in that cluster, all the hits were triggered by distinct F-wave arrivals, so the calculations would be valid (the F-wave velocity was being used). On the other hand, events that were located outside that cluster typically had one or more hits that were triggered at times other than the F-wave arrival. This is the classic nature of AE source location physics, that errors occur when calculations are based on ill-defined parts of the waveforms. In this case we had a mix of "good" and "bad" events from the standpoint of simple source location based on F-wave arrivals. There was a good quota of events coming from a tight cluster (+/- 2" as calculated), with confirmed F-wave timing. The F-wave velocity was confirmed by pencil lead break and it was verified that small changes did not significantly affect the calculated position for purposes of this reporting. This gave confidence in reporting the location of a source at (3'6", 18'9"), the very tight cluster near the bottom of the expanded view shown in Fig. 6.

Fig. 3 File pf1: All Data

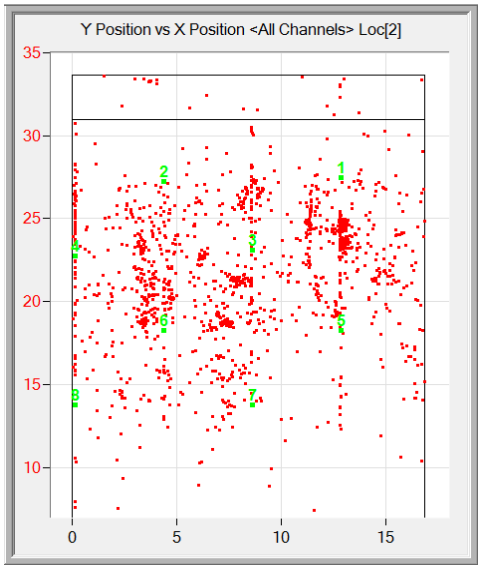


Fig. 4 File pf2: Area of Interest Selected

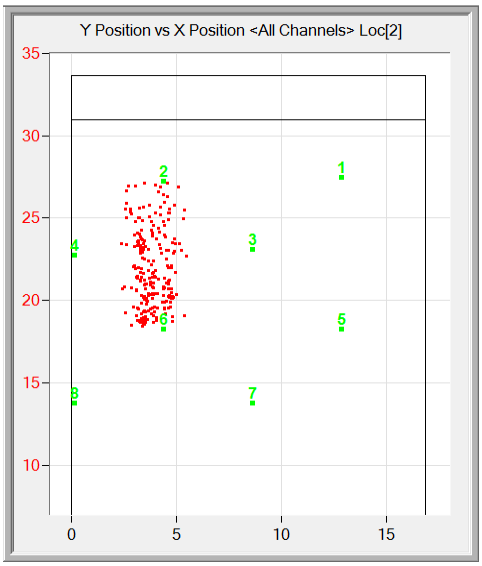


Fig. 5 Amplitude > 50dB Selected

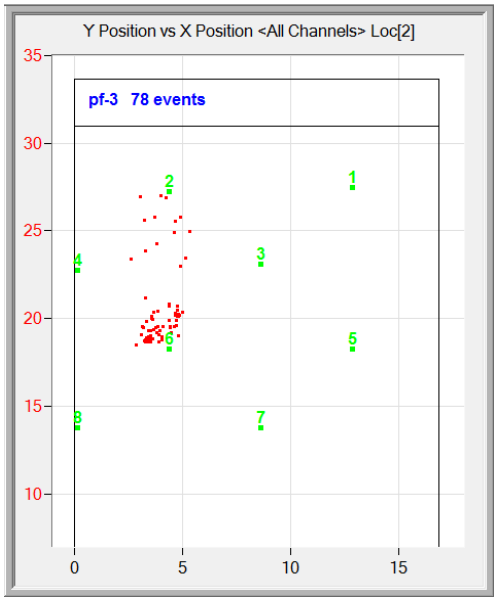
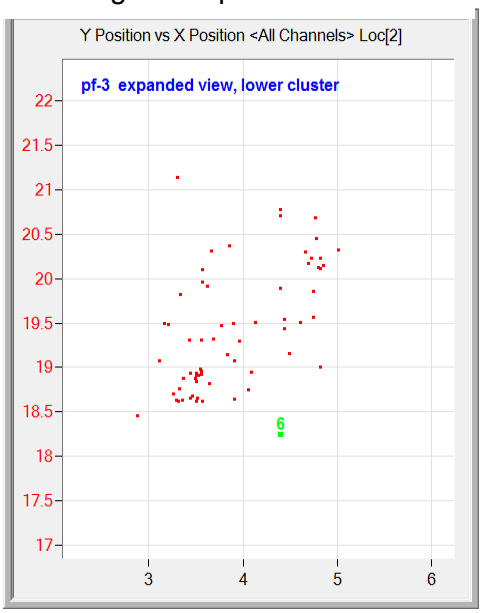


Fig. 6 Expanded View



Conclusions (On Site Preliminary Report)

We can therefore report the finding of this leading source at co-ordinates (3'6", 18'9"). That is the y-coordinate in the agreed reference frame; for measurement purposes, it is 12'2" from the upper closure weld.

As for precision and accuracy, the repeatability of the AE waveforms and the locations calculated from them is +/- 2" as noted above. Sensor positions were carefully measured and it can be argued that since the F-wave arrivals were well-defined, the effects of wall thickness are not significant. Therefore we are cautiously optimistic about the accuracy of the location we are reporting.

As for further characterization of this source, there is considerable E-wave content in many of the recorded waveforms and potentially this could reveal something about the through-wall depth and even the orientation of this apparent flaw. However this is a more complex analysis that cannot be attempted within the time available for filing this on-site, preliminary report.

4.3 Stage 2: Adjusted Location – Reported 9/19

The above-described analysis was checked and reconsidered on the afternoon of Monday September 19. Some shortcomings were identified (the analysis was hasty because of the time spend collecting attenuation data). First, there had been some confusion about sensor locations. Secondly, there were some misgivings on account of the substantial number of location clusters in Fig. 3. Traditional source location technology is prone to several kinds of error especially if the input data is poor quality (badly formed waveforms, falsely long time of arrival differences, etc.). It was suspected that some of these clusters were artefacts arising from low-quality datasets of this kind. It is also suspected that there may have been substantial noise from movement of the vessel on its supports, despite efforts to mitigate this by soft padding. A simple calculation shows that the vessel would have expanded by about 0.1" between timbers during the pressure rise, which could have created substantial AE.

Therefore for this second analysis, an altogether different approach was taken to the challenge of separating genuine emission (and genuine locations) from false ones. In a prior telephone conversation with the AE Subteam, we had described how in some other AE applications, not only in composites but also in metals, much reliance is placed on using AE data from hold periods. This data can be of higher quality than the data during rising or falling load, because noise sources tend to be less active (less structural movement), while structurally significant flaws will tend to continue to emit because of the stress concentrations they produce in their immediate neighborhood. These are

longstanding principles that have played their part in the AE testing of metal structures for 25 years and more.

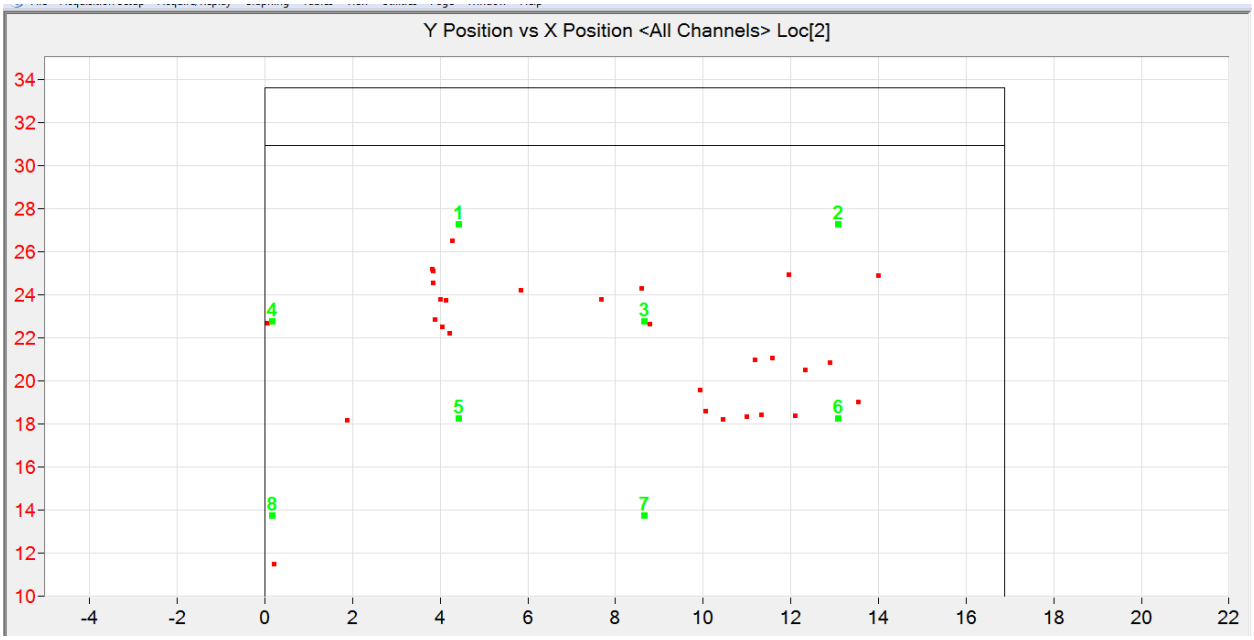
A data filter was accordingly applied to the test file, creating a new file that contained only the hits recorded during the hold periods. Another filter was applied to reduce the threshold from its as-recorded level of 30 dB, to 25 dB to improve the quality of the location analysis. Lowering the threshold moves the effective hit time closer to the first motion of the arriving wave, giving a better location result when used in conjunction with a high wave propagation velocity (in this case the E-wave velocity, 18,000 ft/s).

The result of limiting attention to AE during the pressure holds was twofold. First, there was a drastic reduction in the number of calculated event locations, from 1522 in the raw data file (Figure 3), to just 26. Secondly, there was a complete shift in the location emphasis. Instead of multiple sources competing for further analytical attention, there was a single cluster that was obviously of greater interest than anything else: an axially oriented string of 9 events, a third of the total population. This linear cluster lay in the general area indicated by Wyatt Hunter as containing the flaw (upper east quadrant of the vessel as it lay in its supports); and its axial orientation was suggestive of an extended source lying along a weld line.

This result was reported by e-mail to Ed Johnson in the early evening of Monday, September 19th, in the following manner:

Vessel V0023 – Recommended Places for Attention (Radiographic and Destructive Testing)

Below are the AE event locations found when focusing attention on the hold periods (90%, 100% and 110% of the nominal working pressure of this bank of vessels, 3100 psi).

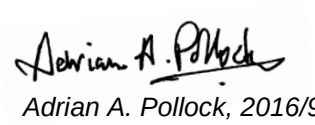


This data was obtained with post test analysis, 25dB adjusted threshold, 18000 ft/sec, 3-8 hits/event.

Cluster of main interest (x = 4, y = 22 to 25) is 4'0" down from the top dead center line, on the east side of the vessel (the side farther from the main bank of vessels) as it lies on the cribbing, and 6' to 9' axially from the upper head-to-cylindrical-section girth weld.

The question may be asked, whether any of the layers has a longitudinal seam weld corresponding to this linear AE indication.

This supersedes the information in the On Site (Preliminary) Report delivered to Ed Johnson on 2016/9/16, which was obtained by a different line of analysis and was also subject to some confusion over sensor co-ordinates.



Adrian A. Pollock, 2016/9/19

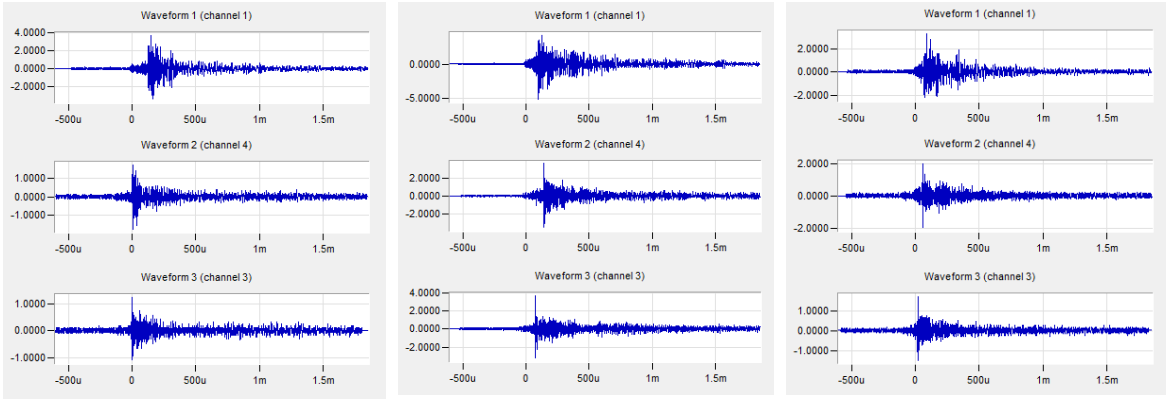
4.4 Stage 3: Additional (MAE) Analysis of Linear Cluster – Current Report

With the most significant source satisfactorily located, our main effort in further analysis was to see what further information could be gained about this source by the application of modal acoustic emission (MAE) techniques. MAE emphasizes the capture and examination of entire AE waveforms, in contrast with traditional AE which works with measured signal features, singly or in combination. MAE is capable of improving source location accuracy, and in favorable cases (especially in composite materials) identifying AE source mechanisms. Classical MAE is rooted in the recognition of extensional and flexural waves in the signal waveform. MAE also uses frequency spectra, although the use of frequency spectra is not unique to MAE.

4.4.1 Illustrative Waveforms, Waveform Interpretation and Source Discrimination

Variations between waveforms from the events in the cluster of interest are illustrated in Fig. 7. For easy comparison, events with the same channel hit sequence (1-4-3) were selected for this Figure. These events occurred at 5087 s, 6932 s and 7091 s (left to right). There are subtle but real patterns in waveform shape, comparing events and comparing channels. For example, the signals on Channel 3 have relatively low-amplitude precursors followed by very sharp main arrivals. These characteristics are more pronounced on Channel 3 than on the other channels.

Fig. 7 Waveforms from Three Events, All with Channel Hit Sequence 1-4-3



Signal waveforms are a concatenation of source function, wave propagation in the structure, sensor response and signal processing. The salient aspects of the source function are its time and frequency characteristics and the directionality of the energy release. The effect of wave propagation can be described as a Green's function which depends both on material properties and on the spatial relationship between source and sensor including source depth, source-sensor distance and plate thickness. The sensor has its characteristic frequency response which is also a function of the directionality of the impinging wave. These are the facts of how AE signal waveforms are developed.

Evidently the analysis and interpretation of AE waveforms is a difficult business. Formation of the waveform is complex and there are many possible analytical approaches. It might be said that the objective of "source discrimination" is to discriminate between the effects of the concatenating factors and thereby produce useful conclusions about the actual AE source. Use of broadband sensors is a very important step towards this objective.

In Figure 7, scanning from top to bottom we see the effects of wave propagation, the same source event being detected at different sensors. Scanning from left to right, the differences between the three sets of waveforms could be due to differences either in source function (time, frequency, directionality characteristics), or in source location giving rise to different Green's functions.

4.4.2 Calculating Source Locations using a Lowered Threshold

A well-known limitation of traditional Δt-based source location is that it is subject to the vagaries of the timing of the threshold crossing. Calculations based on first threshold crossing are often in error insofar as the threshold crossing can occur at any time between first motion and signal peak. The arbitrary, amplitude-dependent nature of this timing process leads to scatter and error in the computed locations. One way of describing this problem is to say that the wave velocity is ill-defined.

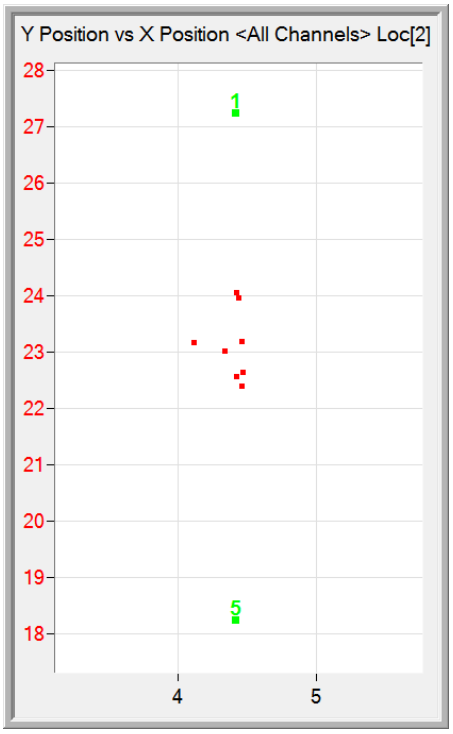
A simple way to come up with a better-defined velocity is to use an AEwin utility to lower the effective threshold, so that the calculations can be made from times closer to the actual first motion in the arriving wave. A high velocity corresponding to the fastest wave mode is then used in the source location calculation. This is the approach used to generate the 9/19/2016 report to Ed Johnson, see page 8 above.

4.4.3 Calculating Source Locations using a Specific Mode

At the next level of technical advancement, the threshold crossing is dispensed with altogether. Instead of timing from a threshold crossing, signals are timed by recognizing a specific feature in the waveform that can be recognized in terms of wave mode theory. In the case of this cluster, having only 9 events to deal with, it was not burdensome to examine their waveforms individually. It was found that about 90% of them had a well-defined F-wave arrival. The AEwin software has a feature that allows hit times to be adjusted by hand to match, precisely, recognized features such as these F-wave arrivals. This was done by with the help of a cursor moved along the waveforms. Source locations were then recalculated using these operator-

selected hit times in conjunction with a well-established velocity for the F-wave arrival in steel, 10,700 ft/s. The result is shown in Fig. 8.

Fig. 8 Cluster Processed at 10,700 ft/s after Adjusting Hit Timings to F-wave Arrivals



Comparing Fig. 8 with the cluster position reported on September 19 (page 8), there are two differences:

- In the x-direction (circumferential), Fig. 8 shows the cluster 6” further round from the zero reference line.
- In the y-direction (axial), Fig. 8 shows a significant reduction in spread, from 36” to 20”.

4.4.4 Estimation of Source-Sensor Distance using MAE; Dispersion Curves

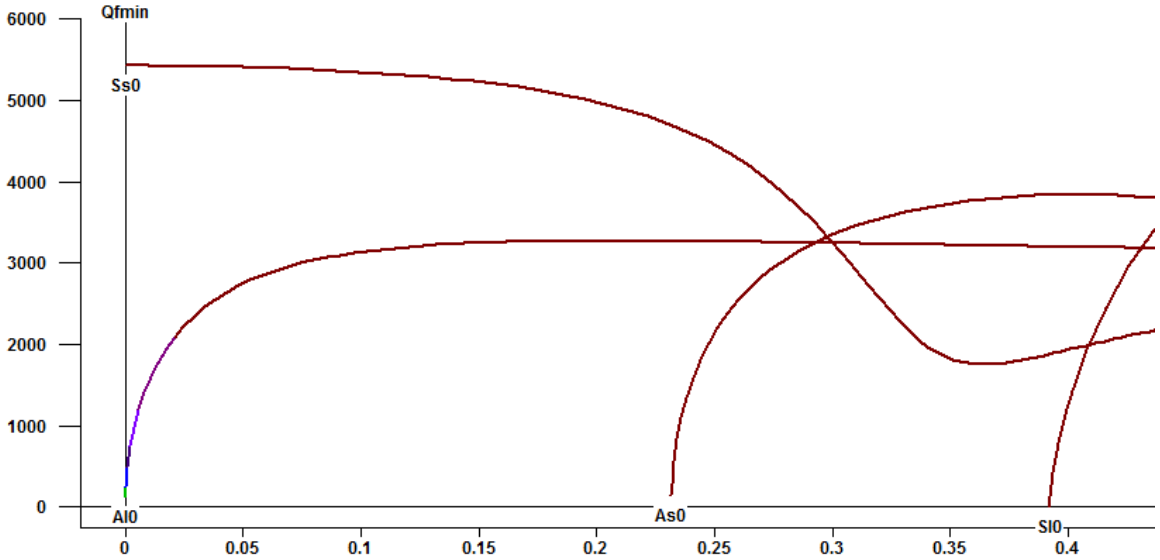
The apparent spread of these locations along the y-axis is about 18 inches. This raises the interesting question whether the source is truly extended like that, perhaps along a weld, or whether the axial alignment of the indication is due to wave propagation, signal processing, computational or other non-relevant factors.

To address this question, modal analysis approach can be taken to the next level. An attractive feature of MAE technology is the ability to determine source-sensor distance (SSD) from a single waveform. This is done by recognizing two or more modes in the waveform, measuring the difference between their arrival times, and combining those time differences with the known mode velocities to find the SSD.

Dispersion curves for a steel plate are shown in Fig. 9. The y- aspect of these curves depends only on material properties, while the x-aspect scales with the plate thickness. These curves are calculated for a typical steel, having a plate of thickness 0.277” (7.04 mm), the nominal

thickness of a single layer according to the A. O. Smith vessel drawing. These curves are calculated by a part of the PERFPAC software suite known as PlotRLQ

Fig. 9 Dispersion Curves (Group Velocity, m/s vs Frequency, MHz) for a 0.277" Steel Plate



According to these curves, the first-arriving modes in the 50-400 kHz frequency range will be s_0, a_0 and a_1. These modes can indeed be discerned in the waveforms from the events of the cluster of interest, with varying degrees of clarity (see Fig. 7). The a_0 mode arrival (aka the F wave) showed high amplitude and a sharp onset identifying its arrival time. The a_1 mode arrived several tens of microseconds earlier than the F-wave. Its amplitude was much less, but it had a sharp onset. It was characterized by its high frequency content which made it relatively easy to recognize. The s_0 mode (E-wave) was the fastest travelling part of the total AE wave and created the first motion in the frequency range we are monitoring.

4.4.5 Comparison between Measured and Theoretical Waveforms

An additional waveform is shown on expanded scale in Fig. 10. This signal was selected as showing the best modal clarity of all the 27 waveforms from the 9 events in the cluster of interest. This was the signal on Channel 1 from the event at 4793 s. The three modes are nicely shown arriving one after another.

The program that generated the dispersion curves (Fig. 9) can also compute the theoretical surface movement for a specified source-sensor distance. This is another capability of the PERFPAC software suite. Inputs to this computation also include the source moment tensor, depth in the material etc. A goal of PERFPAC is source discrimination by matching of measured and theoretical waveforms. Fig. 11 shows a theoretically generated waveform that can be compared with Fig. 10. The source moment tensor has been adjusted to give the best attainable fit. The similarity between observed and theoretical waveforms is very good.

Fig. 10 Signal from Channel 1, Event at 4973 s.

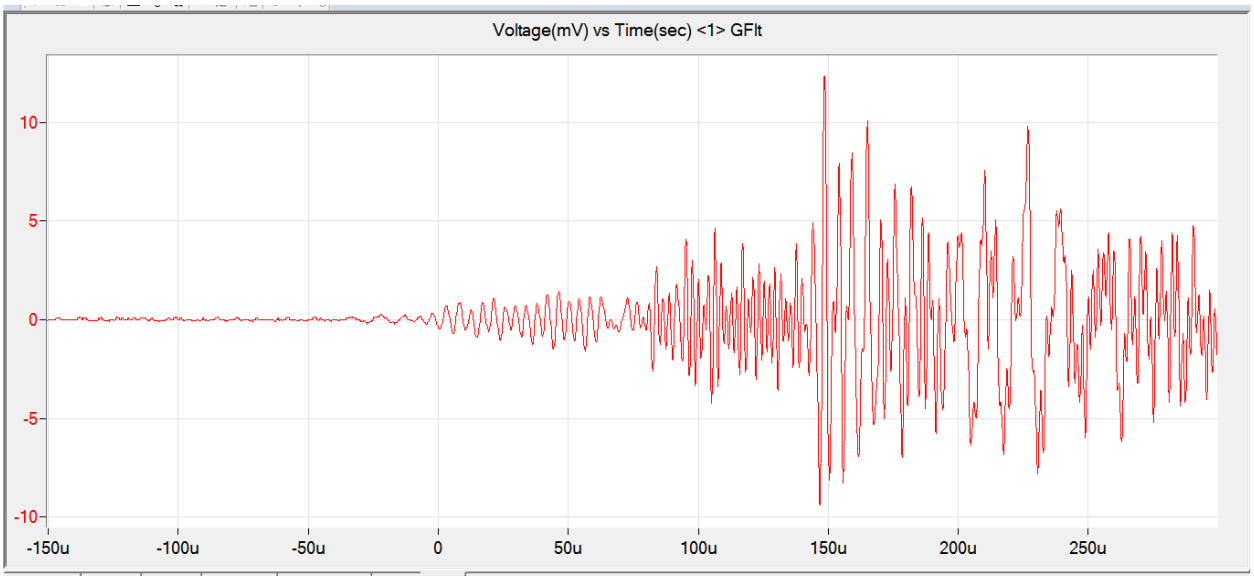
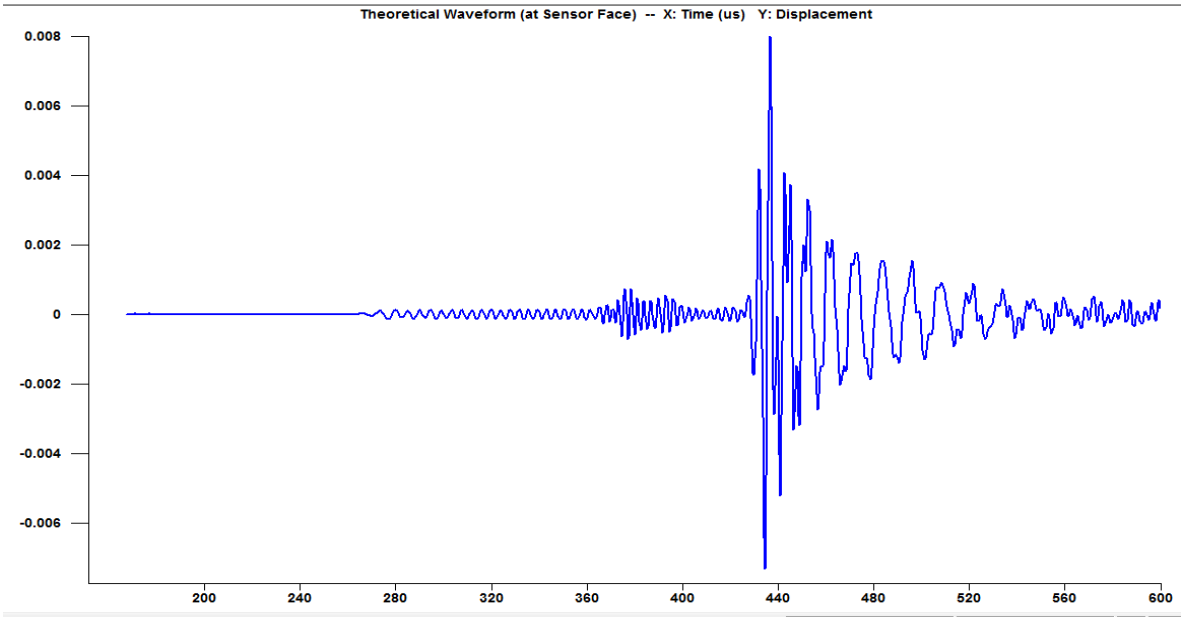


Fig. 11 Theoretical Out-of-Plane Surface Movement for 55.3” Source-Sensor Distance



4.4.6 Wave Propagating as in a Single Layer

An important question, to which there seemed to be no clear answer before this test, was how acoustic waves would propagate in the layered structure of this and similar vessels. There were only speculations about the questions such as:

(a) Would the layers be coupled together tightly enough for the vessel wall to behave like a monolithic piece of steel more than 3” thick? Or,

(b) Would the waves propagate within the individual layers in which they originated until they reached a circumferential weld, at which point they would likely diffract and spread the wave energy across the whole wall thickness? Or,

(c) Would there be some kind of cross-coupling of acoustic energy from layer to layer, in a way that would vary from spot to spot according to the effectiveness of the local coupling? If so, how would this depend on pressure and how would it work out in terms of Lamb wave content? For example, might there be regions where just two or three layers were coupled tightly enough together to act like monolithic plates with thicknesses equal to two or three layers?

These questions were addressed by examining the s_0 mode visible in the waves emitted by the source of interest. The s_0 mode has a highly dispersive region, in which the group velocity falls rapidly as the frequency increases. This is the region where the wavelength is comparable to the plate thickness. In steel, this occurs when the frequency-thickness product is around 1.6 to 2.0 mm.MHz. As the frequency-thickness product varies within this limited range, the velocity varies from 4700 m/s to 3600 m/s. This manifests as the so-called “E-wave” which gives the visual impression of a sinusoidal precursor, running in advance of the main (F-wave) arrival for a length of time that depends on the source-sensor distance. This is the precursor visible in the first part of the waveforms shown in Figs. 10 and 11.

Since the oscillation recognizable in the E-wave occurs at a specific, limited range of frequency-thickness product, it is possible by measuring its frequency to estimate the thickness of the plate. The frequency is inversely proportional to the thickness.

The natural AE waveform (Fig. 10) has 8 cycles in 33.3 μs, a frequency of 240 kHz. The theoretical waveform (Fig. 11), calculated for a single layer thickness, has 8 cycles in 31.3 μs, a frequency of 255 kHz. This good agreement between these numbers shows that as far as this signal is concerned, we are looking at the acoustic behavior of a single layer, not at two or more layers connected monolithically.

Not all the waveforms from the source of interest had the excellent modal clarity shown in Fig. 10. But since they all traversed essentially the same acoustic path, it is not likely that the differences were due to adjacent layers interfering with the wave propagation. It is more likely that the lack of modal clarity resulted from source functions that were not simple impulses, but had fine structure over a time frame of a few tens of microseconds. This smeared the acoustic response, making the distinction between the mode arrivals less clear.

4.4.7 Using MAE to Validate the Linear Nature of the Source

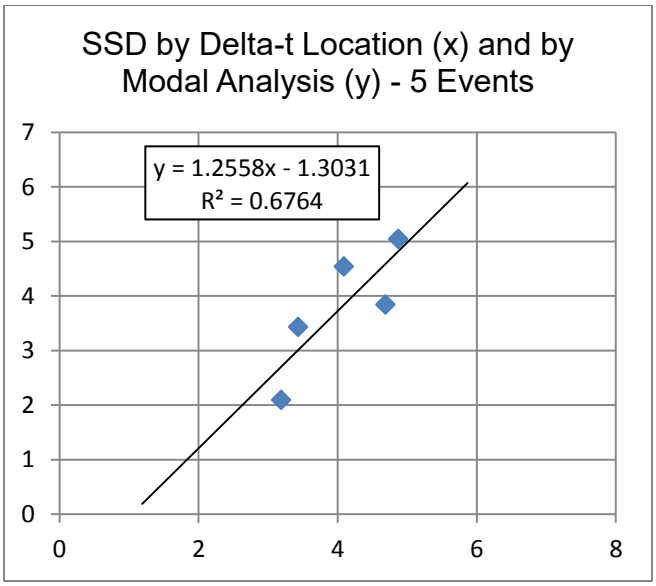
There is another useful technique in MAE, that allows source-sensor distance (SSD) to be calculated from a waveform received at a single sensor. If the waveform contains two recognizable modes whose arrival times can be measured, and whose velocities of propagation are known, it is straightforward to calculate the SSD. This approach (used also in seismology) is radically different from traditional Δt-based technique, in that the former gives useful information from a single channel while the latter necessarily requires the detections on more than one channel.

This second approach outlined above was used as an independent check on the interesting result obtained from 3-sensor Δt-based location, namely that the source appeared to be distributed in a linear manner along the axis of the vessel. Is this real or is it an accident of the location process and its remaining errors? Let us see whether the single-sensor, modal SSD determination confirms or disconfirms the apparent linear nature of this source.

SSD calculations, using two modes, are most commonly based on the time difference between the s_0 and a_0 arrivals. In this case however, because the arrival time of the s_0 mode was often not well defined, it was decided to use the a_0 and a_1 modes. The SSD's thus calculated would be compared with SSD's calculated from the Δt-based source locations. The SSD's to Sensor 1 were of primary interest since these related directly to the axial position of the source. Agreement between the two approaches would verify that the source really did extend over an 18 inch length along the axis of the vessel.

Five of the nine events had their mode arrivals well enough defined to make this comparison. The result of the comparison is shown in Fig. 12. There is a positive correlation. For the three events above the line, the two estimates of SSD agree with one another to within less than 6 inches. For the two events below the line, they agree to within less than 13 inches. Compare this with the 20-inch spread of the Δt-based SSD's and the 36-inch spread of the mode-based SSD's. This agreement between wave-based and Δt-based analysis is strong evidence that we are indeed dealing with an elongated source.

Fig. 12 Axial Position of Events in Cluster, Calculated Two Different Ways



4.5 Discussion

What could be the meaning of such an elongated source (at least 18” in the axial direction)? Two main explanations/rationalizations come to mind: crack, or friction. These are discussed below. It would be nice to pursue the AE analysis in a further effort to diagnose which was the case, but it is may be a better use of time resources to defer this until the results of the destructive examination are available. What we can do here is discuss a little how either of these mechanisms might lead to an elongated source cluster. These ideas can be used going forward, for the integration of the NDT results with the destructive test findings.

A. Crack

(1) This could be a long crack that was too tight to have been detected by RT over most of its length. It could have grown in the 1983 period and then stabilized due to redistribution of the load to neighboring layers. The oral reports that the 1983 AE emission was impressive and cracklike is compatible with relatively low toughness of the steel in this particular set of vessels, especially considering the fact that the vessel had been in hydrogen service.

(2) Pursuant to (1), the AE detected now in 2016 may not necessarily have been associated with actual extension of the crack. It may have been associated with breaking of oxide that had built up over the 30 year intervening period, bridging the two faying surfaces of the crack and/or bridging any two adjacent layers of the vessel. The supposed oxide bridges connections would be brittle, but weak. The oxide might get broken in tension, shear and/or compression depending on its location. There might for example be shear and/or compression between the outermost layer and the next one in. Breakage of oxide between these layers, or on the surfaces of a crack in the layer immediately below the outermost layers, could launch monolayer Lamb waves in the outermost layer to produce waveforms of the kind observed.

(3) Also pursuant to (1), we can propose an explanation why the crack did not start again at ~2750 psi to produce the high-intensity, high-activity AE that had caused the vessel to be removed from service in 1983. The proposed explanation is that all hydrogen had diffused out of the steel in the intervening 30 years and the material was left in a much tougher condition. With this factor in conjunction with the above-mentioned load redistribution into adjacent layers, the crack front did not advance notably in this 2016 test. The plastic zones at the crack tips, on the other hand, may have grown especially during the final pressure rise after all the pressure holds had been completed.

B. Inter-layer rubbing

(1) Rubbing along part of the length of an axially oriented seam weld would be consistent with the observed locations – if a seam weld is indeed present at this circumferential position. Rubbing along the line of the weld could easily happen if the weld bead was not completely ground down in this region. There may have been a prominence making early contact with the adjacent layer over the ~ 18 inches of the AE source. The inner layer would tend to expand more than the outer layer, to an extent determined in part by the rigidity of the girth welds. Local slippage would result from the overcoming of local constraints. Axial or hoop components, either could be considered.

(2) Because of this possibility, we recommend close visual examination of the weld line in the region of the AE source, for any indications of rubbing. This could be metal-to-metal, or oxide-enhanced or oxide-dominated.

5. Summary and Conclusions

1. During pressurization to 4317 psi the vessel produced a large but not overwhelming amount of AE. 41118 hits were recorded, and 1514 events were located using cylindrical location.
2. The priority on-site goal was to reactivate and locate the 1983 source, so that it could be examined with radiography and destructive tests. Three assessments of the 1983 source position were delivered, the first an on-site report submitted in advance of the radiographic testing, and the others coming after more time had been spent on the analysis. The successively identified source positions are shown in the following table:

Date Reported; Technical Approach	Circumferential Position (x)	Axial Position (y)
9/16/2016 Friday (on-site report); various data filters applied.	3'6"	Cluster, centered at 18'9" (corrected next business day)
9/19/2016 Monday (amendment); focus on AE during pressure holds. First threshold crossing after reducing threshold from 30 dB to 25 dB; s_0 mode velocity.	4'0"	Linear indication, extending 36" from 22'3" to 25'3" from "bottom" closure weld
10/19/2016 (this report): focus on AE during pressure holds. a_0 mode arrival picked by hand; a_0 mode velocity.	4'6"	Linear indication, extending 20" from 22'4" to 24'0" from "bottom" closure weld

3. Emission continued during the pressure holds. Those AE events are considered to have been the best quality data. Locations during the hold periods fell along a linear cluster running along the axis of the vessel, about 20 inches long (see table above).

4. Waveform synthesis and modal analysis (MAE) techniques proved their value in several ways:
   - 4.1 A captured AE waveform from the 1983 source agreed with a theoretical waveform computed for the same source-sensor distance and a plate of the same thickness as a single layer in this vessel. This indicated that over a distance of 4' from the 1983 source to an axially aligned sensor, wave propagation was occurring as if in a single layer of the vessel, without serious interruption by the adjoining layer(s).
   - 4.2 Examination of the apparent frequency content of the E-wave led to the same conclusion.
   - 4.3 Hit timing based on the arrival of the a_0 mode led to a substantially tighter cluster than hit timing based on first threshold crossings, even when the latter were improved by lowering the threshold in order to get closer to timing based on first motion.
   - 4.4 The linear nature of the source (see table above) was confirmed by calculating source-sensor distances (SSD's) using a_1-a_0 intermodal time differences. These SSD values correlated quite well with SSD values calculated from the Δt-based source locations.

5. As regards source discrimination (e.g. telling the difference between crack growth and friction), it is recommended to examine and document very carefully, after cutting up the vessel, the condition of any surfaces that could have been involved in rubbing, between vessel layers and/or between crack surfaces, oxidized or otherwise. It may be unusual, but from the standpoint of AE application to this class of vessels this may be no less important than normal fractographic examination of any crack(s) that may be found. Time being limited, it may be more practical to do any further AE analysis in the light of the destructive testing results, rather than trying to predict them.

ADDENDUM

The following remarks are added October 21st, 2016, after the October 19th version of this report had been submitted and reviewed by Ed Johnson. In a follow-up telephone conversation on October 21st, Mr. Johnson hinted that the correlation between our findings and Wyatt Hunter's might be less than complete, and wondered whether we might have anything to add. We mentioned that we had not made much of the fact that there some of the data displays indicated not one but two clusters, axially adjacent in the area of interest, not just one. Reviewing this after the end of the conversation, we could see what had happened. The path chosen on September 16th for removing noise was to concentrate on the emission during the pressure holds. The number of events during the pressure holds was small. It was enough to direct full attention to the linear source discussed in the body of this report, but it was not enough to show two distinct clusters within it. After interest turned to the capabilities of modal AE techniques, the double-cluster aspect of the source was not given any more attention.

More information on the double-cluster aspect of the source is given in this Addendum.

Fig. A1 is a straightforward source location display of the full set of test data, with minimal filtering to remove the initial center punch and the worst of the early scrapes. Fig. A2 shows events and energy scanning the clusters along the y-axis within a limited range of x. Their distinct nature is clear. Their peaks are at 23'1" and 24'4", falling within the range previously reported from closer analyses of the individual events detected during pressure holds.

Fig. A1 Locations (file p-1)

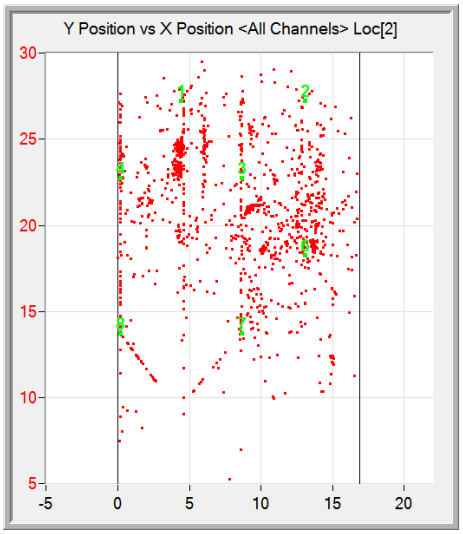
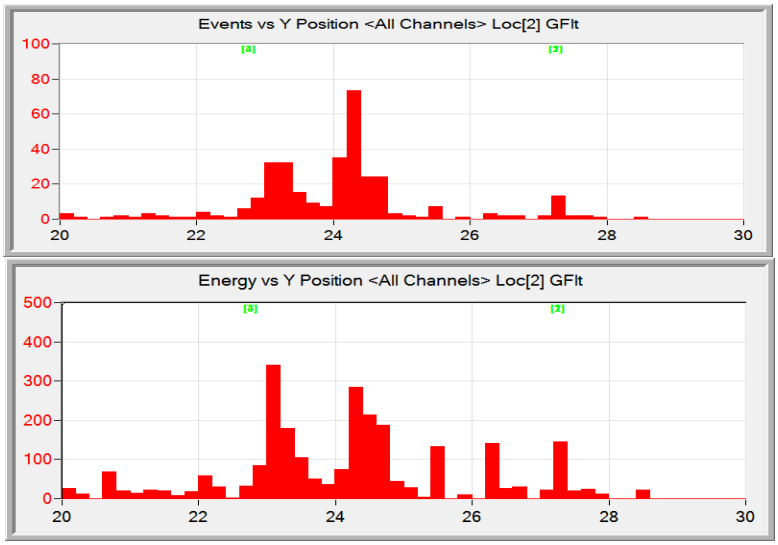


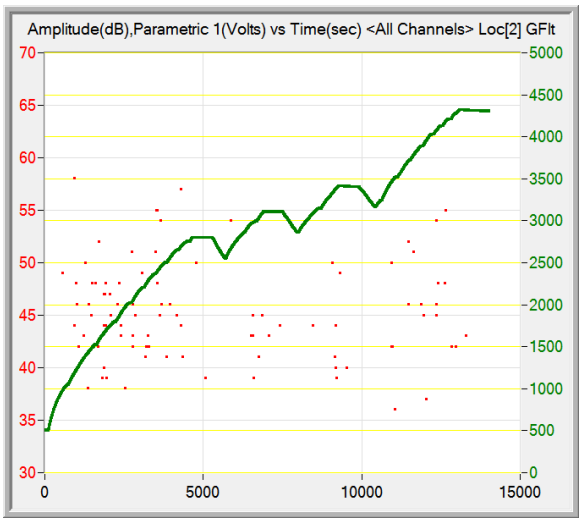
Fig. A2 Scanning Two Prominent Clusters along Y-Axis



Activity plots for the clusters behaved are shown in the graphs below. There is some difference in the activity patterns of the two clusters. The cluster nearer to the end of the vessel was substantially more active at low pressures, but the cluster farther from the end of the vessel became more active at higher pressures so at the end of the test, their total emitted energies were much the same. This can be seen in Figs. A3 and A4.

Fig. A3 First Hit Amplitudes vs Time for Two Clusters, along with Pressure

22.7 < y < 23.6



23.9 < y < 24.8

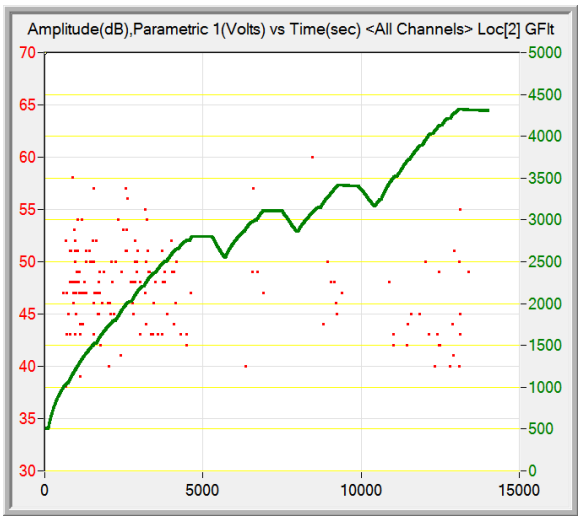
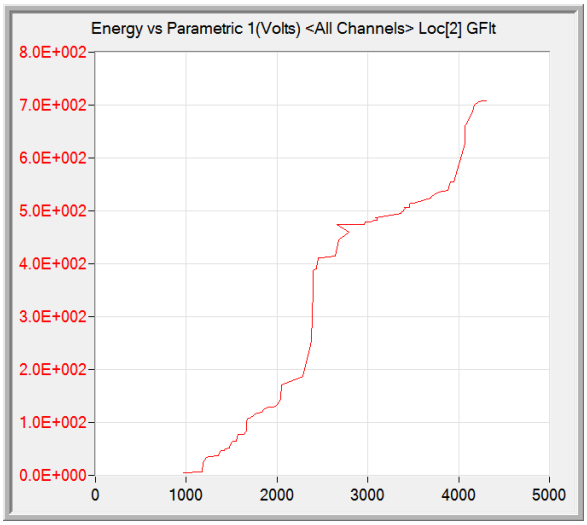
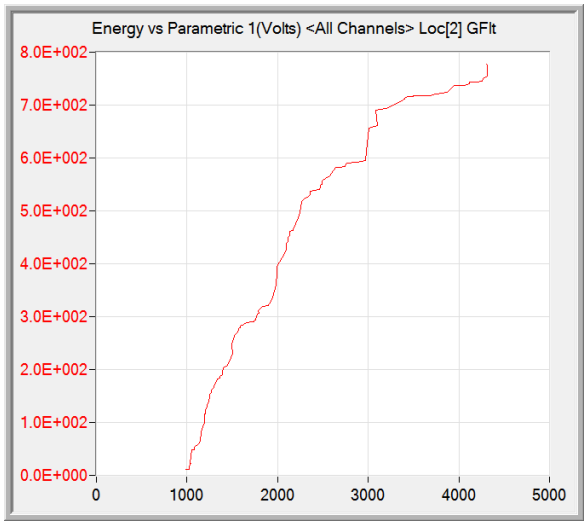


Fig. A4 First Hit Energy vs Time for Two Clusters

22.7 < y < 23.6

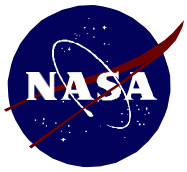


23.9 < y < 24.8



In conclusion, it seems that we had a linear source about 15” long, with most of the activity concentrated at its two ends. The end closer to the top of the vessel showed more of a growth type AE pattern, while the end closer to the vessel legs showed more of a stabilizing pattern.

Appendix U: Acoustic Emission Test Report for Vessel V0023, Report No. AE-V0023-2016



George C. Marshall Space Flight Center
Engineering & Science Services
& Skills Augmentation
Contract NNM12AA41C

Acoustic Emission Test Report for Vessel V0023



Report No.: AE-V0023-2016

Prepared by: Jacobs ESSSA Group

Claud Wyatt P. Hunter

September 13, 2016

ESSSA Group
Wyatt P. Hunter
Digitally signed by Claud Hunter (affiliate)
DN: c=US, o=U.S. Government, ou=NASA, ou=People, 0.9.2342.19200300.100.1.1=cwhunte2, cn=Claud Hunter (affiliate)
Date: 2016.10.06 08:33:04 -05'00'

JACOBS
ESSSA Group

Jacobs ESSSA Group
1500 Perimeter Parkway, Suite 400
Huntsville, AL 35806

TABLE OF CONTENTS

1. Summary 3

2. V0023 Test 4
2.1 Test Equipment 4
2.2 Instrument Set-up Parameters 4
2.3 System Performance Check 5
2.4 Sensor Positions 7
2.5 Test Procedure 10
2.5.1 Pre-Test Background Noise Check 10
2.6 Actual Loading Sequence 11
2.7 Test Data Acquisition 12
2.8 Data Quality Analysis 12
2.9 Analysis (time and time order filters only) 13
2.9.1 Cylinder (3D) Wide Band Sensors (WDI) Location Accuracy Verification 13
2.9.2 Cylinder (3D) Wide Band Sensors (WDI) Location Analysis results 14
2.9.3 WDI Source Location Evaluation 15
2.9.4 Cylinder (3D) Mid-Range Sensors (R15I) Location Verification 19
2.9.5 Cylinder (3D) Mid-Range Sensors (R15I) Location Analysis results 20
2.9.6 R15I Source Location Evaluation 21

3. Conclusion and Recommendation 23

APPENDIX I
VESSEL DOCUMENTATION AND GRAPHS

Vessel Manufacturers Data Report 26
Vessel Drawing 27
ASME Required Documentation 28
R15I Sensor versus WDI sensor data comparison 29
WDI primary source versus time and psi (pre-test pressure ramps and actual test) 30

1.0 Summary

In collaboration with the NASA Layered Pressure Vessel (LPV) Working Group – AE Sub-team, Jacobs ESSSA Group performed an Acoustic Emission (AE) test on layered pressure vessel V0023 on September 13, 2016. Vessel V0023 is an out-of-service LPV located at B4699-B in the West Test Area, Marshall Space Flight Center, Huntsville, AL. The vessel was removed from the vertical bottle battery of 20 identical vessels as shown in Photo 1 and then laid horizontal for test. Following the test and inspection process, the vessel will be dissected by the MSFC Material and Processes Laboratory for characterization of any substantial defects noted and for further material testing. The vessel was instrumented with 43 acoustic emission sensors, (36 R15I sensors and 7 broadband sensors) held in place with magnetic hold-downs. All 43 sensors were attached to a Physical Acoustics Corporation (PAC) DisP System and sensitivity checks were performed. Relevant crack-like signals were identified during the test and verified during post-test data analysis. Suspect areas of V0023 were marked in preparation for follow-up radiography and vessel sectioning.

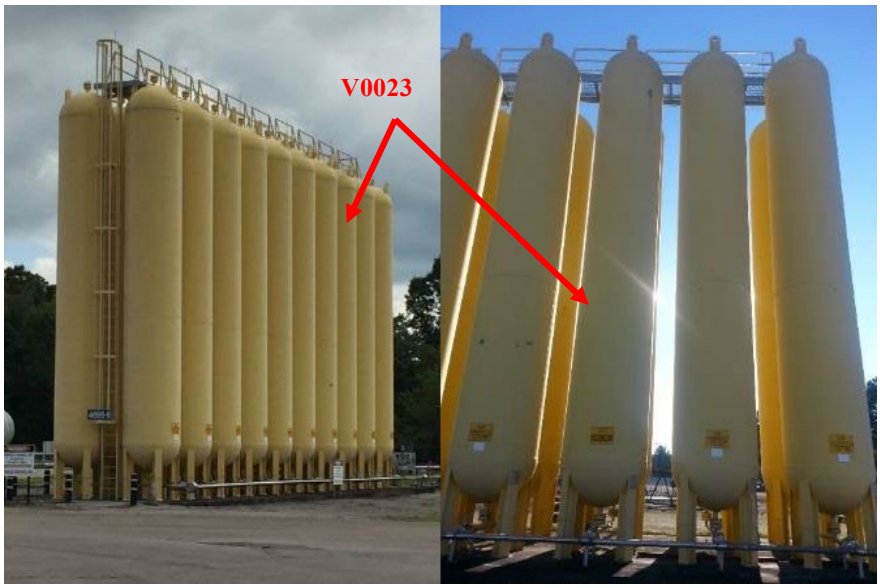


Photo 1 - West Test Area Bottle Bank Including V0023

2.0 V0023 Test

2.1 Test Equipment and Setup

AE INSTRUMENTATION MFR.:	PHYSICAL ACOUSTICS CORP. (PAC)
AE INSTRUMENTATION TYPE:	PAC DiSP System
AE EQUIPMENT CALIBRATION DUE:	August 31, 2017 Certificate No:006175
SENSOR TYPE:	R15I (150kHz)/WDI (broad band)
RESONANT FREQ.:	R15I (150kHz)/WDI (broad band)
PREAMP TYPE:	Integral to Sensor
FILTER:	R15I (100 - 400 kHz)/ WDI (20 kHz highpass)
SENSOR COUPLANT:	Silicon grease
SENSOR ATTACHMENT METHOD:	PAC Magnetic Hold-downs
TEST MEDIUM EMPLOYED:	Water
TEST MEDIUM TEMPERATURE:	Ambient
TEST PROCEDURE	V0023 Document# PVS-16-009

2.2 Instrument Set-Up Parameters

DETECTION THRESHOLD	50dB FIX determined during 2 1000 psig pressure ramps
PREAMP GAIN:	40dB
SENSOR TYPES:	R15I (36 sensors) and WDI (7 sensors)
INSTRUMENT GAIN:	23dB
REARM TIME/HLT	10000 us
HDT	2000 us
RISE TIME/ PDT	1000 us
Max Duration:	99 us
Waveform length	10k
Sample Rate	5 MSPS
Pre-Trigger	512

2.3 System Performance Check Note: Units are in decibels (dbAE.)

The pre-test amplitude readings for V0023 were higher than the average in-service vessel readings at MSFC.

Mean:	92	Minus	5	Plus:	5	System/Sensor Type	Avg. of 3 LB's for calibration
R15I sensors		Min:	87	Max:	97	*µDisP 56/R15I*	

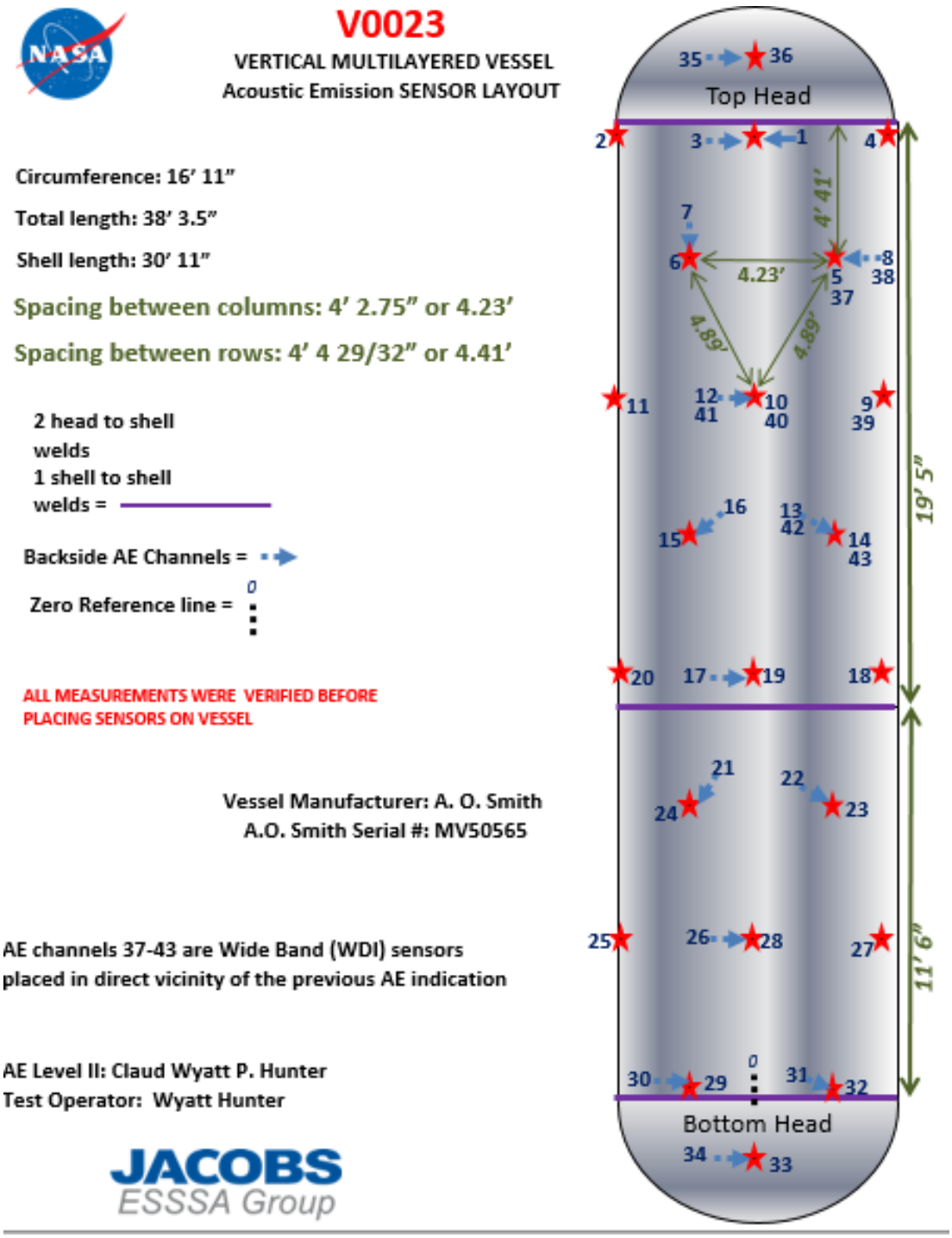
	North			
CH	A	B	C	Avg.
1	97	96	97	97
2	91	91	91	91
3	91	92	96	93
4	91	92	96	93
5	90	91	92	91
6	95	95	96	95.33333
7	93	93	94	93.33333
8	91	92	92	91.66667
9	89	88	90	89
10	96	96	96	96
11	91	96	91	92.66667
12	92	92	92	92
13	90	90	89	89.66667
14	95	97	95	95.66667
15	95	97	95	95.66667
16	95	96	97	96
17	90	89	88	89
18	92	91	91	91.33333
19	93	93	95	93.66667
20	96	95	97	96
21	91	92	91	91.33333
22	91	92	91	91.33333
23	91	92	92	91.66667
24	89	89	88	88.66667
25	92	95	93	93.33333
26	90	90	91	90.33333
27	92	95	96	94.33333
28	97	97	97	97
29	95	91	92	92.66667
30	91	91	91	91
31	89	89	89	89
32	91	92	92	91.66667
33	90	90	88	89.33333
34	89	89	91	89.66667
35	89	88	87	88
36	89	88	87	88

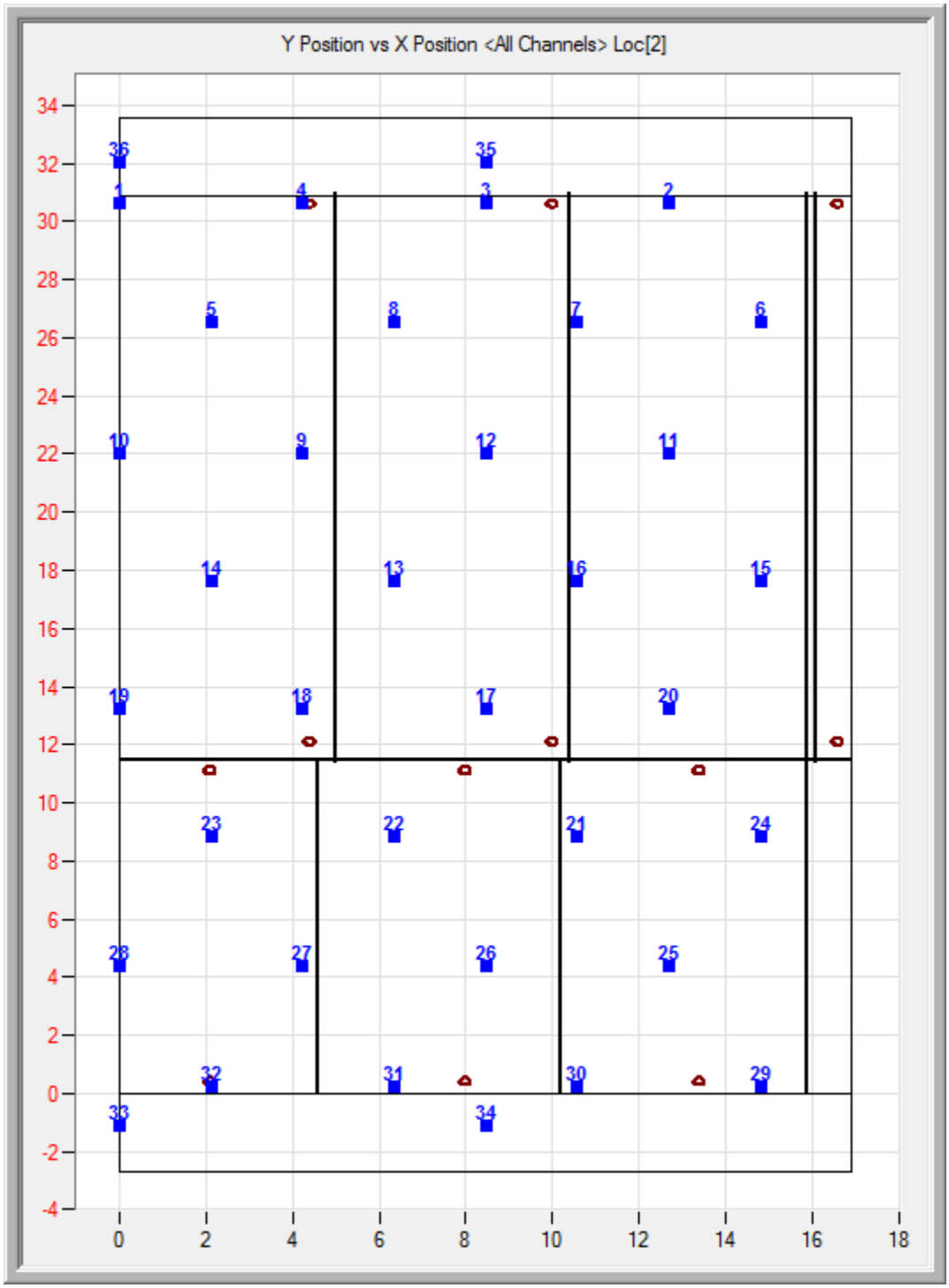
WDI sensors are less sensitive than R15I, lower amplitude readings were recorded for pre -test calibration. Every effort was made to increase amplitude readings prior to testing. V0023 pre-test WDI amplitude readings appear to be about average for WDI sensors.

Mean:	87	**Minus**	5	**Plus:**	5	**System/Sensor Type** **Avg. of 3 LB's for calibration**
WDI sensors		**Min:**	82	**Max:**	92	***DisP 56/WDI***

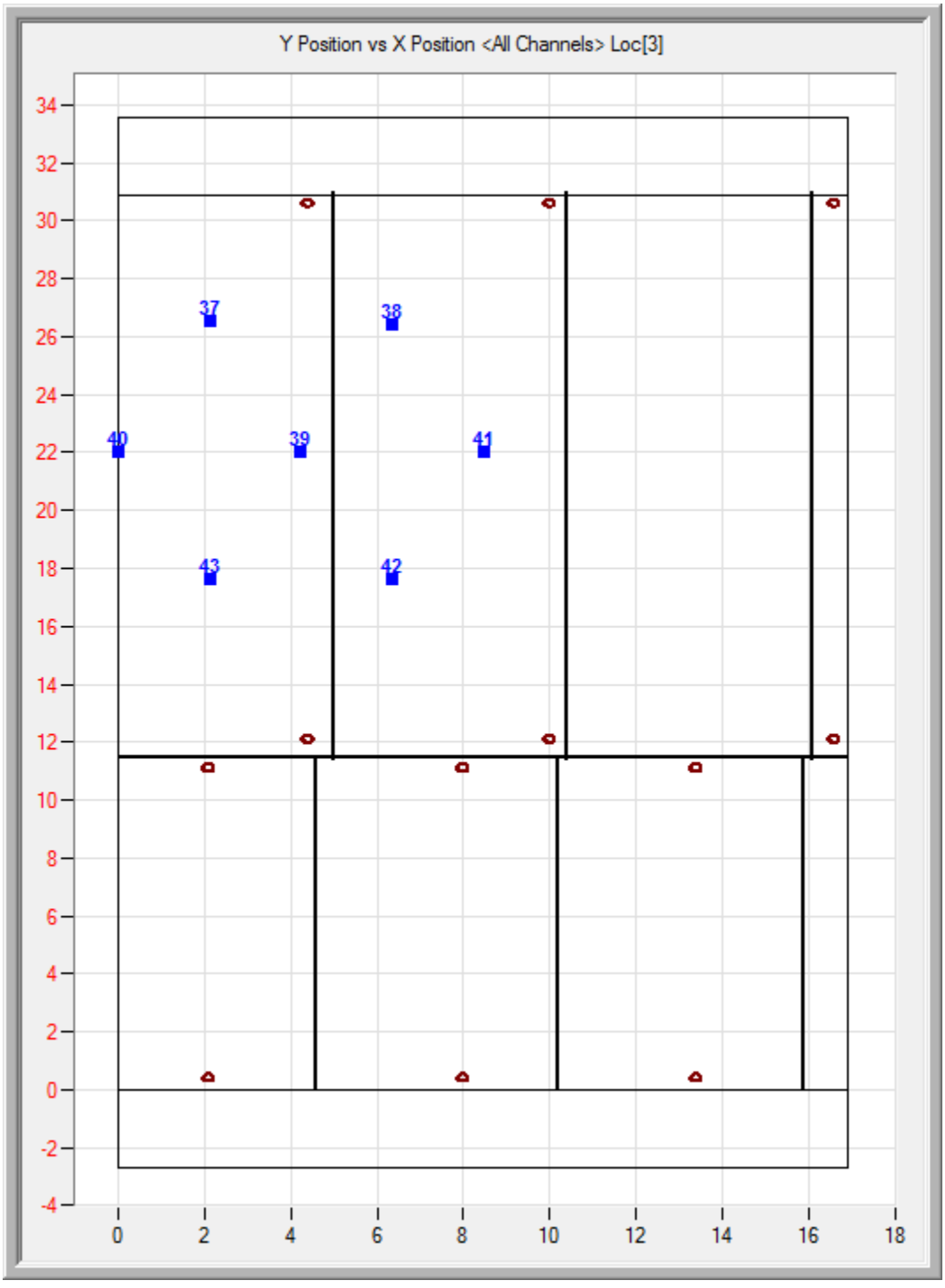
CH	North A	B	C	Avg.
37	91	88	87	89
38	85	85	86	85
39	87	89	89	88
40	91	86	88	88.33333
41	89	88	92	89.66667
42	89	87	86	87.33333
43	82	83	84	83

2.4 Sensor Positions





R15I Sensor Positions
(OD) Longitudinal Welds and Weep-Hole Locations Shown)



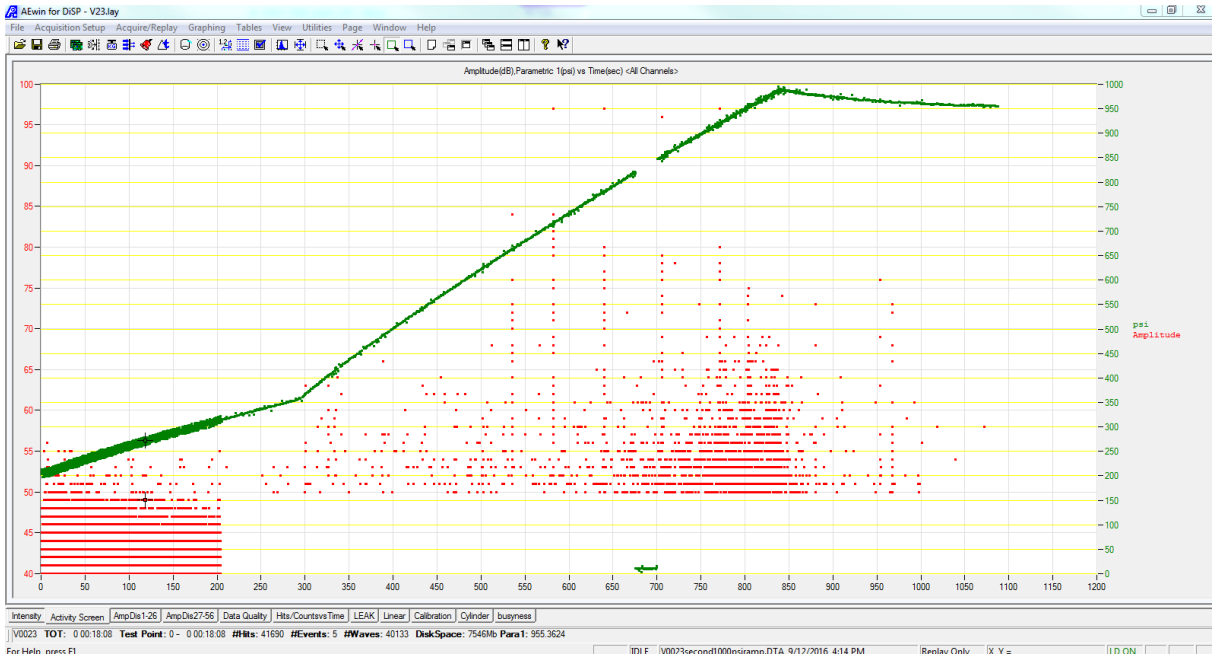
WDI Sensor Positions
(OD) Longitudinal Welds and Weep-Hole Locations Shown)

2.5 Test Procedure

The V0023 Document# PVS-16-009 test procedure, drafted by MSFC personnel and revised with input from the Agency AE Sub-team, provides the planned loading sequence (pressurization schedule) to be used for this test. The target pressurization rate was 1.5 psig/second. It should be noted that V0023 has been out of service since 1983 and disconnected from any pressure source since that time.

2.5.1 Pre-Test Background Noise Check

Two pressure cycles to 1000 psig were performed the day before the actual test to exercise the vessel and determine the level of extraneous background noise which could be anticipated the day of test. The background noise, which is presumed to be a combination of layer rubbing and/or corrosion between the layers of material, was very high during the first loading sequence to 1000 psig. During the second loading sequence, the layer rubbing and/or corrosion noise was not present at low pressure and the flow noise was easily identified, this allowed a 50 dbAE threshold selection to remove flow noise for both the R15I and WDI sensors. Such high levels of background noise could potentially mask relevant indications. Although ASME code requires the AE technician to minimize extraneous noise levels, the technician has no control over extraneous noise generated within the layers. This test was experimental (i.e., not a fitness-for-service evaluation) and the background noise was accepted and the test performed. The graph below demonstrates the flow noise being removed by raising the threshold from 40 to 50 dbAE during the 2nd ramp to 1000psi. (It should be noted that three data files were generated, two for the pre-test 1000 psig cycles, and one for the day of test.)



2.6 Actual Loading Sequence

The day-of-test loading sequence began at 500 psig as shown in the figure below. The initial pressurization of V0023 was slow (below target pressurization rate) until the ullage in V0023 was collapsed. The initial stage of pressurization also resulted in high extraneous noise levels. For this reason, a decision was made to pressurize V0023 to 500 psig to collapse the ullage, allow final leak checks to be performed at the vessel and then proceed with the pressurization and data recording.

SEQUENCE	PRESSURE (psi)	HOLD TIME (MIN)	COMMENTS
1	0-1000-0	0	Performed day before test
2	0-1000-0	0	
3	500-2790-2540	10	Recording started at 500 psig due to high extraneous noise level and slow initial pressurization
4	2540-3100-2850	10	
5	2850-3410-3160	10	
6	3160-4317	15	

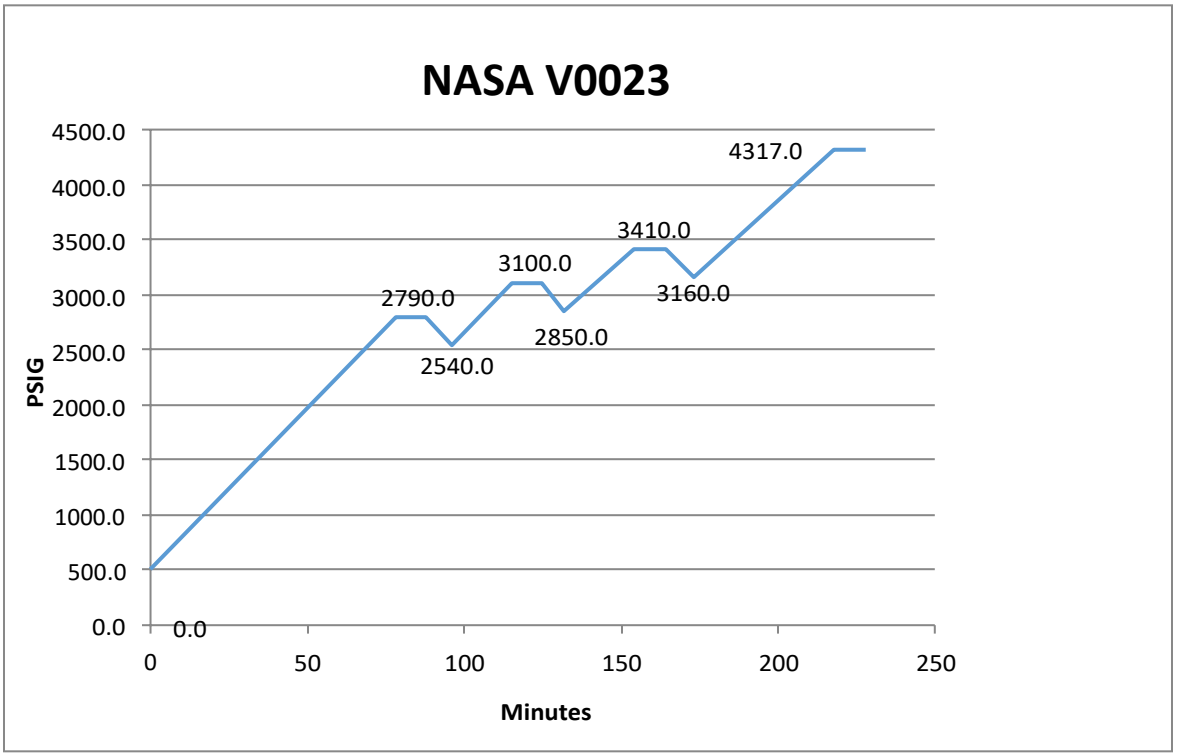
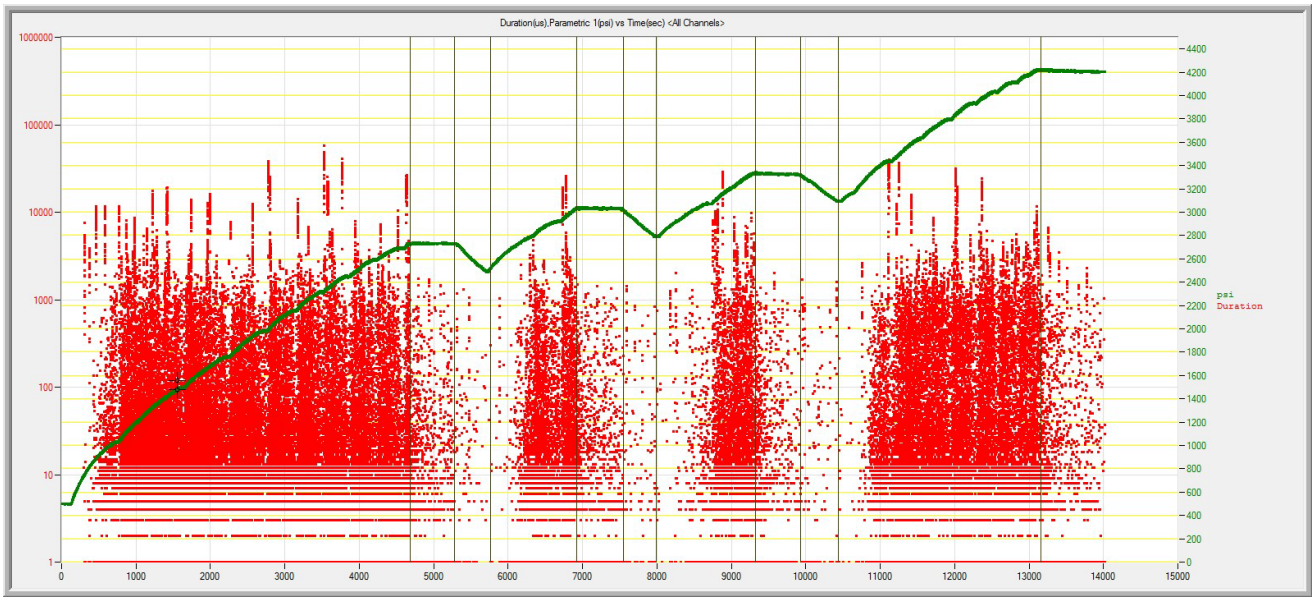


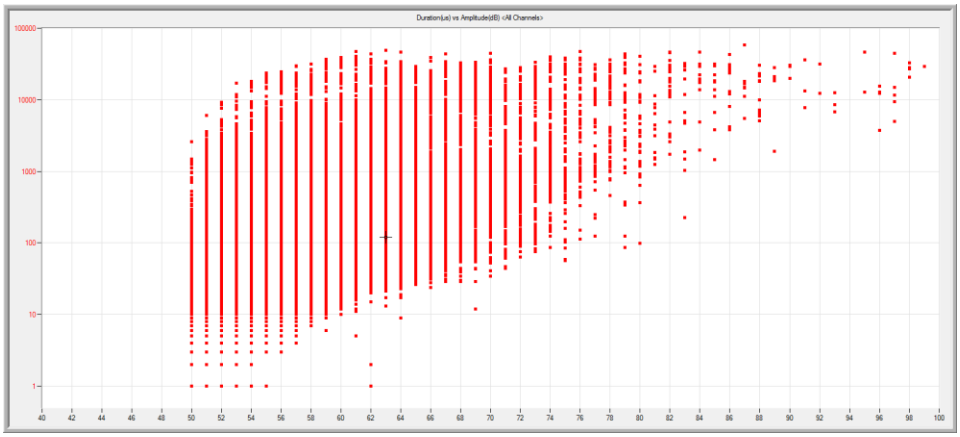
Figure 1

2.7 Test Data Acquisition **Duration vs psi vs Time**



2.8 Quality Analysis

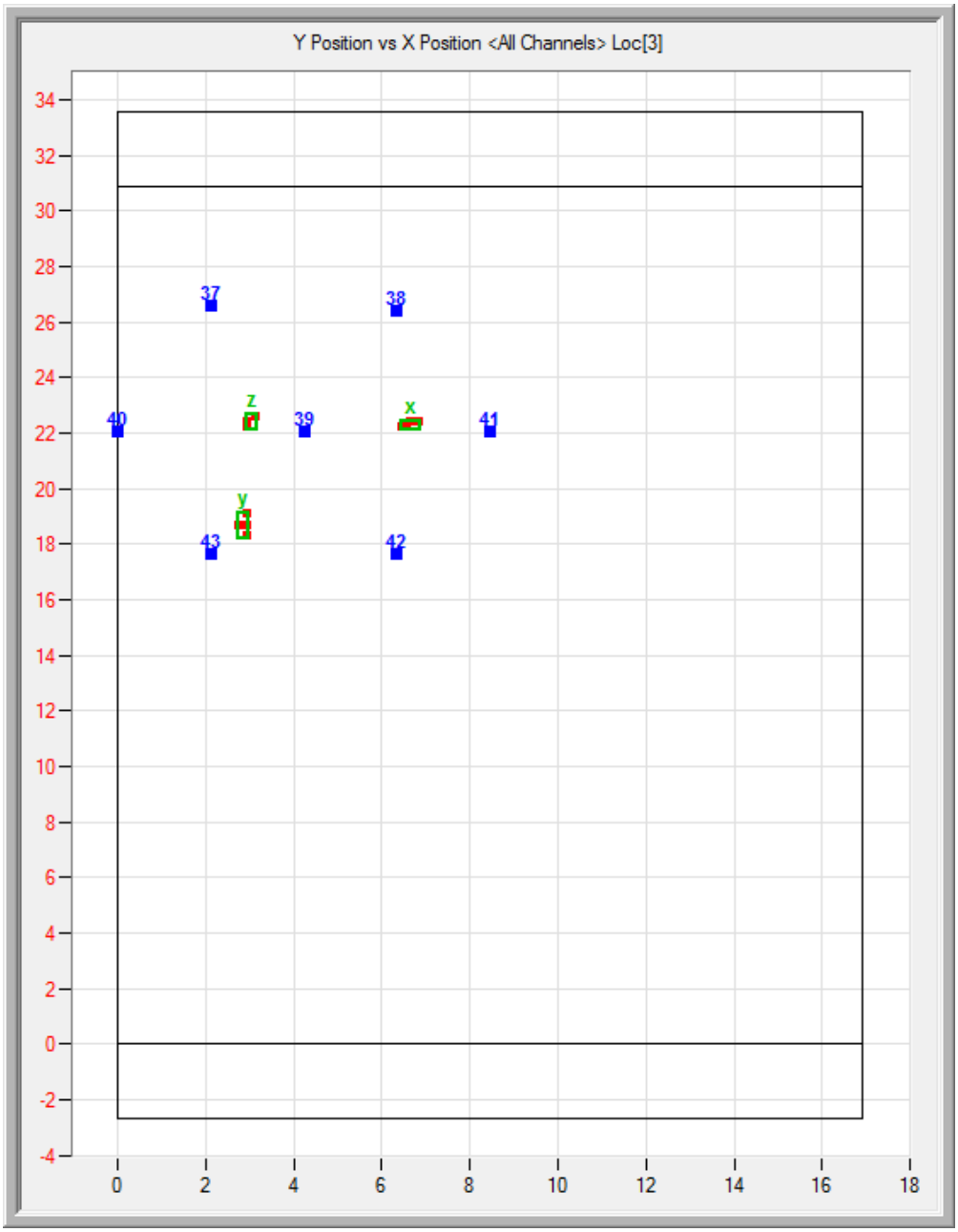
Acquisition of genuine, valid, acoustic emission data is essential to the success of the test. To achieve this, the following actions are required: (1) thoroughly check the instrumentation performance prior to the start of the test; (2) identify and characterize extraneous noise and judge its impact on data quality; (3) carefully monitor the performance of the instrumentation during the test. RFI (Radio Frequency Interference, EMI (Electromagnetic Interference) can be recognized during the background check and during the test. Examples of EMI are a faulty cable or sensor, or an electric motor up or down stream. Flow noise is identified by pre-test pressurization. These extraneous AE sources shall be minimized as much as possible before the test or before resuming the test. Data quality was good for V0023 AE test, the 5 center punch's at the beginning of the test were filtered out and the data was sent through a time-order filter.



2.9 ANALYSIS (time and time order filters only)

2.9.1 Cylinder (3D) Wide Band Sensors (WDI) Location Accuracy Verification (graph units in feet)

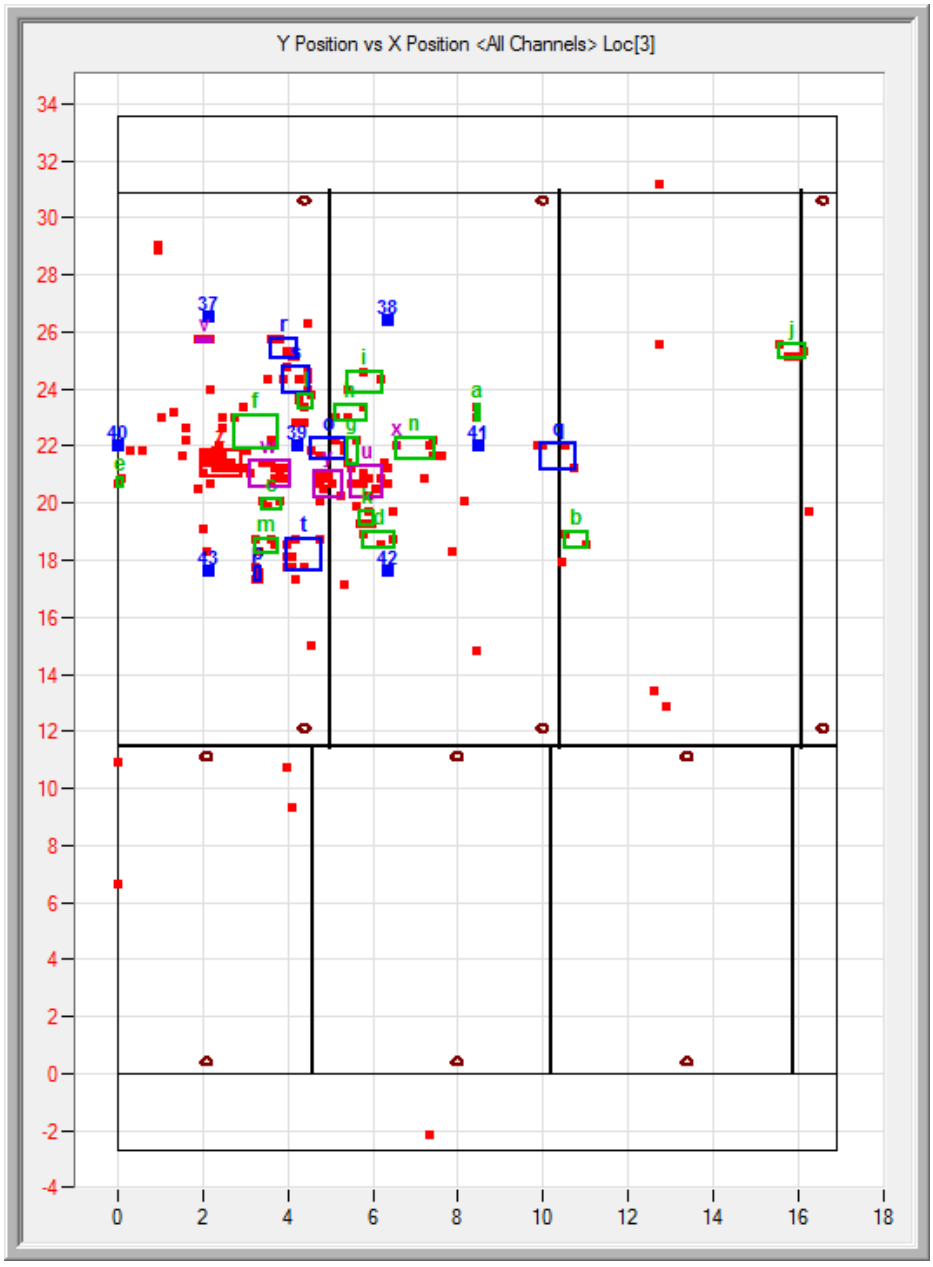
- Verification accepted. Error distance: 0.25’
- Z: 5 LB’s Y-22, X-3
- X: 5 LB’s Y-22, X-6.5
- Y: 5 LB’s Y-19, X-3



2.9.2 Cylinder (3D) Wide Band Sensors (**WDI**) Location Analysis results (graph units in feet)

Source location isolated clustering can be set for grading “points” which is total number of hits, or energy or counts. The box size can be selected to narrow the area of interest or make it broad. The “points” grading was used for this test. A plot of the hits is shown below.

Source location clustering is also presented in a tabular format.
The clusters correspond to those shown in the plot form.



Plot of Hits Detected with WDI Sensors (units in ft.)

Cluster	ID	Points	Total Energy	Total Counts	X avg.	Y	min Xrange	max	min Yrange	max
z	1	30	69	237	2.40	21.45	1.98	2.87	21.13	21.75
y	4	14	44	152	4.85	20.82	4.68	5.23	20.32	21.06
x	21	13	0	14	6.53	22.04	6.52	6.54	22.03	22.05
w	5	12	25	71	3.67	21.12	3.10	3.96	20.76	21.49
v	26	11	0	11	2.11	25.74	1.90	2.15	25.71	25.76
u	9	10	26	91	5.80	20.77	5.51	6.17	20.35	21.23
t	6	9	22	108	4.16	18.01	3.95	4.75	17.66	18.65
s	2	8	11	37	4.31	24.42	3.87	4.50	23.99	24.69
r	10	6	46	137	3.95	25.42	3.65	4.13	25.20	25.80
q	12	6	1	11	10.46	21.91	9.95	10.72	21.30	22.04
p	17	6	29	111	3.27	17.51	3.22	3.30	17.27	17.81
o	3	5	348	379	5.04	21.92	4.58	5.34	21.67	22.22
n	7	4	4	19	7.15	21.99	6.52	7.45	21.74	22.19
m	13	4	56	117	3.47	18.58	3.21	3.72	18.41	18.69
l	14	4	14	42	4.39	23.60	4.29	4.59	23.35	23.73
k	20	4	60	135	5.84	19.35	5.74	5.95	19.21	19.60
j	30	4	19	86	15.89	25.22	15.62	16.19	25.08	25.46
i	8	3	605	699	5.78	24.34	5.37	6.14	23.98	24.59
h	15	3	2	6	5.44	23.13	5.12	5.81	22.93	23.49
g	19	3	11	20	5.53	22.03	5.42	5.59	21.47	22.32
f	22	3	414	346	3.34	22.43	2.73	3.66	22.02	22.99
e	24	3	29	65	0.06	20.77	0.01	0.11	20.67	20.82
d	25	3	27	72	6.15	18.75	5.78	6.47	18.58	18.96
c	32	3	2	9	3.57	20.02	3.46	3.75	19.95	20.09

Table of Hits Detected With WDI Sensors
(X and Y in ft.)

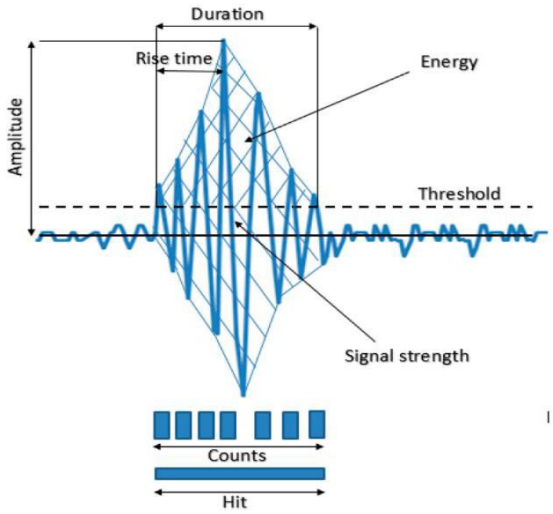
2.9.3 WDI Source Location Evaluation

The V0023 area "**Z**" located source indication is relevant containing "crack-like" signals, high # of isolated hits, medium to high energy, and high counts. Follow-up radiography is recommended at this location. It is suspected that the source will be shallow, closer to outside surface than inside surface, from the lack of signal distortion through the layers. The figures below show basic signal parameters, actual relevant crack-like signatures recorded at location "z" and non-relevant signatures recorded during test. Crack-like signals are sharp with low rise-times. All 30 hits located at source "z" were relevant crack-like signals. No emission during hold periods indicates source not critically active.

"**Z**" is the primary source indication for WDI sensors.

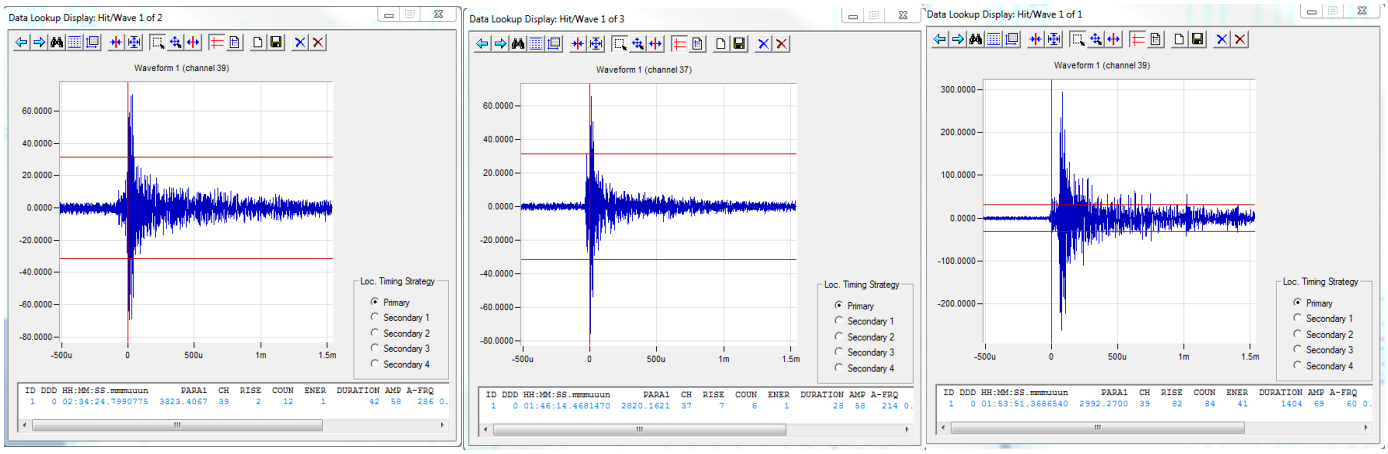
Relevant Source: Combination of High Amplitude, Low Rise time, high hits, high counts, high frequency, high energy, relevant signals

Non-Relevant Source: Combination of Lower Amplitudes, high rise times, low hits, lower counts, lower frequencies, low energy, non-relevant signal

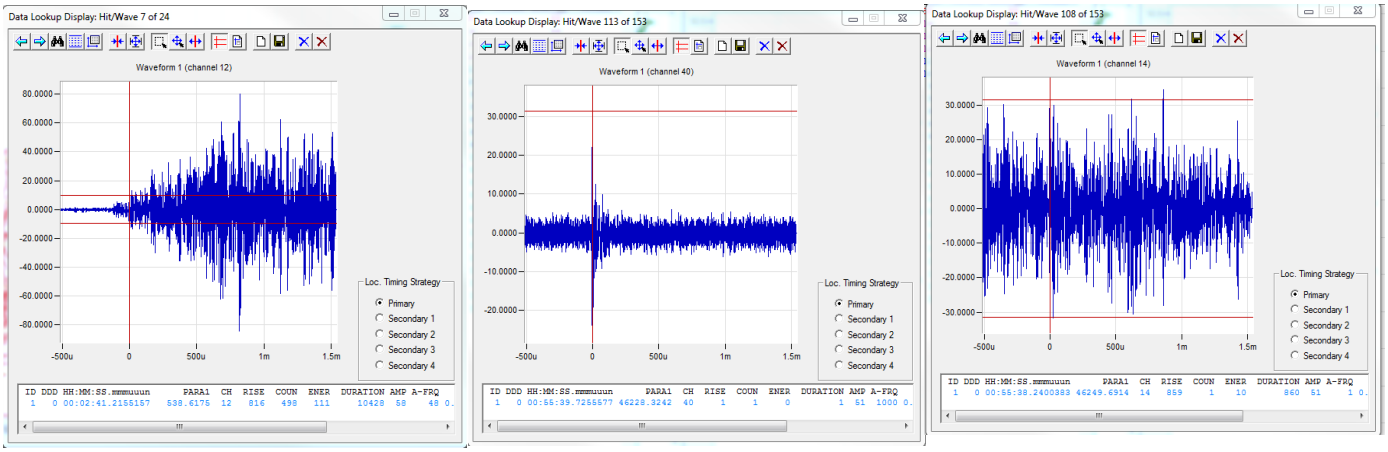


Basic Acoustic Signal Parameters

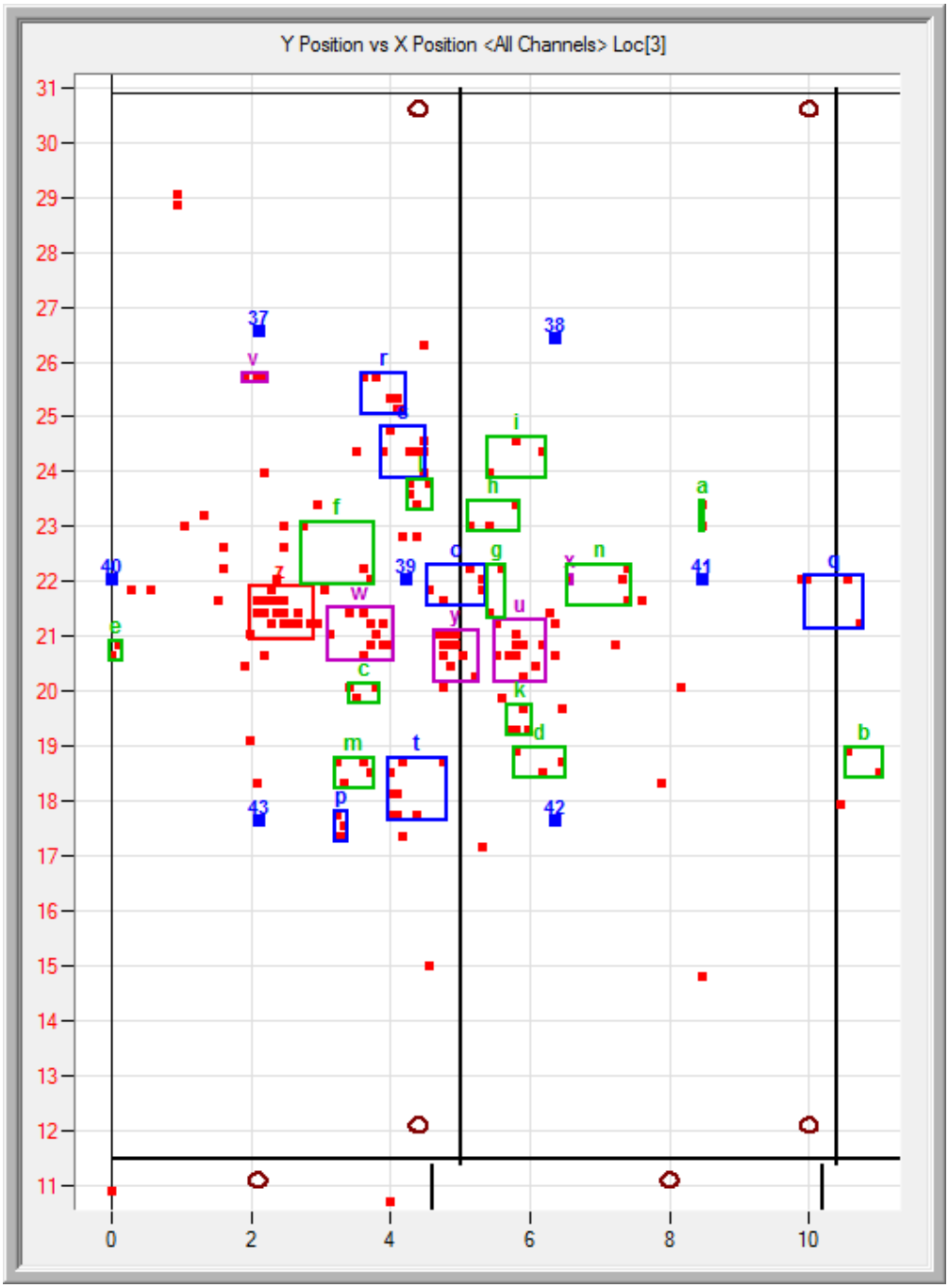
Crack-like signatures from hits located within the “z” cluster are shown below.



Non-relevant signature for comparison to crack-like signatures are shown below.



An exploded view of the hit and cluster locations recorded with WDI sensors is shown below.



2.9.3.1 WDI Source Location Evaluation Continued

The **"y"** located source indication contains low hits (14), 10 relevant and 4 non-relevant signals, low energy and counts. Source "y" is evaluated non-relevant.

The "**x**" and "**v**" located source indications contain low hits (11), low energy and counts. non-relevant

The "**w**" located source indication contains low hits (11), 8 relevant and 3 non-relevant, low energy and counts. Source "w" is evaluated non-relevant.

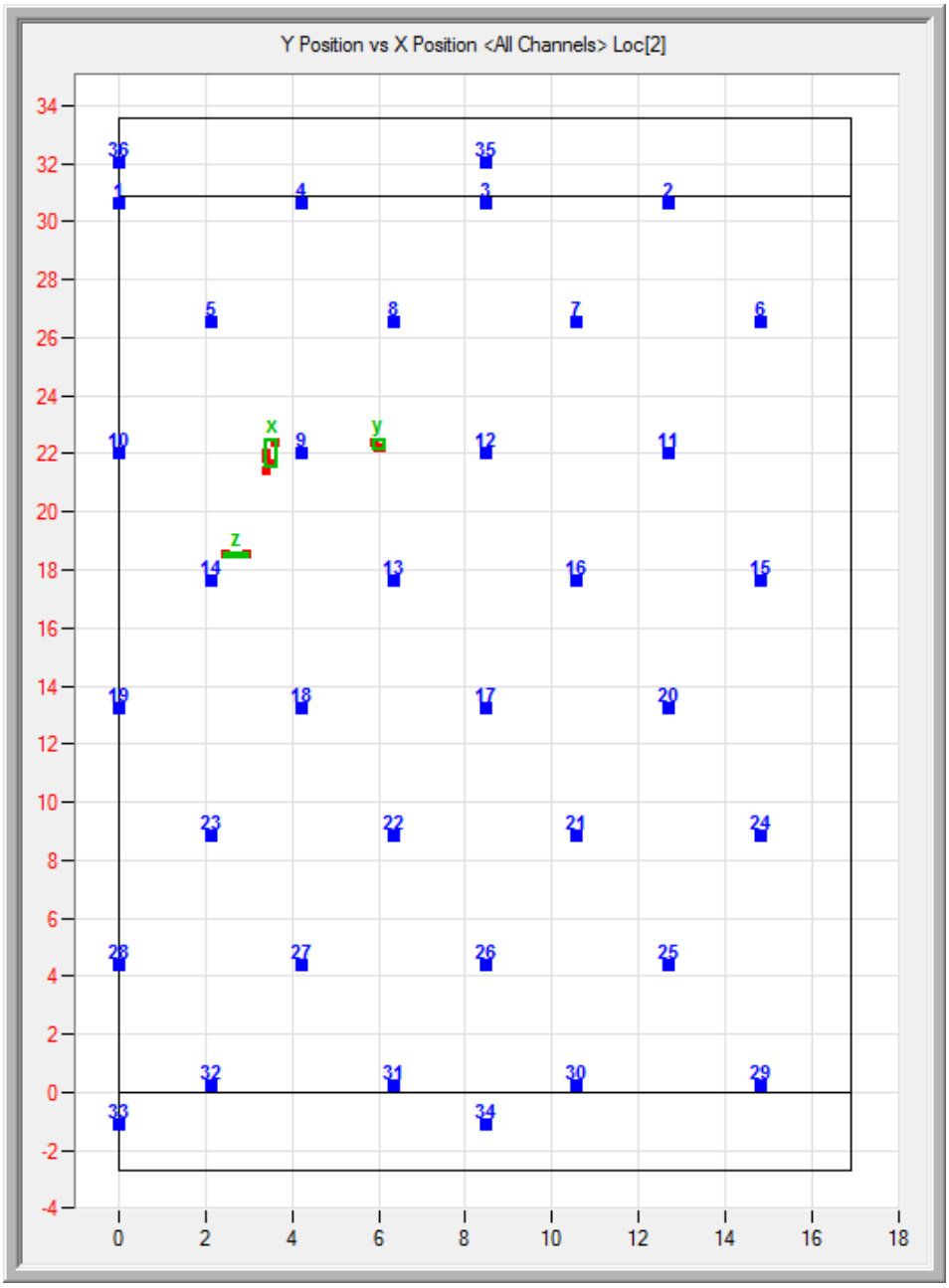
The "**u**" located source indication contains low hits, low energy and low counts. non-relevant

The "**t**", "**p**", and "**m**" located source indications contain (21) relevant signals and have similar locations to the "**z**" source located with the R15I sensors. Combined they have high energy and counts. "**t**", "**p**", and "**m**" are evaluated relevant.

All other located source indications are evaluated non-relevant.

2.9.4 Cylinder (3D) Mid-Range Sensors (R15I) Location Accuracy Verification (graph units in feet)

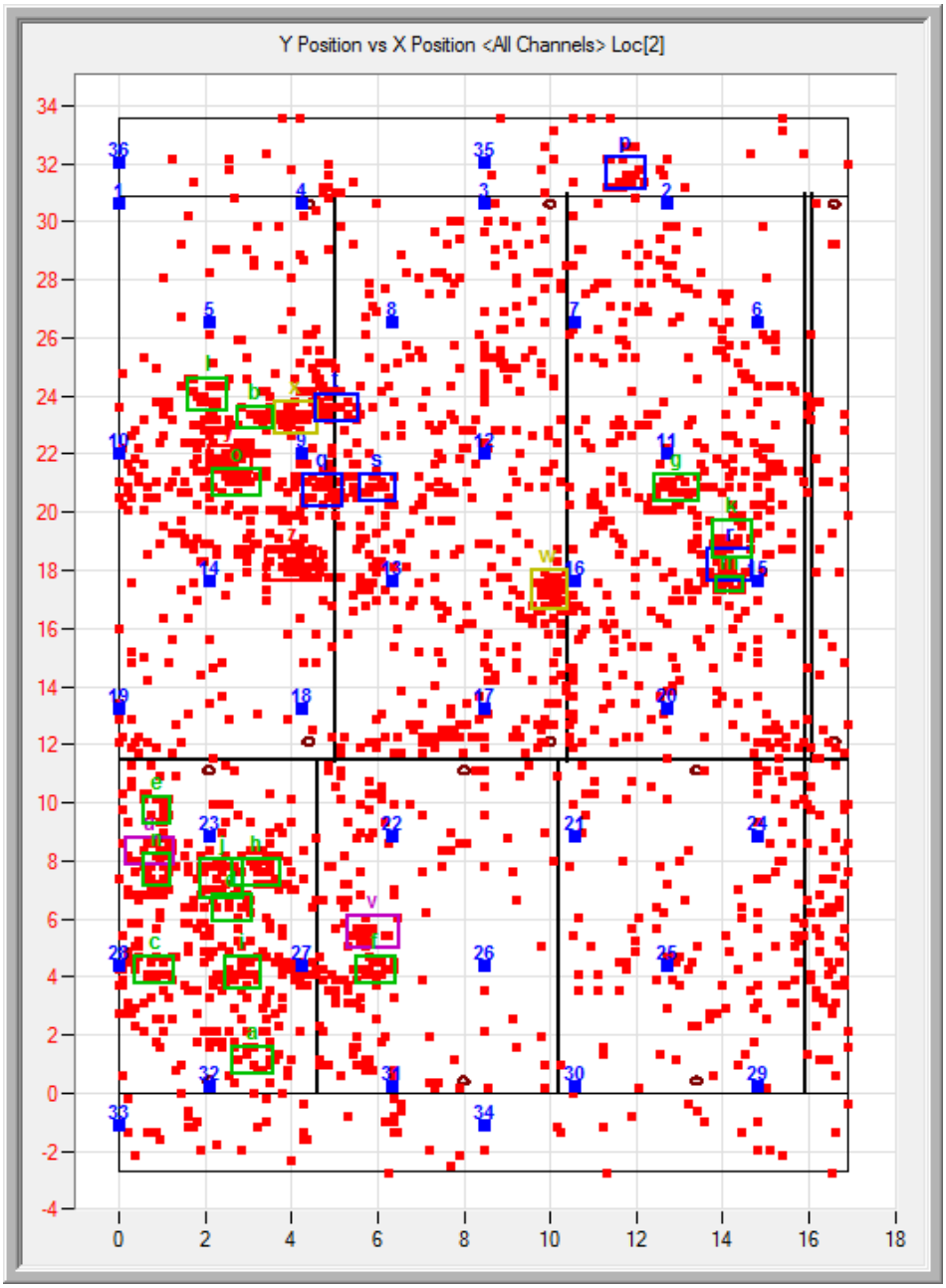
- Verification accepted. Error distance: 0.5’
- X: 5 LB’s Y-22, X-3
- Y: 5 LB’s Y-22, X-6.5
- Z: 5 LB’s Y-19, X-3



2.9.5 Cylinder (3D) Mid-Range Sensors (R15I) Location Analysis results (graph units in feet)

AE equipment source location isolated clustering can be set for grading “points” which is total number of hits, or total energy or total counts. The box size can be selected to narrow the area of interest or make it broad. The “points” grading was used for this test.

Source location clustering is also presented in a tabular format.
The clusters correspond to those shown in the plot form.



Plot of Hits Detected with R15I Sensors (units in ft.)

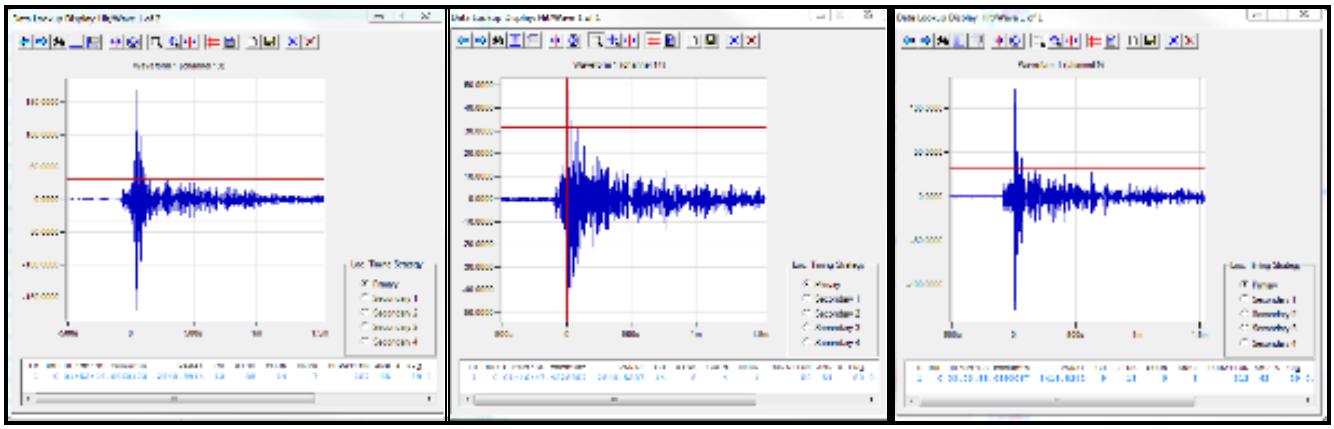
Cluster	ID	Points	Total Energy	Total Counts	X avg.	Y	min Xrange	max	min Yrange	max
z	11	68	195	384	4.17	18.22	3.41	4.66	17.68	18.71
y	35	51	369	625	2.54	21.78	2.08	3.00	21.37	22.20
x	9	47	552	737	4.02	23.36	3.64	4.55	22.87	23.84
w	13	45	358	581	10.02	17.29	9.59	10.40	16.86	17.90
v	60	29	142	223	5.66	5.37	5.27	6.13	5.07	5.83
u	16	27	136	243	0.76	8.31	0.21	1.22	7.92	8.85
t	27	26	254	375	4.85	23.56	4.52	5.47	23.18	23.98
s	17	23	75	154	5.92	20.90	5.59	6.35	20.45	21.31
r	5	22	513	807	14.12	18.08	13.67	14.66	17.70	18.77
q	71	21	124	164	11.73	31.50	11.34	12.12	31.11	32.17
p	59	20	237	376	4.78	20.81	4.27	5.13	20.38	21.22
o	26	19	470	719	3.22	7.86	2.67	3.55	7.52	8.31
n	28	18	190	286	0.81	7.55	0.61	1.14	7.12	8.17
m	30	18	320	511	14.13	17.56	13.83	14.48	17.29	17.80
l	74	18	200	333	2.71	21.09	2.14	3.02	20.67	21.37
k	47	16	273	346	2.79	4.10	2.44	3.20	3.73	4.59
j	68	16	104	204	2.01	24.08	1.58	2.44	23.68	24.56
i	22	15	343	486	2.37	6.81	1.94	2.75	6.43	7.10
h	57	15	218	378	5.96	4.27	5.55	6.38	3.91	4.66
g	4	14	240	375	14.11	18.97	13.80	14.60	18.57	19.70
f	15	13	444	639	12.89	20.87	12.47	13.28	20.45	21.35
e	41	13	84	136	0.86	6.95	0.39	1.11	6.55	7.67
d	21	12	140	214	3.21	23.31	2.79	3.52	22.97	23.61
c	56	12	43	72	3.95	19.89	3.71	4.29	19.62	20.14
b	88	12	89	131	8.60	25.50	8.38	8.90	25.07	26.16
a	53	11	107	165	16.38	6.28	15.84	16.75	5.77	6.67

Table of Hits Detected With R15I Sensors
(X and Y in ft.)

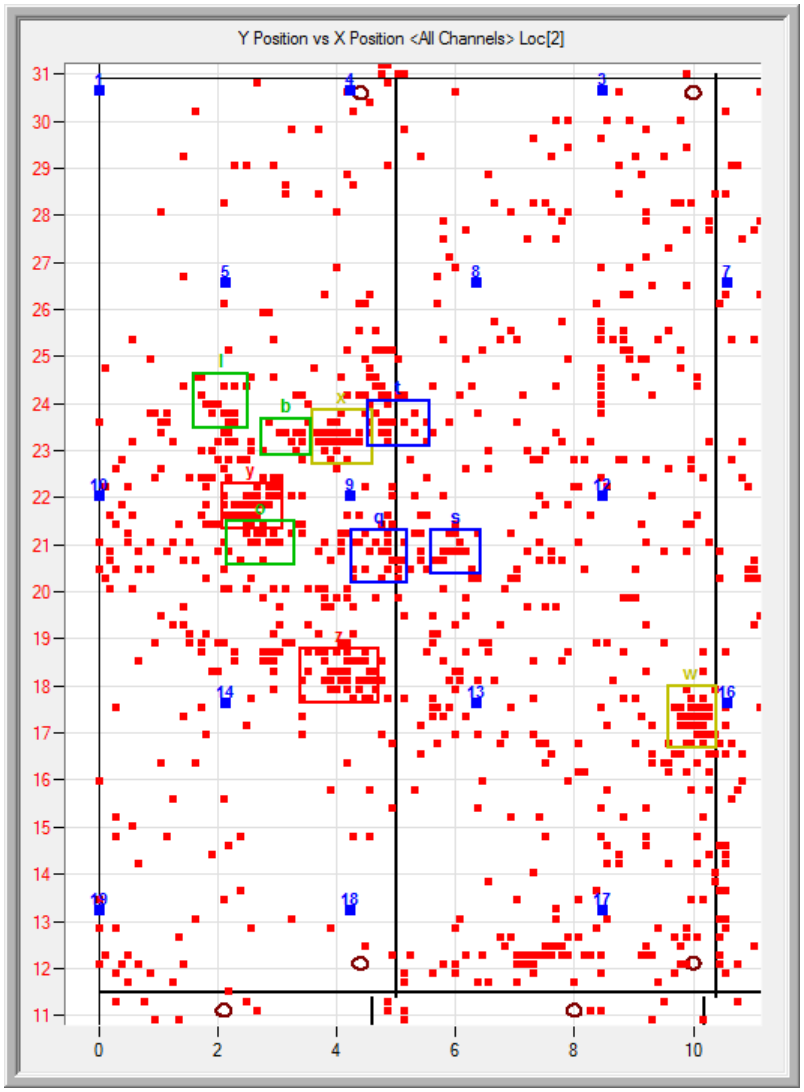
2.9.6 R15I Source Location Evaluation

"**z**" and "**y**" located source indications are relevant containing "crack-like" signals, high number of isolated hits, high energy, and high counts (perform radiography here.) . It is suspected that the source will be shallow, closer to outside surface than inside surface, from the lack of signal distortion through the layers. The following three signals were all recorded at the "y" location. Crack-like signals are sharp with low rise-times.

"y" is the primary source indication for R15I sensors.



An exploded view of the hit and cluster locations recorded with R15I sensors is shown below.



The "**y**" located source indication is relevant containing "crack-like" signals (perform radiography here). Signal continuous throughout test except for pressurization hold periods. No emission during hold periods indicates source not critically active.

The "**z**" located source indication is relevant containing "crack-like" signals (perform radiography here).

The "**x**" and "**w**" located source indication are relevant containing "crack-like" signals, high number of isolated hits, high energy, and high counts (perform radiography here).

The "**t**" located source indication is relevant containing "crack-like" signals. (perform Radiography here)

3.0 Conclusion and Recommendations

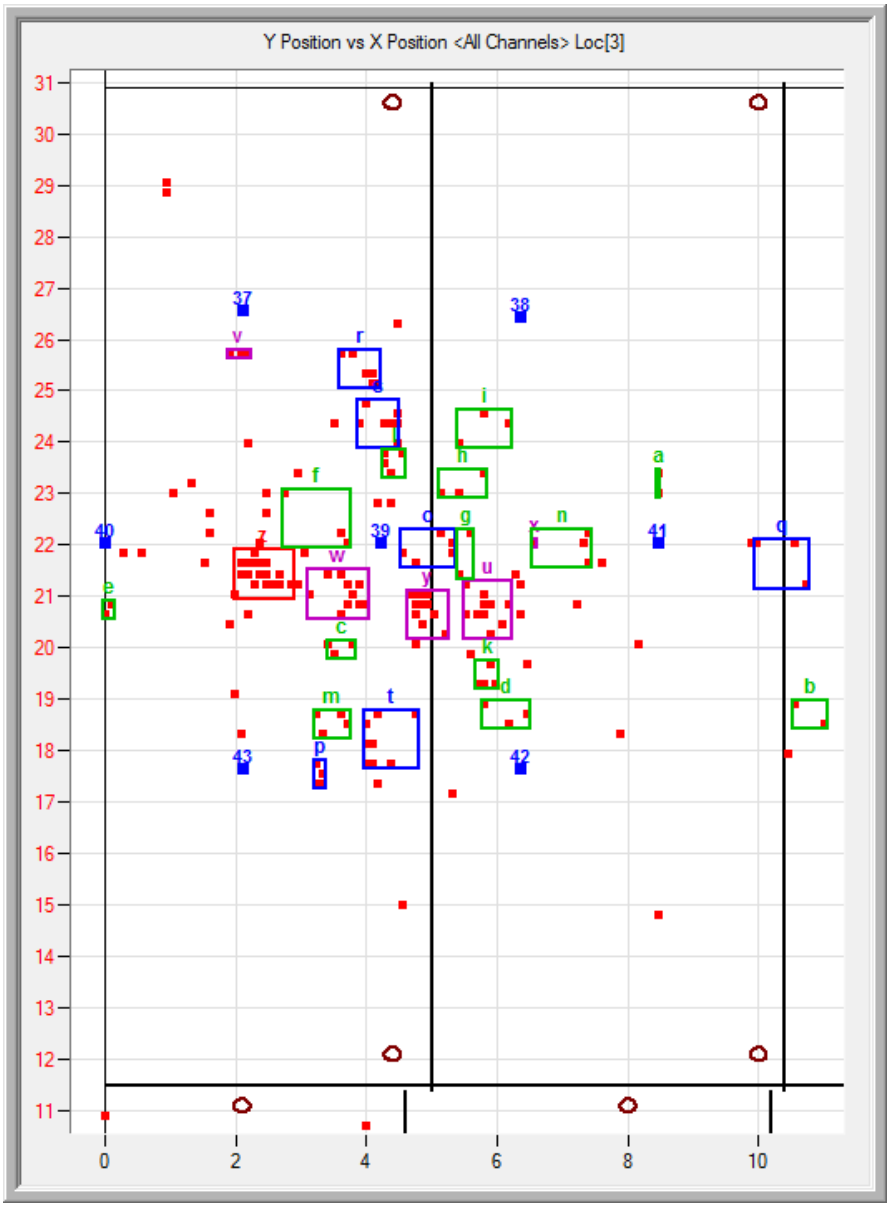
During this test, relevant located source indications that contain “crack-like” signals were detected. See page 26 in appendix 1 for R15I and WDI data comparison.

Recommend performing follow-up Radiography. (WDI) Area for RT

“z” Y: 21.13 to 21.75, X: 1.98 to 2.87

“t”, “p”, and “m” Y: 17.27’-18.69’, X: 3.21’-4.75’

WDI sensors are much less sensitive than R15I’s, recommend using a 32-35 dbAE threshold for the WDI sensors in future testing.



Recommend performing follow-up Radiography. (R15I) Areas for RT

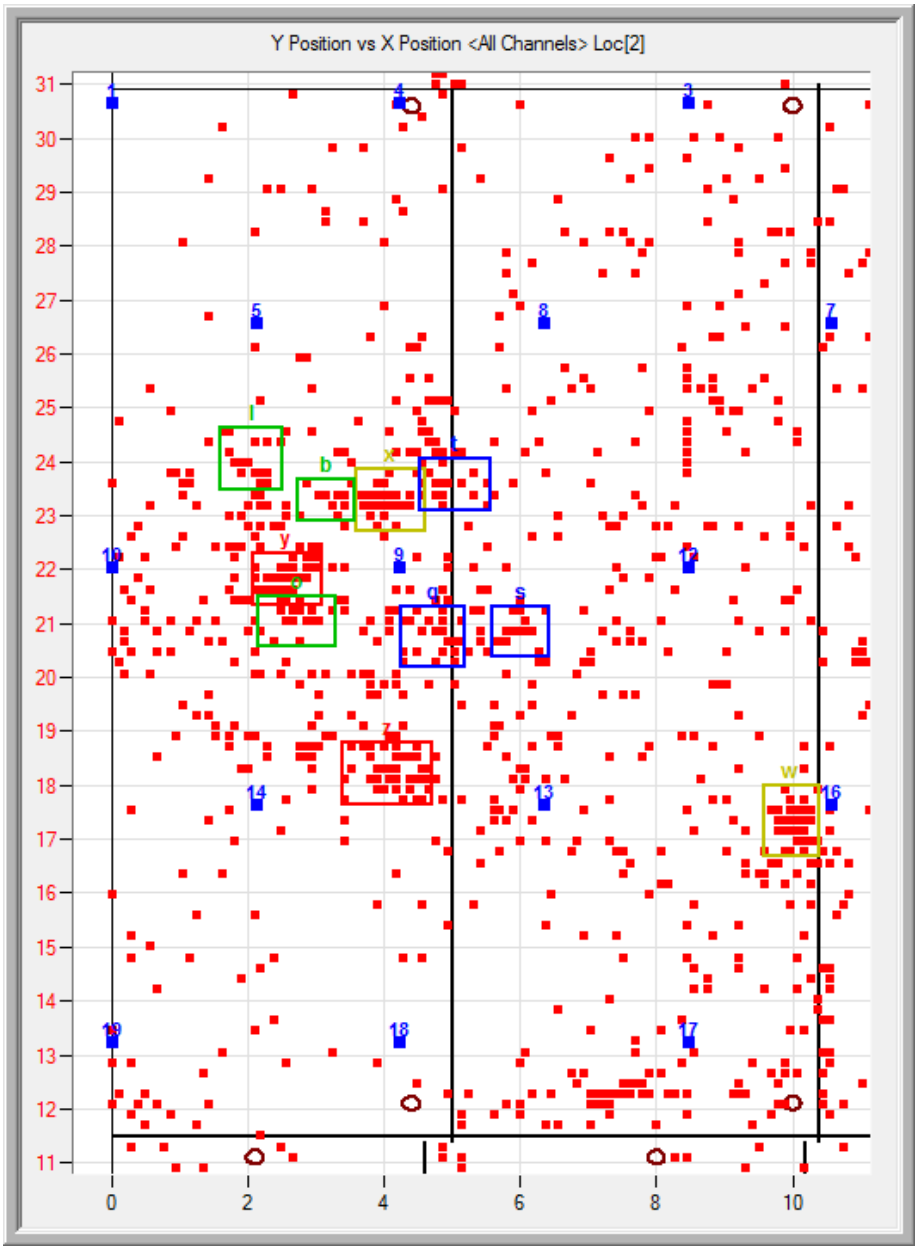
"y" Y: 21.5-22.5, X: 2-3

"z" Y: 17.75-18.75, X:3.5-4.75

"X" Y: 22.75'-23.75', X: 3.5-4.75'

"w" Y: 16.75'-18', X: 9.5'-10.5'

"t" Y: 23.1'-24.1', X: 4.5'-5.5'



APPENDIX I

Vessel Documentation and AE Graphs

VESSEL MANUFACTURERS DATA REPORT

A. O. SMITH CORPORATION

Milwaukee, Wisconsin

Manufacturers' Report on an Unfired Pressure Vessel

Manufactured by A. O. Smith Corporation, Milwaukee, Wisconsin (Name and address of the manufacturer) Mfrs. Shop Job No. MV 50565

2. Manufactured for Western Contracting Corp., Sioux City, Iowa (Name and address of the purchaser) Purchaser's Order No. 22-604

3. Type Vertical (Horizontal or vertical—when in service) Vessel No. MV 50565-17 (Mfg. Ser. No.) To be installed in Lincoln, A.F.B. (Nebraska) (State and State No.) Date Built December, 1960 (Month and Year)

4. Have mill test reports been checked on all the plates or seamless vessel forgings entering this unfired pressure vessel Yes

Does material conform to specification? Yes

5. Shell or Drums: No. 1 Diameter 4 Ft. 10 In. Length over all 38 Ft. 3 1/2 In.

6. Stamps on Shell Plates A.O.Smith 11466 (Brand and lowest tensile strength) Bolts ASTM A193 Gr.B-7 (A. S. T. M. or Other specs. Carbon Steel or Alloy)

ASTM A225 Gr.B FBQ (or High) 43,000 Y.P. 75,000psi MTS-Heads 82,500 YP,110,000psi MTS-Shell

7. Shell plates *3.305 (Thickness) in. Style of Seams: Longitudinal d.w.b.j. and s.w.b.j. with backup

8. Joints Radiographed See 12 Vessel Stress Relieved See 12 (Yes or No) Efficiency of Joint 100 %

9. Girth Joints d.w.b.j. and s.w.b.j. with backup No. of Courses inner shell-4, shell layers-2

10. Outer Shell — (If jacketed, thickness) in. Style of Seams: Longitudinal — Girth — Length of Section or Course — ' — "

11. Heads: (thickness) 3.03 in. Radius of dish 29 spherical in. Radius of knuckle —

Flat, dished, elliptical, integral — Ratio of Ellipse axis — (Side to pressure) Top or one end concave

~~Conical~~ Hemispherical top and bottom Included angle if conical — Bot. or opp. end concave

If removable, head bolts used — — (Number and Size) or method of fastening — (Describe or sketch on separate sketch sheet)

12. w Radiographic Inspection All or Per Cent Thickness

a Longitudinal Joints inner shell 15/32 in.

b Circumferential Joints Nozzle to head seams 3.03 ~~inner shell~~ ~~15/32~~ in.

w Stress Relieving	Heads	Ring Nos.	Controlling Thickness	Temp. of Vessel	Time Temp. is Held
a If part of vessel only	2	inner shells	3.03 15/32 in.	1150° F.	3 1/2, 1/2 Hr.
b If entire vessel	—	—	in.	F.	Hr.

13. Nozzle Outlets in Heads: No. 2 Size 2" Material of Nozzle or Reinforcement ASTM A105 Gr.II How attached welded

Nozzle Outlets in Shell: No. — Size — Material of Nozzle or Reinforcement — How attached —

14. Handholes or Sight Holes — — — (Number, size, and location)

15. Manholes: In Heads — — — Reinforcement —

In Shell — — — Reinforcement — (Number) (Size and location of each, distance off center of head) (Riveted, welded, etc. outside only or also inside)

16. Method of supporting vessel 4 legs (Legs, skirt or ring if on end, or saddles or lugs if horizontal)

17. a Allowable working pressure at atmosphere temperature (See W, R and F-525) 4400 Psi

b Hydrostatic test pressure 7475 Psi

c Hydrostatic test pressure when hammer tested — Psi

d Proof test pressure if applied — Psi

e Location of yield if yielding occured —

f Hydrostatic test stress in longitudinal joints (W. vessels only) 69,328 Psi

g Allowable operating stress ~~Psi~~ stress obtained in f) 40,806 Psi

18. Constructed for pressure of 4400 Psi. With specified operating temperature -40 to 135° F. With corrosion allowance — in.

Remarks Oxygen Storage Bottle *15/32" inner shell and ten .277" layers

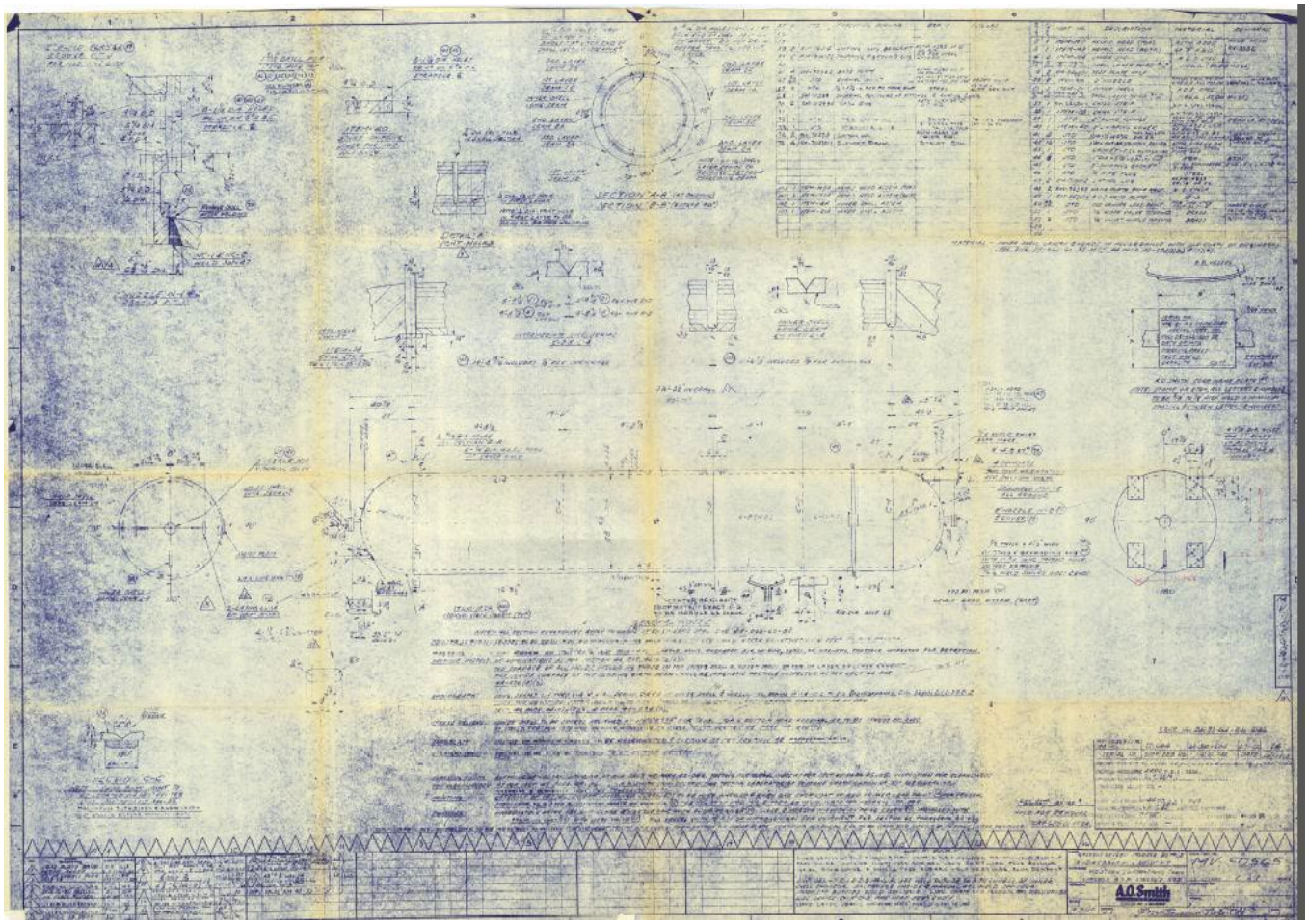
S.F. is 2.0 on Y.P.

WE CERTIFY the above data to be correct and that all details of material, construction and workmanship on this unfired pressure vessel conform to A. O. Smith Drawing No. MV 50565

Date December 5, 1960 Signed A. O. Smith Corporation Manufacturer By John L. Iverson

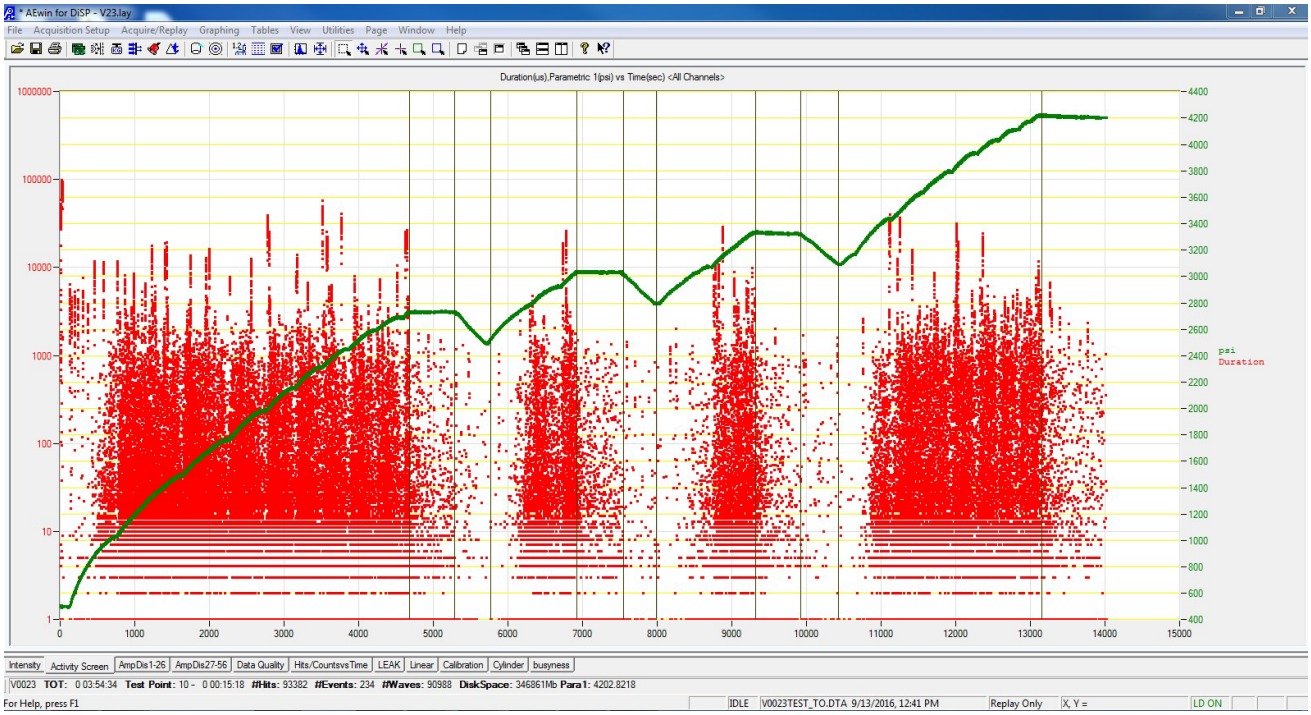
December 5, 1960 Checked by Carlos J. Klem Inspector For Maryland Casualty Co NCC 16284

VESSEL DRAWING

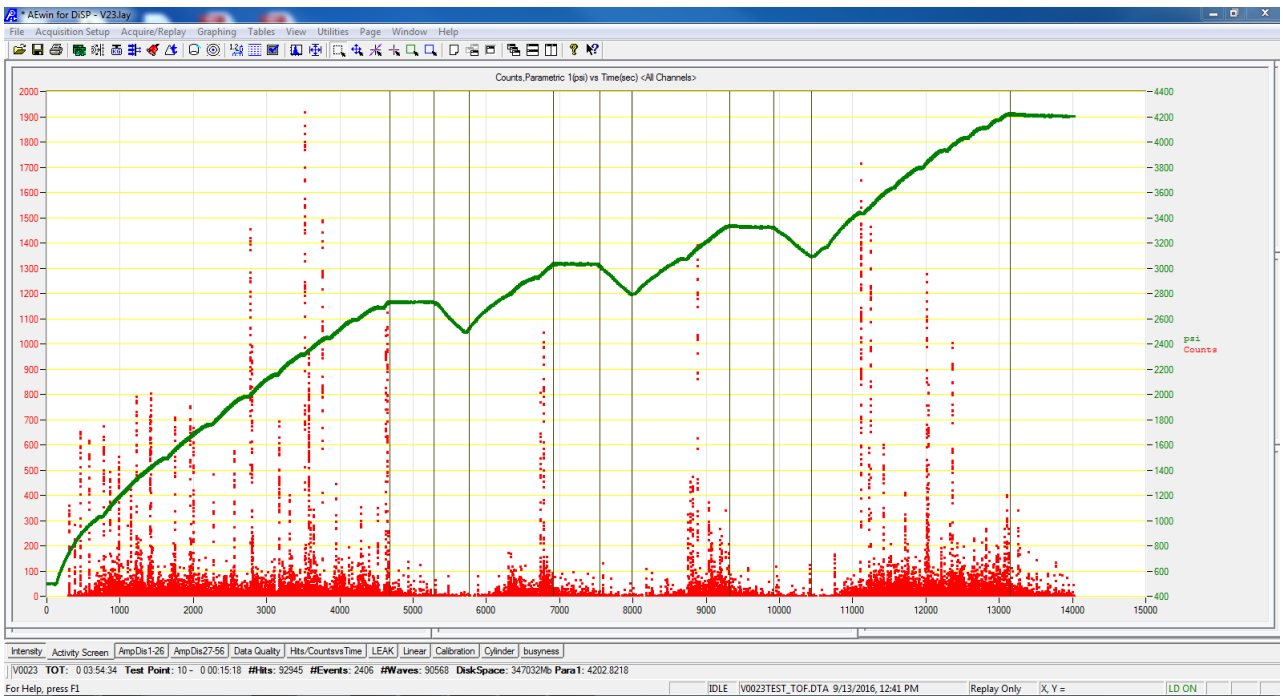


ASME REQUIRED DOCUMENTATION
T-1292 Record

AE hits (# units) above threshold vs time (seconds) and pressure (psi) for zones of interest

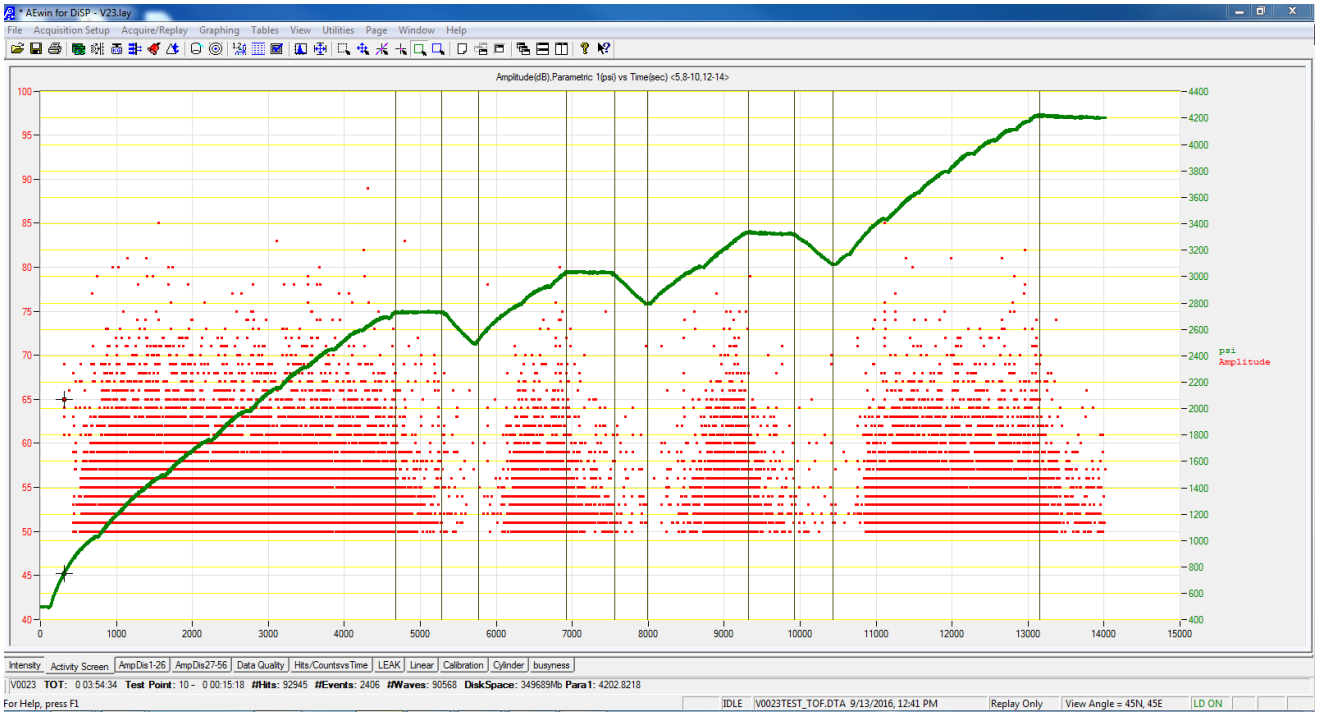


AE Counts (# units) above threshold vs time (seconds) and pressure (psi) for zones of interest

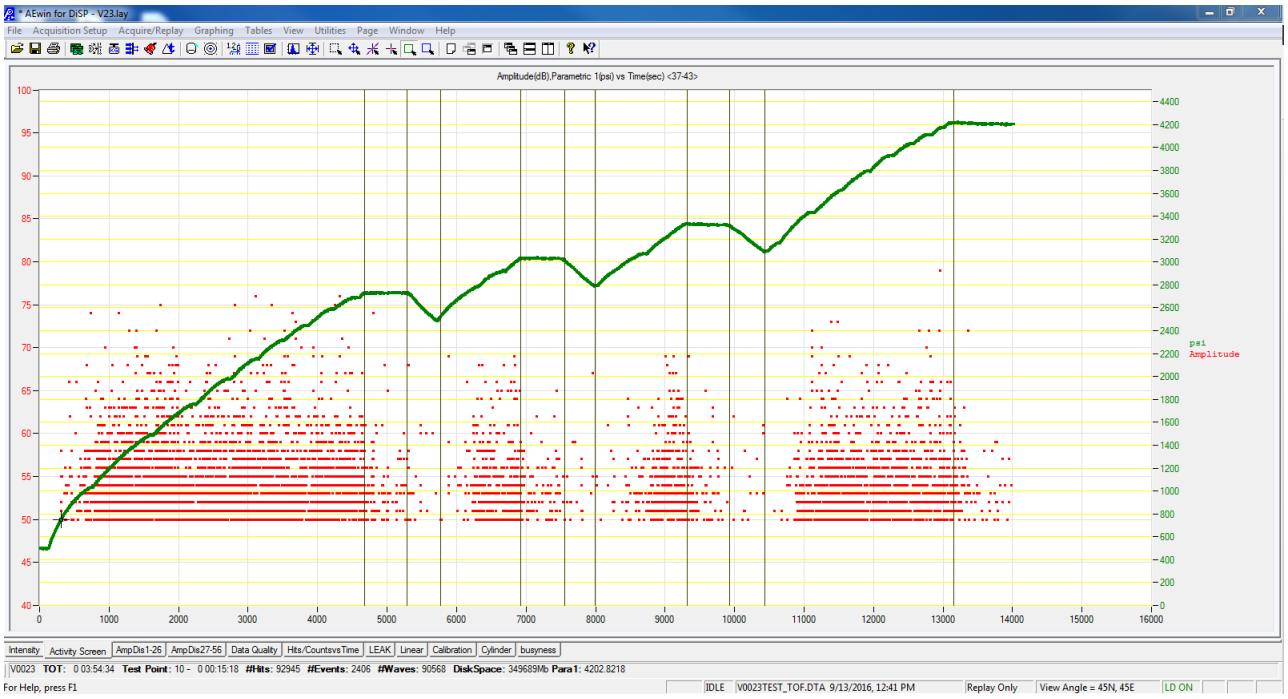


R15I Sensor versus WDI sensors side by side data comparison
(7 WDI sensors placed beside R15I Sensors) (50 dbAE threshold)

R15I (31,178 hits)

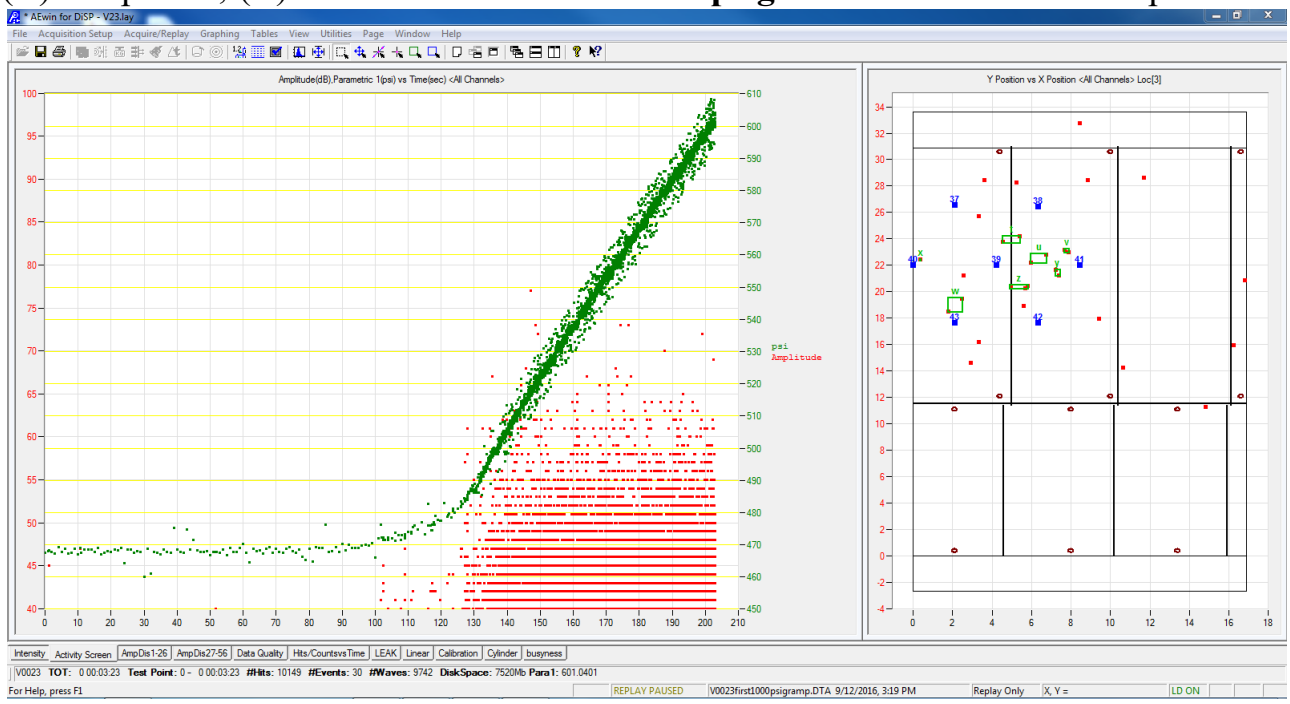


WDI (7,702 hits)

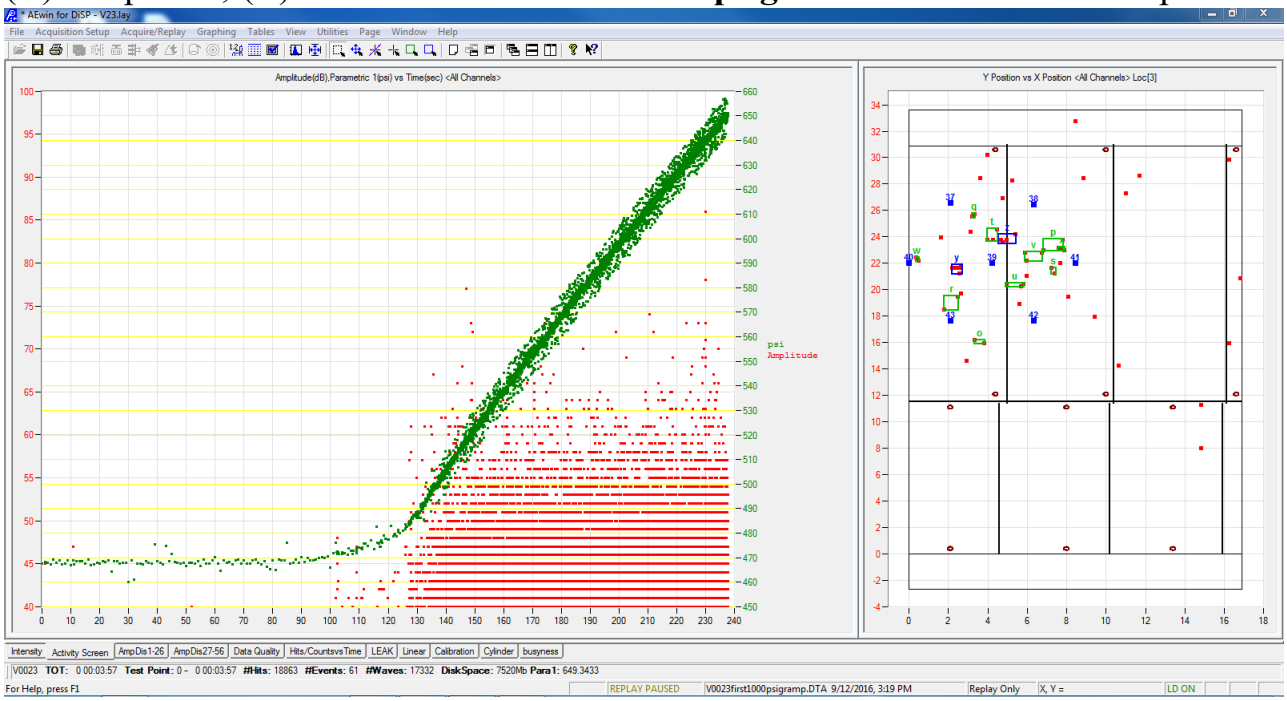


Pre-Test First Ramp (WDI)
V0023first1000psigramp.DTA

(Y) Amplitude, (X) PSI **600 psig** Location Graph

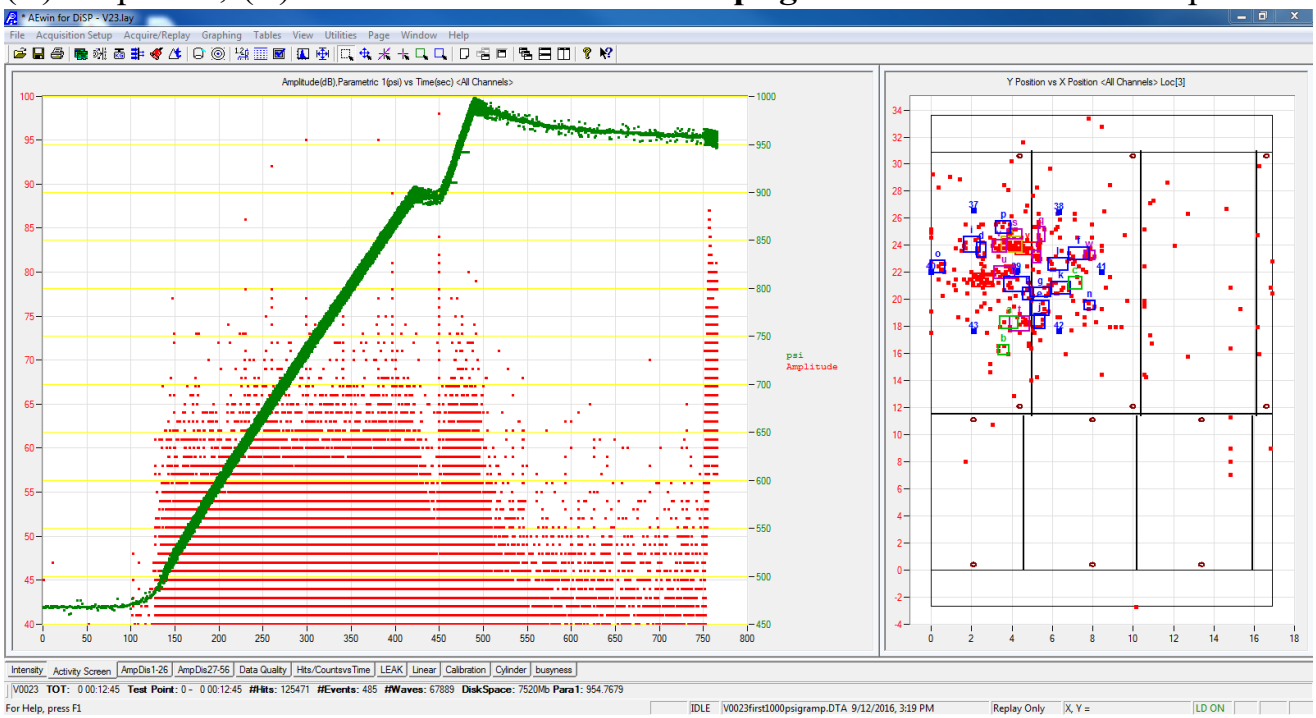


(Y) Amplitude, (X) PSI **650 psig** Location Graph



First Ramp

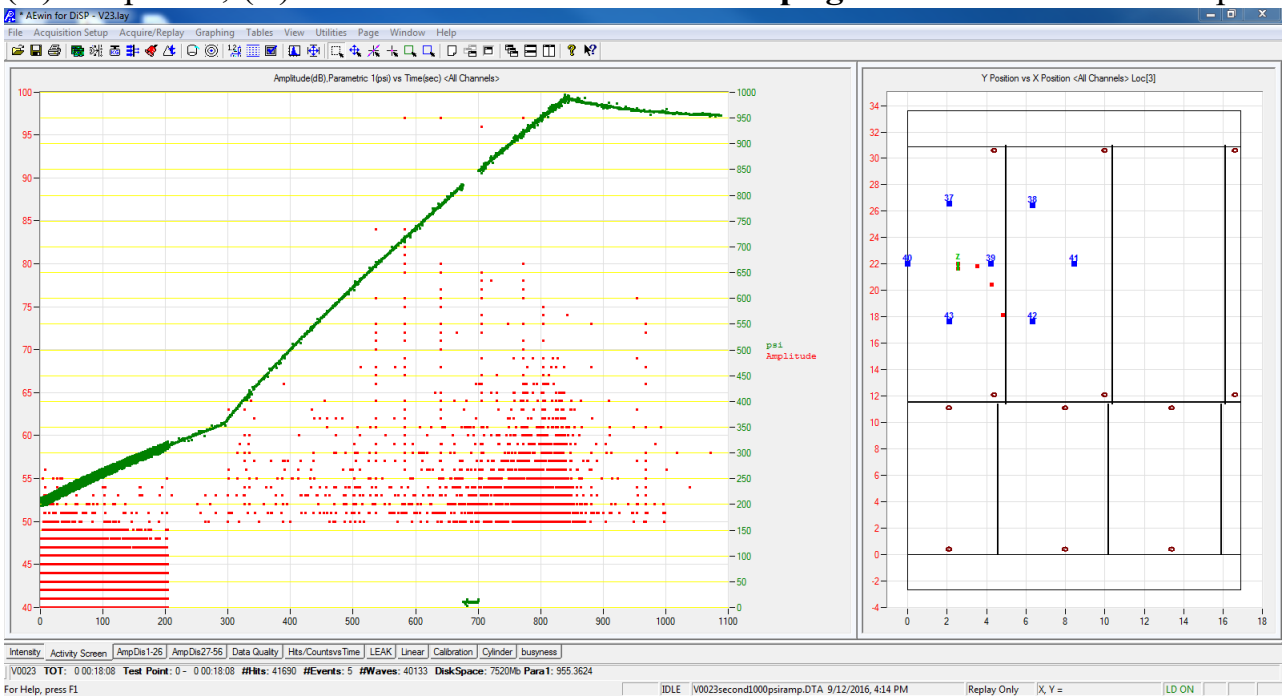
(Y) Amplitude, (X) PSI **1000 psig** Location Graph



Pre-Test Second Ramp (WDI)

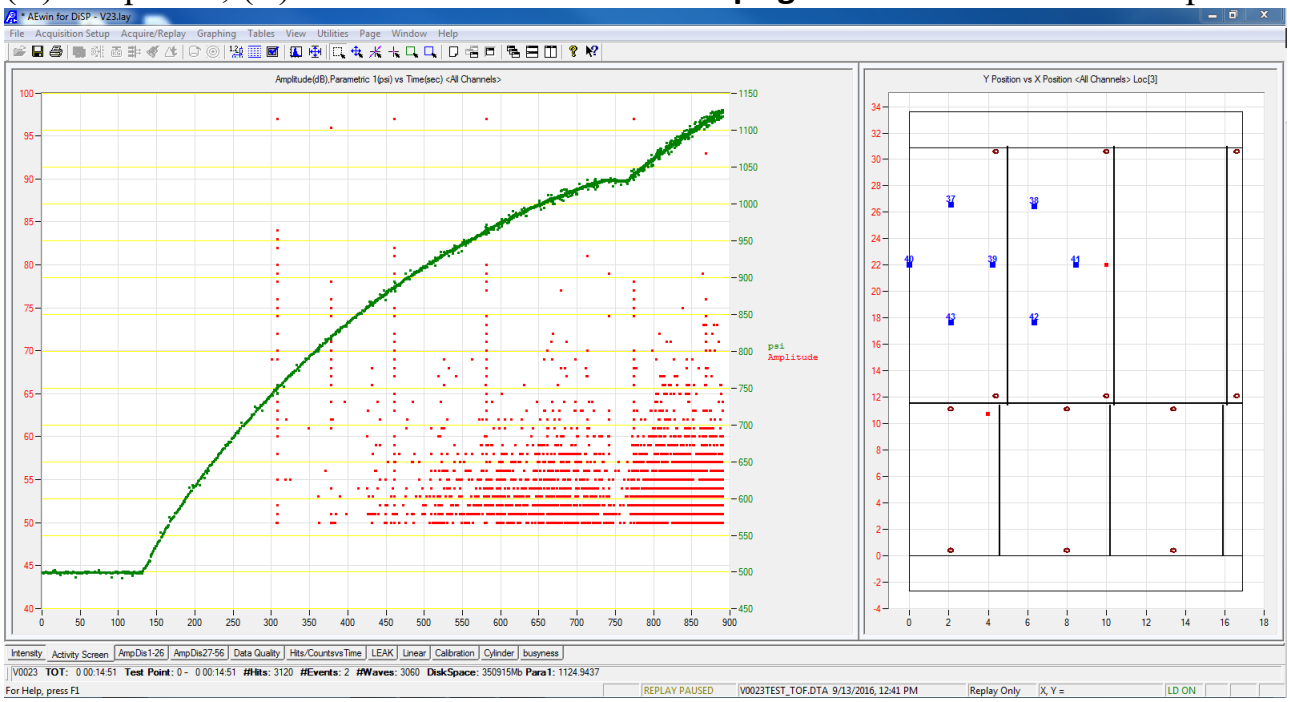
V0023second1000psiramp.DTA

(Y) Amplitude, (X) PSI **1000 psig** Location Graph

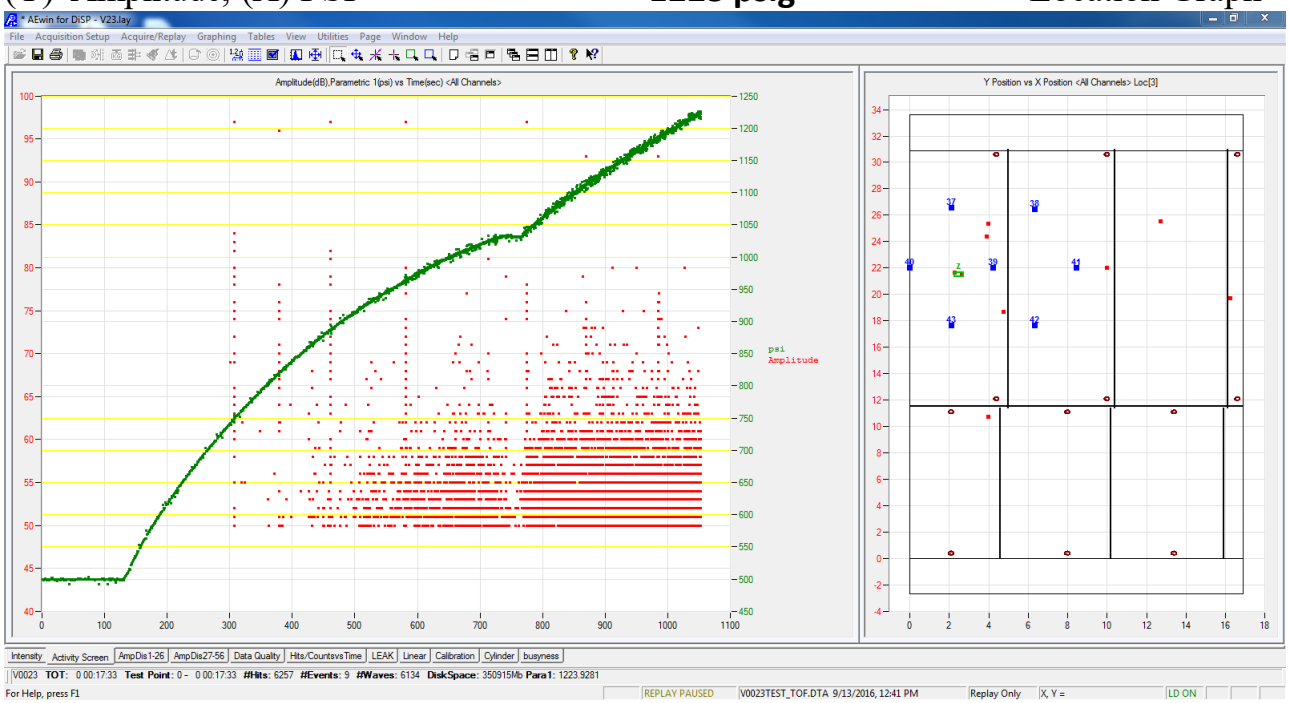


WDI Primary Source Development
Actual Test
V0023TEST_TOF.DTA

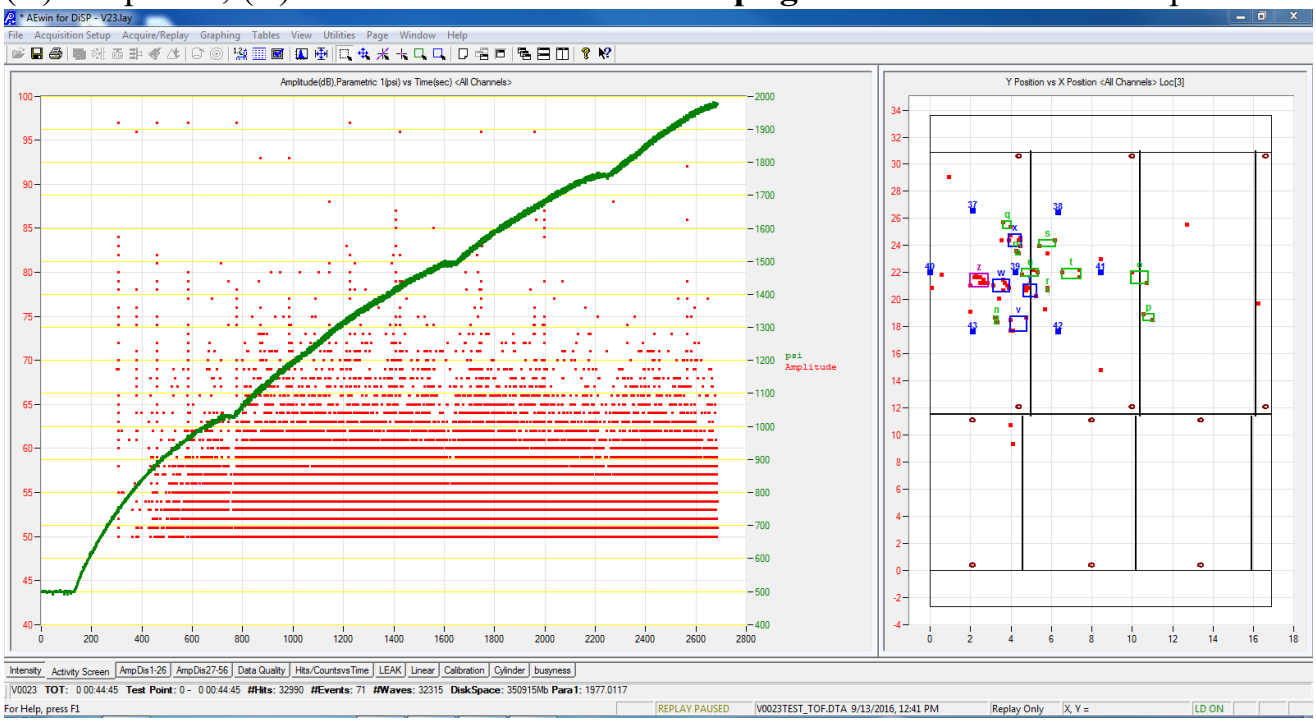
(Y) Amplitude, (X) PSI **1125 psig** Location Graph



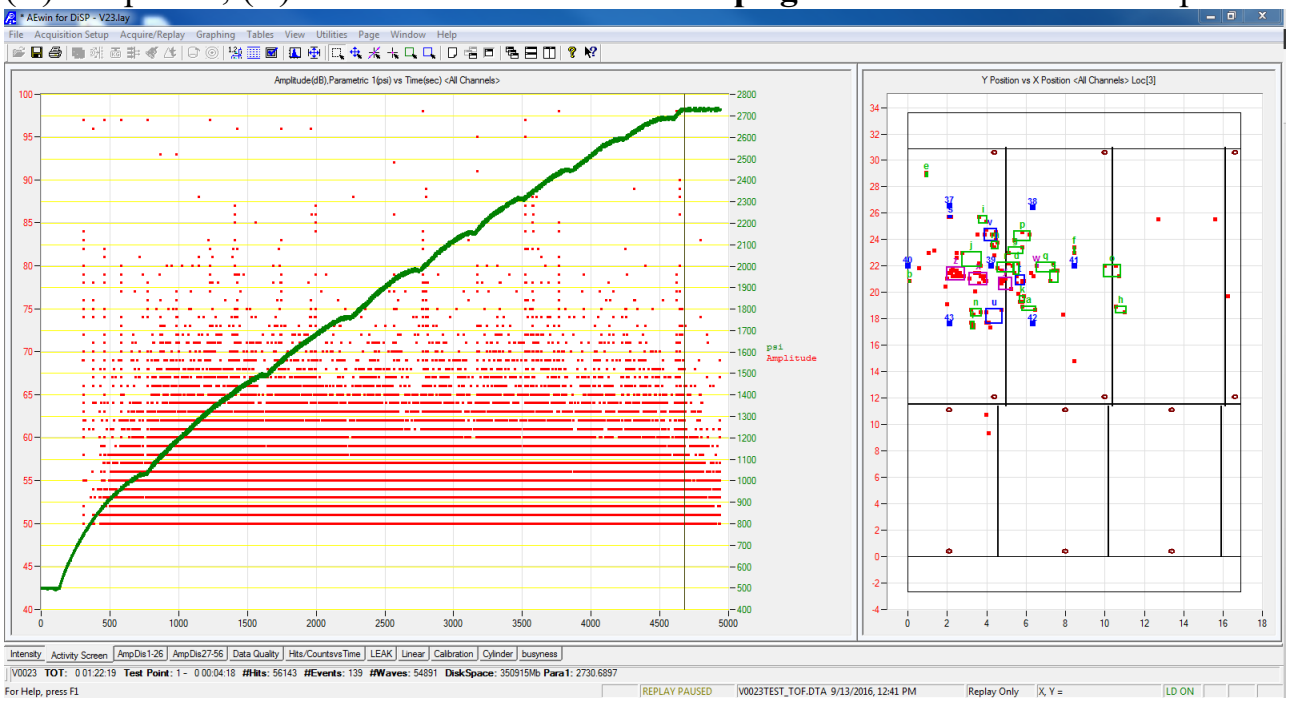
(Y) Amplitude, (X) PSI **1225 psig** Location Graph



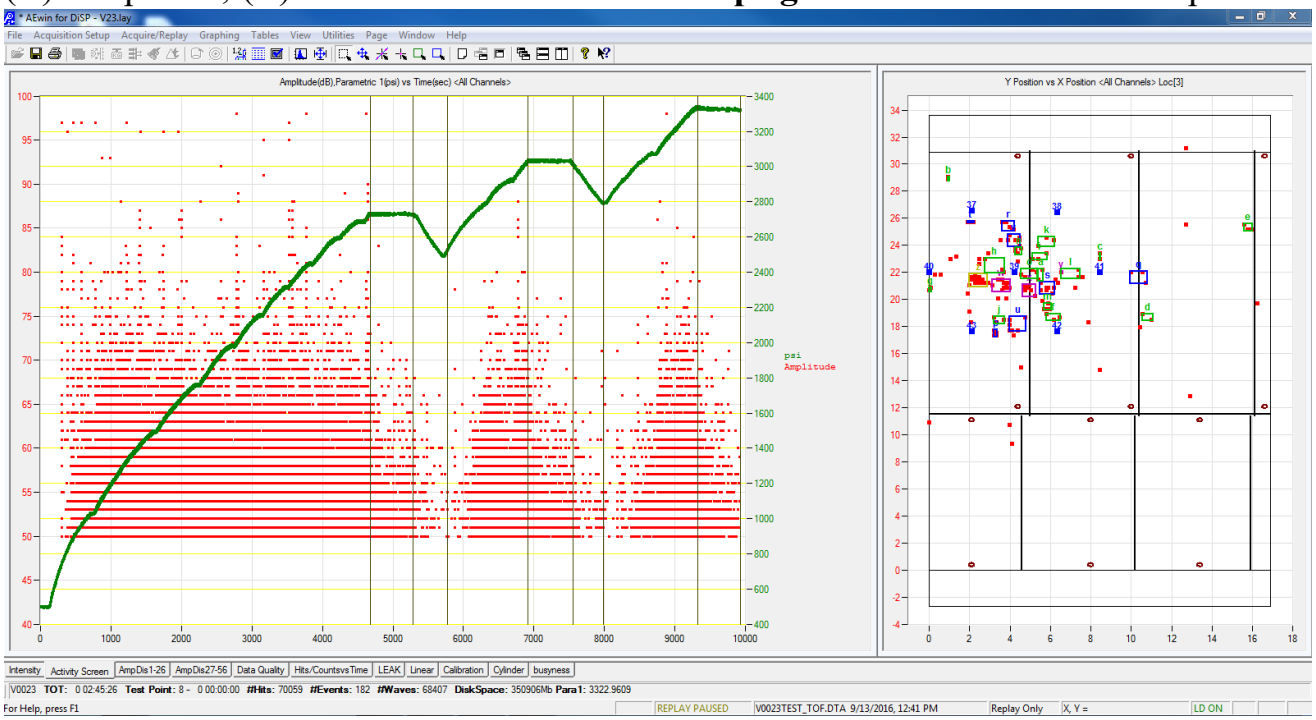
(Y) Amplitude, (X) PSI **1975 psig** Location Graph



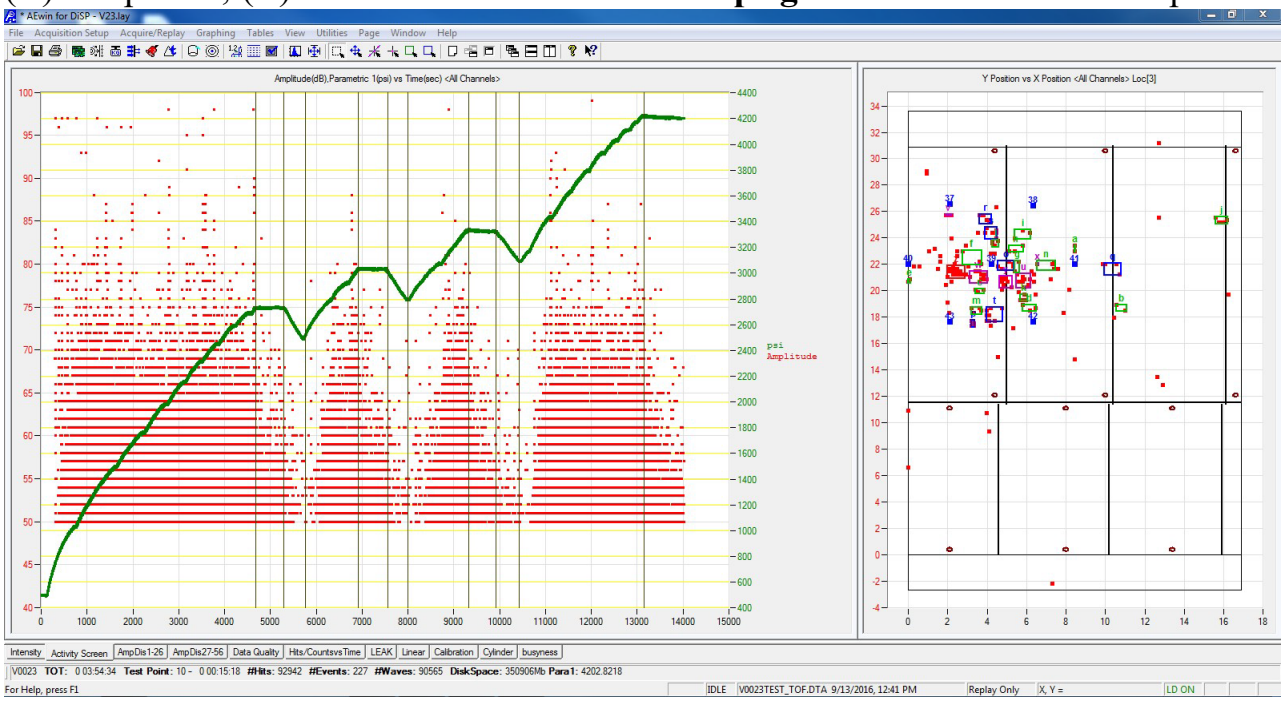
(Y) Amplitude, (X) PSI **2730 psig** Location Graph



(Y) Amplitude, (X) PSI **3325 psig** Location Graph



(Y) Amplitude, (X) PSI **4300 psig** Location Graph



Appendix V: V0023 Vertical Multilayered Vessel Acoustic Emission Sensor Layout

- Approximate Locations of Stuff

V0023

VERTICAL MULTILAYERED VESSEL Acoustic Emission SENSOR LAYOUT

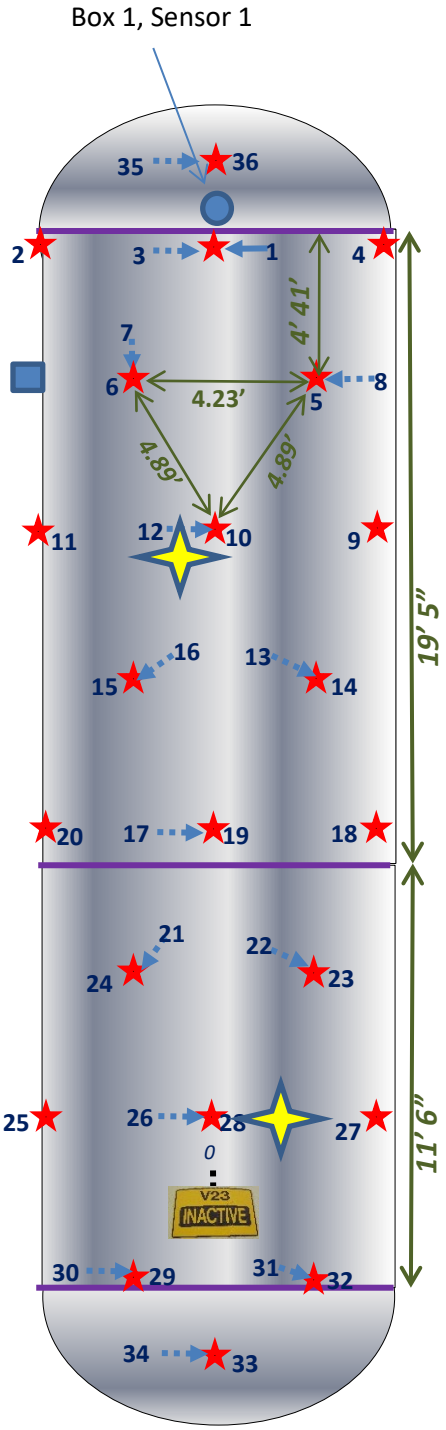
Circumference: 16’ 11”

Total length: 38’ 3.5”

Shell length: 30’ 11”

Spacing between columns: 4’-2.75” (4.23’)

Spacing between rows: 4’-4 29/32” (4.41’)



Backside AE Channels =

Zero Reference line = 0

ALL MEASUREMENTS SHALL BE VERIFIED BEFORE PLACING SENSORS ON VESSEL

Vessel Manufacturer: A. O. Smith
A.O. Smith Serial #: MV50565

AE channels 37-45 will be Wide Band (WDI) sensors placed in direct vicinity(TBD) of the previous AE indication and directly adjacent to the R15I sensors

AE Level II: Claud Wyatt P. Hunter
Test Operators: James Walker/ Wyatt Hunter

JACOBS
ESSSA Group

Appendix W: Report on the Modal Acoustic Emission Testing of A.O. Smith Pressure Vessel V0023

Report on the Modal Acoustic Emission Testing of A. O. Smith pressure vessel V0023

Location: NASA Marshall

Test Date: September 13, 2016

Report Date: November 2, 2016

By: Digital Wave Corporation

Executive Review

- Modal Acoustic Emission testing was performed on September 13, 2016 at NASA Marshall on the A. O. Smith pressure vessel V0023.
- Twenty eight sensors were arrayed on the vessel to detect emissions from sources
- Two locations had groups of events, one at (102, -12) and one at (315, 10) inches.
- The waveforms from either of these locations showed no active crack growth indications
- The waveforms from these locations occurred at pressures well below the prior maximum pressurization, indicating these emissions are not from active crack growth
- Based on the analysis, no active crack growth occurred
- The indications observed at one of the locations were consistent with cold weld cracking of crack faces

Introduction

Digital Wave Corporation performed Modal Acoustic Emission (MAE) testing at NASA Marshall on September 13, 2016 on A. O. Smith pressure vessel V0023. The following sections will detail the test setup, data analysis and results of the testing. Much of the data analysis is covered in NASA/CR-2014-218156, NF1676L-18207, *Cyclic Crack Growth Testing of an A. O. Smith Multilayer Pressure Vessel with Modal Acoustic Emission Monitoring and Data Assessment*. The report can be accessed at:

https://ntrs.nasa.gov/search.jsp?R=20140008836

This report will only touch on the data analysis since it is covered in great detail in the above report.

Modal Acoustic Emission

Modal acoustic emission uses wideband sensors and instrumentation to acquire the out-of-plane surface displacement of a propagating wave in a structure. Wideband (high fidelity) systems provide a true representation of the surface displacement. These waves will consist of various wave modes depending on the source orientation and part geometry. From the wave modes, the source orientation can be determined, absolutely. In thinner structures, this usually simplifies to only two possible propagating wave modes - the two lowest Lamb modes, S_0, the lowest order symmetric Lamb mode, and A_0, the lowest order asymmetric Lamb mode. These modes are also referred to as plate modes. There are many references in the literature describing these modes. In thicker structures, such as the multilayer A. O. Smith pressure vessels, higher order modes can be created, and must be accounted for.

MAE is a deterministic analysis, unlike acoustic emission (AE). Because of the resonant instrumentation used in AE, different sources and source orientations can create the same parameters (amplitude, duration, counts, energy, etc.) in a signal. This makes source identification impossible. Furthermore, the parameters used are not independent. Since the sensors used are resonant, they decay in an exponential fashion. Thus, if one knows the amplitude, then the other parameters, such as counts, duration, and energy, are all related. A final point to make on AE is that the sensors are resonant over a very narrow bandwidth. Outside of this bandwidth, the response decreases dramatically. Many sources contain frequencies of interest that are outside of the high response of the transducer. This leads to poor source identification results.

The final piece to the puzzle is that MAE measurements can be related to fracture mechanics theory. Energy release in a known source can be calibrated and related to the fracture growth of a material. When this energy is calculated for conventional, stable crack growth in metallic materials, it is a very small release. AE analyses that rely on large amplitude signals to warn of crack growth, have made an incorrect assumption about flaw growth in metallic materials and will lead to false positives, or, worse yet, false negatives.

Instrumentation

The digital waveform acquisition instrumentation used for the testing was Digital Wave Corporation's DM series. This system uses four channel acquisition modules, which can be either bussed together to

create larger channel systems, or used separately as multiple four channel systems. These systems are connected to the display, storage and analysis computer via an Ethernet connection. Digital Wave Corporation preamplifiers were used. These are computer controlled, and have gain selections from 0 to 72 dB in 6 dB steps. Finally, a Digital Wave Corporation B454 wideband transducer was used.

This system is designed to have the lowest noise (highest sensitivity) of any AE or MAE system in use. This is done by moving the gain amplifiers to within a foot of the sensors, using shielded Ethernet cable to carry the analog signal, and digitizing the signal at the test article and then sending the high level digitized signal back to the storage computer. This results in a 20 mVp-p noise level at a gain of 66 dB.

Sensor Layout

Figure 1 below shows the sensor layout used for the test. Twenty-eight (28) sensors were used to monitor the vessel.



Figure 1. Sensor layout for V0023. The top of the vessel is at 0 on the Y-axis, the top head-to-shell weld is at 0 on the X-axis, the domes are shown as the semi-circles, and the dome with the legs is on the right-hand side of the plot. The line at 233 inches is the girth weld in the vessel.

Sensors were in arrays of four, with 60 inches between sensors within an array, and sensors within the array rotated by 90 degrees. The next array was overlapped by a foot, with again a 60 inch spacing. This approach was used to provide both coverage of the vessel and source location within each array, with a slight overlap between each array.

System Settings

The instrumentation was set accordingly to ASTM E1419 for the monitoring of seamless steel tubes used in tube trailers. This document suggests a sensitivity of 32 dB_{AE} for detection of flaws in these steel tubes, and through our testing, that sensitivity is at the edge for detection of typical fatigue crack growth in steel, and suitable for crack jumps due to over-pressurizations that exceed the prior loading (if the crack tip has been sharpened due to fatigue crack growth). For this testing the following gain and digitization settings were used:

Gain: 66 dB
Threshold: 0.08 V
Sensitivity: 32 dB_{AE}
Highpass Filter: 20 dB
Lowpass Filter: 1 MHz
A/D Rate: 1.25 MHz
Samples per Waveform: 2048

Data Analysis

Data was captured throughout the pressurization, and stored to digital media. The hardware filter settings were chosen to reduce data from rubbing and fretting sources, as well has high frequency sources such as EMI.

Post-test processing was performed to eliminate noise signals from the data. After all processing was performed to remove noise and extraneous events, the remaining locations were plotted. These are shown in Figure 2.



Figure 2. Location of events from the MAE testing of V0023. The event clusters are circled in the figure for clarity.

There were two clusters of events that occurred during the pressurization. The cluster of events at approximately (102, -12) inches, contained higher frequency components (400-500 kHz) as well as extensional mode characteristics exhibited by in-plane (crack growth) sources. A representative waveform and its Fourier frequency transform are shown in Figure 3. However, the events began to occur at very low pressures (approximately 1000 psi, Figure 4), and the signal duration was much longer, (as shown in Figure 3), than that due to the short (delta function) energy release found in true crack growth. Based on the signals from this area, it was concluded that these sources were from the fracture of cold welds as the vessel was pressurized. These were formed during depressurization as the two irregular crack surfaces from the pre-existing defect came together and were “welded” together via the high compressive loading of the vessel wall at zero pressure. This type of source has been observed previously in the fatigue monitoring of aircraft structures (U. S. Airforce’s Smart Metallic Structures Program, DWC was a subcontractor to Northrup Grumman, 1993). If the vessel is re-pressurized, these sources are re-activated, typically at low pressures or stresses, and detected via the MAE monitoring. But, the waveform frequency content coupled with the stress state is not correct for active crack growth.

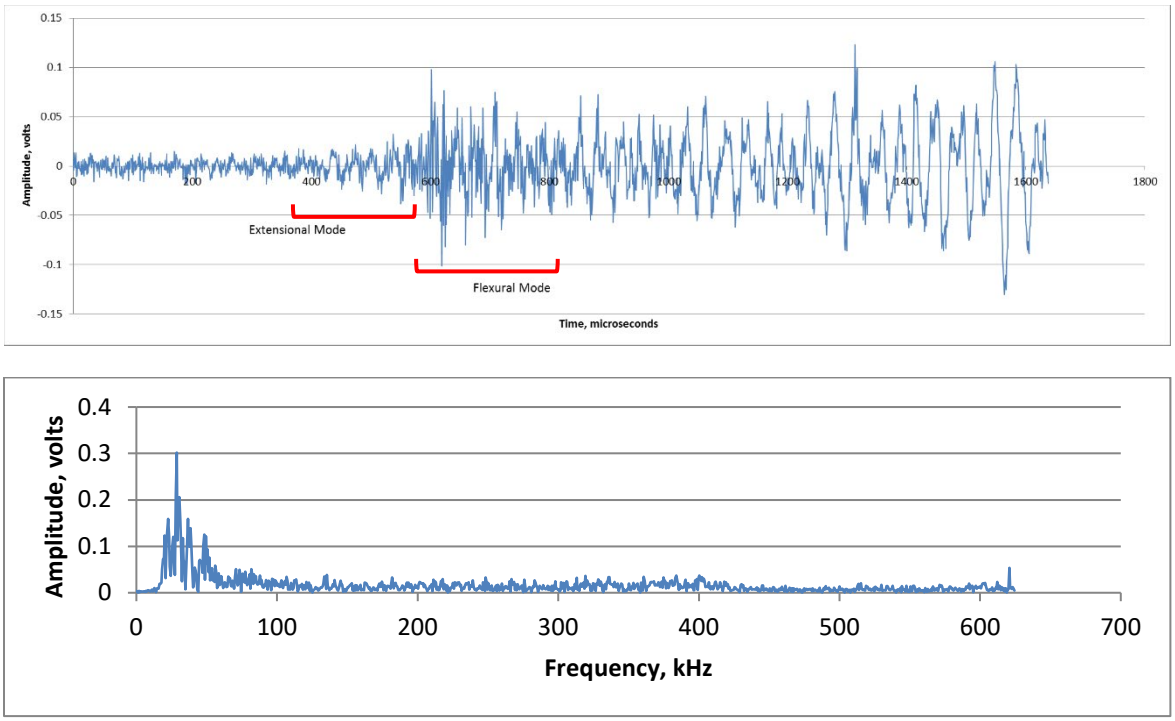


Figure 3. The top figure shows the waveform from the cold weld source, the bottom figure the frequency content of the signal.

It was reported prior to the testing that this source occurred every time the vessel was previously pressurized, as well as during pressure holds. The cold weld phenomena would support this observation. Furthermore, this would also explain why this source was detected upon multiple pressurizations as it would occur whenever the vessel is depressurized and then re-pressurized. Fracture mechanics has shown that stable crack growth only occurs when the prior pressure or stress has been exceeded, not at pressures far below the previous loading. Unstable/stable phenomena (thermally activated sources) proposed prior to the testing do not support the results of this testing.

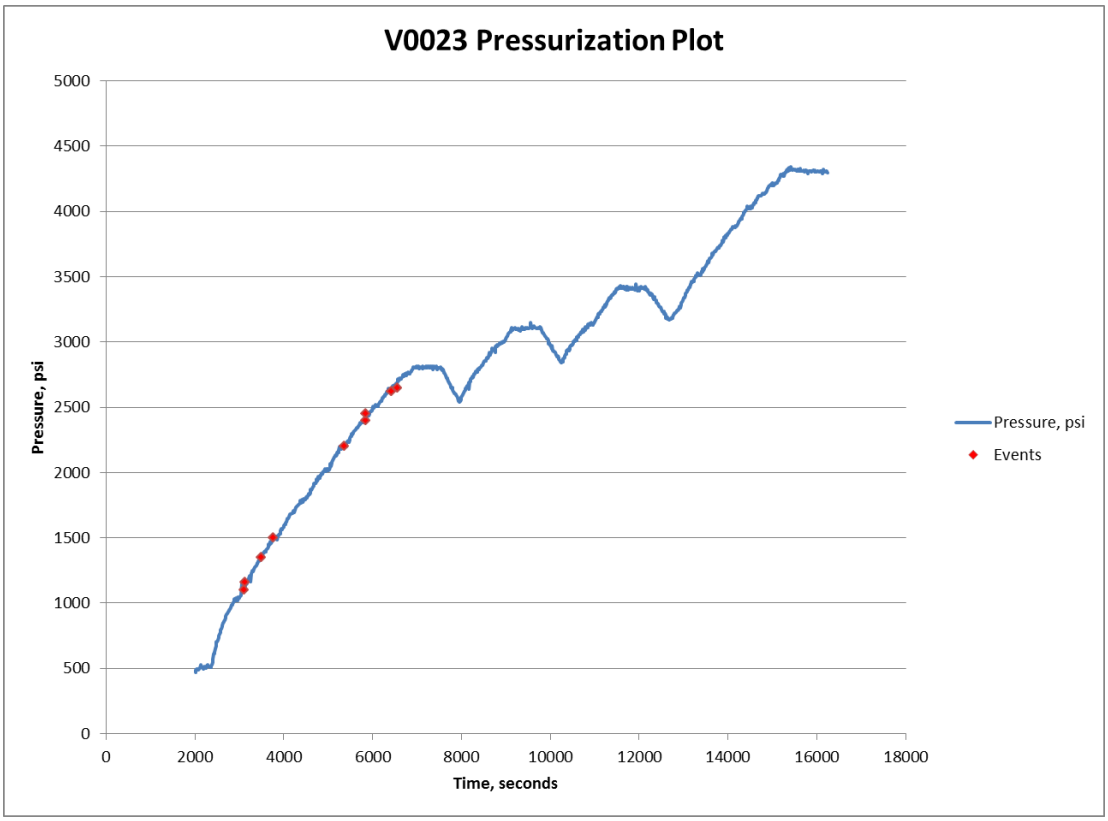


Figure 4. This figure shows when the events occurred in pressure for the events located at (102, -12) inches. Occurrence of the MAE was well below the previous pressurization of 2700 psi.

There was a second source (315, 10) inches on the vessel that had very large amplitudes, and was detected by all sensor arrays down the length of the vessel. There is no explanation for this source, as it saturated all seven systems, so wave mode and frequency content information was lost. These large signals typically are not indicative of crack growth and are related to large out-of-plane fretting or rubbing sources.

There were no significant events from either head-to-shell welds or the girth weld in the vessel. These were the areas of most interest, as they are single points of failure due to the weld through the entire thickness. While cracks in the individual layers are interesting, they do not lead to catastrophic failure since they are arrested by the individual thickness layers. This is similar to aircraft structures, both civilian and military, that are flown with known and active cracks, but are allowed to fly due to the multiple load paths in these structures.

Finally, no events were detected during load holds, showing that no unstable or thermally activated crack growth was occurring, and, no single events occurred that would indicate crack growth in any other area of the vessel.

Conclusion

- Modal Acoustic Emission testing was performed on September 13, 2016 at NASA Marshall on the A. O. Smith pressure vessel V0023.
- Twenty eight sensors were arrayed on the vessel to detect emissions from sources
- Two locations had groups of events, one at (102, -12) and one at (315, 10) inches.
- The waveforms from either of these locations showed no active crack growth indications
- The waveforms from these locations occurred at pressures well below the prior maximum pressurization, indicating these emissions are not from crack growth
- No crack events were detected during load holds, ending the speculation that unstable/stable crack growth was occurring
- No single events occurred in the vessel showing crack growth in other areas
- Based on the analysis, no active crack growth occurred

The conclusion is that no crack growth occurred during the pressurization, and that the cracks found were created during the proof pressure testing that occurred at time of manufacture.